The transport properties of Earth's upper mantle materials : insights from in situ HP-HT experiments

Damien Freitas

UNIVERSITE CLERMONT AUVERGNE

Collegium des Sciences Fondamentales

ECOLE DOCTORALE DES SCIENCES FONDAMENTALES

N°178

Thèse de doctorat

Présentée pour obtenir le grade de

DOCTEUR D'UNIVERSITE

Spécialité : Structure et évolution de la Terre et des autres planètes

Par

Damien FREITAS

Titulaire du Master 2 Recherche

« Magmas et Volcans »

The transport properties of Earth's upper mantle materials: insights from *in situ* HP-HT experiments.

Les propriétés de transport des matériaux du manteau supérieur terrestre, enseignements des expériences *in situ* à HP et HT.

Soutenue publiquement le 12 décembre 2019 devant le jury :

Didier Laporte	DR, CNRS, Université Clermont Auvergne, Clermont-Ferrand	Président du jury
Yanbin Wang	PR, University of Chicago, APS, Chicago,	Rapporteur
Helène Bureau	DR, CNRS, Sorbonne Université, Paris,	Rapporteure
Eric Debayle	DR, CNRS, Univeristé Claude Bernard, Lyon	Examinateur
Jean-Phillipe Pérrillat	MdC, Univeristé Claude Bernard, Lyon	Examinateur
Muriel Laubier	MdC, Université Clermont Auvergne, Clermont-Ferrand	Examinatrice
Denis Andrault	PR, Université Clermont Auvergne, Clermont-Ferrand	Directeur de thèse
Geeth Manthilake	CR, CNRS, Université Clermont Auvergne, Clermont-Ferrand	Co-Directeur de thèse

Remerciements - Acknowledgements

Ce travail de thèse n'aurait pas pu être possible sans l'implication et le soutien d'un nombre important de personnes issues du milieu de la recherche et en dehors. Je vais me risquer ici à les remercier sans oublis.

Pour commencer, il convient de remercier les jurys : Hélène Bureau, Yanbin Wang, Eric Debayle, Jean-Phillipe Pérrillat, Didier Laporte et Muriel Laubier qui ont accepté de lire et d'évaluer ce travail. J'ai particulièrement apprécié les discussions qui ont suivi la soutenance et je les remercie pour cette superbe journée.

Je remercie les encadrants de cette thèse Geeth Manthilake et Denis Andrault. Merci pour cette belle opportunité de travail, de ces choix de thématiques qui ne furent pas toujours aisées, mais hautement intéressantes et prometteuses.

Je remercie tout particulièrement mes collaborateurs, sur les travaux publiés ou en cours de publication. Pour leurs intérêts, leurs discussions et leurs expertises augmentant grandement la portée de nos travaux.

Je remercie grandement Julien Chantel, pour toute l'aide qu'il m'a fourni avec le traitement des signaux acoustiques (coriaces ceux-ci !!), les nombreuses discussions que l'on a eu ensemble et son aide importante sur les nombreuses « reviews » des papiers et questions pointues sur les ondes acoustiques.

Je remercie Frederica Schiavi, sans qui je n'aurais pu faire les nombreuses mesures Raman et qui largement outrepassé son rôle lors de mon master 2, se plaçant comme une encadrante au moment où j'en ai eu besoin, depuis la correction du manuscrit jusqu'à la soutenance.

Je remercie Julien Monteux pour son aide et sa contribution pour la partie thermique et modélisation de cette thèse, quand ce n'était pas pour parler de guitare, de foot ou du Hellfest !

Je remercie Nathalie Bolfan-Casanova pour son apport considérable sur tout ce qui a touché à la thématique de l'eau dans le manteau terrestre. Ainsi qu'Ali Bouhifd pour son expertise sur les densités des magmas.

Je remercie plus largement les collègues de l'équipe de pétrologie du LMV ainsi que les personnels des équipes techniques avec qui nous avons pu échanger et partager les nombreuses galères du quotidien d'expérimentateur ! Je remercie en particulier Jean-Louis Fruquière et Cyril Guillot qui m'ont rendus de nombreux services et ont fourni un travail impeccable sur mes commandes de pièces et assemblages multi-enclumes. Claire Fonquernie qui a été précieuse pour l'utilisation des broyeurs. Mhammed Benbakkar, pour les analyses ICP et sa bonne humeur. Eric Brut pour ses nombreux coups de mains pour tout ce qui a touché à l'électronique et ses petits montages maisons qui m'ont sauvé la mise à de nombreuses reprises.

Parmi ceux-ci, il y en a quand même trois à qui je dois des salutations particulières. Je parle bien entendu du trio essentiel de la pétro exp : Franck Pointud, Nicolas Cluzel et Antoine Mathieu. Je remercie Franck pour les nombreux coups de main, sa réactivité quand nous avions des soucis avec les presses et sa précieuse gestion des stocks de consommables.

Je remercie tout particulièrement Nico, qui a été bien plus qu'un collègue pendant ces années. L'une des seules personnes à savoir écouter et être disponible quand j'en avais le plus besoin. Je le remercie de m'avoir introduit au « foot du mercredi » où nous avons passé de sacrés matchs ensemble.

Enfin, je remercie très sincèrement Antoine Mathieu. En plus d'être un ingénieur extrêmement compétant, il m'a suivi, aidé et partagé mes nombreuses galères au cours de mes travaux sur le thermique. Son apport, que ce soit sur l'Angström ou le pulse est majuscule. Antoine a été le seul à me filer un coup de main et à chercher à comprendre les problèmes sur les différents systèmes quand certains « experts » ont soigneusement éludé le sujet. Cela mérite un remerciement à la hauteur de l'aide fournie.

Je remercie tout particulièrement Christian Nicollet, qui aura été définitivement mon guide, coach et ami depuis la L3. Je n'aurais jamais été si loin sans son intervention.

Plus personnellement, il y a un certain nombre d'amis, de proches et de connaissances qui doivent être également remerciées pour leur contribution et les marques d'attentions qu'elles ont portées pour permettre la réalisation de ce travail. Cette thèse ne fut pas toujours une partie de plaisir et m'a beaucoup couté. Pour mener à bien ce travail, j'ai pu compter sur mes amis, ma famille de thèsards qui m'ont donné ce supplément de force. Il y a bien évidemment le trio puis duo du bureau : Alexis Richie, Simo et Nathan pour les lourdes

tranches, les bastons de nerfs, vous allez me manquer putain ! Les Valentins, Père Gueugue et Thundervalou qui ont tranchés tout autant ainsi que Swetha, membre inconditionnel de la soirée qui fissure. Merci Pierre, Paul et Claudine pour tous les afters, sessions jeux et dégustations ! Une pensée également à Loïs frère de la petro et de métal, JM mon valeureux époux, Giacomo, Gioachino, Diego, Cyril, Remy, Marie-Anne, Juliette, Taya, Vincent, Melo, Marion, Luca, Baraa, Popaul, Guillaume, Roxane, Sophie, Masa etc.

Je remercie mes amigos: Robinet, Camille & Seb, Charles et les Joan's, les anciens de Descartes et du stade, la bande de fou furieux du Hellfest : Manon, Romeo, CC, père Mamet, Simon, Loutre Adri, Boudha et compagnie. Aux copains du Raymond et aux vieux de la CARA !

Je remercie ma famille Péruvienne pour tout l'amour que vous envoyez malgré la distance : la senora Yvonne, Roger, Nelida, Saida, presidente Patricio et vos familles !

Je remercie ma famille, mes grand mères, mes oncles et tantes, les counzinzins, ma belle-famille qui ont été des soutiens permanents. Mes parents et ma sœur qui m'ont permis de faire ce que je voulais et m'ont donné les moyens d'y arriver. Dois Freitas c'est três fois mieux !

Enfin, je tiens à remercier Laura Domas. Que dire... Je me suis occupé de la science, tu t'es occupé de tout le reste, évidemment cette réussite est aussi la tienne. Merci à sainte mémère Mimine de veiller sur nous et de nous rendre toujours plus maousses.

Il y a quelques artistes que dois remercier, la musique fut un compagnon quotidien durant ces trois années, je remercie tous ces groupes qui m'ont tant donné : Amorphis, Insomnium, Trivium, Gojira, Parkway Drive, le punk rock en général, le synthwave et the Prime Thanatos, la deep house, EM, les Casseurs Flotteurs, les Fatals Picards, Little Big et tous les autres. Je remercie aussi les podcasts de France Inter, rien de mieux pour remonter le moral qu'un billet, un ptit Guillermo, moment Meurice ou Tanguy, le pied.

Je remercie les bourses de l'enseignement secondaire et supérieur ainsi que la région Auvergne d'avoir cru en mes capacités et me permettre de poursuivre mes études qui aboutissent avec cette thèse de doctorat.

Résumé

Les propriétés de transport des roches mantelliques sont des paramètres importants pour interpréter aussi bien qualitativement que quantitativement les informations géophysiques, telles que la vitesse des ondes sismiques, les flux de chaleurs et les profils magnétotelluriques terrestres. L'origine des anomalies géophysiques du manteau supérieur, comme la zone de faible vitesse (LVZ ; 70-150km de profondeur) et le niveau de faible vitesse (LVL ; 350-410 km de profondeur), est peu renseignée et demande des contraintes expérimentales.

Au cours de cette thèse, nous avons étudié les propriétés électriques, sismiques et thermiques des péridotites solides et partiellement fondues via le développement de techniques géophysiques *in situ*. Nos expériences à hautes pressions et températures, en presse multi-enclumes, nous ont permis d'établir les effets de la fusion sur ces différentes propriétés physiques aux conditions mantelliques.

Nous avons, pour la première fois, réalisé des mesures combinées de conductivité électrique et de vitesses des ondes sismiques en une seule et même expérience. Grâce à cette technique, nous avons réconcilié les mesures du taux de fusion impliquées dans la LVZ estimées par les deux signaux géophysiques avec 0.3-0.8%vol. de fusion partielle. L'équilibre textural entre les phases liquides et solides s'est révélé être fondamental pour la comparaison des mesures en laboratoire.

Nous avons ensuite procédé à la première reproduction de fusion par déshydratation durant l'ascension des péridotites hydratées depuis la zone de transition mantellique vers le manteau supérieur (entre 12 et 14 GPa). Au cours de la fusion partielle, les signaux sismiques et électriques mesurés sont comparables aux observations géophysiques confirmant l'hypothèse de fusion au niveau de la LVL. Les taux de liquides impliqués à la base du manteau supérieur seraient alors modestes (< 2 %vol). La composition des magmas produits précise le rôle de filtre chimique de ce niveau situé entre les manteaux supérieur et profond. La densité estimée du magma confirme sa flottabilité neutre, favorisant la stabilité de ce niveau au cours des temps géologiques. Les analyses des éléments volatils et les modélisations des transferts d'hydrogène prouvent que ce niveau est un réservoir potentiel d'eau profond et favorise l'hypothèse d'une hydratation par la base du manteau supérieur.

Enfin, des méthodes de mesure de diffusivité thermique (Angström, pulse) ont été adaptées à la presse multi-enclumes du LMV. Des procédures de traitement et des modélisations des transferts thermiques ont été développées Les premières mesures de diffusivité thermique de verres et liquides réalistes aux conditions mantelliques ont pu ainsi être réalisées. De plus, la caractérisation d'échantillons aux structures variées a pu être effectuée à l'aide de la méthode Angström (périclase, olivine, péridotite partiellement fondue).

Mots clés : Fusion partielle. Manteau supérieur. Zone de transition mantellique. Conductivité électrique. Vitesse sismique. Diffusivité thermique. Presse multi-enclumes.

Abstract

The transport properties of mantle rocks are key parameters to qualitatively and quantitatively interpret direct and indirect geophysical information such as seismic velocities, heat fluxes and electromagnetic profiles across Earth's and planetary interiors. The origins of upper mantle geophysical anomalies such as the Low Velocity Zone (70-150 km deep) and the Low Velocity Layer (350-410 km deep) are poorly known and require experimental constraints.

In this PhD thesis, we have explored the electrical, seismic and thermal properties of realistic solid and partially molten peridotites via the development of geophysical *in situ* techniques. Performed at high pressures and temperatures in multi-anvil apparatus, our experiments allowed the characterization of the effect of melting on these different physical properties at mantle conditions.

We performed the first experimental combination of electrical conductivity and sound wave velocity in a single multi-anvil experiment. Thanks to this technique, we reconciled electrical and seismic estimations of the melt fraction implied in the LVZ with 0.3-0.8 Vol.% of partial melting. The textural equilibration between melt and solid phases was found to be crucial for the comparison of laboratory estimations.

We then realized the first reproduction of the dehydration melting process during the ascend of hydrous peridotites from the mantle transition zone to the upper mantle, between 12 and 14 GPa. Measurements during partial melting gave acoustic and electrical signals comparable to geophysical observations favoring partial melting explanation of the LVL anomaly. The implied melt fractions at upper mantle base were quantified to be moderate (<2 Vol.%). The chemical composition of produced melts confirmed the role of chemical filter of this melt layer located between upper and deep mantle. The calculated density confirmed the neutral buoyancy of the melt layer, making it a stable feature over geological times. Volatiles analyses and hydrogen transfer modeling confirmed this layer as a potential deep water reservoir and favored a bottom-up hydration of Earth's upper mantle.

Thermal diffusivity characterization techniques (Angström and pulse heating methods) were adapted to the LMV multi-anvil apparatus. Improved treatment procedures were elaborated for thermal transfer characterization under HP and HT conditions. The first thermal diffusivity characterization of glasses and melts at realistic mantle conditions were performed. In addition, thermal diffusivities of various samples (periclase, olivine, peridotite) were investigated with different structures (solid, solid+melt etc.) using Angström method.

Keywords :
Partial melting. Upper mantle. Mantle Transition Zone. Electrical conductivity. Seismic velocity. Thermal diffusivity. Multi-anvil apparatus.

Table of contents

Chapter II: Experimental and analytical methods

Chapter III Electrical conductivity and acoustic wave velocity in partially molten systems

Chapter IV Experimental evidence of a global melt layer above the Mantle Transition Zone

Chapter V Dehydration melting at the 410-km discontinuity and the bottom-up hydration of Earth's upper mantle

Chapter VI: Thermal diffusivities measurements of geomaterials at high pressure and temperature using Angström method in multi-anvil apparatus

General introduction

Planetary bodies' formation, histories and structures are some of the most fundamental scientific themes. Starting from naturalistic and simple observations, the understanding of planets and celestial objects quickly achieved the results that most of the matter is not visible, in most of the cases, unreachable and confined into planets interiors. However, internal structures and properties govern the evolution of the planetary bodies and are responsible of their external aspects and dynamics. Surface manifestations of the Earth's internal dynamic and properties are numerous. Their observables range on different timescales, but their consequences can greatly impact surface conditions and habitability. The most impressive short-scale manifestations in surface such as seismicity, magnetic field or volcanic activity were the motivating source of the first representations of Earth's interior.

Historically, the first ideas and representations of the Earth (or at least the first traces) were made during Greek civilization (IVth century BC) when the first philosophers started to think about the working of Nature and the origin of mankind. Aristotle (384-322 BC) proposed a spherical Earth composed of "dirt element" surrounded by water and air in a spherical space ending with a fire layer. Earthquakes were induced by wind circulation in internal cavities and the presence of small particles will ignite and create volcanoes. This vision of the Earth's interior will last during the antiquity and the middle-age and will only be revised after the great discoveries of the XVth century. The astronomical progress with the revolution made by Corpernicus (1473-1543) definitely buried the old Greek models. Descartes (1595-1650) is one of the first to imagine the Earth internal structure linked to its genesis. Starting from the hypothesis that Earth is an old star, he proposed a "star" matter core surrounded by dirt, water and air layers covered by a surface crust. Oceans were then created by collapsed parts of the crust and mountains by an original cataclysm. Other models were proposed at this time, notably the model of Kirsher (1602-1680), who proposed a "fire" nucleus and reservoirs at different depths to explain the occurrence of volcanism.

The development of naturalistic geology and outcrops studies during the XVIIth century led the geologists to propose that sedimentation is the process that created all variety of rocks at Earth's surface. This deposit should result from the initial biblical flood. The Neptunism school of thought grew considerably in these decades with the important fieldwork contribution of Woodward (1665-1728). Numerous models (Haley, Moro etc.) were then proposed. However, the absence of scientific arguments and demonstrations prevent the

adoption or rejection of a given model. Buffon (1707-1787), using the first rigorous methodology, proposed a solid Earth using the anomaly gravity made by mountain massifs. The planet interior should be hot (via the discovery and measurements of the geothermal gradient) and initially fully molten to explain the flattened spherical shape of the Earth. These thermal concepts were progressively reinforced by the works of Fourier (1768-1830) and Cordier (1777-1861), which depicted a fully molten inner Earth. At the opposite from previous works, most of rocks would then be the result of a fusion episode. The discovery of pressure dependence of rock solidus by Hopkins (1793-1866) marks an important step to a hot, but solid, inner Earth's conception. The end of the XIXth century is marked by the development of modern physics and allowed Kelvin (1824-1907) to give a first estimation of global rheological parameters, Earth's elasticity is comparable to steel and so, must be solid. The composition of the inner Earth also remained largely debated even if, models based on density were, at this time, proposing a metallic core surrounded by rocky shells in different proportion. The last word has returned to seismologists who precised the structure and the composition of the inner earth. The discovery of the mantle-crust transition by Mohorovicic (1857-1936), the core mantle discontinuity by Gutenberg (1889-1960) and inner core by Lehmann (1888-1993) settle the framework of the present Earth's structure.

Nevertheless, the knowledge on inner Earth's structure and composition, thanks to geophysical measurements such as seismology, is limited, as none of probed materials are directly available. The advent of experimental petrology considerably helped into the understanding of the inner Earth at large scales. The development of Bridgeman anvil apparatus, piston cylinder, diamond anvil cells and multi-anvil apparatus (1910-1960) considerably changed our vision on the Earth's interior. The discovery of Wadsleyite, Ringwoodite and Mg-Perovskite (after called Bridgemanite) during the late 60's finally put a name and mineral structure on the major component of each reservoir of the inner Earth. These funding works developed the whole experimental petrology field in which this work modestly takes place. The experimental petrology aims, from the very beginning, to compare the laboratory results with geophysical observables. These observables can be rock samples. However, such samples of deep mantle are very scarce and often have undergone re-equilibration, melting and/or contamination on their path toward the surface. On the other hand, geophysical observables such as seismic or electrical properties provide direct information on the present Earth's mantle. The increase of number and quality of seismometers, magnetic stations/satellites, computational methods and databases allow

nowadays the study of fine structures (variations < 1% in velocities and objects of size up to 5-20 km for body waves in Earth's upper mantle). These geophysical observations motivated the development in the 70's, but mostly since the 80's, of apparatus dedicated to *in situ* measurements during high pressure and high temperature experiments. Several types of analyses can be performed such as structural, chemical analyses (interaction energy/matter such as X-rays analyses), rheological studies (uniaxial compression, deformation) and transport properties.

This PhD work focuses on transport properties measured *in situ* during high pressure and temperature experiments for several reasons. First, they represent the most direct properties to compare with geophysical observables. Their observations are the unique direct information retrieved from the present deep mantle. Second, by similar reasoning, the geophysical observations are also the unique information that can be obtained during HP-HT experiments (if we except synchrotron experiments), and the importance of the quantification of physical parameters at a given pressure and temperature can't be neglected. In addition, from these observables one can infer numerous other physical parameters. These parameters help to physically understand Earth's mantle at these conditions and can be used as inputs for modeling purposes.

However, the interpretation and quantification of seismological or magneto-telluric observations (*inter alia*) remain a very challenging task with our present knowledge. The main quantification technique relies on the calibration of the geophysical observations via *in situ* laboratory measurements. In front of the various possible conditions and parameters (P, T, FO_2, chemistry, texture etc.), the number of geologically relevant systems characterized is limited. Depending on the type of signal, the number of studies investigating *in situ* properties is in a growing trend, from which some fields such as electrical conductivity are well developed. At the opposite, several others fields on are much less understood such as thermal properties, in particular for deep Earth conditions. Despite continuous developments since the 70's, for almost each kind of *in situ* technique, this type of measurement still appears as one of the most difficult to perform. This difficulty is translated by a complex adaptation of the high pressure apparatus to the measurement and the technical realization as some assemblies can be unpretentiously qualified as "haute couture" of experimental petrology. Both of these aspects significantly restrained a wider spread of these techniques. As a result, a tremendous amount of work is still required to investigate the factors influencing the transport properties of geomaterials at mantle conditions.

The aim of this PhD work is to better constrain Earth's upper mantle geophysical observables and anomalies using *in situ* high pressure and high temperature measurements of transport properties. It focuses on anomalous zones detected by geophysical signals, as their origins and quantification remain not fully understood. This work also aims, to a lesser extent, to increase the knowledge on physical and chemical properties of geomaterials at mantle conditions. To do that, different types of *in situ* characterizations will be performed using multi-anvil apparatus. Measurement of electrical and acoustic properties will allow discussion and interpretation of two main geophysical anomalies of upper mantle: the Low Velocity Zone and the Low Velocity Layer between 70-200 km and 350-410 km depths, respectively. In parallel, measurements of thermal properties of solids and melts will help to precise the thermal structure of the present and past mantle. This work, as a contribution to experimental petrology and mineral physics field, also encompasses significant development and improvements of the existing techniques and methods. These aspects will be particularly detailed in thermal conductivity chapters.

In details, this PhD thesis is composed of 7 chapters, each investigating some aspects of these geophysical properties and their impact in our understanding of Earth's mantle.

- The Chapter I aims to present the subject via a state of art on electrical, seismic and thermal observations and the presentation of the main results obtained from previous mineral physics experiments. Each part will describe the geophysical observations for each field on Earth's mantle and provide the physical basement of each transport property (theory and mechanisms), whose are of significant interest for geological materials at mantle conditions.
- The Chapter II is a presentation of experimental and analytical methods. First, experimental methods will be described with multi-anvil apparatus and its associated *in situ* geophysical techniques. The second part of this chapter will be dedicated to analytical tools used for *post-mortem* sample characterizations.
- The Chapter III is a presentation of results on electrical conductivity and acoustic wave velocity measured in partially molten systems. This study describes the results of the first simultaneous measurements of electrical conductivity and acoustic wave velocity on partially molten samples. The effect of melt texture was found to be particularly important for electrical conduction process. The implication on the melt fraction quantification of the Earth's asthenosphere Low Velocity Zone is given. This study was published in Physics and Chemistry of Minerals in 2019.

- The Chapter IV is focused on the first experimental evidences confirming the presence of a partially molten layer above the mantle transition zone (MTZ). Based on *in situ* acoustic wave velocity measurements and a new experimental procedure, especially developed for the reproduction of dehydration mechanism in laboratory, an explanation to seismic anomalies detected above the MTZ is proposed together with important insights from melt chemistry and density on layer. These results were published in Nature communication in 2017.
- The Chapter V deals about the electrical properties of partially molten peridotites at different conditions and their use to precise the extent of melting in the upper mantle together with the role of water coming from the low velocity layer (350-410 km depths). The experimental *in situ* electrical conductivity measurements helped to precise and understand the water content and melt presence at various depths in Earth's mantle. With these experimental determinations, different scenarios for the bottom-up hydration of the upper mantle due to the possible presence of the melt layer and hydrous MTZ have been explored. This study was published in Earth and Planetary science letters in 2019.
- The Chapter VI is a presentation of the development and the realization of *in situ* thermal diffusivity measurements with Angtröm method using multi-anvil apparatus (MAA). The improvement and new development on LMV 1500 Ton MAA heating system to allow these measurements will be explained as well as the development of a complete and improved (errors propagation, Monte Carlo inversion etc.) data processing procedure. The results on thermal diffusivity measurements of various geological materials, such as known standards (MgO, olivine), geological materials such as peridotites of natural glasses and melts, are provided.
- The Chapter VII is focused on the development of a portable "pulse heating" apparatus for thermal diffusivity measurement in MAA. The goals of this new apparatus development as well as its technical realization will be given. Data modeling and experimental design will be also carefully detailed to allow further application of such device. Experimental results from different series of tests (LMV and SOLEIL) and experiments will be given and discussed.

For editorial and embargo reasons, the published scientific manuscripts have been used in their post-print version without journal formatting. Their formats have been reworked for this PhD manuscript. Similarly, the reference sections of each paper have been merged into our final bibliography section.

Chapter I

State of art:

Geophysical seismic, electromagnetic and thermal observations from Earth's mantle and mineral physics constraints

Chapter 1: State of art: Geophysical seismic, electromagnetic and thermal observations from Earth's mantle and mineral physics constraints

1) Introduction

The research problem of this work is to understand, reproduce and constrain the geophysical observables measured on Earth's mantle by different geophysical techniques such as seismic velocities, electromagnetic and thermal properties. This work will in particular focus on upper mantle features, where significant seismic and electrical anomalies have been reported. The two main, somewhat global-scale features, are the Low Velocity Zone (LVZ) located at the top of the asthenosphere (70-200 km deep) and the Low Velocity Layer observed between depths of 350-410 km.

This chapter aims to give an overview on geophysical observables on the Earth's mantle. The seismological, electrical and thermal observations on present Earth's mantle will be successively described. The associated up-to-date constraints from mineral physics *in situ* characterizations will be also provided as well as their implications into the interpretation of geophysical observables. This general background remains an important pre-requisite to help the reader understanding the following chapters III, IV, V, VI and VII of this manuscript. The dedicated experimental methods, used to realize geophysical *in situ* characterization, are given in the methodology section in our next chapter II.

In this section each geophysical observable that was studied, quantified and discussed further in this manuscript will be described with a special focus on upper mantle features and encountered anomalies, as they are the main targets of this manuscript.

2) Seismic observations and experimental characterizations

Detections and measurements of seismic waves at Earth's surface allow retrieving information on Earth's interior. The types of waves, their shapes and travel times can be interpreted in terms of mineralogy, structure and temperature of mantle rocks. The development of seismology allowed to precise Earth's present structure and gave the bulk properties of the great internal reservoirs such as mantle and core. In this section, a presentation of seismological observations and derived models on Earth's internal structure and composition will be realized. In addition, mineral physics constrains on theoretical and experimental aspects will be given along with their implications on observables interpretation.

a) Seismic observables

The structure of the Earth is now well established and documented. The development of deep Earth seismology by the late 19th century, and the successive discoveries of crust-mantle, core-mantle discontinuities and inner core by Mohorovicic, Guttenberg and Lehmann respectively, settled the definitive structure of the Earth (Fig. I.1).

The present structure of the Earth, obtained from seismology, makes the distinction between the crust (oceanic and continental) and the mantle separated by the Moho discontinuity between 7 and 150 km according to the geodynamical context. The mantle is divided in 3 subparts, the upper mantle, mantle transition zone (MTZ) between 410 and 660 km and lower mantle until 2900 km. An additional layer named D" has also been more recently discovered. This layer has a thickness of 200 km (2700-2900 km deep) and is located above the core-mantle boundary (CMB). The core is also subdivided in two parts, outer and inner-core (ICB at 5100 km). Seismology does not only provide the structure of the planet but also information on its chemical composition and mineralogy. One dimensional physical models have been built since 1980, based on compilation of thousands of seismic events. The measurement of travel times and seismic amplitudes for the large earthquakes allowed retrieving the elastic and anelastic properties of the crossed media. These spherically symmetric models named PREM (Dziewonski and Anderson, 1981), AK135 (Kenett et al., 1995) or IASP91 (Kenett and Engdahl, 1991) allow the representation of an Earth's average for compressional (Vp), shear waves (Vs) and attenuation to retrieve Earth's density profile. These different models have been constructed using various databases, computational procedures and parameterizations (see table I.1), however, they compare fairly well at global scale (Fig. I.2).

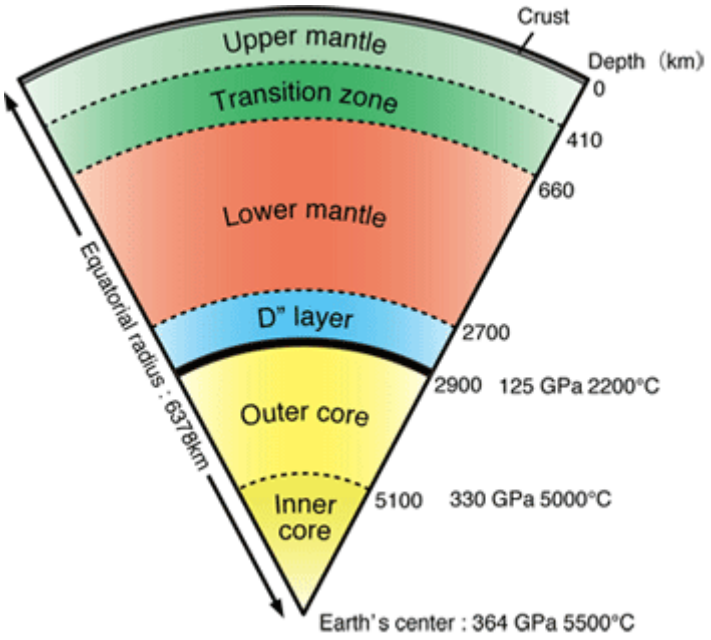

Figure I.1 Earth's present structure (Spring-8, 07/03/2019 http://www.spring8 .or.jp/en/news_publications/research_highlights/no_57/)

The velocity and density profiles are highlighting well the early observations of the discontinuities that allowed the determination of the structuration of our planet. These changes of density and velocities are due to changes in minerals structures such as phases transition (olivine to wadsleyite and then to ringwoodite) or changes of the mineral or material composition (mantle silicates to metallic core). The change of physical state can also be a source of observed discontinuities such as the liquid outer core (S waves loss for this zone). Globally, the seismic velocities increase with increasing depths as results of increasing density with pressure.

The seismic wave velocities can be used to test petrological models with different mineralogy as a function of depth. Among these, one of the preferred models is the pyrolite (pyroxene-olivine-rock), which is a hypothetical primitive mantle model that is obtained using actual depleted mantle and basaltic melts extracted from this mantle. Elaborated by Ringwood in 1975, this model proposed to mix basalts (MORB-like) and refractory mantle with a ratio of 1/3 to 1/4. Converting this compositional model, via modal proportion of mineral phases for such composition, into velocity or density profiles allows interpreting seismological data in terms of mineralogical content and composition (Canamaro et al., 2005; Li and Liebermann, 2007; Kaminsky et al., 2012) (Fig. I.3).

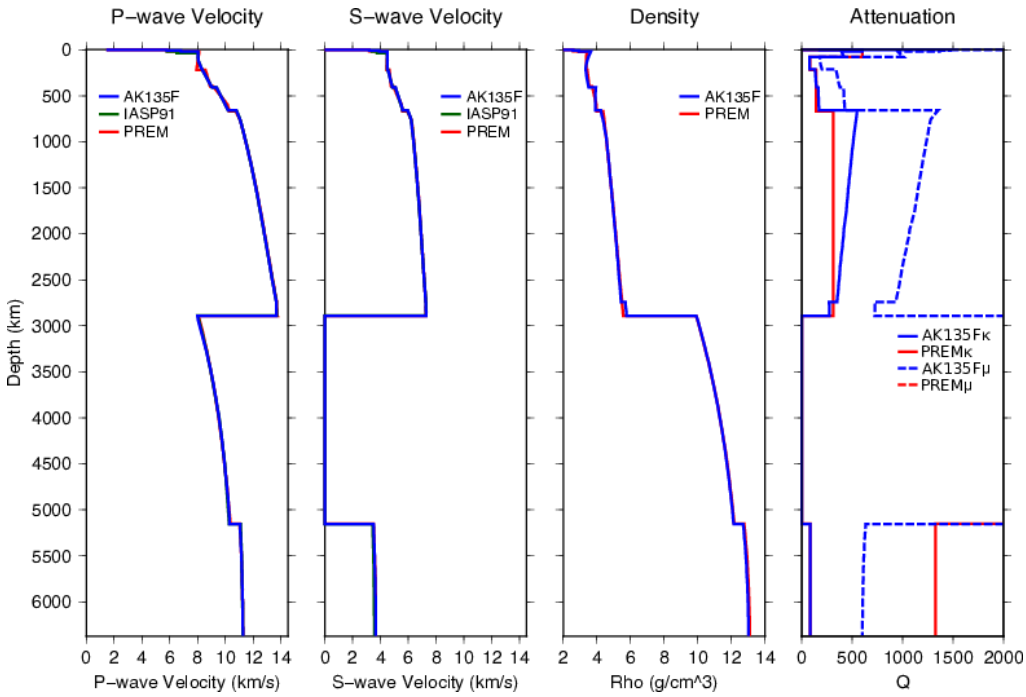

Figure I.2 Whole mantle profiles of Compressional and Shear waves velocities, density and seismic attenuation for the 3 most common reference models. (Figure from Berkeley University CIDER's website, the 07/03/2019. http://seismo.berkeley.edu/wiki_cider/REFERENCE_MODEL)

Table I.1 Summary of common reference models (table from Berkeley University CIDER's website, the 07/03/2019 http://seismo.berkeley.edu/wiki_cider/REFERENCE_MODELS)

Model	**PREM**	**IASP91**	**AK135 and AK135-F**
Reference	Dziewonski and Anderson, 1981, PEPI	Kennett and Engdahl, 1991, GJI	*Kennett et al., 1995* and *Montagner and Kennett, 1996*, GJI
Data used	Body waves, normal modes, surface waves, surface wave dispersion, astronomical observations	Bodywaves ($6*10^6$ measurements)	Bodywaves relocated with IASP91, bodywave differentials, plus normal modes (in AK135-F only)
Period	1 s with attenuation corrections for 200 s	1 s	1 s
Regional bias	Crust thickness is weighted average of continent and ocean, mantle unbiased	Continental crustal thickness used as seismometers are on continents. Upper mantle more biased than lower mantle	AK135: continental thickness used as seismometers on continents, upper mantle more biased than lower mantle. AK135-F: Average crustal structure, upper mantle more biased than lower mantle.
Water layer	Yes: 3km thick	No	Yes: 3km thick
Resolved parameters	Vp, Vs, Q, density	Vp, Vs	Vp, Vs, plus Q and density (in AK135-F only)
Features	Upper mantle discontinuity at 220 km depth	Vp better resolved than Vs	Outer core well resolved by PKP differential travel times, density and Q from Montagner and Kennett (1996)
Anisotropic/Isotropic	Transverse anisotropy of 2-4% from 80-220 km depth	Isotropic	Isotropic
Best uses in seismology	Long period studies	Body-wave studies, earthquake relocation	Body-wave studies specifically core, earthquake relocation

In addition to 1D observation and models, numeral seismic studies addressed the radial and lateral variations of the arrival times (velocities) observed at regional and local scales. It is now well established that the mantle is heterogeneous at various scales. It results into a large potential variation in seismological parameters (travel-times, scattering, attenuations, anisotropy etc.) that can be quantitatively addressed by comparison with averaged 1-D profiles. These variations can then be translated into compositional (major elements, isotope), structural (anisotropy, scattering, crystallography), mineralogical (minerals, phase transition, melt) or physical state (FO_2, temperature) heterogeneities. These heterogeneities are remarkably well highlighted by tomographic studies. In the upper mantle, the coupling to geodynamical setting is striking, with slabs or cratonic roots that are highly visible (Fig. I.4 and I.5).

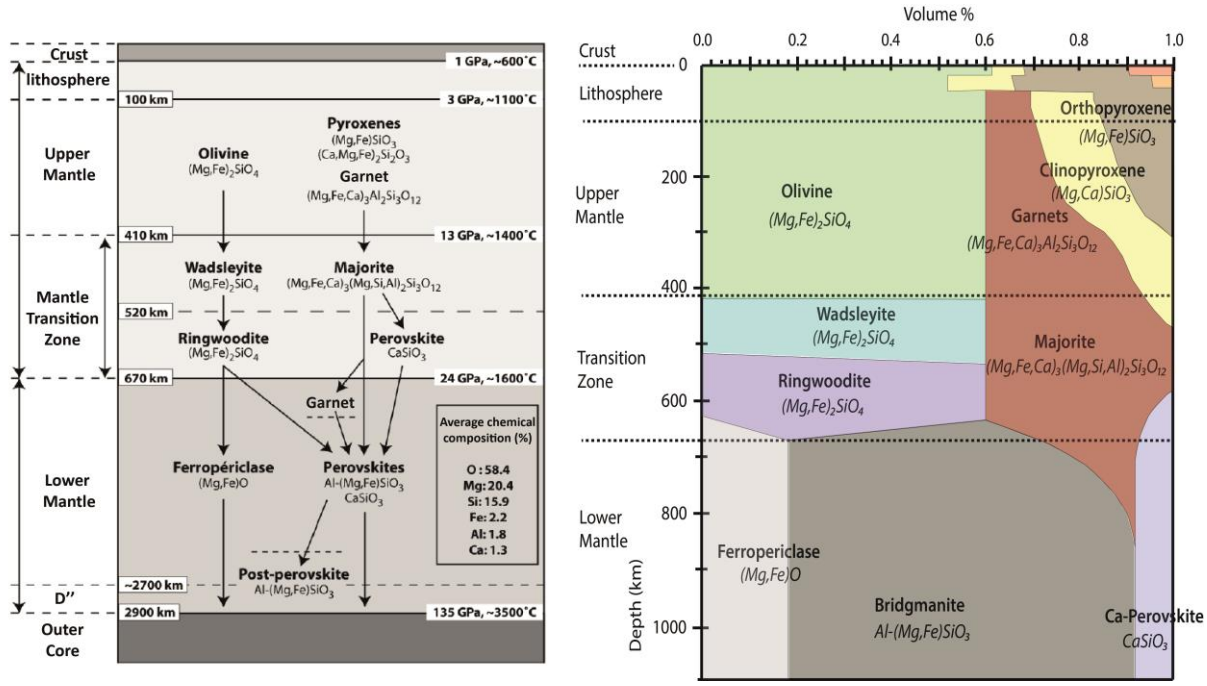

Figure I.3 Mantle mineralogy and proportions as a function of depths for the different subdivisions for a pyrolitic composition. Left panel is modified after Brunet et al., 2007 and right one is modified after Kaminsky et al., 2012.

Lateral heterogeneities studies and seismic imaging also highlighted that depths of major discontinuities such as UM-MTZ and MTZ-LM regions at 410 and 660 km respectively are not fixed but vary significantly. These differences are due to varying depths of phase's transitions which translate temperature and/or chemical composition variations. Hence, the boundaries between the different layers of the Earth are not fixed and terms used as "410" or "660" discontinuities are often used to refer to the transition that are occurring at slightly different depths in reality (Tauzin et al., 2010; Hier-Majumder and Tauzin, 2017).

Furthermore, the temperature alone cannot account to all the variations observed in the present mantle. As an example, slab regions exhibit higher velocities compare to surrounding mantle. This stiffer behavior cannot be explained only by colder temperatures and requires logically taking in account that MORB mineralogy significantly differs from peridotite or pyrolite at high pressures.

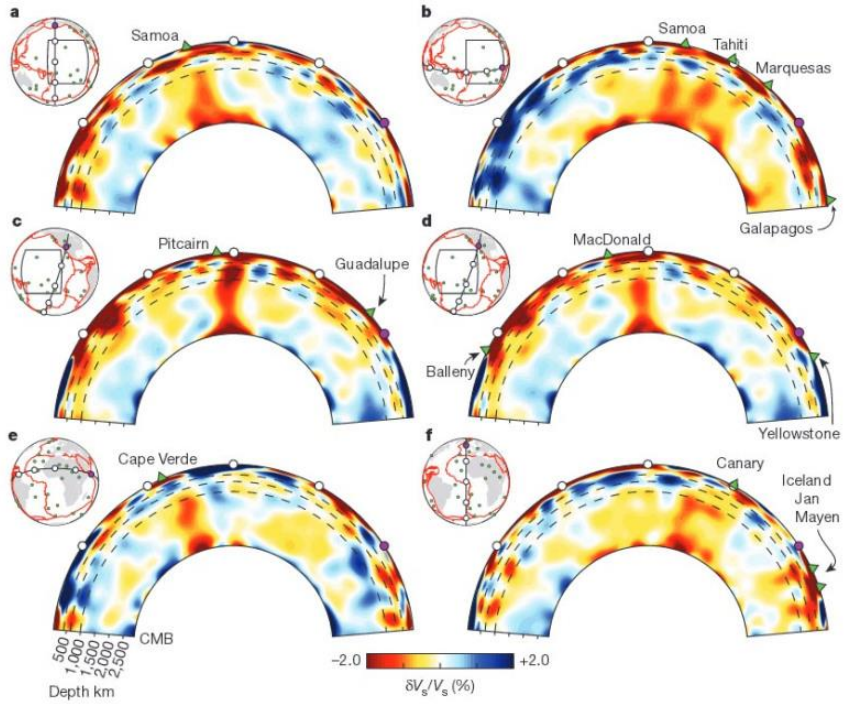

Figure I.4 Whole mantle seismic tomography cross sections beneath a variety of volcanic islands from French and Romanowicz (2015).

Seismic velocities observations provide numerous fundamental insights on Earth's interior structure and materials properties. However, to obtain more quantitative information on mantle rocks from seismic waves, comparisons and calibrations from elastic properties measurements made in laboratory at relevant conditions of Earth's interior are required, as well as theoretical elasticity models. For these reasons, laboratory experimental setups were developed on high-pressure and high-temperature apparatus. With these apparatus, a large amount of geomaterials from single crystals to rocks were investigated on a large pressure and temperature range. Solids are pretty well known for the most common phases and compositions for upper and lower mantle. However, the potential presence of partial melting, as suggested by the recent detection of anomalous zones at multiple depths in the mantle, remains yet poorly constrained. Their qualitative and quantitative interpretations are a function of our understanding of the elasticity of the geomaterials.

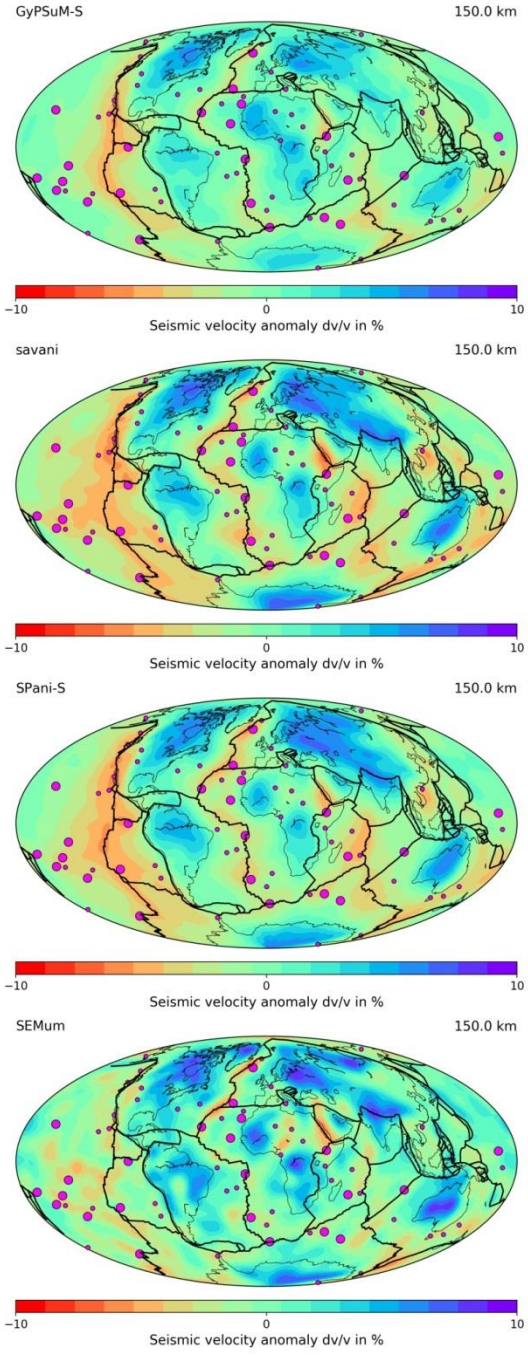

Figure I.5 S wave velocities variation at 150 km depth for different models. Figure made with Submachine website, (Hosseini et al.,2018).

(https://www.earth.ox.ac.uk/~smachine/cgi/index.php). GyPSum-S uses body waves (Simmons et al., 2010). Savani uses surface waves and body waves (Auer et al., 2014). SPani-S uses surface waves and body waves. SEMum uses waformed (Lekic and Romanowicz, 2011).

b) Sound velocity mechanisms

Acoustic waves are waves of energy generated by a disturbance (movement, rupture or explosion) that travels in a material. The velocity of propagation of the wave depends on the density and the elastic properties of crossed materials. The first observations from Love (1927) shown that any disturbance in an unbounded isotropic medium is propagated with a constant compression velocity. After this description, the discovery of additional body and

surface waves by seismologists completed to set up the energy propagation mode through waves at geological scales in the Earth (Fig. I.6).

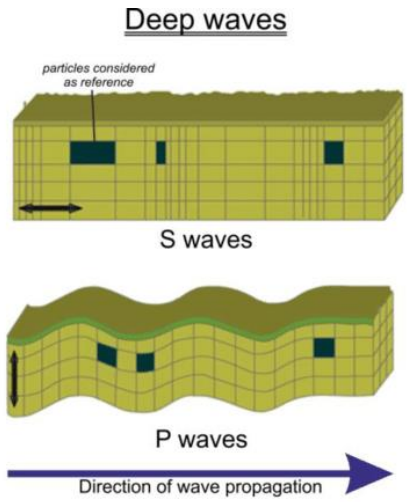

Figure I.6 Body waves mechanism compared to their direction of propagation. Modified after Martinez Moreno, (2015) and Grotzinger and Jordan, (2010).

Body waves are composed of primary (compressional) waves and secondary (shear waves). Primary waves (P) are compression/longitudinal waves. They are the faster type of waves, they define the speed of sound and their velocity is expressed as it follows:

$$V_p = \sqrt{\frac{K + \frac{4}{3}\mu}{\rho}} = \sqrt{\frac{\lambda + 2\mu}{\rho}}$$

Secondary waves are shear or transverse waves. They have a perpendicular motion to the direction of wave's propagation. This wave is the second fastest body wave and its velocity can be written:

$$V_s = \sqrt{\frac{\mu}{\rho}}$$

Starting for these two types of waves the bulk sound speed, often used in theoretical works, can be expressed:

$$V = \sqrt{V_p^2 - \frac{4}{3}V_s^2} = \sqrt{\frac{K_s}{\rho}}$$

Where μ is the shear modulus, ρ the density, λ the 1st Lamé coefficient and *Ks* the isentropic bulk modulus.

c) Experimental determination of sound velocity on geomaterials and their implications on Earth's mantle structure

Using the techniques described in Chapter II, elasticity of numerous geomaterials and ceramics have been measured over a quite significant pressure and temperature range. The most significant results per phase/mineral family will be given here (Fig. I.7).

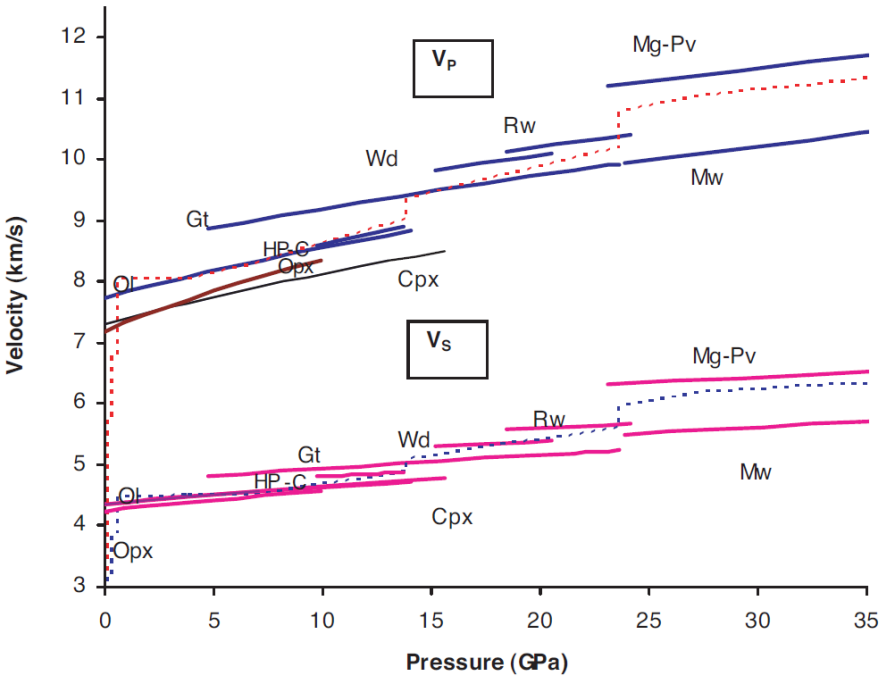

Figure I.7 Acoustic wave velocities of major mantle phases (solid lines) as a function of pressure along a 1,600-K adiabatic geotherm, compared with global seismic model AK135 (dotted lines). Ol, olivine; OPx, orthopyroxene; CPx, clinopyroxene; HP-C, high-pressure clinopyroxene; Wd, wadsleyite; Rw, ringwoodite; Gt, garnet; Mg-Pv, magnesium silicate perovskite; Mw, magnesiowüstite. Figure taken from Li and Libermann, (2007).

i) Olivine

As the main mineral component of the Earth's upper mantle, olivine has been well studied under almost all its possible aspects. Its elastic properties has been known since the 1990's for its entire stability range (0-12 GPa) and were measured with almost all the modern techniques (ultrasonics, ISS, Brillouin scattering, RUS, etc.). This compound served as a comparison standard between techniques. However, the exact values of pressure derivatives of its shear and bulk moduli remain long discussed due to different data processing methods (Libermann and Li, 1998). The accepted values based on velocities and volumes measurements (Liu et al., 2005) are given in the table I.2. The recovered data from experiments at different pressures highlighted a decrease of the adiabatic bulk modulus (Ks) with increasing pressure. Similarly, the increase temperature was translated by a decrease of both shear and bulk moduli. However, with the measured olivine seismic velocities along the

geotherm, the calculated upper mantle profile increases gradually for both Vp and Vs as well as its density. This behavior matches very well with global seismic models which also have a gradual increase on velocities in the upper mantle.

ii) Wadsleyite and Ringwoodite

For the high pressure polymorphs of olivine: wadsleyite and ringwoodite, the sound velocities increase with pressure. This is translated by the changes of structures and a significant density increase (0.25 g/cm^3 from forsterite to Mg-wadsleyite and 0.076 g/cm^3 for mg-Wd to Mg-ringwoodite). The superior density dependence to iron content of these high pressure phases also favors the velocity contrast at transition zone depths. As a function of a more compact structure, bulk and shear moduli were shown to increase at each step for wadsleyite and ringwoodite. The temperature dependence of these moduli is similar with slightly lower and higher values for wadsleyite and ringwoodite respectively.

iii) Pyroxenes

Pyroxene family encompasses a wide variety of possible composition and structures. From orthopyroxene to clinopyroxene, the proportion of the different phases (Opx disappears around 10 GPa) and their compositions evolve with increase pressure up to the transition zone and a final dissolution into the majorite. Among this variety, Mg-Fe end-members were mostly studied for their elastic properties. Surprisingly, pyroxenes sound velocities exhibit a nonlinear behavior with increasing pressure. Above 9 GPa, elastic softening was reported, which should translate a transition to a metastable phase between ortho-enstatite and high pressure clino-enstatite (Kung et al., 2005). Cpx and Opx have similar elastic properties and are relatively soft compare to olivine. At the opposite, the high pressure clino-enstatite is much stiffer with a higher bulk and shear moduli (table I.2).

iv) Garnet and Majorite

Garnet, similarly to pyroxene, encompasses a great variety of chemical species. Pyrope-almandine series are the most studied species, because of their relevance in mantle (Chantel et al., 2016), and over a quite wide range of P and T. Progressive transformation of pyrope into majorite is translated by a smooth increase of velocities with pressures. The elastic moduli of majorite and pyrope have been found to be roughly similar (Sinogeïkin et al., 2002).

Table I.2 Elasticity of major upper mantle and transition zone minerals. Modified after Li and Liebermann (2007),See each mineral references therein.

Mineral	Density (g/cm^3)	K_{s0} (GPa)	K_{s0}'	$\partial K_s/\partial T$ (GPa/K)	G_0 (GPa)	G_0'	$\partial G/\partial T$ (GPa/K)
Olivine	3.222 + 1.182 X_{Fe}	130	4.6	-0.017	77	1.6	-0.014
Wadlseyite	3.472 + 1.24 X_{Fe}	173	4.5	-0.014	108	1.4	-0.016
Ringwoodite	3.548 + 1.30 X_{Fe}	185	4.5	-0.019	119	1.5	-0.015
Clinopyroxene	3.277 + 0.38 X_{Fe}	117	4.5	-0.015	67	1.7	-0.014
Orthopyroxene	3.204 + 0.799 X_{Fe}	114	6.6	-0.013	74	1.6	-0.011
HP Clino-enstatite (6.5 GPa)	3.460	157	5.6	-0.017	99	1.5	-0.015
Pyrope	3.565 + 0.76 X_{Fe}	171	4.1	-0.016	91	1.5	-0.010
Majorite	3.518 + 0.97 Xfe	168	4.1	-0.015	88	1.5	-0.010

v) Melt and partially molten materials

Melts and partially molten materials represent a potential important component of Earth's mantle. This is even more important for seismic properties where partial melts, with elastic properties that differ largely from solids, were early suggested to account for velocities anomalies of upper mantle (Anderson and Sammis, 1970; Romanowics, 1995).

However, knowledge of seismic behavior of melts is very limited. In fact, because of their near zero shear modulus and experimental difficulties, melts are very difficult to characterize. The work of Rivers and Carmichaels (1987), on an important number of melts, highlighted that sound velocities are not very sensible to chemical composition in case of geological materials. The inferred bulk moduli, were similar with a very low value compared to solid of 20 ± 2 GPa. In addition to seismic velocity measurement at high temperature, Rivers and Carmichaels (1987) provided also one of the most important works to discuss attenuation by melts. Since then, no systematic experimental study investigated in more details the seismic properties of melts, and pressure effects are only little known.

Partially molten systems have been mostly studied by theoretical and analogue systems (Takei, 2000; Yoshino et al., 2005), until the recent measurements performed by our group: Chantel et al. (2016), setting the framework of this PhD work. Significant disagreements have

been pointed out by the comparison of the different techniques and highlighted important effect of textural arrangement of the melt solid-mixture. This effect has been investigated in details in this PhD work, as well as the extension of acoustic measurements on partially molten rocks to pressures up to 14 GPa (Chapters III and IV).

vi) *Earth's seismic velocity depth profile and associated anomalies*

Earth's upper mantle and transition zone velocity profile is well explained by a combination of the major rock forming mineral: olivine, garnet and pyroxenes and their respective high pressure forms. Calculated velocity profiles from the different minerals using pyrolite model yield to very similar profiles to global seismic reference models (Li and Liebermann, 2007). The profiles are indeed very close to olivine for Vp and Vs and their deviations can give clues on mineralogical composition of the mantle. For example, the discontinuities around 220-300 km can be explained with transition to the high pressure forms of pyroxenes (Li and Liebermann, 2007). The intensity of the jump at 410 km during the wadsleyite/olivine transition was used to quantify the quantity of olivine in the upper mantle in dry or wet scenarios (Liu et al., 2005). Similarly, jumps and velocity gradients before and after "410" discontinuity have been used by Li et al. (2001) to confirm the good agreement on seismic velocities between pyrolitic composition and lower parts of upper mantle (>200 km).

Despite global profiles have a good agreement with simple mantle mineralogy at most of depths, several global and local anomalous zones have been detected. The magnitudes, the vertical and lateral extent quantification of these zones remain difficult and increase significantly with increasing depths and decreasing the zone size and/or magnitude. The early detection of a given zone (Revenaught and Spikin, 1994) is often followed by series of detailed studies focusing on the depths of interest and using more adapted methods for precise quantification (Tauzin et al., 2013; Hier-Majumder and Tauzin, 2017). Most of the detected zones are located in the upper mantle with the Low Velocity Zone (LVZ) located between 70 to 150 km deep, the Low Velocity Layer (LVL) above the Mantle transition zone between 350 and 410 km. Both LVZ and LVL have been detected at a somewhat global scale (Tauzin et al., 2010) (Chapters III, IV and V).

The LVZ has been shown to have a large velocity decreases with absolutes S waves velocities decreasing from 4.55 to 4.1 Km/s (~10% drop) (Evans et al., 2005; Anderson and Sammis, 1970; Romanowicz, 1995). Important P wave velocities decrease have also been reported as well as significant increase of Vp/Vs ratio. Present at variable depths, the LVZ

also seems to have a varying thickness depending on the geological context (slab, plumes reading ridges; see Chapter III) with a varying thickness velocity.

At greater depths, the LVL is characterized by an important thickness variation (up to 50 km), locations from the 410' and intensity of S wave decrease (up to 9%) (Revenaught and Spikin, 1994; Tauzin, 2010; Hier-Majumder and Tauzin, 2017) (Fig. I.8).

Presence of anomalies in the mantle transition zone and lower mantle are less documented due to the difficulty of data interpretation and distinction with inversion artifacts. Nevertheless some anomalous batches around 590 km have been found by Tauzin et al., (2013). Zones of anomalies have been also locally detected at the top of the lower mantle between 660 and 1000 km depths (Schmandt et al., 2014). Finally, a great interest has been shown by seismologists to the D" layer in the recent years with possible anomalies due to thermal or chemical heterogeneities as well as zones of bridgemanite and post-perovskite transitions (Thomas et al., 2004; Granero, 2000).

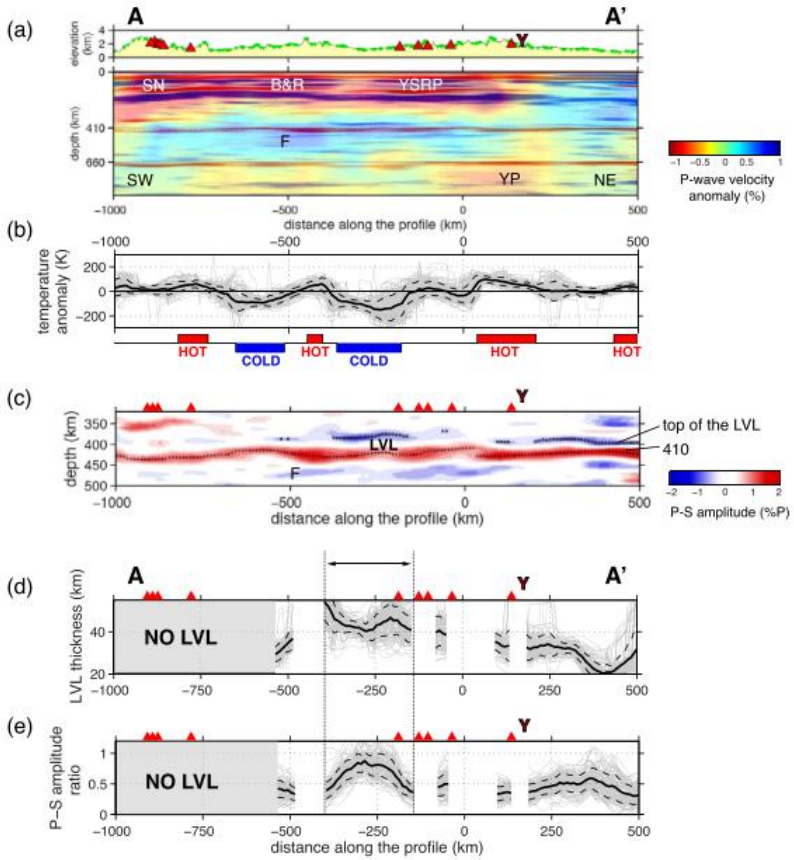

Figure I.8 Example of observed LVL anomalies in the western USA in term of P wave velocity anomaly (a), temperature anomaly (b), location depths (c), thickness (d) and P-S amplitude ratio (e) from Hier-Majumder and Tauzin (2017). See details therein.

3) Magnetotelluric observations, experimental determinations and interpretations

Electrical conduction results from the ability of a material to transport electrical charges, and so currents and magnetic fields. Thus, electrical properties of mantle rocks are important because they control the transmission and the resulting "shape" of Earth's magnetic field initiated by the core. At the opposite of seismology, the first studies on Earth's conductance at global scale are recent, with pioneer works of Hirayama (1934), Rikitake (1948, 1951 parts I to IV), Tikhonov (1950) and Cagniard (1953).

a) Magnetotelluric observations

The electrical conductivity profile of the Earth's mantle can be inferred from electromagnetic induction studies. Earth's primary magnetic field is generated by the geodynamo from the core. A secondary internal field is also created due to the effects of electrically conductive rocks. In addition, the external electrical and magnetic field is significantly affected by solar winds, Earth's magnetosphere, ionosphere and lightning/thunderstorm. These events and induced changes create a consequent electromagnetic induction. Measurement of primary, secondary and induced electromagnetic fields can be used to probe the inner Earth.

Two methods are mainly used to infer electrical conductivity of the deep Earth: magnetotelluric sounding (MT) and geomagnetic depth sounding (GDS). The Earth's naturally varying electric and magnetic fields are usually measured for a wide range 10^4 to 10^{-8} Hz. The periods are usually shorter than 1 year for GDS, mainly due to the decrease of induced components as frequency decreases, and can be even shorter for MT. The penetration depth of the electromagnetic field depends on its sounding period. Greater depths investigations require measuring lower frequencies, which requires longer recording times. As conventional sounding depth are usually less than 10 km, deep Earth sounding implies very long-period measurements, recordings of several days to weeks or more to obtain good data quality. Horizontal resolution of MT data is a function of the distance between sounding locations, as closer sounding locations will result into an increase of the horizontal resolution. Vertical resolution of MT mainly depends on the frequency being measured. The resolution decreases with the increasing periods and so decreases with increasing investigation depths.

However, in this large frequency range several excitation mechanisms coexist (Kuvshinov, 2008). For periods longer than 24 hours, that are commonly used to study Earth's mantle, the magnetic field signal is dominated by magnetospheric ring currents (Püthe et al., 2015). The data treatment is often difficult and the presence of different mechanisms requires adjustments in the source parameterization during data processing and modeling stages (Gravyer et al., 2017). The interpretation of sounding data is usually done by separation of each mechanism inducing a weaker resolution and inconstancies between models. Most of the global or regional mantle conductivity models (Olsen, 1998 and 1999; Neal, 2000; Utada et al., 2003; Constable and Constable, 2004; Tartits et al., 2004; Kuvshinov et al., 2005; Kuvshinov and Olsen, 2006, Toffelmier and Tyburcy 2007; Baba et al., 2010) are based on inversion of C-response derived from observatory or satellite data in the frequency domain by GDS method. The recent development of simultaneous inversions methods by ETH group (Grayver et al., 2017) aims to resolve these disagreements. The joint inversion of different mechanisms would provide a better resolution by combination of land observatory and satellite data (Champ, Sac-C, Swarm etc.) which usually requires a more significant computational treatment (correction of time variations in magnetic and tidal magnetic field, etc.).

The actual GDS + MT data allows a precise characterization of the crust and upper mantle. For higher pressures, the associated errors are very large and do not allow a fine resolution of mantle features. Despite a significant scatter between the studies, some general trends can be drawn. The electrical conductivity of Earth's material increases with depth, this is mostly due to increase of both P and T conditions. Important variations can be expected at the mantle transition zone where water content in wadsleyite and ringwoodite has been shown to have a crucial effect on the bulk electrical properties of the rocks (Manthilake et al., 2009; Yoshino et al., 2005; Xu et al., 1998). Electrical properties of lower mantle and core are yet only broadly constrained. A quite constant EC profiles with depth have been reported in lower mantle (Kuvshinov et al., 2005; Kuvshinov and Olsen, 2006; Olsen et al., 1999; Grayver et al., 2007) with values between 0 and 10 S/m and a pronounced effect of D" layer is also expected (Velimski et al., 2006). For the core, electrical conductivity values remains scarce and unconstrained by direct measurements.

In this PhD, the regional and global electrical conductivity profiles and their reported anomalies are of significant interest. The upper mantle electrical properties are pretty well constrained nowadays with values ranging from 0.01 to 0.1 S/m until 410 km (Fig. I.9). The

EC slightly increases in upper mantle but is severely marked by the presence of a high conductivity layer at depths corresponding the lithosphere-asthenosphere boundary (LAB) and the seismically defined low velocity zone (LVZ) between depths of 70-150 km. Above this layer, very resistive asthenosphere rocks are characterized by conductivities between 10^{-4} and 10^{-3} S/m. This layer marks a very strong increase in EC up to values higher than 0.05 S/m. This high conductivity anomaly is of significant interest as many possible scenarios were built to explain it. Indeed, ranging from solid state hypotheseis: presence of hydrogen, olivine anisotropy and presence of preferential orientation zones (Karato, 1990, Goetze, 1977) to partial melting scenarios: low melt fractions, melt localized in sheared zones and anistropically distributed (Caricchi et al., 2011; Zhang et al., 2014; Pommier et al., 2015 and Chantel et al., 2016). A detailed study of this anomalous layer is proposed in the chapter III.

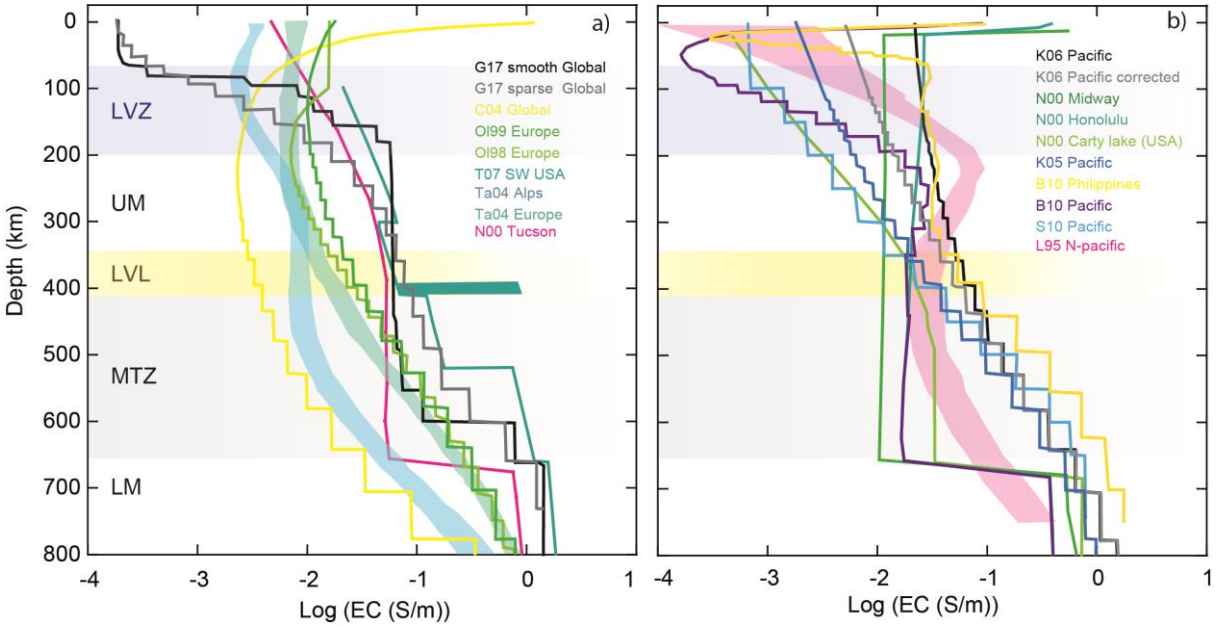

Figure I.9 Sum up of MT + GDS deep electrical conductivity profiles made in the Earth's mantle. a) is for Global, Europe and USA profiles. G17 refers to Grayver et al. (2017) (satellite + ground), C04 is Constable and Constable (2004) (satellite), Ol98 is Olsen (1998) and Ol99 for Olsen et al. (1999) (satellite). T07 is Toffelmier and Tyrbucy (2007), the profiles is measured in SW USA, the anomaly at LVL is modeled. T04 refers to profiles by Tarits et al. (2004) (ground) in western Alps and Europe. N00 refers to Neal et al. (2000) (ground) B) is only for profiles made in the Pacific region, which was importantly studied. K05 andK06 refers to two profiles made by Kuvshinov (2005) and Kuvshinov and Olsen (2006) (satellite) over the pacific. N00 refers to Neal et al. (2000) (ground) for three different locations in the pacific. B10 are profiles from Baba et al. (2010) in pacific and Philippines (ground). S10 correspond to profiles made by Shimizu et al. (2010) (ground) and L95 refers to Lizarralde et al. (1995).

On the other hand, another anomaly has been suggested in the upper mantle. As for seismic velocity, an electrically conductive layer atop the mantle transition zone has been suggested (Tofflemier and Tyrburcy, 2007). However, this anomaly has been more modeled than directly measured mainly due to problems of resolution and the strong influence of a very conductive MTZ (values between 0.1 to 1 S/m). The problem of lateral heterogeneity of

the LVL at 350 km and its thickness variations may also represent a difficulty to observe with global electrical conductivity models. The electrical properties of such anomalous layer will be discussed in the Chapters VI and V. Finally, significant increase of electrical conductivity has also been reported at the "660" discontinuity, at the transition between MTZ and lower mantle, by the recent inversion of Grayver et al. (2017). This feature may also represent a significant zone of interest for future MT+GDS studies, as resolution at this depth is still preventing a detailed electrical conductivity profile.

b) Electrical conduction processes

The development of dedicated apparatus to measure both magnetotellurics (MT) and electrical conductivity of rocks in laboratory provided a new source of complementary information to seismology. In fact, electrical conductivity of rocks is function of a number of parameters: pressure, temperature, chemical composition (including important effect of volatiles), oxygen fugacity, crystalline orientation and rock textures (Yoshino et al., 2010; Manthilake et al., 2009; Freitas et al., 2019; Chapter III). As any electrical circuit, the bulk electrical conductivity of a rock can be short-circuited by a very small amount of a very conductive phase. As a consequence, the presence of interconnected melts (Roberts and Tyburcy, 1999; Ten Grothenhuis et al., 2005), fluids (Glover et al., 1990), hydrogen/water rich phases (Karato, 1990) or metals (Yoshino et al., 2003, 2004; Manthilake et al., 2019) will be translated by a huge increase of electrical conductivity. At the opposite, a small fraction of conductive material isolated into an insulating matrix will result into low bulk conductivity. The presence of water as defects into nominally anhydrous minerals (NAMS) also results into a serious increase of electrical conductivity (1 to 2 orders of magnitude for olivine) (Yoshino, 2008; Poe, 2010). The understanding of mantle MT profiles, thanks to laboratory determinations, would allow better constrains on chemical content, presence of melts/fluids and minor/trace element presence. In addition, the effect of temperature which activates different conduction mechanisms is very strong with variations up to 10 orders of magnitude from room to melting temperatures. Again, the comparison with MT profiles could help to decipher temperature variations in Earth's mantle.

Electrical conduction mechanisms are not unique and depend on temperature. Temperature activates different mechanisms which are in competition. The resulting bulk electrical conductivity is usually dominated by one mechanism at a given temperature. However, at pivotal points a sum of contributions is expected. In practical case, most silicate

minerals act like an insulator at room temperature. Their electrical conductivities are usually hard to measure because they are below the detection limit of conventional multimeters. Silicate minerals are regarded as ionic insulators with large energy gaps, for example, 6.4 eV for forsterite at surface conditions. However, when temperature rises to the mantle conditions, these minerals behave as a semiconductor. Mobility of lattice defects and a small amount of impurity such as hydrogen and ferric iron enhances electrical conduction of silicate mantle minerals at mantle temperatures.

The Nersnt -Einstein relation describe the electrical conductivity for an ionic-bounded crystal. In this equation, the electrical conductivity (S/m) depends on the number of electric charge carriers per unit volume (N), the charge number Z, the electron charge e (C) and μ its mobility (m²/V/s).

$$\sigma = NZe\mu$$

In the case of plural contributions, the bulk electrical conductivity of a material can be expressed as the sum of the contributing mechanisms:

$$\sigma = \sum_i N_i q_i \mu_i = \sum_i N_i (ez)_i \mu_i$$

Where N_i is the density of the $i\text{-}th$ type charge carrier (m^{-3}), q the effective charge (z) and μ its mobility (m²/V/s).

The mobility of the charge carriers is described by an Arrhenian behavior due to the diffusion of the charges carriers (the thermal process responsible of the mobility).

$$\mu = \frac{\mu_0}{T} exp\left(\frac{-\Delta H}{kT}\right)$$

Where μ_0/T is the pre-exponential factor, ΔH is the activation enthalpy (J), k is the Boltzmann constant (J/K), and T is the absolute temperature (K). In practice, the $1/T$ factor in the pre-exponential term is not always used. From this, the electrical conductivity equation can be written, where σ_0 is the pre-exponential factor (S/m), ΔH is the activation enthalpy (J), k is the Boltzmann constant (J/K), and T is the absolute temperature (K).

$$\sigma = \sigma_0 exp\left(\frac{-\Delta H}{kT}\right)$$

Boltzmann constant can be replaced by gas constant (R in J/mol/K) in the previous formula to have activation enthalpy expressed in J/mol. This equation is, the most commonly used to interpret electrical conductivity measurements in geoscience. In fact, as direct measurement of sample resistance allows retrieving sample conductivity knowing sample/electrode dimensions, the representation of the data into an Arrhenius plot (*ln(EC) vs 1/T*) allows a direct visualization of activation enthalpy (e.g. slope of the linear fit). Activation enthalpy is defined thermodynamically by a combination of activation energy (ΔE in J) and activation volume (ΔV in m^3). The electrical conductivity (S/m) can then be written as a function of T (K) and pressure P (Pa):

$$\sigma = \sigma_0 exp\left(\frac{-\Delta E + P\Delta V}{kT}\right)$$

As expressed above, the bulk electrical conductivity of a rock is a sum of different mechanisms. Different types of mechanisms exist, their dominance is a function of the mechanism characteristics (chemistry, structure, etc.) and their thermally activation. Each conduction mechanism as a characteristic energy (slope in the Arrhenius plot), which can help deciphering a given regime.

i) Proton conduction

At low temperature, the proton conduction mechanism dominates. The activation energy of proton conduction is usually much less than 1 eV. This low activation energy allows its presence even at very low temperatures (1000 K), making it the dominant process within this range. It is commonly observed that hydrous minerals have much higher electrical conductivity than dry ones (Manthilake et al., 2009; Karato, 1990; Yoshino, 2006). The reason of this common feature is due to the size of the proton (H^+) which allows a relatively fast diffusion in solids compared to other, much larger, ions. Proton conduction does not require hydrogen rich minerals to occur, as smalls quantities in NAMS were shown to be enough to initiate conduction (Karato, 1990). Proton conduction occurs by charge transfer by H^+ hopping between the different point defects in host crystals. The electrical conductivity, when dominated by proton conduction, is thus a function of the water content. The electrical conductivity increases with the number of protons per unit of volume as suggested by the Nernst-Einstein equation. The pre-exponential term was observed to decrease with increasing the water content as well as activation enthalpy for different silicate crystals (Manthilake et al., 2009; Yoshino et al., 2006 and 2008). For an isotropic distribution of protons in the host

crystal, the activation enthalpy is expected to be proportional to the cubic root of the concentration with a correction factor for the geometry. Yoshino et al. (2010) applied the equation of n-type semi-conductor (Debye and Conwell, 1954):

$$\Delta H_p = \Delta H_{0p} - \alpha_p (N_p)^{1/3}$$

Where ΔH_p is the activation enthalpy at a given concentration *Np*. *Np* is the number of proton and ΔH_{p0} is the activation enthalpy at a very low hydrogen concentration. α_p is the geometrical correction factor described above. Then, using Nernst-Einstein equation, the conductivity can be expressed as a function of the water concentration (or proton):

$$\sigma = \sigma_{0p} C_w exp\left(\frac{-\Delta H_{0p} - \alpha C_w^{\frac{1}{3}}}{kT}\right)$$

C_W is the water content in weight, α is a geometrical factor, and H_{0p} is the activation enthalpy observed at very low water content.

In addition to proton conduction, a highly conductive feature can be observed at low temperature in EC experiments. The so called "moisture" patterns can be easily found in experiments, where adsorbed water from atmosphere by samples and parts can give electrical conductivities 1 to 2 orders of magnitudes higher than solid ones at low temperatures. The presence of this adsorbed water probably short circuit the high resistance sample using proton diffusion. The persistence of this adsorbed moisture up to high temperatures can be a significant problem as it will start to diffuse in crystal or melts. However, staying at moderate temperatures (500 K) for a prolonged time results in a progressive loss of moisture and a significant increase of EC, coherent with solid values (moisture removal procedure by Mantilake et al., 2009).

ii) Small polaron conduction

At moderate temperatures, solids such as silicate rocks are dominated by small polaron conduction also called hopping conduction. In ionic crystals such as oxides and types II-VI semiconductors, the Coulomb interaction between a conduction electron (or hole) and the lattice ions are strongly coupled (electron-phonon coupling). This "phonon" like motion can be seen as the effect of the electron/hole that is pulling nearby positive ions towards it and pushing nearby negative ions away. This electron/hole and associated virtual phonons is often

treated as a single composite particle, the so-called polaron first defined by Landau in 1933 (Landau, 1965; Devreese, 1996).

Hopping conduction in Earth's mantle minerals (silicate with cation such as Ca^{2+}, Mg^{2+}, $Fe^{2+/3+}$ etc.) is due to charge transfer from neighboring ions of different valence such as Mg and Fe in olivine, pyroxene or garnet (Fig. I.10). Because of the oxygen fugacity, T, P, crystal structure and mantle composition, a certain amount of iron is present in its oxidized form: 3^{+}, thus presenting an electron hole (missing electron). The transfer of this electron hole from one crystallographic site to another implies the transfer of an electric charge and so produces a conduction mechanism ($Fe + H^{\cdot} = Fe^{\cdot}$). The electron hole transfer is theoretically easy to activate in terms of energy. However, the transfer of an electron hole generate trouble for the local structure with an excess of positive charge, the neighboring atoms then accommodate the charge difference by attraction of anions and repulsion of cations (artificial phonon motion). This motion and generated strain are defined as the small polaron, and its relative activation energy is then much higher (usually >1 eV). In most of mantle minerals ferric iron is not present as structural compound but is present as impurities in Mg-Fe site and so is a function of both oxygen fugacity and crystal structure. The electrical conduction is thus proportional to ferric irons in the system. The charge carrier density can be expressed as the ratio of ferric iron over total iron:

$$n = \frac{ZsX_{Fe}}{V} = Z\frac{\frac{Fe^{3+}}{\sum Fe}X_{Fe}}{V}$$

Where V is the unit cell volume, Z the number of formula unit per cell and X_{Fe} is the atomic fraction of iron per formula unit. The mobility of a small polaron can be written:

$$\mu = \frac{A}{T}exp\left(\frac{-\Delta E_h}{kT}\right)$$

where E_h is hoping activation energy (J) and A is a term function of hopping distance and so crystal structure.

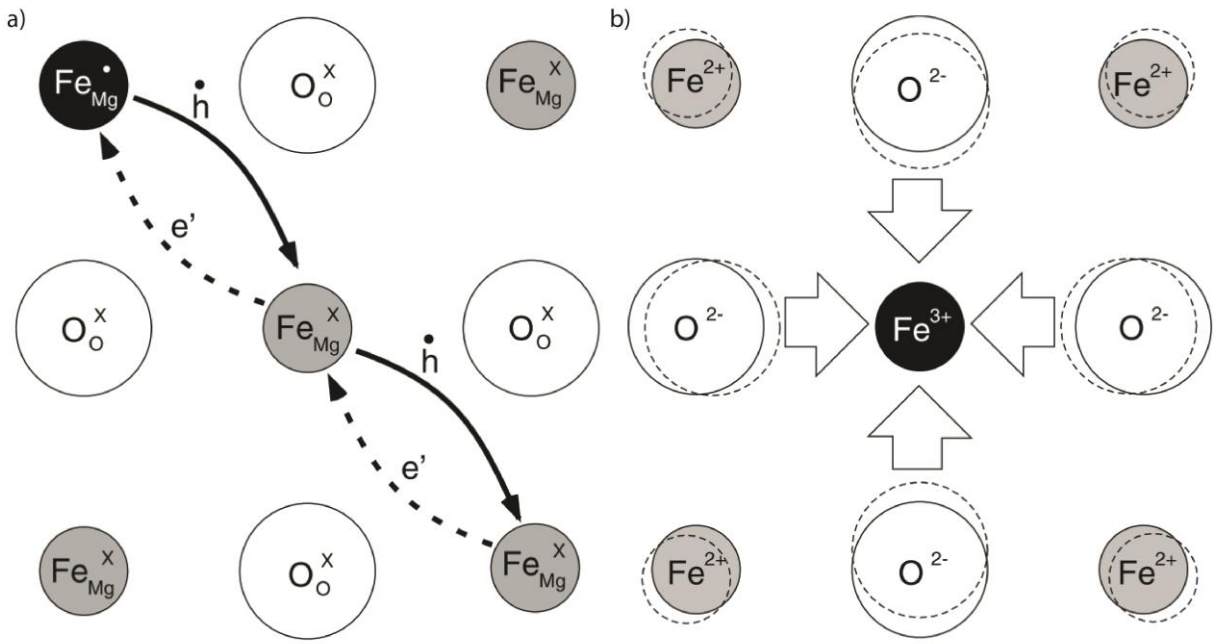

Figure I.10 a) Schematic diagram of hopping conduction (small polaron). Electron hole (h) transfer, symbolized by the arrows from Fe in Mg sites carries an electric charge. B) Schematic effect of charge transfer by small polaron on local lattice. Presence of Fe^{3+} induces repulsion of other Fe^{2+} cation and attracts O^{2-} anions. This process creates a resistance of the lattice to hopping conduction which is responsible of its high energy of activation. a) and b) were modified after Yoshino (2010).

iii) Large polaron conduction

Large polaron or Fröhlich polaron conduction mechanisms have been reported in very few specific cases for geological materials: Pericalse and Ferro-periclase (Sempolinski et al., 1980; Dobson et al., 1997; Dobson and Bordholt, 2000). Large polaron conductivity results in electron-lattice interaction due to long-range coulombic interaction between solid ions and electronic carrier. The large polaron is larger than electron hoping phenomenon, larger than the lattice constant of the material (Byrnes, 2008) and so must require higher energies. The mobility of large polaron is usually limited by scattering with optical phonon and strong electron-optical phonons coupling is expected in these materials. The mobility of large polaron charge carriers takes the mathematical expression:

$$\mu = \mu_0 T^{\frac{1}{2}}$$

iv) Ionic conduction

Ionic conduction mechanism occurs at high temperature in various geological materials. It occurs into Fe-Mg bearing silicates minerals such as olivine polymorphs, pyroxenes or garnets but also in silicate melts. However, the exact mechanism slightly differs between melts and solids.

For systems that undergo partial melting at moderate temperatures, near melting temperature, the slope of the conductivity curve is marked by a jump. After the jump, the slope of the conductivity trend as a function of temperature is almost vertical. This slope is a clue of a new conduction regime which corresponds to ionic conduction characterized by very high activation enthalpy. The bulk electrical conductivity contains contribution from each ion. Previous work on realistic melts (Gaillard and Marziano, 2005) demonstrated that the electrical conduction should be dominated by light alkalis (Li and Na). Na diffusivity in basaltic melts has activation energy of 160 kJ/mol at 1673 K (Ni et al., 2011) which is consistent with conductivities in basaltic melts 120-150 kJ/mol early measured by Tyburczy (1983). In molten systems, in which we consider Na transport as the dominating mechanism (other contributions negligible), the equation of the electrical conductivity becomes:

$$\sigma = \frac{1}{H_R}\frac{Dc(zF)^2}{RT}$$

Where D is the Na diffusivity (m²/s), c the concentration of Na, z the charge, F the Faraday constant (c/mol) and H_R the Haven ratio (the ratio of the tracer diffusion coefficient, D^*, to a diffusion coefficient, D_0, dependent on the ionic conductivity, see Murch (1982) for a detailed review). The Haven ratio is a correlation factor of the diffusion process and is determined by the diffusion mechanism by a competition between vacancies and interstitial atoms.

Therefore, in solid systems (such as Fe-Mg bearing silicates), the ionic mobility varies with temperature. Charge carriers are often vacancies in magnesium site with cation (Fe, Mg etc.) movements, requiring therefore a large energy of activation (>2eV) (Fig. I.11). The ionic mobility can then be written as a function of temperature:

$$\mu = \frac{\mu_0}{T} exp\left(\frac{-\Delta E_i}{kT}\right)$$

where ΔE is the activation energy (J) for the mobility of the ions and μ_0 is the pre-exponential term.

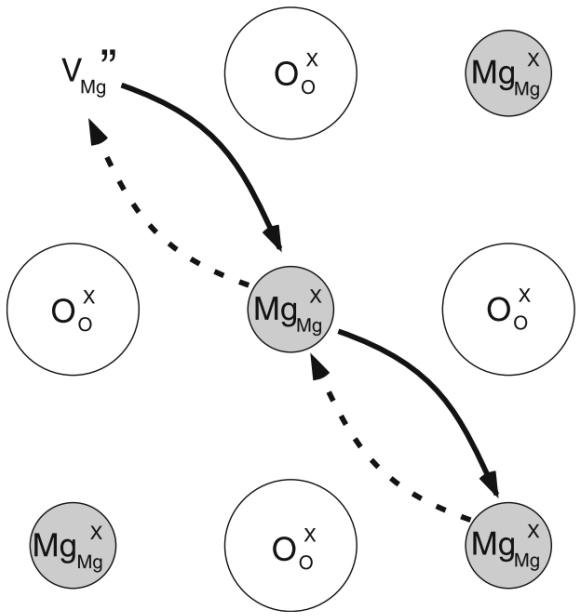

Figure I.11 Schematic diagram showing the ionic conduction process in Mg bearing minerals. The conduction occurs with migration of vacancies in the magnesium site as indicated by the arrows. Figure from Yoshino (2010).

c) Electrical conductivity of geological materials at mantle conditions

Electrical properties of geomaterials at mantle conditions are of significant interest to interpret magneto-telluric profiles as well as understanding Earth's geomagnetic field properties. To understand these data, laboratory electrical conductivity measurements techniques were developed on high pressure apparatus during the late 70's and early 80's. Nowadays, most of major phases were studied in details, such as olivine, pyroxene, garnets and their high pressure polymorphs. However, the variety of phases and rock assemblages, conduction process and parameters, influencing electrical conduction along P and T range of Earth's interior, prevent yet a complete understanding.

Here, only upper mantle and transition zone minerals will be succinctly described (Fig. I.12), a detailed review with summarizing tables for activation energy and conduction processes can be found in Yoshino et al. (2010).

i) $(Mg,Fe)_2SiO_4$ polymorphs

Olivine is the most abundant phase in the upper mantle, for these reasons (together with moderate P and T conditions) it was extensively studied. The conduction mechanisms were estimated to be dominated by small polaron until 1200°C and then a combination of ionic and polaron (Omura, 1991; Xu et al., 1998) and finally ionic at very high temperature (>1600 K) (Yoshino et al., 2009; Fei et al., 2018). Activation enthalpies have been reported to be around

1.3-1.6 eV and above 4 eV for small polaron and ionic conduction respectively. Numerous studies address the importance of anisotropy in electrical conduction with measurement or oriented single crystals and polycrystalline samples. Indeed, olivine is quite anisotropic with a factor 2 to 3 of difference between faster [001] and slower [010] axis (Schock et al., 1989; Hirsch et al., 1993; Du Frane et al., 2005; Poe et al., 2010). Electrical conductivity is a function of chemical composition, and was found to heavily depend on the total iron composition (Hirsh et al., 1993; Farla et al., 2010). In addition, electrical conduction is also a function of oxygen fugacity (Wanamaker and Duba, 1993; Hirsh et al., 1993; Constable, 2006).

At low temperature proton conduction appears in olivine sample containing small amount of water as defects. The effect of water in olivine has been strongly debated (Karato, 1990; Yoshino et al., 2006; Wang et al., 2006; Poe et al., 2010) with important implications for the water content inferred in the upper mantle.

High pressure polymorphs of olivine have been also consequently studied. As major phases of the mantle transition zone, wadsleyite and ringwoodite represent a significant amount of mantle proportion. Thus, they are important for interpretation of global MT/GDS studies. Xu performed the first measurements of their electrical conductivities in 1998. These were estimated to be 1 to 2 orders of magnitude higher than olivine. However, the high pressure and temperature range implies difficult measurement in particular due to presence of volatiles. In fact, complementary analysis of Xu samples by Huang et al. (2005) showed the presence of water which increases the electrical conductivity. The new measurements by Yoshino et al. (2008) and Manthilake et al. (2009), helped to distinguish small polaron and proton conduction mechanisms of wadsleyite and ringwoodite in a wider temperature range. As for olivine, small polaron should be the dominant mechanism at mantle conditions. The proton conduction is, however, strongly dependent on hydrogen amount as activation enthalpies for protron conduction decreases with increasing water content for wadsleyite (Manthilake et al., 2009) but inverse results were also reported (Yoshino et al., 2008). Similarly to olivine, bulk EC increases with iron content and depends also on oxygen fugacity (Yoshino and Katsura, 2009).

ii) Garnets

Garnet is important stable phase in the upper mantle and MTZ. Its proportion increases with pressure as CPX starts to dissolve in it. Its composition changes at higher pressure to

majoritic composition with important incorporation of Si. Majorite is quite abundant in the MTZ and may represent also a significant part of the subducted slabs (MORB bulk composition). Unlike olivine, garnets have a very wide combination of compositions, and so solid solutions. Thus, investing garnet electrical properties as a function of composition remains important as the compositional changes are observed while increase pressure. Studies of Xu and Shankland (1999), Romano et al. (2006), Yoshino et al. (2008) and Dai et al. (2012 and 2013) helped to precise these compositional effects on pyrope-almandine solid solutions and majorites at very high pressures (18-23 GPa). High Fe content in garnet and majorite would induce way higher electrical conductivity and activation enthalpies for small polarons reported are similar to other silicate compound: 1.4 eV. The effect of water into garnets as point defects, as reported by recent studies (Mookherjee and Karato, 2010), remains yet unknown.

iii) Pyroxenes

Pyroxene is also an important mineral in the Earth's upper mantle. Opx is only present at low pressures (<5 GPa) and represents a small fraction, on the other hand Cpx are quite abundant before dissolving into the majoritic garnet. However, dedicated high pressure studies on electrical properties of Cpx are scarce (Yang et al., 2011 and 2012). These studies report also an important effect of water of bulk electrical conductivity, as well, with possible effects of anisotropy but also a significant effect of iron oxidation state (and so oxygen fugacity) for small polaron conduction process.

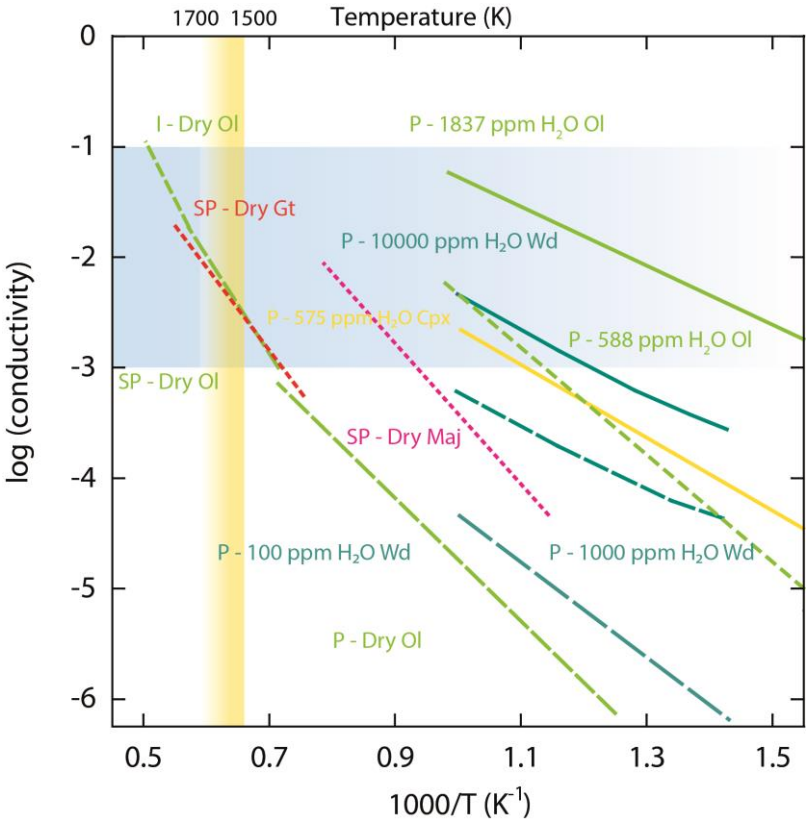

Figure I.12 Electrical conductivities (log) of the most common upper mantle and transition zone minerals as a function of reciprocal temperature (modified Arrhenius plot). P, Sp and I refer to the conduction mechanism: proton, small polaron and ionic conduction respectively. Phases name and water contents were labeled near the profiles. Dry olivine is from Yoshino et al. (2006), hydrous olivines (average of 3 crystalline directions) by Poe et al. (2010). Wadsleyite sample are from Manthilake et al. (2008). Cpx are from Yang et al. (2012), Garnet Romano et al. (2006) and majorite from Yoshino et al. (2008). Yellow shadow area is the upper mantle temperature range according the adiabat from Katsura et al. (2010) and blue area represents upper mantle electrical conductivity range.

iv) *Melts and partially molten rocks*

Electrical properties of melts at upper mantle and MTZ conditions are of a great interest for detection of melting regions in the mantle. As melt properties are a function of pressure and temperature as well as chemical composition, it appears mandatory to determine via laboratory measurements the electrical properties of geological plausible melts in order to interpret quantitatively the geomagnetic profiles.

Melts and partial melts have been extensively studied because of their potential geological implications. However, the wide variety of possible configurations, the large sets of influencing factors and technical limitations makes our understanding incomplete yet. First studies on geological melts (Khitarov et al., 1970; Presnall et al., 1972; Murase and McBirney, 1973; Waff and Weill, 1975; Tyrburcy and Waff, 1983) highlighted their high ability to conduct electricity and invoked partial melting hypothesis to explain the high

conductivities observed between 70-200 km deep (asthenosphere LVZ). These studies highlighted that electrical conductivity critically depends on the melt composition and major elements such as iron and alkalis. The bulk EC was found to significantly increase at higher alkalis and in particular Na contents (Gaillard et al., 2004; Pommier et al., 2008; Gaillard and Marziano, 2005; Ni et al., 2011).

In addition, the effect of dissolved volatiles (H_2O and CO_2) in the melt was found to be very important. In fact, impact of these volatiles on thermodynamics and transport properties of the melt have been reported (Shaw, 1963; Watson, 1979; Ochs and Lange, 1997; Zhang et al., 2010). Recent studies have highlighted that only small amount of water (<1%) can significantly increase the melt conductivity (Gaillard, 2004; Pommier et al., 2008; Ni et al., 2011), this observation also apply for CO_2 in a smaller amplitude (Ni et al., 2011). Finally, changing from silicate to carbonatitic melt was shown to have a very important effect. Carbonatites were shown to be very conductive (>100 S/m) (Gaillard et al., 2008) even if these values have been challenged by more recent estimations (Yoshino et al., 2010).

Dry or hydrous silicate melts exhibit a non-arrhenian behavior (*log(EC)* does not depend on *1/T* linearly) at high temperature probably due to thermal effects (Ni et al., 2011) and translated by fragile behavior on viscosity's temperature dependence. By consequence, Vogel-Fulcher-Tammann equation is preferred to illustrate the temperature dependence of melts electrical conductivity:

$$\sigma(T) = \sigma_0 exp\left(\frac{A}{T-B}\right)$$

Where σ_0, A and B are adjustable parameters. Similarly, activation energy of silicate melt cannot be fitted in Arrhenius plot and is often fitted using $\Delta H = \frac{RT^2 \partial ln\sigma}{\partial T}$.

Melt electrical conduction mechanism is ionic and dominated by diffusion transport of light elements such as Na. Activation enthalpies of ionic conduction in silicates melts are usually very high (120-170 kJ/mol) (Gaillard and Iacono-Maraziano, 2005; Tyburcy and Waff, 1983; Ni et al., 2011). In cases of hydrous melts, the diffusion Na is enhanced by presence of water (decrease of viscosity) and EC is also believed to increase by H diffusion (Gaillard et al., 2004). At the opposite, CO_2 has much less effect on melt structure explaining a more moderate effect on the bulk EC. The intensity of the effect of dissolved volatiles in melts is also a function of the melt chemistry, as more pronounced increase due to water were

reported for basaltic melts compared to phonolites or rhyolites (Ni et al., 2011; Gaillard et al., 2004).

In cases of partial melting, which is the most common case in Earth's mantle, properties of the bulk rock is a function of solid and melt characteristics with additional "mixing" terms. Of course the intrinsic properties of the solid and melt which are linked to their compositions and structures are important, however the grain-melt distribution at small scale have a great impact. The variety of melt microstructures, mostly due to minimization of interfacial energy, affects the melt distribution, the porosity/permeability of the rock and so their electrical conduction. The melt interconnectivity, translated by the dihedral angle estimation, is also a key factor controlling the efficiency of electrical conduction. Indeed, as melt is much more conductive than solid, the interconnected melt network will "short-circuit" the solid skeleton and give very high bulk conductivity. At the opposite, a non-wetting isolated melt, will not produce a very strong increase of EC. The bulk partially molten rock electrical properties are then a function of textural characteristics and melt fractions. These textural considerations will be investigated in Chapter III.

Classically, the melt-solid electrical properties have been described by different possible theoretical and empirical relationships (Fig. I.13). These different simplifying laws were established to give a physical framework to understand experimental data. They will be detailed in this section because some of them are used in the following chapters (III and V). In the following equations X_m is the melt fraction, σ_m is the melt electrical conductivity, σ_t the bulk rock electrical conductivity and σ_s the solid electrical conductivity.

Cubes model (Waff, 1974): $\sigma_t = \left[1 - (1 - X_m)^{2/3}\right]\sigma_m$

Hashin-Shtrickman upper bound (H^+) (Sphere): $\sigma_t = \sigma_m + \frac{(1 - X|m)}{1/(\sigma_s - \sigma_m) + X_m/3\sigma_m}$

Hashin-Shtrickman lower bound (H^-) (Sphere): $\sigma_t = \sigma_s + \frac{X_m}{1/(\sigma_s - \sigma_m) + (1 - X|m)/3\sigma_s}$

Tube model (Grant and West, 1965; Schmelling, 1986): $\sigma_t = 1/3\sigma_m X_m + (1 - X_m)\sigma_m$

Archie's law (Watanabe and Kurita, 1993): $\sigma_t = C X_m^n \sigma_m$

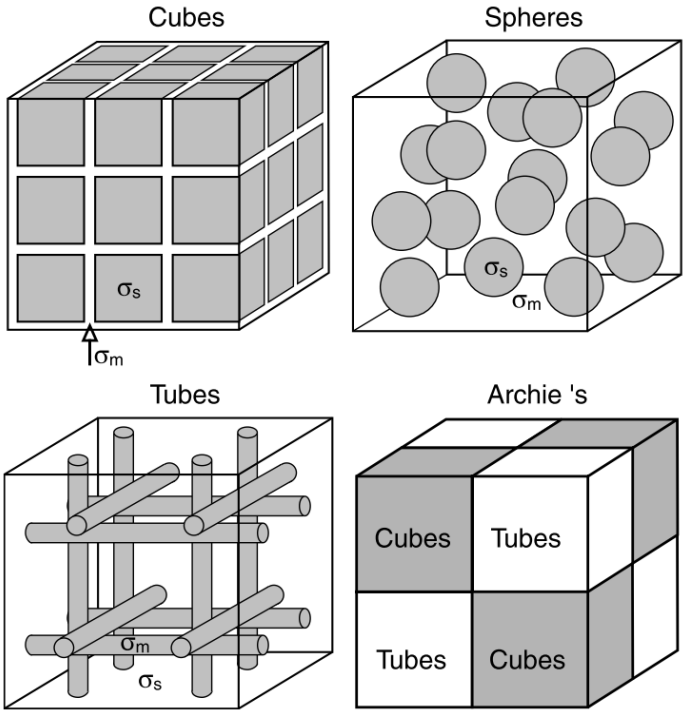

Figure I.13 Illustration of the different simplified physical models of melt/solid textures. Figure from Ten Grotenhuis et al. (2005).

The cube model considers cubes of solid material (with low conductivity) surrounded by a melt layer of uniform thickness. Sphere models, also named Hashin-Shtrickman upper and lower bounds, consider isolated spheres of solid material in highly conductive melt for H^+ and the reversed configuration in case of H^-. Tubes model uses equally spaced melt tubes within a solid matrix. Finally, Archie's law is an empirical relation and so does not have a clear geometrical representation. It is based on resistor network theories and can be visualized as a mixture between tubes and cubes models according Ten Grothenuis et al. (2005).

This recent study highlighted that Archie's law reproduces well the experimental data with fitting coefficient of $C = 1.47$ and $n = 1.3$ for basaltic melt into an olivine matrix. However, the Archie's law fails at 0 melt fraction as solid electrical conductivity is not present in the calculation as it can be present in H^+. By consequence, Archie's law tends to 0 in $X_m = 0$, which has no physical meaning and give lower EC at low melt fraction than H+. This drawback can become an advantage when solid electrical conductivity is not known, still allowing a quite precise data fitting. At large melt fractions > 5% Archie's law and H^+ model give similar results.

4) Heat budget of Earth and thermal properties of mantle rocks

Measurements and estimation of Earth's total heat flux provides unique information to understand its internal vigorous activity. Depending on the method of estimation, a large debate remains on deep mantle contributions. The review here proposed highlights the crucial importance of new and extensive characterization of thermal properties at mantle P-T conditions. In addition, mineral physics constrains on theoretical and experimental aspects will be given via important theoretical consideration for the heat transfer types and their effects on global observed properties.

a) Past and present constrains on heat budget and thermal evolution of the Earth

i) Present constraints

Earth is a massive and complex heat engine with heterogeneous repartition of temperature in its interior due to different heat sources and sinks. The sources of heat are well known with a combination of different origins: accretionary heat, latent heat released by core crystallization, differentiations heat and radioactivity. To understand Earth's thermal evolution, the overall heat budget and its distinct contributions have to be estimated. Despite the total heat budget is pretty well constrained with the quantification of releasing sources in surface (heat conducted in surface rocks, volcanic and hydrothermal activities, etc.), the contributions to this budget remain tainted by large errors and uncertainties. The global heat flow was estimated to be 46±3 TW (Fig. I.14). This estimation was made thanks to direct global measurements of thermal gradients in boreholes, with laboratory calibrated thermal conductivity on the rock samples, which is corrected with oceanic thermal models that accounts to the underestimation due to hydrothermalism. Between the different contributions, radiogenic heat production is fairly well constrained with 20 TW estimated by bulk silicate Earth model of a chondritic composition. Among them, the crust has a significant role with 6-8 TW, which is restrained in a shallow volume.

If we take in account the tidal heating estimated to 0.4 TW, mantle cooling and core heat flow are the two other main poles of heat sink and production (respectively). The flow from core and the lower mantle into the upper mantle parts may be then significant (>30 TW) (Kellogg et al., 1999; Nolet et al., 2006; Lay et al., 2007). Both contributions are yet badly constrained in particular for lower mantle (the cooling flux ranges between 5-25 TW) and core mantle boundary heat flux (varying according the different studies) (Lay et al., 2008; Buffett et al., 2003; O'Rourke et al., 2017). However, as the global budget is robust,

constraining one of the unknown will allow having good estimation of the remaining others. To do this, the heat flow coming from the core has been targeted as the problem to solve. However, both early and recent estimations are conflictual despite the constraints from different techniques such as temperature, dynamo, buoyancy of plumes etc.

The CMB heat flow estimation indeed requires models on temperature and composition as well as materials properties. The temperatures at the CMB have been estimated by the estimation of the solidus curves (Holland, 1997; Boehler et al., 2000; Akins et al., 2004) to 3400 to 4300 K. However, our group recently challenged the previous estimations (Andrault et al., 2011, 2016, 2016b and 2019). In fact, its thermal evolution may not vary as previously thought (Andrault et al., 2016b). Previous calculations estimated the TBL at CMB as a 200 km thick layer with a thermal conductivity of 10 W/m/k for 5-13 TW of CMB heat flow. Such high thermal conductivity hasn't been proved yet and must imply radiative component given that thermal diffusivity decreases with increasing temperature. This hypothesis is not supported by spin transitions observations on lower mantle minerals (Goncharov et al., 2006). Moreover, the presence of chemical heterogeneities at the CMB with the D" layer detected by seismological studies, shows that heterogeneous thermochemical boundary layer will introduce significant uncertainties in thermal parameters estimations.

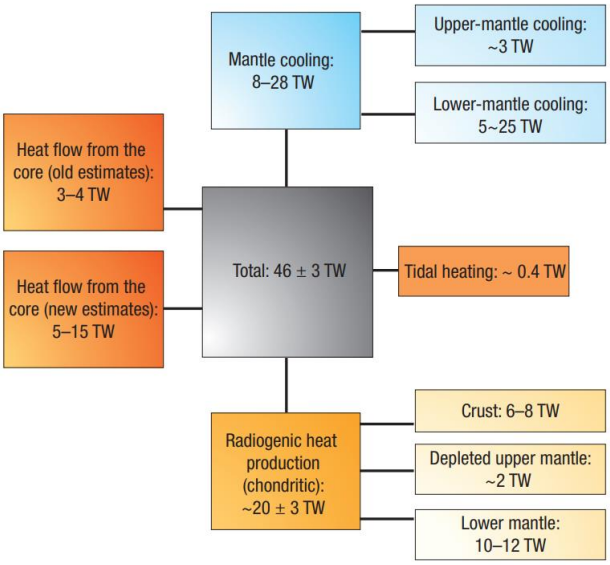

Figure I.14 Global heat flow balance from Lay et al. (2008).

Other estimations from geodynamo have been proposed. Indeed, the present magnetic field suggests that vigorous convection is present in outer core to sustain this magnetic field over geological timescales. Some dissipation may be related to these movements generated by

either compositional sources such as exclusion of light elements (Buffett et al., 2003; O'Rourke and Stevenson, 2016; O'Rourke et al., 2017) or growth of the inner core and solidification of the outer core. The CMB heat flow would be then controlled by the thermal conductivity of the metallic outer core. However, it's thermal conductivity is very debated with values ranging between 10 and 150 W/m/K (Fig. I.15) and the numerical models have still strong limitation to reproduce realistic core convection (small scale flows, very turbulent convection etc.). The resulting estimated dissipation as very large range 1-10 TW as well as uncertain CMB heat flow evolution with time (>8 TW in the past, 3-4 TW actually (Buffett et al., 2002)).

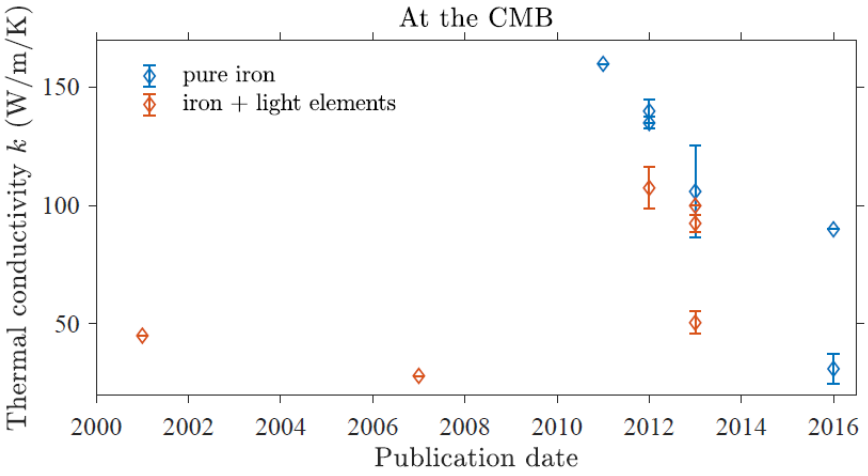

Figure I.15 Determination of thermal conductivity of the core at CMB conditions. A great variability of estimations with distinct techniques yield pretty large uncertainties on resulting CMB heat flow. From R. Deguen (Houches summer school, 2017).

The presence of mantle plumes generated at the base of the CMB, in the D" layer, also provides constraints on CMB heat flow because they represent local excess of heat (or entropy). However, their number and fate in the past is still unclear (Lay et al., 2008). The different models suggest values between 5-15 TW at the CMB to explain the plumes generations.

Finally, constraints from perovskite and post perovskite phases transitions and possible double crossing near the CMB would also help estimating the CMB heat flux. The phase transition is, with laboratory calibrations, a precise *in situ* thermometer. Its Clapeyron slope is well known as well as its acoustic properties allowing a better interpretation of deep earth seismic profiles. The double crossing of post perovskite stability due to high temperatures near CMB was observed. It fixes a second absolute temperature near the CMB (~4000 K) and

yield to CMB fluxes of 7-15 TW (with assumed thermal conductivity between 5-10 W/m/K) (Van der Hilst et al., 2007).

ii) *Early Earth and past constraints*

Earth's formation, differentiation and large scale dynamics over geological time scales are the results of the ongoing cooling process. Heat is transported from the inner parts of the Earth to its surface and then loss into space. At a first glance, as the Earth is still internally active and hot inside after 4.568 Ga, one could guess that the transport of heat must be pretty slow, inefficient or that additional heat producing processes were active in its history.

Understanding the formation of the Earth and its thermal history requires considering the formation processes. At the end of accretion, in the first 10's of Ma (after CAI), the early Earth was molten, hot and had vigorous convection and one or several phases of magmatic oceans may have been present. The magmatic oceans are due to the presence of important heat released during accretion, making the temperature profile crossing the solidus. After this initial magma ocean phase (+ basal magma ocean ?), probable other phases could occur thanks to meteoric impact creating large regions of partial melting up to a complete mantle melting as suggested for the moon forming impact (Canup, 2012).

The thermal history of this stage is badly constrained because thermal properties of molten rocks or partially molten rocks are not well known, in addition to large possible ranges of pressure, temperature, chemistry and oxidation states of the materials. In the case of magma oceans, the temperature profile will be mostly quickly homogenized by vigorous convection. The convective geotherm is however, limited at the top and its bottom by two thermal boundary layers in which the thermal gradients are very steep and controlled by diffusion transfers. The nature of the thermal boundary layer is not precisely known in the past as the presence of a crust at Earth's surface, its nature and its potential thickness are really debated (Abbott et al., 1994; Korenaga et al., 2008; Davies, 2009; Herzberg et al., 2010). Higher mantle potential temperature in the past, as inferred by Herzberg et al. (2007 and 2010) on komatiites, will imply steeper gradients in the crust (Fig. I.16). The thickness of the thermal crust should also be greater in this conditions and chemistry of the produced crust must be different with changing depths of melting (komatiite, basalt, anorthosite etc.). However, the exact frontier between the thermal boundary layer and the "chemical" crust issued from mantle melting is still unconstrained, as only poor amount of rock archives survived through geological times. The present of a basal magma ocean (BMO) after the moon forming impact

has been also suggested (Labrosse et al., 2007) and its implication on the conductive and convective profiles into Earth's mantle have been recently investigated in Andrault (2019) (Fig I.17).

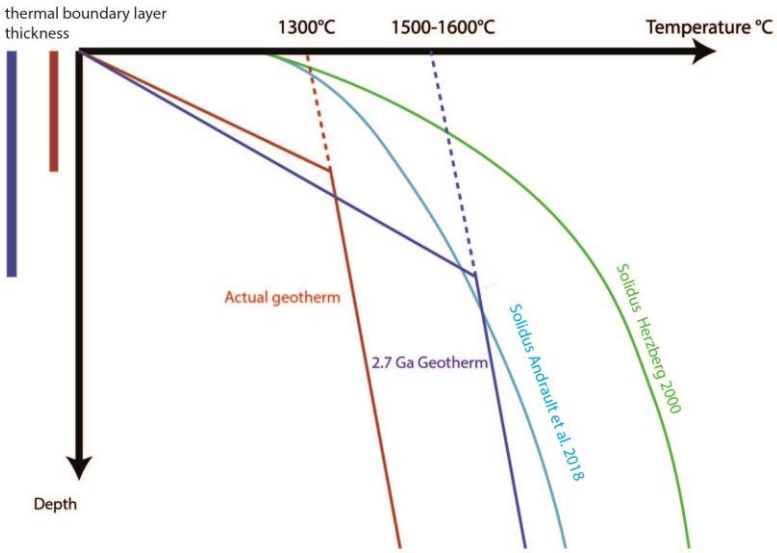

Figure I.16 Simplified and schematic illustration of thermal boundary layer thickness evolution with time, considering a single solidus and higher mantle potential temperature in the past. Such difference of temperature should imply thicker thermal boundary layers and/or steeper gradients. Variations of crust composition, physical state and thickness will change the thermal properties of this layer with potential influence of mantle cooling.

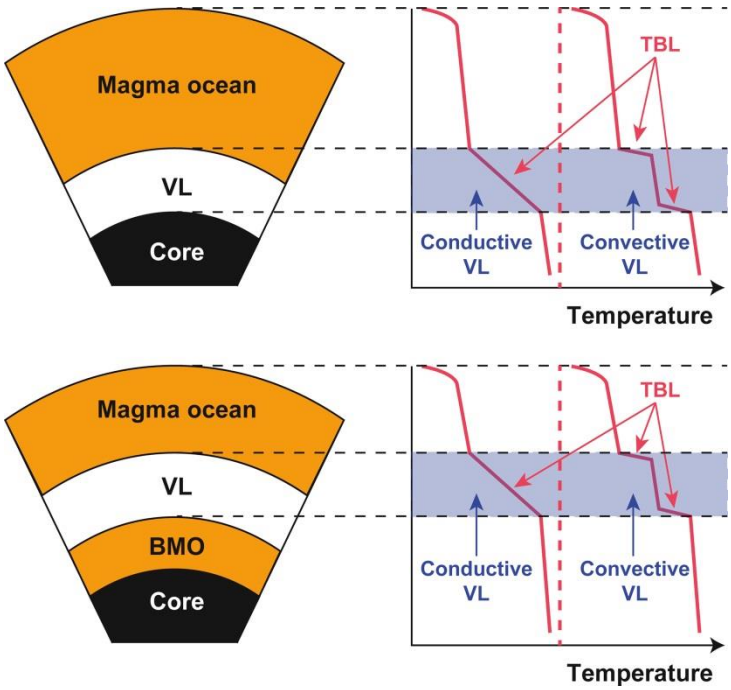

Figure I.17 Role of a viscous layer made of Bridgmanite on the mantle geotherms considering both BMO or standard magma ocean cases (bottom or middle crystallization cases respectively) and conductive or convective viscous layer into the establishment of thermal boundary layers (TBL). Figure from Andrault (2019) (see discussion therein for further explanations).

The role of core mantle boundary appears, similarly to actual debates on heat fluxes, crucial into the control of internal heat flow. This layer is the interface between the core and the mantle, from which a tremendous source of energy has been transferred in the early Earth due to inner core crystallization. Several constrains of CMB heat flow has been proposed by numerous recent studies with a potential CMB heat fluxes up to 8-10 TW (2 to 3 times the actual) (Stacey and Looper, 1983; Young and Lay, 1989; Lay, 2007; Lay et al., 2008; Gocharov, 2009; Buffett, 2003). However, its estimation in the past is much more uncertain and requires important modeling step in which inputs (thermal properties *inter alia*) have wide error bars.

Earth's thermal history can be inferred from these new studies. Indeed the flux at CMB should have evolved through time in different possible ways (Lay et al., 2008, Andrault et al., 2016b). The age of the inner core which solidifies while cooling depends directly on the CMB flux. Starting from an initial very high temperature stage during the planet formation and core segregation, the core and mantle were fully molten. When the mantle mostly solidified, the heat removal was much more inefficient and helped into keeping high temperatures in the deep Earth. The temperature profile after moon forming impact was commonly proposed as significantly decreasing with time to supply and sustain the dynamo. Energy in the order of 4 TW would have been reconciling an early inner core growth and a sustained dynamo. At the opposite CMB larger flow would imply a late inner core formation (~1 Ga) and very high rates in the past to sustain the dynamo (Labrosse et al., 2001). Recent suggestion by Andrault et al. (2016b) challenged this vision, while proposing a very quick temperature decrease after moon forming impact, and quasi stable temperature at CMB since then and that geodynamo was only enhanced by mechanical forcing by tidal distortion and precision due to the presence of the Moon, which energy ranges near 4 TW. Moreover, the other sources of energy such as light element expulsion form the core, potential presence of radioactive elements such as K or short life isotopes are also possible sources of energy.

To sum up, actual and past CMB heat fluxes are yet still very debated. Their estimations impose both the understanding of the core and mantle materials thermal properties. Among them, the mantle present at the D" layer is very peculiar and probably heterogeneous. In fact, in addition to metal/rocks interactions and mixing, a large amount of light elements are released by the core (Buffett, 2003) changing the local compositions. The presence of slabs materials as well as partially molten rocks of different natures (LLVP) is also probable. In addition to these actual constraints, the previous setting of the mantle during the early stages

with magmas oceans and thermal boundary layer of different natures (and depths) as shown by Andrault (2019) is yet only qualitatively constrained. Similarly, the presence of large partially molten zones in the actual or past upper mantle as suggested by the presence the LVZ and LVL anomalies may also influence the establishment of these conductive TBL, their effects remain yet unknown.

As a consequence, thermal diffusivity of various geomaterials such has solids rocks, metals glasses and melts, have to be determined experimentally on a wide possible P-T range. The temperature dependence of thermal parameters has to been properly constrained in order to build models to suit the numerous geological implications (which is also often overcome in actual models, Monteux, personal communication). The present constraint from theoretical considerations and mineral physics experiments are thus provided in the following section.

b) Physics of thermal transfers applied to Earth

In this section, the general concepts of thermal transfers are explained and detailed with their respective mathematical and physical expressions. Indeed, they represent an important pre-requisite to understand our two chapters (VI and VII) dedicated to thermal diffusivity measurements.

i) General theory and origin of heat diffusion equation

The importance of heat transfers in geophysics has been early recognized in the modern science developments. Fourier (1820) and Kelvin (1897) used the geothermal gradients and heat conduction theories to estimate the age of Earth.

The first key equation is Fourier's law which links thermal conductivity and temperature to the heat flux.

$$Q = -\kappa \nabla T$$

This can be expressed in one dimension, where *n* is the length scale normal to the surface.

$$Q = -\kappa \frac{dT}{dn}$$

Fourier's law implies that the Earth surface flux is function of its inner temperature and its thermal conductivity. The thermal conductivity can define the thermal diffusivity by the following relation:

$$D = \frac{\kappa}{\rho C_p}$$

Where ρ is density and Cp heat capacity.

The total heat flux by conduction is known to be the density of thermal transfer current by conduction and is defined by the surface integral of the heat flow by conduction:

$$total\ flux = P_{cond} = -\oiint_S \overrightarrow{\|Q_{cond}\|} dS$$

For a given medium with an entering and outgoing thermal flux by conduction and internal heat production (Pe), one can express its energy (U) variation in function of internal energy U_{int} and fluxes.

$$\frac{dU}{dt} = d\frac{\iiint U_{\int}\ d\tau}{dt} = \iiint_{Vol} Pe\, d\tau - \oiint_S \overrightarrow{\|Q_{cond}\|}\, dS$$

Where τ is the volume of the medium. Using Green-Ostrogradski theorem, the formula can be written:

$$\iiint \frac{U_{\int}}{dt} d\tau = \iiint Pe\, d\tau - \iiint \left(\overrightarrow{\|Q_{cond}\|}\right) d\tau$$

In each point the equation become:

$$d\frac{U_{\int}}{dt} = Pe - \left(\overrightarrow{\|Q_{cond}\|}\right)$$

If both convection and radiations energies are taken in account, this becomes the thermal equation viewed from energy:

$$\iiint \frac{U_{\int}}{dt} d\tau = \iiint Pe\, d\tau - \iiint \left(\overrightarrow{\|Q_{cond}\|}\right) d\tau - \oiint \left(\overrightarrow{Q_{conv}} - \overrightarrow{Q_{rad}}\right) dS$$

Using Fourier's law for conduction process for uniform κ material and internal energy function of heat capacity (Cp) and density (ρ):

$$\iiint Cp\rho \frac{dT}{dt} d\tau = \iiint Pe\, d\tau - \iiint \left(\kappa \overrightarrow{gradT}\right) d\tau - \oiint \left(\overrightarrow{Q_{conv}} - \overrightarrow{Q_{rad}}\right) dS$$

If only conduction is considered the relation can be simplified to:

$$Cp\rho\frac{dT}{dt} = \left(\kappa\overrightarrow{gradT}\right) + Pe$$

Using the divergence and gradient properties, the general equation of heat transfer by conduction in an isotropic medium can be expressed:

$$\kappa\nabla^2 T + \frac{d\kappa}{dt}\left[\left(\frac{dT}{dx}\right)^2 + \left(\frac{dT}{dy}\right)^2 + \left(\frac{dT}{dz}\right)^2\right] + H\ (internal\ heat) = Cp\rho\frac{dT}{dt}$$

The heat diffusion equation can be expressed in its conventional form:

$$\Delta T + \frac{1}{\kappa}\frac{d\kappa}{dt}\left(\overrightarrow{gradT}\right)^2 + \frac{Pe}{\kappa} = \frac{Cp\rho}{\kappa}\frac{dT}{dt} = \frac{1}{\alpha}\frac{dT}{dt}$$

Where α is thermal expansivity, Δ is the Laplacian operator and *Pe* is the internal heat, generally a radioactivity term can be added for additional internal heat.

This ubiquitous heat diffusion equation is used in all thermal diffusion studies. Its solving represents of major problem due to the temperature derivatives of *D* or *κ* and the Laplacian operator which imply to constrain perfectly the problem in several dimensions.

ii) Heat diffusion in solids: Debye's model

In solids, such as natural rocks and ceramics, the heat diffusion process is the main source of heat transfer. At lattice and atomic scales, the heat is translated by agitation of the lattice. These movements have been described as phonons and are thermally active. Debye's model is the most used theory to characterize phonon vibration modes which is a key point into the understanding of conductive heat transfer. Debye's model also predicts the heat capacity /specific heat and the so-called Debye temperature (T_D) which defines the activations of all the phonon's modes.

Debye's model was developed in 1912 and is based on particles statistics approach of phonons. These lattice vibrations can be treated as quantum harmonic oscillators and can only accept discrete amount of energy ($\Delta E = h\nu$) as they obey to Bose-Einstein statistics. The total energy in the lattice vibration (*U*) can be inferred from Bose-Einstein relation:

$$U = 3\int_0^{E_{max}} \frac{E}{e^{E/kT} - 1} dE$$

With *E* is the following relation considering a cube of dimension *L*, where the wavelength (λ) is given by *2L/n*. *h* is the Planck constant, *k* is the Boltzmann constant and *n* is an integer.

$$E = h\nu = \frac{hc}{\lambda} = \frac{hcn}{2L}$$

Using the three modes of phonon vibration in 3D space (one longitudinal and two transverse modes) and integration in spherical coordinates, the integration can be done making the substitution of *x* by:

$$x = \frac{hcn}{2LkT}$$

The upper limit of the integral in *x* is so defined by:

$$x_{max} = \frac{hcn_{max}}{2LkT} = \frac{hc}{2kT}\left(\frac{6N}{\pi V}\right)^{1/3} = \frac{T_D}{T}$$

With *N* is the number of atoms in the solid and *V* is solid volume.

The T_D constant is associated to the highest allowed mode of vibration. By consequence, for a given solid, the phonon excitation modes will increase in energy with temperature until the Debye temperature is reached. At Debye temperature, all the modes are exited and the specific heat of the solid reaches a value close to its maximum. Also it is very common to find thermal calculation where only $T > T_D$ because it allows to simplify the specific heat relations and phonon energies.

Using all the constant, the total energy integral becomes:

$$U = \frac{9NkT^4}{T_D^3}\int_0^{T_D/T} \frac{x^3}{e^x - 1}dx$$

The Debye specific heat expression is the derivative of this formula. The integral cannot be evaluated in a direct way but numerical evaluation shows a good agreement with the experimentally measured specific heat for the full range of temperature. It approaches at high temperature the Dulong-Petit law with a characteristic behavior in T^3 at very low temperaturse (Fig. I.18).

$$C_v = 9Nk\left(\frac{T}{T_D}\right)^3 \int_0^{T_D/T} \frac{x^4 e^x}{(e^x - 1)^2}dx$$

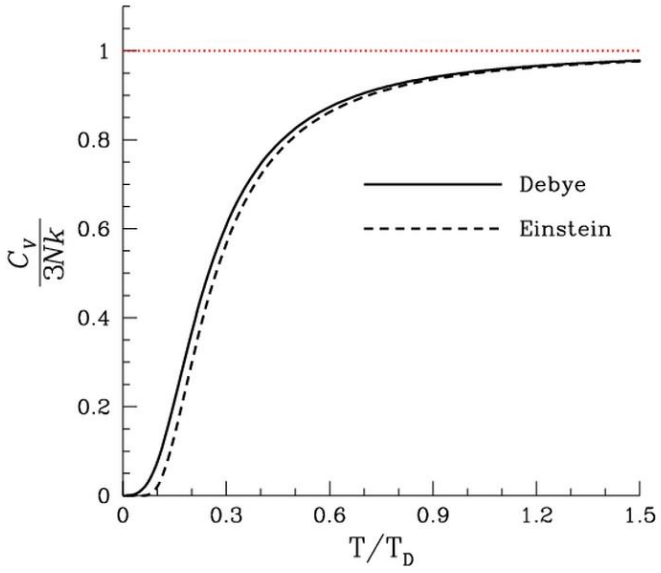

Figure I.18 Debye estimation of specific heat compared with Einstein model, at Debye temperature all the phonons modes are exited and the specific heat is almost at its maximal value. From Wikipedia 30/12/2016.

The heat capacity, which is commonly used for thermal conductivity calculation, can be expressed from the specific heat inferred from Debye's model using the thermodynamic relation. Heat capacity is a measurable physical quantity equal to the ratio between heat added to an object and its resulting temperature change. The heat capacity at constant volume is used into Debye models whereas heat capacity at constant pressure is more used in Earth science.

$$\left(\frac{dU}{dT}\right)_V = \left(\frac{dQ}{dT}\right)_V = C_v$$
$$\left(\frac{dU}{dT}\right)_P = \left(\frac{dQ}{dT}\right)_p = C_p$$

Where U is the internal energy and Q the amount of heat.

$$C_p - C_v = T\left(\frac{dP}{dT}\right)_V \left(\frac{dV}{dT}\right)_P$$
$$C_p - C_v = VT\frac{\alpha^2}{\beta_t}$$

Where α is the coefficient of thermal expansion and β is the isothermal compressibility.

iii) *Types of heat transfer in the inner Earth*

Thermal transport properties play a crucial role in Earth evolution, in fact several types of heat transfers exists in the Earth interior, acting at different lengths and timescales. Heat transfer is the exchange of thermal energy between physical systems, the rate of the heat transfers depends on the temperature of the system and the properties of the intervening medium. In the Earth, the three fundamental modes of heat transfer are represented: conduction also known as diffusion, convection and radiation. The studied scale is also important when considering the mode of heat transfer.

Geophysical studies concerning heat transport have shown different behaviors for Earth's envelopes due to variation of chemistry. In fact, the type of heat transport mechanism is function of the optic and electrical properties of the materials. For metals, that are the main compound of the Earth's core, the main heat transport is done by electron scattering and lattice vibrations: phonon scattering. As the metal is conductor and opaque, it does not show significant radiative contribution at core conditions. Thus, thermal conductivity of metals have been poorly directly measured but estimated via the Wiedemann-Franz law using their electrical conductivity which is easier to obtain at HP and HT conditions (Manthilake et al., 2019).

$$\kappa = LT\sigma$$

Where σ is the electrical conductivity and L is the proportionally constant Lorenz number. This type of estimations is still currently used for metallic core alloys.

Mantle minerals can be divided in two groups according their optical and electrical properties (Fig. I.19). First, the opaque insulators, those behave like metal for radiative part of heat transfer but are insulating materials (wüstite, troïlite). Their thermal properties are then only controlled by phonon scattering. The second group, which contains the silicates, the most common Earth materials, belongs to the partially transparent insulators. Their thermal transport properties depend both on lattice vibration and radiative conductivity. This group is submitted to ballistic photons, when important thermal gradients are observed, which can be the case of high pressure and temperature experiments.

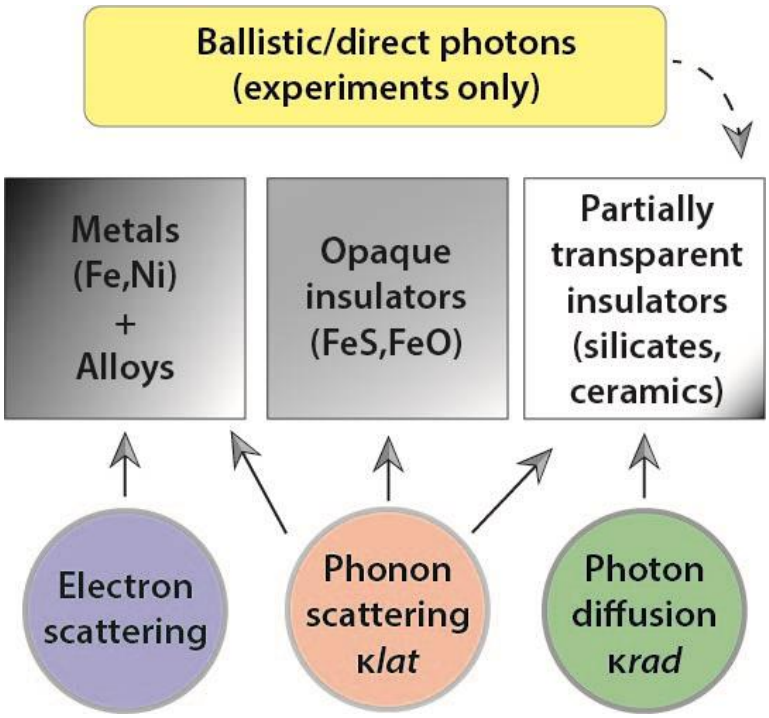

Figure I.19 Type of heat transport associated to the different types of Earth material. Only the 3 bottom circles are naturally present. Modified after Hofmeister and Brandlund (2015).

(1) Conduction heat transfer

In Earth, the heat transfer is conductive/diffusive at microscopic scale. Transport of heat is achieved by scattering of quantized lattice vibrations: the phonons. The phonons are of two types: optic and acoustic mode. In optic modes, the atoms move in opposite directions giving strong interactions with damped and localized oscillations. At the opposite, acoustic modes atoms translate in phase with the unit cell, the interaction are weaker but can be propagated on long distances. Both modes involve transverse and longitudinal components that are generally described as compressional and shear waves. The phonon scattering is an energy transfer between neighboring particles by successive molecules, atoms and electrons collisions. The collisions transfer kinetic and potential energies (internal energies) between the colliding objects. The transport of heat by scattering of phonon within each mineral grain is named "lattice conductivity" and written κ_{lat}. The conductive transfer is quantified by Fourier's law and depends on material temperature and thermal conductivity.

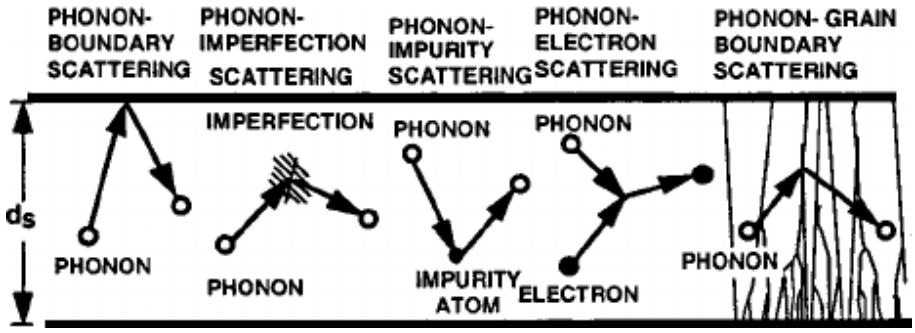

Figure I.20 the different type of phonon scattering present in solid materials from Asheghi et al. (2002).

The vibrational heat transport can be modeled by Debye's model (see previous section), using the analogy of phonon scattering with molecules collisions in a gas which is the base of thermal transport theory in electrical insulators (Fig. I.20). The summations can be derived and were achieved by Peierls (1929) and Klemens (1958):

$$\kappa_{lat} = \frac{1}{3}\frac{\rho}{ZM}\sum_{j=1}^{3}\sum_{i=1}^{3NZ} C_{ij}{u_{ij}}^2\tau_i$$

Where *M* is the molar formula weight, *Z* the number of formula units in the primitive cell, C_{ij} the Einstein heat capacity of each vibrational mode, u_{ij} the group velocity (d_w/d_S) where *S* is the wave vector ($w = 2v\pi$), *v* is the frequency, and $\tau_i$is the mean free lifetime. The sum is up to 3 on *j* for the three orthogonal directions and *3NZ* for *i* which correspond to the normal modes of a crystal with *N* atoms.

The lattice thermal conductivity can thus be expressed using different models:

(a) Acoustic model

The Debye theory for *Cv* has generally been used to estimate the lattice thermal conductivity (κ_{lat}) but the phonon lifetime had to be estimated. The phonon lifetime (τ_i) is assumed to go as *1/T* above Debye temperature (θ) which reproduces Eucken's empirical law (1911):

$$\kappa_{lat} = \frac{B}{T} for T > \theta$$

B is fitting parameters that can be estimated by dimensional analysis and corrected by different authors. The first estimation of Dugdale and MacDonald (1955) *eq.a* was later improved by Julian (1965) *eq.b* and Roufosse and Klemens (1973) *eq.c*.

$$eq.a = \kappa_{lat} = \frac{Cv}{3\alpha}\frac{u}{\gamma_{th}}\frac{a}{T} = \frac{VK_t}{3}\frac{u}{{\gamma_{th}}^2}\frac{a}{T}$$

$$eq.b = \kappa_{lat} = \frac{24}{20}\frac{4^{1/3}}{{\gamma_{th}}^2}\left(\frac{K_b\theta}{h}\right)^3\frac{ZMa}{T}$$

$$eq.c = \kappa_{lat} = \frac{1}{\pi^{1/3}2^{1/6}}\frac{3^{1/3}}{{\gamma_{th}}^2}\left(\frac{K_b\theta}{h}\right)^3\frac{ZMa}{T}$$

Where $\gamma_{th}$is the thermal Grüneisen parameter (= $\alpha V K_t/Cv$, K_t is the bulk modulus, α is thermal expensivity, V the molar volume, h the Planck constant and a is the unit cell parameter. These equations are only valid above Debye temperature.

The pressure dependence of κ is important since the measured thermal diffusivity/conductivity values require extrapolation for estimations at Earth's mantle conditions. Based on Debye heat capacity model, one can write (using $\alpha \propto v$ in equations *b* and *c*):

$$\frac{\delta\left(ln(\kappa_{lat})\right)}{\delta P} = \frac{1}{K_t}\left(3\gamma_{th} + 2q_{th} - \frac{1}{3}\right) \approx \frac{6}{K_t}a\ t\ T > \theta$$

Where the second Grüneisen parameters is $q_{th} = \delta ln\,\gamma_{th}/\delta lnV$. The Debye model restricts the values of the Grüneisen parameter assuming a linear dispersion of the phonons, which can be written for the simplest cubic lattice $u_i\gamma_i v_i V^{1/3}$ using ν as frequency.

(b) Bulk sound model

Phonons can be approximated as the propagation of a wave through the crystalline middle. Thus, sound velocity which is determined accurately by experimental measurements can help to precise thermal conductivity estimations.

The Debye summation can be simplified to:

$$\kappa_{lat} = \frac{\rho}{3ZM}Cv\langle u\rangle^2\tau$$

Where $\langle u\rangle$ is the bulk sound velocity, the pressure derivative is:

$$\frac{\delta\left(ln(\kappa_{lat})\right)}{\delta P} = \frac{1}{K_t}\frac{\partial K_t}{\partial P} + \frac{1}{Cv}\frac{\partial Cv}{\partial P} + \frac{1}{\tau}\frac{\partial \tau}{\partial P} \cong \frac{K'}{K_t} \approx \frac{4}{K_t}$$

The pressure derivative of *Cp* is close to zero and is often dropped in front of the magnitude of the experimental error.

(c) The damped harmonic oscillator (optic model)

The lifetime of optic modes are obtained using the Damped Harmonic Oscillator (DHO) of Lorentz introduced by Hofmeister et al. (Hofmeister, 2007, 2001; Hofmeister and Yuen, 2007). The lifetime of the phonon modes are expressed from any mode as a function of the *FWHM*, which is the Full Width at Half Maximum from individual peaks in the dielectric functions that are extracted from the IR spectra.

$$\tau_i = \frac{1}{2\pi FWHM}$$

FWHM can be obtained by Raman or IR spectra. It reflects the phonon interaction with all the modes in the crystal, taking in account scattering by defects, anharmonicity and represents an average in the Brillouin zone. For average properties (dependence of sound velocity according the mode is not well constrain) the thermal conductivity can be written:

$$\kappa_{lat} = \frac{\rho}{3ZM} Cv\langle u\rangle^2 \tau = \frac{\rho}{3ZM} \frac{Cv\langle u\rangle^2}{2\pi\langle FWHM\rangle}$$

FWHM is estimated from IR reflectivity data from spectroscopy measurements (FTIR) or, but more rarely, from experiments through a transparent middle (LFA, DAC…). But the temperature and pressure derivative are now well known due to both presence of longitudinal and transverse modes (Hofmeister, 2007). If one assume the mode Grüneisen parameter ($\frac{\gamma_{i=K/\nu_i} * \partial \nu_i}{\partial P}$) where *K* is roughly equal to the volume of the vibrating unit we can obtain:

$$\frac{\delta\left(ln(\kappa_{lat})\right)}{\delta P} = \frac{1}{K_t}\left(m\gamma_{ave} - 2q_{ave} + \frac{1}{3}\right) - \frac{1}{\langle FWHM\rangle}\frac{\delta\langle FWHM\rangle}{\delta P} \approx \frac{4}{K_t}$$

Where $m = 2$ at θ > 250 K, 3 for θ > 400 K and θ at T > 550 K and so depending on the mineral studied. The term γ_{ave} is roughly equal to γ_{th}.

(2) Convection/advection heat transfer

Convection is present in Earth's mantle at large scales. At this scale, the mantle can be considered as a viscous fluid which is able to flow by buoyancy forces resulting from density contrasts in the fluid by differences in temperature. The convective heat transfers mechanism heat by fluid displacement and so by mass transfer, but heat is also partly moved by diffusive process (small scale) (Fig. I.21).

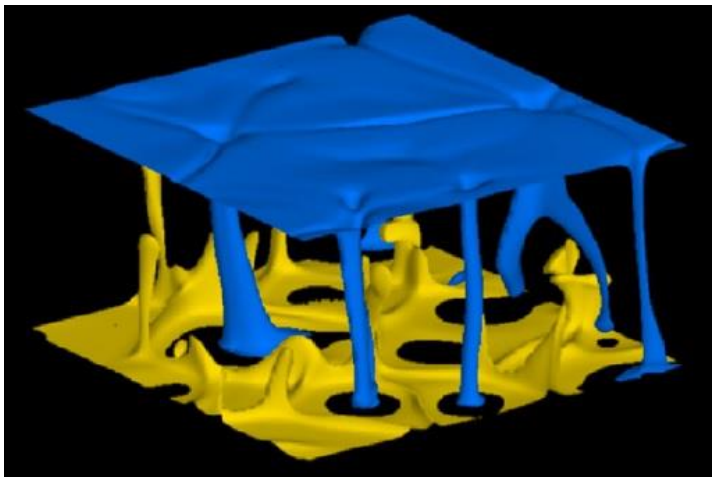

Figure I.21 Example of convection transfer where yellow color represents heat flux to the surface and blue color downwelling of cold materials. From Labrosse et al. (2007).

In a body of fluid, as can be considered Earth's mantle, convection and conduction process, at large scale, are considered to compete for the dominance of heat transfer mode. The buoyancy of the fluid is enhanced by the presence of important thermal gradient and thus, high heat conduction will inhibit convection by reducing temperature variations. Thus, according Fourier's law, the dominant mode depends on thermal properties (thermal conductivity) of the mantle material which controls the conductive heat. The Rayleigh number (Ra) determines the balance between conduction and convection by making the ratio between buoyancy forces and inertial forces.

$$Ra = \frac{g\Delta\rho L^3}{\alpha\mu} = \frac{g\beta\Delta T L^3}{\alpha\nu}$$

Where g is the acceleration due to gravity, ρ is density and $\Delta\rho$ the density contrast between lower and upper end-members, L the characteristic length, α thermal diffusivity, μ the dynamic viscosity, β the volume thermal expansion and ν the kinematic viscosity. The critical Rayleigh number is between 1000 and 2000 and convection is likely to occur above these values. The mantle Rayleigh number can be simply estimated using glacier isostatic rebound for mantle viscosity. Its value is usually in the order of 10^6 and explains why mantle is convecting at regional scale.

Dimensionless numbers are well used by the geophysicists for their usefulness as they permit to characterize regimes and heat transfer modes without requiring a full model of Earth's mantle. Rayleigh number is commonly used for convection but two other dimensionless numbers are also important in heat transfer science.

The Prandtl number (Pr) is defined as the ratio of viscous diffusion to thermal diffusion rate.

$$Pr = \frac{\nu}{\alpha} = \frac{Cp\mu}{\kappa}$$

Where ν is the kinematic viscosity, α thermal diffusivity, Cp specific heat, κ thermal conductivity and μ dynamic viscosity. This number is in the order of 10^{25} for the mantle meaning that the momentum diffusivity dominates the behavior. Large Prandtl number indicates that convection is more efficient than conduction. This number controls the thickness of the thermal boundary layers of the mantle.

The third important dimensionless number to constrain mantle heat transfer is the Nusselt number. This dimensionless number is the ratio of convective to conductive heat transfer across a boundary.

$$Nu = \frac{total\ heat\ transfer}{conductive\ heat\ transfer} = \frac{hL}{\kappa}$$

Where h is the convective heat transfer coefficient of the flow and L the characteristic length. Nusselt number characterizes the type of flow with laminar characteristics for Nu close to 1 and turbulent flow for values above 100. This number is particularly useful for the study of thermal boundary layers.

(3) Radiative

Earth's mantle minerals are electrical insulators, heat transfer is also diffused radioactively by photons which can be represented by an effective thermal conductivity κ_{rad} that can be calculated from the InfraRed spectrum. Radiative transfer occurs through any transparent or partially transparent medium, which is true for most of minerals but not for metals. The energy transfer is made by photons in electromagnetic waves because thermal radiation is a direct result of random movements of atoms and molecules. The motion of these charged particles induces the emission of the electromagnetic wave which is able to carry the energy out of the middle. The thermal radiations involve grain to grain progressive absorption and re-emission of photons directed by the temperature gradient of the medium. The radiative transfer is described by the Stefan-Boltzmann equation from an object in vacuum based on blackbody emissions spectrum.

$$Q = \sigma \epsilon T^4$$

Where Q is the heat flux, ε is the emissivity (1 for blackbody), σ is the Stefan-Boltzmann constant and T is temperature.

However, the radiative transfer in the laboratory experiments, whose are submitted to steep temperature gradients, can also involves a special kind of radiative transfer which does not exist in the nature: the ballistic photons (can also be found under the name of direct or boundary-to-boundary photons). Ballistic photons are produced from the source (heater or laser) and are directly transferred to the probe/thermocouple and warm it with minor or without participation of the sample medium.

Radiative transfer is temperature and frequency dependent and it also depends on three different length scales: the particle size, the distance of photon absorption and the distance of significant temperature change (Fig. I.22). Photon mean free path is important and defines if radiative transfer is diffusive or direct. It depends on the optical conditions, where thick conditions are required to be diffusive (mantle case) or direct if optically thin conditions are present (experiments). The average mantle grain size is estimated to be around 1 mm, the scattering of light for such a grain size should vanish at distances between 1 and few hundred meters with no absorbance for typical temperature gradient of < 10 K/km. In the mantle, the emitted light from a grain should not reach another grain with a temperature difference of 1 K (given the gradient). For this reason, direct or ballistic radiative transfer is not possible and photon transport is diffusive by grain to grain process. The diffusive radiative transfer can be estimated by IR spectra of the considered phase is frequency dependent (Goncharov et al., 2008; Hofmeister, 2014, 2007).

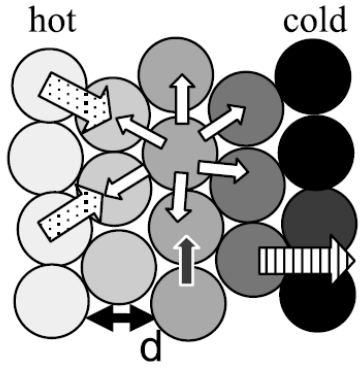

Figure I.22 Photon diffusion in a grainy medium with grain to grain transfer. According second principle of thermodynamics only the net flow is counted (stripped arrow). From Hofmeister (2014).

The quantity of light crossing a sample at any frequency can be expressed in function of the sample thickness (d) and the true absorption coefficient ($A(v)$):

$$A(v)d = -ln\left[\frac{I_t(v)}{I_0(v)}\right] + 2ln[1 - R(v)]$$

Where I_0 is the intensity entering and I_t is the intensity of light exiting the crystal. R is the reflectivity, the ratio between reflected intensity and entering intensity (I_R/I_0), it can also be expressed in function of the refraction index (n) in case of weakly absorbing spectral regions $R = (n-1)^2/(n+1)^2$. We can note that if additional scattering can be present (defects, boundary effects…) A should be treated in consequence (baseline of the spectra). Optical thickness can considered in function of $A(v)d$ term with thin medium for values < 1 and thick for values > 2, the difference of optical thickness can be translated by an important difference in transmitted amount of light with > 36% thin and < 14% for thick conditions.

Radiative heat transfer under diffusive (thick) conditions can be modeled by the commonly used mean free gas model (Hofmeister, 2014). The energy and the intensity of the radiated light can be obtained from Planck (1914) blackbody functions:

$$e(v) = 4\pi n\, I_{bb}/c$$

$$I_{bb}(v) = \frac{2hv^3}{c^2}\left[\frac{1}{exp\left(\frac{hv}{k_bT}\right) - 1}\right]$$

Where e is the energy density and I is the intensity of the blackbody. The emission power can be related to the emissivity (ε) and reflectivity (R):

$$\xi = (1 - R)\varepsilon I_{bb}$$

In the mantle, each grain is a source of radiation. Emissivity can also be retrieved from Kirchhoff's law of dielectrics:

$$\xi = 1 - exp\left(-dA(v)\right)$$

The mean free path (Λ) is controlled by both scattering and attenuation and depends on the grain size (d):

$$\frac{1}{\Lambda} = \frac{1}{d} + A(v)$$

Thus using the Clausius' kinetic of gas model can be applied to diffusion of photon:

$$\kappa_{rad,diff} = \frac{1}{3}\int_0^\infty u\Lambda C_v dv$$

Where *u (c/n)* is the phase velocity. A new general equation was provided by Hofmeister (2014) for calculation of diffusive radiative thermal conductivity which can be simplify according the case considered (see the reference for further discussion):

$$\kappa_{rad,diff}(T) = \int_0^{\infty} \left[\frac{d}{1+dA(v,T)}\right] \frac{c}{n(v,T)} \frac{\partial}{\partial T} \left[(1-R)\left(1-e^{-dA(v,t)}\right) \frac{8\pi n h v^3}{3c^3} \frac{1}{e\left(\frac{hv}{k_B T}\right)-1}\right] dv$$

c) Experimental constrains on minerals and rocks thermal diffusivities and conductivities

The characterization of thermal properties of mantle in the P-T conditions of deep mantle requires significant experimental work. This work started with the pioneer work of Birch in the 20th century, Eucken (1911) and Bridgman (1924). It was then followed by several generations of researchers from both condensate matter physics and Earth science communities. Several techniques were developed in order to constrain thermal conductivity and thermal diffusivity of single phases or polycrystalline rocks. The first observation is that measuring these parameters is not an easy task. Since more than 50 years, significant improvements were made into the understanding of the upper mantle phase's thermal properties but measurements at conditions of deep upper mantle and lower mantle remains exceptional and important extrapolations are nowadays are still current.

The data table I.3, presented under, highlights the increasing number of studies on thermal properties associated with the development of more complex techniques allowing a much wider exploration of P and T space. Despite early developments in the early 70's, most of the experimental works on geological materials were conducted since 2000. The recent apparition of diamond cell techniques associated to laser heating and thermal emission monitoring allowed very different approaches than measurements in conventional high pressure devices such as multi-anvils apparatus.

This table highlight that most of common minerals have been quantified over a significant P and T range and various techniques. Rock quantification have been very limited too few peridotites and crustal rocks and limited P-T conditions. Glasses and melts have only been recently investigated (Hofmeister et al., 1999; Romine et al., 2012) at RP-HT conditions. Most of these data obey to simple 1/T law as suggested by Debye model (Hofmeister and Brandlund, 2015).

Table I.3, non-exhaustive list of thermal diffusivities studies with their associated techniques, P and T ranges and measured sample until 2016.

Phase(s)	P (GPa)	T(K)	1st Author	Year	Method
-	RP		Parker	1961	Flash
MgO	RP	Cryogenic	Slack	1962	Steady state
Ol (Fo,Fa), NaCl	5	1300	Fujisawa	1968	Angström
Gt,Qz	RP	823	Kanamori	1968	Angström
Qz, basalt, sepentinite	RP	RT	Kanamori	1969	Angström
Gt	RP	Cryogenic	Slack and Oliver	1971	Angström
Ol, Opx	RP	723	Kobayashi	1974	Angström
Ol(Fo92, SC)	RP	Low T	Schärmeli	1982	Thin wire
MgO	RP	RT	Andresson and Bäckström	1986	Two-strip
Orthoclase	RP	Cryogenic	Cahill	1992	Radial
Silica glass	9	1300	Katsura	1993	Angström
Ol, Opx, Gt	RP	RT	Chai	1996	Picosecond spectroscopy
MgO	5	1500	Katsura	1997	Angström
Orthoclase	RP	300	Höfer and Schilling	2002	RHTM
Ol, Gt	8.3	1100	Osako	2004	Pulse
Ol, Wd, Rg	20	1300	Xu	2004	Angström
Ol, peridotite	RP	1400	Gilbert	2005	Flash
Ol, Qz, NaCl	RP	1200	Hofmeister	2005, 2008	Flash
Ol (% Fo)	RP	RT	Petermann and Hofmeister	2006	Flash
Pv, Fp	133	800	Goncharov	2008	IR Krad only
SiO2 polymorphs	RP	1273	Branlund and Hofmeister	2008	Flash
Ablite, feldspar, pyroxene glasses and melts	RP	1600	Hofmeister	2009	LFA
MgO	32	RT	Goncharov	2009	IR + pulse
Muscovite	24	RT	Hsieh	2009	Thermoreflectance
Pv	125	?	Goncharov	2010	Pulse DAC
Pv compound	RP	1800	Hofmeister	2010	Flash
MgO, NaCl, SrTiO3	RP	RT	Hofmeister	2010	Flash
Mg(OH)2	57	RT	Ohta	2010	Thermoreflectance
Pv, Fp	26	1300	Manthilake	2011	Angström
Pv, PPV	144	RT	Ohta	2012	Thermoreflectance
Ryholite glass melt	RP	1650	Romine	2012	LFA
Archean rocks	RP	1273	Merriman	2013	Flash
Dense silicate melt	85	RT	Murakami	2014	IR+ DAC
Silica glasses	RP	1273	Hofmeister	2014	Flash
Cpx glasses and melts	RP	1100	Hofmeister	2014	Flash
Pv	46	RT	Goncharov	2015	Pulse DAC
FeO6, FeCO3	73	1600	Lobanov	2016	Pulse DAC

Chapter II

Experimental and analytical methods

Chapter II: Experimental and analytical methods

1) General introduction

This chapter aims to present the experimental and analytical parts of this PhD, with a presentation of experimental methods and experiments realization. The main apparatus of this work: multi-anvil apparatus (MAA), will be presented as well as its technical implication such as pressure and temperature control and measurements. These points are an important pre-requisite for the thermal parts of this PhD, where important technical developments linked to heating system were made (chapters VI and VII). The geophysical *in situ* characterization methods will be then detailed and explained for sound velocity, electrical conductivity and thermal diffusivity measurements. In a second step, analytical techniques will be presented as experimental petrology heavily relies on experimental and post mortem characterizations. A succinct description of the main analytical apparatus used during this PhD will be made.

2) Experimental methods

a) Multi-anvil experiments

Multi anvil apparatus (MAA) is the main tool used during this PhD and the angular stone of our works. This section aims to summarize its principles together with a brief historical description. More details can be found in the recent eloquent reviews of Liebermann (2011) and Ito (2007).

i) The multi-anvil apparatus (MAA)

Multi-anvil press is an experimental apparatus developed to carry high pressure and high temperature experiments keeping large volume samples (in the order of mm^3). This technique allows a relatively homogeneous heating in the sample chamber and a quasi-hydrostatic pressure for relatively wide range of conditions (pressures < 1-100 GPa and temperatures from 0 to 3000 K). The great adaptability of the MAA allows a full set of geometries and combination required by the different type of experiments and measurements. These experiments allow a wide scientific community: geoscientists, chemists and physicists, to better understand materials at extreme conditions. I often describe this apparatus as the “Swiss army knife” of experimental petrology in vulgarization talks to illustrate the variety of possible experiments. The increasing number of *in situ* and synchrotron techniques also reinforces this statement.

The Multi-anvil apparatus (MAA) was invented in 1958 by T. Hall (Fig. II.1). It differs from other presses, such as the so called “large volumes” apparatus (piston cylinder, belt and Paterson presses or Brigdman/Drickamer apparatus, *inter alia*), by a simple technical definition. The definition provided by Liebermann in 2011 is in agreement with original concept from T. Hall defining MAA as a “High pressure apparatus with more than one axis of loading and four or more anvils compressing sample”. This definition includes tetrahedral, cubic and octahedral anvils apparatus, which are still used today.

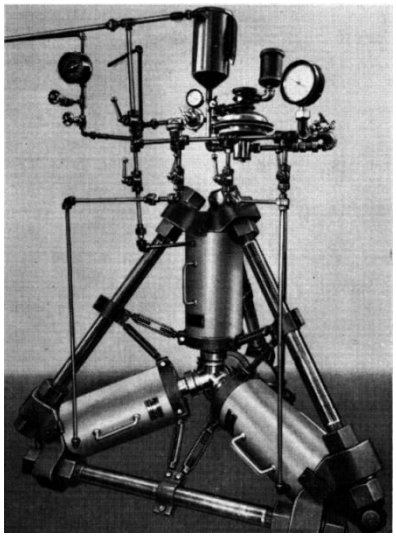

Figure II.1 The first tetrahedral MAA of Tracey Hall built in 1958 (image from Libermann, 2011).

The first works of Hall in 1958 and the following by Akimoto and Fujisawa in 1968, with their own version of tetrahedral apparatus build in Japan, are the pioneer studies. In the late 60’s, cubic anvil apparatus were developed simultaneously by Hall (1962 and 1967), Zeitlin and Brayman (1963) and Wakatsuki (1971, 1982), models derived from these works are used today in synchrotrons or with uni-axial and tri-axial differential ram MAA (also named DIA and D-DIA for deformation). The octahedral-anvils apparatus also named Kawai-type multi-anvils after their development by Kawai in the 70’s with japanese groups. The first publication of Kawai and Endho (1970) is one of the fundamental works in the multi-anvil history, because most of the modern apparatus uses the Kawai octahedral geometry (Fig. II.2). Kawai geometry uses split-spheres primary anvils made of steel divided by three plans making a cavity for 8 secondary anvils made of tungsten carbide, named the Kawai cell. The sphere was initially placed in an oil reservoir but later Kawai group attached it to steel guideblocks allowing vertical/uniaxial compression. Developed between 1970 and 1975, this kind of setup was adapted to high tonnage presses with examples of presses of 10000 tons and 5000 tons present at Osaka and ISEI Misasa respectively. The expansion of the Kawai type

MAA is greatly due to E. Ito from ISEI Misasa, as it is the case for our apparatus at LMV (Fig. II.2). Walker module, that equips the 1000 tons MAA at LMV, was developed in the early 90's (Walker et al., 1990 and 1991) to simplify and provide more affordable apparatus. This ring type guideblock also contributed to the widespread of MAA.

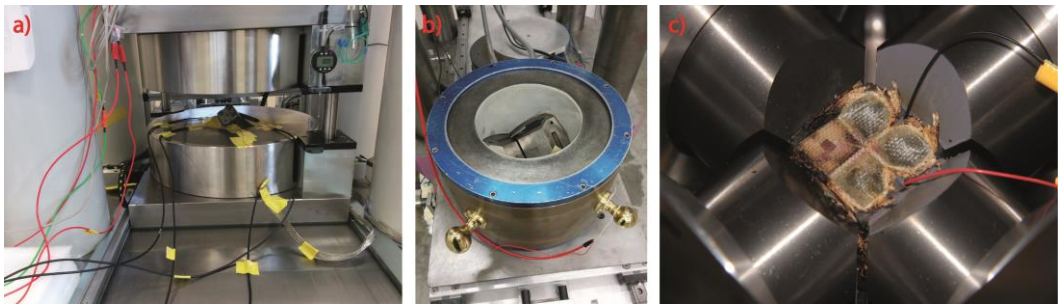

Figure II.2 Comparison of the different type of MAA. a) Kawai type MAA (1500 T at LMV) b) Walker module on a MAA (1000 T at LMV) c) DIA type MAA with primary anvils made of WC (1200 T press SOLEIL synchrotron PSICHE beamline).

The octahedral-anvil MAA is a technique that relies on a hydraulic system which is constituted by two opposite cylinders. The bottom cylinder is static and fixed on the apparatus, the top one can move vertically from open to close position (or the opposite). Air pumps are used to bring oil to a multiplying cylinder to pressurize oil that drives the upper hydraulic ram. The pressure is transmitted to a module that can be Walker, Kawai type (octahedral) (Walker et al., 1990; Kawai and Endho, 1970) or (D-DIA) (Fig. II.2). The modules form a cylindrical/spherical cavity which is filled by two stages of anvils. The first 6 primary anvils are made of steel and are disposed three facing up and three facing down. This geometry forms a cubic cavity in which are inserted the 8 secondary anvils made of tungsten carbide (or sintered diamond). This typical setup of two stages of anvils gave the name to the technique: multi-anvil press, furthermore, this geometry allows to transmit the vertical (uniaxial) force from the upper ram to tri-axial forces on the assembly with a quasi-hydrostatic pressure. For DIA and D-DIA types of multi anvils, different configuration can be used. In case of standard experiment, the 6 primary anvils made of WC form a cubic cavity in which are inserted the secondary WC cubes, whereas for deformation experiments, differential compression can be made by an independent control of each anvil (Fig. II.3).

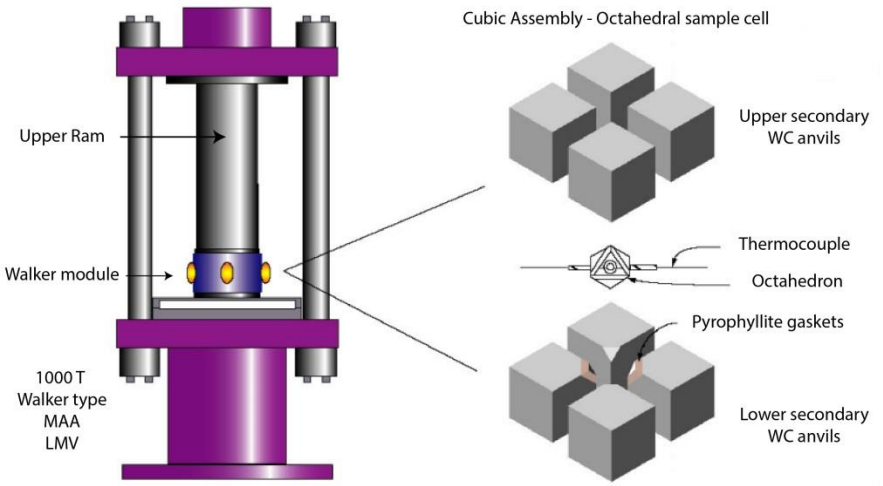

Figure II.3 Schematic view of the 1000 T Walker type MAA at LMV. Modified after Boivin (1998).

The MAA technique is particularly well adapted for material and Earth sciences studies, with the capacity to work from less than 1 GPa to 30 GPa with secondary anvils made of tungsten carbide but can rich up to 110 GPa with the recent developments of japanese groups using sintered diamond secondary anvils (Kunimoto and Irifune, 2010). The first apparatus developed were only able to reach limited pressures as 10 GPa for Hall tetrahedral's press (Hall, 1958). Then, with high tonnage presses (2000, 5000 and 10000 Tons), high pressures were reached up to 30 GPa in the end of 70's (Ohtani et al., 1979), but our increasing knowledge and technological progress lead recently the Misasa and Ehime group to surpass pressures of 1 megabar (Yamazaki et al., 2014; Kunimoto and Irifune, 2010), in more classical configurations (WC anvils) pressures up to 26 GPa have been performed using 1500 Ton press at LMV.

These performances place the MAA as one of the best tools to study high pressures and temperatures domains. The apparatus covers a large part of the Earth's P-T space and is probably the most powerful tool for upper mantle and uppermost lower mantle studies (Fig. II.4) as it keeps large sample volume, near hydrostatic pressure (see dedicated section) and a good control of temperature (in comparison of LH-DAC).

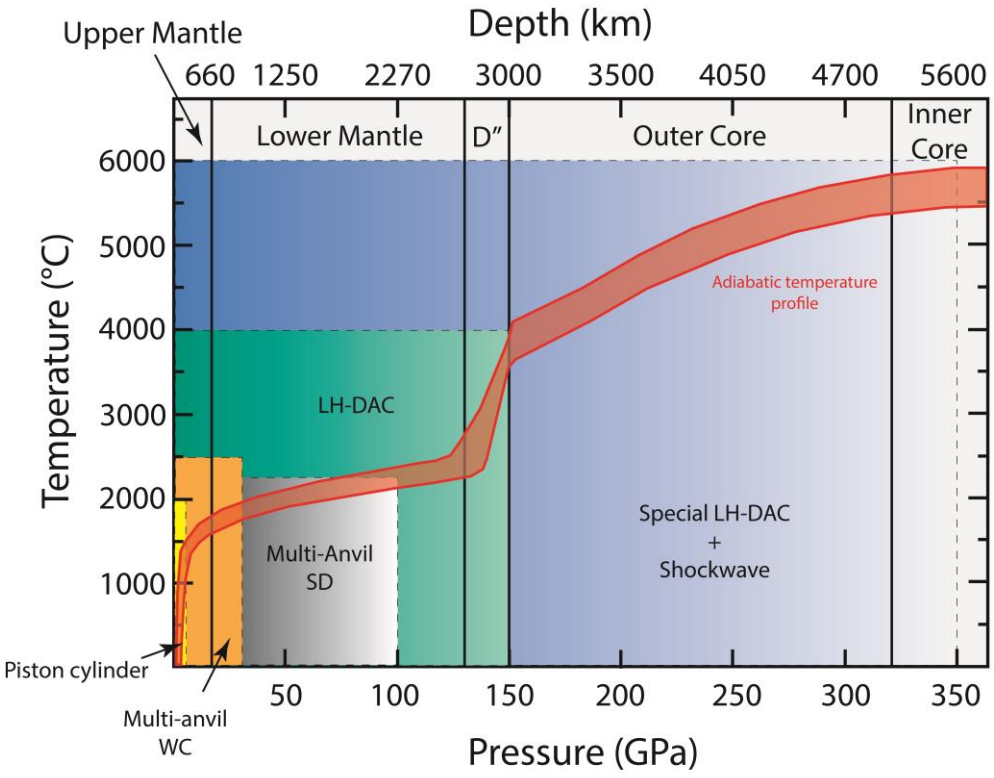

Figure II.4 Pressure vs Temperature plot with inner Earth conditions (red geotherm). The domain of study of each tool is represented in color. SD: sintered diamond, WC: tungsten carbide, LH-DAC: laser heated diamond anvil cell. The fields are based on highest measurements performed, however it is very difficult (for each tool) to reach both P and T limit in the same experiments.

ii) Multi-anvil assemblies (octahedral-anvil MAA)

The secondary tungsten carbide anvils are truncated in their inner edge to form an octahedral cavity. The truncated edge size can vary according the targeted pressure and sample volume. Obeying to the simple pressure (P) law in function of applied force (F) and surface of application (S):

$$P = \frac{F}{s}$$

The greater is the target pressure, the smaller has to be the truncated edge of the secondary anvil. Different types of couples of octahedron edge size and anvil truncated edge size ($1^{st}/2^{nd}$) are commonly used in multi-anvil apparatus: 25/17 for pressures < 5 GPa, 18/11 up to 10 GPa, 14/8 and 14/6 up to 20 GPa and 10/4 and 7/3 for pressures up to 30 GPa. 25/17 corresponds to 25 mm which is the size of the octahedron edge which is compressed by 17 mm edge size WC anvil. The central octahedrons always have a larger size than the truncated anvil to avoid contact between the anvils during the compression (break-up).

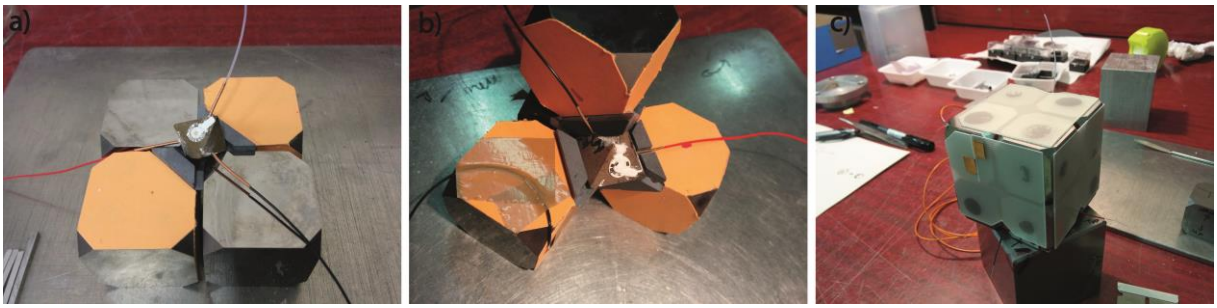

Figure II.5 Illustration of the assembly steps of an experiments, with a) the octahedron on the secondary anvils with gaskets and cardboard paper. b) fixation steps of the octahedron on the cube to make the cubic assembly, one can remark the notches in pyrophyllite gaskets to let the wires go out of the assembly. c) Final cubic assembly ready to be disposed in the primary anvils. The cubes are hold and insulated by epoxy sheets. The copper strips are for electrical current transmission between the two opposite anvils for heating.

The assembly is composed of the secondary anvils on which pyrophyllite gaskets are glued around the truncated edges. These gaskets surround the octahedron and prevent, with their extrusion during compression, the contact between the cubes. The gaskets are blocked laterally by cardboard paper which is pasted at the back of the gasket on the anvil side (Fig. II.5). The whole assembly, once the octahedron is inserted in the eight secondary anvils, is fixed by epoxy sheets before setting up into the primary anvil cavity. The epoxy sheets act as a structure that maintains 4 different cubes and also helps to keep the cubic geometry given that the cubes are not in contact. The epoxy sheets act as lubricant between primary and secondary anvils, and finally they allow, by insertion of copper strips, to heat the assembly.

Inside the octahedron the sample is inserted in a specific series of ceramics to transmit the pressure to the sample and heat it. The configuration of the inner parts of the assembly is adaptable, and optimized to the type of experiments which is realized. The assembly is composed of:

- An MgO octahedron, doped with 5% Cr_2O_3, acts as pressure transmitter middle.
- A Zirconia sleeve (ZrO_2). This part acts as a thermal insulator to reduce heat loss from the heater and prevent octahedron and cubes to reach high temperatures.
- A heater, which is composed of cylindrical resistance that will, while crossed by current, heat by Joule effect. The heater can be a metal: rhenium foils, graphite etc. or a semi-conductor ceramic as lanthanum chromite ($LaCrO_3$). The heater is connected to the two opposite secondary anvils by the heater itself (folded metal foils) or by a metal electrode: molybdenum or graphite.

- A MgO inner sleeve, inserted in the heater; acts as an electrical insulator for the sample and a pressure transmitter. The nature of this part can be changed (for example HBN in chapter III) to prevent chemical reaction between sample and its surroundings.
- The sample which is in the center part of the assembly. It is usually inserted in a capsule (Re, Au-Pd, graphite, MgO etc.) and is compressed top and bottom by ceramic pistons: MgO or Al_2O_3.
- A thermocouple is used to monitor the temperature. It is constituted by two types of metal wires brought in contact near the sample. The thermocouples commonly used in LMV are type C, they are composed of two wires of W-Re alloy (5% Re and 26% Re). The thermocouple is insulated from the heater by the MgO inner sleeve and is often inserted in 4 holes alumina/mullite piston.

The assemblies developed for *in-situ* measurements are less common and are adapted for the specific requirements of each measurement. For example, electrical conductivity assemblies need to be optimized for electrical insulation of the sample and connect electrodes around the samples. Details about each assembly are given in the dedicated method sections and chapters. A very nice work to elaborate standardized assemblies have been performed by Leinenweber et al. (2012), and worth being an inspiration for more standardized experiments allowing a better reproducibility between laboratories.

iii) Pressure in Multi-anvil experiments

The pressure generation and apparatus characteristics have been described in the parts above. However, one of the main challenges of experimental petrology is the control of pressure during the experiment. In opposition to temperature, which can be followed by thermocouples, pressure can't be monitored during experiments (except with synchrotron radiation facilities) and has to be calibrated prior. Indeed, the relationship of applied press force to pressure in experiment is not easy to calculate forward as it depends on the press characteristics and tuning as well as the material used (type of secondary anvils, with differences on each brand) and the assembly (size, materials, gaskets etc.). The high pressure groups calibrate their instruments with experiments, thanks to known phase transition and phase diagrams of different compounds that can be estimated *in situ* or *post mortem*. The pressure calibration can be performed with metals transitions: Bi I-II, Ba I-II, Ba II-III, ZnTe I and II, ZnS, GaAs, GaP as well as silicate phase transition: quartz and olivine multiple transitions, GaGeO3 compound. They allow covering a wide range of anchor points to make

calibration curves (from 1 to > 20 GPa). The transitions have a significant temperature dependence (depending Calpeyron's slope) and calibrations are usually made both at room temperature and high temperatures. Some works nicely details the pressure (and temperature) calibration of MAA: Frost et al. (2004), Leinenweber et al. (2012) and Knibbe et al. (2018).

At the LMV, multi-anvil presses were calibrated by the experimental petrology team (< 2010) for different assemblies sizes. Because the material used in other types of experiments are almost the same (in particular WC cubes of a given trademark, MgO octahedron and gaskets), the calibration should apply to all of our assemblies without important deviations. Calibrations were made at room and high temperatures (1200 to 1400°C) to better constrain the effect of temperature. Our apparatus were calibrated with coesite/stishovite, GaGeO3, ZnS, olivine-wadsleyite and wadsleyite-ringwoodite transitions both low and high temperatures (Fig. II.6). The relation of cell pressure versus loading force is then established and can be used as calibration for a given cell assembly. The calibration is almost linear for large assemblies. However, it becomes more nonlinear at very high pressure and using smaller ones. This calibration covers the entire range of pressure allowing constraining pressure with a precision better than 0.5 GPa in our experiments.

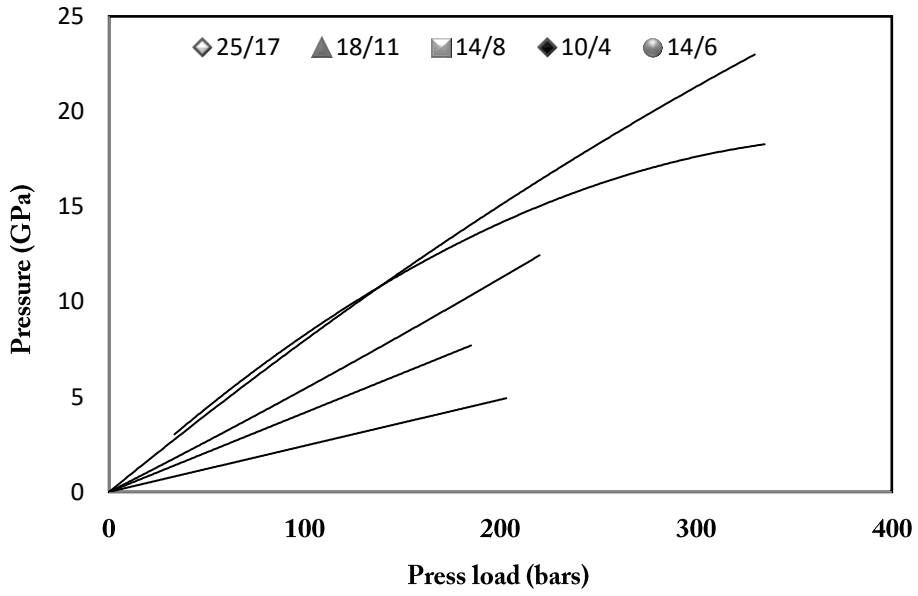

Figure II.6 Multi-anvil calibration at the LVM for different types of assemblies as a function of press load. (Personal communication from Manthilake).

Pressure control in MAA allows a somewhat fine exploration of the pressure range of Earth's upper mantle. However, the comparison of the experimental data to natural systems encompasses the assumption that generated pressure is hydrostatic. Several studies tried to

assess the pressure gradients and estimated the strain tensor for different kind of apparatus (Yagi et al., 1975; Li et al., 2004, Libermann, 2011 and references therein). On this aspect, the MAA is one of the most hydrostatic tool for mantle pressures range with pressure gradient that are not exceeding 0.1 GPa in the sample cell as well as quasi null deviatoric stress.

iv) Temperature in Multi-anvil experiments

Along with considerations on pressure, the generation, the control and the accuracy on temperature during MAA experiments is a very important point. In fact, considerations on temperature during the experiments are even more important for our *in situ* experiments and are the basis of thermal diffusivity determinations. Despite recent technical improvements, estimate properly the exact temperature of multi-anvil experiments is a tricky point.

(1) MAA heating system configuration

First, the heat generation part has to be carefully thought during the building of the heating system as well as the assembly design for each requirement. The heating system must have different electrical transformers allowing switching between different configurations for metal or ceramics heaters to ceramics (see hereafter). The system can be controlled manually by adjusting the values, with Eurotherm devices or homemade software such as LabVIEW programs developed at LMV-OPGC. The quality of the electronic part is not negligible, as it allows fine control and reactive apparatus (small increment of voltage/intensity for small temperature steps). In addition, a modulator can be inserted in the device for special requirements: ramps, oscillation etc. This apparatus is used to perform Angström method measurements. The heating system frequency must be significantly higher than oscillations made by the modulator. The heating system of the MAA must be easily tunable and accessible for both new developments and modifications.

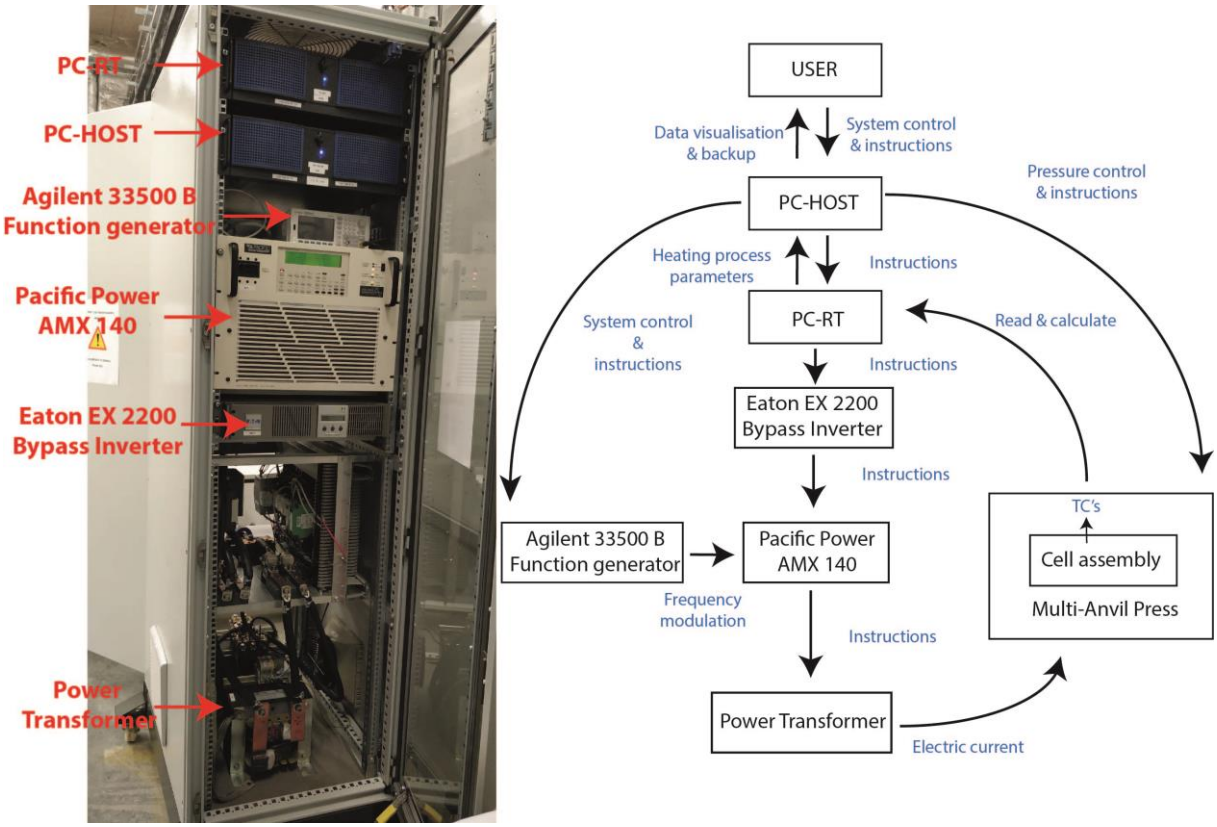

Figure II.7 LMV 1500 Tons multi-anvil press heating system. Photography of the electrical cabinet with the different constituent of the system is given on the left. On the right, a schematic view of the system and its operation.

At LMV the heating system was build thanks to LMV and OPGC laboratories, it is succinctly presented in the figure II.7. It is composed of a series of 3 electric transformers (64A/62.5V, 7.8V/512A and 31.3V-128A) used depending on the furnace type. There are controlled by a Pacific AMX 140 smart source which allows controlling the delivered power, current intensity or voltage. The Pacific source is connected to an Eaton (EX2200) bypass inverter which ensures a continuous delivery of electrical current (no clipping) to the transformers. The pacific source can also be controlled by an Agilent function generator (Agilent 33500B series) to modulate the frequency of the power source. In fact, the frequency of the Pacific source can be varied from 1 KHz to 100 Hz but requires an external modulation to produce long period signal (~Hz) required for Angström method. The Pacific source and Agilent function generator are connected to two computers. First, the PC-RT is only dedicated to the control of the heating system and the acquisition of temperature. It controls the heating parameters such as instruction on current intensity and regulates the power supply. In the meantime, this computer reads the thermocouples values (from the electromagnetic force) and converts these signals into temperature applying the classical correction of cold junction temperature. Our system is in charge of 5 temperatures channels: 2 non filtered type C, 1

filtered type C and 1 non filtered type S thermocouples in addition to one additional thermocouple (type S) to measure primary anvils temperature. The PC-RT has no interface in addition to a low data storage capacity (it only calculates). Thus, it is controlled by a second computer named the PC-HOST which serves as an interface for the user to control the whole system, saves recovered data as well as control the pressure of the MAA. The PC-host is connected to the PC-RT via a GPIB cable which limits the speed of communication between the two computers (limited to 140 ms). The whole system is piloted by a LabVIEW interface developed by A. Mathieu. The LabVIEW programs allow the control of the whole system temperature and its regulation. An additional pane on the standard heating software was developed for the control of Agilent 33500b and allows the generation and the backup of thermal oscillation necessary for Angström method (see dedicated chapter).

(2) Experimental assemblies, the importance of heater type…

The choice and the design of the cell assembly is the crucial step for temperature control in the experiments. A clever design will result in a reduction of thermal gradients in the sample zone as well as minimizing heat loss. Depending on experimental requirements it can be various and must be adapted for targeted purposes:

- Metallic furnaces (rhenium) are convenient for *in situ* measurements such as electrical conductivity because they are thin (maximize sample volume) and they can be cut precisely by laser. They provide stable heating over the whole MAA pressure range and can reach temperature >2300°C. At the opposite, they are expensive and produce important thermal gradients. They also are sensible oxidizing conditions.
- Graphite furnaces are also commonly used for synthesis, element partitioning melting experiment etc. They are affordable, easy to machine and able to provide long and stable heating. They are stable to high temperatures (>2000°C) but moderate pressures (< 8GPa). The heat transmission is efficient and thermal gradient less important than in metal heaters. Molybdenum electrodes are often used to prevent material flowing.
- $LaCrO_3$ and ceramic furnaces are common pressures above 8 GPa. The drawbacks of $LaCrO_3$ are important, first the cost (REE are expensive) and is toxic. We observe the heating to be less controllable and stable than other heaters. Maximum reachable temperature is also lower than other heater types. As graphite, it also requires molybdenum electrodes.

Usually straight wall ceramic/graphite heaters are used. However, stepped furnace can be preferred. They imply making furnace from different pieces but permit to have thicker

walls around sample cell for a more efficient heating and a strong reduction of thermal gradients (Fig. II.8). Steeped wall furnace are commonly used for large assemblies (difficult to machine for 10/4 and 7/3) and used when temperature control really matters. The use of straight or stepped furnaces changes the power versus temperature relationship and temperature calibration have to be done for each type of assembly (if performed without thermocouple).

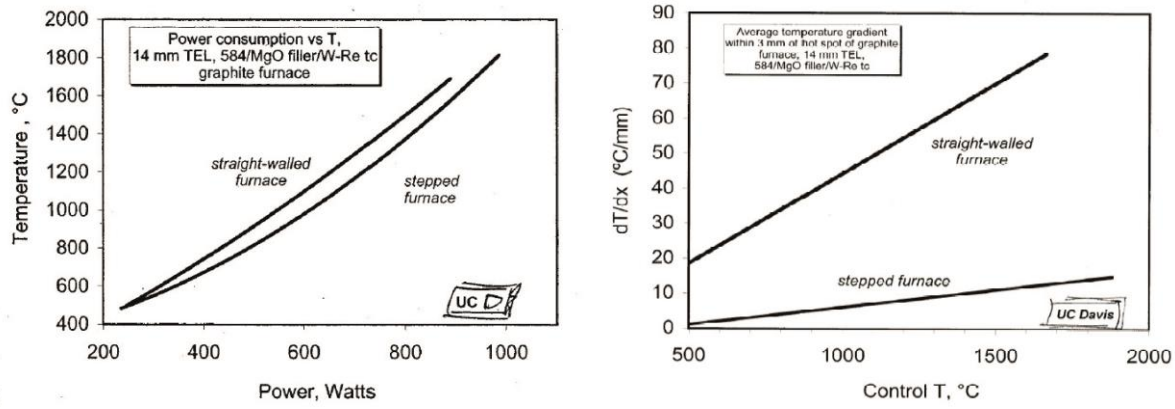

Figure II.8 a) Illustration of power vs temperature curve estimate for stepped and straight furnaces for graphite type in 14 mm truncation geometry. b) Estimations of thermal gradient with a 3mm hotspot in graphite furnace for 14 mm truncation. Graphs from C.E. Lesher, UC Davis, COMPRES 2005 workshop.

(3) Thermal gradients and their modeling

Thermal gradients are one of the major problems of the high pressure experiments. Natural thermal gradients have been estimated to be around 1°C/km, whereas in experiment it can be up to tens of °C/mm or even greater. In MAA, thermal gradients are not very easy to measure because the control of thermocouple position is not accurate and that TC can't be moved during an experiment. The gradient can be measured via different runs of calibration or modeling. Gradients using melting technique or geothermometers such as enstatite/diopside (Gasparik, 1989) revealed gradients up to 200°C in 2 mm capsules (100°C/mm).

The thermal gradients were estimated in our experiments using the model from Hernlund et al. (2006) and corrected for the thermocouple offset to the center of the sample. The software allows drawing the assemblies in an interface with a limited choice of materials (rhenium replaced by platinum) and calculated the gradient at a desired temperature. No pressure dependence is available for thermal conductivities whereas, as seen in experimental calibration, pressure changes heater power/temperature curve as well as TC EMF. The results must also have an uncertainty in the order of 5-10°C at moderate temperature and pressure (> 10 GPa and 1300°C) and probably higher above.

The model drawn is a quarter of the real assembly as its axis is symmetrical along the cylinder axis and has a mirror plane perpendicular to it. The position and the size of the parts are given from our assembly's dimensions and corresponding materials selected. Anvils positions are also represented because they act as strong heat sink from the assembly and boundary conditions are important. For the simulations performed with 14/8 geometries, thermal gradients in the sample (~1.2 mm large for 1 to 1.5 mm thickness) are small: in the order of 5 and up to 10°C at high temperatures: 30°C/mm vertically (1200°C) and 9°C/mm radially (800°C) (Fig. II.9). For our larger assemblies (18/11 and 25/17) gradients are greater but mainly due to the larger size of the sample e.g 15°C/mm vertically in 25/17 assembly (1200°C) (Fig. II.10).

(4) Thermocouples

Temperatures in the high pressure assemblies are measured using thermocouples. It consists in measuring the electromagnetic force (EMF), under the form of a tension in V, between two metallic wires of different composition forming an open wire (no current). Temperature is estimated using parameterized calibration of EMF vs temperature.

The accuracy of thermocouple temperature measurement relies on several factors. Uncertainties on supplier calibrations are often only considered. However, the pressure dependence of the electromagnetic force is never given and poorly taken in account. Getting and Kennedy (1970), reported for type S thermocouples differences up to 300 μV at pressure of 5 GPa and high temperatures (Fig. II.11) which can be translated into a difference up to few 10's of degrees. A potential dependence of thermocouple EMF on oxygen fugacity can't be ruled out as metals are often sensible to oxidation. However, this potential effect is very poorly documented for high pressure devices.

A strong issue to thermocouple used in multi-anvil experiments has been also pointed-out by Nishihara et al. (2006), where the effect of copper coils has been found to lower considerably the measured EMF. According the study, the effect of coil, which is more conductive than thermocouple wires, imply underestimation of temperatures up to 100 to 150 K in comparison with thermocouples without coils at high temperatures (1600-2000 K). The corrections of our data, if the effect is confirmed, has to be performed and temperatures have to be shifted high according the trends (experiment or theoretical) given by Nishihara et al. (2006).

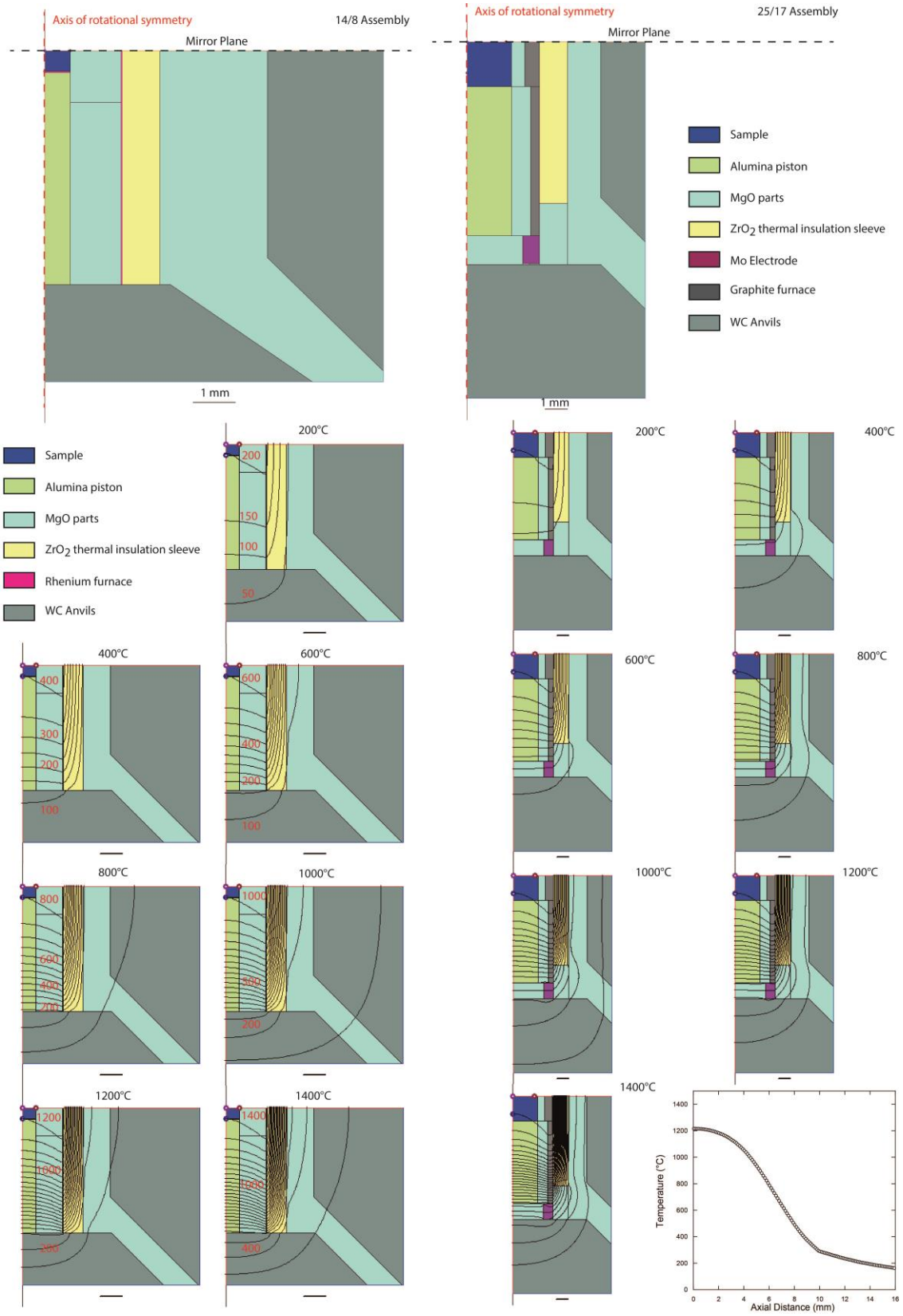

Figure II.9 and II.10 Results of the thermal gradient modeling for 14/8 and 25/17 geometry with rhenium and graphite furnaces, respectively. The detailed drawing with color legend is given atop; results of models at different temperature are displayed. Profile displayed for 1200°C simulation parallel to the assembly.

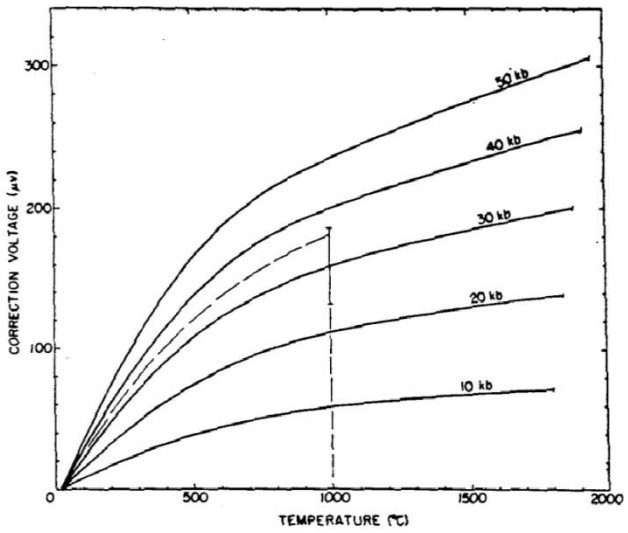

Figure II.11 Pressure dependence of the electromagnetic force on type S thermocouple. Values obtained at 20°C, dash line indicate the upper limits of the experimentally explored region. From Getting and Kennedy (1970).

The second problem of thermocouples is the exactitude of their indications. In fact, we observed while having experiments with similar assemblies that the power-temperature trend is not strictly identical for all of our experiments. These deviations are due to the extrusion/offset of the thermocouple junction. This deviation from assembly's center is translated to a lower temperature measurement at equivalent power due to thermal gradient. Making a calibration requires ensuring none of the calibrating experiment underwent offset compared to the hottest central point. This is difficult to prove but can be checked in *post mortem* analyses. If thermocouple is placed at the back of a sample, temperature should be corrected for the offset (half sample thickness if centered) using thermal gradient estimation from modeling software (see above).

Here are given some Power vs Temperature curves measured during our and LMV colleges experiments (Figs. II.12 and II.13). These values are not corrected from temperature gradients and offset position to illustrate the observed variation. The graphs highlight trends that are followed by the majority of the experiments, but little offsets due to sample size variations and assemblies differences are observed. Some, such as M374 in Figure II.12, are typical patterns due to TC offset by extrusion. Heating power vs temperature profiles for 25/17 in thermal diffusivity measurements are provided in the dedicated section (Appendix D).

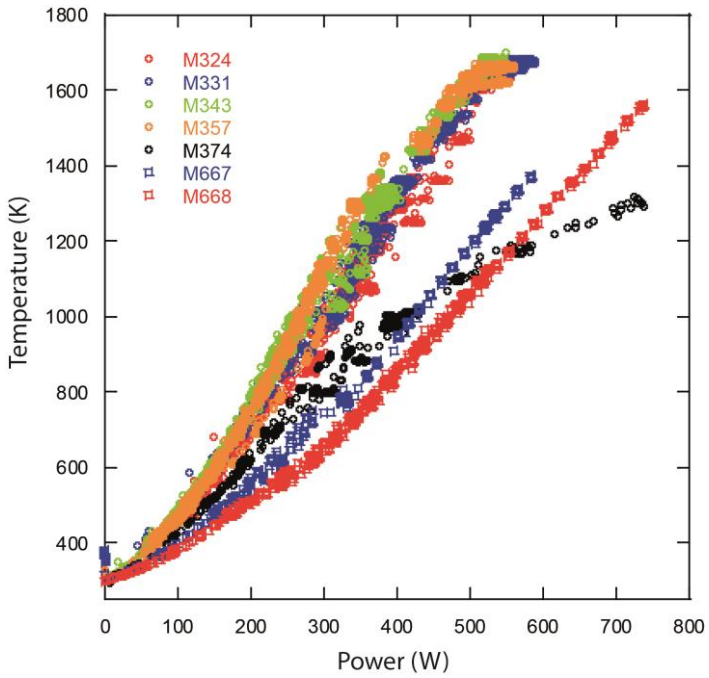

Figure II.12 Heating profiles of our 18/11 rhenium furnace electrical conductivity experiments on 1500T Kawai type MAA. Circle experiments were performed at 2.5 GPa. M667 and M668 were performed at 6 and 9 GPa respectively. The slope variation is due to pressure effect on heater heating efficiency as well as ceramics behavior

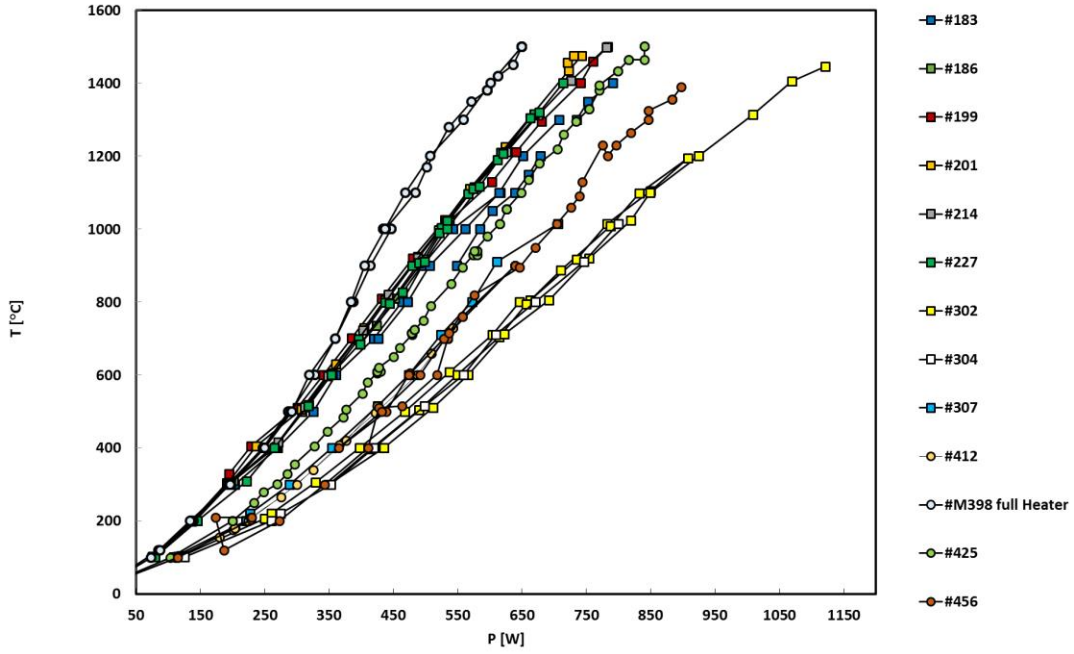

Figure II.13 Heating profiles of our 14/6 rhenium furnaces experiments. The squared data points are from experiments of G. Pesce PhD work, they are electrical conductivity experiments, various pressures. Circle are our data and are electrical conductivity + sound wave velocities experiments at 12 GPa, they differ slightly from EC experiments with a probably lower heating efficiency (different sample capsules, pistons, sizes etc.).

b) Geophysical *in situ* measurements in HP-HT multi-anvil experiments

In this section each experimental method for geophysical *in situ* measurement during MAA runs will be introduced. Acoustic waves, electrical conduction and thermal transfer techniques and their adaptations to multi-anvil apparatus will be given for solids and molten rocks characterizations. As the main techniques used during our experimental studies, specific considerations for our systems will also be given in these subsections.

i) Laboratory characterization of elastic properties

Over the past 50 years, the elastic properties of a various set of minerals and their high pressure phases have been studied. To do that, a set of different physical techniques were used from static and shock compression measurements as well with various spectroscopy techniques. These techniques can provide measurement of numerous elastic parameters such as bulk and shear modulus or more complex data such as elastic tensor etc.

However, most of the techniques do not measure directly seismic wave velocities and are in several cases not performed at mantle conditions (P, T) (Li and Liebermann, 2007). Their extrapolation via finite strain theory models and equation of state are required for their comparison to seismologic data. On the other hand several techniques based on physical acoustics have been developed to measure directly the elastic behavior of mantle minerals. Four main techniques have achieved significant results in the Earth's science field: Resonant Ultrasound Spectroscopy (RUS), Impulsive Stimulated Light Scattering (ISLS), Brillouin spectroscopy and ultrasonic interferometry (over various frequency ranges). Among these techniques, ultrasonic spectroscopy and X-rays techniques are the most used in geophysical sciences. In this PhD work, only ultrasonic interferometry was used due to its well established protocol (Chantel, 2012) and successful adaptation to LMV 1500 ton multi-anvil apparatus (Chantel and Manthilake).

Ultrasonic interferometry methods have been extensively used by mineral physics community since their development in the 50's by McSkimin (1950). Several types of frequencies can be used between kHz, MHz and GHz. The frequency choice is governed by two main factors: the excitation frequencies of piezoelectric transducers and the sample size. Indeed, the acoustic wavelength should be small compared to sample size, by consequence very high pressure studies requires small samples. For LH-DAC, GHz ultrasonic interferometry has been developed (Jacobsen et al., 2004; Reichmann and Jacobsen, 2004;

Kantor et al., 2004) using different type of transducers such as sapphire and YAG buffer rods with different metal sputtering (Freitas and Yoneda, unpublished, ISEI summer school, 2016). For multi-anvil experiments, MHz ultrasonic interferometry techniques are used. Two main methods coexist: pulse echo overlap (PEO) (Papadakis, 1990; Kono et al., 2012) and phase comparison methods (Rigden et al., 1988). As phase comparison technique is not used at LMV, only PEO will be described.

(1) Pulse echo overlap

The pulse echo overlap, is a popular method used in acoustic velocity measurements for MHz ultrasonic interferometry. It relies on the transfer function of the measured echoes of the entire system: transducer, anvil, buffer rod and sample. The experimental setup is simple and can easily be transported (useful for synchrotron studies). It is composed of a waveform generator, which creates the initial signal, and sends it to the transducer. The transducer converts the signal and simultaneously records the reverberated echoes. This transducer conversion is recorded by an oscilloscope which is triggered by the initial signal. Then, the procedure is repeated hundred to thousand times to reduce signal noise ratio by stacking the signals and can be saved via oscilloscope's interface (Fig. II.14).

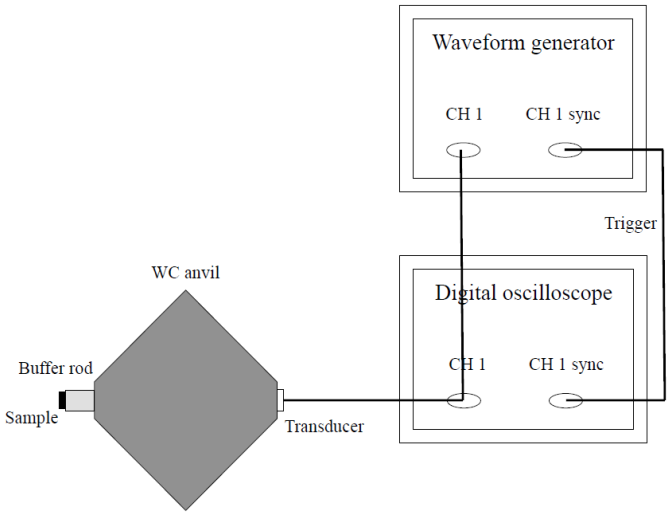

Figure II.14 Ultrasonic velocity measurement set-up used at the LMV and APS. Figure from Chantel, (2012).

Raw data acquired during the experiments usually have a quite high noise level and does not allow distinguishing very precisely the sample echo. The raw signal needs to be processed before correctly interpreted, making sound velocity measurements inappropriate tool for real time monitoring of *in situ* experiments (compared to electrical conductivity for example). The signal quality can however, be improved using an amplifier placed before the oscilloscope.

The signal (response function, *y(t)*) is a convolution of a transfer function (*h(t)*) and the stimulus function (*x(t)*). The transfer function estimation requires some important analysis that will be detailed in the following part.

In linear time invariant systems, which are the case of electrical systems but also simple seismological ones, time domain and frequency domain are linked by Laplace transforms. The convolution products of the transfer function and stimulus function can be obtained by multiplying Fourier transforms in the frequency domain.

For the relation in time domain:

$$y(t) = h(t) * x(t)$$

Becomes in frequency domain:

$$Y(f) = H(f).X(f)$$

With:

$$H(f) = \int_{-\infty}^{\infty} h(t)e^{-i2\pi ft}\,df$$

And:

$$X(f) = \int_{-\infty}^{\infty} x(t)e^{-i2\pi ft}\,dt$$

The stimulus function can be retrieved by preforming the inverse Fourier transform of *H(f)* limiting the frequency range from minimum and maximum frequencies ($f_{min} = f_c-\Delta f$, $f_{max} = f_c-\Delta f$) and considering a central frequency (f_c).

$$x(t) = \int_{f_c-\Delta f}^{f_c+\Delta f} X(f)e^{i2\pi ft}\,df = 2\frac{sin(2\pi\Delta ft)}{2\pi\Delta ft} = 2sinc(2\pi\Delta ft)$$

The response function (*y(t)*) is finally expressed:

$$y(t) = h(t) * x(t) = [LTI - system] * 2sinc(2\pi\Delta fT)$$

Several improvements allowed this technique to be probably the most adapted for mantle elasticity studies. Among them, the adaptation to the different types of multi-anvil apparatus and the use of synchrotron radiation allowed significant democratization of the technique. The synchrotron radiation is crucial because it allows monitoring changes of

sample length, estimate pressure, temperature and density in addition to the acoustic velocity measurements. The calibration of sample lengths and measurements of thermal expansion with these online experiments also permitted the realization of off-line measurements with length correction models (Chapter III). The recent introduction of dual mode transducers (see hereafter) to perform simultaneous measurement of P and S waves and improvement of electronics and mathematical treatments consequently improved the *in situ* technique (Li and Libermann, 2007).

(2) Pizeo-electric transducer

To generate acoustic waves at high frequency, piezo-electric transducers are used. Piezo-electricity is a physical property only occurring in crystals with crystallographic polar axis. The crystal can electrically polarize under the action of a mechanical stress, the corollary is also true (direct vs reverse piezoelectric effect) (Fig. II.15). Piezoelectricity is a quite common behavior in material as 32 crystal classes exhibit this behavior. Among them, some natural crystals have been widely recognized such as Quartz or Topaz, even if most of the known materials are (synthetic) ceramics.

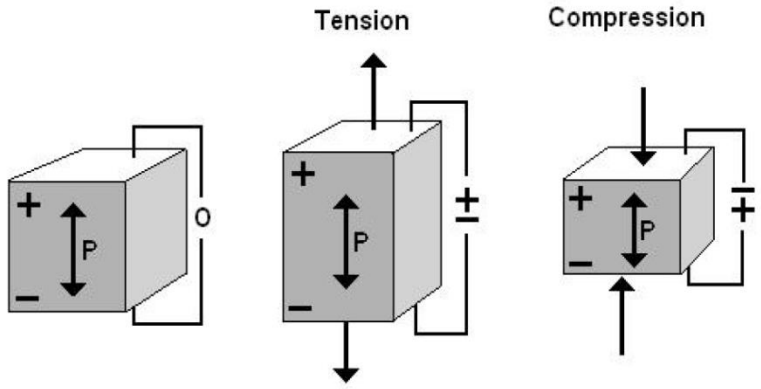

Figure II.15 The principle of piezo-electric effect on a crystal (converse geometry). Figure from Chantel, 2012.

Piezo-electric transducers are a chips cuts from a polar crystal in a specific manner (angle of cut) to produce compressional waves when electrical AC potential is applied. The most modern version of these piezo-electrics crystals can also produce shear and compressional waves at the same time (so-called dual mode transducers), whereas different crystals or conversion angles were used classically. The transducer maximum amplitude and signal efficiency is obtained at crystal resonant frequency.

In this PhD work, we used 10° rotated Y-cut $LiNbO_3$ dual mode transducers with a gold cover furnished by Boston piezoelectrics. Resonance frequency given by the supplier is 16.7

MHz for P waves and 10 MHz for S waves. AC field is applied at different frequencies of 30 and 50 MHz for measurement of P and S waves simultaneously (50 MHz for P wave and 30 MHz for S wave) to have excitation at ~2^{nd} and 3^{rd} (for 30 MHz) and 3^{rd} and 5^{th} (for 50 MHz) harmonics for P and S waves respectively. The transducers are then fixed on a corner of a polished secondary WC anvil. It is fixed using high temperature epoxy and welded to a coaxial cable that allows the connection to the wave function generator and oscilloscope for recording. The "transducer" anvil must be grounded to provide signal and anvil temperature should not excess 70° C because $LiNbO_3$ undergoes phase transition above this temperature and is not piezoelectric anymore.

(3) Sample fabrication of monomineralic and polycrystalline aggregates for acoustic wave velocity measurements

The sample fabrication for accurate measurements of sound wave velocity needs to be carefully considered in order to produce strong signal reflections and high signal to noise ratio. First of all, the attenuation was found to be a function of the grain size as well as the wavelength of acoustic signal (Mason and McSkimin, 1947). As our experiments are performed at almost constant wavelength (30-50 MHz, corresponding to a wavelength of 89-161 nm (50 MHz) and 149-269 nm (30 MHz) using PREM velocities at 70 km for P and S waves) grain size can be considered as the controlling factor of signal attenuation. Qualitatively Mason and McSkimin (1947) expressed attenuation *(A)* as a function of grain size *(a)* ($A = f(a)^2$). The grain size must be kept small and sample anisotropic. Anisotropy is favored by large grain size in sample (which can also be check via textural and EBSD analyses) and the ratio between signal wavelength and grain size must be above 10 (Lieberman et al., 1975). With a grain size of 1-20 microns in our experiments, the *l/a* ratio lies between 4.5 and 269 providing suitable conditions for elastic measurements.

In addition, possible boundary effect during measurements can occur. They commonly are presented as negligible for high aspect ratios (for a cylinder here, sample width/sample length). For that, sample aspect ratio around 1 or above are used to avoid any kind of boundary effect. The ratio between sample diameter and signal wavelength was also determined to necessarily be above 2.4 (Tu et al., 1955; Silaeva and Shaminan, 1958) in order to measure the longitudinal wave velocity in an infinite medium and not "reverberation" lowered velocity. In our case, the smaller samples had minimal diameter of 1.2 mm and the ratio can be estimated to be 4.46-13.41 ensuring optimal conditions for measurements.

Finally sample density must be very close to the theoretical value (99%) in order to avoid the presence of a too great porosity and micro cracks. Low sample density/high porosity will have two main effects. The first effect is the sample compaction during the high pressure and temperature experiment which is adding uncertainties on sample length (and possible movement in the cell assembly). Second, the measured acoustic velocities are usually lower than non-porous material. Finally, presence of important porosity will also enhance inelastic absorption in the sample. For these reasons, we synthesized our samples in prior experimental runs at the target pressure conditions and fairly high temperatures (> 1100 K) (Chapters III and IV).

ii) *Electrical conductivity measurement, visualization and results processing*

To measure electrical conductivity over a very wide pressure and temperature range (from crust to core), measurements setups have been developed for a wide variety of high pressure apparatus. Actual measurements are performed in routine on three of the most common high pressure devices: piston cylinder, multi-anvil apparatus and diamond anvil cells (DAC) but using the same technique: impedance spectroscopy. At LMV, impedance spectroscopy technique is performed using a SOLARTRON impedance spectrometer, frequency sweep technique is used and frequency ranges from 1 Hz to 1 MHz.

The complex impedance is defined similarly to the concept of resistance. Ohm's law described the ability of a circuit element to resist the flow of electrical current. The resistance (R) is then defined by the ratio between voltage (V) and intensity (I).

$$R = \frac{U}{I}$$

The use of Ohm's law is frequent in simple circuits. However, it only applies to ideal resistor, which resistance value is independent of frequency. Rocks, similarly to other real electrical circuits exhibit a more complex behavior and have a frequency dependent resistance. Impedance then replaces the concept of resistance, which also measure the ability of the system to resist the flow of an electrical current but is not limited by assumptions on frequency. The electrochemical impedance is measured by applying an AC current to the sample and estimating the current into it. Usually small currents are applied as excitation signal resulting into a pseudo linear response of the sample cell. The current response to a sinusoidal potential will be a sinusoid of the same frequency shifted in phase. The current signal can also be analyzed as a sum of sinusoidal function by Fourier series.

If we consider a sinusoidal excitation signal of the form:

$$U_t = U_0 sin\,(\omega t)$$

Where U is the electrical potential, t is the time and U_0 the amplitude at $t = 0$ and ω the angular frequency ($\omega = 2\pi f$ in rad/s) and f the frequency (Hz). The associated response in a linear system (or pseudo linear) is:

$$I_t = I_0 sin\,(\omega t + \varphi)$$

Where I is the amplitude (different from U) and is shifted in phase (φ).

The impedance Z can be defined similarly to Ohm's low:

$$Z = \frac{U_t}{I_t} = \frac{U_0 sin\,(\omega t)}{I_0 sin\,(\omega t + \varphi)} = Z_0 \frac{sin\,(\omega t)}{sin\,(\omega t + \varphi)}$$

Historically, the representation of $U(t)$ vs $I(t)$ forming the Lissajous figure on oscilloscopes was the accepted method for impedance measurements. However, using Euler relationship, potential and current response can be expressed as a complex number:

$$exp(j\varphi) = cos(\varphi) + jsin(\varphi)$$

Impedance can be written:

$$Z(\omega) = \frac{U}{I} = Z_0 exp(j\varphi) = Z_0\big(cos(\varphi) + jsin(\varphi)\big)$$

Or

$$Z(\omega) = Z' + jZ''$$

Where Z' and Z'' are the real and imaginary parts of impedance, respectively.

For rocks and mineral samples the Resistance-Capacitance (R-C) parallel circuit is conventionally used to determine electrical conductivity. In the Nyquist plot, X axis is represented by the real part of the complex impedance and the Y axis is the opposite of the imaginary part (Fig. II.16). The plotted data for simple R-C circuit (single time constant) make a semi-circle in which the vector $|Z|$ is the impedance and the angle with this vector is the "phase": $\varphi = arg(Z) = artan(Z''/Z')$. When the phase angle is infinite, the circle is at the origin, when it is 0° the sample resistance is equal to the real part of the impedance. The data

can also be represented in the Bode plot which displays the log of impedance and phase as a function of angular frequency (Fig I.14).

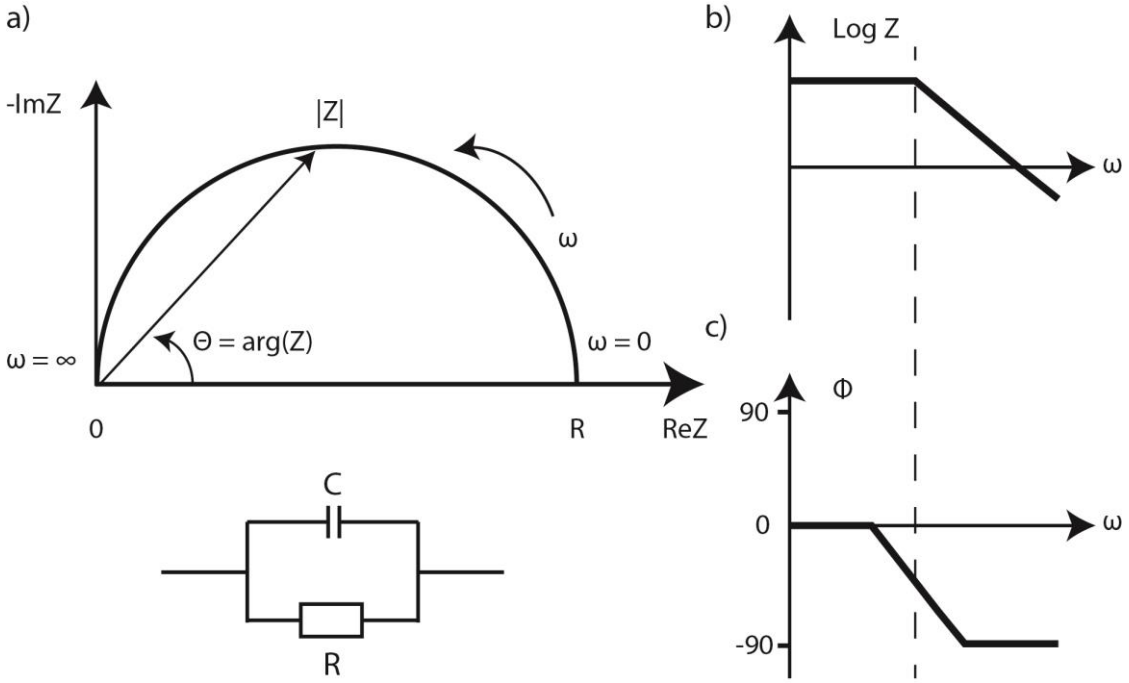

Figure II.16 a) Nyquist plot with impedance vector for a single time constant (R-C circuit, here under). Position of angular frequencies and phase angle are indicated. B) Bode plot for a single phase constant, log of impedance and phase angle are represented as a function of frequency for this simple theoretical case, such shape correspond to grain interior information in geological studies.

In reality, impedance spectra obtained in the Nyquist plot shows only parts of semi-circle as a function of temperature (decrease of the resistance with temperature). Several arcs in the complex plane can also be observed as the consequence of sur-imposition of different process: grain interior, grain boundary and electrode reaction observed for three successive arcs by Robert and Tyburcy (1999). The second and third arcs are not often seen in HP-HT experiments for dry solids. However, presence of fluids/melt or adsorbed moisture can be evidenced by the creation of a second arc, which can be modeled as a series of R-C circuits (series or parallel, non-unique solution) (Fig. II.17). Presence of adsorbed water is often highlighted by a second arc that is making a “tail shape” toward very low frequencies and not closing the circle.

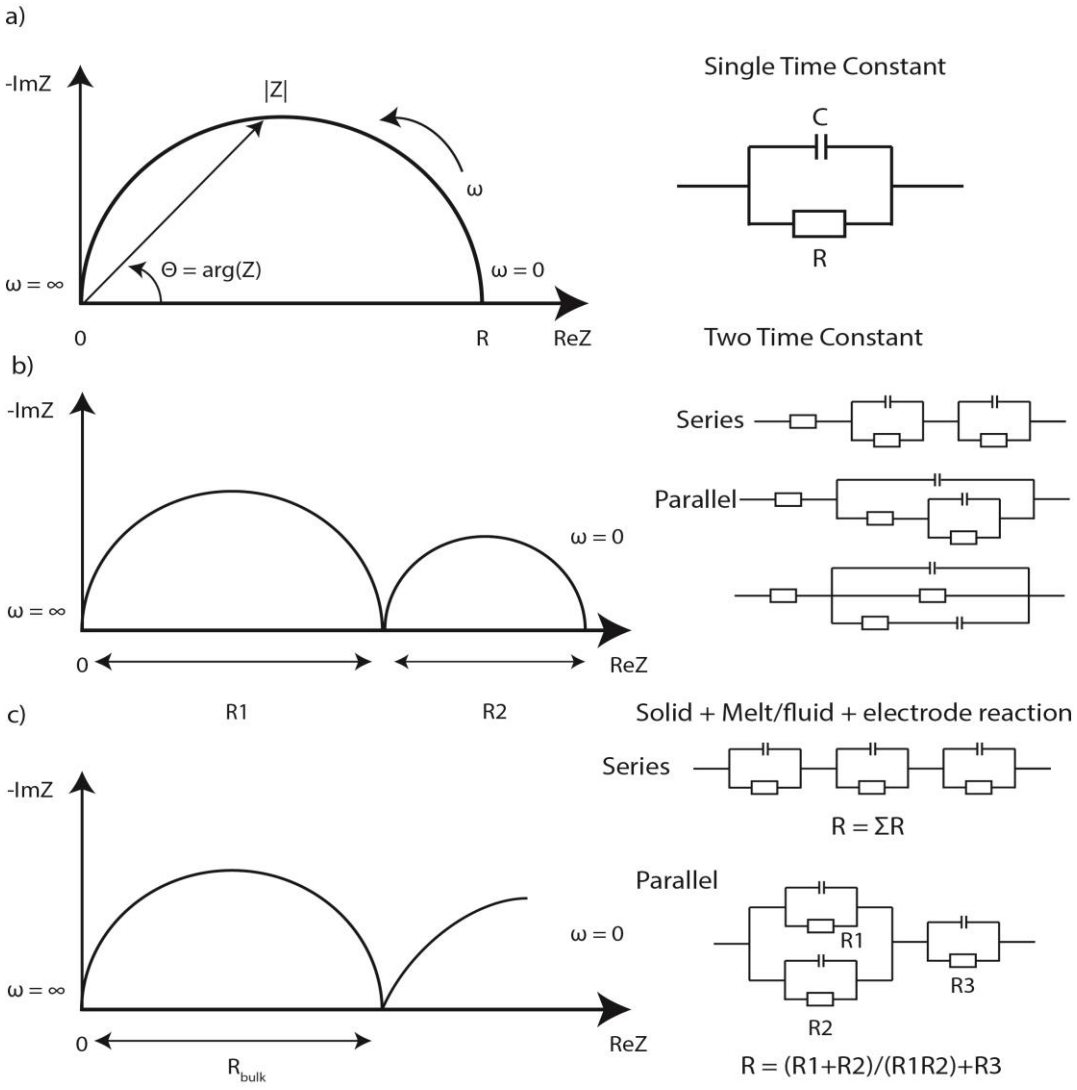

Figure II.17 schematic diagrams of Nyquist plots a) with one Time Constant (simple RC circuit) which is similar to experimental grain interior impedance spectra b) with two Time Constant (a solid + a fluid for example), different types of equivalent circuit can be fitted to this spectra (non-unique solutions) considering series or parallel circuits. c) Example of impedance spectra with 3 contributions: solid+melt+electrode. This type of spectra can be fitted by also several types of equivalent circuits (parallel or series) which induce different estimation of the total sample resistance.

Low temperature measurements are difficult because the resistance of minerals and rocks are very high, close to the limit of the apparatus (0.1-1 GΩ). Some devices were adapted to these low frequency data (Katsura et al., 1998) even if circular fitting of arc data sampling provides satisfying results. The high intercept of the circular fit to the impedance arc corresponds to the 0 frequency/phase angle impedance and so sample resistance. Insulation tests prior the measurement of a sample at low temperature must be performed. Tests are usually made by measurements of a known, high resistance ceramics such as alumina or periclase (Yoshino et al., 2004; Yoshino et al., 2008; Manthilake et al., 2008).

At high temperature, electrical conductivity measurements are also difficult as induction is very likely to occur in the whole impedance spectrometer circuit. In specific case, such as ionically conductor (like metal or melt), the sample can have a resistance which is inferior to the resistance of the cables and spectrometer electrical circuit. To overcome these issues, impedance spectrometers are no longer used and a more simple direct measurement with high precision multi-meter can be used. Frequency sweep is no longer used as frequency variations are small for conductive materials.

The sample cell for electrical conductivity measurement can have several shapes. The most common setup consists into inserting the sample in insulating sleeve (MgO, Al_2O_3, BN etc.) and connecting the sample with two metal discs placed at top and bottom of the sample (sandwich electrodes). The discs are in metal, which can be of various compositions (Ni, Au, Fe, Mo, Pt, Re, Ir etc.). Re, Ni or Mo discs are mostly used as they can also control to some extend oxygen fugacity (Re-ReO, Mo-MoO_2 or Ni-NiO). However, these discs are not real buffers as oxides and metal are not coexisting (Chapter V). One disc is usually connected to the thermocouple whereas the other side to single wire. All the wires are insulated by ceramic or plastic insulator (inside and outside the cell assembly respectively) for heater and cubes. Electrical conductivity is then retrieved knowing electrode surface, which is usually precisely known as electrodes are cut with laser.

$$\sigma = \frac{l}{SR}$$

Where l is sample length, S electrode/sample cross-sectional surface and R sample resistance.

Furthermore, other geometries have been developed to measure electrical conductivity via impedance spectrometry. Among them, the cylindrical electrode technique is a quite widespread practice, in particular in piston cylinder but also multi-anvil experiments (Xu et al., 1998; Ni et al., 2011; Gardes et al., in review). In this configuration the sample is surrounded by a metal shield, a thin metal foil that can be made of different materials such as disks electrodes (see above). The shield is grounded and is separated from the heater by an insulation sleeve. The advantage of this technique is the lower disturbance from the heater which can make important induction effects. It also helps minimizing thermal gradients and sample current leakage into the assembly and wires. The sample preparation is then more difficult as sample needs to be drilled in the center to insert a metal rod that will act as an electrode. The obtained data must be then corrected by a geometrical factor to take in account

the cylindrical geometry. The main disadvantage of this technique is the low insulation resistance of the foils due to moisture adsorption.

Data processing and fitting is performed according to the setup measurement. For standard impedance spectroscopy technique, semi-circles are fitted in the Nyquist diagram to obtain sample resistance at each temperature. Electrical conductivity can be retrieved knowing sample and electrodes dimensions. For a more precise estimation, sample diameter and radius can be measured (if on-line synchrotron experiments) or recalculated using thermal expansion at each pressure and temperature step. Data are then represented in modified Arrhenius plot (which is used by convention), plotting natural logarithm or base 10 logarithm of electrical conductivity as a function of 1/T or 1000/T. The solid data, that follows an arrhenian behavior, draws linear trend over a given range of temperature that is a direct consequence of the conduction process. The fit of these trends allows retrieving activation enthalpy of the given process (with a correction factor due to the use of log instead of ln):

$$\sigma = \sigma_0 exp\left(\frac{-\Delta H}{kT}\right) \leftrightarrow ln(\sigma) = ln(\sigma_0) - \frac{\Delta H}{kT} \leftrightarrow Y = B + A * X$$

Where *A (-H/K)* and *B* ($log\sigma_0$) are the fitted parameters and *X* is *1/T*.

iii) *In situ thermal diffusivity characterization techniques*

In this section both Angström method and pulse heating technique will be described in order to understand the present developments proposed by this study (Chapter VI and VII respectively).

The literature on experimental characterization on thermal conductivity and diffusivity of mantle materials is nowadays important and the methods used are plural (Angström, pulse heating, Laser Flash Analysis (LFA), etc.). Nevertheless, these successive developments testify the vigorous discussions, disagreement and limitations between the different groups and techniques.

The main point motivating the present developments/improvements is the limitation in both pressure and temperature of most of the tools. The first objective of the *in situ* techniques is thus, to be able to probe the whole range of mantle conditions. LFA measurements are fairly easy and Hofmesiter's group already characterized every type of materials presenting a geological interest. However, these measurements are only available at room pressure and never exceed 1800 K in a gas mixing furnace. Angström as well as pulse heating techniques

adapted to multi-anvil covers a wide range of P and T with pressures up to 30 GPa and temperatures over 2000 K (simultaneously!). On the other hand, the techniques developed on diamond anvil cells are the most adapted for the lower mantle studies with a range covering up to 150 GPa and high temperatures thanks to laser heating, but these techniques are for technical issues (sample size notably) not able to perform simultaneous HP and HT *in situ* measurements. In fact, most of experiments reported in the literature for pressure > 50 GPa are realized at RT and only few experiments were made with temperature which never exceed 1000 K (Chapter I). For these reasons, we found that multi-anvil characterizations of thermal properties at realistic P and T conditions is still of a significant interest.

Contact methods such as Angström and pulse heating techniques using thermocouples and secondary heaters suffered from a reduced precision of the inferred thermal parameters. It has been argued that contact free methods such as LFA have a much greater accuracy on the absolute conductivity at RP and RT with accuracy less than 5% (Hofmeister, 2007). In the same way, the same author claimed that pressure and temperature derivatives obtained by multiple contacts are not accurate and yield to values that are not absolute, even at high pressure, despite they seemed to show compatibles values once back-calculated to RP and RT. The contact methods have been found to have a precision of 20% based on the reproducibility of measurements at RP and RT (Ross et al., 1984). They involve systematic errors due to the thermal contact resistance and the differential thermal expansion between the thermocouple and the sample. The sample surface roughness also affects the contact by presence of gaps between the sample and the thermocouple wires. These gaps create additional sample thermal resistance because phonons cannot propagate in the air. The thermal resistances (Q) are additive and so the bulk conductivity is underestimated (Hofmeister, 2007), such as expressed in the following equation of Carslaw and Jaegger (1959):

$$\frac{1}{\kappa_{measured}} = \frac{1}{\kappa_{sample}} + Q$$

Added to these mechanical disadvantages, spurious radiative process can also affect the measurements. The radiative effects are function of the mineral phases present (opaque or semi-transparent) and grain size of the sample. Furthermore, the experiments can be submitted to a special type of photons named ballistic photons (Chapter I), which can directly warms the thermocouple with minor participation of the sample (Hofmeister and Criss, 2005).

To sum up, none of the current available technique surpasses entirely the others. This is why we opted for these two contacts techniques to provide new estimates at the mantle P-T conditions in particular for melts and glasses. However, it appears mandatory to keep in mind the drawbacks of both techniques when comparisons with other literature studies are made.

(1) Angström method

The Angström method is one of the first techniques developed for thermal diffusivity measurements with funding publications of Fujisawa et al. (1968) and Kanamori et al. (1969) for high pressure experiments. This technique, initially developed for measurements at room pressure and temperature, was well adapted for measurements during MAA experiments at HP and HT.

It was developed by Angström for experiences designed on long metal bars of a small cross section (Carslaw and Jaegger, 1959). The end of the bar was subjected to periodic changes in temperature, being alternatively heated or cooled for equal intervals. The bar was allowed to radiate into a medium at constant temperature. The bar reached a periodic state behavior which was measured with temperature at two points at different lengths. These points were measured, analyzed harmonically and conductivity was determined independently of the surface conductance.

The Angström method relies on the fundamental equations of linear flow of heat in a rod. For the first experiments, a semi-infinite rod was considered where the flow is one dimensional in x direction for a uniform rod. The equation can be written (Carslaw and Jaegger, 1959):

$$\frac{dT}{dt} = \kappa \frac{d^2T}{d^2x} - \nu T$$

Where T is temperature, t is the time, κ is thermal diffusivity and ν is radiation constant (Carslaw and Jaegger, 1959, p19). For a semi-infinite rod and harmonic excitation the temperature at the end of the cylinder vary as:

$$T = A_0 + A_1 \cos(wt)$$

Where w is the angular frequency, $w = 2\pi/t$. If we assume the boundary conditions that temperature is equal to 0 at infinite, the solution of the first equation is:

$$T = A_0 exp(-q_0 x) + A_1 exp(-q_1 x) cos(wt - q_1' x)$$

Where:

$$q_0 = (\nu/\kappa)^{1/2}$$

$$q_1 = \left[\left(\frac{\nu}{2\kappa}\right) + \left(\frac{\nu^2}{4\kappa^2} + \frac{w^2}{4\kappa^2}\right)^{1/2}\right]^{1/2}$$

$$q_1' = \left[-\left(\frac{\nu}{2\kappa}\right) + \left(\frac{\nu^2}{4\kappa^2} + \frac{w^2}{4\kappa^2}\right)^{1/2}\right]^{1/2}$$

If we further consider a finite rod the temperature at x = 0 is still defined by the equation but the boundary condition has to be change at the final length *l*.

In the Angström method adapted to high pressure apparatus the heat flow is generated radially in the sample rod. The sample is drilled in the center and thermocouples are fixed both in the center of the cylinder and on the edge, blocked with the sample capsule. The heat is generated by a temperature wave by the heater of a controlled frequency and period (Fig. II.18). In this case a radial flow in an infinite uniform cylinder equation is used:

$$\frac{dT}{dt} = \kappa\left(\frac{d^2T}{dr^2} + \frac{1}{r}\frac{dT}{dr}\right)$$

Where *r* is the radial distance from the axis. The boundary condition of this setup is:

$$\frac{dT}{dr} = 0, at\ r = 0$$

If we consider harmonic excitation at a distance $r = R$ from the axis:

$$T_R = B_0 + B_1 cos\ (wt)$$

This can also be written in its complex form:

$$T_R = b_0 + b_1 R$$

Where B_0, $B_1, b_0$and b_1 are constants. The solution of the radial flow equation with the boundary conditions developed above.

$$T_R = b_0 + b_1\left[J_0 \frac{\left(\sqrt{-i} * x\right) * exp\ (iwt)}{J_0\left(\sqrt{-i} * l\right)}\right]$$

Where:

$$l = \left(\frac{w}{\kappa}\right)^{1/2} R$$

$$x = \left(\frac{w}{\kappa}\right)^{1/2} r$$

At $r = 0$ and $r = R$ we have:

$$T_R = b_0 + b_1 cos wt$$

$$T_0 = b_0 + b_1 \theta cos(wt|-\varphi)$$

Where:

$$\theta = \frac{1}{\sqrt{bei(u)^2 + ber(u)^2}}$$

$$\varphi = tan^{-1}\left(\frac{bei(u)}{ber(u)}\right)$$

The two parameters $\theta \wedge \varphi$ are able to be retrieved by the experimental observations. The solution to the first equation can be writen using the dimensionless argument u, from which thermal diffusivity (D) can be directly estimated knowing angular frequency (w) and sample radius (d).

$$u = d(w/D)^{1/2}$$

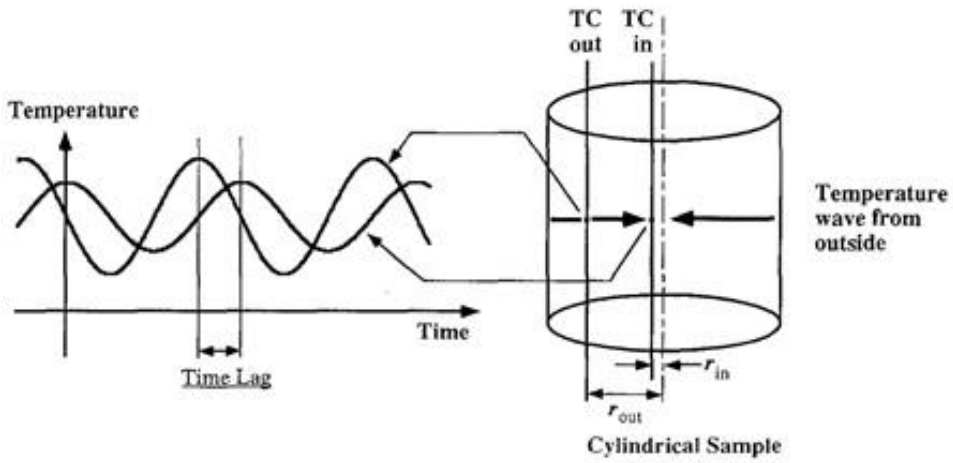

Figure II.18 The Angström method for radial heat flow in a cylindrical sample. After Katsura,(1993)

The Angström method was adapted to multi-anvil apparatus for high pressure measurements under the impulsion of Bayreuth team with the work of Katsura in 1993. He adapted this technique to the multi-anvil device, which design was reproduced in most of the following studies on this apparatus (Xu et al., 2004). The Angström method is adapted for multi-anvil assemblies using two thermocouples that are inserted through the octahedron and passing by the center and the edge of the sample. The wires are protected from the heater by the MgO inner sleeve.

Using this given configuration, a sinusoidal temperature wave is generated by the oscillation of the electric power supply by using a function generator. The frequencies of the measurements are commonly between 0.3 to 1.5 Hz (Katsura, 1993; Xu et al., 2004). The power modulation and data collection system were significantly improved with time (Fig. II.19). Furnace temperature has to be applied with high frequency (1 KHz) to avoid thermal response of the sample. The measurements are then made using a superimposed low frequency temperature wave. Sine waves are successively used to modulate the heater current at each temperature. Measurements last a minimum of 10 periods and the interval between measurements have to be important (> few minutes) to reach steady state before new temperature perturbations.

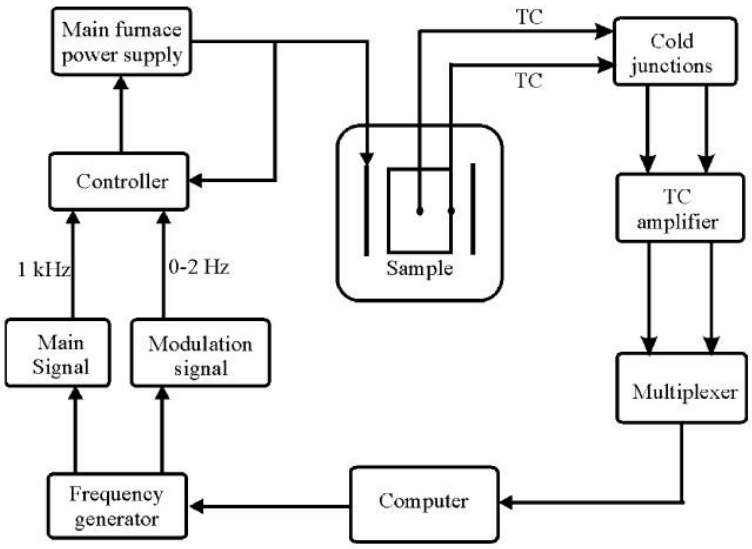

Figure II.19 Example of power modulation system and data collection improved from Katsura (1993) by Xu et al. (2004).

(2) Pulse heating

The pulse heating method is the second main method developed to provide measurements of thermal conductivity of minerals. The original development was made by Dzhavadov in 1975. It was later used and improved by Misasa group with the work of Osako in 2004 (Fig. II.20).

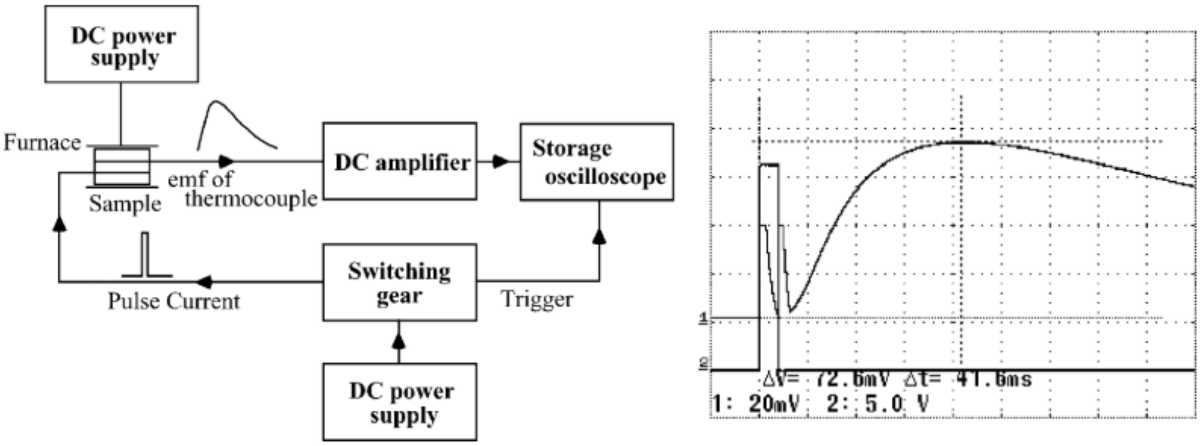

Figure II.20 Schematic of the electronic device for the pulse heating method and associated records from Osako et al. (2004)

The technique allows estimating *D*, *κ* and also can gives clues on *Cp* at high pressure. The original work was done on large samples (up to 2 cm in diameter) but significant size reduction have been made for analyses at high pressure and high temperature using multi anvil press (Osako et al., 2004). The strength of the technique is to work on anisotropic material and is particularly well suited for oriented single crystal studies.

It consists in the assembly of 3 identical disks of sample. An impulse heater is placed on one interface of the disks and a thermocouple is inserted at the other interface with the respective x positions: 1/3 and 2/3. A pulse of heat is generated that will create a temperature wave through the sample (Fig. II.21).

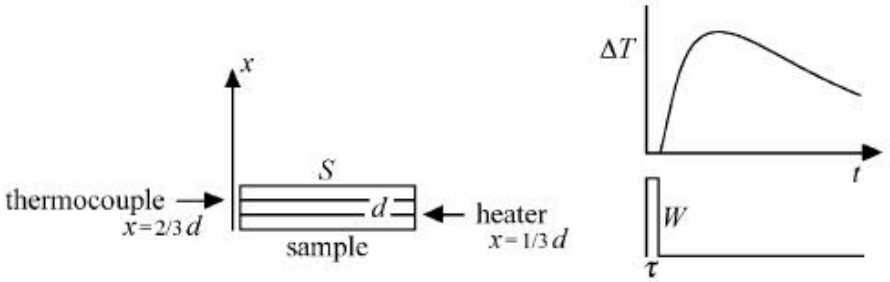

Figure II.21 representation of the pulse heating method with the signal impulse on the lower graph and it's consequence on the thermocouple on the upper one from Dzhavadov, (1975).

The sample is introduced into a specially designed multi-anvil assembly from (Osako et al., 2004). The ambient temperature is produced and controlled by the plate heaters connected to the secondary anvils with a bend surrounding the zirconia + MgO vertical plug. The central thermocouple is flat with a thickness of 0.03 mm and a width of 0.3 mm and the additional impulse heater is made of Ni-Cr with photo-etched slot which helps to produce one dimensional heat flow in the sample (Fig. II.22).

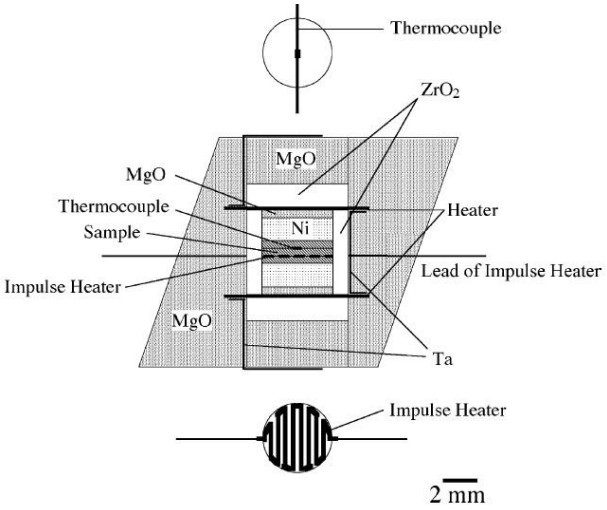

Figure II.22 Multi-anvil assembly for pulse heating technique from (Osako et al., 2004)

The temperature variation at the position of the thermocouple can be expressed as (modified from Dzhavadov, 1975):

$$\Delta T = A\sum_{n=1}^{\infty}\frac{1}{n^2}sin\frac{n\pi}{3}sin\frac{n\pi x}{d}exp(-n^2Bt)*[exp(-n^2B\tau)-1]$$

Where t is time from the onset of heating, x is the position from the end of the sample, d the total high of the disks and τ is the duration of the heating pulse. A and B are:

$$A = \frac{2Wd}{\pi^2\kappa S}$$

$$B = \frac{\pi^2 D}{d^2}$$

Where W is the power of impulse heating, S the surface of the heater. These parameters are fitted with the data recovered from the experiments. Summations over $n>10$ converges relatively fast.

3) Analytical methods

a) Sample preparation

Our sample preparation was similar in most of our cases because of the necessity to analyses the chemical composition, imaging and get information on sample's texture.

After each multi-anvil experiment, the octahedron was recovered and was cut with a diamond wire or disk saw to obtain a flat surface, parallel to the heater. The remaining part of the assembly was loaded into epoxy resin (Epofix^{TM} from Struers), impregnated under vacuum and polished with coarse grain silicon carbide sandpaper (#220 sandpaper → 68 μm grains) until the sample was brought to surface. Each sample was then polished up to its center with decreasing the sandpaper grain size with: #600 (40 μm grains), #800 (22 μm grains), #1200 (15 μm grains) and #2400 (9 μm grains) sandpapers. The sample is then mirror polished with diamond pastes, successively with 9 μm, 6 μm, 3 μm, and 0.25 μm diamond size. Polishing can be manual or automatic using a polishing machine. We used polishing machine (Mecapol P200) for solid samples, easy to polish, whereas hand polishing was preferred for delicate ones. For difficult samples, not well sintered or loosing grains, a second epoxy or superglue impregnation under vacuum was realized.

The recovered samples were metalized for scanning electron microscope imaging and electron microprobe analyses. It consists into the deposit of a thin film of carbon under secondary vacuum by the vaporization of a carbon string with current heating. This step helps to ground samples to avoid charge building at sample surface under an electron beam.

For micro-Raman analyses, the samples are not metalized due to the strong perturbation on OH frequency region induced by carbon coating. The metallization, if present is then removed by quick polishing with ¼ micron diamond. The samples are usually cleaned with ethanol in ultrasonic bath, carefully dried and stored under vacuum.

b) Scanning electron microscope (SEM)

The scanning electron microscopy was used during this study for imaging the recovered samples, measuring of their dimensions, identifying their phases with the Backscattered Electrons (BSE) photographs and chemical mapping using the Energy Dispersive X-Ray spectrometer (EDS) detector.

The scanning electron microscopy consists into the projection of a focused electron beam. The projected electrons react with atoms of the sample producing large spectra of particles

and radiations. The emitted signals contain information about the chemical composition, crystallography and topography of the probed area.

The electrons are generated by a thermo-ionic gun from which the electrons are extracted from a tungsten wire while heating. At high temperature the electrons have enough energy to extract from filament (overshot the potential barrier) and are released in the high vacuum of the chamber, then accelerated by electrical field and focused to the sample. The electron beam is scanned with a raster scan pattern. The SEM apparatus is usually composed of a column with an electron gun, a series of condenser lens and apertures/slits to focus and tune the intensity of the beam. A stigmator leads the beam to the sample chamber. The chamber is composed by the specimen holder which can rotate and be moved in the 3 axis and the detectors for SEI and BSE electrons (Fig. II.23). The system is then connected to a computer for data visualization, processing and storage.

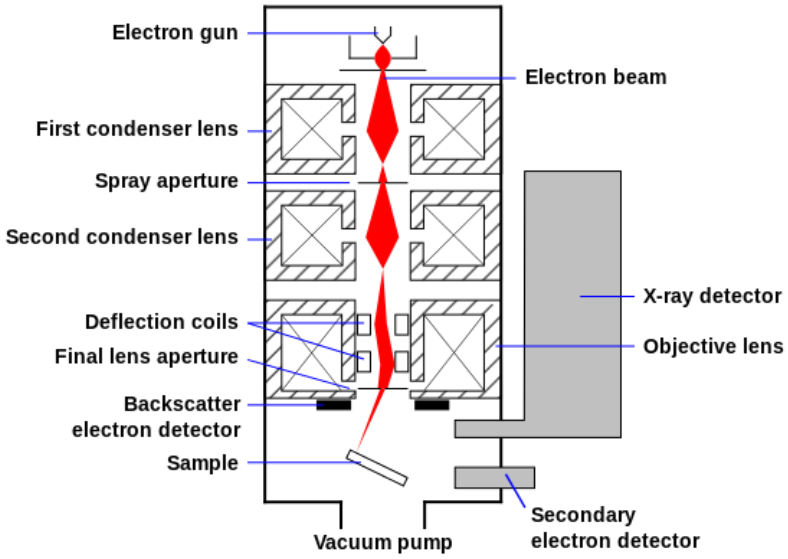

Figure II.23 Schematic of the electron beam propagation inside a scanning electron microscope. The electron beam and its shape is drawn in red, the different components of the SEM are labeled. The effect of each component is highlighted by the shape change of the electron beam (e.g condenser to focalize the beam etc.). The analytical part is represented by the black parts with the detectors. In LMV different types of detectors are avaible: EDS, WDS and cathodolimuniscence (not represented here). Figure taken from Wikipedia 16/12/2016.

For imaging, two types of signals were used: Secondary Electron Image (SEI) and Back Scattered Electrons (BSE). SEI is a common detection mode: primary electrons are emitted from the source close to the sample surface. Their interactions with the electronic cloud of the atom will enhance, by giving a fraction their energy, the ejection of secondary electrons from the K-shell (outermost layer). The secondary electrons are collected and detected by an Everhart-Thornley detector which is a type of scintillator-photomultiplier system. Because the secondary electrons have a low energy, the use of a photomultiplier is

mandatory to increase their energy to emit light. This light signal is recorded and can be saved as an analog or digital image. The number of secondary electrons emitted directly depends on the angle between the beam and the sample. The interaction volume increases with the angle of incidence and so more secondary electrons are produced. Thus the number of electrons is correlated to the sample surface characteristics and will display in bright the steep surfaces and edges. The SEI appears particularly well suited for texture analysis and its high resolution allows details observations (up to few nm).

The second detection mode is the Back Scattered Electrons (BSE) also named reflected electrons. The BSE consists in the reflection of the high energy electrons from the beam by quasi-elastic scattering interaction with the atom and its electronic cloud. The heavy atoms (high Z) are recognized to backscatter more electrons than light elements. It appears that this technique is particularly suited to detect contrasts between areas with different chemical compositions, such as minerals in our samples. The scattered electrons are collected by a scintillator and have a high energy. This high energy implies they can come from deeper into the sample than the SEI (Fig. II.24). By consequence, they are not really well adapted for high resolution information given that their excitation is fairly large at high tension of acquisition making an “excitation pear”. The size of the pear is function of the beam size, acceleration tension, density and chemical composition of the sample and the characteristics of the detector. This volume is the real volume analyzed and is bigger than the spot size itself. This effect has to be taken in account for the analysis of small objects such as melt pockets (see hereafter).

During this study, we used two types of SEM. A conventional SEM at the LMV and a Field Emission Gun (FEG SEM) Scanning Electron Microscope at 2MaTech in Aubière were used. The SEM at the LMV is a JEOL Jeol JSM-5910 LV and the used EDS detector was a SPIRIT PGT type. For imaging, the accelerating voltage was 15 kV and working distance of 11.4 mm and accelerating voltage of 10 kV and working distance of 19.3 mm was used for chemical mapping. Some samples were also analyzed with a field emission gun (FEG) SEM ZEISS supra 55VP with an acceleration voltage of 15 kV and working distance of 9.7 mm. The FEG SEM is used for imaging smaller samples and structures than a conventional SEM. The electron generation is different in this device with a field emission gun from where the electrons are extracted by applying high tension to a tungsten tip. The electrical field in the pin is very intense and allows by quantum tunnel effect the extraction of the electrons from the metal. This apparatus is capable to produce high primary electron brightness with a small

spot size and this at low voltage. It allows analyzing thinner samples than the conventional SEM by a significant reduction of the excitation volume and gives spatial resolution of the order of few nanometers.

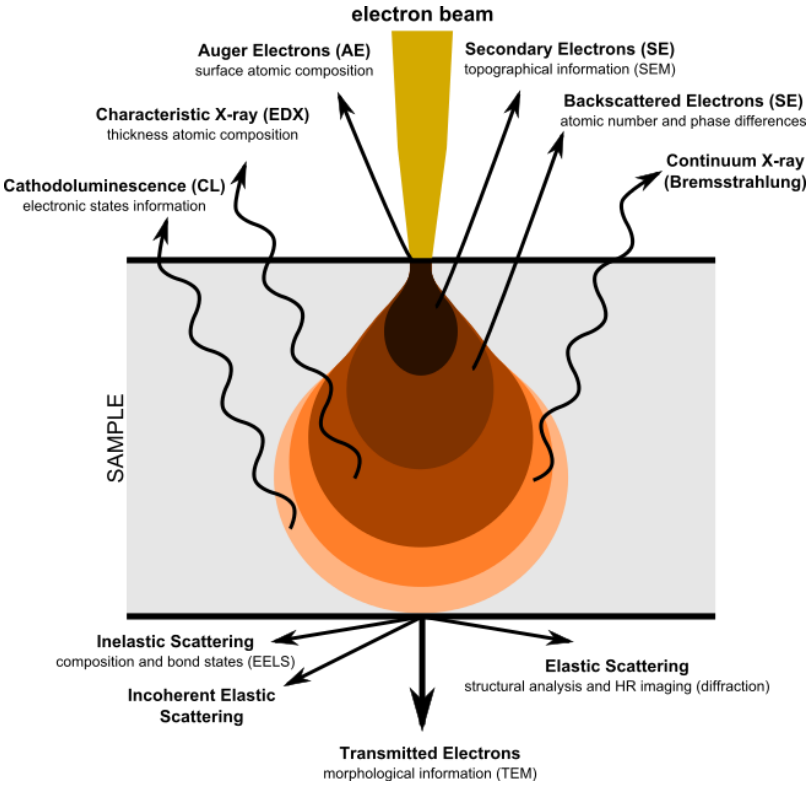

Figure II.24 Schematic view of the excitation pear in a sample induced by an electron beam (valid for SEM but also EMPMA). The depth of excitation and the associated physical phenomenon are given and labeled for both transmitted/scattered phenomenon and reflected/back emitted ones. The interest of each phenomenon is written under it. For SEM, SEI and BSE, signals are used for surface analysis and phase identification respectively. Chemical analyses are carried using EDX emissions. Cathodoluminescence can be used to map zoning crystals such as zircons (main use at the LMV). Image taken from Wikipedia 16/12/2016

The SEM apparatus at the LMV also allows obtaining quantitative analysis via punctual measurements or chemical mapping. In this mode the energy dispersive X-ray (EDS or EDX) detector is used to measure EDS spectra on a small spot. EDS uses a solid state semiconductor detector to analyze at the same time all the wavelengths produced by the sample, coupling the EDS detector with the scanning mode of the apparatus allows to perform chemical mapping of the sample where each pixel is a quantitative analysis of the sample. It presents the advantage of having a small spot size and both select small areas with the software to have phase average chemistry which can be particularly useful for molten samples which are generally affected by quench crystallization. The drawbacks of the technique are a lower precision in the analysis than electron probe microanalyzers (EPMA). Also the total of the analysis is usually not equal to hundred and must be normalized, which is problematic for hydrous phases (H and OH are not analyzed).

c) Electron Probe Micro-Analysis (EPMA)

The electron microprobe was used during this study to measure the chemical composition of our samples. This apparatus allows, similar to the SEM, to analyze in a non-destructive manner a small volume of sample. The principle is close to the SEM (see above), by the acceleration of electrons to bombard the sample surface. The sample phases react with the electron beam and emit X-rays at characteristic wavelengths of the elements being analyzed. The incident beam induces the X-fluorescence of the sample: the emitted primary electrons excite the atom by energy transfer, moving the atom away from its fundamental state. To return to this lowest energy level, the atom emits an electron on the electronic layers that are close to the atom (K), this vacant place will be filled by another electron from a higher energy bound shell (L, M …) and this electron transition emits X-rays that are characteristic of the atoms (Fig II.25). The energy and the wavelength of the X-photon is equal to the difference in binding energy between the electron shell with the vacancy and the shell from which the electrons comes to fill the vacancy. Depending on the layer origin of the electron, the energy of the emitted rays will produce K_α for L layer or K_β for M layer that are used to quantify the atoms fractions.

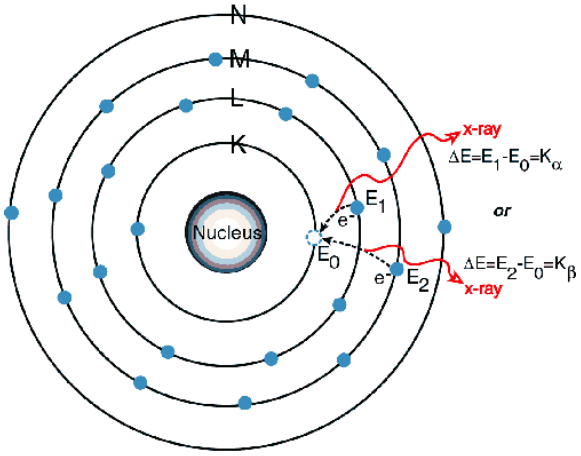

Figure II.25 Illustration of atomic electron shell, with K, L, M and N layers. The transition of an electron from a layer to another will induce an x-ray emission characteristic in energy of the transition and the element. A transition from L layer to K layer will induce a Kα emission and Kβ emission from transition from M layer to K layer. These two types of transition are commonly used for EPMA quantifications. Figure from amptek.com 19/12/2016

The electron microprobe is composed of an electron gun from which the electrons are produced using a tungsten filament (lanthanum hexaboride crystal also exist as a source). The filament is the cathode and the electrons are accelerated through vacuum to the anode plate. The anode has apertures and electron flow is collimated and focused by electromagnetic

lenses and apertures. The beam enters in the sample chamber and interacts with the sample. An optic system and a BSE detector allow the imaging of the samples and help to select the area of analysis. The X-photons detector can vary according the apparatus setup: energy dispersive X-ray (EDS) or wavelength dispersive X-ray spectroscopy (WDS) (Fig. II.26).

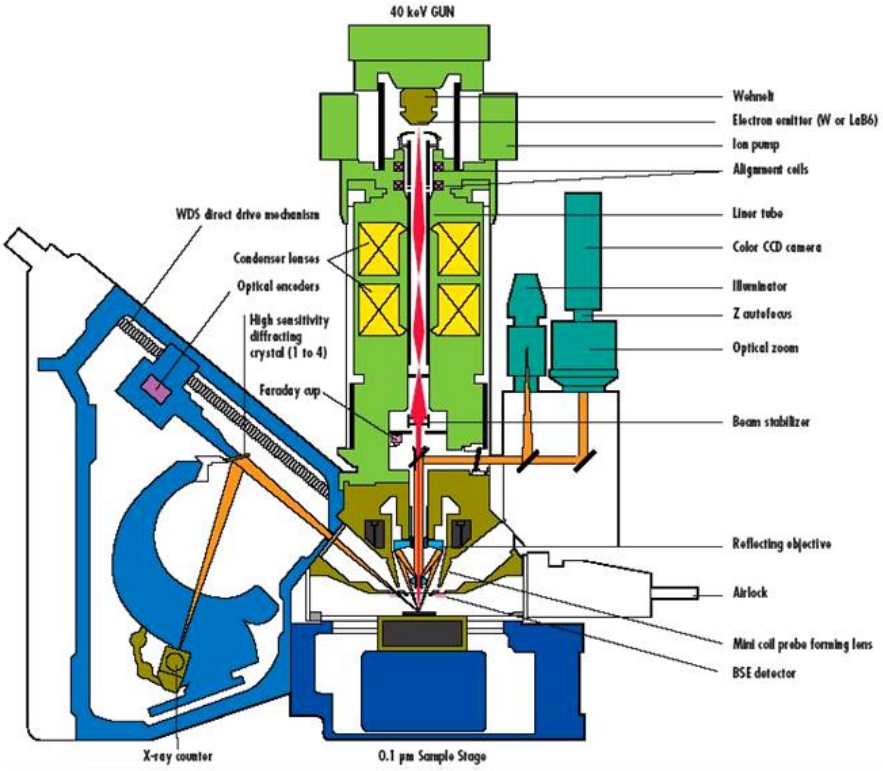

Figure II.26 schematic view of an Electron Probe MicroAnalyzer (EPMA) Cameca SX 100.

EDS uses a solid state semiconductor detector to analyses at the same time all the wavelengths produced by the sample. EDS is fast and can analyze almost all atomic numbers but its precision is not as good as the WDS. The WDS is composed of monochromators crystals and uses the Bragg law to select the X-ray wavelength. Thanks to the Bragg relation, the link between the incident angle θ, the interplanar spacing $d_{(h,k,l)}$ of the crystal and the wavelength of X-photons is the following:

$$d_{hkl} sin\theta = n\lambda$$

The WDS spectrometer has the capacity to vary the incident angle via both the detector and crystal rotation. The rotation of the couple is mechanized and follows a Rowland circle that allows sweeping a large range of angle (Fig II.27). Each spectrometer is limited, according the crystal used, in angle that is why it is necessary to use several spectrometers to probe all the wavelengths and analyze the quasi totality of the atomic numbers (Z >5).

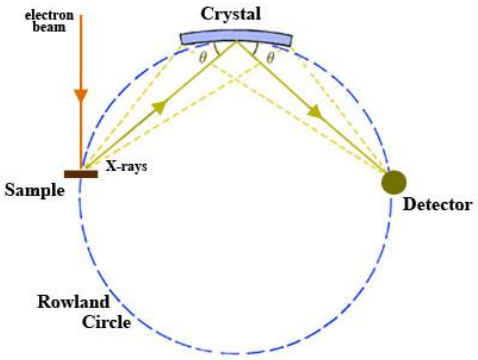

Figure II.27 Rowland circle showing the different positions of the electron beam, sample, crystals and detector. The moving detector and analyzer crystal permits them to be positioned on this circle for probing a wide range of angles. Figure taken from Carleton university website: http://serc.carleton.edu/research_education/geochemsheets/wds.html 19/12/2016

During this study, the chemical analyses were realized by a Cameca SX100 at the LMV. The accelerating voltage used was 15 kV and the 4 WDS spectrometer were parameterized for major elements.

The analysis with the EPMA requires previous measurements on standards to calibrate the apparatus. Thus, the standards used must have a chemical composition close to the sample in similar conditions. Moreover, the efficiency of the analysis and the spatial resolution depends on the source characteristics (field emission vs thermos-ionic), tension of acquisition, spot size, chemical composition and density of the sample and detector counting time. For efficient analyses, different sets of analyzing crystals are available depending on the number of crystals on each WDS spectrometer and the number spectrometers (Table II.1). The most common analyzing crystals are given in the next table and their properties as well as ranges of elements.

Table II.1 Different types of analyzing crystals are given in this table with their chemical composition, d-spacing values as well as their possible analysis range for K rays. Source of data: http://www.get.obs-mip.fr/en/equipements/Services-Communs/c3/microsonde_principes 19/12/2016

Name	Type	Formula	2d ()	K Rays
LIF	Lithium fluoride	LiF	4.027	From Mn to Ga
PET	Pentaerythritol	$C_5H_{12}O_4$	8.742	From S to Cr
TAP	Thallium acid phtalate	$C_8H_5O_4TI$	25.9	From N to P
PC1	Multi-layer	W/Si	60	N,O and F
PC2	Multi-layer	Ni/C	95	B and C
PC3	Multi-layer	Mo/B_4C	210	Be and B

At LMV, the EPMA is tuned in function of the types of analyses and standard routines have been made to improve analyses quality depending analyses are made on glasses, crystals and the type of element analyzed. The common configuration is using accelerating voltage of 15 kV, available analyzing crystals are LIF, PET and TAP. Usually two LIF are used with one TAP and one PET on the 4 WDS spectrometers. The measurement time is 10 s by element

and 5 s or less for alkalis (to prevent element migration under the electron beam). Time can be more important if precise analyses of minor or trace elements are wanted (F, S or Cl for example). For glasses and not perfectly quenched melts with quench crystals, the analysis can be tuned differently. In case of large melt fractions, the beam of the EPMA is defocused and large beam spots (20-50 microns) are used for averaging the sample with large probed zone (increase beam current and/or tension). Conventional beam size is a few microns (1-5 µm), however volume probed is always more important than just the spot size. This problem was one of our main concerns for melt pockets and films analyses as well as small grains we often have in high pressure experiments.

We have considered different aspect to decrease the sample volume analyzed while keeping enough signal to provide a good analysis. To do that, we performed a set of simulations using CASINO software (https://www.gel.usherbrooke.ca/casino/What.html, 16/08/2019). We considered simple chemistry with olivine end-members: forsterite and fayalite. We lunched a set of Monte Carlo simulations with various accelerating voltage and beam size to have an idea of their impact on sampled volume.

First, the simulations give a complete characterization of the beam fate with very detailed technical information on electron absorption and BSE emission, which are useful when fine tuning of the apparatus is required. The simulation (run with 10000 electrons) draws a very nice pear shape such as in the figure II.24. The composition influences the affected area and volume, as the compositions with heavy elements absorb more efficiently the electron beam than lighter ones. On fayalite, we observed a strong reduction of affected volume with around 1/3 less than forsterite. For accelerating voltage influence, rise of the tension results in an increase of both depth of penetration and width of excited sample. The higher tension simulations show a more pronounced pear shape than lower tension one. The volume probed is more spherical in case of low accelerating voltage, and a better control of the analyzed zone is possible.

For our simulations in forsterite, the excited volume is not elliptic with maximum widths and depths that can be significantly different (1.32 (width) - 0.7 (depth) µm for 10 kV, 1.7 - 1.38 µm for 15 kV and 2.6 - 2.3 µm for 20 kV). If we assume a spherical excited volume calculated from the average of the two parameters of the ellipse, we can see that exited volume increase of a factor 3 to 4 for each 5 kV increase of accelerating tension.

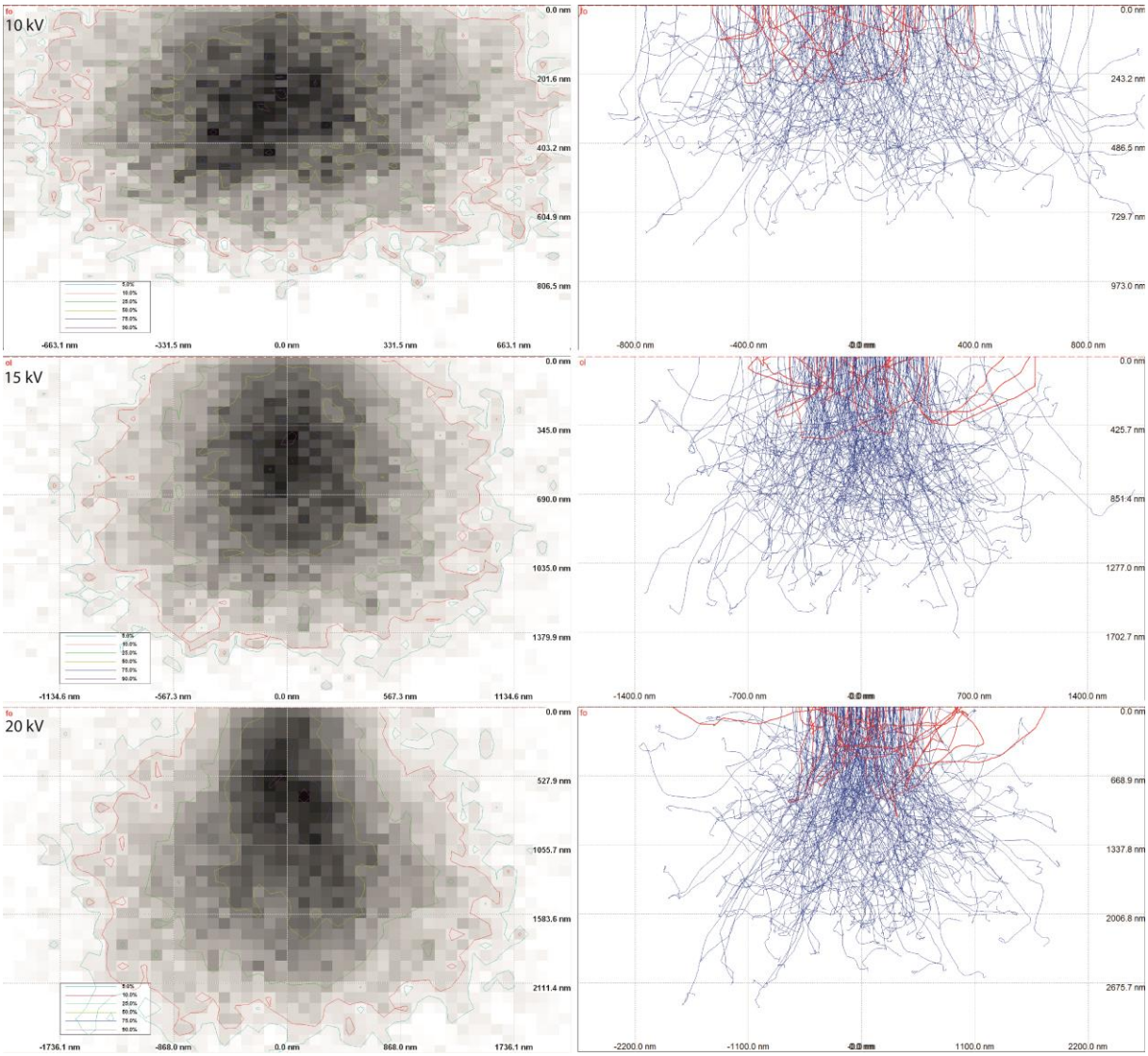

Figure II.28 CASINO simulation for forsterite substrate using 10000 electrons (2000 displayed) for different accelerating voltage and fixed beam size (1 µm). Left side image shows absorption contours of the beam where darker zones are the more excited, right panel shows the electrons trajectories for the same simulation.

For spot size of the beam influence, the relation is very clear: the depth of penetration is almost constant and the excited surface is proportional to beam size. Figures II.28 and II.29, shows the influence of beam size at a constant accelerating voltage (15 kV), the lateral extension of energy absorption maps almost double between 1 and 2 microns beam and multiplied by 5 for 5 microns, the extension is always slightly bigger than the spot size (e.g ~1.2 µm for 1 µm spot). This cross section can be converted in surface. The increase of a factor 2 of the spot diameter is translated into a factor 4 of surface increase and assuming spherical shape a factor 8 in volume.

To decrease the analyzed volume, the beam size has to be kept at minimum and accelerating voltage should be moderate. However, reducing accelerating voltage significantly

decreases signals quality, work on L rays for heavy elements can be a solution. We also observed that compositional effect can be important and this aspect is important in case of Fe rich melts, strong absorption is expected and sample volume is estimated to be significantly reduced limiting surrounding olivine contamination.

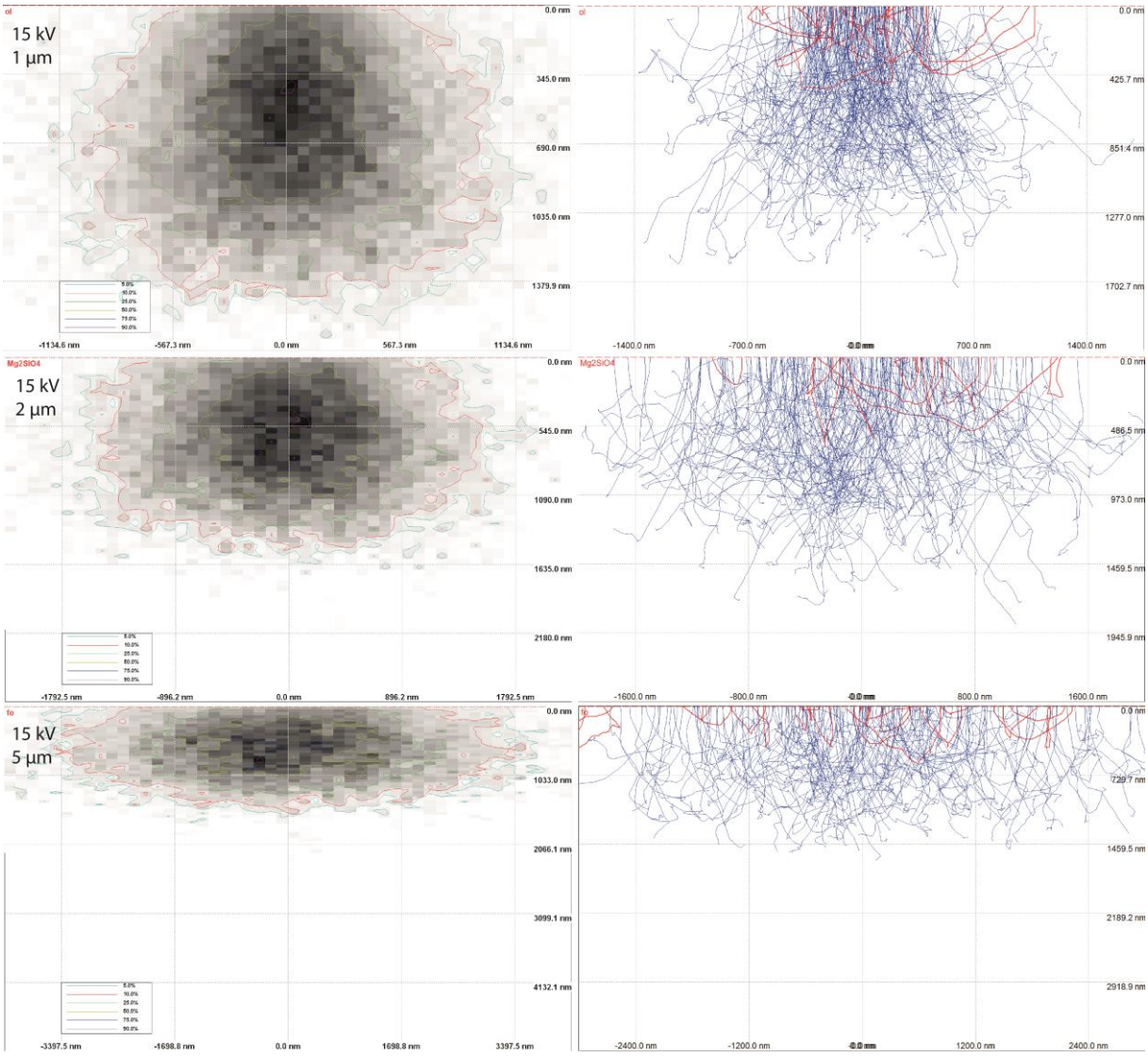

Figure II.29 CASINO simulation for forsterite substrate using 10000 electrons (2000 displayed) for different beam size and fixed accelerating voltage (15 kV). Left side images shows absorption contours of the beam where darker zones are the more excited, right panels show the electrons trajectories for the same simulation.

d) Raman spectroscopy

Raman spectroscopy was used during this study to characterize sample phases as well as estimating volatile contents of crystal and glasses.

The Raman spectroscopy is a non-destructive technique (if the user is reasonable with the laser power…) used to observe low frequency modes in a system such as vibrational and rotational modes. It relies on Raman (Stokes) scattering which is inelastic of a monochromatic light send by a laser. The wavelength of the laser used depends on the machine but is generally in the visible range. The laser interacts with the vibrations and phonon of the crystalline structure of the sample. The energy of the laser photon is offset due to these interactions. The inelastically scattered photons can be either higher or lower energy than the incoming laser photon defining anti-Stokes and Stokes scattering. The Raman shifts gives clues on the vibrational modes of the sample because it gives the difference in energy between the original rovibronic (rotation and vibration) state of the molecule and the rovibronic state under exited conditions (Fig. II.30). Reported Raman shifts are in wavenumber, have unit of inverse length and are related to energy. To convert recovered wavelength in Raman shift the following formula is used:

$$\Delta w(cm^{-1}) = \left(\frac{10^7}{\lambda_0(nm^{-1})} - \frac{10^7}{\lambda_1(nm^{-1})}\right)$$

Where Δw is the Raman shift, λ_0 is the excitation wavelength and λ_1 the Raman spectrum wavelength (Stokes).

The structure of the apparatus can be quickly resumed to a monochromatic source that illuminates the sample by a laser beam. Electromagnetic radiation from the illuminated spot, containing the vibrational information of the sample, is collected with a lens and sent through a monochromator. Because only inelastic scattered radiation of the sample is wanted, the inelastic radiation at the wavelength of the laser line (Rayleigh scattering) is filtered out by either a notch filter, edge pass filter, or a band pass filter. The remaining collected light is dispersed onto a spectrometer and CCD detector (Fig. II.31).

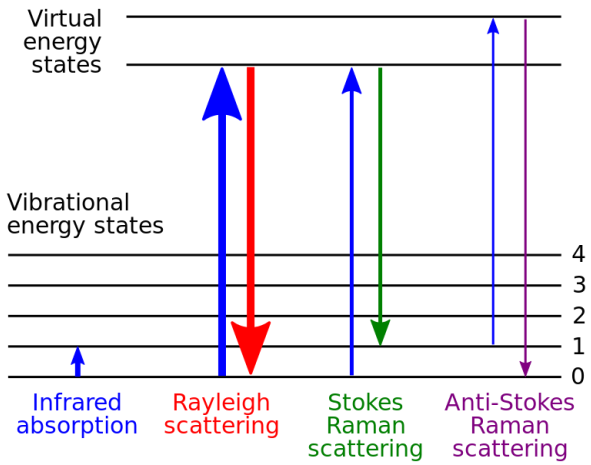

Figure II.30 Energy states involved in the Raman spectra (Wikipedia 21/12/2016)

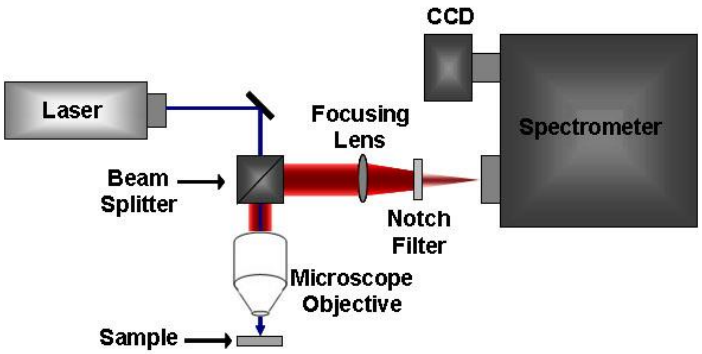

Figure II.31 a) Raman schematic principle (http://archive.cnx.org/contents/f8a19258-739c-43d6-9b26-cc6b9cf70821@1/surface-enhanced-raman-spectroscopy-for-the-study-of-surface-chemistry) 21/12/2016

Raman spectroscopy is a powerful technique to identify the chemical bounds and the symmetry of the molecules. Thus, each crystal will have a typical pattern which is easy to recognize, the peaks of these pattern depend on the crystal structure, chemistry and impurities contents such as volatiles that have specific bands than can be measured for quantification using known standards.

For our different studies, Raman spectra were collected using an InVia confocal Raman micro spectrometer manufactured by Renishaw, equipped with a 532 nm diode laser (output power of ~140 mW), a Peltier-cooled CCD detector, a motorized XY stage and a Leica DM 2500 M optical microscope. The Raman spectroscopy technique was preferred over FTIR analysis mainly due to its capacity to analyze both OH and Si bonds in a non-destructive manner (double polished samples are not required) and its small spatial resolution allowing the analysis of small melt pockets. Scattered light was collected by a back-scattered geometry; the laser power on the sample was reduced to ~9, 16.5 or 75 mW (5, 10 or 50%) and the slit aperture was set to 65 µm (standard confocality setting) or 20 µm (high confocality setting). A

set of 5x, 20x, 50x objectives are used to locate interesting zones and crystals and gradually focus, a 100x objective and 2400 l/mm grating were used for the analyses. These analytical conditions result in spatial resolution of ~1 μm and spectral resolution better than 1 cm^{-1}. Daily calibration of the spectrometer was performed based on a Si 520.5 ± 0.5 cm^{-1} peak. The spectra were recorded using Wire 4.2 Software from ~100 to 1300 cm^{-1} (alumino-silicate network domain) and from ~3000 to 3800 cm^{-1} (water domain). Acquisition times are commonly between 30-600 s for the high-frequencies domain and 5-120 s for the low frequencies. The Raman spectra of given species were compared with Renishaw library, RRUFF and ENS Lyon databases to ensure crystal determination and conformity with the compositions obtained via the EPMA acquisitions.

For quantification, Raman analyses were performed on mineral phases (wadsleyite, olivine, pyroxene, garnet, etc.) and on the interstitial glass phase. Difficulties in Raman analyses of the glass phase were caused by the very small size of glass pockets (sometimes < 1 μm), general instability of the water- and iron-rich glass under the laser beam, and overlapping of the surrounding olivine Raman peaks on the silicate glass bands. For hydrous crystals, analyses were not easy due to dehydration and reaction under the laser together with a small crystal size. This is why these analyses were performed at low laser power (5%). For determination of water content in glasses, we used both the external calibration procedure (Mercier et al., 2010), which is based on a set of hydrous basaltic glass standards (Médard and Grove, 2008; Médard et al., 2008; Sisson and Grove, 1993) and the absolute intensities of the water band area, and an internal calibration procedure, based on the correlation between the glass-water concentration and the relative areas of the water and silicate Raman bands. The two methods gave comparable results. Water contents of the standards were determined using both FTIR and SIMS techniques. Standards were analyzed at the same conditions as the samples. The method for glass quantification and calibration curves are given in the appendix A. Analytical precision calculated based on repeated daily measurements of standard glasses is generally better than 6 % relative (Schiavi et al., 2018).

During this PhD work, Raman spectroscopy was intensively used because of the importance of volatiles in the studied fields and the accessibility of the apparatus. As the tool was often used, a serie of tests were performed by the author to check the impact of user while doing baselines and provide different comparisons of methods. We estimate important to keep this data to have an idea of the tool reproducibility fitting errors etc. This data is given in the appendix A.

Chapter III

Electrical conductivity and acoustic wave velocity in partially molten systems

Chapter III Electrical conductivity and acoustic wave velocity in partially molten systems

1) General introduction

Geophysical properties of Earth's materials have been extensively studied by *in situ* experiments in order to interpret the geophysical measurements made on Earth and other planetary bodies. A consequent number of studies focused on electrical conductivity aims to quantify both partially molten systems and end-members to determine possible melt fraction in the Earth's asthenosphere (Presnall et al., 1972; Tyburczy and Waff, 1983; Ni et al., 2011; Yoshino et al., 2010; Zhang et al., 2014; Caricchi et al., 2011; Maumus et al., 2005; Laumonier et al., 2017). At the opposite, studies based on the effect of partial melting on acoustic velocities remained mostly theoretical (Takei et al., 2000, 2002; Yoshino et al., 2010). The recent measurements of Chantel et al. (2016) highlighted a consequent disagreement between experimental and theoretical quantifications on sound wave velocity in the case of geological partially molten materials. In addition, melt fractions inferred from laboratory measurements of electrical conductivities and acoustic wave velocities are not compatible (Pommier and Garnero, 2014; Karato, 2014) and yield to a large possible range of melt fractions inferred in the literature for natural cases.

During this PhD work, we aimed to investigate the *in situ* geophysical properties of partially molten geological materials to better constrain Earth's mantle structure. This strong debate on possible melt fractions implied in asthenosphere LVZ, if partial melting hypothesis is considered, motivated this study. Such work will aim to understand the factors influencing the *in situ* geophysical measurements.

In this work, we aimed to search for possible answers to the discrepancies observed between the different *in situ* techniques as well as conflicting results within a given technique. The recent results of our group (Chantel et al., 2016) on acoustic wave velocity provided the framework for an innovative technical development and perform the first simultaneous measurements of electrical conductivity and acoustic wave velocity.

In situ geophysical measurements were measured simultaneously during high pressure and high temperature experiments (2.5 GPa and up to 1650K) for simplified, but realistic binary system composed of MORB + San Carlos olivine. Interpretation of the results, to the light of textural processes upon partial melting, allowed determining that electrical conductivity is

critically sensible to solid-melt arrangement. The amount of partial melt required to explain the both electrical and seismic anomalies of mantle asthenosphere's LVZ are significantly lower than previously expected.

2) Résumé

Les comparaisons entre observations géophysiques et mesures de laboratoire aboutissent à des estimations antagonistes des fractions de liquides magmatiques impliqués dans les régions partiellement fondues du manteau terrestre. Ces estimations conflictuelles traduisent vraisemblablement des différences entre les mesures expérimentales de conductivités électriques et d'ondes acoustiques. Dans cette étude, nous avons réalisé des mesures simultanées des vitesses des ondes acoustiques et de la conductivité électrique d'un analogue à la fusion partielle (Olivine + basalte de ride médio-océanique MORB) à 2.5 GPa et jusqu'à 1650 K. Le but de l'étude est d'estimer les effets de la modification texturale d'un analogue à la fusion péridotitique sur les signaux géophysiques. La vitesse des ondes acoustiques (*V*p et *V*s) et la conductivité électrique sont mesurées sur le même échantillon, présentant une texture liquide/solide identique, le même gradient de température, le même état de contrainte et les mêmes impuretés. Une forte diminution des vitesses sismiques et une augmentation de la conductivité électrique ont été observées en réponse à la fusion partielle du composant basaltique. Stabilisée à une température constante de 1650 K, la conductivité électrique augmente graduellement alors que la vitesse des ondes acoustiques reste relativement constante. Alors que la totalité du composant basaltique (MORB) fond instantanément au-dessus de son solidus, l'inter-connectivité du liquide et sa distribution évoluent au cours du temps, affectant la conduction électrique. Nos observations expérimentales suggèrent donc que les vitesses des ondes acoustiques répondent immédiatement à la fraction volumique de liquide silicaté dans le cas d'un liquide très mouillant. La conductivité électrique est en revanche significativement affectée par les modifications texturales du liquide. La vitesse des ondes acoustiques semble être plus adaptée pour l'estimation des fractions de magmas dans un échantillon partiellement fondu aux échelles de temps de laboratoire (~ h). À partir de nos résultats, la réduction de la vitesse des ondes de cisaillement (*V*s) dans la partie majeure de la zone de faible vitesse, à distance des rides médio-oceaniques, peut être expliquée par 0.3-0.8 vol% de liquide magmatique ayant des volatils. Les rapports élevés de *V*p/*V*s (1.82–1.87) mesurés pour ces fractions de liquide sont également compatibles avec les observations géophysiques.

3) Simultaneous measurements of electrical conductivity and seismic wave velocity of partially molten geological materials: effect of evolving melt texture

Published article in Physics of Chemistry and Minerals (accepted 1St January 2019, online 12th January 2019).

Post print version, official version: https://link.springer.com/article/10.1007%2Fs00269-019-01021-5

Simultaneous measurements of electrical conductivity and seismic wave velocity of partially molten geological materials: effect of evolving melt texture

D. Freitas[1*] · G. Manthilake[1] · J. Chantel[2] · M. A. Bouhifd[1] · D. Andrault[1]

*Corresponding author: (damien.freitas@uca.fr +334.73.34.67.23, ORCID: 0000-0002-1722-4081)

[1] Université Clermont Auvergne, CNRS, IRD, OPGC, Laboratoire Magmas et Volcans, F-63000 Clermont-Ferrand, France

[2] UMET, Unité Matériaux Et Transformations, Bâtiment C6, University of Lille, Villeneuve d'Ascq, 59655 Lille, France

a) Abstract

Comparison between geophysical observations and laboratory measurements yields contradicting estimations of the melt fraction for the partially molten regions of the Earth, highlighting potential disagreements between laboratory-based electrical conductivity and seismic wave velocity measurement techniques. In this study, we performed simultaneous acoustic wave velocity and electrical conductivity measurements on a simplified partial melt analogue (olivine + mid oceanic ridge basalt, MORB) at 2.5 GPa and up to 1650 K. We aim to investigate the effect of ongoing textural modification of partially molten peridotite analog on both electrical conductivity and sound wave velocity. Acoustic wave velocity (*V*p and *V*s) and EC are measured on an identical sample presenting the same melt texture, temperature gradient, stress field and chemical impurities. We observe a sharp decrease of acoustic wave velocities and increase of electrical conductivity in response to melting of MORB component. At constant temperature of 1650 K, electrical conductivity gradually increases, whereas acoustic velocities remain relatively constant. While the total MORB components melt instantaneously above the melting temperature, the melt interconnectivity and the melt distribution should evolve with time, affecting the electrical conduction. Consequently, our experimental observations suggest that acoustic velocities respond spontaneously to the melt volume fraction for melt with high wetting properties, whereas electrical conduction is significantly affected by subsequent melt texture modifications. We find that acoustic velocity measurements are thus better suited to the determination of the melt fraction of a partially molten sample at the laboratory time scale (~ h). Based on our estimations, the reduced *V*s velocity in the major part of the low velocity zone away from spreading ridges can be explained by 0.3–0.8 vol.% volatile-bearing melt and the high *V*p/*V*s ratio obtained for these melt fractions (1.82 – 1.87) are compatible with geophysical observations.

Keywords: Electrical conductivity · Acoustic wave velocity · Low velocity zone · Dihedral angle · Melt fraction · MORB

b) Introduction

The Earth's asthenosphere is characterized by a region of high electrical conductivity (> 0.05 S/m) (Shankland and Waff, 1977), ~ 3–8% reduction of seismic wave velocity and high seismic attenuation (Anderson and Sammis, 1970; Romanowicz, 1995). A low degree of partial melting has often been considered as a viable explanation (partial melting hypothesis), because the magnitude of seismic and electrical anomalies cannot be explained by the temperature effect alone (Fischer et al., 2010). Alternative mechanisms based on solid state processes, such as anelastic relaxation (Goetze, 1977; Stixrude and Lithgow-Bertelloni, 2005) and hydrogen diffusion (Karato, 1990) in mantle minerals have also been proposed (null hypothesis). However, the recent finding of young alkali basalt (< 10 Ma) on the 135 million-year-old Pacific plate (Hirano et al., 2006) provides strong physical evidence for partial melting at the top of the asthenosphere.

The criteria for melting in the asthenosphere have been discussed in a number of recent papers (Galer and O'Nions, 1986; Plank and Langmuir, 1992; Dasgupta and Hirschmann, 2006). Volatile-assisted melting in the asthenosphere is favored as the mantle temperatures at the relevant depths are expected to be lower than the dry peridotite solidus (Dasgupta and Hirschmann, 2006). The volatile contents of the primitive mantle samples suggest mantle abundances of ~ 150 ppm wt of H_2O and ~ 100 ppm wt of CO_2 (Saal et al., 2002), while CO_2 contents of up to 1800 ppm wt have been reported in undegased sources (Cartigny et al., 2008). The recent discovery of young alkali basalt associated with volcanism along fractures in the lithosphere indicates up to 5 wt% CO_2 and 1.0 wt% of H_2O volatile contents (Okumura and Hirano, 2013). However, the measurements based on melt inclusions in minerals and quenched glasses indicate a global average of about 3000 ppm wt of H_2O and 170 ppm wt of CO_2 in natural mid oceanic ridge basalt (MORB) (Naumov et al., 2014). A substantial contribution of volatiles to the melting can be expected at low temperature regions in the asthenosphere (Sifré et al., 2014; Yoshino et al., 2010). The reduced seismic velocity and elevated electrical conductivity have been widely used as evidence for the presence of melt in the Earth's interior (Anderson and Sammis, 1970). The magnitudes of the seismic velocity and conductivity variations are directly linked to the melt fraction, therefore comparison of geophysical data with laboratory models has long been considered as the most plausible way to quantify the melt contents in partially molten regions of the Earth (Anderson and Sammis, 1970; Shankland and Waff, 1977). The accurate determination of melt volume fraction in the asthenosphere is a key constraint for the plate tectonics and mantle convection models (Schmerr, 2012). Apart from identifying the partially molten regions and quantifying the melt fractions, the seismic and electrical methods can also be used to characterize their spatial distribution. For example, laboratory-based experiments (Caricchi et al., 2011; Zhang et al., 2014; Pommier et al., 2015) have been able to attribute the seismic and electrical anisotropies observed at spreading ridge environments to the shear localization of melt due to plate motion.

The presence of a melt significantly modifies the viscoelastic properties of mineral assemblages. The critical parameters are the volume fraction and the melt microstructures (Kohlstedt, 1992). Unfortunately, experimental determinations of seismic velocity on realistic melt compositions are limited to a few studies. An early measurement of *V*p and *V*s in a melt-bearing peridotite reported no significant effect of melt fractions below 3.0 vol.% (Sato et al., 1989). The measurements based on torsional forced oscillation of melt-bearing olivine indicate reduced seismic velocities, and high attenuation can be observed for melt fractions as low as 0.01 vol.% (Faul et al., 2004), suggesting a possible melt fraction of 0.1 – 1 vo.l%, for the average grain size variation in the upper mantle from 1 to 10 mm, respectively. The recent experimental developments allow accurate determination of seismic velocity measurements of partially molten rocks at the pressure and temperature conditions expected at the Earth's interior (Chantel et al., 2016) and predicted about 0.2 vol.% melt content in the asthenosphere. On the contrary, the melt fraction estimations based on the acoustic velocity of analogue systems (Takei, 2000) indicate significantly higher melt fractions than those predicted using realistic upper mantle melts (Faul et al., 2004; Chantel et al., 2016). For example, the 6.6% melt required to explain 10% *V*s reduction in Borneol-diphenylamine analogue system (Takei, 2000) is considerably higher than the about 1% melt required by basaltic melt to explain a similar velocity reduction (Chantel et al., 2016).

The dependence of acoustic wave velocities and attenuation upon melt fraction and grain-scale melt distribution has also been discussed in several theoretical studies. These studies were based on ideal melt geometries and explained using the oblate spheroid model (Schmeling, 1986), tube model

(Mavko, 1980), the crack model (O'Connell and Budiansky, 1974) and models based on grain boundary wetness or ''contiguity'' (Takei, 1998, 2002; Yoshino et al., 2005; Hier-Majumder, 2008). The calculations based on the finite element method on melt geometries led (Hammond and Humphreys, 2000) to conclude more than 1% melt is required to explain 3.6% and 7.9% velocity reduction for *V*p and *V*s respectively, which is significantly lower than the 6.2% and 11% reductions observed in laboratory measurements for similar melt fractions (Chantel et al., 2016). The naturally occurring, randomly distributed melt (Faul et al., 2004; Chantel et al., 2016) is shown to have a significant effect on seismic velocity compared to the simplified melt textures assumed in theoretical models (Hammond and Humphreys, 2000; Takei, 2002; Yoshino et al., 2005) or analogue systems (Takei, 2000). The considerably higher melt volume fractions required in theoretical models can be attributed to the idealized geometries, such as planar cracks, spheres, ellipsoids, or simplified cuspate forms, which may not represent the true melt geometries in naturally occurring melt (Kohlstedt, 1992; Faul et al., 1994; Hammond and Humphreys, 2000), limiting their applications to partially molten regions in the asthenosphere.

An early electrical conductivity measurements on basaltic melt suggested 5 – 10 vol.% melt needed to account for the observed electrical anomalies in the asthenosphere (Tyburczy and Waff, 1983; Maumus et al., 2005). However, recent studies suggest the presence of much lower volume fractions; 0.3–3.0 vol.% for hydrous basaltic melt (Yoshino et al. 2010; Ni et al. 2011), or less than 0.3 vol.% for carbonatitic melt (Gaillard et al., 2008; Yoshino et al., 2010). The electrical conductivity of volatile enriched basalt (15 – 35 % CO_2 and about 2 – 3 wt% H_2O) indicates about 0.1 – 0.15 vol.% melt could explain the observed conductivity anomalies (Sifré et al., 2014). The development of melt interconnectivity in partially molten rocks is known to have a profound effect on electrical conductivity (Waff, 1974; Maumus et al., 2005). However, the number of studies investigating the influence of melt microstructures on EC is extremely limited. The study by ten Grotenhuis et al. (2005) showed that a melt geometry evolving from isolated triple junction tubes at 0.01% of melt to a network of interconnected grain boundary melt layers at 0.1% of melt has a greater effect on electrical conductivity.

Various other experimental techniques have been used to constrain the melt fraction associated with the low velocity zone (LVZ) in the Earth's asthenosphere. Geochemical constraints from trace elements partitioning suggest that low degree of melting (less than 1%) can be generated at greater depth (below than 100 km) (Salters and Hart, 1989). Similarly, studies based on experimental petrology, such as volatile (H_2O and CO_2) effect on peridotite solidus, indicate the melt fraction in the asthenosphere LVZ has to be 0.1 vol.% or less (Plank and Langmuir, 1992; Dasgupta and Hirschmann, 2007).

Both experimental and theoretical models acknowledge that the volume fraction and spatial distribution of melt play an integral part in modifying the seismic and electrical properties of partially molten rocks. However, large discrepancies still remain in the laboratory estimations (regardless of the technique) of the amount of melt volume fraction present in the asthenosphere (Pommier and Garnero, 2014; Karato, 2014). Due to the large number of studies addressing the electrical properties of melt, the disagreement between laboratory-based electrical conductivity measurements is highly visible (Karato, 2014). The influence of volatile contents could be one of the key parameters controlling the conductivity of the resulting melt (Yoshino et al., 2010; Ni et al., 2011; Sifré et al., 2014). A model based on chemical variation in the melt has been proposed to explain the apparent disagreement on melt fraction estimations between electrical conductivity measurements and seismic models (Pommier and Garnero, 2014). The discrepancy may primarily stems from the absence of systematic experimental investigation into the structural factors influencing the EC in partially molten systems. The effect of melt fraction on seismic velocity has been mostly limited to numerical models. Significant disagreement between these theoretical models is still present due to the choice of melt geometries (Yoshino et al., 2005). A comparison with recent laboratory based seismic velocity measurements on realistic partially molten materials (Chantel et al., 2016) indicates a significant underestimation of seismic response by theoretical models (Takei, 2000; Yoshino et al., 2005). The cross-correlation of melt fraction estimations based on theoretical seismic models and laboratory electrical conductivity is at present a highly uncertain exercise.

The effect of melt texture and chemical compositions (volatiles) have long been assumed for the observed inconsistency, but there has never been a systematic study on how the evolving melt textures influence the electrical conductivity and seismic velocity (SV). Similarly, melt textures and melt contents during high pressure, high temperature experiments are strongly affected by the stress field

and the temperature distribution within the sample and it is highly unlikely that two experiments would yield identical melt distributions.

In this study, we aim to investigate the effect of ongoing textural modification of partially molten peridotite analog on both electrical conductivity and sound wave velocity. Here we have developed a novel high-pressure multi-anvil cell design to investigate simultaneously the seismic and electrical properties of partially molten samples. Acoustic wave velocity (*V*p and *V*s) and EC are measured on an identical sample presenting the same temperature gradient, stress field and the chemical impurities, which all influence the melt content and the melt texture in partially molten high pressure samples. This critical improvement enables us to compare the seismic and electrical responses to the onset of melting, to different melt volume fractions and to the evolution of melt interconnectivity of a partially molten sample. Based on our observations, we suggest possible scenario which may resolve the observed discrepancy of melt fraction estimations based on EC and SV measurements.

c) Methods

i) Sample preparation

Samples used in this study were a powder mixture of natural San Carlos (SC) olivine and volatile-rich natural MORB glass (location 6°44′N, 102°36′W, collected during the Searise-1 research cruise). The volatile content is estimated to be 2730 (± 140) ppm wt H_2O and 165 (± 40) ppm wt CO_2 (Andrault et al., 2014), comparable with the average H_2O and CO_2 levels observed in MORB from diverse geological settings (Naumov et al., 2014). The MORB glass and inclusion free, hand-picked, SC olivine crystals were crushed separately and reduced to fine grain powders (see grain size distribution in Fig. III.S1). The water content analysis of the San Carlos olivine indicates less than 1 ppm wt of water (Soustelle and Manthilake, 2017). These powders were then mixed in predetermined weight proportions to obtain the desired melt fractions at high temperature. The accurate determination of melt fraction using the image analysis is an uncertain exercise. The mixing of MORB with olivine results in an accurate control of the melt fraction in the sample as the MORB component melts instantaneously above its melting temperature, which is significantly lower than the olivine solidus. This procedure has been extensively used to obtain a controlled melt fraction in high-pressure experiments (Faul et al., 1994; Cmíral et al., 1998; Maumus et al., 2005; Yoshino et al., 2010; Caricchi et al., 2011; Zhang et al., 2014; Chantel et al., 2016). While this technique is suitable for obtaining controlled melt fractions (nominal melt fractions) in laboratory experiments, it cannot be used as a substitute for the physical property measurements of incipient melting scenarios (Sifré et al., 2014). We prepared different starting materials with MORB volume fractions of 0.1, 0.5, 1 and 2 vol.% mixed with San Carlos olivine. The powder mixtures were ground with an automatic agate mortar for more than 2 h to obtain a homogeneous distribution of the MORB component. The average grain size of the starting powder size was estimated to be 3.74 ± 3.32 μm (Fig. III.S1). To achieve high accuracy during weighting of the powder, we prepare more than 5 g for each composition. The resulting powder mixtures were then hot pressed at 2.5 GPa and 1100 K for 2 h using a 1500 ton multi-anvil apparatus. The low temperature for hot pressing experiments (below the melting temperature of MORB) ensures that the starting materials are melt free and thus that the evolution of melt texture occurs during the conductivity and velocity measurements.

ii) High-pressure high-temperature experiment

High-pressure, high-temperature experiments were performed using a 1500 ton Kawai-type multi-anvil apparatus at Laboratoire Magmas et Volcans, Clermont-Ferrand, France. For experiments conducted at 2.5 GPa, we used octahedral pressure media composed of MgO and Cr_2O_3 (5 wt%) in an 18/11 multi-anvil configuration (octahedron edge length/anvil truncation edge length) (Fig. III.1). The assembly was designed to accommodate the geometrical requirements for measurements of *V*p, *V*s and EC in a single high pressure cell. The pre-synthesized cylindrical sample was inserted into a hexagonal boron nitride (hBN) capsule. The use of high-purity hBN sintered at high temperature and pressure without binder (Type—BN HP, FINAL Advanced Materials) prevents the B_2O_3 reacting with the silicate melt. The hBN capsule also helps to electrically insulate the sample with respect to the furnace. The furnace is composed of a 25 μm thick cylindrical Re foil, with apertures for the electrode and the thermocouples wires. A zirconia sleeve was placed around the furnace to act as a thermal insulator. Oxygen fugacity of the sample was not controlled during the experiments, but should be below Re-ReO_2 buffer. We placed two electrodes made of Re discs (25

μm thick) at the top and bottom of the cylindrical sample. A tungsten rhenium ($W_{95}Re_5$–$W_{74}Re_{26}$) thermocouple junction was placed at one end of the sample to monitor the temperature. On the opposite side it was connected to a single W95Re5 wire (see Fig. III.S2 for details on electrode connection). We collected impedance spectra between the two $W_{95}Re_5$ wires. Cylindrical MgO ceramic sleeves were used to insulate the electrode wires from the furnace. A dense Al_2O_3 buffer rod was placed between one of the tungsten carbide (WC) anvil truncations and the sample to enhance the propagation of elastic waves and to provide sufficient impedance contrast to reflect ultrasonic waves at the buffer rod-sample interface. Both ends of the anvil, the alumina buffer rod and the samples were mirror polished using 0.25 μm diamond pastes to enhance mechanical contacts. All ceramic parts of the cell assembly, including the pressure media, were fired at 1373 K prior to the assembling to remove any absorbed moisture.

iii) Acoustic wave velocity measurements

Acoustic wave velocities of samples were measured using the ultrasonic interferometry technique (Chantel et al., 2016; Freitas et al., 2017). In this method, electrical sine wave signals of 20–50 MHz (3–5 cycles) with *V*peak-to-peak of 1–5 V were generated by an arbitrary waveform generator (Tektronix AFG3101C) and were converted to primary (*V*p) and secondary (*V*s) waves by a 10° Y-cut $LiNbO_3$ piezoelectric transducer attached to the mirror polished truncated corner of a WC anvil. The resonant frequency of the transducer is 50 MHz for compressional waves (P-waves) and 30 MHz for shear waves (S-waves). Elastic waves propagated through the anvil, the alumina buffer rod (BR) and the samples, and were reflected back at the anvil-BR, BR-sample, and sample-electrode interfaces. We also consider possible reflections from the Re electrodes (Davies and O'Connell, 1977; Jackson et al., 1981; Nielser and Jackson, 1989) (Text III.S1c). The reflected elastic waves were converted back to electrical signals by the transducer and captured by a Tektronix DPO 5140 Digital Phosphor Oscilloscope at a rate of 5×10^9 sample/s. Signals at 20, 30, 40 and 50 MHz were recorded at each temperature step. The two-way travel time for the acoustic waves propagating through the sample can be determined by the time difference between the arrivals of the echoes from the BR sample interface and the sample-electrode interface by the pulse-echo overlap method (Kono et al., 2012).

iv) Electrical conductivity measurements

EC measurements were performed using the ModuLab MTS Impedance/Gain-phase analyzer in the frequency range of 10^6– 10^1 Hz. Polyphasic samples are characterized by a combination of resister-capacitor/constant phase element (R-C/ CPE) circuits and the resistance can be obtained by fitting the impedance spectra to appropriate equivalent circuits (Fig. III.S3). Once the sample resistance has been determined, conductivity can be calculated using the sample dimensions determined at each temperature using the thermal expansion of the constituent phases. The insulation resistance of the assembly was determined in a preliminary experiment using an hBN rod at similar pressure–temperature conditions and was observed to be lower than the sample resistance. At the target pressure of 2.5 GPa, the sample was kept at 500 K for more than 12 h. While maintaining 500 K, the electrical resistance of the samples, measured at regular intervals, usually increases due to the removal of the moisture absorbed by the sample and surrounding materials. This step is crucial to prevent the moisture (H_2O) being incorporated into the sample at higher temperatures (Manthilake et al. 2009). The next heating cycle started once the resistance reached a steady value, which is often 1–2 orders of magnitude higher than the resistance measured at the beginning of the heating cycle. We generally performed several heating–cooling cycles at temperature steps of 50–100 K, until sample resistance was reproducible between the heating and cooling paths. This procedure minimizes the uncertainty of EC measurements due to adsorbed moisture. Once the solid sample EC was reproducible, the temperature was gradually increased in smaller temperature steps (25 K) to initiate melting. Sample melting is characterized by a drastic decrease in the sample resistance (increase in conductivity). Finally, the temperature was kept constant at 1650 K and impedance spectra were collected at regular intervals for more than 1 h.

v) Melt textures and Dihedral angle measurements

Micro-textures of the recovered samples were investigated with a Field Emission Gun Scanning Electron Microscope (FEG-SEM) with an accelerating voltage of 15 kV and working distance of 9–11.6 mm.

High magnification back scattered electron (BSE) images were obtained to identify the degree of interconnectivity and the structure of the melt at the grain boundaries in partially molten samples after SV and EC measurements. The presence of the hard alumina piston may introduce differential stresses to the sample, resulting in a shape-preferred orientation (SPO) in partially molten samples (Bussod and Christie, 1991). To characterize the possible melt alignment in an olivine matrix, we performed image analyses on BSE images along a section parallel to the axis of the cylindrical sample. The orientation of the long axis of melt pockets and area of the melt pockets were obtained by image processing techniques using Matlab software (Fig. III.S4).

vi) Grain size and grain orientation distribution

The grain size of our samples was estimated using two different techniques: the intercept method, and using FOAMS software (Shea et al., 2010). The intercept method estimates the number of intersections of grain boundaries with a random line drawn across the sample. The length of the line is important to statistically cross enough grains. The FOAMS software measures every isolated particle from skeletonized images and estimates its morphological parameters: area, perimeter, shape from 2D ellipse with a long and short axis, etc. The program also calculates 2D parameters such as aspect ratio and elongations. From the binary images, the code can convert 2D morphological information into 3D information using the equivalent diameter for spherical geometry by means of stereological conversion equations from (Sahagian and Proussevitch, 1998). This program works properly for all type of samples for 2D information. Volumetric estimations (2D – 3D) can be performed when the grains are mostly rounded and do not show strongly elongated shapes. Results are given in Table III.S1.

vii) Experimental uncertainties

Experimental measurements of *V*p, *V*s and EC are subjected to uncertainties originating from the estimation of temperature, pressure, sample dimensions and fitting errors. Errors have been estimated to be 2.5% for seismic velocities (2σ), 5% for velocities drops (2σ) and 5% for EC values (2σ). Errors on the melt fractions are less than 1% relative (ex: 1 ± 0.01% of MORB). Detailed sources of uncertainties for each technique and error propagation calculations are given in supporting information (Text III.S1) (Bouhifd et al., 1996; Gillet et al., 1991; Li et al., 2007). Error bars are reported in each figure when larger than the symbol size except Figs. III. 2 and III.8a for visibility.

d) Results

i) Acoustic velocity

The acoustic wave velocities obtained for samples containing SC olivine and 0.1, 0.5, 1, and 2% nominal volume fractions of melt are shown in Fig. III.2. Below the melting temperature, *V*p and *V*s decrease with increasing temperature, emphasizing the characteristic decrease of bulk and shear modules with temperature. Upon melting of the MORB component, which is at about 1590 K, both *V*p and *V*s decrease significantly for the samples with 0.5–2% MORB. The magnitude of the velocity drop is positively correlated to the MORB fraction in the sample, but no significant change is observed at the melting temperature for pure olivine and the sample with 0.1 vol.% melt. After the initial decrease in response to the MORB melting, the acoustic velocities *V*p and *V*s remain unchanged while maintaining the sample at a constant temperature of 1650 K.

ii) Electrical conductivity

The electrical conductivity of samples containing 0.1, 0.5 and 2 vol.% of nominal melt fractions are shown in Fig. III.3. At the melting temperature of MORB (~ 1590 K), the samples with 0.5 – 2 vol.% melt indicate sudden increases in conductivity (up to a factor of 5), compared to their solid counterparts. However, no immediate change in conductivity is observed for 0.1 vol.% melt upon crossing the temperature threshold. EC of all melt-bearing samples continues to increase after the melting event, while being kept at a constant temperature of 1650 K. The rate of increase of conductivity gradually decreases with time (Fig. III.3), probably approaching a steady-state with time, however, these 1-h duration experiments did not reached a stable EC value overtime. The conductivity values after being kept at 1650 K for more than 30 min indicate an increase in conductivity of 0.6 log units, a factor of 3.98, for the 0.1% melt sample compare to the value obtained before melting. The conductivity variations after being kept for more than 50 min at 1650 K, are about 0.6 log units, a factor of 3.98, for the 0.5%, and a 0.4 log units, a factor of 2.51, for the 2% melt-bearing samples.

iii) Textural analyses of samples and melt

The presence of melt is clearly visible for all samples, with melt distributing along the grains boundaries as well as triple junction tubes. Interconnected melt networks are visible over a large part of each sample including the sample with 0.1 vol.% of melt (Fig. III.4). Using the high resolution SEM images, we determined the wetting angles of the melt-solid interfaces, which indicate a median angle of 27° ± 4°.

Table III.S1 presents the grain size and grain orientation parameters derived from both intercept and FOAMS software, samples average grain size are similar and between 7 and 15 µm. The eccentricity is calculated from the best fitting ellipse foci and circle center. This parameter indicates how far the best fitting ellipse deviates from perfect circularity, the values from 0.76 to 0.84 in our samples indicate that grains are mainly rounded but not perfect spheres. Elongation parameter is expressed by $\varepsilon = (a - b)/(a + b)$, which characterizes the difference between the long (a) and short (b) axes of the fitting ellipse; large values (close to 1) indicate elongated particles. Our average values trends from 0.25 to 0.36, meaning grains have an elliptic cross section which slightly deviates from circularity. Aspect ratio is expressed as $A = b/a$, and characterizes the shape of the particle; large aspect ratios (close to 1) indicate particles are rounded and not elongated; our high-intermediate values are in good agreement with this observation.

The analyses based on the orientation of the long axis of melt pockets indicate random distribution of melt within the olivine matrix (Fig. III.S4). The associated histogram indicates no significant preferential orientation.

e) Discussion

i) Effect of evolving melt texture on acoustic wave velocity and electrical conductivity

Upon melting, partially molten samples evolve toward textural equilibrium with time, thus improving the melt interconnectivity and melt redistribution within the olivine matrix (Fig. III.4). The comparison of images of samples before melting and after keeping prolonged time above the melting temperature of MORB clearly demonstrate the evolution of Ol + MORB powder mixture from initial non-equilibrium state (MORB is randomly distributed) to the extensive wetting of crystal faces and the smoothly curved solid-melt interfaces (Fig. III.S5). The textural equilibrium depends on several factors such as melt fraction, melt chemistry and grain size distribution (Laporte and Provost, 2000). The melt geometries in olivine-basalt systems consist of grain boundary melt layers, triple junction networks (Yoshino et al., 2005, 2009) and ellipsoïdal discs (Faul et al., 1994). The continuous increase of EC observed in our experiments can be attributed to the gradual development of an interconnected network of melt channels, which facilitate the movement of charge carried through the melt. In contrast, acoustic wave propagation in a partially molten media should be more affected by the presence of melt in its path (volume fraction), than its fine geometrical evolution subsequent to melt interconnection. We note that the EC increased rapidly in the first tens of minutes and appeared reaching near steady-state after about 1 h, indicating that the textural modifications that influence the interconnectivity of the melt can be mostly achieved within few hours. The melt takes its final like shape very rapidly (in the first hour), however complete equilibration between melt and host olivine matrix in both chemical and textural aspects require several weeks of annealing (Waff and Blau, 1982; Laporte and Provost, 2000).

(1) Interpretation of acoustic wave velocity results

The magnitude of the drop in seismic wave velocity in response to melting is proportional to the melt volume fraction in the sample (Fig. III.2). Compared to the higher melt fractions, the sample containing 0.1% melt does not show abrupt variations of acoustic wave velocity in response to the onset of melting of MORB components. This observation suggests that the volume fraction of melt has to be sufficiently large (higher than 0.1 vol.%) to alter the seismic wave propagation through partially molten rock. Additionally, associated errors to seismic wave velocity measurements and fitting does not allow distinguishing significant drop for low melt fractions (~ 0.1%). Further, the relatively constant seismic velocity at a constant temperature of 1650 K, after the melting of MORB, suggests that the seismic velocity is less sensitive to the ongoing textural equilibration of the sample. The melt fraction in a partially molten rock with complete wetting properties is observed to be the key parameter controlling the magnitude of seismic velocity in geological systems. The secondary waves (Vs) are more sensitive to the presence of melt

due to their near zero shear modulus, which further enhances their ability to detect and quantify melting in laboratory samples.

The comparison of present data with previous experimental and theoretical estimations of seismic velocity is shown in Fig. III.5. While our results are consistent with that of Chantel et al. (2016), there are considerable deviations in our experimental values from those estimated based on theoretical approximations (Takei, 2000). As explained previously, the disagreement may arise due to the simplified melt geometries assumed in theoretical models. This observation can be further corroborated by comparing two theoretical models, one based on natural melt geometries (Yoshino et al., 2005), and the other on ideal melt geometries (Takei, 2000). The model with melt arrangements similar to naturally occurring melt record a significant velocity drop for a given melt fraction compared to the one assuming ideal melt distribution. However, the model based on grain boundary wetness (Yoshino et al., 2005) also predicts the seismic velocities are significantly affected by modifications on the pore geometry. It has been shown that the melt wetting properties vary significantly with increasing pressure and volatile content (Yoshino et al., 2007). The slight discrepancy between the present study and that of Yoshino et al., (2005) can be explained by the change in wetting properties, due to improved melt wetting properties at high pressure and the presence of both H_2O and CO_2 in our samples.

(2) Interpretation of electrical conductivity results

The electrical conductivity variation while kept at constant temperature (at 1650 K) provides valuable insights into the development of interconnected melt channels in partially molten samples. For larger melt fractions (above 0.1%), the melt network forms efficiently as shown by an order of magnitude conductivity increase observed at the onset of melting. However, after the onset of melting and the associated EC jump, while kept at constant temperature of 1650 K, the increase in electrical conductivity for larger melt fractions (2% with 0.4 log unit increase of EC) is smaller than the sample with a low melt fraction (0.1% with 0.6 log unit increase of EC). This potentially indicates that when the melt fraction is sufficiently large, the major portion of melt is already arranged into a well distributed network of melt channels. On the other hand, the subsequent modifications improving the melt interconnectivity have a significant effect on low melt fractions. It has been shown that the melt geometry in a mineral-melt aggregate is determined by the solid–solid and solid–liquid interfacial energies (Laporte and Provost, 2000). The solid–liquid interfacial energies may control the interconnectivity of a partially molten medium at low melt fraction; the network of melt could be limited in its 3D extension between the olivine grains, with some surfaces remaining initially non-wetted due to surface tension.

As for acoustic velocity, a sharp variation in electrical conductivity was not immediately apparent for the sample with 0.1% melt fraction. However, when maintained at 1650 K, EC continued to increase for the 0.1% melt sample, after 1 h to 0.6 log unit higher than the conductivity of the sample before melting. This observation suggests that the electrical conductivity method can be used to detect melt fractions lower than 0.1% as long as the measurements are performed on texturally equilibrated samples. This indicates that EC is extremely sensitive to the onset of melting. Furthermore, the sample resistance measurement is instantaneous and can be a powerful tool to detect the onset of melting during an experiment.

The electrical conductivity of similar olivine-basalt systems has been investigated in previous experiments (Maumus et al., 2005; Yoshino et al., 2010; Caricchi et al., 2011; Zhang et al., 2014; Laumonier et al., 2017) (Fig. III.5). While measured conductivities are located within the individual EC measurements of olivine (Constable, 2006; Laumonier et al., 2017) and basaltic melt (Presnall et al., 1972; Tyburczy and Waff, 1983; Ni et al., 2011; Laumonier et al., 2017), the partially molten systems do not display good agreement between different studies. The slightly higher EC observed for partially molten samples in Yoshino et al.(2010), compared to our study may have been due to their use of texturally equilibrated melt-bearing samples (pre-synthesized samples in a piston cylinder apparatus) in electrical conductivity measurements, which compare favorably with our observations. EC values comparable to texturally equilibrated samples can be obtained by extrapolation of our EC data for timescales of days and weeks (Fig. III.6).

ii) The source of discrepancy

The interpretation of seismic and electrical anomalies in terms of melt fraction often results in conflicting estimations as to the extent of melting in the asthenosphere (Pommier and Garnero, 2014;

Karato, 2014). A conductivity model based on major element chemistry of melt attributed the apparent inconsistencies in conductivity measurements to possible chemical variations in the melt (Pommier and Garnero, 2014). Their model predict that low degree melting of peridotite produces melt that is more conductive than basaltic compositions. We find their approach is an important step towards unifying the seismic and electrical observations. However, the melt fractions estimations used in their study were based on theoretical models, which appear to underestimate the effect of melt fraction on seismic velocity. Monitoring the behavior of melt-bearing samples for an extended period of time at high pressure and high temperature remains a challenging exercise. Escape of melt during prolonged heating is one of the major sources of failure, and experimental studies often overcome this issue by shortening the duration of the in situ measurements at high temperature. However, our results demonstrate that the EC values can vary significantly with time within the first hour of measurements, and relatively stable EC values can be obtained once the 3D interconnected network has been established. Texturally non-equilibrium melt can lead to an underestimation of the total effect on EC of a given melt fraction (Fig. III.6). Comparison of such measurements with geophysical profiles, therefore, results in an overestimation of the melt fraction in the corresponding region in the Earth's mantle. Values here provided after 1 h at 1650 K are not fully stabilized as highlighted by the subtle slope of the fit. We also note that once the sample conductivity stabilized, as a result of improved melt interconnectivity, electrical conductivity values of samples containing 0.1, 0.5, and 2% are not considerably different (less than one order of magnitude). This difference becomes subtle, close to the uncertainty of measurements, for higher melt fractions according to the trend shown in Fig. III.6. This implies that uncertainties on inferred melt fractions from EC can be very important if implied melt fractions are higher than few percents. This observation is particularly crucial for magnetotelluric (MT) profiles with low spatial resolution. For these reasons, EC values here provided will not be further used for geophysical implications. However, we note that the electrical conductivity measurements are superior over acoustic wave velocity for qualitative detection of low melt fractions for samples with evolved melt textures. If the wetting properties of the melt are modified by the presence of significant amounts of volatiles in the melt (H_2O and CO_2) the electrical response for low melt fractions is instantaneous (Sifré et al., 2014).

In this study, we observe real-time *V*p, *V*s and EC responses during melting and consecutive textural evolution of melt. The variation of electrical conductivity subsequent to the melting of MORB can also be caused by the chemical changes occurring at high temperatures for a prolonged period of time. The effect of change in chemical composition on electrical conductivity in melt has been investigated in previous studies (Roberts and Tyburczy, 1999), with a general trend showing an increase in conductivity with increasing alkali and Fe + Mg contents and a decrease with increasing silica content. However, we observe that the melt composition stays similar to the starting MORB composition during the experiments, except for a minor decrease in Fe content (Table III.1). The Na is an important charge carrier in silicate melt (Pfeiffer, 1998; Gaillard and Marziano, 2005; Ni et al., 2011) and Na contents in our melt remains similar to the starting composition. Based on the totals of chemical analyses of melt, we confirm that significant volatile enrichments may not occur in our melt. Therefore, the observed conductivity increase with time is not expected to be caused by any chemical modification to the melt. This observation also confirms that the final melt fraction in the sample stays similar to the starting material. Similarly, due to the low partition coefficient between olivine and melt (~ 0.004) (Novella et al., 2014), the water is mostly retained by the melt phase, so proton (H+) diffusion in olivine affecting the electrical conductivity at high temperature can also be ruled out. The constant velocity after the melting of MORB components also rules out the possible increase in melt fraction in the sample at constant temperature, which is also supported by image analysis and chemical mapping of the sample. Further, analyses on the orientation of the matrix and melt pockets in our samples indicate random shape-preferred orientation (SPO) ruling out melt channeling due to possible anhydrostaticity in the high-pressure cell assembly (Fig. III.S4).

iii) Applications of laboratory results to the Earth's interior

The comparison between laboratory data and seismological signals requires experiments in which the molten phase is in textural equilibrium with the solid matrix. Due to time-limited laboratory experiments, transient conditions may affect the results of acoustic velocities. In this case, textural analysis is important for correct interpretation of

experimental data and run products. In a partially molten system at given pressure and temperature, the melt network can evolve to minimize the energy of melt-solid interfaces. This equilibration process concerns the wetting angle θ at solid–solid melt triple junctions, the area-to-volume ratio of melt pockets at grain corners and the melt permeability threshold (Laporte et al., 1997). The small dihedral angles estimated for our partially molten samples ensures complete grain boundary wetting and melt interconnectivity even for extremely low melt volume fractions (von Bargen and Waff, 1986; Laporte et al., 1997; Laporte and Provost, 2000), which is crucial for propagation of seismic waves. The solid-melt dihedral angle is known to vary with pressure, temperature and with the composition of the melt phase (Minarik and Watson, 1995; Yoshino et al., 2005). Experimental studies suggest that textural equilibration is a time-dependent process, which usually requires long annealing times (weeks or months) (Waff and Blau, 1982; Laporte and Provost, 2000; Maumus et al., 2005). Still, small dihedral angle (10° – 30°), the extensive wetting of crystal faces and the smoothly curved solid-melt interfaces observed in our samples are strong indications that the microstructure has reached transient conditions and forming a melt-solid network close to equilibrium textures (Cooper and Kohlstedt, 1984; Waff and Faul, 1992; Cmíral et al., 1998) (Fig. III.4). Further, after reaching the peak temperature, the acoustic velocity remains nearly constant (Fig. III.2), suggesting that the samples are well relaxed, enabling a safe comparison of our seismic wave velocity measurements with geophysical observations.

In addition, the extrapolation of laboratory acoustic wave velocities measurements to natural observations require the consideration of both anelasticity and frequency effects. Laboratory experiments (when not torsional) are usually performed at the frequency range from 20 to 50 MHz. The choice of this frequency range is determined by both requirements on excitation frequencies for the piezo-electric transducer as well with the restricted size of the probed samples in HP-HT apparatus.

Both anelasticity and anharmonicity that are accounting for the temperature dependence of sound velocity could lower the observed velocities. These are functions of frequency, temperature, pressure, mineral/melt intrinsic properties (including the chemical composition) as well as grain size and grain boundaries micro-textures (Rivers and Carmichael, 1987; Karato, 1993; Jackson et al., 2002, 2004; Faul et al., 2004). In solids, anharmonic effects related to thermal expansion ($\partial\rho/\partial T$) were found to be important in high frequency (MHz) experiments. This process does not imply energy loss and remains nearly insensitive to frequency (Karato, 1993). On the other hand, anelasticity is associated to energy loss and depends on frequency and relaxation effects. Relaxation effects are thermally activated, hence anelasticity must be accounting for a significant part of the attenuation at high temperatures. Anelasticity of partially molten system have been poorly studied (Faul et al., 2004; Jackson et al., 2004). Because our melt fractions are small ($\leq$ 2%) and similar to melt fraction estimated in the mantle, the assumption of using anelastic values of pure olivine is reasonable (Jackson et al., 2002; Chantel et al., 2016), also partially molten systems were found to have similar grain boundary sliding process to solid (Jackson et al., 2002; Faul et al., 2004). Nevertheless, this process is more easily activated in melt-bearing samples, where weaker grain boundaries have been reported (Faul et al., 2004). In addition, most of silicate melts have very high absorption in this frequency range and signals are seriously attenuated (Rivers and Carmichael, 1987). However, this study showed that the echo overlap technique is suitable for high-Q melts, and thus appropriate for MORB melts. This study also stressed that for low viscosity melts (< 1000 Pa·s), which is the case of MORB melts at high temperature (presence of volatiles will significantly increase this effects), velocities are independent from frequency, as expected when wave's period is much smaller than the characteristic relaxation time ($1/f \ll \tau$). Relaxation time was estimated using the relation $\tau = 0.01 \times \eta \times \beta$, where β is the inverse of adiabatic compressibility and η the melt viscosity, used for fitting of theoretical and experimental dispersion curves by Rivers and Carmichael (1987). Calculation using their parameters for the Kilauea basalt (1700 K) yields relaxation time of 0.467 nanoseconds for frequency of 30 MHz (used in our study). The product of angular frequency by relaxation time between 10^{-2} and 10^{-1} (0.088) can be converted into a $C/C0$ ratio (see Fig. 10 in Rivers and Carmichael, 1987). It estimates the measured velocity to be similar to the relaxed one as the ratio is very close to unity ($1 \leq C/C0 < 1.10$), pointing a very small effect of anelastic behavior. Our moderately hydrous MORB probably have a lower viscosity and accordingly a shorter relaxation time favoring our conclusions. Detailed discussion on quality factor (Q) estimation by ultrasonic experiments, on similar compositions, has already been made by Chantel et al. (2016). However, our $\partial\ln(Vp)/\partial T$ and $\partial\ln(Vs)/\partial T$ values of − 4.95 and − 8.78 ($\times 10^{-5}$) K^{-1}, of our

olivine + MORB samples prior melting, are somewhat similar with temperature dependence values calculated by high-*Q* from Karato (1993), indicating a good agreement with pure olivine data up to melting point with anharmonic plus anelastic behavior.

Finally, the use of MHz frequencies tends to underestimate the effect of anelasticity. This increases the uncertainty on our measurements, but this uncertainty must be reasonable as shown by the small errors estimated in absorption calculations (4%) (Rivers and Carmichael, 1987), as well with near relaxed sound speed found for melt. In this study, we thus report a minimal effect of the presence of partial melt on the acoustic wave velocities and consider similar bias as estimated for solids (anelasticity and anharmonicity) because small fraction of melt seems to have only a moderate effect. Our extrapolation suffers also from grain size considerations as detailed by Jackson et al. (2002), even though this process was found to be nearly frequency independent for attenuation at mantle conditions.

iv) Geophysical implications

Our study demonstrates that the melt content in a partially molten media can be better quantified using the reduction of seismic velocity for melt fractions with a minimum detectable melt fraction between 0.5 and 0.1% (no seismic velocity drop seen for 0.1%). On the other hand, for the studied melt fractions of 0.1–2.0% with well-developed interconnectivity, electrical conductivity, varies within a strict range of about 0.5 log units even if transient values were only reached, too narrow to resolve fine melt structures without introducing significant uncertainties.

In this study, we specifically use the % drop in acoustic wave velocity as a measure to determine the melt fraction. Our study indicates that the 3–8% global reduction in seismicvelocity (*V*s) observed at the top of the asthenosphere (Anderson and Sammis, 1970; Widmer et al., 1991; Romanowicz, 1995) can be explained by 0.3–0.8% volatile-bearing melt (Fig. III.7a). However, these values may vary laterally depending on the extent of melting at the corresponding temperatures and the volatile contents in the mantle (Sifré et al., 2014). Regional *V*s variations of up to 10% observed below the Pacific plate (Schmerr, 2012) indicate large melt fractions of up to 1% present in some parts of the asthenosphere, suggesting large heterogeneities in terms of melt distribution. Apart from the global reduction of seismic velocity, numerous studies report velocity perturbations in various geological settings such as spreading ridges, intraplate mantle plumes and subduction (e.g., Pommier and Garnero, 2014). Assuming melt chemistry does not have any significant influence on acoustic wave velocity (Rivers and Carmichael, 1987); we compare our melt fraction estimations to those reported using theoretical models (Table III.S2 and Fig. III.7b).

In addition to the use of absolute sound wave velocities and velocities drop, the use of *V*p/*V*s ratio can be of significant interest for comparison with seismological data. Bulk and shear moduli of a partial melt system (a solid containing pore spaces saturated with melt) varies as a function of melt volume fraction. Accordingly, the relative change of *V*p/*V*s ratio could indicate the presence of melt in deep mantle conditions. As detailed in Chantel et al. (2016), the absolute velocities values measured on analog systems do not compare well with real seismic velocities measurements. It is mainly due to the difference in mineralogy (e.g., pure olivine against peridotites) and relaxation effects due to differences in frequencies between natural and experimental seismic velocities estimations (see discussion therein). However, the use of *V*p/*V*s ratios and its variations allow a relevant comparison of our analog data to natural system as changes are relative and not based on absolute velocities values.

Our data indicate that below melting point, *V*p/*V*s ratio increases from 1.75 to 1.8 from room temperature up to 1650 K (Fig. III.8). These values are consistent with values observed for solid upper mantle ranging from 1.7 to 1.8 given by standard models such as PREM (Dziewonski and Anderson, 1981) or AK135 (Kennett et al., 1995). These values are also consistent with moderate *V*p/*V*s values obtained from upper mantle minerals, ranging also between 1.7 and 1.8 for olivine (1.8), clino and orthopyroxenes (1.72 and 1.74) at the same pressures (Li and Liebermann, 2007). At melting, we observe a strong and sudden increase of the *V*p/*V*s ratio. The magnitude of the increase correlates positively with the melt fraction. *V*p/*V*s ratios above 1.9 are observed for sample with 2% melt fraction (Fig. III.8c). Our *V*p/*V*s ratio values compare favorably with LVZ estimations with ratios given by global models ranging between 1.8 and 1.85 and requiring only moderate amount of melt (< 1% of melt). However, our data implies very high melt fractions involved in local anomalies where *V*p/*V*s ratios up to 2.5 or more have been reported (Schaeffer and Bostock, 2010; Hansen et al., 2012). These very high anomalies imply higher melt fractions (12.5% for *V*p/*V*s ratio of 2.5, based on the trend defined in Fig. III.8c) even if other physical processes such very high

volatiles contents in melts could explain these anomalies.

In general, we find that the melt contents reported in previous geophysical studies are consistently higher than the estimations based on laboratory measurements of seismic wave velocities. The majority of these studies used the theoretical prediction of velocity reduction for partially molten rocks, which underestimate the effect of melt fraction on seismic velocity. The use of our laboratory measurements provides melt fractions that are consistent with petrological models. Further, we believe that the refined melt fraction estimations would provide a solid platform to constrain a meaningful cross-correlation between field-based seismic and electrical observations. The effect of the chemical composition of melt on acoustic wave velocity is one of the important aspects worth exploring in future studies.

f) Conclusions

This study presents the first simultaneous measurements of electrical conductivity and acoustic wave velocity of partially molten samples of geophysical importance. The results highlight how electrical conductivity and acoustic wave velocity respond to the evolving melt texture from a completely random melt distribution. The continuous increase of electrical conductivity at constant temperature, after melting of MORB, indicates that the melt interconnectivity evolves with time. In contrast, constant seismic velocity after the melting suggests acoustic velocity is sensitive to the melt volume fraction in the sample, but less affected by the evolving melt texture. Our results suggest that the electrical conductivity of partially molten materials measured before reaching the evolved melt interconnectivity can lead to an underestimation of the EC for a given melt fraction. This may result in an over-estimation of melt fraction in geological settings. Overall, the *Vs* measurements appear to be a more appropriate method for determining the melt fraction in a partially molten system with complete wetting properties. The previous approximations based on theoretical models of seismic velocity appear to overestimate the extent of melting in the mantle. This study demonstrates the importance of using electrical conductivity values from texturally equilibrated partially molten sample for comparison with geophysical data.

g) Acknowledgements

We thank J.-M. Henot for the SEM analyses, J.-L. Devidal for the electron microprobe analyses and A. Mathieu for the technical assistance. We thank F. Gaillard for beneficial discussions. DF acknowledges S. Thivet for FOAMS assistance and starting powder analysis. GM acknowledges funding from the French PNP program (INSU-CNRS) and Actions initiatives OPGC 2014. DA is supported by ANR-13-BS06-0008. This research was financed by the French Government Laboratory of Excellence initiative no ANR-10-LABX-0006, the Région Auvergne and the European Regional Development Fund. This is Laboratory of Excellence ClerVolc contribution number 326. All of the experimental data and numerical modelling are provided in the figures and tables obtained by methods described in the text.

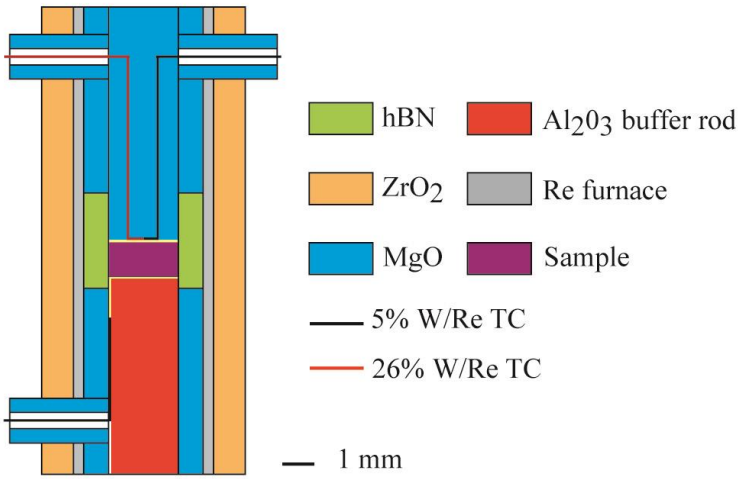

Figure III.1 Schematic cross section of the high pressure cell assembly for simultaneous acoustic velocity and electrical conductivity measurements. The assembly was designed to place the sample at the center of the cell at high pressure due to differential compression of alumina and MgO pistons. The respective pistons lengths were calibrated in prior experiments

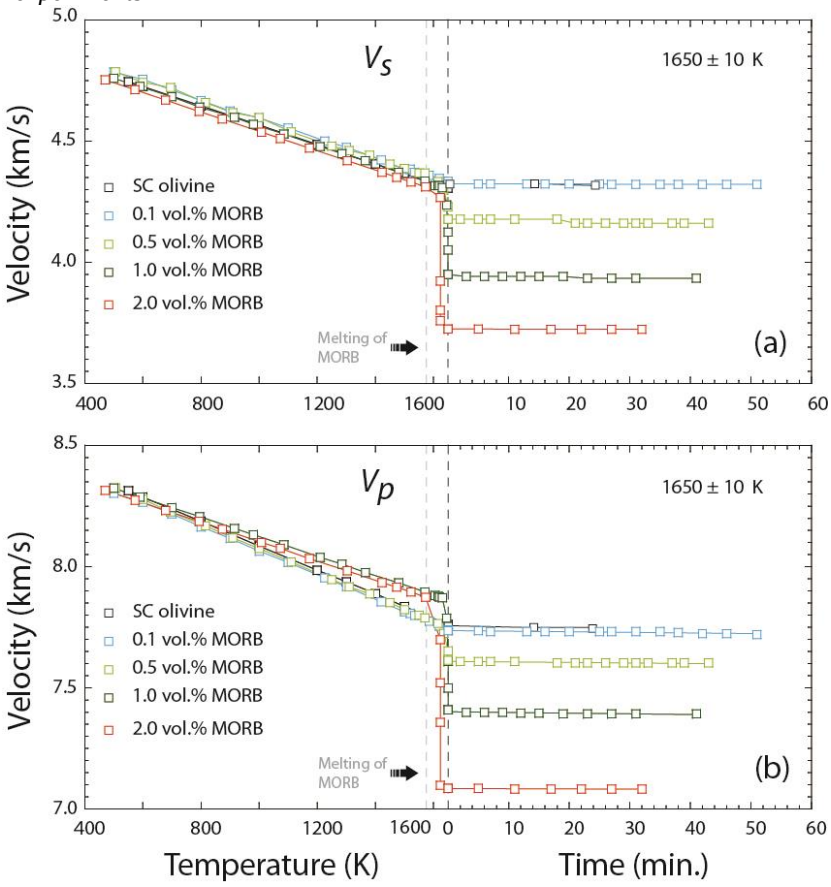

Figure III.2 a S- and b P-wave velocities as a function of increasing temperature (left) and as a function of time at a constant temperature (right) for olivine- and melt-bearing samples investigated in this study. The uncertainty results from the estimations of temperature, pressure, sample dimensions and data fitting errors are estimated to be lower than 2.6% (2σ) of the value. Errors are not represented for visibility. Temperature error [10 K (2σ)] is within the symbol for all data points

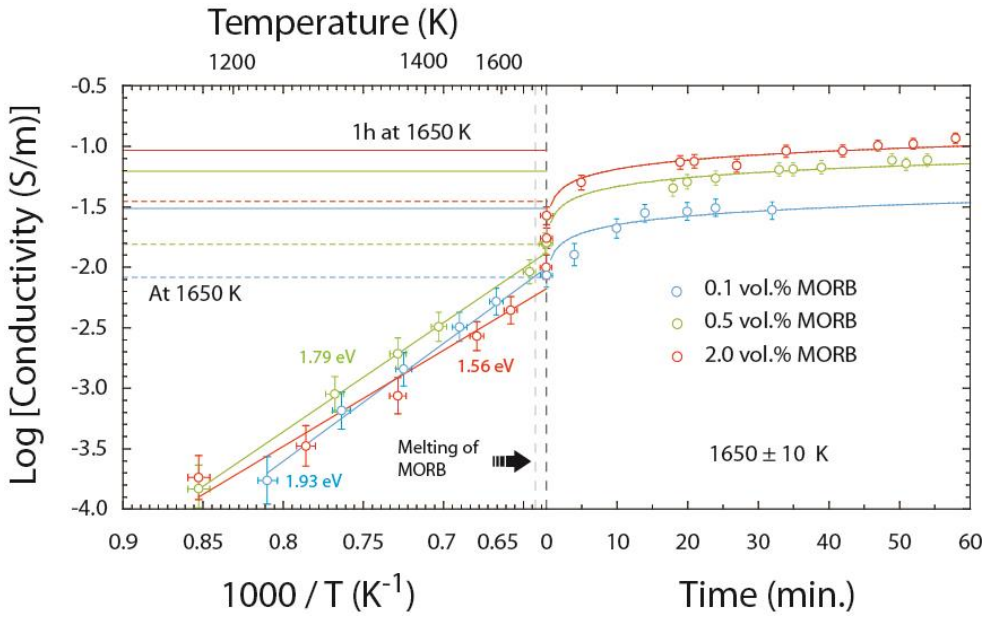

Figure III.3 Electrical conductivity as a function of reciprocal temperature (left) and, as a function of time at a constant temperature (right), for the samples containing 0.1, 0.5 and 2 vol.% melt fractions. Solid and dashed lines indicate the corresponding conductivities immediately after melting and after 1 h at constant temperature of 1650 K. The uncertainties associated with the electrical conductivity data measurements are less important at high temperatures. The uncertainty results from the estimations of temperature, pressure, sample dimensions and data fitting errors are less than 5% (2σ) of the value for EC. Error in temperature is 10 K (2σ)

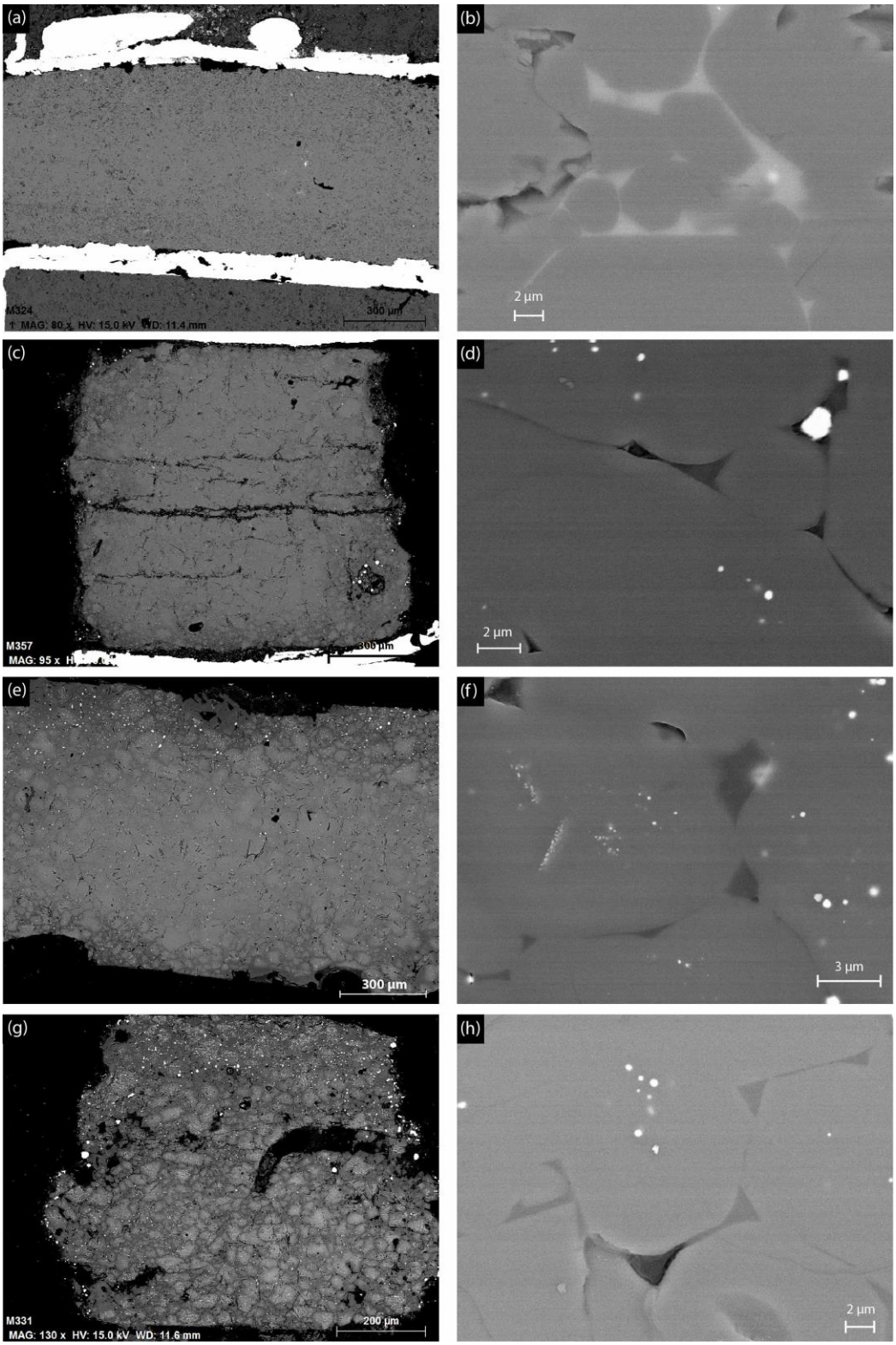

Figure III.4 Backscattered electron (BSE) images showing near equilibrium melt textures at melt- olivine interfaces at 1650 K. Well-developed interconnected melt channels in samples with a, b 2.0%, c, d 1.0%, e, f 0.5% and g, h 0.1% melt volume fractions. The bright particles attached on sample surface and holes are rhenium pellets coming from polishing (TC's, furnace and electrodes are made of Re). Biggest particles are presents in samples holes and along sample/capsule interface (c, g) whereas smallest particles are attached to sample surface along polishing scratches (well visible in f)

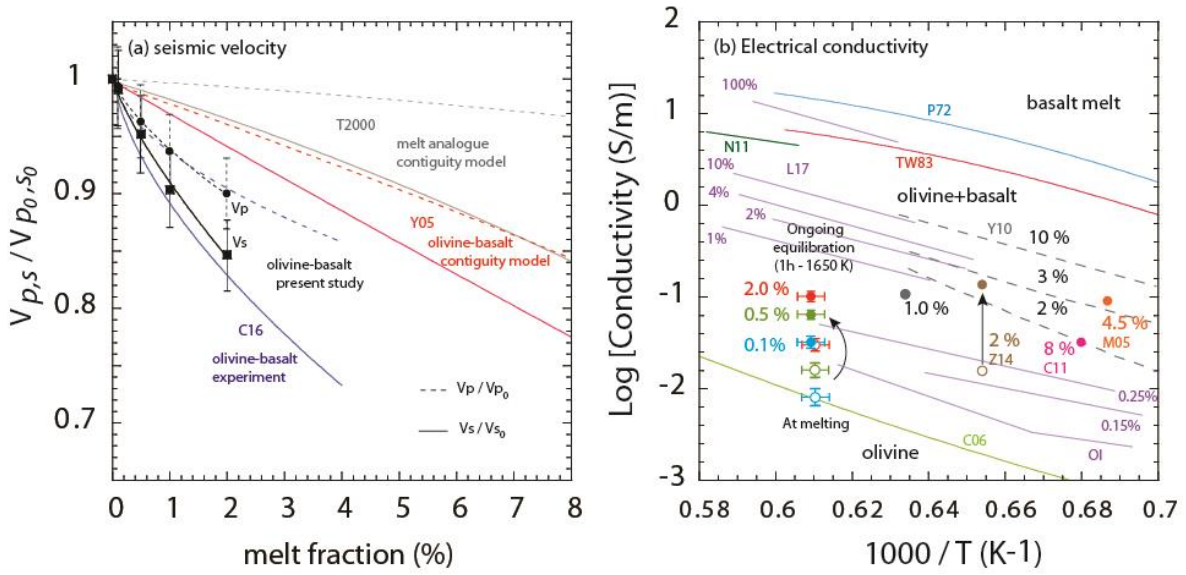

Figure III.5 Comparison of reported acoustic velocities and electrical conductivities for partially molten systems. a Vp,s/Vp0,s0 ratios for various melt fractions. Experimentally determined velocities for the olivine-basalt system (Chantel et al., 2016) and theoretical estimations for olivine-basalt (Yoshino et al., 2005) and melt analogue systems (Takei, 2000) are shown for comparison. Errors in SV ratio are 3.6% (2σ), errors in melt fraction are within the data symbol (1% relative). b Reported electrical conductivity values for olivine, MORB and olivine + MORB compositions. Open circles and filled circles indicate our conductivity data for our volatile-bearing partial melts at melting and data after 1 h at 1650 K. The conductivity values presented in the figure are C06 (Constable 2006), P72 (Presnall et al., 1972), TW83 (Tyburczy and Waff, 1983), N11 (Ni et al., 2011), Y10 (Yoshino et al., 2010), Z14 (Zhang et al., 2014), C11 (Caricchi et al., 2011), M05(Maumus et al., 2005) and L17 (Laumonier et al., 2017). The EC values reported in Zhang et al. (2014) indicate melt conductivity before (open circle) and after (solid circle) the textural modifications due to the shear deformation. Errors on our data points are 5% (2σ) on EC value and 10 K (2σ) in temperature.

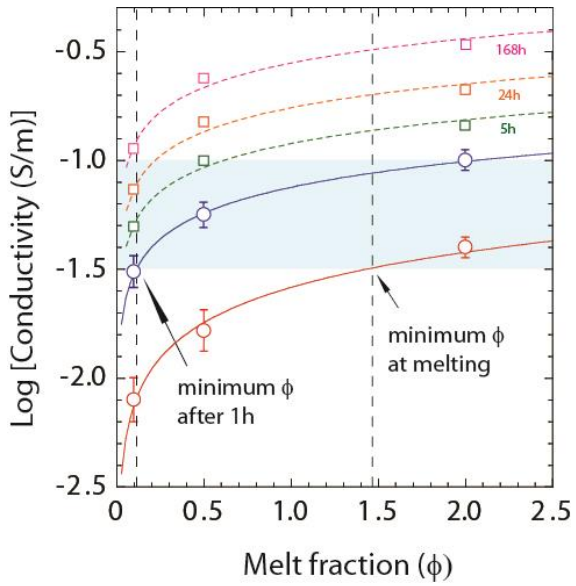

Figure III.6 The comparisons of electrical conductivity before and after 1 h at 1650 K for studied melt fractions. The conductivity corresponding to the LVZ is shown by the blue shaded area. The vertical lines indicate the minimum melt fractions required to explain the high conductivity zone in the asthenosphere. Extrapolated data using the logarithmic laws fitted from data in Fig. III.3 was represented from relevant time-scales with squares. This slow increase shows that weeks of equilibration will be necessary to have half an order of magnitude increase of EC. Such an increase is compatible with measurements performed on equilibrated material after weeks of annealing. Errors on EC are 5% (2σ) and within the data symbol for melt fraction (1% relative). Errors on extrapolated values are 10% (2σ) and we not displayed for distinction with measured data points

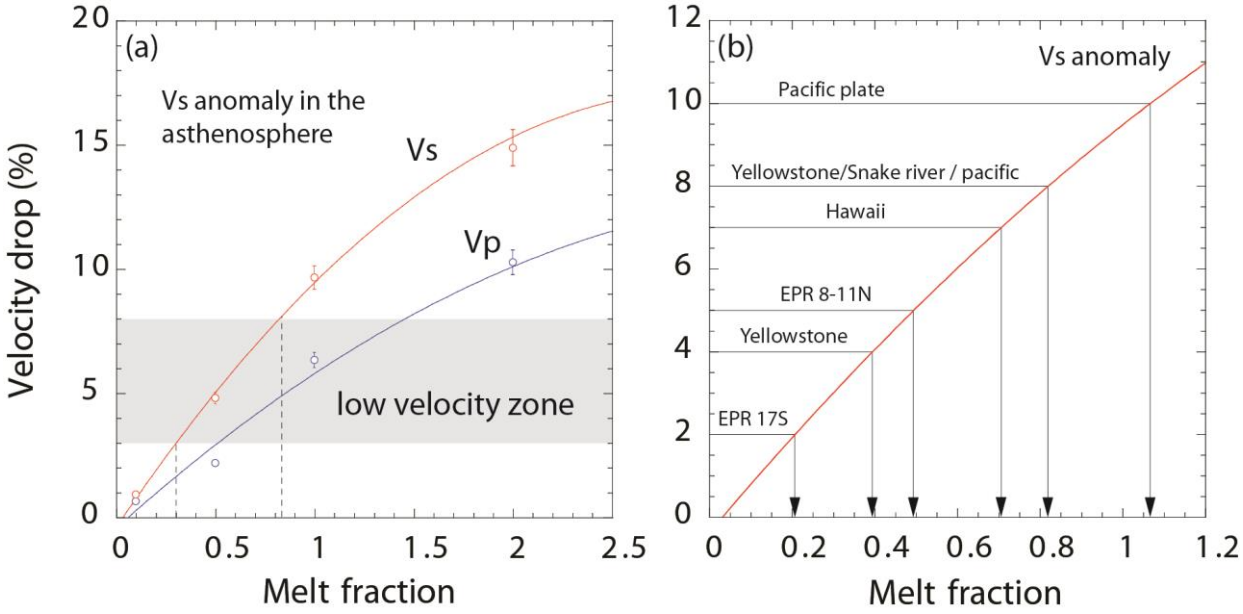

Figure III.7 (a) The % drop in P- and S-wave velocity as a function of the sample melt fraction. The geophysically observed S-wave velocity anomaly for the LVZ in the asthenosphere is shown by the shaded rectangle. Note that the 3–8% Vs drop observed for most of the asthenosphere can be explained by 0.3–0.8% melt. (b) Vs velocity anomalies observed at various geological settings and the possible melt fraction estimations based on our model. The Vs anomalies presented in the figure are from EPR 17S (Toomey et al., 1998), EPR 8-11N (Toomey et al., 2007), Yellowstone-Snake River (Wagner et al., 2010), Hawaii (Laske et al., 2011), and the Pacific (Kawakatsu et al., 2009; Schmerr, 2012). Errors on velocity drops are 5% (2σ) relative and within the symbol for melt fraction (1% relative)

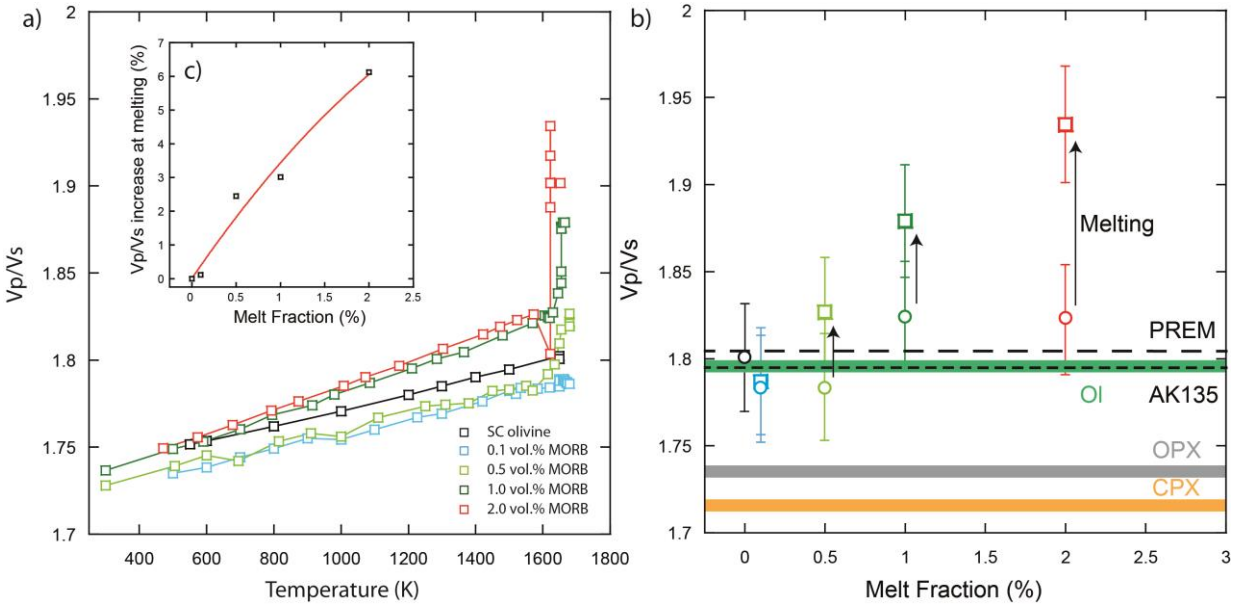

Figure III.8 a) Vp/Vs ratio of our experiments reported as a function of increasing temperature. The standard deviation on the data lies between 0.0305 and 0.0335 (lowest to highest temperature values) corresponding to an error majored by 1.75% of the Vp/Vs ratio (1σ). b) Vp/Vs ratio as a function of the volume melt fraction (MORB content). Values for solid sample before melting are represented by circles and values after partial melting occurred with squares. Vp/Vs ratios from seismological data: PREM (Dziewonski and Anderson 1981) and AK135 (Kennett et al., 1995) are represented in black dashed lines. Vp/Vs ratios from nominal minerals are represented by colored zones (green for Olivine, grey for OPX and gold for CPX), velocities data at 2.5 GPa was taken from Li and Liebermann (2007). c) Inset figure in a Vp/Vs ratio increase at melting in function of melt fraction, quantifying the magnitude of increase of the ratio in response to partial melting

Table III.1 Chemical composition of MORB and olivine before and after the experiments.

	MORB initial	MORB final	Olivine initial	Olivine final
SiO_2	50.73 (0.28)	51.15 (0.1)	41.97 (0.8)	41.43 (0.4)
TiO_2	2.00(0.02)	2.22 (0.27)	0.06 (0.02)	0.03 (0.02)
Al_2O_3	13.73 (0.18)	14.54 (0.1)	0.1 (0.03)	0.1 (0.01)
FeO	11.29 (0.13)	9.20 (0.1)	9.3 (0.3)	9.15 (0.2)
MnO	0.2 (0.2)	0.22 (0.1	0.11 (0.03)	0.12 (0.04)
MgO	7.1(0.12)	6.94 (0.09)	48.65 (0.9)	49.69 (0.7)
CaO	10.94 (0.22)	11.41 (0.03)	0.23 (0.1)	0.22 (0.01)
Na_2O	2.83 (0.07)	2.26 (0.3)	<0.01	<0.01
K_2O	0.15 (0.08)	0.35 (0.1)	<0.01	<0.01
Total	**98.79 (0.5)**	**98.29 (0.2)**	**100.4 (0.2)**	**100.7 (0.8)**

h) Supplementary materials

i) Introduction

This supporting information contains detailed error estimations on sound wave velocity (SV), electrical conductivity (EC) and melt fractions of starting samples (Text III.S1).

Additional tables are given for:

- Grain size and textural parameters of each recovered sample from FOAMS analysis (table III.S1).
- Estimation of melt fraction using previous literature reported S wave's velocities anomalies and inferred melt fractions for comparison (table III.S2).

Additional figures are given for:

- Average grain size of the starting powder (2 vol.% MORB) composition (Fig. III.S1).
- Electrode connection in the EC/SV high pressure assembly, 3D schematic view. (Fig. III.S2).
- Impedance spectra of solid and partially molten samples (Fig. III.S3).
- Melt texture with absence of the melt preferred orientation (Fig. III.S4).
- Evolution of melt texture, showing samples at different maturity stages (Fig. III.S5).

ii) Supplementary Text

Text III.S1. Experimental uncertainties and error estimations

Experimental measurements of the sound velocity of primary waves (Vp), secondary waves (Vs) and electrical conductivities (EC) are subjected to uncertainties originating from the estimations of temperature, pressure, sample dimensions, and data fitting errors. The errors given in this manuscript in percentage (1 or 2σ) are always relative, even on a percentage (example: SV drop of 10% with 5% relative error results in: 10 ± 0.5%)

Errors on sample dimensions (a):

Sample lengths, prior to sample loading and after the melting experiments, were determined with a high precision digital height-gauge (accuracy of 0.1 μm) and using the Field Emission Gun scanning Electron Microscope (FEG-SEM) respectively. Sample length at target pressure and temperature were estimated using elastic deformation and thermal expansion. Possibility of significant length change due to plastic deformation at melting was considered and ruled out after on-line experiments with the 13-ID-D beamline on the APS (Chantel et al., 2016) study where no abrupt changes were observed. Estimation of the length at 1650 K and 2.5 GPa was made using:

$$d = d_0 \left[\frac{\rho_0}{\rho}\right]^{\frac{1}{3}} = d_0 \left[1 - \alpha(T - T_0) + \frac{P}{K}\right]^{\frac{-1}{3}}$$

with α equal to 2.7 e^{-5} K^{-1} (Bouhifd et al., 1996) at T_0 = 300 K, K = 125 GPa (Li et al., 2007; Gillet et al., 1991) and d_0, initial sample length. This estimation is made using initial sample lengths because recovered samples after high P-T experiments showed decompression cracks, and often lost edges during the sample cutting and polishing procedures. However, the maximum length changes observed in our recovered samples were mostly within 5% of the initial length.

Errors on sound wave velocities (b):

Based on sample dimensions and SV signal considerations, errors on P and S waves velocities can be quantified using error propagation formula. Covariance term was neglected in the calculation. Uncertainties on velocities can be expressed as a function of sample length (d) and time (t).

$$\sigma_V = \sqrt{\left(\frac{1}{t}\right)^2 * {\sigma_d}^2 + \left(\frac{-d}{t^2}\right)^2 * {\sigma_t}^2}$$

We found that our standard deviation was usually lower than 1.25% (1σ). Using the same treatment, the errors on acoustic wave velocity drops, used from comparison with

geophysical data, can be estimated. Where V_{melt} is velocity for partially molten material (at steady state) and V_{ini} is the velocity before melting. Errors on sound wave velocity drops are less than 2.6% (1σ).

$$\sigma_{drop} = \sqrt{\left(\frac{Vmelt}{Vini^2}\right)^2 * {\sigma_{Vini}}^2 + \left(\frac{-1}{Vini}\right)^2 * {\sigma_{Vmelt}}^2}$$

Sound velocity ratio used, in the Fig. III.5a is calculated via the ratio between V_{melt} and V_{ini}. The resulting error's propagation formula is given under. Errors were found to be majored by 1.8% (1σ).

$$\sigma_{Vmelt/Vini} = \sqrt{\left(\frac{Vmelt}{-Vini^2}\right)^2 * {\sigma_{Vini}}^2 + \left(\frac{1}{Vini}\right)^2 * {\sigma_{Vmelt}}^2}$$

We note that because our discussion is mostly based on the relative variations of acoustic wave velocity with the occurrence of melting, and with the melt fraction in the sample, a slight variation of the sample dimensions during the experiment would not influence our conclusions.

Bond-effect estimation (c):

We have considered the effect of a possible bound-effect on sound wave velocity as suggested by Davies and O'Connell (1977), Jackson et al.(1981), Niesler and Jackson(1989). This bound effect might originate from the 25 µm Rhenium foil placed between the sample and the buffer rod. A 25 µm foil was necessary in order to maintain electrical contact between sample and the electrode wires. However, the presence of the discs enhances the mechanical contact and might allow a more efficient transmission of acoustic waves from the buffer to the sample. The reflection from the rhenium foil was not observed in any of our experiments.

To estimate the potential effect of the Re foil, we have calculated the Vp and Vs velocities using the elastic properties of rhenium available at 1 atmosphere (bulk modulus of 383 GPa and shear modulus of 180-273 GPa). Despite variations observed on the shear modulus, Vp was estimated between 5.45 - 5.96 km/s and Vs to 2.94 - 3.61 km/s. The time shift associated is 4.59 - 4.19 and 8.52 - 6.93 nanoseconds for Vp and Vs respectively. This translates into only a few percent (< 5 % for Vp and < 1.5 % Vs) of the observed travel time for our samples. The foil echo should then be small, both in amplitude and duration. This echo might be hidden in the buffer rod echo which is coherent with our observation of the absence of foils echo. This estimation underlines that bond effect is negligible or rather small if present (within our considered error for acoustic waves velocities).

Errors on electrical conductivity (d):

Electrical conductivity is subjected to the same type of errors than seismic wave velocity, mostly due uncertainties on sample dimensions. The electrical conductivity is calculated by fitting the resistance and then using:

$$\sigma = \frac{L}{A * R}$$

Where L is the sample cylinder length, A the sample circular face area and R the resistance. By the same formulas the error can be estimated. Estimating sample dimensions at P and T using the relations here above, the error propagation can be written as:

$$\sigma_c = \sqrt{\frac{-L}{RA^2}^2 . {\sigma_A}^2 + \frac{1}{AR}^2 . {\sigma_L}^2 + \frac{-L}{R^2A}^2 . {\sigma_R}^2}$$

We estimate that the experimental errors on the absolute values of Vp, Vs and EC are within 5% (2σ).

Errors on the melt fractions (e)

The volume melt fraction in the samples was controlled by the amount of MORB powder added to the mixture. The starting powders were prepared for at least 5 grams of mixture to ensure a sufficient precision on the melt fraction (83.94 to 4.18 mg of MORB from 2 vol.% to 0.1%). The uncertainty on melt fraction estimations is mostly related to the uncertainty of weighing, which has an accuracy of 0.01 mg. The overall uncertainty of melt fraction estimation is less than 1% (relative: 1 ± 0.01% of MORB, 2σ).

iii) Supplementary tables

Table III.S1 Grain size and grain orientation distribution in our samples for various melt fractions. The grain size estimations are from intercept method (avg. Grain size column) and image processing by FOAMS (Avg. Eq. Diameter). Other textural parameters are derived from FOAMS software (see description in sections 2.6 and 3.3). Errors (1σ) are given in parenthesis.

Melt fraction	Avg. Grain size (µm)	Avg. Eq Diameter (µm)	Eccentricity	Elongation	Aspect ratio	Regularity
2%	10.48 (5.24)	7.69 (4.64)	0.81 (0.14)	0.32 (0.16)	0.53 (0.18)	0.86 (0.10)
1%	8.68 (4.34)	7.67 (5.77)	0.84 (0.13)	0.36 (0.16)	0.50 (0.18)	0.84 (0.10)
0.50%	15.16 (7.58)	13.07 (7.12)	0.76 (0.14)	0.26 (0.14)	0.61 (0.17)	0.89 (0.08)
0.10%	7.20 (3.60)	5.58 (5.02)	0.84 (0.14)	0.35 (0.17)	0.50 (0.19)	0.86 (0.10)

Table III.S2 Estimation of the implied melt fractions in different asthenopheric regions where LVZ have been detected. S wave velocity drop are given and our inferred melt fractions are compared with previous literature estimations.

Location	Vs drop	Previous estimation	Reference	Our model
East Pacific Rise (8 - 11 N)	5%	1-3%	Toomey et al. 2007	0.5%
East Pacific Rise (17 S)	2%	1%	Toomey et al. 1998	0.2%
Hawaii region	3-7%	0.75-2%	Laske et al. 2011	0.3-0.7%
Yellowstone/ Snake River Plain	4-8%	1-2%	Wagner et al. 2010	0.4-0.8%
Pacific Plate	8-10%	3.5-4%	Kawakatsu et al. 2009	0.8-1.1%

iv) Supplementary figures

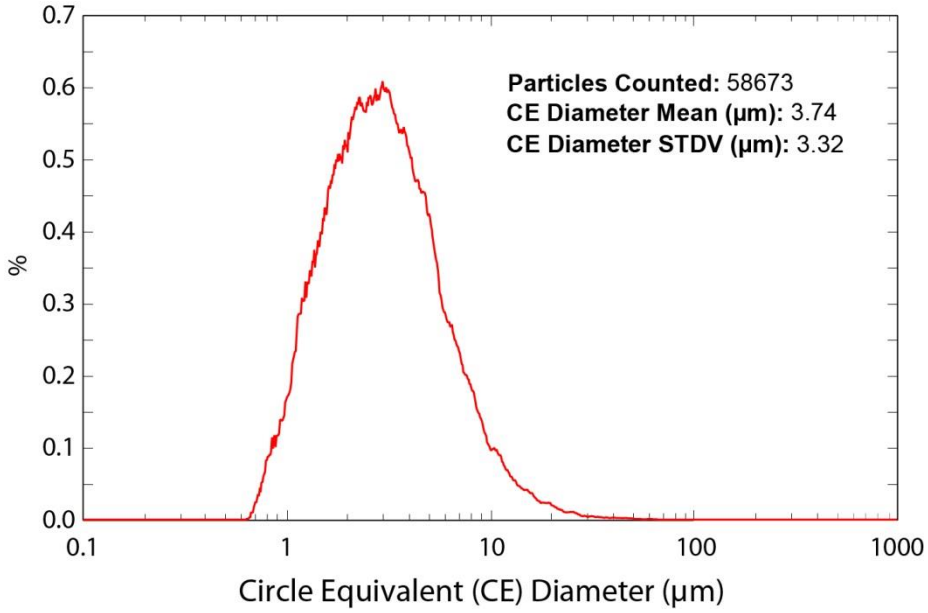

Figure III.S1 Circular equivalent diameter of "olivine + MORB" grains of our starting 2% MORB powder. Analysis is performed using a MALVERN Morphologi G3 apparatus using 5 mm^3 of powder. Only a restricted area was analyzed because of the important number of particles recovered (enough for statistical considerations). Average grain size is 3.74 µm which is clearly thinner than grain size estimations on recovered samples (Table III.S1) suggesting a consequent grain growth at during HP-HT experiments.

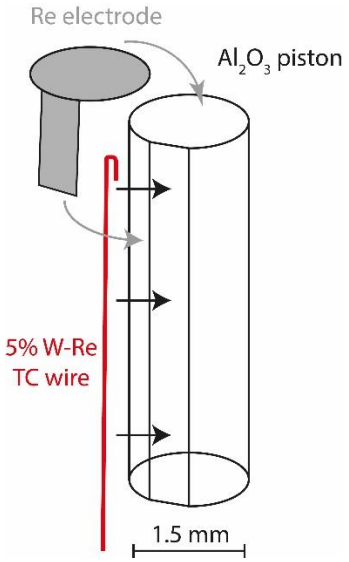

Figure III.S2 Schematic diagram showing the electrode connection on the buffer rod in the high pressure assembly for EC/SV measurements. The rhenium electrode is connected via a single 5% W-Re thermocouple wire. The electrode has a tongue, which is folded downward along the alumina buffer rod. The wire and electrode are inserted along the piston and the hook shape help maintaining a good electrical contact. The contact between the electrode and the wire is purely mechanical and is better achieved with confining pressures.

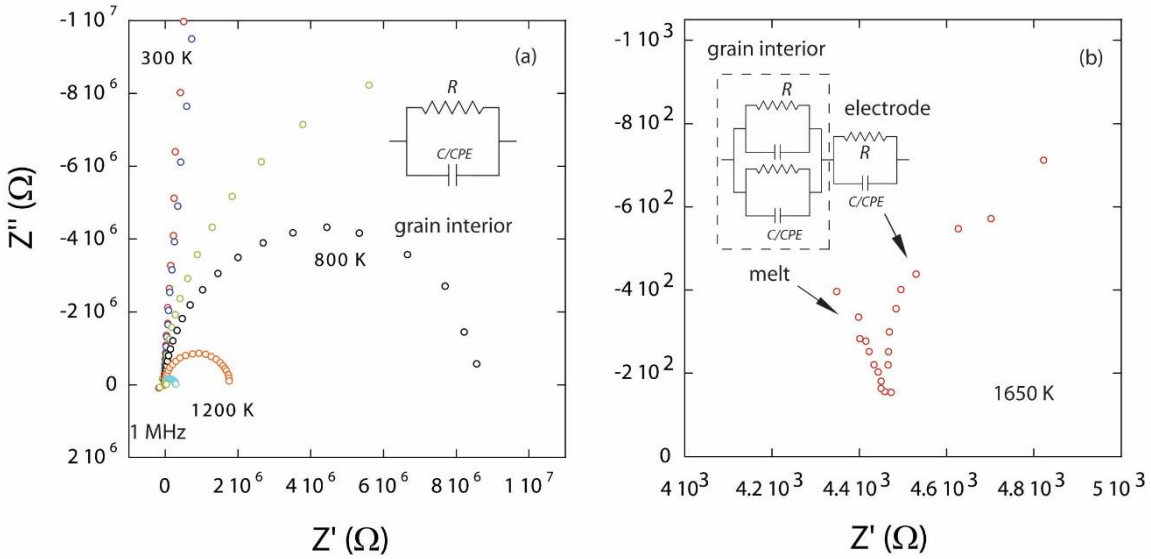

Figure III.S3 Impedance spectra of the sample at different stages of heating, (a) before melting (b) after melting at 1650 K. Errors on impedance are within the symbol (± 150 Ω for 1 MΩ impedance).

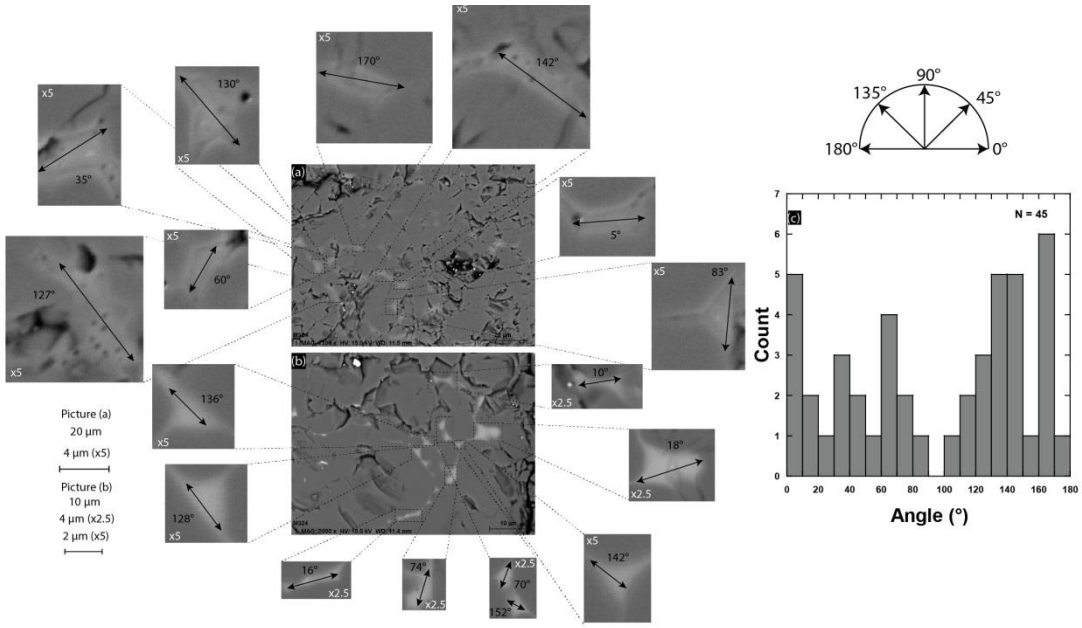

Figure III.S4 Orientation of melt pockets along the long axis (SPO) as a percentage of the total melt area in a section cut parallel to the axis of the cylindrical sample. Images a and b were selected from 2% melt sample. The black arrows in enlarged images of selected melt pockets display the orientation of the long axis. (c) Histogram of the orientation of melt pockets (SPO) with the bin size of 10° for 45 measurements.

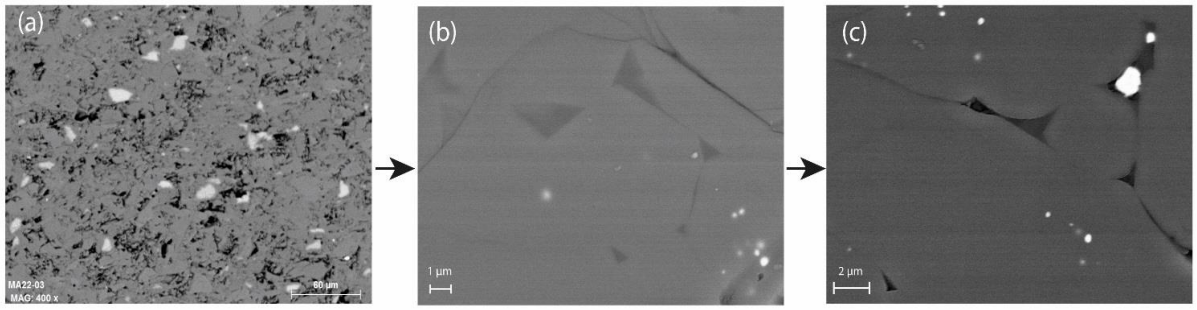

Figure III.S5 SEM images showing (a) distribution of MORB powder in a 2% melt sample prior to the melting experiments. (b) Melt pockets with angular grain interfaces (c) melt pockets in the same sample after melting experiments after 1 hour at 1650 K showing more rounded and smoothed interfaces.

4) Notes and additional information

Additional data that has not been inserted in published work will be provided and commented in this section. This will help to precise the technical aspects of this work as well as results on textural analyses and electrical conductivity.

a) Experimental assemblies, set up and starting materials

Additional figures and tables are given to provide more details on the starting materials choices, experimental conditions and precise the data obtained on the experiments of this chapter.

In this study, samples were composed of a powder mixture of natural San Carlos (SC) olivine and volatile-rich natural MORB glass. The San Carlos Olivine (SC) crystals were selected from peridotites enclaves obtained by G. Manthilake. The MORB glass and inclusion free, hand-picked, SC olivine crystals were crushed separately and reduced to fine grain powders (see Fig. III.S5 above). These powders were then mixed in predetermined weight proportions to obtain the desired melt fractions at high temperature, with MORB volume fractions of 0.1, 0.5, 1 and 2 vol.%. The calculated mixing ratios are given in the table III.2 for a total amount of 1g of powder of each composition, in total 5g of each were prepared to ensure a minimum errors due to weighting.

Table III.2 Calculated ratio of the mixture of San Carlos Olivine and MORB (wt%) for a total of 1 g

	2 vol.%	**1 vol.%**	**0.5 vol.%**	**0.1 vol.%**
MORB %wt	0.01679	0.0838	0.00419	0.00084
Sc Ol %wt	0.98321	0.99162	0.99581	0.99916

These powders were hot-pressed for 2 hours at 2.5 GPa and 1100K using 25/17 graphite furnace assembly. The schematic plan of this assembly is given in the figure III.9. During experiments, the sample temperature was measured by a type C W5% Re-W26% Re thermocouple, which was located on the outside of the Re capsule. Retrieved samples from the synthesis experiment were cut into a section around 1.5 mm in thickness for 2.3 mm of diameter. The samples were mirror polished on both faced with, in first, sandpapers of tungsten carbide of 1024 and 2048 and then with diamond solution with a succession of diamond size of 6, 3 and 0.25 μm. The final length (about 1 mm) and diameter of the samples were measured with digital high gauge Mitutoyo apparatus (table III.3), giving an accuracy of ± 0.005 mm. The homogeneity of the samples was also checked by binocular lens before and after polishing.

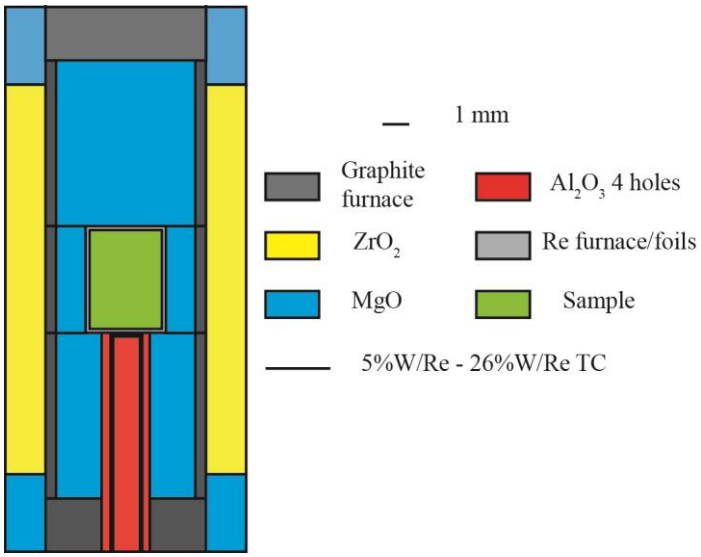

Figure III.9 Schematic cross section of the assembly used for syntheses. The synthesis of the olivine + MORB mixtures were performed using a 25/17 assembly with graphite furnace and rhenium capsule. The experimental conditions were 2.5 GPa and 1100 K for 2h. The recovered samples were cut in two with diamond wire saw and double polished for EC/SV experiments.

Figure III.10 Photograph of the synthesis products after double polishing. Sample was then inserted in the EC/SV experiments.

Sample lengths were measured to range between 500 and 1000 microns after double polishing and sample radii were adjusted from synthesized sample to 1000 microns. This estimation is made using initial sample lengths because recovered samples, after high P-T experiments, showed decompression cracks, and often lost edges during the sample cutting and polishing procedures. However, the maximum length changes observed in our recovered samples were mostly within 5% of the initial length. Initial estimated lengths and radius are given in the following table. Sample radius was manually adjusted from starting and so, is nearly constant.

The radiographic image analyses provide the most accurate information on the change of sample length in response to increasing temperature. In off-line experiments such as ours, we

use the thermal expansion of constituent materials to estimate the length change. Detailed information on the length estimations are given in the following table III.3.

Table III.3 Estimated lengths of our samples with measurements prior the EC/SV experiment, estimated length at HP and HT and the measured sized after. One can see that the sample size reduction is almost negligible thanks to the synthesis at similar conditions. Measurements on M324 were not accurate after the experiments due to problem in SEM software for scale estimation during the measurement.

Sample	Initial length (µm)	Initial diameter (µm)	Estimated length at 1650 K (µm)	Size after experiment (µm)	% reduction
M324-2%	831.5	1000.0	836.11	-	-
M357-1%	1021.0	1000.0	1026.66	989.5	3.09
M343-0.5%	526.5	1075.0	529.42	468.6	11.00
M331-0.1%	758.5	1000.0	762.71	738.5	2.64

The recovered syntheses run products were also analyzed with Scanning Electron Microscope. The images of these samples confirmed the presence of MORB fragments within an olivine matrix. The quantity of the MORB observed in 2D sections is coherent with the volume fraction inserted in each composition (see Fig. III.11). The MORB grains do not show any melting process and appear to be homogeneously distributed through the sample.

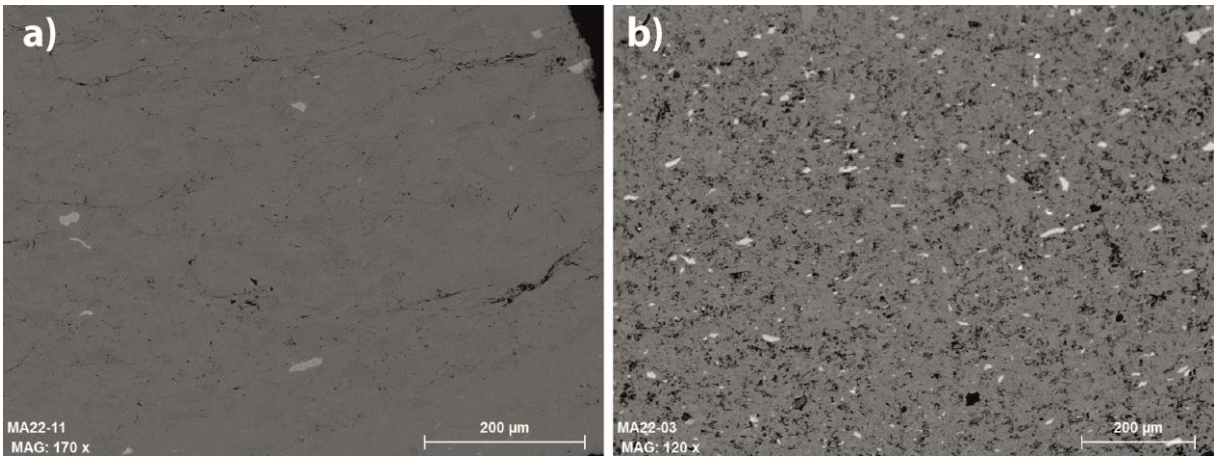

Figure III.11 Backscattered electrons microphotographs of samples after the synthesis run. a) is a microphotograph of 0.5 vol.% of MORB and b) is microphotograph of 2 vol.% of MORB

The experimental setup for *in situ* EC/SV measurements is detailed in the figure III.12 and the recovered acoustic signals are detailed in the figure III.13.

Figure III.12 Photographs illustrating the preparation of high pressure and high temperature experiments and their realization. From top left to bottom right: a) experimental assemblies (25/17 and 18/11) used for this study with graphite heater and rhenium capsules. b) Assemblage of octahedron on the cubes. One can remark the specific geometry required for the thermocouple and electrode wires which is unique for this experiment given that the position in the primary anvils guide block is fixed for the transducer. c) Boston Piezoelectric LiNbO3 transducer fixed (tin solder) at the polished corner of 11 mm truncation anvil. d) Tektronix digital phosphor oscilloscope (left) and Tektronix AFG3101C wave function generator (right) used for sound velocity generation and record. e) 1500 Ton (Voggenreiter Mavo press) multi-anvil apparatus used at the Laboratoire Magmas et Volcans. f) Solartron ModuLab MTS Impedance/Gain-phase analyzer used to measure electrical conductivity. For scale octadreon side length is 24 and 18 mm (a), 18 mm (b), truncation corner 11 mm (c), computer mouse at foreground (d), Multi-anvil apparatus is 3.2 m high (e), 15'' laptop (f).

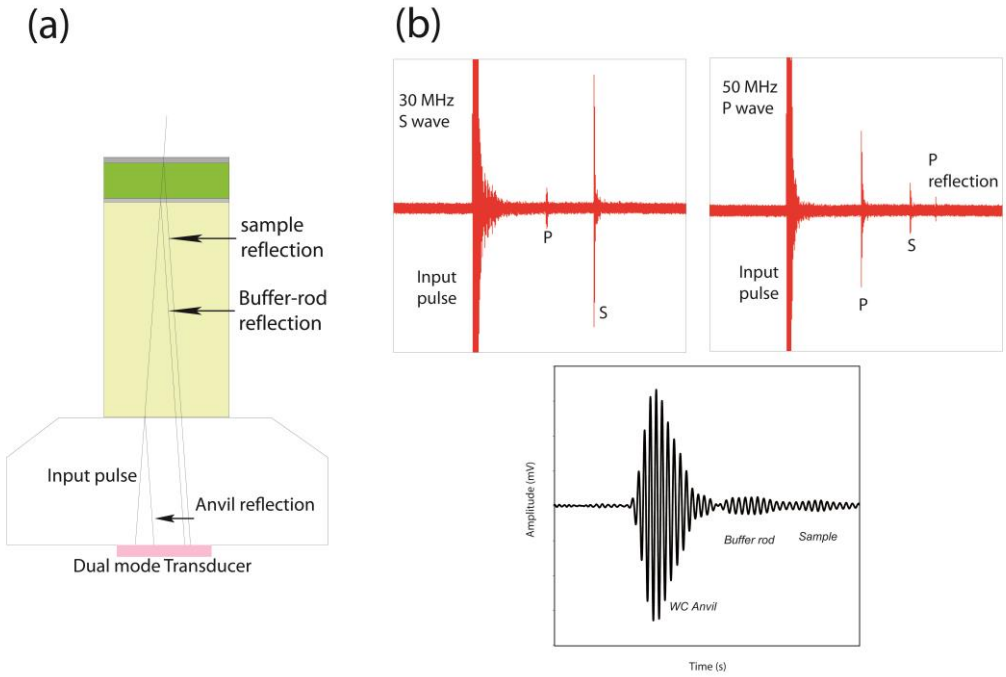

Figure III.13 (a) Schematic of acoustic wave propagation in the experimental configuration for simultaneous measurement of P- and S- wave velocities during high pressure-temperature experiments. (b) Acoustic signals (P- and S-) generated and received by the dual-mode lithium niobate transducer.

b) Samples textures and micro-textural analyses

The micro-textural analyses have been described in our published work (see here-above). Main results have been given in the supplementary table III.S1. The associated data on texture such as binary image and histograms of size distribution and grain orientation are given in the appendix B. The determination of our dihedral angle for our four experiments is also provided in this section (Fig. III.14).

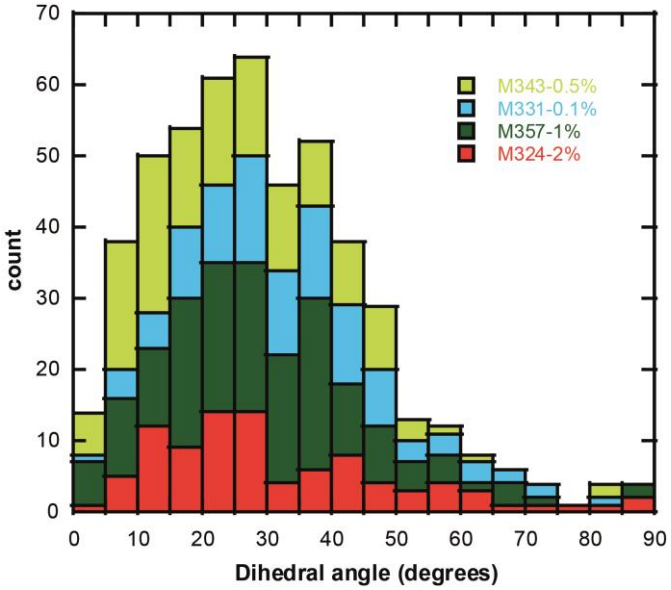

Figure III.14 Dihedral angle histogram estimated for our four samples. The median value is 27 ± 4° (1σ). The angles were measured using high resolution FEG SEM apparatus and on BSE microphotograph. The tangent method was applied with a Matlab® code developed by the author.

c) Electrical conductivity mechanisms

A more detailed consideration of electrical conduction is resented here with presentation of additional data (EC of all cycles for each experiment, Fig. III.15). Measured activation enthalpies and conduction processes are interpreted and discussed.

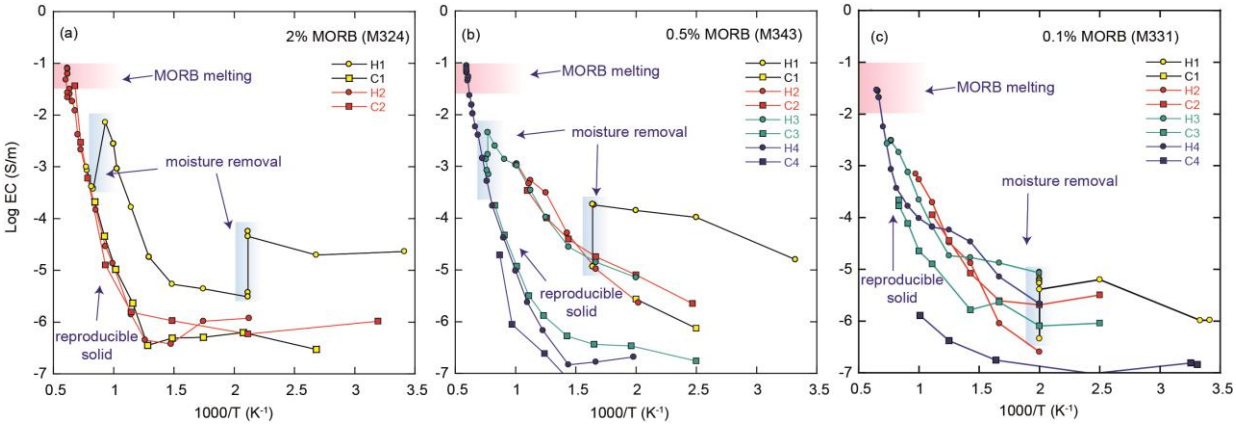

Figure III.15 Electrical conductivity measurements during each experience: (a) 2%MORB (b) 0.5% MORB, (c) 0.1% MORB. First heating and cooling cycles were performed to remove adsorbed moisture according the procedure developed by Manthilake et al. (2008), these steps are crucial to avoid any contamination from surrounding material (in particular volatiles) into our melt. Melting cycle was performed when reproducible solid electrical conductivity values were obtained. An important slope change was observed above 1000/T = 1.5 highlighting the transition from proton (at low T) to small polaron (high T).

Electrical conduction processes existing for silicates have been described in the Chapter I. Silicate minerals are regarded as ionic insulators at low temperature. However, these minerals behave as a semiconductor at mantle conditions. Mobility of lattice defects and a small amount of impurities, such as hydrogen and ferric iron, enhance electrical conduction of silicate mantle minerals at mantle temperatures. The Nersnt -Einstein relation describe the electrical conductivity for a crystal or a solid rock (see chapter I):

$$\sigma = \sigma_0 exp\left(\frac{-\Delta H}{kT}\right)$$

where σ_0 is the pre-exponential factor, ΔH is the activation energy, k is the Boltzmann constant, and T is the absolute temperature.

Our experiments show similar electrical conductivities values for different runs from room temperature to 1500 K despite the different melt contents (-7 to -2 in log unit) . Moreover, the conductivity systematically increases with increasing temperature. The different values observed for the last heating cycle of 0.1% melt sample can be explained by the persistent

presence of moisture because the last cooling cycle of the same sample is characterized by a similar value to all the other samples cycles, so the moisture was lost during the heating cycle.

Each sample shows the same transition of conductivity dynamics throughout the different heating and cooling cycles. Between room temperature and 700 K, conductivity values are small and with a very weak activation enthalpy, this suggests that proton conduction dominates at low temperature (Table III.4). At higher temperature, an inflexion of the conductivity curve is always present and highly visible. The activation enthalpy of this part between 700 K and 1650 K is significantly higher; this slope difference suggests a different conduction process which can be explained by small polaron conduction (Yoshino et al. 2010).

At high temperature, small polaron conduction dominates the proton conduction. Activation enthalpies observed are similar to olivine values with values between 1 and 2 eV. Therefore, the conductivity of the mixture is expressed as:

$$\sigma_{sample} = \sigma_{Ol} * \%ol + \sigma_{MORB} * \%MORB$$

Table III.4 Values of activation enthalpy and pre-exponential factor for the two conduction mechanism fitted. First, lower temperature range corresponds to proton conduction mechanism whereas high temperature range corresponds to small polaron.

Sample	σH (S/m)	ΔH (eV)
2 vol.% MORB		
300-700K	1.16E-06	0.0648
700-1650K	1089.43	1.57004
0.5 vol.% MORB		
300-700K	8.40E-08	0.004066
700-1650K	47.68	1.30243
0.1 vol.% MORB		
300-700K	1.56E-07	0.003630
700-1650K	4.32	0.96979

Where σ_{fe} and σ_{H+} are conductivities by small polaron and proton conductions, respectively. So the bulk conductivity is the result of the sum of crystal contributions normalized by their respective fraction. Thus, combining small polaron and proton conductions, the electrical conductivity of the sample (and each component) can be expressed as:

$$\sigma = \sigma_{0Fe} exp\left(\frac{-\Delta H_{Fe}}{kT}\right) + \sigma_0$$

Where the first term is small polaron conduction and the second one the proton conduction.

In our case, MORB component before melting is glassy and can partly recrystallize at high temperature, mostly in pyroxene and olivine. Olivine is at least 98% of the crystal contribution and so the other phase's contributions can be negligible at solid state as shown by our activation enthalpies compatible with olivine.

At melting temperature, the slope of the conductivity curve is marked by a jump which is the conductivity drop. After the drop, the slope of the conductivity values is almost vertical. This slope is a clue of another conduction regime which corresponds to ionic conduction characterized by very high activation enthalpy. The bulk electrical conductivity contains contribution from each ion. Previous work (Gaillard et al., 2005) demonstrated that the electrical conduction should be dominated by light alkalis (Li and Na). Na diffusivity in basaltic melts has activation energy of 120 - 160 kJ/mol (Ni et al., 2011; Tyburczy and Waff, 1983). The ionic conduction was however, not measured due to our experimental strategy.

d) Sample/capsule/electrode interfaces and additional chemical maps

To ensure the increase of electrical conductivity was not due to sample reaction with surrounding materials such as rhenium electrodes or BN capsules, we performed additional SEM imaging. Our sample does not show any reaction with both BN and electrodes (Fig. III.16) confirming that the small rhenium pellets found in the sample are due to polishing and that sample chemistry did not change during the experiments.

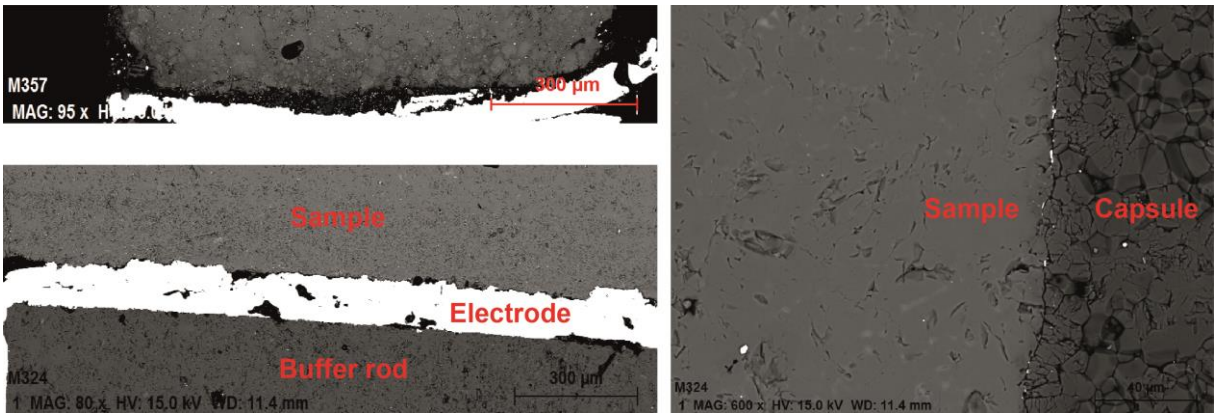

Figure III.16 Sample interfaces boundaries studied with SEM apparatus (backscattered electrons microphotograph). A possible reaction of the sample with its surrounding has been also considered, in additions to details given in the published article, to explain the increase of electrical conductivity with time. On these pictures taken on different samples, we can observe the absence of reaction between samples and rhenium electrodes as well with surrounding capsule. In addition no melt pools or infiltrations were observed along these discontinuities.

We also took the opportunity to give our 2% sample for tests performed on a new EMP JEOL JXA-8530F Hyperprobe apparatus at the University of Lausane. The tests were made to check the resolution of the apparatus with chemical maps on small objects (such as melt pockets) with chemical compositions that are not way different than the surrounding materials such as it occurs in natural samples. These maps highlight that our melt chemistry is quite homogeneous through the sample and that a small quench crystallization rim can be observed in our melt pockets (which was not possible with our LMV apparatus) (Fig. III.17). Measured chemical composition at pocket center is similar to what we gave in the table III.1.

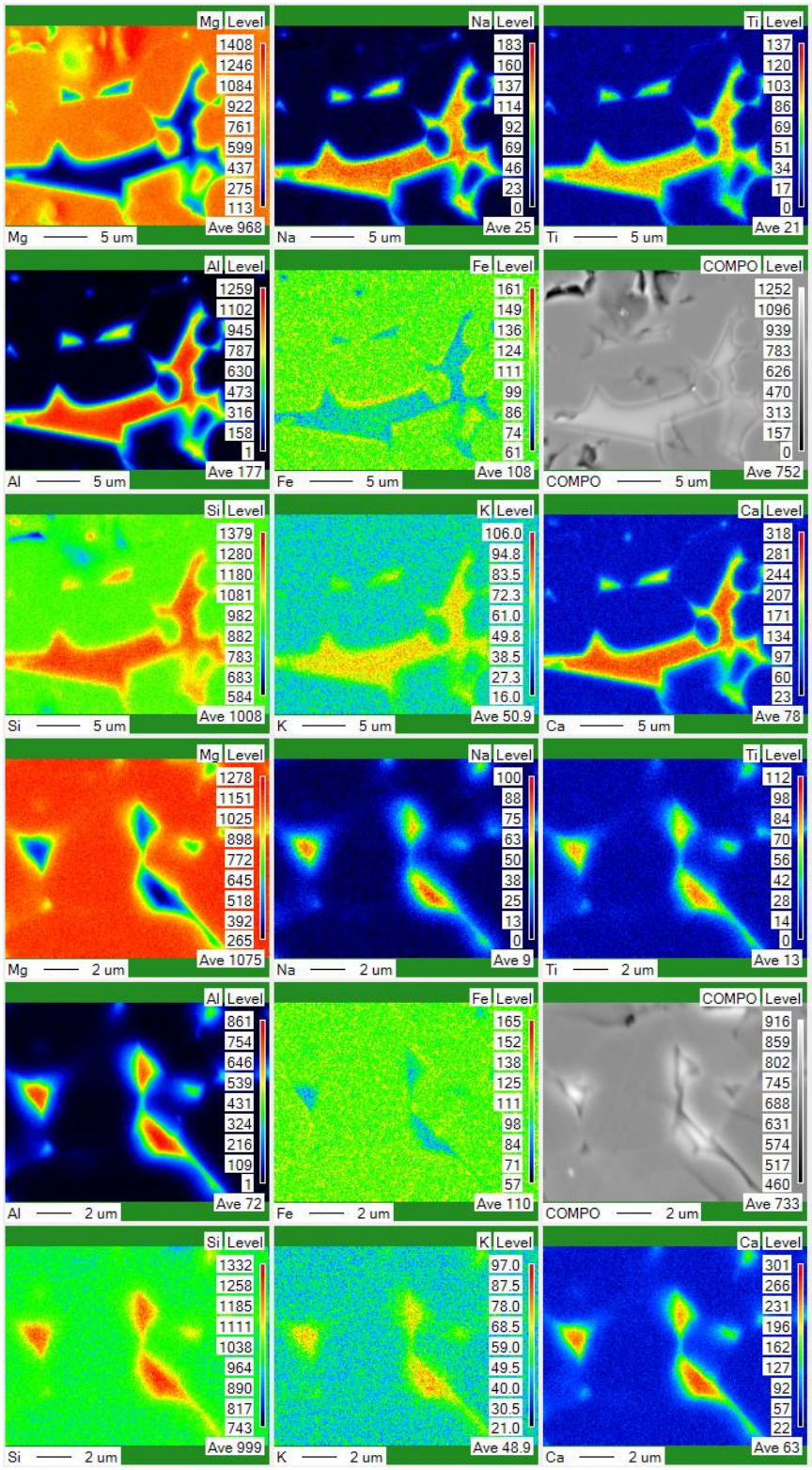

Figure III.17 Chemical maps of melt pockets from our 2 % MORB sample. Chemical homogeneity of our melt pockets were checked using FEG-EMP apparatus JEOL JXA-8530F Hyperprobe at the University of Lausanne. The analyses were kindly performed by J.L Devidal and T. Hammouda (tests of the apparatus). The analyses revealed, for almost all elements, a good homogeneity of the pockets and the presence of a thin quenched rim (<100 nm) as expected for these experiments. The used of Ca and Na maps is of a great interest to see the interconnection of the melt pockets and melt films at very low pocket size compared to standard BSE images. The analyses given in Freitas et al. (2019) were taken at the center of pockets similar or larger than these displayed in the first map (10-30 microns).

5) Summary

This work aimed to better understand and quantify the process that influences geophysical properties of partially molten rocks at upper mantle conditions. With a new assembly and experimental set-up, designed especially for this study, we report the first simultaneous measurements of electrical conductivity and sound wave velocity. The application of this new experimental system on geological materials allows investigating in a same experiment, which experienced the very same conditions (eg temperature and pressure gradients, chemical impurities and solid/liquid textures), the response of each geophysical signal to the onset of melting. Motivated by the discrepancies between *in situ* laboratory estimations, from sound wave velocity and electrical conductivity, of potential melt fractions implied in asthenosphere LVZ (70 - 220 km depth), this innovative study suggest that experimental issues can be the source of the disagreements between the different research groups. In fact, our experiments highlighted strong electrical conduction improvement due to the evolution of texture from a random to 3D interconnected network of melt. This process is time dependent, might require days or weeks for a complete equilibration, vary very importantly within the first hour after reaching melting temperature for a liquid with good wetting properties (dihedral angle = 27°). Because laboratory estimations of electrical conductivity are usually shortened to avoid melt escape or reactions, the measured values can underestimate the total effect of partial melting, on electrical conduction and require larger melt fractions to explain geophysical anomalies. Electrical conductivity appears to be a precise tool to detect the onset of melting, over its use to quantify melt fractions should be made with caution, as it both depends on textural state and chemical composition (including volatile). At the, opposite we found sound velocity to be a reliable tool to quantify melt fraction as it is way less sensible to both texture, composition or P/T effect. Experimental sound wave velocity was estimated to be much more reduced than theoretical prediction, which was also a source of disagreement between geophysical techniques, implying less than a percent of partial melting to explain most of the LVZ anomalies. Additional details to the published work were also given in this chapter to give full information about these samples, in particular with the melt and solid textures.

6) Perspectives

As described above, this work aims to be funding stone for new in depth studies. It offers a great variety of perspectives that were, for some, investigated in this PhD work, and others that remain of a significant interest for further projects.

a) Extended use of the EC/SV technique and experimental setup

Further experiments using combined EC/SV on the same sample to investigate other P-T range (See chapters IV and V) can be realized with the aim of a better understanding of other geophysical anomalies both on Earth or other planetary bodies (SEIS data from Insight on Mars?).

To do these, similar experiments can be adapted with our setup to other configurations (small truncation for higher pressure). This can be performed not only on partially molten systems but can be applied for phase transitions that can be monitored with both geophysical signal or other processes such as chemical reactions, grains growth, sample hardening/weakening or dehydrations/decarbonation of hydrous/carbonated minerals or rocks. This technique can also be performed under synchrotron radiation if EC and SV apparatus can be brought to the beamline. In this case, the assembly parts have to be optimized to reduce X-ray absorption, with rhenium heater with laser cut windows and full BN electrical insulation sleeves for example.

This experimental strategy can also be adapted to other melt compositions, as the effect of the melt composition in sound velocity in partially molten systems with real melt compositions and fraction is currently unknown. Rivers and Carmichael (1984) have shown that compositional effects on acoustic wave velocities are very moderate, however their study focuses on fully molten samples whereas effects on samples with intermediate to low melt fraction should be considered. Among chemical composition, the presence of volatiles and their effects on melt texture (dihedral angles) must be considered for a wider range.

As highlighted by this work, the experimental procedure was found to be crucial for the reproducibility and comparison between different experiments and laboratories. The dehydration procedure proposed by Manthilake et al. (2008), is a key step into the realization of electrical conductivity measurements to get rid of adsorbed water. This water could otherwise diffuse into the melt once solidus temperature is reached. The development of standardized assemblies is difficult among *in situ* EC/SV experimental community because

each experiment has its own requirements. However, a standardized procedure for both for EC/SV measurements and sample characterization as proposed in this paper would help comparison between studies.

b) Quantification of textural parameter time evolution with respect to geophysical signals

In this chapter, we suggest that the increase of electrical conductivity with time in a partially molten sample with a controlled melt fraction and relatively unchanged chemical composition is due to melt textural evolution. Our study is a first observation of this mechanism, even if data reported by Yoshino et al. (2005) also suggested the same trend. The next experimental step would be proposing a quantification of textural parameters with time and measure their effect on *in situ* geophysical measurements. A mathematical characterization would allow corrections of each experiment to compare values at the chemical and so textural equilibrium. This type of study was asked several times by reviewers of our work as it represents one of the most crucial points controlling geophysical properties. However, perform it would require a very careful consideration and a consequent number of experiments and time.

Quantify the SV or EC values with a given texture would be difficult as textural modifications are highly sensitive to different experimental settings. A very reproducible assembly and apparatus must be used, as well with standardized procedure. Perform "Quench experiments", which are a standard procedure in phase relation, melting relation and partition/diffusion experiments can be imagined for this study. Series of EC or EC/SV experiments can be performed with the same melt fraction sample and quenched at different times (each 20 minutes). The melt fraction should be intermediate as our study highlighted that large melt fraction instantaneously interconnect well and show less pronounced evolution with time. Very low melt fraction will induce small pocket size and fewer statistics. *Per contra,* these experiments will be very difficult to realize, the main reason is the sensibility to the experimental setting, and each experiment will have its own path toward equilibrium. Then, quench experiments will produce a variety of texture that will provide only a qualitative view of the ongoing maturation. Textural parameters can be measured, even if the use of dihedral angle will require a statistically important number of measurements to distinguish tiny variations from the error bar. However, because each sample will have slight variations due to the unique experimental setting, correlate a textural parameter to a value of electrical conductivity is risky as it depends on other parameters as well. The textural parameters must

be very finely resolved (great number) to be able seeing variation on short time scales. The infinite set of possible paths from initial state to equilibrium state (in thermodynamic point of view) will not allow a quantification of how EC evolves with texture but rather qualitative characterization.

c) The importance of anelastic and anharmonic effects

A detailed study on anelastic and anharmonic effects on sound velocity of partially molten materials would be also of a great interest. This point will allow better understanding of the bulk effect of the presence of melt on acoustic wave velocity. This effect was discussed in our published work and Chantel et al. (2016) for Q considerations. However, this MHz or GHz ultrasonic experiments lacks of a systematic investigation on these parameters. Because we compare experiments and natural measurements, at very different frequencies, the effect of these non-ideal behaviors directly impact our conclusions. The realization of such measurements will be difficult as high frequencies are taken in laboratory due to restricted sample size (HP) and technical limitation of piezoelectric transducers. Experiments can be performed on the same sample at different frequencies. On the other hand, this would imply distinct apparatus and setup, and so many sources of uncertainties.

Chapter IV

Experimental evidence of a global melt layer above the Mantle Transition Zone

Chapter IV Experimental evidence of a global melt layer above the Mantle Transition Zone

1) General Introduction

The Earth's mantle encompasses several zones of anomalies detected by geophysical observables such as seismicity and electromagnetic sounding. Among them, recent observations, inferred from receiver functions, highlighted a significant decrease of P and S wave velocities and high attenuation at the base of the upper mantle, between 350 and 410 km depth (Revenaugh and Sipkin, 1994; Song, 2004; Schaeffer and Bostock, 2010; Tauzin et al., 2010, 2013; Hier-Majumder et al., 2014). This anomalous layer was observed at a nearly global scale and its thickness (averaged to 50 km) (Tauzin et al., 2010) was shown to be very variable, even at regional scale (Tauzin et al., 2013; Hier-Majumder et al., 2014).

The source of such anomalies and geophysical properties of mantle rocks at this pressure and temperature range remains poorly constrained. By consequence, several hypotheses were brought to explain these anomalies. Solid state process were, one time invoked such as mineralogical anisotropy, however, the geodynamical context does not favor these hypothesis compared to plausible example such as lithosphere asthenosphere boundary (LAB). Partial melting hypothesis was then brought as the most probable explanation, despite here again a variety of possible scenarios and melting process. Revenaugh and Sipkin (1994), who first reported these anomalies, used subducted slab partial melting scenario and melt migration to the base of upper mantle to explain these anomalies. This scenario was challenged by the latter global seismological studies of the anomalous zone where no strong correlations of anomalies with slab location were observed. The proximity of the mantle transition zone and associated phases transitions complicate the observations, in particular for magnetotelluric studies in which jump of electrical conductivity at the mantle transition is difficult to resolve (see chapter I). Nevertheless, the particularity of this zone is probably related to the specific anomalies here observed. Bercovici and Karato proposed in 2003, the transition zone water filter model, which theoretically explains the presence of a global melt layer atop the MTZ by dehydration melting. In fact, the MTZ is composed of high pressure polymorphs of olivine, wadsleyite and ringwoodite. The transition can be expected to be isochemical, but implies different crystal structures and so physical properties (Ringwood, 1991). Among them, water solubility has been shown to increase significantly for these polymorphs compared to nearly dry olivine (Kohlstedt et al., 1996; Bolfan-Casanova et al., 2000; Férot and Bolfan-Casanova,

2012). If the MTZ is hydrous and its content in wadsleyite exceeds olivine solubility, the passive upwelling of MTZ rock across 410' discontinuity will oversaturate the rock during the back-transformation into olivine. Free aqueous fluids can be released and induce rock partial melting by significantly decrease of its melting point. This process should operate at nearly global scale where MTZ material upwells passively in response to slab injection in the deep mantle.

The absence of clear quantifications of these anomalies by other techniques than seismology and the lack of experimental *in situ* geophysical measurements prevent the confirmation of melting hypothesis and the definitive adoption of a given melting scenario. In this chapter, we report the first experimental reproduction of dehydration melting scenario together with *in situ* acoustic wave velocity measurements in order to better understand the seismological information. The indoor seismology also allows the recovery of rock samples and performs textural as well as chemical analyses. Results of these measurements were published in an experimental confirmation article in Nature Communication (see under). Additional details on experimental setup, texture and chemistry will be given in this chapter to complete this study.

2) Résumé

Le niveau de faible vitesse sismique situé au-dessus de la discontinuité à 410 km du manteau terrestre a souvent été attribué au phénomène de fusion partielle par déshydratation. Dans cette étude, nous avons reproduit expérimentalement la transformation de phase wadsleyite/olivine du matériel traversant la discontinuité à 410 km et mesuré *in situ* la vitesse des ondes acoustiques durant la fusion partielle de la péridotite hydratée. Notre modèle de vitesse sismique reproduit les anomalies négatives (dVs = -4 %) globales avec des taux de fusion partielle de l'ordre de 0.7 % (< 1%) des péridotites situées à la base du manteau supérieur. Les liquides produits sont enrichis en eau (~16.5 wt.%) et en fer (~ 33 wt.%) et leurs densités ont été estimées entre 3.56 et 3.75 $g.cm^{-3}$. La teneur en eau d'un liquide gravitationnellement stable au niveau de faible vitesse sismique (LVL) implique une zone de transition mantellique hydratée avec 0.22 ± 0.02 wt.% d'eau. Une telle concentration est compatible avec les estimations basées sur les données magnétotelluriques.

3) Experimental evidence supporting a global melt layer at the base of the Earth's upper mantle

Published article in Nature Communication (accepted 16th November 2017 online 19th December 2017).

Post print version, official open access version: https://www.nature.com/articles/s41467-017-02275-9

Experimental evidence supporting a global melt layer at the base of the Earth's upper mantle

D. Freitas[1], G. Manthilake[1]*, F. Schiavi[1], J. Chantel[2], N. Bolfan-Casanova[1], M.A. Bouhifd[1], D. Andrault[1]

[1.] Université Clermont Auvergne, CNRS, IRD, OPGC, Laboratoire Magmas et Volcans, F-63000 Clermont-Ferrand, France

[2.] Department of Earth, Environmental and Planetary Sciences, Case Western Reserve University, Cleveland, OH 44106, USA

*corresponding author (geeth.manthilake@uca.fr)

a) Abstract

The low velocity layer (LVL) atop the 410-km discontinuity has been widely attributed to dehydration melting. In this study, we experimentally reproduced the wadsleyite-to-olivine phase transformation in the upwelling mantle across the 410-km discontinuity and investigated in-situ the sound wave velocity during partial melting of hydrous peridotite. Our seismic velocity model indicates that the globally observed negative Vs anomaly (-4 %) can be explained by a 0.7 % melt fraction in peridotite at the base of the upper mantle. The produced melt is richer in FeO (~ 33 wt. %) and H_2O (~16.5 wt. %) and its density is determined to be 3.56 - 3.74 $g.cm^{-3}$. The water content of this gravitationally stable melt in the LVL corresponds to a total water content in the mantle transition zone of 0.22 ± 0.02 wt. %. Such values agree with estimations based on magneto-telluric observations.

b) Introduction

The origin of the low velocity layer (LVL) atop the 410-km discontinuity has long been attributed to the presence of melt (Song et al., 2004; Bercovici and Karato, 2003; Revenaugh and Sipkin, 1994; Schaeffer and Bostock, 2010; Tauzin et al., 2010; Vinnik and Farra, 2007). The LVL is reported to be a widespread seismic anomaly (Tauzin et al., 2010), with an average 4 % Vs velocity drop across a narrow, ~ 50-60-km-thick region atop the mantle transition zone MTZ. The presence of a partially molten layer at the base of the upper mantle has a wide range of geological implications. In particular, it is directly linked to H_2O contents in the MTZ, which plays an important role controlling the global water circulation (Bolfan-Casanova et al., 2000; Karato, 2011). It promotes the material exchange between the upper and lower mantle without requiring a whole mantle or layered convection model (Schaeffer and Bostock, 2010) and could help to explain the chemical differences between mid-ocean-ridge and ocean-island basalts (Bercovici and Karato, 2003). Refining the LVL properties may provide unique insight into the nature of deep mantle plumes and their interactions with the surrounding mantle (Bercovici and Karato, 2003; Vinnik and Farra, 2007). Further, a melt layer may influence mantle dynamics by decoupling the upper mantle and the MTZ above the 410 km discontinuity along this low viscosity layer and allowing coherent motion between lithosphere and the underlying mantle (Vinnik and Farra, 2007).

Numerous studies predict the melting of peridotite under deep mantle conditions if water is present (Bercovici and Karato, 2003; Inoue, 1994; Sakamaki et al., 2006). The magnitude of the Vs velocity drop at the LVL is directly related to the melt volume fraction. The melt fraction in the LVL should be the key parameter controlling the stability of the melt layer and the subsequent element fractionation between upwelling mantle and the melt. The highly wetting character of hydrous silicate melt at high pressure (Yoshino et al., 2007) implies that even a small degree of melting can dramatically affect the propagation of seismic waves at high depths. Both experimental (Chantel et al., 2016; Faul et al., 2004; Sato et al., 1989) and theoretical models (Hammond and Humphreys, 2000; Hier-Majumder, 2008; Mavko et al., 1979; O'Connell and Budiansky, 1974; Schmeling, 1986; Takei, 2002, 1998; Yoshino et al., 2005) have investigated the magnitude of the velocity drop that would be associated with the melt fraction. However, the current velocity models are based on either low pressure (< 2.5 GPa) laboratory measurements or simulations based on simplified melt geometries, limiting their applications when interpreting the seismic anomaly at the base of the upper mantle. Thus, systematic laboratory measurements of the effect on seismic velocity of a melt generated at deep mantle conditions are central to establishing the dehydration-melting scenario at the base of the upper mantle.

Density is a key parameter controlling the stability of a melt layer in the LVL (Bercovici and Karato, 2003; Karato et al., 2006; Leahy and Bercovici, 2010, 2007), and is determined by chemical composition as well as pressure and temperature. However, experimental investigations of the hydrous peridotite melt composition are limited to 6 GPa (Novella and Frost, 2014). Other systematic works have explored the density of hydrous silicate melts at high pressure, assuming variable concentrations of FeO and H_2O (Jing and Karato, 2012, 2009; Matsukage et al., 2005; Mookherjee et al., 2008; Ohtani et al., 1995; Sakamaki et al., 2006; Suzuki and Ohtani, 2003; Suzuki et al., 1998). While these studies provide useful relations between melt density and composition, knowledge of the melt composition as a function of the degree of melting is currently lacking, adding notable uncertainties to current geodynamic models (Karato et al., 2006).

In this study, we experimentally simulate upwelling of peridotite mantle across the 410 km discontinuity by synthesizing variably hydrated peridotites in the wadsleyite stability field (14 GPa) and measuring the sound wave velocity of re-equilibrated peridotite in situ in the olivine stability field (12 GPa) as a function of increasing temperature. Then, using ex situ characterization of the melt chemical composition and microstructures, together with numerical calculations, we constrain the partial melting scenario during peridotite dehydration above the MTZ. Using sound wave velocity, we determined the melt volume fraction and, from chemical systematics, the composition of the melt that would be consistent with seismic observations. Finally, we discuss the geophysical and geochemical consequences of a globally distributed melt layer at the base of the Earth's upper mantle.

c) Results

i) Sound wave velocity

At a fixed pressure of 12 GPa, the sound velocity of peridotite before melting is characterized as expected by a gradual decrease of compressional and shear wave velocities with increasing temperature. For peridotite containing 600 ppm wt H_2O, we observe one abrupt drop of velocity corresponding to the wadsleyite-to-olivine phase transformation (Fig. IV.1). For peridotite samples with > 3000 ppm wt. H_2O, we observe two distinct velocity perturbations: a first velocity drop at 1000-1100 K and a second at 1450-1500 K (Fig. IV.1). For comparison, the dry peridotite sample (synthesized in the olivine stability field) does not show any abrupt variation in sound wave velocity (Fig. IV.1).

The first velocity perturbation observed upon increasing temperature for hydrous peridotite samples synthesized in the wadsleyite stability field is explained by the back-transformation of wadsleyite into olivine. The second velocity drop observed at around 1450 K exclusively in the most hydrous peridotites (> 3000 wt. ppm H_2O) can be attributed to the onset of melting. In the temperature range between the two velocity jumps, the released fluid is likely incorporated back into the remaining wadsleyite fraction.

ii) *Chemical and micro-texture analysis*

Analysis of experimental run products after the velocity measurements had been completed confirmed the presence of melt in H_2O-bearing samples (Fig. IV.2), while no sign of melting was observed in the H_2O under-saturated peridotite sample with 600 wt. ppm H_2O. Chemical analyses of the melt show a significant enrichment in incompatibles elements: Ca, Al, Na, K, together with increasing H_2O and FeO contents with decreasing melt fractions (Supplementary Table IV.S1).

The melt is distributed in a network of interconnected grain boundary tubes and melt-filled triple junctions within the host mineral matrix (Fig. IV.2). Using the high resolution SEM images, we have determined the sample melt fractions as well as the wetting angles of melt-solid interfaces for samples with different melt fractions. Dihedral angles are < 10° for all measured samples and the median angle slightly increases with increasing melt fraction (Fig. IV.3).

The small dihedral angles observed in the present melts (Fig. IV.3) ensures complete grain boundary wetting and melt interconnectivity even for extremely low melt volume fractions (Laporte et al., 1997; Laporte and Provost, 2000; Von Bargen and Waff, 1986), which is crucial for propagation of seismic waves**.** The solid-melt dihedral angle is known to vary with pressure and with the composition of the melt phase (Minarik and Watson, 1995; Yoshino et al., 2005). The slight increase of dihedral angle with increasing melt fraction (Fig. IV.3) is a unique observation and can be explained by the decrease in H_2O content in melt at higher degrees of melting. Owing to the high wetting properties of the melt, we assume that slight changes in dihedral angle with melt fraction may not affect the seismic wave velocity in our samples.

d) Discussion

Quantitative comparison between laboratory data and seismological signals requires experiments in which the molten phase is in textural equilibrium with the solid matrix. Due to time-limited laboratory experiments, transient conditions may affect the results of sound velocities. Therefore, texture analysis and interpretation are important. In a partially molten system loaded at given pressure and temperature, the melt network can evolve to minimize the energy of melt-solid interfaces. This equilibration process concerns the wetting angle θ at solid-solid-melt triple junctions, the area-to-volume ratio of melt pockets at grain corners and the melt permeability threshold (Laporte et al., 1997; Laporte and Provost, 2000). Experimental studies suggest that textural maturation is a time-dependent process, which usually requires long annealing times (weeks or months) (Laporte and Provost, 2000; Waff and Blau, 1982). Still, the near-zero dihedral angle (< 10°) the extensive wetting of crystal faces and the smoothly curved solid-melt interfaces observed in our samples are strong indications that the microstructure has reached an equilibrium (Cmíral et al., 1998; Cooper and Kohlstedt, 1984; Waff and Faul, 1992) (Fig. IV.2). Further, after reaching the peak temperature, the sound velocity remains nearly constant, suggesting that the samples are well relaxed, enabling a safe comparison of our measurements with geophysical observations.

We pointed out the change in melt chemistry with the degree of melting of our peridotite samples. Recent studies have shown that such compositional variations do not influence the propagation of seismic waves significantly (Afonso and Schutt, 2012; Hier-Majumder et al., 2014). Accordingly, based on the sound wave velocity of our melt-free and melt-bearing samples, we derive a relation between the % drop in shear wave velocity and the sample melt fraction. According to this model, the negative 4 % shear wave velocity anomaly of the mantle can be explained by the presence of 0.7 % volume fraction of hydrous silicate melt in the LVL (Fig. IV.4). Regional variations in the melt fraction, possibly induced by lateral temperature variations, could cause variable Vs velocity anomalies, reported elsewhere, in the low velocity layer (Revenaugh and Sipkin, 1994; Vinnik and Farra, 2007).

Our laboratory experiments demonstrate that partial melting can be triggered by upwelling of hydrous transition zone material. Still, the stability of a melt layer at the base of the upper mantle is critically linked to its density (Karato et al., 2006). Based on the chemical composition of the hydrous silicate melts obtained in this study, we determined the melt density using the third-order Birch–Murnaghan equation of state, taking into account their concentrations of H_2O, FeO, CO_2, Na_2O and K_2O (Karato et al., 2006; Matsukage et al., 2005; Sakamaki et al., 2009) (See methods for details). Our calculations suggest that the presence of incompatible elements such as CO_2, Na_2O

and K_2O have a negligible effect on melt density (less than 1% variation for the maximum possible abundances) compared to FeO and H_2O. The melt with 33 wt.% FeO and 16.5 wt.% H_2O, which corresponds to a melt fraction of 0.7 vol%, presents a density of 3.58 - 3.74 $g.cm^{-1}$ in the pressure range of 12-14 GPa (~350 -410 km depth) (Fig. IV.5). For comparison, the density of the ambient mantle varies from 3.51 to 3.72 g cm^{-1} (Dziewonski and Anderson, 1981) indicating that the melt is neutrally buoyant at those depths.

The stability of the melt layer at the base of the upper mantle is determined by the efficiency of melt generation and melt extraction processes. Hydration of MTZ mineral phases is key and the downwelling slabs can continuously provide a subsequent amount of water to the MTZ due to entrainment of hydrous phases from the lithosphere (Ohtani et al., 2004). The transition zone water filter (TZWF) model (Bercovici and Karato, 2003; Karato et al., 2006) details possible interactions between a melt layer and the surrounding mantle. For example, melt entrainment in downwelling slab components provides a plausible mechanism for recycling of H_2O and incompatible elements back to the MTZ and the lower mantle. The lateral variations in temperature (Yan et al., 1989), water content and/or the rate of mantle upwelling could affect significantly the degree of partial melting in the LVL, and therefore the melt density. For example, relatively hotter regions should produce more melt with lower density than those subjected to smaller degrees of melting. Even subtle variations in melt density could result in upward or downward movement of melt, toward the Earth's surface or back to the MTZ, respectively. Such melt migration could be a controlling parameter of the LVL thickness.

In this study, we show that a melt fraction of 0.7 vol.% is compatible with the seismological observations in the LVL. With the working hypothesis of melt fraction in the LVL being similar to the degree of partial melting (i.e. the batch melting scenario), we estimate the water content in the source material. Our calculations show that 0.7 vol. % melt with 33 wt.% FeO requires 16.5 wt.% H_2O in order to be gravitationally stable at 350-410 km depth. Knowing the H_2O partitioning coefficient between the melt and the peridotite residue (Novella et al., 2014), we calculated the H_2O contents in the MTZ to be 0.22 ± 0.02 wt.%. These water concentration values are in good agreement with previous estimations based on electrical conductivity (Huang et al., 2005; Karato, 2011). However, variation of melt fraction within the LVL may indicate regional variations of water content in the MTZ. The water depleted (Yoshino et al., 2008) or water saturated models for the MTZ (Fei et al., 2017; Pearson et al., 2014) cannot be corroborated by the findings of the current study. Particularly, the near-water saturated conditions implied by hydrous ringwoodite inclusions found in natural diamond (Pearson et al., 2014) may not be representative of the whole MTZ but instead may represent an episode of subduction-zone-related melting.

e) Methods

i) Sample preparation

Starting materials with a composition similar to KLB-1 peridotite (Wang and Takahashi, 2000) were prepared using regent grade oxides, initially mixed in the absence of the required amount of $Al(OH)_3$ to yield the correct mineral composition. These powders were dried at 300 °C overnight to remove any adsorbed moisture. Na and K were added as $NaCO_3$ and K_2CO_3 and then de-carbonated. The decarbonation of the oxide mixtures was carried out by slowly increasing the temperature to 1000°C (1.6°C/min) and keeping it at 1000°C for about 10 hours to ensure complete decarbonation. The decarbonated powder mixture was then cooled to 200°C and stored in a high vacuum furnace at 120°C prior to the hot pressing runs. The required amount of $Al(OH)_3$ was then mixed with the decarbonated powder mixture to obtain the desired amount of water in peridotite samples. The resulting powder mixtures were hot pressed to obtain solid sintered samples for seismic velocity measurements. The dry samples were synthesized at 5 GPa and 1473 K for 2 hours in rhenium (Re) foil capsules. The low water storage capacity in peridotite at this pressure (Férot and Bolfan-Casanova, 2012) helps maintain relatively water-poor conditions in the nominally dry sample. Hydrous samples were synthesized at 14 GPa and 1373 K for 2 hours in Gold-Palladium (Au-Pd) capsules. Given that the water storage capacity of wadsleyite is 4-5 times high than olivine (Férot and Bolfan-Casanova, 2012) and that the water storage capacity of clinopyroxene and garnet increases with pressure, the synthesis of hydrous samples at 14 GPa allows incorporation of more water into minerals phases. The wadsleyite-bearing sample with relatively low water content was synthesized by first hot-pressing in the olivine stability field (2.5 GPa and 1473 K) to lower the initial water content in minerals, and then by hot-pressing the pre-sintered sample at 14

GPa and 1473 K in an Au-Pd capsule. Si-metal powder was also used to surround the capsules in order to reduce the influence of adsorbed moisture on the synthesis process. Water under-saturated conditions are required during the synthesis process, in order to avoid hydrous silicate melts along grain boundaries, which could otherwise interfere with the conductivity and sound wave velocity. Cylindrical core samples ~1.0 mm in length and ~1.2 mm in diameter were prepared from these pre-synthesized sample specimens. In situ measurements were performed on double-polished core samples of the starting material. The final length and diameter of the samples were measured with an accuracy of ± 0.1 μm. The chemical composition and the water contents of the starting samples were analyzed using electron microprobe and micro-Raman, respectively.

ii) High-pressure, high temperature experiments

Simultaneous high-pressure and high-temperature experiments were performed using a 1500-ton Kawai-type multi-anvil apparatus at the Laboratoire Magmas et Volcans, Clermont-Ferrand, France. Both sample synthesis and the in situ measurements were performed using an octahedral pressure medium composed of MgO and Cr_2O_3 (5 wt.%) in a 14/8 multi-anvil configuration (octahedron edge length / anvil truncation edge length) For in situ measurements, the assembly was designed to accommodate the geometrical requirements for measurements of Vp, Vs and EC within a single high-pressure cell. The pre-synthesized cylindrical sample was inserted into a single-crystal MgO sleeve. The sleeve also helps to insulate the sample electrically from the furnace. This furnace, composed of a 50 μm thick cylindrical Re foil, has apertures for the electrode and the thermocouple wires. A zirconia sleeve around the furnace was used as a thermal insulator.

We placed two electrodes, made of Re discs, at the top and bottom of the cylindrical sample. A tungsten-rhenium ($W_{95}Re_5$-$W_{74}Re_{26}$) thermocouple junction was placed at one end of the sample to monitor the temperature. The opposite end was connected to a single $W_{95}Re_5$ wire. We collected impedance spectra between the two $W_{95}Re_5$ wires. A dense Al_2O_3 buffer rod was placed between one of the tungsten carbide (WC) anvil truncations and the sample to enhance the propagation of elastic waves and to provide sufficient impedance contrast to reflect ultrasonic waves at the buffer rod-sample interface. Both ends of the anvil, the alumina buffer rod and the samples were mirror-polished using 0.25 μm diamond paste in order to enhance mechanical contacts. All ceramic parts of the cell assembly, including the pressure medium, were fired at 1373 K prior to their assemblage in order to remove any adsorbed moisture, and kept (as the samples) in vacuum furnaces (10^{-2} Torr and 150°C) before assembling the experiment. Oxygen fugacity of the sample was not controlled during in situ measurements, but was expected to remain below the Re-ReO_2 buffer.

The upwelling of the hydrous mantle transition zone across the 410 km discontinuity was simulated by synthesizing hydrous samples at conditions corresponding to the wadsleyite stability field (14 GPa), and then reloading them to 12 GPa (conditions corresponding to ~350 km in depth) in order to observe their melting behavior by monitoring their Vp, Vs, and electrical conductivity responses. Thus, more water, exceeding the storage capacity of olivine, can be incorporated as a point defect dissolved in the structure of wadsleyite. This procedure also ensures that a hydrous melt does not form during the synthesis process. Upon re-equilibration in the olivine stability field, the wadsleyite transforms to olivine and the new mineral assemblage cannot store the original water content; consequently a free fluid is liberated that triggers melting. By changing the initial water content of the wadsleyite sample or by increasing the sample temperature, we observe seismic velocity responses of five different samples with melt fractions of 0, 2, 3.5, 7 and 25 %. For comparison, we have also measured seismic wave velocity of anhydrous peridotites at 12 GPa pre-synthesized, guaranteeing melt-free conditions in water under-saturated upper mantle.

iii) Seismic wave velocity measurements

Sound wave velocities of the samples were measured using the ultrasonic interferometry technique(Li et al., 2004). In this method, electrical signals of sine waves of 20–50 MHz (3–5 cycles) with $V_{peak\text{-}to\text{-}peak}$ of 1–5 V were generated by an arbitrary waveform generator (Tektronix AFG3101C); they were then converted to primary (V_P) and secondary (V_S) waves by a 10° Y-cut $LiNbO_3$ piezoelectric transducer attached to the mirror-polished truncated corner of a WC anvil. The resonant frequency of the transducer is 50 MHz for compressional waves (*P*-waves) and 30 MHz for shear waves (*S*-waves). Elastic waves propagated through the tungsten carbide

(WC) anvil, alumina buffer rod (BR), and the sample, and were reflected back at the interfaces between the anvil-BR, the BR-sample, and the sample-electrode. The reflected elastic waves were converted back to electrical signals by the transducer and captured by a Tektronix DPO 5140 Digital Phosphor Oscilloscope at a rate of 5×10^9 sample/s. Signals at 20, 30, 40 and 50 MHz were recorded at each temperature step. The two-way travel time for the sound waves propagating through the sample can be determined by the time difference between the arrivals of the echoes from the BR-sample interface and the sample-electrode interface by the pulse-echo overlap method[59]. Sample lengths, prior to sample loading and after the melting experiments, were determined with a high precision digital multi-meter (accuracy of 0.1 μm) and using the BSE images obtained using Field Emission Gun scanning electron microscope (FEG-SEM), respectively. The change of sample length due to the thermal expansion at high temperature was corrected using the equations of state of olivine and wadsleyite, the principal mineral phases present in the samples.

iv) Chemical and microstructural analysis

The chemical composition of pre-sintered samples and experimental run products after seismic velocity measurements were investigated using the Cameca SX100 electron probe micro analyzer at the Laboratoire Magmas et Volcans of Clermont-Ferrand. Energy-dispersive X-ray spectroscopy (EDS) chemical mapping was used to determine the mineral proportions. Micro-textures of the samples were observed with a Scanning Electron Microscope (SEM) JEOL Jeol JSM-5910 LV at the Laboratoire Magmas et Volcans of Clermont-Ferrand. For imaging, an accelerating voltage of 15 kV and working distance of 11.4 mm were used, and for chemical mapping an accelerating voltage of 10 kV and working distance of 19.3 mm were used. The fine melt micro-textures were observed with ZEISS supra 55VP field emission gun (FEG) SEM with an acceleration voltage of 15 kV and working distance of 9.7 mm (2MATech, Aubière, France).

Powder X-ray analysis using Philips PW 1830 (Cobalt wave-length) was carried out prior to the seismic velocity measurements to ensure the absence of additional hydrous phases such as super hydrous phase-B in pre-sintered samples. No evidence for additional hydrous phases was found in the pre-synthesized hydrous peridotite samples.

v) Water content estimations

Raman spectroscopy was used to estimate the water contents of mineral and melt phases. Raman spectra were collected using an InVia confocal Raman micro spectrometer manufactured by Renishaw, equipped with a 532 nm diode laser (output power of ~140 mW), a Peltier-cooled CCD detector, a motorized XY stage and a Leica DM 2500 M optical microscope, housed at the Laboratoire Magmas et Volcans (Clermont-Ferrand). Scattered light was collected by a back-scattered geometry; the laser power on the sample was reduced to ~9 or 16.5 mW and the slit aperture was set to 65 μm (standard confocality setting) or 20 μm (high confocality setting). A 100x objective and 2400 l/mm grating were used for the analyses. These analytical conditions result in spatial resolution of ~1 μm and spectral resolution better than 1 cm^{-1}. Daily calibration of the spectrometer was performed based on a Si 520.5 ± 0.5 cm^{-1} peak. The spectra were recorded using Wire 4.2 Software from ~100 to 1300 cm^{-1} (alumino-silicate network domain) and from ~3000 to 3800 cm^{-1} (water domain). Acquisition times were 60-240 s for the high-frequencies domain and 30-60 s for the low frequencies. Raman analysis was performed on mineral phases (wadsleyite, olivine, pyroxene and garnet) and on the interstitial glass phase. Difficulties in Raman analysis of the glass phase were caused by the very small size of glass pockets (sometimes < 1 μm), general instability of the water- and iron-rich glass under the laser beam, and overlapping of the surrounding olivine Raman peaks on the silicate glass bands. For determination of water content in glasses, we used both the external calibration procedure(Mercier et al., 2010), which is based on a set of hydrous basaltic glass standards (Médard and Grove, 2008) and the absolute intensities of the water band area, and an internal calibration procedure, based on the correlation between the glass-water concentration and the relative areas of the water and silicate Raman bands. The two methods gave comparable results. Water contents of the standards were determined using both FTIR and SIMS techniques. Standards were analyzed at the same conditions as the samples. Analytical precision calculated based on repeated daily measurements of standard glasses is generally better than 6 % relative.

vi) Experimental uncertainties

Experimental measurements are subjected to uncertainties originating from the estimations of temperature, pressure, sample dimensions, data fitting errors and estimation of melt chemistry. The estimated experimental errors on the absolute values sound wave velocity are within 5 % and it sis less than 6 % for chemical analysis.

vii) Calculations of silicate melt density at high-pressure

We estimated the density of silicate melts (compositions similar to the peridotite melts at 10 – 20 GPa pressure range) and found that the most important melt oxides that control peridotite density (SiO_2 content is roughly constant) at high pressures are FeO and H_2O, consistent with previous studies (Jing and Karato, 2008; Matsukage et al., 2005; Sakamaki et al., 2009).

The first step of our calculations was to determine the density of dry peridotite and hydrous peridotite melt (5 wt.% H_20) at high pressure, in order to estimate the effect of H_2O on melt density in the 10 to 20 GPa pressure range. We used the third-order Birch-Murnaghan equation of state (EOS):

$$P = \frac{3}{2}K_T\left(\left(\frac{\rho}{\rho_0}\right)^{\frac{7}{3}} - \left(\frac{\rho}{\rho_0}\right)^{\frac{5}{3}}\right) \times \left(1 - \frac{3}{4}(4 - K') \times \left\{\left(\frac{\rho}{\rho_0}\right)^{\frac{2}{3}} - 1\right\}\right) \quad (1)$$

Where ρ is the high-pressure density, ρ_0 is the zero-pressure density, K_T is the isothermal bulk modulus and K' is its pressure derivative. The temperature effect on K_T is expressed with the following equation:

$$K_T = K_{T_0} + \left(\frac{\partial K_T}{\partial T}\right)_P (T - T_0) \quad (2)$$

With the following parameters (Sakamaki et al., 2009) used for hydrous peridotite (5 wt% H_2O) at 1773 K: ρ_0 = 2.40 g/cm^3, K_T = 8.8 ± 1.9 GPa, K' = 9.9 ± 3.6, and = -0.0022 ± 0.0015 (GPa/K)and the following parameters for dry peridotite at 2100 K: ρ_0 = 2.72 g/cm^3, K_T = 24.0 ± 1.3 GPa, K' = 7.3 ± 0.8, and $\left(\frac{\partial K_T}{\partial T}\right)_P$ = -0.0027 ± 0.0017 (GPa/K). We found that H_2O decreases the density of peridotite melt in the 10 – 20 GPa pressure range at 1770 K by about 0.02 g/cm^3 for every 1 wt.% H_2O This result is in good agreement with the previous studies in the pressure range of 10 to 16 GPa (Matsukage et al., 2005). However, for lower pressures (1 to 5 GPa pressure range), water decreases the density of silicate melt by about 0.04 g/cm^3 for every 1 wt.% H_2O (Agee, 2008). This is consistent with the fact that water is more compressible than the major oxides of silicate melts at upper mantle conditions (SiO_2, Al_2O_3, FeO, MgO, CaO) (see Matsukage et al.(2005) for more details).

The computed partial molar volume of H_2O, $_{H2O}$ = 7.6 cm^3 mol^{-1} at 15 GPa, is in good agreement with the ~ (8 ± 2) cm^3 mol^{-1} of Matsukage et al.(2005).

The effect of iron was examined by using the data of Matsukage et al.(2005) at pressure and temperature conditions for a depth of 410 km. Supplementary Figure VI.S1 reports the variation of the isothermal bulk modulus (K_T) as a function of the FeO content in silicate melt (mol.%). For the value of K', although its value must be > 4 for silicate melts at high pressure(Guillot and Sator, 2007), we assumed a value of 4 in our calculations (mainly due to the limited experimental data on silicate melts at high pressure).

To estimate the effects of Na_2O, K_2O and CO_2 on the density of silicate melt at high pressure, we used the reported partial molar volumes (Karato et al., 2006) in conjunction with the volume of hydrous peridotite melt (5 wt.%). In the 10 -20 GPa pressure range, adding a total of up to 1 wt.% of these oxides does not drastically change the density of the silicate melt. For instance, adding ~ 2000 ppm wt. CO_2 (maximum possible value for our composition, based on Raman spectra), ~ 2000 ppm wt. Na_2O and ~ 8000 ppm wt K_2O to a hydrous peridotite melt (with 5 wt. % H_2O) will lower the density from about 3.5 to 3.47 g/cm^3 at 16 GPa. So, in the following calculations we take into account only the effects of H_2O and FeO on the density of silicate melts at high pressure, and ignore the effects of the other oxides.

To determine the density of our melt (that contains 20.2 mol. % FeO) at high pressure we used the following steps:

We determined the density of our Fe-rich hydrous melt (~ 14 mol. % H_2O) at high pressure using the Birch-Murnaghan EOS

with K' = 4 and K_T = 17.462 – 0.12154 × FeO (mol. %)

$$P = \frac{3}{2} K_T \left(\left(\frac{\rho}{\rho_0} \right)^{\frac{7}{3}} - \left(\frac{\rho}{\rho_0} \right)^{\frac{5}{3}} \right) \quad (3)$$

ρ_0 of our composition was determined using the Ochs and Lange (1999) model at 1 bar and 1773 K.

Then we estimated the effect of H_2O (up to 40 mol. %) on the density of the Fe-rich hydrous melt by using the partial molar volume of water:

$$V_{\text{FeO and H2O-rich melt}} = (1 - \delta x_{H2O}) \times V_{\text{FeO-rich melt}} + \delta x_{H2O} \times V_{H2O} \quad (4)$$

where δx_{H2O} is the difference in molar fraction of water between the FeO-H_2O-rich melt and the FeO-rich melt.

Another way to estimate the effect of water on the density of silicate melts at high pressure is to assume (as noted above) that H_2O decreases the density of silicate melts in the 10 – 20 GPa pressure range at 1770 K by about 0.02 g/cm^3 for every 1 wt. % H_2O:

$$\rho_{\text{FeO and H2O-rich melt}} = \rho_{\text{FeO-rich melt}} - 0.02 \times \delta X_{H2O} \quad (5)$$

here the δX_{H2O} is the difference in wt. % of water between the FeO-H_2O-rich melt and the FeO-rich melt.

f) Acknowledgments

We thank S-I Karato and an anonymous reviewer for their constructive reviews that benefited the manuscript. GM acknowledges funding from the French PNP program (INSU-CNRS). NBC is supported by ANR-11-JS56-01501 and DA is supported by ANR-13-BS06-0008. This research was financed by the French Government Laboratory of Excellence initiative n°ANR-10-LABX-0006, the Région Auvergne and the European Regional Development Fund. This is ClerVolc contribution number 274.

g) Figures and Captions

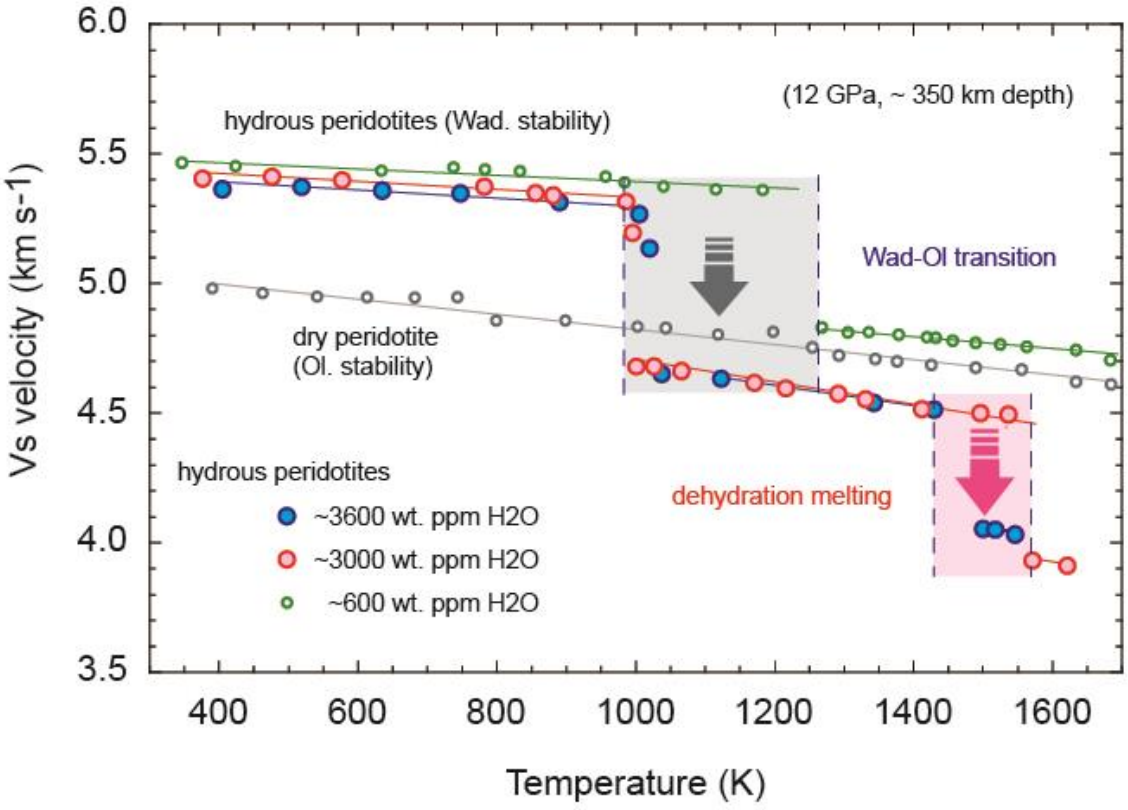

Figure IV.1 Secondary wave velocity as a function of temperature for hydrous peridotites. Hydrous peridotites synthesized in the wadsleyite stability field (14 GPa) and then re-equilibrated in the olivine stability field (12 GPa) demonstrate two distinct velocity drops: the first corresponding to the wadsleyite to olivine transition at low temperature, and the second corresponding to the onset of melting at higher temperature. The hydrous peridotites with low water contents indicate velocity decrease corresponding to the wadsleyite-to-olivine phase transformation The velocity variation of dry peridotite, synthesized at olivine stability field does not indicate any abrupt variation in sound wave velocity and follow the trend for general decrease of bulk and shear moduli with temperature. The blue, red and green circles represent hydrous wadsleyite with 3600, 3000 and 600 wt. ppm of H_2O, synthesized at wadsleyite stability field. The grey circle is for dry peridotite synthesized at olivine stability field.

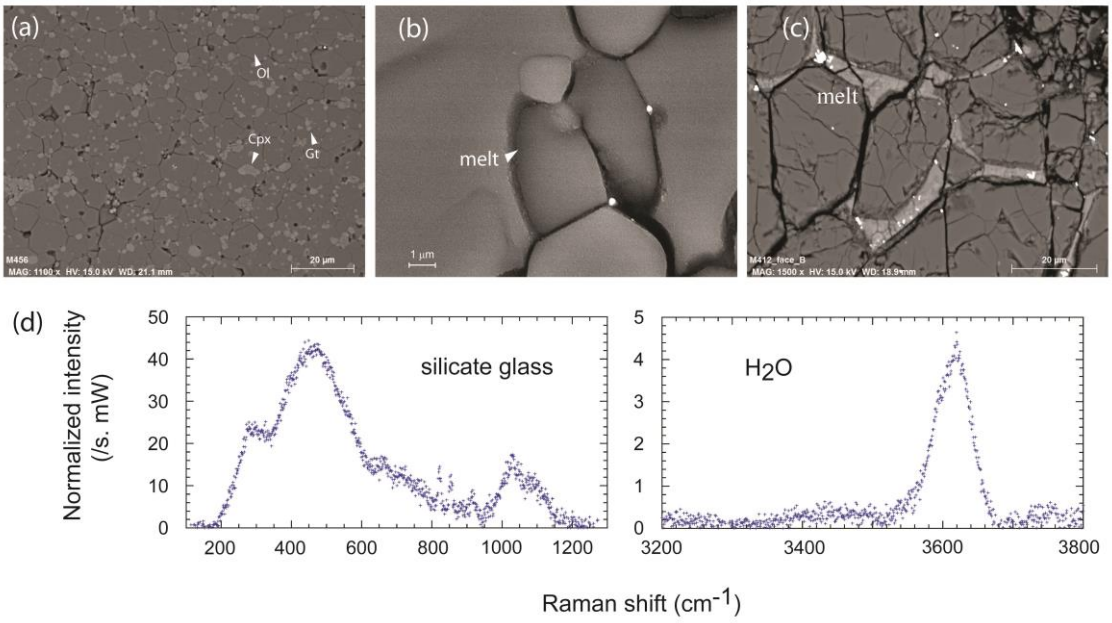

Figure IV.2 Sample characterization after high-pressure, high-temperature experiments. (a), (b) and (c) FEG SEM images showing mineral and melt distribution in recovered samples. (d) Micro Raman spectra of preserved hydrous silicate glass. In silicate vibration region low-wavenumber bands corresponds to vibrations of the alumino-silicate network (weak olivine peaks at 824 and 856 cm^{-1} overlap the silicate glass spectrum); In H_2O vibration (high-wavenumber) region corresponds to water-stretching vibrations of OH groups and H_2O molecules.

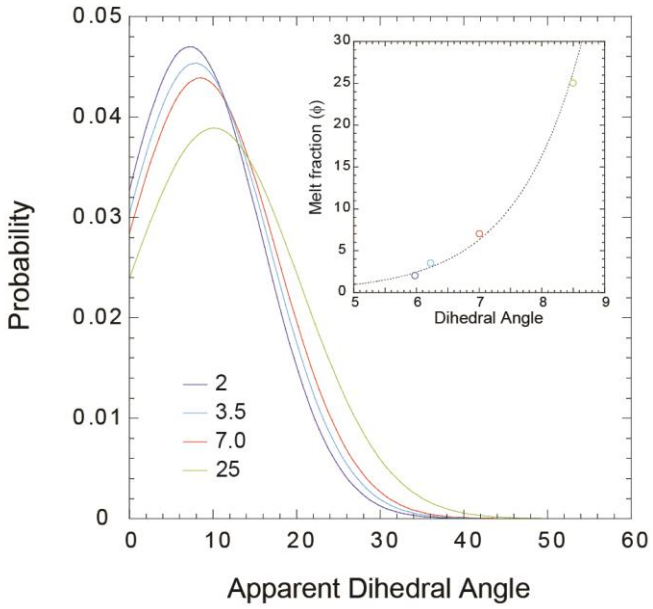

Figure IV.3 Variation of dihedral angle with the melt fraction. The probability curves indicate a slight increase in dihedral angle with increasing melt fraction. The majority of melt occurs as melt-filled grain boundaries. A total of more than 50 measurements were used for the fitting. (Inset) the change of dihedral angle with the melt fraction. The dihedral angle for the 0.7 % melt fraction should be less than 5°.

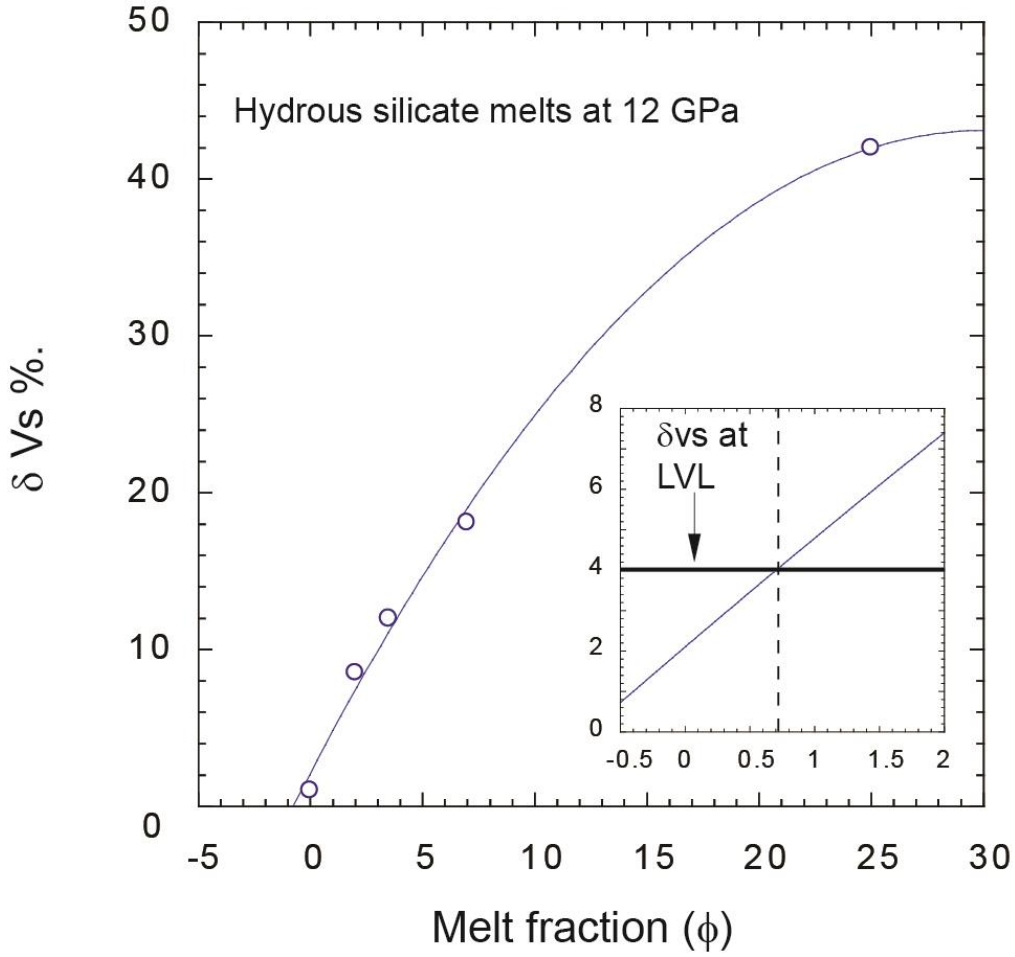

Figure IV.4 % drop in secondary wave velocity as a function of sample melt fraction. The second order polynomial fitting indicates the best fitting line up to 25 % melt fraction. The inset figure indicates the melt fraction required to explain the geophysically observed -4 % ∂Vs, yielding 0.7 % of melt fraction for the LVL above the mantle transition zone.

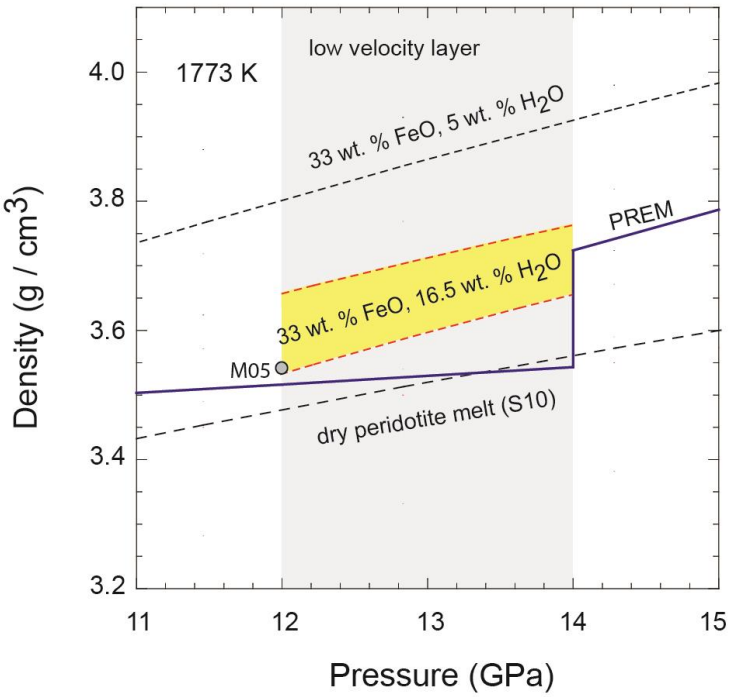

Figure IV.5 Density of hydrous silicate melts occurring at the base of the Earth's upper mantle. The density of hydrous melt is determined by the third order Birch–Murnaghan equation of state (see Methods for details). The yellow shaded ara indicate the possible range of densities obtained for the 0.7 % melt fraction with 33 wt.% FeO and 16.5 wt. % H_2O. The calculated density for melt with 33 wt.% FeO and 5 wt.% H_2O in indicated in black broken line. The experimental data for hydrous rich melt (Matsukage et al., 2005) (M05) and dry peridotite melt (Sakamaki et al., 2010) (S10) are shown for comparison. The mantle densities are taken from PREM (Li et al., 2004) with corrections applied for the thermal expansion.

h) <u>Supplementary materials</u>

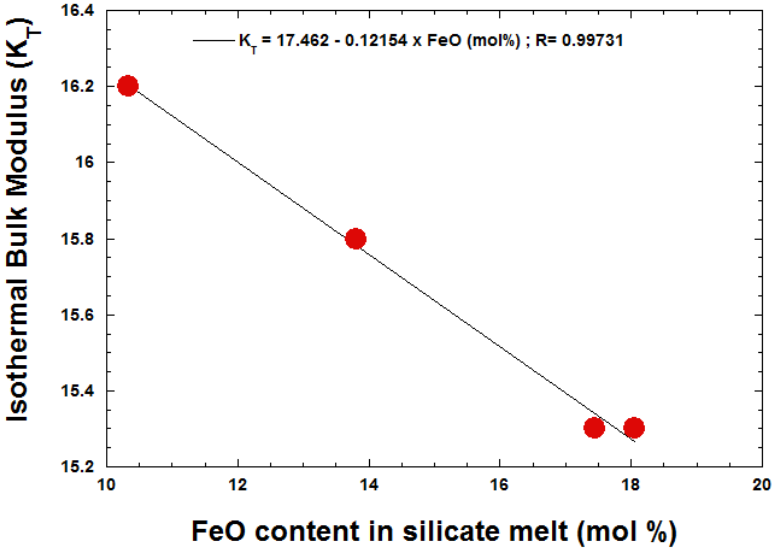

Supplementary Figure IV.S1 Isothermal bulk modulus (K_T) as a function of the FeO content (mol.%).

	Peridotite	2 % melt	7 % melt	25 % melt
SiO_2	44.48	39.74	45.59	45.09
TiO_2	0.16	0.00	0.93	0.52
Al_2O_3	3.59	2.55	10.09	11.20
Cr_2O_3	0.3	0.00	0.00	0.00
FeO	8.1	21.23	11.34	6.48
MnO	0.12	0.00	0.05	0.00
MgO	39.22	2.62	10.69	16.01
CaO	3.44	8.95	16.63	14.75
Na_2O	0.3	0.07	1.52	1.63
K_2O	0.02	0.13	0.16	0.04
H_2O	0.02	12.00	4.20	0.30
Total	**99.75**	**87.30**	**101.22**	**96.01**

Supplementary Table IV.S1 Chemical compositions of the initial peridotite mixture and the resulting hydrous silicate melts.

4) Notes and additional information

Additional data that has not been inserted in published work will be provided and commented in this section. This will help to precise the technical aspects of this work as well as results on textural analyses, acoustic velocities and chemistry of our samples.

a) <u>High pressure experimental assemblies and setup details</u>

Additional information is given in this section on the high pressure assemblies and starting materials. Pictures of the experimental device and similar assemblies are given in the previous chapter III.

For these experiments, synthesis and *in situ* acoustic wave velocities assemblies are given here (Fig. IV.6). The uses of the same assembly to accommodate both electrical conductivity and acoustic wave velocities (as developed for chapter III, results on electrical conductivity in chapter V) required a special adaptation of the EC/SV assemblies developed by our group for these high pressures conditions. The geometry developed on 18/11 configuration was

translated over a 14/8 geometry (synthesis runs assemblies are displayed with 6 and 9 GPa ones in chapter V).

At high pressure, risks of short circuits and electrical conductivity measurement failure dramatically increase. In addition, the position of the transducer imposes a specific geometry for our assembly in the multi-anvil guide block. For these reasons, we paid specific attention to the wire exit of the thermocouple from both the assembly and the cubes. We opted for the fixation of the TC by copper coils every two edges to fix each wire to a different cube (see configuration in figure IV.7). The wires were afterward attached to the cubes, covered by cardboard paper, with Teflon tape to reach the proper exit.

In addition, example of acoustic waves velocities recorded during the experiments and their paths in the high pressure assemblies are given in the figure IV.8.

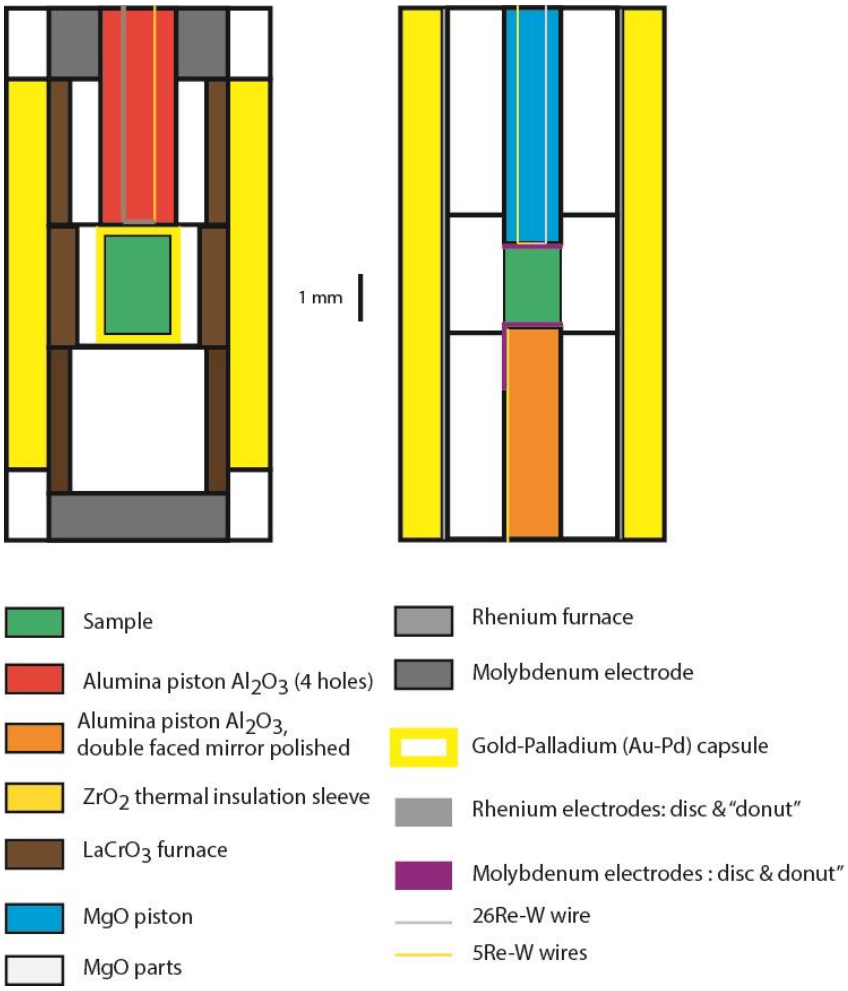

Figure IV.6 Schematic cross sections of the high pressure assemblies used for the synthesis of peridotite samples (left) and acoustic wave velocities measurements (right). For the synthesis of hydrous samples, Re capsule was replaced by sealed Au-Pd capsule.

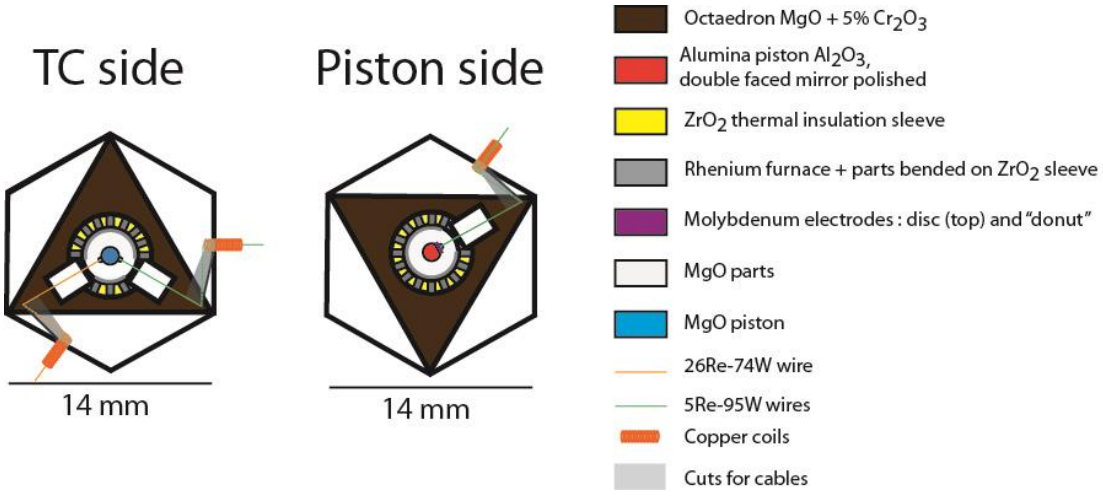

Figure IV.7 Top and bottom view of the octahedron faces highlighting the wires configuration of the assembly.

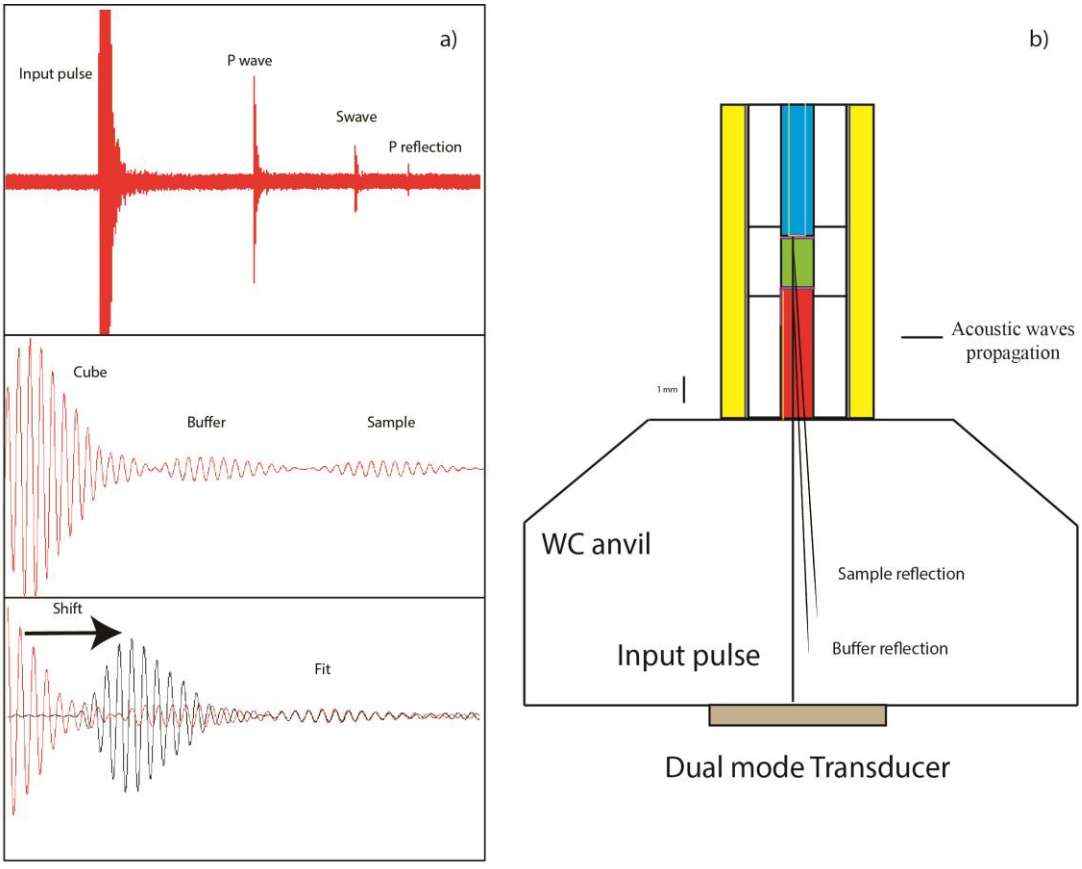

Figure IV.8 a) S and P waves recorded during the experiment. The top image shows the raw signal recorded during the experiment. The intermediate picture displays P wave signal convolved from the raw data above where each part echo can be identified. The bottom image represents the shifted spectra necessary to fit and get the reflection delay between the buffer rod and the sample. b) Schematic of acoustic wave propagation in the experimental configuration for simultaneous measurements of P and S wave velocity through the secondary tungsten carbide (WC) anvil and the assembly.

b) Textural analyses

Micro-textures of our samples have been described in the published work with dihedral angle estimations. Complementary analyses were also realized with a combination of image surface analysis based on SEM chemical maps and back-scattered electron images, with the procedure detailed in our published work (Freitas et al., 2019; see Chapter III).

First, samples texture and aspect were examined with conventional scanning electron microscope (SEM) and Field Emission Gun Scanning Electron Microscope (FEG-SEM) for the characterization of the melt pockets in low melt fraction samples. In addition to melt texture microphotographs given in the paper, representative views of our samples after EC/SV experiments at 12 GPa are shown in appendix B (Figs. B.4, 5 and 6).

From these back-scattered electron images, binary/skeletonized images were made as well as melt fraction determination via surface analysis. These images are binarized with Gimp software using color threshold and hand drawing of grain boundaries and melt pockets. Binary images are given in appendix B (Figs. 7, 8 and 9).

From these binary images, we performed series of textural analyses using FOAMS software and simple methods such as the intercept method to get the average grain size of each sample (appendix B; figs. B.10, 12, 14, 16 and 18) and the aspect of the grains (Figs B.11, 13, 15, 17 and 19). Indeed, our previous work showed crucial importance of texture for the proper interpretation of *in situ* geophysical measurements.

The final results of such analyses are given in the next table IV.1. We can observe that both our samples are homogeneous in term of grain size and phase repartition. The grain size is small showing a log-normal unimodal repartition with a mode around 5 microns for all of our samples. The volume conversion highlights that most of the sample's volume is carried by grains slightly larger, with modes between 5 and 10 microns. The equant texture is confirmed by the orientation histograms, where no significant grain orientation is observed (as for melt). The textural parameters indicate the rounded shape of our grains with low elongation and high regularity. These quantifications confirm our sample and melt texture is homogeneous and might be representative of a natural sample with a given amount of melt.

Table IV.1: Textural parameters and modal proportions of experiments at 12 GPa. Each sample texture is quantified using image analysis and FOAMS software (Shea et al., 2010) on BSE microphotographs and chemical maps, for detailed methods description (Freitas et al., 2019). % refers to the modal proportion. EqDi corresponds to each phase equivalent diameter (circle of equivalent area) which is for rounded grains a good estimation grain size. Area perimeter long and short axis describes grain aspects (all of these are in mm). Orientation quantify the angle of long axis with vertical direction (sample cylinder axis). Eccentricity, elongation, aspect ratio and regularity are textural parameters that quantify the geometrical aspects of each phase. N is the number of grains analyzed (on 2-5 images). Avg Gs to the average grain size of the sample obtained by intercept method. On some samples BSE contrast was not good enough to separate Cpx and garnets, they have been treated together in these cases. Each averaged data is followed by the associated standard deviation.

M412 - 12 GPa (7.00±1.77%)													
Olivine	%	EqDi	Area	Perimeter	Long-axis	Short-axis	Orientation	eccentricity	elongation	aspect ratio	regularity	N	AVG GS
AVG	66.15	0.010354	0.000124	0.039304	0.014673	0.008367	92.79	0.78	0.28	0.59	0.90	679	10.20
STD	1.77	0.007159	0.000197	0.028696	0.010161	0.006013	55.25	0.15	0.14	0.17	0.08		0.51
CPX+GT		EqDi	Area	Perimeter	Long-axis	Short-axis	Orientation	eccentricity	elongation	aspect ratio	regularity	N	
AVG	15.11	0.008359	7.32E-05	0.030256	0.011377	0.006922	85.48	0.75	0.24	0.62	0.91	266	
STD	1.77	0.004836	9.21E-05	0.019929	0.006912	0.004207	57.43	0.15	0.13	0.17	0.07		
Melt		EqDi	Area	Perimeter	Long-axis	Short-axis	Orientation	eccentricity	elongation	aspect ratio	regularity	N	
AVG	7.00	0.00655	4.69E-05	0.034366	0.013192	0.005516	91.57	0.85	0.38	0.47	0.77	317	
STD	0.27	0.004108	6.75E-05	0.040128	0.012627	0.005241	51.64	0.13	0.18	0.19	0.18		
M425 12 GPa (2.00±0.45%)													
Olivine	%	EqDi	Area	Perimeter	Long-axis	Short-axis	Orientation	eccentricity	elongation	aspect ratio	regularity	N	AVG GS
AVG	61.52	0.004009	1.59E-05	0.01508	0.005336	0.003378	82.53	0.73	0.22	0.65	0.91	936	3.77
STD	3.98	0.002047	1.61E-05	0.008556	0.00281	0.001822	46.44	0.15	0.12	0.16	0.07		0.50
GT		EqDi	Area	Perimeter	Long-axis	Short-axis	Orientation	eccentricity	elongation	aspect ratio	regularity	N	
AVG	16.92	0.002147	4.31E-06	0.008107	0.002983	0.001746	96.87	0.75	0.25	0.62	0.92	775	
STD	1.99	0.000944	4.15E-06	0.004187	0.001531	0.000803	50.53	0.17	0.15	0.18	0.06		

CPX		EqDi	Area	Perimeter	Long-axis	Short-axis	Orientation	eccentricity	elongation	aspect ratio	regularity	N	
AVG	19.56	0.003007	8.35E-06	0.010718	0.003798	0.002547	97.53	0.70	0.21	0.67	0.95	753	
STD	1.99	0.001272	6.71E-06	0.004816	0.001584	0.001186	50.00	0.16	0.12	0.16	0.04		
M456 12 GPa (3.5±2.44%)													
Olivine	%	EqDi	Area	Perimeter	Long-axis	Short-axis	Orientation	eccentricity	elongation	aspect ratio	regularity	N	AVG GS
AVG	66.70	0.003152	1.02E-05	0.012102	0.004116	0.002675	87.81	0.72	0.22	0.66	0.92	568	3.16
STD	4.27	0.001747	1.09E-05	0.007335	0.002297	0.001569	47.72	0.16	0.12	0.16	0.06		0.44
CPX + GT	%	EqDi	Area	Perimeter	Long-axis	Short-axis	Orientation	eccentricity	elongation	aspect ratio	regularity	N	
AVG	29.80	0.001387	2.21E-06	0.004853	0.001798	0.001162	86.65	0.71	0.21	0.67	0.94	1078	
STD	4.27	0.000947	4.34E-06	0.00367	0.001301	0.000794	48.51	0.15	0.12	0.16	0.05		
M490 12 GPa (25.65±2.50%)													
Olivine	%	EqDi	Area	Perimeter	Long-axis	Short-axis	Orientation	eccentricity	elongation	aspect ratio	regularity	N	AVG GS
AVG	64.01	0.006815	4.81E-05	0.025912	0.009555	0.005489	93.21	0.78	0.27	0.59	0.91	408	6.87
STD	3.99	0.003853	5.77E-05	0.015635	0.005471	0.003343	48.94	0.15	0.14	0.17	0.06		0.33
CPX + GT		EqDi	Area	Perimeter	Long-axis	Short-axis	Orientation	eccentricity	elongation	aspect ratio	regularity	N	
AVG	10.34	0.005979	3.77E-05	0.023298	0.008767	0.004746	96.97	0.79	0.30	0.56	0.89	87	
STD	2.86	0.003514	5.25E-05	0.014534	0.005162	0.003029	55.47	0.15	0.15	0.18	0.09		
Melt		EqDi	Area	Perimeter	Long-axis	Short-axis	Orientation	eccentricity	elongation	aspect ratio	regularity	N	
AVG	25.65	0.007206	9.31E-05	0.048496	0.013549	0.006416	80.34	0.84	0.35	0.50	0.79	70	
STD	2.50	0.008222	0.000237	0.096567	0.018722	0.008817	54.10	0.11	0.15	0.16	0.16		
M492 12 GPa (0.00%)													

Olivine	%	EqDi	Area	Perimeter	Long-axis	Short-axis	Orientation	eccentricity	elongation	aspect ratio	regularity	N	AVG GS
AVG	72.19	0.003613	1.31E-05	0.012945	0.004926	0.002953	88.50	0.76	0.25	0.61	0.91	2046	4.29
STD	3.49	0.001908	1.61E-05	0.007331	0.002608	0.001652	51.33	0.15	0.13	0.17	0.06		0.50
CPX + GT		EqDi	Area	Perimeter	Long-axis	Short-axis	Orientation	eccentricity	elongation	aspect ratio	regularity	N	
AVG	27.81	0.003748	1.53E-05	0.013926	0.005245	0.003037	87.30	0.77	0.27	0.60	0.90	639	
STD	3.49	0.002321	2.57E-05	0.009394	0.003264	0.001995	48.22	0.15	0.14	0.17	0.07		
M421 12 GPa (0.00%)													
Olivine	%	EqDi	Area	Perimeter	Long-axis	Short-axis	Orientation	eccentricity	elongation	aspect ratio	regularity	N	AVG GS
AVG	61.48	0.004185	2.3E-05	0.016287	0.005968	0.003363	98.87	0.79	0.29	0.57	0.90	1208	5.21
STD	1.44	0.00343	4.75E-05	0.014316	0.004613	0.003005	46.84	0.14	0.15	0.18	0.07		0.53
CPX + GT	%	EqDi	Area	Perimeter	Long-axis	Short-axis	Orientation	eccentricity	elongation	aspect ratio	regularity	N	
AVG	38.52	0.003665	1.42E-05	0.013389	0.005023	0.002974	97.11	0.76	0.26	0.61	0.92	1372	
STD	1.44	0.002144	1.86E-05	0.008591	0.00299	0.001827	48.93	0.15	0.13	0.16	0.06		

c) Chemical analyses

A detailed analysis on the chemistry of solid and melt phases, measured on the recovered experimental runs after *in situ* geophysical measurements at 12 GPa, will be given together with 6 and 9 GPa additional experiments performed in the next chapter V. A part of this data such as major element proportion on each phase was also published in Freitas and Manthilake (2019) (Chapter V).

d) Erratum

A slight mistake has been made in the published work on figure IV.4. Indeed, in the figure used in the Nat.Com paper, the fit of ∂Vs versus melt fraction is not passing by origin point which must be used as an anchor point. This point has been corrected in the updated version here (figure IV.9), with only minor changes on inferred melt fractions considering the error bar of 5% on ∂Vs values.

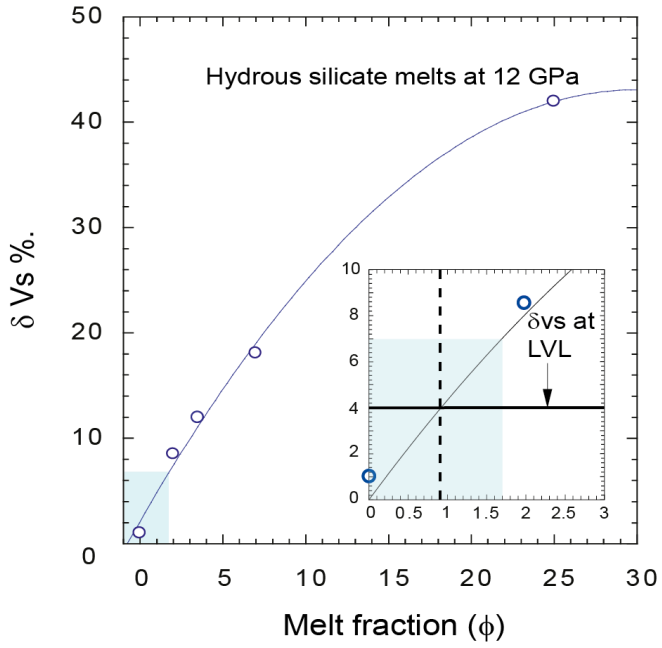

Figure IV.9 The % drop in secondary wave velocity as a function of sample melt fraction. The second order polynomial fitting indicates the best fitting line up to 25 % melt fraction considering the anchor point at (0;0). The inset figure indicates the melt fraction required to explain the geophysically observed -4% ∂Vs, yielding 0.9 % of melt fraction for the LVL above the mantle transition zone.

5) Summary

This work aimed to realize the first experimental reproduction of dehydration melting process suggested by models such as the Transition Zone Water Filter (Bercovici and Karato, 2003). In such models, mantle transition zone material is passively upwelling across the 410 km discontinuity. This limit represents the P-T conditions for the main mineral transformation from wadsleyite to olivine. If MTZ materials water content is higher than olivine solubility, partial melting should occur via the release of a significant amount of free fluids. This passive ascension is difficult to reproduce in a single experiment, however it can be approximated into the realization of two successive experiments to first synthesize the wadsleyite bearing peridotite and then, in a second, run in olivine stability field, undergo partial melting thanks to the phase transition.

Using a modified setup for *in situ* electrical conductivity and acoustic wave velocity developed in the precedent chapter, the geophysical properties of the system were measured during phase transformation and dehydration induced melting. This first characterization on realistic system (chemical, volatile contents, etc.) and pressure and temperature conditions are of significant interest to interpret seismological information at the LVL depths. The commonly observed *Vs* decrease of few percent (4 - 9%) can be explained invoking realistic small fraction of melt (< 2%).

Such melt chemistry was quantified by EMP, FEG-SEM and micro-raman analyzes. Despite very important difficulties to perform these measurements (it mostly hold on few points and luck) and the consideration of all uncertainties behind, we found that these low degrees partial melts are very different from classical low pressure melts such as MORB or alkalis basalts. These “first juices” melts are much enriched in incompatibles elements in particular water and iron and depleted in magnesium. This observation matches pretty well with recent observations of carbonates and fluids rich melt at really low melt fraction at intermediate pressures from natural peridotites (Gardès et al., in review). The density of extrapolated melt compositions for realistic melt fractions (<< 1%), was found to be denser than surrounding mantle favoring a melt layer trapped at the base of the upper mantle.

The variations of the magnitude of the sound velocity drop observed at LVL depths should then reflect the intensity of melting, its lateral movements or the compositional variations of MTZ source mantle. In particular, variation of water contents in the mantle

transition zone would imply large variation of melt fractions and melt densities favoring the creation of upper mantle plumes in the more volatile-rich cases.

6) Perspectives

This study is the first reproduction of a complex melting process and its geophysical characterization at important pressures. Thus, implications and perspectives of this works are plural. In this section we propose a series of perspectives and future works that can be performed:

a) Treatment of electrical conductivity signals on the experiments and their implications

In the experiments presented in this chapter, electrical conductivity was used to detect the melting point and stop the temperature increase during the experiment to keep small melt fractions and have a good coverage of realistic melt fraction range that are possible in the geological cases. Indeed sound wave velocity does not offer the possibility to live monitor the onset of melting and require significant treatment that prevents the real time following of sample state (see chapter III). However, the electrical conductivity signal was measured during the experiments and its comparison with magnetotelluric signals is of significant interest. One of the great interests of such geophysical signal is also its sensitivity to volatile content which would be of a crucial importance to decipher water repartition in the uppermost mantle and understand its dynamics. This work will be detailed in the next chapter V.

b) Accurate chemical characterization and high resolution 3D imaging

The main challenge of our experiments characterization remained to have a reliable chemical analysis of the melt. Because of their size or their fragility (during polishing or sensibility to Raman laser beam), it is very difficult to have good analyses without significant contamination of surrounding materials, presence of quench crystals and difficulty to analyze such small pockets. Similarly texture and melt fraction quantification heavily depends on 2D plans made during the polishing. This 2D information coupled with very wetting low melt fractions reduces significantly the available number of pockets/tubules or films and results in larger uncertainties on melt fraction and textural parameters such as dihedral angles.

For chemistry, we tried various setups and machines available at the University Clermont Auvergne. However, the size of the melt pockets is particularly small and successful analyses were only obtained on the largest pockets found (> 2 microns).

The recent development of FIB-SEM to perform 3D analysis by the realization and imaging of thin slices in the sample by E. Gardès in CIMAP/GANIL in Niort, France is extremely promising. The system was in fact already used on natural peridotite partial melts at lower pressure by Gardès et al. (Submitted) and gave nice 3D maps of melt distribution. Melt chemical analysis was performed via a FIB separation of the melt pocket from the matrix for a better analytical precision. Contacts were taken with E. Gardès but for time reasons and funding, such analyses were not performed during this PhD. However, it represents a very strong perspective to such works and open many possibilities to the submicron level (very low melt fraction, near 0 °dihedral angle melts, improved chemistry etc.).

The 3D analysis can also be carried out during synchrotron experiments. This would imply larger melt fraction but with appropriate markers, melt distribution and chemical composition estimation can be live monitored via X-rays imaging/tomography and X-ray diffraction. Such 3D tomographic device is now available in SOLEIL synchrotron at PSICHE beamline. The recent work of Boulard et al. (2018) after numerous efforts in the technical development is also very promising inspiration for such analyses.

c) <u>What about Carbon?</u>

A special interest is given to water (hydrogen) in this study and next chapter. However, we performed our experiments in carbon free (as much as possible) environment. However, in natural cases some carbon must be present in the materials. Even if the amount of carbon present in the mantle transition zone and its maximum solubility in high pressure polymorphs is still discussed, its presence might strongly influence the chemistry of partial melts at very low fusion rate.

Thus, it would be of great interest to perform experiments with carbon in controlled quantity and realize chemical analyses of melts at low melt fraction to see the dominance/miscibility of carbonatites or silicate melts together with the presence of fluids. The effect of such melt on geophysical properties is currently unknown at these pressures and would be a very difficult but interesting study.

d) <u>Toward very high pressures?</u>

In addition to the observed seismic anomalies above the 410 km discontinuity, several other seismic features have been detected at higher pressures. Indeed, strong anomalies have been detected along the 660 km discontinuity and dehydration induced partial melting was

also proposed as a possible explanation (Schmandt et al., 2014). Similarly, the zone at 520 km seems to have also unpredicted characteristics in particular showing strong velocity gradients near this discontinuity (Shearer et al., 1996).

The only few experimental studies performed at this pressure were made with diamond anvil apparatus, which implies large limitations for the interpretation of seismic velocities measurements such as large thermal gradients, small samples, heterogeneous presence of melt due to laser heating, etc. The translation of our experimental technique and devices into very high pressure experiments would be difficult but possible using the state of art apparatus and analytical techniques such as synchrotron radiation. They will provide a better quantification of the effect of partial melting onto the geophysical signals, as well as possible quantification of implied melt fraction and advanced chemical analyses. Such a project is under evaluation for a JSPS postdoctoral fellow with GRC laboratory at Ehime University

.

Chapter V

Dehydration melting at the 410-km discontinuity and the bottom-up hydration of Earth's upper mantle

Chapter V Dehydration melting at the 410-km discontinuity and the bottom up hydration of Earth's upper mantle

1) General introduction

The detection and the confirmation of regions of partial melting in the Earth's mantle is, in most of the cases, directly linked to the presence of volatiles into the Earth's interior (Daguspta and Hirschmann, 2006; Plank and Langmuir, 1992; Sifré et al., 2014). The recent studies focused on the mantle transition zone and the associated low velocity layer located atop, pointed out the crucial role of water into the generation of the melt layer and the control of its physical and chemical properties (Bercovici and Karato, 2003; Freitas et al., 2017). The dehydration melting process was shown to occur when mantle transition zone material upwells passively in response to slab injection into deep mantle. If the water content of this wadsleyite bearing material exceeds the olivine water storage capacity, the free fluids released during the upwelling and associate phase transition could help the mantle rock to undergo partial melting. This melting scenario heavily depends on the water content of the MTZ materials as well as its importance for the melt layer repartition. According to the original theory of the transition zone water filter model (Bercovici and Karato, 2003; Karato et al., 2006; Leahy et al., 2010), the presence of the melt layer would have great implications into the Earth's mantle differentiation by melting as well as numerous incompatible elements storage such as volatiles. The water circulation at the planetary scale, should then be reconsidered for its deep, long term cycle.

The confirmation of the presence of partial melts based on *in situ* sound wave velocities and their comparisons to seismic observations made by our previous study (Freitas et al., 2017, Chapter IV) highlighted the major role of water into this melting region above the MTZ. We pointed out that only small amount of partial melt (< 3%) can explain the observed geophysical anomalies and that this melts are very enriched in incompatible elements and water. Such high melt water content (up to 16.5% for realistic melt fraction < 1%) and enriched compositions was not really considered in previous work, suggesting more basaltic composition due to larger melt fractions. However, the modality of melting remains poorly constrained and the melt characteristics and its effect on electrical conduction would imply an important positive anomaly. This anomaly has been thought but not directly observed yet, mostly due to important difficulties to obtain resolved geomagnetic data at these depths. Forward models and regional inversion have been made by Toffelmier et al. (2007) based on

electrical properties of basaltic melts. This work is the first study to propose electrical conductivity profiles with consideration of this Low Velocity Layer (LVL). However, our recent work has shown that our melt are significantly different and so the magnitude of their effect on electrical conduction for a binary melt/solid system at high pressure and temperature is currently unknown.

In this chapter, we investigate the electrical properties of partially molten peridotites at relevant conditions of the upper mantle up to its base. Indeed, the electromagnetic profiles provide important information on the physical state of the mantle and are (at the opposite of acoustic wave velocities) heavily depending on the volatile content of the rock. In addition to experiments performed at 12 GPa, in which electrical conductivity and acoustic waves velocities were measured (chapter IV), additional analyses and experiments at 6 and 9 GPa have been carried out in order to precise these profiles. Based on the major interpretation of melt free but hydrous under-saturated conditions in the main part of the upper mantle (180-350 km), we derived several models to better constrain the fate of water in this "410" partial melt layer and its integration in a mantle scale water circulation model. Our conclusions are reported in a paper published in Earth and Planetary Sciences Letters. Our results suggest a possible hydration of the upper mantle by partial melting at the LVL and a bottom up process. In this bottom up process, a contribution from both diffusion and passive upwelling terms are expected. Our calculations showed that diffusion cannot be achieved over upper mantle temporal and spatial scales and that upwelling would initiate residual peridotite (and so water) transport progressively filling the whole upper mantle. The melting residues can have relatively various water content given the olivine melt partition coefficient and mainly depends on the initial MTZ water content. In case of moderately hydrated MTZ (< 1500ppm H_2O) residual peridotites with moderate water content can be obtained (200 ppm).

2) Résumé

La remontée passive du matériel issu de la zone de transition mantellique induit une fusion par déshydratation au-dessus de la discontinuité à 410 km. Dans cette étude nous avons mesuré la conductivité électrique de systèmes partiellement fondus hydratés, dans une gamme de pression correspondant à des profondeurs entre 200 et 400 km, et exploré si cette fusion partielle peut être le processus d'hydratation du manteau supérieur. Nos données électriques démontrent que le manteau supérieur entre 180-350 km est majoritairement solide (non fondu) confirmant également la présence de conditions hydratées inférieures à la saturation.

La fusion partielle d'un manteau remontant, depuis la zone de transition avec un contenu en eau inférieur à 1500 ppm, produit des péridotites résiduelles avec des teneurs en eau de l'ordre de 200 ppm. Cette remontée de matériel vient progressivement remplir et remplacer les roches du manteau supérieur par ces péridotites résiduelles modérément riches en eau en moins de 260 Ma. Dans cette étude, nous proposons un processus d'hydratation par la base du manteau supérieur engendré par la fusion par déshydratation à la discontinuité située à 410 km de profondeur. La fusion partielle hydratée reportée à la base de l'asthénosphère est alors une conséquence directe de la saturation en eau des péridotites résiduelles lors de leur remontée.

3) Bottom up hydration of Earth's upper mantle

Article accepted at EPSL, the 13/07/2019.

Electrical conductivity of hydrous silicate melts: Implications for the bottom-up hydration of Earth's upper mantle

---

D.Freitas[1*], G. Manthilake[1]
[1]Université Clermont Auvergne, CNRS, IRD, OPGC, Laboratoire Magmas et Volcans,
F-63000 Clermont-Ferrand, France
([*]corresponding author: damien.freitas@uca.fr)

a) Abstract

The upwelling of the hydrous mantle transition zone triggers dehydration-induced partial melting atop the 410-km discontinuity. Here we investigate the electrical conductivity of hydrous silicate melts in the 200 - 400 km depth range and explore whether melting at the 410-km depths is responsible for the hydration of the upper mantle. Our experimental electrical conductivity data demonstrate that the mantle at 180 - 350 km depth is mostly melt free, confirming the H_2O under-saturated conditions. However, residual mantle from partial melting atop the 410 km may contain various possible amounts of water according to the initial mantle transition zone and melt concentrations. This residual H_2O could contribute to the hydration of the upper mantle either through diffusion or material replacement by upwelling. Our calculations suggest that the diffusion may not be responsible for the hydration of the upper mantle to present H_2O concentration of 50 – 200 ppm wt. Melting of the upwelling mantle transition zone with less than 1500 ppm wt. H_2O produces residual peridotites with ~ 200 ppm H_2O at the 410-km discontinuity. Continuous upwelling of such hydrous residues would gradually replace the dry upper mantle with depleted residual hydrous peridotites in less than 260 Ma. In this study, we propose a bottom-up hydration mechanism for the Earth's upper mantle driven by dehydration-melting at the 410-km discontinuity. The hydrous partial melting at the top of the asthenosphere appears to be a consequence of H_2O saturation in the upwelling residual peridotites.

Keywords: electrical conductivity, water storage capacity, hydrous melt, upper mantle, mantle upwelling, mantle transition zone

b) Introduction

The average H_2O content of the Earth's upper mantle is determined to be about 50-200 ppm wt. (Hirschmann, 2006; Michael, 1988; Saal et al., 2002; Simons et al., 2002). These estimates are significantly lower than the H_2O storage capacity of peridotite mineral assemblages (Ardia et al., 2012; Demouchy and Bolfan-Casanova, 2016; Férot and Bolfan-Casanova, 2012), indicating water undersaturated conditions for the Earth's upper mantle. The origin of H_2O in the upper mantle is still a subject of debate. However, two possible scenarios have been proposed. In the first hypothesis, the H_2O in the upper mantle has been attributed to hydrous residues left behind following partial melting in the upper mantle. In the second scenario, H_2O in the upper mantle can be derived from the mixing of dry upper mantle with a hydrous primitive source (Hirschmann, 2006).

At present, three distinct partial melting regimes, that could explain the origin of H_2O in the upper mantle have been proposed; dehydration melting at the 410-km discontinuity (Bercovici and Karato, 2003), melting in mantle wedges (Hirth and Kohlstedt, 1995) and partial melting of mantle plumes (Morgan and Morgan, 1999), all arguing that the residues left behind by the melting events could be responsible for H_2O contents in the upper mantle. While the depleted signature of mid oceanic ridge basalt (MORB)-source upper mantle strongly favors the partial melting hypotheses, the exact nature of the melting regime that led to the hydration of the upper mantle, consistent with geochemical, geophysical and geodynamic observations, remains poorly constrained (Hirschmann, 2006).

A recent study based on *in situ* sound velocity measurements confirmed the dehydration induced melting in the upwelling mantle across the 410-km discontinuity (Freitas et al., 2017). Geophysical observations of high electrical conductivity (up to 1 S/m) (Toffelmier and Tyburczy, 2007) and reduced seismic wave velocities (δVs 4 - 9%) (Revenaugh and Sipkin, 1994; Tauzin et al., 2010) suggest a 50-60 km thick melt layer above the Mantle Transition Zone (MTZ) (Revenaugh and Sipkin, 1994; Song et al., 2004; Tauzin et al., 2013, 2010; Vinnik and Farra, 2007). The upwelling of hydrous MTZ with ~ 0.1 - 0.2 wt.% of H_2O (Freitas et al., 2017; Huang et al., 2005; Karato, 2011) and the significant differences in H_2O storage capacities between the MTZ (Bolfan-Casanova et al., 2000; Hirschmann et al., 2005; Kohlstedt et al., 1996) and the overlying mantle (Demouchy and Bolfan-Casanova, 2016; Férot and Bolfan-Casanova, 2012) is the governing factor that triggers melting in the upwelling mantle across the MTZ (Bercovici and Karato, 2003; Freitas et al., 2017). The reported 3.6 - 9.4 % shear wave velocity drop is compatible with a 0.5 - 2.5 % melt fraction (Freitas et al., 2017) in the partial melt layer.

The melt produced at the 410-km discontinuity is found to contain high H_2O contents (Freitas et al., 2017; Matsukage et al., 2005). The mineral-melt equilibrium following melting at the top of the MTZ causes H_2O to diffuse from the hydrous melt into solid mineral phases both above and below the melt layer. The H_2O diffusion may occur between melt and wadsleyite, transferring H_2O back into the underlying MTZ and between melt-olivine/pyroxene/garnet, hydrating the overlying mantle. In addition to the diffusion process, the mantle upwells passively away from subduction zones in response to intrusion of slab material into Earth's interior (Bercovici and Karato, 2003; Karato et al., 2006). The mantle upwelling is significantly faster than H_2O diffusion into mantle minerals (Bercovici and Karato, 2003), replacing the dry upper mantle with residual peridotites. The dehydration melting in the upwelling mantle and subsequent H_2O transport mechanisms therefore play a crucial role in water transfer between the upper mantle and the mantle transition zone (Bercovici and Karato, 2003).

Laboratory measurements of electrical conductivity have been extremely useful in characterizing the material circulation in the Earth's mantle (Dai and Karato, 2009; Yoshino, 2010). The laboratory measurements suggest electrical conductivity is a powerful tool for detecting melt or fluid and their occurrence within the solid mineral matrix at deep mantle conditions (Freitas et al., 2019; Grotenhuis et al., 2005; Manthilake et al., 2016, 2015; Maumus et al., 2005). It is also sensitive to the chemical composition of melt, particularly to volatiles (Gaillard et al., 2008; Karato, 1990; Manthilake et al., 2009; Yoshino, 2010) and alkalis (Ni et al., 2011). In this study, we measure the electrical conductivity of hydrous peridotite at various pressures up to 12 GPa above their melting temperatures. The results were compared with magnetotelluric profiles to gain insight into the extent of melting and melt percolation if hydrous conditions are assumed for the Earth's upper mantle. Based on our results, we discuss different

scenarios that could be responsible for the H_2O circulation in the upper mantle.

c) Materials and Methods

i) Starting materials

Starting materials with a composition similar to KLB-1 peridotite (Wang and Takahashi, 2000) were prepared using reagent grade oxides, initially mixed in the absence of the required amount of $Al(OH)_3$ to yield the correct mineral composition (ranging from 1.63 to 4.86 mg to obtain 500 mg of peridotite powder with 400 to 1500 ppm H_2O, respectively). These powders were dried at 300 °C overnight to remove any adsorbed moisture. Na and K were added as $NaCO_3$ and K_2CO_3 and then de-carbonated. The decarbonation of the oxide mixtures was carried out by slowly increasing the temperature to 1000°C (1.6°C/min) and keeping it at 1000°C for about 10 hours to ensure complete decarbonation. The decarbonated powder mixture was then cooled to 200°C and stored in a high vacuum furnace at 120°C prior to the hot pressing runs. The required amount of $Al(OH)_3$ was then mixed with the decarbonated powder mixture to obtain the desired amount of H_2O in peridotite samples.

Samples with ~0, 500, 700 and 1200 ppm wt. H_2O as initial content in powders were prepared in order to have hydrous under saturated conditions at the different targeted pressures. As water solubility increases with pressure in nominally hydrous phases (Ardia et al., 2012; Férot and Bolfan-Casanova, 2012), we always used initial water content under solubility limit at each pressure. However, due to the absorbed moisture in the high pressure synthesis assembly, the water content may be subjected to some possible water (H) diffusion into the samples even with sealed capsules. The X-Rays powder diffraction analyses using a Philips PW 1830 (Cobalt wave-length) and micro-Raman analyses were carried out prior to the electrical conductivity measurements to ensure the absence of additional hydrous phases such as super hydrous Phase-B and partial melts in pre-sintered samples.

ii) Experimental

The resulting powder mixtures were hot pressed to obtain solid sintered samples for electrical conductivity measurements. Hydrous and dry samples were synthesized at different pressures and temperature conditions in a first high pressure run with multi-anvil apparatus, these samples were recovered for *in situ* measurements that were performed in a second multi-anvil run. The details on samples conditions (pressure, temperature and time at temperature) are given in the table V.S1. Dry samples were synthesized at target or lower pressures to ensure low water solubility of the material (Ferot and Bolfan, 2012; Kohlstedt et al., 1996). Hydrous samples were synthesized at target pressure (for 6 and 9 GPa) and 14 GPa. The synthesis of hydrous samples at 14 GPa performing in situ experiments at 12 GPa allows us to simulate the dehydration induced melting at the 410-km discontinuity (Freitas et al., 2017).

Dry samples and hydrous samples were synthetized for ~2 hours in Gold-Palladium (Au-Pd) capsules and temperatures between 1373 and 1573 K (table V.S1). These under saturated conditions are required during the synthesis process, in order to avoid hydrous silicate melts along grain boundaries, which could otherwise interfere with the electrical conductivity. Cylindrical core samples ~1.0 mm in length and ~1.2 mm in diameter were prepared from these pre-synthesized sample specimens.

The high-pressure and high-temperature experiments were performed using a 1500-ton Kawai-type multi-anvil apparatus at the Laboratoire Magmas et Volcans, Clermont-Ferrand, France. Both sample synthesis and the *in situ* measurements were performed in multi-anvil apparatus using an octahedral pressure medium composed of MgO and Cr_2O_3 in a 14/8 multi-anvil configuration (octahedron edge length / anvil truncation edge length) for experiments at 12 GPa and 18/11 for experiments at 6 and 9 GPa (Supplementary Figure V.S1). The pre-synthesized cylindrical sample was inserted into a MgO sleeve. The sleeve also helps insulate the sample electrically from the furnace. This furnace, composed of a 25 µm thick cylindrical Re foil, has apertures for the electrode and the thermocouple wires. A zirconia sleeve around the furnace was used as a thermal insulator. Thermal gradient was also taken in to account for the design of these experiments (Hernlund et al., 2006), and were estimated to be negligible < 5° with our sample dimensions (Supplementary Figure V.S2). We placed two electrodes, made of Mo discs, at the top and bottom of the cylindrical sample. A tungsten-rhenium ($W_{95}Re_5$ - $W_{74}Re_{26}$) thermocouple junction was placed at one end of the sample to monitor the temperature. The opposite end was connected to a single $W_{95}Re_5$ wire. We collected impedance spectra between the two $W_{95}Re_5$ wires. All

ceramic parts of the cell assembly, including the pressure medium, were fired at 1373 K prior to their assemblage in order to remove any adsorbed moisture, and kept in vacuum furnaces (10^{-2} Torr and 150°C) before assembling the experiment. Oxygen fugacity of the sample was not controlled during *in situ* measurements, but was expected to remain below the Mo-Mo_2 buffer.

EC measurements were performed using the ModuLab MTS Impedance/Gain-phase analyzer in the frequency range of 10^1 - 10^6 Hz. Polyphasic samples are characterized by a combination of resistor-capacitor/constant phase element (R-C/CPE) circuits and the resistance can be obtained by fitting the impedance spectra to appropriate equivalent circuits (Supplementary Figure V.S3). Once the sample resistance has been determined, conductivity can be calculated using the sample diameter and length. The experimental procedure for electrical conductivity measurements is discussed elsewhere (Manthilake et al., 2016, 2015). Importance of a moisture removal procedure is crucial in these experiments and is detailed in Supplementary Figure V.S3.

iii) Chemical and microstructural analyses

The chemical composition and micro-textures of pre-sintered samples and experimental run products after electrical conductivity measurements were investigated using a Cameca SX100 electron probe micro analyzer and a Scanning Electron Microscope (SEM) JEOL Jeol JSM-5910 LV, respectively, at the Laboratoire Magmas et Volcans of Clermont-Ferrand. Energy-dispersive X-ray spectroscopy (EDS) chemical mapping was used to determine the mineral proportions and chemical compositions by selecting a large area of each phase. The fine melt micro-textures were observed using a ZEISS supra 55VP field emission gun (FEG) SEM at 2MATech, Aubière, France. Major element compositions of solid phases are given in Supplementary Tables V.S2 and V.S3.

The presence of water (OH) in the crystalline phases of our peridotite samples was qualitatively analyzed both before and after electrical conductivity measurements. These analyzes were performed with micro-Raman spectroscopy (Freitas et al., 2017) (Supplementary Figures V.S4 - S6). Raman spectra were collected using an InVia confocal Raman micro spectrometer, equipped with a 532 nm diode laser (output power of ~140 mW), a Peltier-cooled CCD detector, a motorized XY stage and a Leica DM 2500 M optical microscope, at the Laboratoire Magmas et Volcans, Clermont-Ferrand. The Raman spectroscopy technique was preferred over FTIR analysis mainly due to its capacity to analyze both OH and Si bonds in a non-destructive manner and its high spatial resolution allowing the analysis of small objects (~1 μm). However, due to the unavailability of H_2O calibration curves for pyroxene and garnet, we were not able to perform a complete estimate of the bulk H_2O contents of our samples (qualitative analysis only).

d) Results

The melting of hydrous peridotite can be detected by a sudden or discontinuous increase in electrical conductivity at high temperature (Fig. V.1). The electrical conductivity of partially molten peridotites varies from 0.1 -1 S/m. The activation enthalpies of hydrous peridotites before melting indicate the conduction mechanism is characteristic of electron hopping (small polaron conduction) (Katsura et al., 2009).

The high resolution image analyses of samples after electrical conductivity measurements indicate the presence of melt in hydrous samples (Fig. V.2). The experimental run products indicate well developed polygonal textures with average grain size of < 30 μm. The melt distribution appears to be homogeneous throughout the samples and occurs as thin films along grains boundaries and as small pockets of a few hundred nanometers in size at triple junctions (Fig. V.2 b, c, d). The melt forms an interconnected network showing a very low dihedral angle with complete wetting of the grain boundaries (Freitas et al., 2017) (Fig V.3).

Due to the extremely small size of the melt pockets (< 1 μm), we were not able to measure the chemical composition of the resulting hydrous silicate melt at 6 and 9 GPa. The melt fraction appears to be low (up to a few %). The chemical analyses of melt at 12 GPa indicate significant enrichment in incompatible elements (Ca, Al, Na, K, Fe, Ti) (Freitas et al., 2017).

Samples synthesized prior to electrical conductivity measurements were melt-free (confirmed by X-ray powder diffraction/micro-Raman) and their mineralogy was mainly composed of olivine, clinopyroxene and garnet (Fig. V.2a). No evidence of hydrous phases such as super-hydrous B were found

in the starting materials. The proportions of the different crystalline phases vary between the samples depending on the degree of melting. The starting samples recovered after synthesis at 12 GPa have mineral proportions of about 60 ± 2% olivine, 20 ± 2% garnet and 20 ± 2% clinopyroxene. Upon partial melting at 12 GPa, the proportion of olivine remained almost constant, while the proportion of Cpx decreased with increasing melt fractions. The proportion of garnet slightly increased with melting, as would be expected with mantle mineralogy (Kaminsky, 2012). For all experiments, the Mg number of olivine is between 90 and 93. Nominally anhydrous sample have lower Mg numbers of 88 - 89, which is consistent with melt-absent conditions. Chemistry of solid phases for synthesis and experimental runs are given in Supplementary Tables V.S2 and V.S3.

e) Discussion

i) Melting in the upper mantle

The magnetotelluric and geomagnetic depth sounding profiles of the upper mantle indicate significant regional variation in electrical conductivity (Grayver et al., 2017; Kuvshinov et al., 2005; Toffelmier and Tyburczy, 2007). The majority of geophysical profiles are compatible with electrical conductivity resulting from hydrous upper mantle minerals (Novella et al., 2017b). The comparison of these electrical conductivities of hydrous silicate melts with global electromagnetic and magnetotelluric profiles of the upper mantle implies that the upper mantle in the depth range 180-350 km is mainly melt free (Fig. V.4). However, the estimated high electrical conductivity anomaly above the 410-km discontinuity (Toffelmier and Tyburczy, 2007) appears to be compatible with the presence of melt in this zone (Fig. V.4). Thanks to our measurements, the melt fraction required to explain this observed anomaly is estimated to be < 10 vol. % (Fig. V.4). This estimation is significantly higher than the melt fraction of 0.5 - 2.5 % obtained by sound velocity measurements (Freitas et al., 2017) to explain the shear velocity reduction (δVs) of 3.6 - 9.4 %. The possible over-estimation of melt fraction by laboratory electrical conductivity methods has been discussed in a recent study (Freitas et al., 2019) in addition to assumptions made on forward and inversion models of electromagnetic data (Toffelmier and Tyburczy, 2007). In our discussion, we use our electrical conductivity data to qualitatively determine the vertical extents of melting in the upper mantle.

The absence of melt in the depth range 180 - 350 km confirms that the water content of the upper mantle is below the saturation limits of peridotite (Ardia et al., 2012; Férot and Bolfan-Casanova, 2012). This water undersaturated mid-upper mantle is sandwiched between two partial melt layers. Melting at the top of the asthenosphere (above 180 km) has been discussed in terms of the reduced water solubility of aluminous orthopyroxene (Mierdel et al., 2007), and melting below 350 km has been linked to the reduced water solubility in peridotites, in both cases melting is caused by the presence of excess H_2O. Here we investigate whether the dehydration-induced water saturation and subsequent melting at the top of the mantle transition zone has an influence on water circulation in the Earth's upper mantle.

ii) H_2O circulation in the upper mantle

The strong evidences supporting the presence of a melt layer atop the mantle transition zone and the strict requirement of H_2O for deep mantle melting underline the importance of understanding the mechanism that is responsible for H_2O circulation in the upper mantle. Assuming that the mantle was initially dry and well mixed after the establishment of the vigorously convecting global magma ocean, initiation of subduction in a plate tectonic context can be considered as having been the major process responsible for mantle hydration. With average downward slab velocities of between 5 and 10 cm per year (Gordon, 1995a) and assuming plates 7 km and a total ridge length of 70000 km, the annual amount of subducted material is estimated to be 24 - 49 km (Smyth and Jacobsen, 2006). With a mean age of 80 Ma, the average subducted material is estimated to have between 0.1 and 1.5% of H_2O (Dixon et al., 2002) leading to an H_2O flux of 0.1 to 1 km^3 into the mantle per year. However, studies of ophiolites indicate that most hydrous minerals break down at shallow mantle conditions and subducted rocks in eclogite facies were shown to be significantly impoverished in volatiles, with values of up to 0.25% H_2O (Katayama and Nakashima, 2003). Even in the case of extreme slab dehydration of up to 97% (Dixon et al., 2002), H_2O contents of up to 1000 ppm wt. can be preserved in subducting slabs and transported down to the transition zone (Dixon et al., 2002).

Using slab downward speed of 5 cm per year and the MTZ thickness of 250 km, the time required for a portion of slab to cross the MTZ is estimated to be 5

Ma. While this time is relatively short on a planetary timescale, the slab deflection and stagnation in the MTZ observed in seismic tomography studies (Zhao, 2004) suggests that residence time of subducted material would be much greater than the values assumed in our calculations. With a diffusion coefficient of 10^{-8} - 10^{-10} m²/s (Hae et al., 2006; Richard et al., 2006), a significant transfer of H_2O from the slab to the MTZ could be expected during that time.

The appearance of the melt layer above the MTZ can be inferred given the estimation of H_2O slab fluxes in the mantle transition zone. If we assume 24.5 km^3 slab material reaches the MTZ per year (volume produced at the ridges for 5 cm/year spreading velocity along 70000 km of ridges with an average thickness of 7 km (Gordon, 1995b)), and that these rocks contain 1000 ppm wt. H_2O, a mass of 9.4×10^{10} kg of H_2O is transferred to the MTZ every year. Assuming the volume of the MTZ to be 6.5×10^7 km^3, with a mass of 2.6×10^{20} kg (mean density of 4000 kg/m^3), and assuming complete slab dehydration into the MTZ, only 2.2 - 3.3 Ma after the beginning of modern subduction is required to reach 800 - 1200 ppm wt. in the MTZ, which is roughly equal to the maximum H_2O solubility in nominally anhydrous minerals (NAM's) forming the upper mantle (Ardia et al., 2012; Demouchy and Bolfan-Casanova, 2016; Férot and Bolfan-Casanova, 2012). Using the upper limit of the inferred H_2O content of the mantle transition zone from geophysical methods of about 0.1 - 0.2 wt.% H_2O (Freitas et al., 2017; Huang et al., 2005), the time required to transport H_2O from surface to the MTZ is estimated to be 6 ± 0.6 Ma. This very simple estimation highlights the efficiency of the hydration of the MTZ. It indicates clearly that melting at the 410-km discontinuity would have been initiated early in the Earth's history. However, H_2O diffusion into wadsleyite is a slow process (Hae et al., 2006). For example, the time required to diffuse 2000 ppm wt. H_2O to reach 500 ppm wt. at 500 km laterally along the MTZ is estimated to be 175 Ga. Given that the surface area of the MTZ is significantly large and the number of active subduction zones is extremely limited, it is possible that the H_2O distribution in the MTZ remains heterogeneous, with regions of the MTZ maintaining dry conditions (Yoshino et al., 2008). The absence of seismic anomalies in some regions (Tauzin et al., 2010) indicates that melting is not pervasive above the MTZ. The upwelling of H_2O deprived regions (< 800 - 1200 ppm wt.) of the MTZ may not undergo partial melting upon entering the upper mantle.

The H_2O under-saturated MTZ, as demonstrated by recent experimental studies (Freitas et al., 2017; Huang et al., 2005; Karato, 2011), can be a result of continuous removal of H_2O from the MTZ (upward and/or downward) or partial dehydration of slabs at the MTZ. The first scenario implies the presence of a global H_2O circulation cycle extracting H_2O from the MTZ from an early stage. However, the quantity of H_2O stored in the melt layer above the MTZ together with the moderately hydrous olivine present in equilibrium with melt over the 60 km thick layer, only represents a small portion of the total amount of H_2O in the MTZ (< 1%). This amount is a few orders of magnitude lower than the total amount transported by subducted slabs per year. Similarly, the known deep volcanic sources of OIB show that source material may be only moderately hydrous with H_2O content estimated between 300 and 1000 ppm wt. (Rüpke et al., 2006; Simons et al., 2002). These calculations demonstrate the possibility of large scale melting events occurring periodically in the Earth's history. Large scale deep mantle melting has occurred in the past, as demonstrated by the presence of komatiites, kimberlites and numerous large igneous provinces (Vinnik and Farra, 2007). However, at present, such large scale volcanism does not exist anymore and hot spot volcanism and mantle plumes are alternative candidates for removing H_2O from the deep Earth.

On the other hand, it also appears possible that slabs that are not fully dehydrated at the MTZ, and instead carry a substantial amount of H_2O on down to the lower mantle (Dixon et al., 2002). The high H_2O contents of up to 2 wt. % observed in some enriched mantle sources of oceanic island basalts (OIB) indicate that some H_2O may be incorporated into dense hydrous silicate phases (Nishi et al., 2014; Pamato et al., 2014) that penetrates down into the lower mantle via subduction processes (Rüpke et al., 2006). These would imply a slower hydration rate of the MTZ and more tardive apparition of the LVL.

iii) *Bottom-up hydration of the upper mantle*

In this section, different possible mechanisms of bottom–up hydration of Earth's upper mantle and their consequences are explored.

Due to the H_2O under-saturated conditions of the upper mantle, the water contained in hydrous melts produced at the 410-km discontinuity may diffuse in to the overlying mantle. Based on the one dimensional diffusion equation (Crank, 1975), we calculate the diffusion time required to hydrate the upper mantle assuming that the upper mantle is initially dry (Supplementary Figure V.S7),

$$C(x,t) = C_0 + (C_1 - C_0) * erfc\left(\frac{x}{2\sqrt{D * t}}\right)$$

where C_0 is the initial concentration, C_1 is constant local concentration, x is the distance to the border of concentration C_1, t is the diffusion time and D the diffusion coefficient of hydrogen in olivine. The value for D was estimated to be $7.82\times10^{-9} \pm 6.1\times10^{-8}$ m²/s at 1723 K for a randomly oriented polycrystalline material (average of the three crystallographic direction) (Novella et al., 2017b). Using average H_2O solubility for mantle (Demouchy and Bolfan-Casanova, 2016; Férot and Bolfan-Casanova, 2012), increasing from 300 ppm wt. at 200 km up to 1000 ppm wt. at 410 km, we calculate the time required for peridotite in equilibrium with the hydrous melt layer to reach H_2O saturation. Our results indicate that the time required to reach the H_2O saturation in the uppermost mantle is unrealistically high based on diffusion alone, and cannot be achieved during the planetary life time (Supplementary Figure V.S7, Fig. V.5a).

On the other hand, the mantle away from subducting slabs is rising passively in response to the material injection by subduction. Estimated values using slab flux yield to upwelling velocities of 1 mm per year (Bercovici and Karato, 2003). The estimation based on convection models indicates convection rate as high as 1.5 cm/year (Becker et al., 1999). The upwelling rates from subduction fluxes indicates that only 260 Ma is sufficient to bring rocks from the top of the transition zone to the uppermost mantle (150 km depth) and even faster considering the highest convection rates. This estimation indicates that residual hydrous peridotite should be rising from the LVL to the uppermost mantle and saturates the upper mantle at various depths depending on the initial H_2O contents in peridotite (Fig. V.5b).

Here we investigate the possible H_2O contents of peridotites in contact with the melt layer. The shear wave velocity reduction (δVs) at the melt layer is estimated to vary between 3.6 - 9.4 % (Revenaugh and Sipkin, 1994; Tauzin et al., 2010). Based on our previous study (Freitas et al., 2017), the resulting melt fraction corresponding to the δVs at the low velocity layer is estimated to be 0.5 - 2.5 vol.%

The average water content of the MTZ has been constrained by different methods with variable results. Despite potential high water solubilities of MTZ minerals (Bolfan-Casaonova et al., 2018b), the actual content of the MTZ is believed to be lower than saturation limit. Water contents inferred from inclusions in diamonds (Pearson et al., 2014,) with up to 2 % would suggest potentially high water content which also supported by viscosity measurements (Fei et al. 2017). Particularly, the near-water saturated conditions implied by hydrous ringwoodite inclusions found in natural diamond (Pearson et al., 2014) may represent an episode of subduction-zone-related melting. However, most of geophysical techniques such as elasticity, sound velocities (Inoue et al., 1998, Chang et al., 2015, Freitas et al., 2017) and electrical conductivities (Huang et al., 2005, Yoshino et al., 2008, Yoshino and Katsura 2012) indicating major part of MTZ contains < 0.2 wt. % H_2O.

Assuming a batch melting scenario and H_2O partitioning between peridotite and melt (Novella et al., 2014), readjusted to the mineral proportions expected at 12 GPa (Supplementary Text V-S1), we could estimate the H_2O contents of peridotite in equilibrium with hydrous melt for variable water contents in the mantle source for different melt fractions (Fig. V.6). Different scenarios could occur given the potential range of water content of the residual peridotites (Fig. V.6). Thus, if residual peridotite in the upwelling mantle contains about 200 ppm wt. of H_2O, mantle saturation can be expected at range of depths in the upper mantle (Fig. V.6). If we assume the H_2O saturation curves of Férot and Bolfan-Casanova (Férot and Bolfan-Casanova, 2012), Hirschmann et al. (Hirschmann et al., 2009), Tenner et al. (Tenner et al., 2012, 2009) and Ardia et al. (Ardia et al., 2012) (for garnet/olivine partitioning of H_2O of 9.0), peridotite in the upper mantle reaches H_2O saturation limits above 200 km. In contrast, by using the extreme H_2O saturation scenario proposed by Ardia et al. (2012) with water partitioning between olivine and garnet of 0.9, the mantle saturation above 200 km depths can be expected for the water contents of 450 ppm. However, this value is inconstant with the upper mantle water contents of 50 - 200 ppm.

The ascent of residual hydrous peridotites would initiate melting upon reaching their storage capacities and could be responsible for the hydrous melting at the top of the asthenosphere. Melting above a depth of 180 km can only be explained by moderate water content in the MTZ (< 1500 ppm wt) for geologically relevant melt fractions at the 410-km discontinuity (Fig. V.6). The upwelling of the MTZ with water contents of less than 800 ppm wt. may not undergo melting upon entering the upper mantle and may continue to hydrate the upper mantle. However, such fertile peridotites are not able to explain the depleted signature of the upper mantle. Melting at the 410- km discontinuity is therefore a primary requirement for a compatible hydration of the upper mantle with geochemical constrains.

The lithosphere-asthenosphere boundary (LAB) is defined as intersection of the conductive geotherm of mechanically strong crust with the fluid-saturated peridotite solidus in mechanically weak upper most part of the mantle (McKenzie and Bickle, 1988). The location of the LAB is therefore corresponding to the depth at which the fluid saturation occurs in upwelling peridotites. The geochemical constraints suggests that the LAB is not a stable feature, which appear to move up or down over geological time scale (O'Reilly and Griffin, 2010). If other parameters remain constant, the lateral variation of the depth of the LAB may indicate the variable water contents in residual peridotites, which corresponds to the lateral variations of water contents in the MTZ. Further, the movement of the depth of the LAB at the same location may suggests episodic variation of water contents in the MTZ over geological time scale. The upwelling of MTZ with a water content greater than 2000 ppm wt. ppm could produce residual peridotites reaching the maximum water storage capacity (Fig. V.6). Upwelling of such peridotites could continue to melt and form a gravitationally unstable melt column in the upper mantle. The upwelling of the MTZ with high water contents would trigger large-scale melting (Vinnik and Farra, 2007) and could be responsible for the formation of upper mantle plumes.

iv) *Conclusions*

Based on our data, we propose a hydration mechanism for the Earth's upper mantle that is consistent with geophysical observations (magnetotelluric and seismic profiles) and geochemical constraints. In this bottom-up water transportation mechanism, the residual hydrous peridotites, formed as a result of melting at the 410-km discontinuity, upwell across the upper mantle, replacing initially dry mantle peridotites. The resulting water content in the residues is directly related to the water content of the mantle transition zone and the degree of melting. The upper limit of 200 ppm observed for the upper mantle can be maintained in residual peridotites if the water content of the MTZ is less than 1500 ppm . The slow H_2O diffusion rates in wadsleyite may enforce large gradient in H_2O distribution within the MTZ, and as a result, regional variations of H_2O contents in the upper mantle would be expected. The ascent of residual hydrous peridotites could be responsible for the hydrous melting at the top of the asthenosphere.

f) Acknowledgments

We thank F. Schiavi for the assistance with Raman analyses, A. Mathieu for technical assistance, J.M Hénot, J.L Devidal and 2MAtech staff for their help in SEM and EMP and FEG-SEM analyses, respectively. We appreciate the discussion with J, Chantel, D, Andrault, N. Bolfan-Casanova and M.A Bouhifd. G.M. acknowledges funding from the French PNP program (INSU-CNRS). This research was financed by the French Government Laboratory of Excellence initiative n°ANR-10-LABX-0006, the Région Auvergne and the European Regional Development Fund. This is ClerVolc contribution number xx.

g) Figures

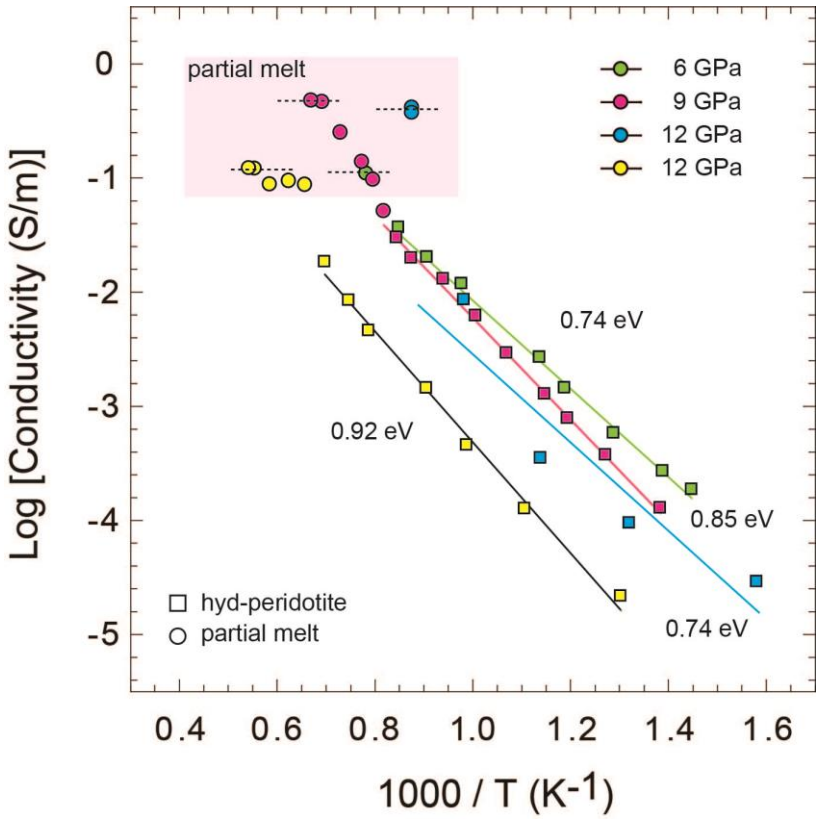

Figure V.1 Electrical conductivity of hydrous peridotites at 6, 9 and 12 GPa. The peridotites before melting are indicated in squares and after partial melting are in circles. The melt conductivities used for the discussion are shown with vertical lines. Activation enthalpies are given in eV, next to the individual fits. The error bars associated with the electrical conductivity data measurements are less than the symbol size at high temperatures. The uncertainties in the estimation of the electrical conductivity result from the estimations of temperature, pressure, and sample dimensions, as well as data fitting errors, are less than 5%.

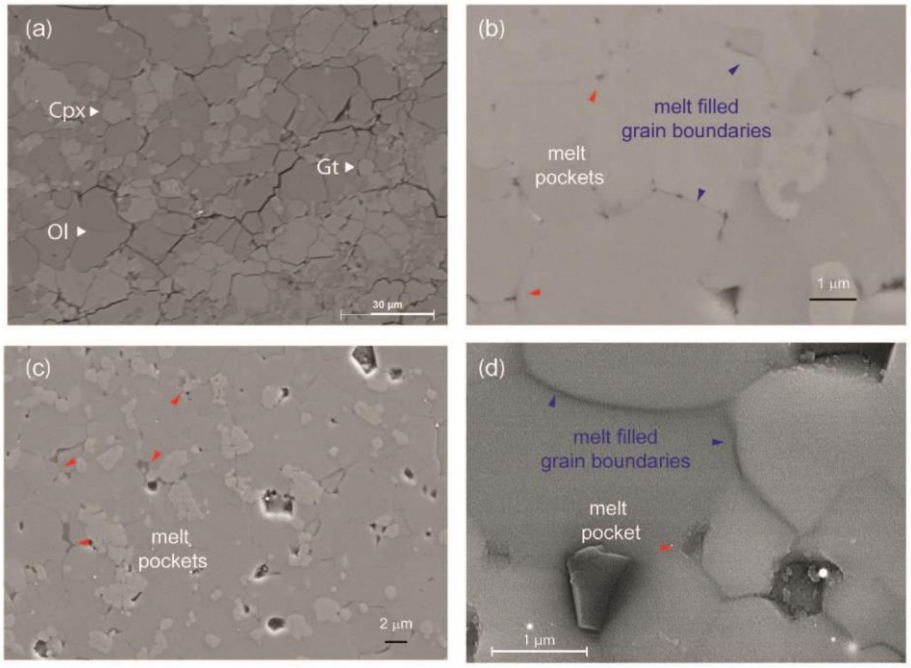

Figure V.2 High resolution microphotographs of the recovered samples before and after the electrical conductivity measurements. (a) Hydrous peridotite sample showing mineral distribution before melting at 12 GPa (M421). (b) The mineral and melt distribution of partially molten sample after the electrical conductivity measurements at 6 GPa (M667), (c) at 9 GPa (M668), (d) and at 12 GPa (M425).

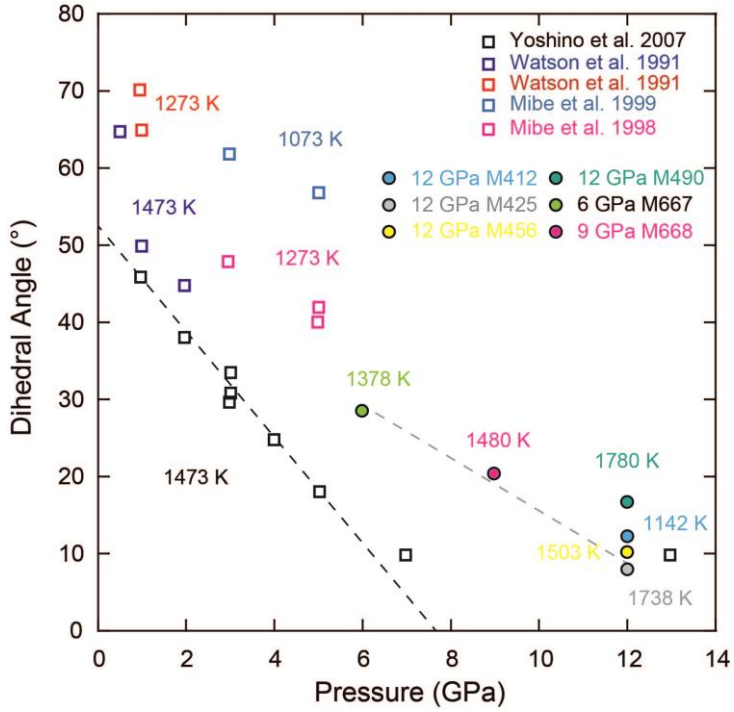

Figure V.3 Dihedral angles estimated in our partially molten samples as a function of pressure. The maximum temperature of each experiment is indicated next to its symbol. Dihedral angles were estimated using FEG SEM and SEM image analysis with Matlab code to measure the angles by the tangent method. Analytical error is estimated to be 5° (1σ). Relevant literature values for similar or analogue systems at lower pressures have been represented for comparison (Mibe et al., 1999, 1998; Watson et al., 1991; Yoshino et al., 2007).

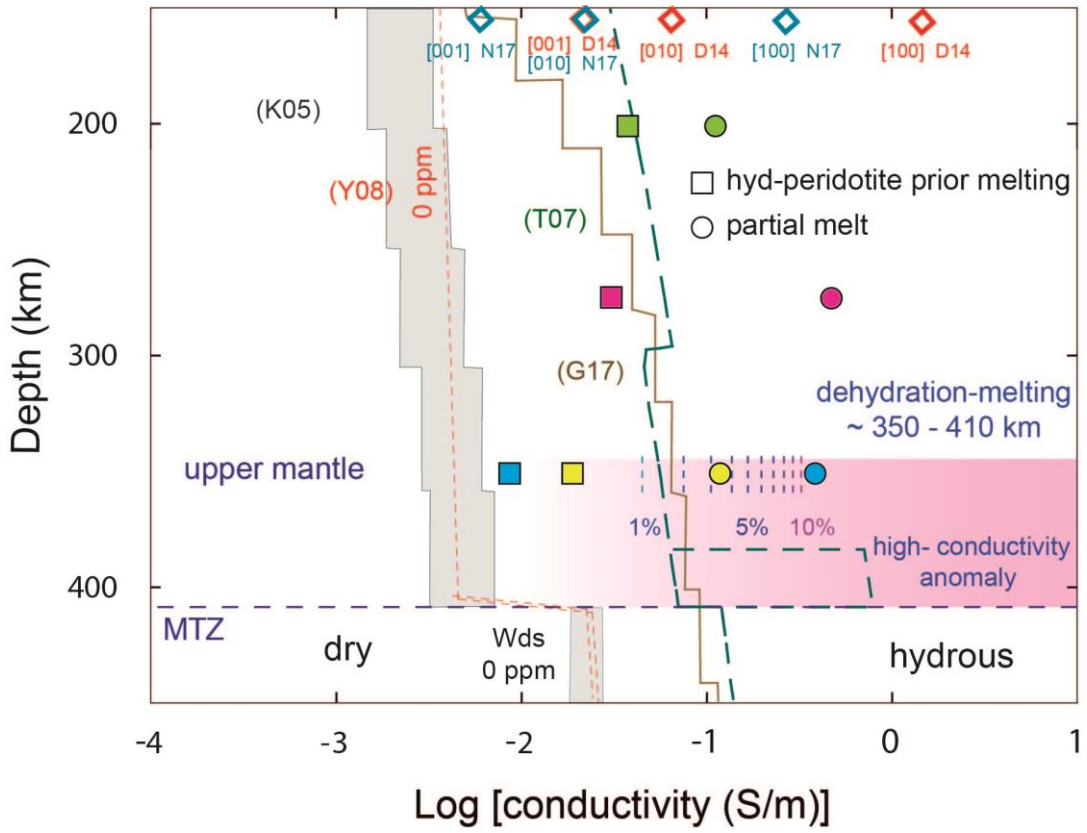

Figure V.4 Electrical conductivity of hydrous silicate melts compared with geophysical profiles. Electrical conductivities of peridotite prior to melting (squares) and partially molten peridotites (circles) at 6, 9 and 12 GPa are displayed as a function of depth. Hashin Shtrikman upper bound (HS+) conductivities for different melt fraction are displayed for 12 GPa samples with dashed lines. The conductivity profiles are for oceanic mantle (pacific, KO5) (Kuvshinov et al., 2005), continental (Tuscan SW USA, T07) (Toffelmier and Tyburczy, 2007) and global electrical conductivity model of Earth's mantle based on inverting satellite magnetic field measurements (G17) (Grayver et al., 2017). Pink shaded area indicates the possible distribution of hydrous melt at the top of the mantle transition zone. In this area the high conductivity anomaly modeled from EM data has been represented (Toffelmier and Tyburczy, 2007). Dry upper mantle electrical conductivity vs depth profile based on high pressure electrical conductivity measurements are also displayed (Yoshino et al., 2008). Electrical conductivities of oriented single crystal olivine from measurements (Dai and Karato, 2014) (4 GPa and extrapolated to mantle temperatures) and diffusion experiments (Novella et al., 2017b) (2 GPa, extrapolated to mantle temperatures and with 80 ppm of water) have been reported. Electrical conductivity anomaly of 350' cannot be reproduced by moderately anisotropic solid rock but rather require presence of melts. Our solid hydrous peridotites conductivities agree well with randomly oriented olivine values.

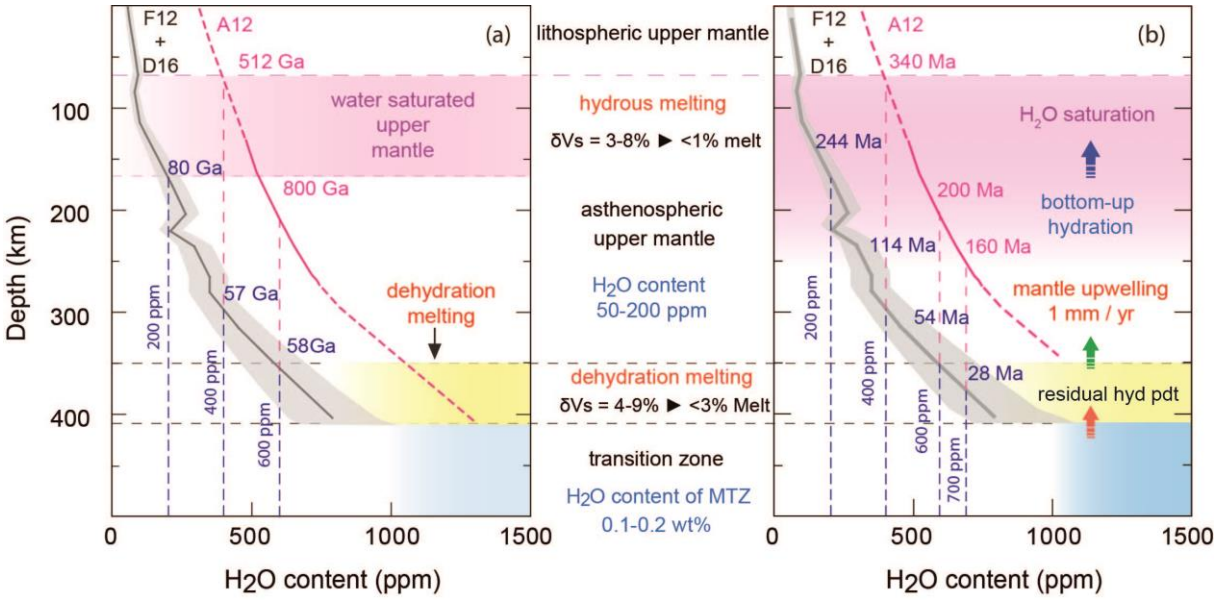

Figure V.5 Comparison of water transport mechanisms of the Earth's upper mantle. (a) Hydration of the Earth's upper mantle by diffusion. The estimations are based on the diffusion coefficient of 7.89×10^{-9} m^2/s (Novella et al., 2017a) at 1723 K with initial H_2O concentration of 800 ppm wt. and variable diffusion lengths (from 410-km to the saturation depth at a given water content) (see also Supplementary Fig. V.S7). The water saturation curves are for peridotite without considering garnet (F12) (Férot and Bolfan-Casanova, 2012) and considering water partition between olivine and garnet (0.9) (A12) (Ardia et al., 2012). The broken lines indicate the time required to saturate the upper mantle by diffusion at given depths for a given bulk water content. The shaded in yellow indicates regions where dehydration-melting is expected. The shaded in pink indicate depth range for mantle H_2O saturation which can't be explained by diffusion process. (b) Hydration by upwelling. The dehydration melting at the 410-km discontinuity (Freitas et al., 2017) produces residual peridotites with different H_2O concentration according melt fractions and compositions. The continuous upwelling of hydrous peridotite replaces the initially dry peridotite in the upper mantle, forming hydrous upper mantle. The ascending peridotite reaches water saturation levels at different depths (Ardia et al., 2012; Férot and Bolfan-Casanova, 2012), and should initiate hydrous melting. The broken lines indicate the time required to saturate the upper mantle at given depths for a given bulk water content. The water saturation curves are for peridotite without considering garnet (F12) (Férot and Bolfan-Casanova, 2012) and with considering water partition between olivine and garnet (A12) (Ardia et al., 2012). The shaded in yellow indicates regions where dehydration-melting is expected. The shaded in pink indicate depth range for mantle H_2O saturation.

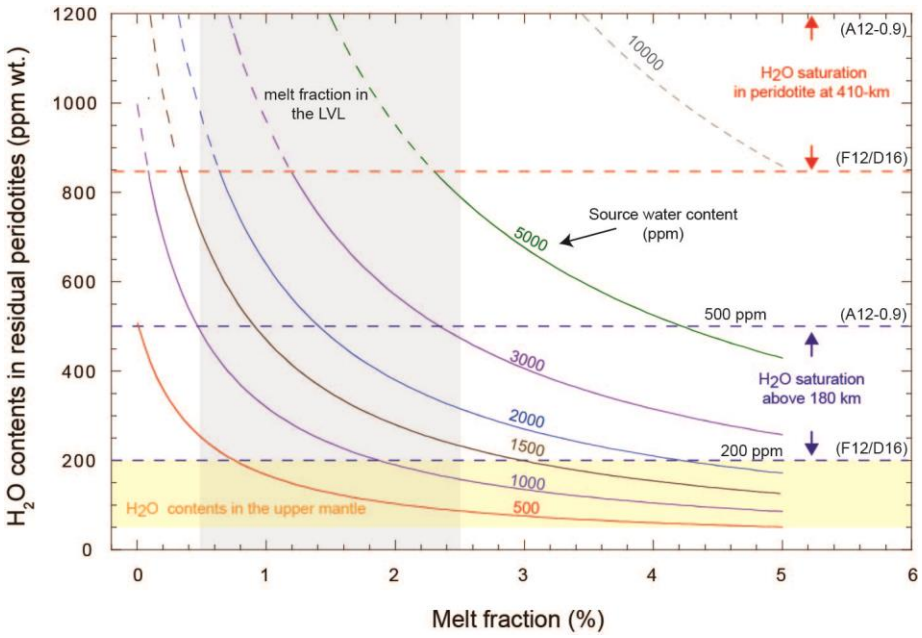

Figure V.6 Bottom-up hydration of the upper mantle. The H_2O contents are calculated assuming batch melting scenario at the 410-km discontinuity. The H_2O contents in the source (MTZ) are marked next to individual lines. The Gray shaded area indicates the melt fraction expected at the partially molten layer above the MTZ. The area shaded in Yellow indicates H2O content of the upper mantle. Vertical lines (F12/D16) (Demouchy and Bolfan-Casanova, 2016; Férot and Bolfan-Casanova, 2012) and (A12) (Ardia et al., 2012) indicate water saturation limits at different depths based on water solubilities of peridotites.

h) Supplementary materials

Supplementary materials for:
Electrical conductivity of hydrous silicate melts: Implications for the bottom-up hydration of Earth's upper mantle

D.Freitas[1*], G. Manthilake[1]
[1]Université Clermont Auvergne, CNRS, IRD, OPGC, Laboratoire Magmas et Volcans, F-63000 Clermont-Ferrand, France
(*corresponding author: damien.freitas@uca.fr)

Supplementary materials

Here we give supplementary information concerning:

- **The estimation of the H_2O partition coefficient for peridotite/melt at 12 GPa (Text V.S1)**
- **Experimental conditions and parameters of syntheses and *in situ* measurements (Table V.S1)**
- **Average chemical composition of solid mineral phases at 6 and 9 GPa both before and after EC measurements (Table V.S2)**
- **Average chemical composition of solid mineral phases at 12 GPa (Table V.S3)**
- **Schematic cross section of the high pressure assemblies (Figure V.S1)**
- **Modeling of thermal gradient in our assembly (Figure V.S2)**
- **Impedance spectra of the sample at different stages of heating (Figure V.S3)**
- **Representative Raman spectra from starting materials and recovered experimental runs at 6 GPa (Figure V.S4)**
- **Representative Raman spectra from starting materials and recovered experimental runs at 9 GPa (Figure V.S5)**
- **Representative Raman spectra from recovered experimental runs at 12 GPa. (Figure V.S6)**
- **Water diffusion calculations for the hydration of Earth's upper mantle. (Figure V.S7)**

i) Supplementary text

Supplementary Text V.S1: The estimation of the H_2O partition coefficient for peridotite/melt at 12 GPa.

The H_2O partition coefficient between peridotite and melt is available at 6 GPa (Novella et al., 2014). Due to the significant variation of mineral proportions at 12 GPa, we have estimate the H_2O partition coefficient between peridotite and melt based on mantle mineralogy at 12 GPa. The bulk partition coefficient can be calculated by:

$$D_{H2O}^{pdt/melt} = \sum X_i Kd_i$$

Where *X* are the fraction of each mineral (*i*) and *Kd* is partition coefficient for water with melt. The *Kd* values are taken from Novella et al. (2014) and mineral proportion where estimated using the mineral proportions estimated at 12 GPa in our study. Mineral proportion at 12 GPa are observed to be 60 % of olivine, 28 % of Garnet (Gt) and 12 % of Clinopyroxene (Cpx).

	Kd (Novella et al., 2014)	STD
Melt/olivine	0.004	0.0006
Melt/Opx	0.0064	0.0004
Melt/Cpx	0.0115	0.0016
Melt/garnet	0.0032	0.0008
$D_{Melt/pdt}$ 6 GPa	0.006288	0.000343
$D_{Melt/pdt}$ 12 GPa	0.004676	0.000424

ii) Supplementary tables

Table V.S1 Conditions of experimental runs (syntheses and in situ measurements). Each run conditions are given in the first section: pressure, temperature and duration at maximum temperature. In situ experiments were only kept for short times above melting temperature (< 1h) to avoid any melt escape or reaction. Water content are then given with the 3 next columns: initial starting water content in powders, water content in solid samples after syntheses and water content after in situ electrical conductivity measurements. Water content on solid samples after in situ measurements was estimated qualitatively (or with large errors) by Raman spectroscopy (see methods section and Freitas et al., 2017). Partially molten samples characteristics are given, with melt fractions and estimated melting temperatures based on electrical conductivity. Dihedral angles measurements are given with average and median angles for each partially molten sample. In the last column (remarks), the type of each experiment is given; synthesis run number used for electrical conductivity measurements is given in parenthesis. Errors given in parenthesis are 1 standard deviation.

[1] *Water content of the bulk sample estimated with quenched glass quantification and partition coefficient (Novella et al., 2014) with mineral proportions inferred from BSE image analyses.*

[2] *Melt fractions estimated by mass balance, partition coefficients and image surface analyses.*

[3] *Melt fractions estimated by image surface analysis only.*

	Experimental conditions			Water contents (ppm)			Partial melting		Dihedral angle Θ			
Run #	Pressure (GPa)	Tmax (K)	Time	initial powder	Solid sample	After *in situ* EC[1]	**%melt**[2]	Tmelting (K)[4]	Number of measurements	Mean	Median	Remarks
M405	5	1523 (20)	3h45	0	-	-	-	-	-	-	-	Synthesis
M407	5	1473 (20)	1h	0	-	-	-	-	-	-	-	Synthesis
M408	14	1373 (20)	7h	≈500	> 3000	-	-	-	-	-	-	Synthesis
M410	14	1373 (20)	2h10	≈500	3267 (650)	-	-	-	-	-	-	Synthesis
M412	12	1738 (5)	< 1h	0	-	3098 (959)	**7.00 (0.27)**	1143 (5)	77.00	12.20 (11.68)	10.51	EC (M405)
M415	5	1450 (20)	2h30	0	-	-	-	-	-	-	-	Synthesis
M421	12	1385 (5)	< 1h	0	-	993 (260)	-	-	-	-	-	EC (M415)
M425	12	1738. (5)	< 1h	≈500	≈3000	3030 (627)	**2.00 (0.45)**	1493 (5)	139.00	7.88 (8.79)	6.23	EC (M408)
M455	14	1373 (20)	2h	≈700	≈3600	-	-	-	-	-	-	Synthesis
M456	12	1503 (5)	< 1h	≈700	≈3600	-	**3.50 (2.44)**	1303 (5)	59.00	10.12 (10.26)	8.50	EC (M455)
M481	2	1473 (20)	2h	0	-	-	-	-	-	-	-	Synthesis
M482	14	1323 (20)	2h10	-	500-700	-	-	-	-	-	-	Synthesis (M481)
M490	12	1780 (5)	< 1h	0	500-700	800-1650	**25.65 (2.50)**	1561 (5)	36.00	16.60 (9.52)	17.09	Freitas et al. 2017 (M481)
M492	12	1363 (5)	< 1h	0	500-700	490 (125)	-	-	-	-	-	Freitas et al. 2017 (M482)
M665	6	1273 (20)	4h15	≈700	1579 (413)	-	-	-	-	-	-	Synthesis
M666	9	1323 (20)	3h30	≈700	1740 (523)	-	-	-	-	-	-	Synthesis
M667	6	1378 (5)	< 1h	≈700	1579 (413)	-	**3.68 (1.86)** [3]	1163 (5)	104.00	28.46 (13.19)	27.26	EC (M665)
M668	9	1480.20 (5)	< 1h	≈700	1105 (422)	-	**6.33 (1.01)** [3]	1181 (5)	109.00	20.32 (9.53)	19.49	EC (M666)

Table V.S2 Average chemical composition of solid mineral phases at 6 and 9 GPa both before and after EC measurements. Each value is an average of 3 to 10 analyses; the standard deviation is indicated in parenthesis. Chemical analyses of quenched melt were not possible due to the extremely small size of the melt pockets.

	Starting material at 6 GPa			**After EC exp. At 6 GPa**			**Starting material at 6 GPa**			**After EC exp. At 6 GPa**		
	Ol	**Cpx**	**Gt**	**Ol**	**Cpx**	**Gt**	**Ol**	**Cpx**	**Gt**	**Ol**	**Cpx**	**Gt**
SiO_2	40.00 (0.90)	54.82 (0.22)	46.13 (0.92)	40.65 (0.87)	54.42 (0.73)	42.13 (2.84)	39.30 (1.00)	53.58 (0.63)	39.81 (2.45)	39.28 (1.39)	51.14 (0.96)	40.68 (0.22)
TiO_2	0.00 (0.00)	0.00 (0.00)	0.00 (0.00)	0.00 (0.00)	0.00 (0.00)	0.00 (0.00)	0.00 (0.00)	0.00 (0.00)	0.00 (0.00)	0.00 (0.00)	0.00 (0.00)	0.00 (0.00)
Al_2O_3	0.29 (0.37)	2.34 (0.64)	14.66 (0.49)	0.44 (0.43)	2.59 (0.36)	15.41 (6.69)	1.03 (0.03)	1.48 (0.15)	18.50 (4.68)	0.20 (0.20)	1.79 (0.22)	20.53 (0.54)
Cr_2O_3	0.00 (0.00)	0.00 (0.00)	0.00 (0.00)	0.00 (0.00)	0.00 (0.00)	0.00 (0.00)	0.00 (0.00)	0.00 (0.00)	0.00 (0.00)	0.00 (0.00)	0.00 (0.00)	0.00 (0.00)
FeO	10.71 (1.86)	3.93 (1.35)	8.80 (0.77)	10.79 (2.54)	2.77 (0.09)	9.01 (1.00)	8.81 (0.22)	4.22 (3.06)	10.84 (1.85)	9.18 (1.34)	3.06 (0.30)	9.17 (0.12)
MnO	0.00 (0.00)	0.00 (0.00)	0.00 (0.00)	0.00 (0.00)	0.00 (0.00)	0.00 (0.00)	0.00 (0.00)	0.00 (0.00)	0.00 (0.00)	0.00 (0.00)	0.00 (0.00)	0.00 (0.00)
MgO	40.00 (0.90)	19.12 (0.46)	22.75 (0.74)	47.17 (2.57)	19.70 (0.68)	42.13 (2.84)	50.00 (1.25)	19.30 (0.94)	23.29 (5.35)	48.25 (2.45)	20.91 (2.57)	20.47 (2.93)
CaO	0.09 (0.05)	18.38 (2.84)	6.79 (1.53)	0.16 (0.11)	18.97 (0.60)	5.04 (2.87)	0.17 (0.01)	18.88 (4.42)	4.81 (1.22)	0.14 (0.10)	18.65 (1.82)	5.87 (0.71)
Na_2O	0.22 (0.28)	1.91 (0.68)	0.72 (0.11)	0.31 (0.37)	1.79 (0.27)	0.60 (0.19)	0.58 (0.02)	1.78 (0.90)	0.49 (0.28)	0.27 (0.24)	1.42 (0.19)	0.17 (0.21)
NiO	0.00 (0.00)	0.00 (0.00)	0.00 (0.00)	0.00 (0.00)	0.00 (0.00)	0.00 (0.00)	0.00 (0.00)	0.00 (0.00)	0.00 (0.00)	0.00 (0.00)	0.00 (0.00)	0.00 (0.00)
K_2O	-	-	-	-	0.01 (0.02)	0.01 (0.02)	0.00 (0.00)	0.00 (0.00)	0.00 (0.00)	-	0.01 (0.01)	0.05 (0.02)
Total	**99.91 (1.15)**	**100.52 (0.57)**	**99.84 (0.86)**	**99.55 (0.94)**	**100.19 (0.33)**	**99.89 (1.36)**	**99.9 (2.50)**	**99.24 (0.47)**	**97.74 (1.11)**	**97.36 (0.28)**	**96.97 (0.58)**	**96.95 (1.53)**

Ol: olivine, Cpx: clinopyroxene, Gt: garnet

Table V.S3 Average chemical composition of solid mineral phases at 12 GPa. Each value is an average of 5 to 20 analyses. The standard deviation is given on the average value in parenthesis.

	M412-7 (0.27)% Melt			**M421-0% Melt**			**M425-2 (0.45)% Melt**			**M456-3.5 (2.44)% Melt**		
	Ol	**Cpx**	**Gt**	**Ol**	**Cpx**	**Gt**	**Ol**	**Cpx**	**Gt**	**Ol**	**Cpx**	**Gt**
SiO_2	41.60 (0.38)	56.48 (1.01)	47.23 (0.89)	40.90 (0.87)	54.62 (0.65)	40.69 (1.38)	41.36 (0.26)	54.78 (0.67)	43.95 (1.46)	41.99 (0.48)	55.73 (0.36)	46.51 (4.01)
TiO_2	0.00 (0.00)	0.03 (0.01)	0.78 (0.38)	0.04 (0.03)	0.10 (0.04)	0.57 (0.39)	0.04 (0.03)	0.06 (0.03)	0.43 (0.16)	0.05 (0.04)	0.10 (0.05)	0.32 (0.26)
Al_2O_3	0.12 (0.02)	2.66 (0.29)	8.87 (2.21)	0.04 (0.08)	1.66 (0.46)	22.19 (3.04)	0.44 (0.60)	1.74 (0.57)	17.13 (5.31)	0.15 (0.04)	1.83 (0.40)	13.17 (10.42)
Cr_2O_3	0.12 (0.02)	0.01 (0.02)	0.01 (0.01)	0.01 (0.02)	0.01 (0.02)	0.03 (0.02)	0.01 (0.01)	0.02 (0.01)	0.03 (0.02)	0.00 (0.00)	0.00 (0.02)	0.00 (0.00)
FeO	7.15 (0.24)	4.83 (0.48)	9.77 (1.77)	8.99 (1.12)	2.97 (0.71)	7.73 (0.58)	7.01 (0.78)	2.90 (0.35)	6.34 (0.61)	5.55 (1.96)	2.96 (0.15)	5.17 (0.99)
MnO	0.02 (0.02)	0.02 (0.02)	0.05 (0.02)	0.02 (0.02)	0.01 (0.01)	0.06 (0.02)	0.02 (0.02)	0.02 (0.02)	0.06 (0.03)	0.01 (0.01)	0.02 (0.01)	0.05 (4.59)
MgO	50.78 (0.58)	33.61 (0.73)	13.64 (8.72)	48.80 (0.68)	18.74 (5.83)	18.51 (4.17)	50.10 (1.20)	19.09 (1.18)	24.97 (7.53)	52.67 (2.02)	17.83 (0.62)	24.57 (4.59)
CaO	0.18 (0.03)	1.70 (0.23)	15.99 (4.72)	0.11 (0.12)	20.04 (4.33)	8.77 (7.09)	0.36 (0.30)	19.79 (1.07)	6.94 (1.97)	0.23 (0.14)	20.96 (0.50)	10.58 (2.07)
Na_2O	0.02 (0.02)	0.21 (0.13)	1.46 (0.42)	0.02 (0.04)	1.31 (0.29)	0.06 (0.02)	0.03 (0.02)	0.97 (0.18)	0.11 (0.07)	0.03 (0.02)	1.23 (0.12)	0.31 (0.25)
NiO	0.01 (0.01)	0.07 (0.02)	0.00 (0.00)	-	-	-	-	-	-	0.01 (0.01)	0.00 (0.00)	0.02 (0.01)
K_2O	0.01 (0.01)	0.01 (0.02)	0.06 (0.06)	0.01 (0.01)	0.03 (0.02)	0.01 (0.02)	0.00 (0.00)	0.01 (0.01)	0.01 (0.01)	0.01 (0.01)	0.02 (0.01)	0.02 (0.01)
Total	**99.88 (0.93)**	**100.16 (1.14)**	**97.86 (5.21)**	**98.94 (0.67)**	**99.50 (1.40)**	**98.62 (1.05)**	**99.38 (0.45)**	**99.39 (0.57)**	**99.95 (1.70)**	**100.70 (0.29)**	**100.68 (0.61)**	**100.71 (1.03)**

Ol:olivine, Cpx: clinopyroxene, Gt: garnet

iii) Supplementary figures

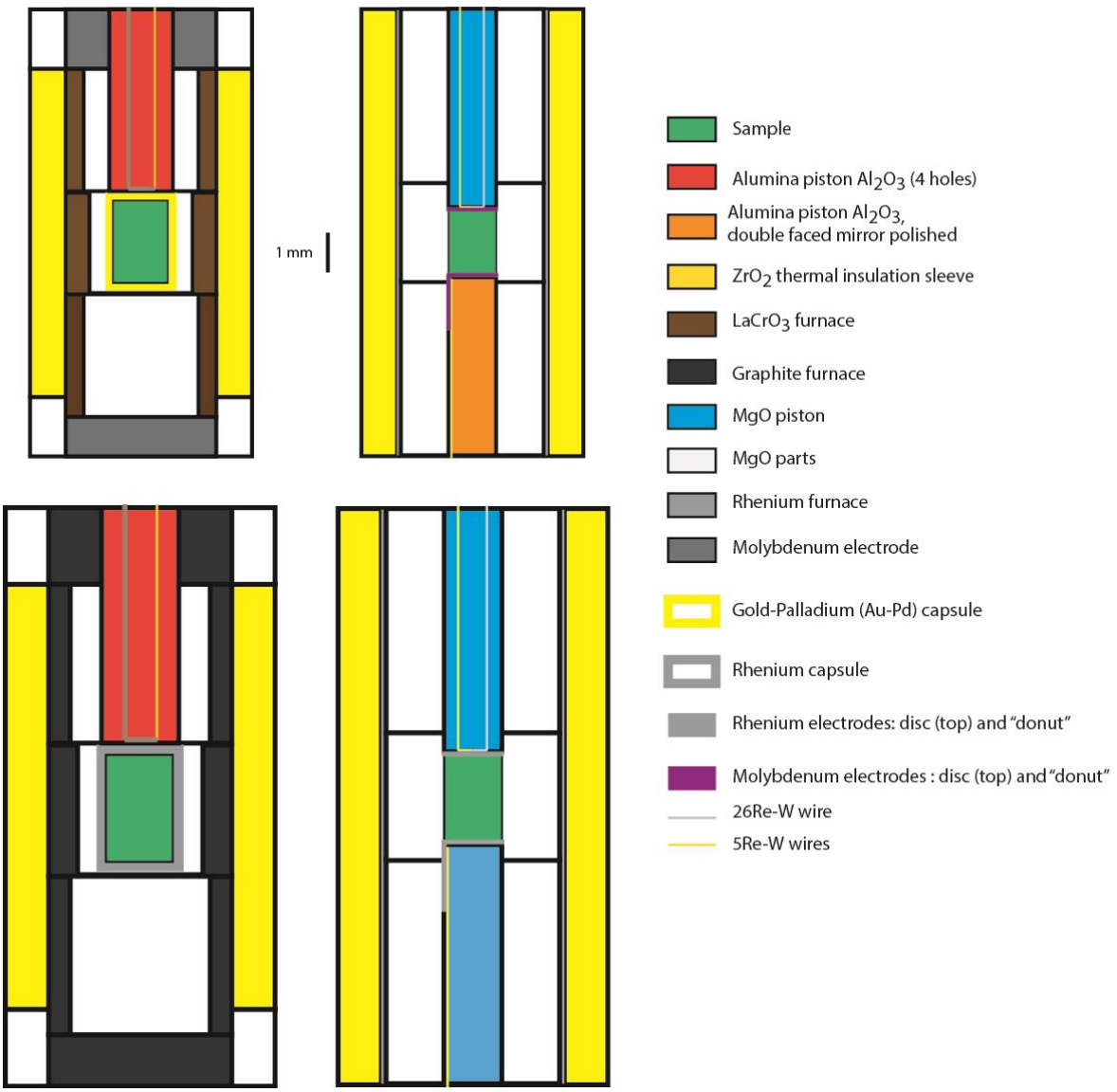

Figure V.S1 Schematic cross section of the high pressure assemblies. Assembly geometries at the left was used for the synthesis of the peridotite samples and on the right was used for electrical conductivity measurements at 6, 9 and 12 GPa

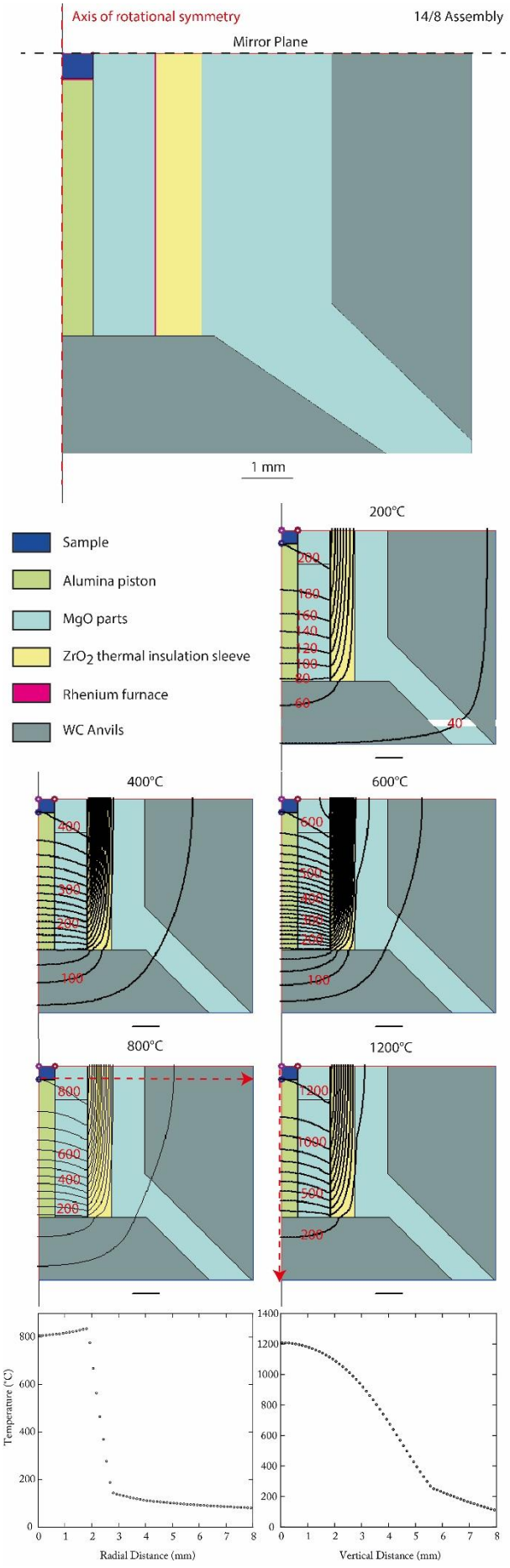

Figure V.S2 Modeling of thermal gradient in our assembly. Results of simulations using the software codes of Hernlund et al. (2006). The maximum temperature gradient of the assembly at 1500 K was estimated to be less than 20 K.

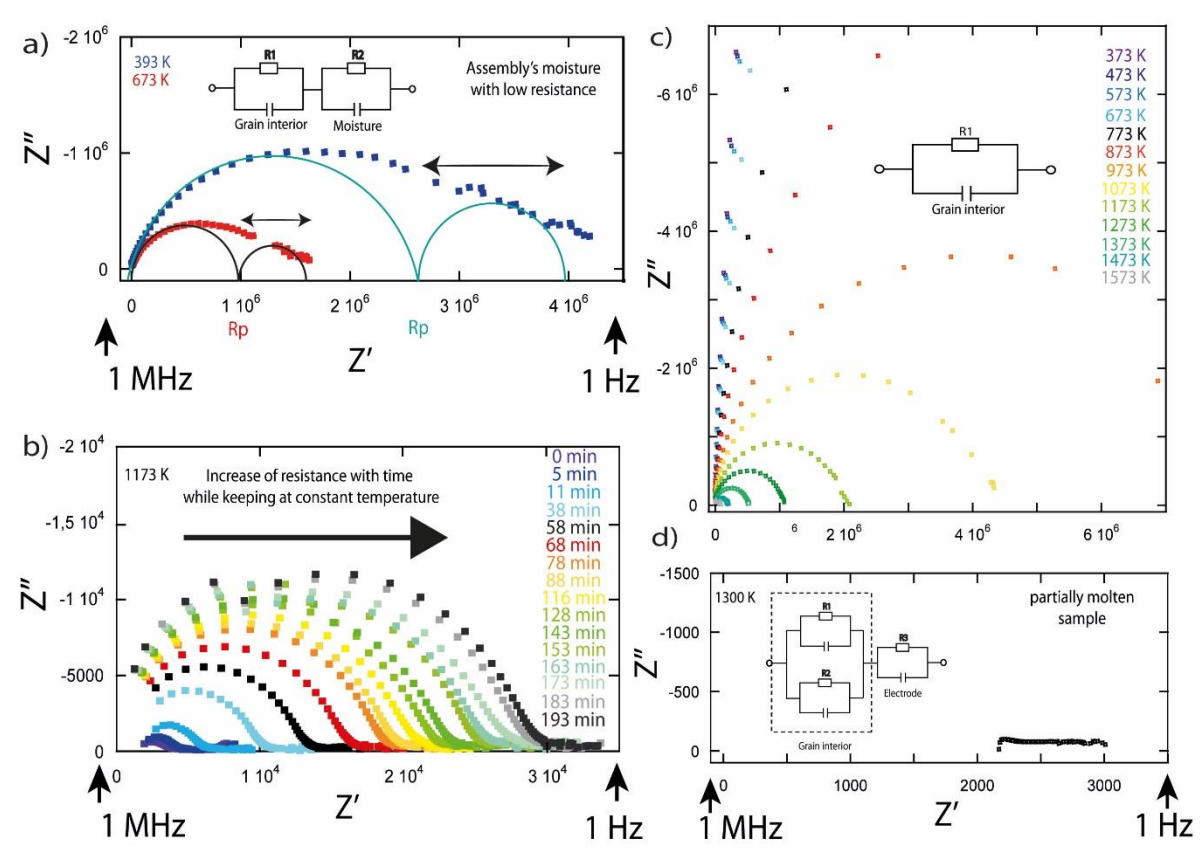

Figure V.S3 Impedance spectra of the sample at different stages of heating: (a) during assembly dehydration at 673 K (b) sample annealing at 1173 K. (c) Impedance spectra recorded after assembly dehydration and sample annealing steps. Moisture tails were not observed anymore during this cycle. (d) Impedance spectra recorded after the onset of melting, these spectra are characterized by the disappearance of the semicircular shape for induction patterns.

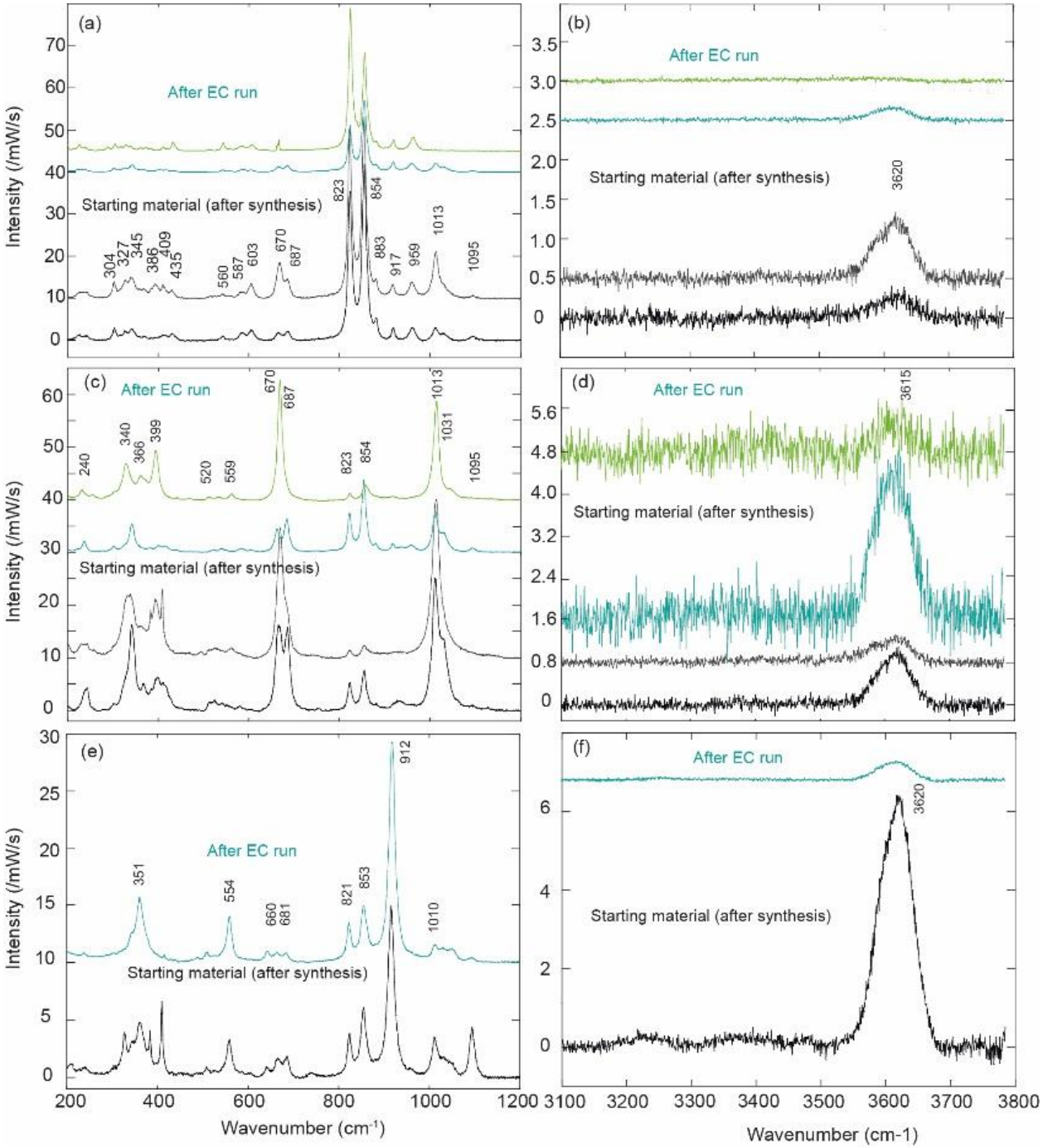

Figure V.S4 Representative Raman spectra from starting materials and recovered experimental runs at 6 GPa. Low-wavenumber (200-1200 cm^{-1}) bands corresponding to vibrations of the silicate network (a, c, e) and high-wavenumber bands (3100-3800 cm^{-1}) corresponding to O-H vibrations (b, d, f) of olivine, pyroxene and garnet, respectively. The presence of H_2O is visible in all samples. H_2O content is significantly reduced in the experiments which undergo partial melting. Black and gray spectra were taken in starting material after the synthesis run, green spectra were acquired on samples recovered after the in situ measurements.

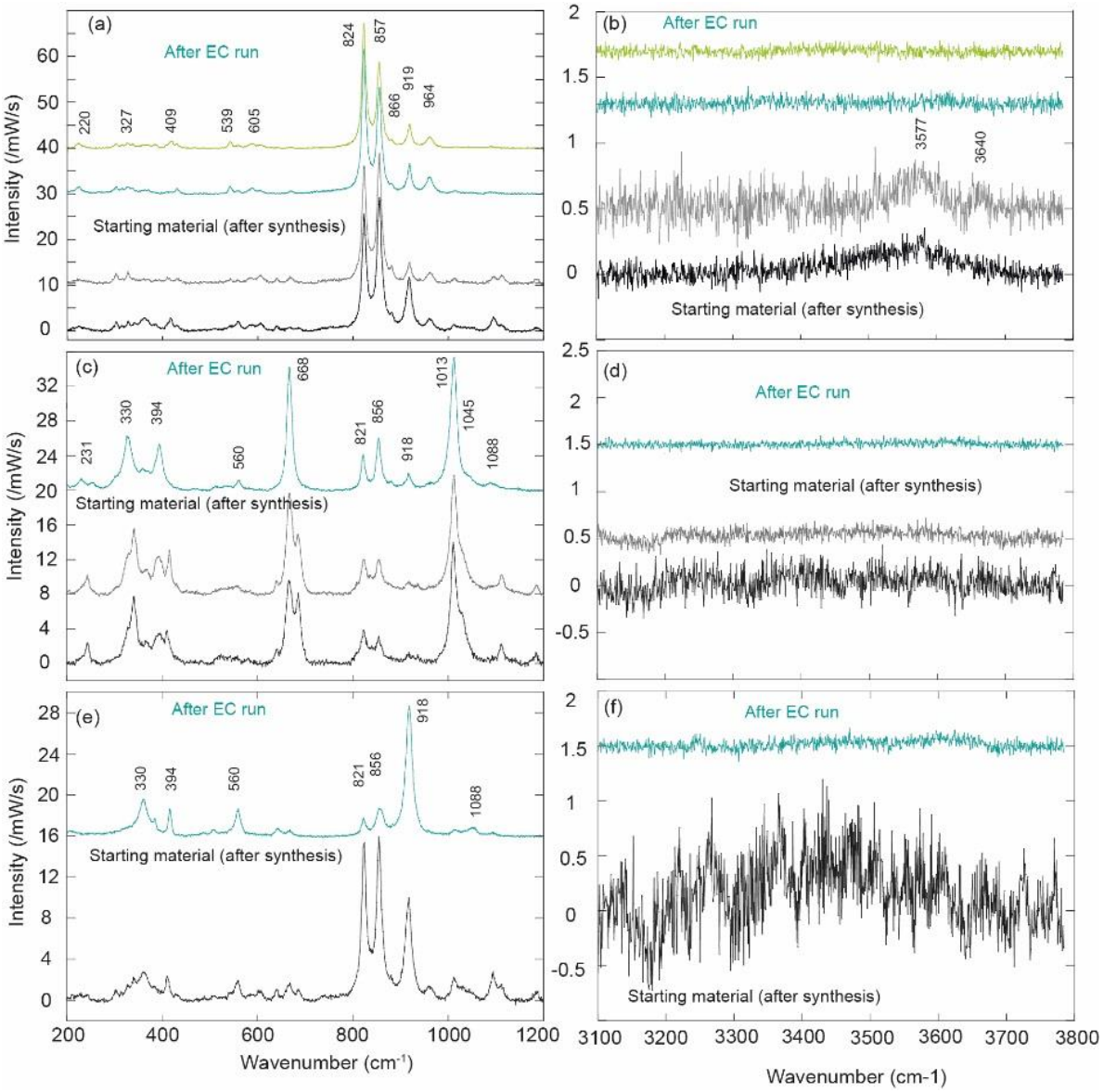

Figure V.S5 Representative Raman spectra from starting materials and recovered experimental runs at 9 GPa. Low-wavenumber (200-1200 cm^{-1}) bands corresponding to vibrations of the silicate network (a, c, e) and high-wavenumber bands (3100-3800 cm^{-1}) corresponding to O-H vibrations (b, d, f) of olivine, pyroxene and garnet, respectively. The presence of H_2O is visible in all samples. H_2O content is significantly reduced in the experiments which undergo partial melting. Black and gray spectra were taken in starting material after the synthesis run, green spectra were acquired on samples recovered after the in situ measurements.

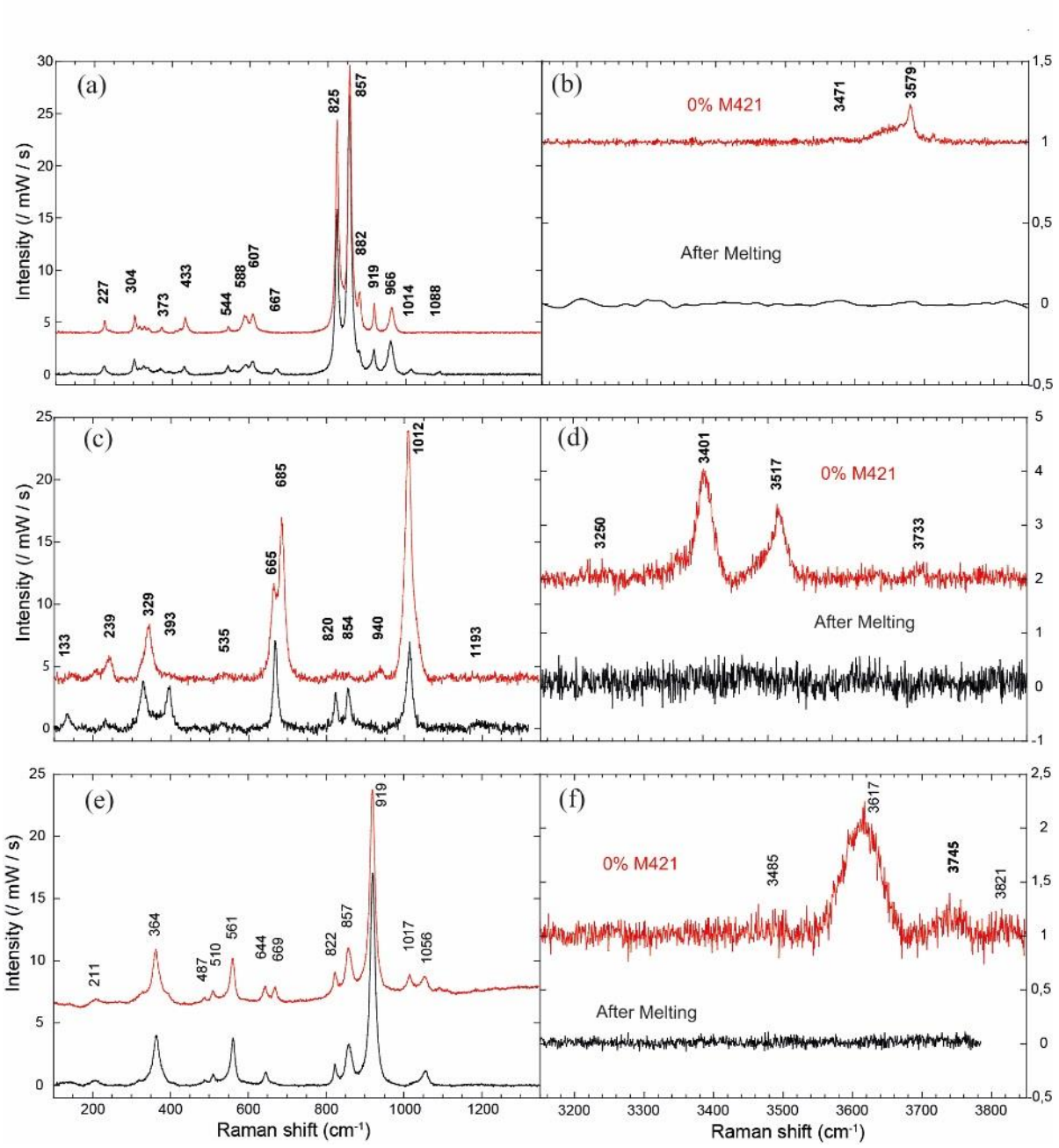

Figure V.S6 Representative Raman spectra from recovered experimental runs at 12 GPa. Red spectra were measured on samples with 600 ppm wt. bulk H_2O contents. The black spectra were acquired on the samples that undergone partial melting. Spectra on the left column (a, c, e) were made on silicate frequency region (200-1200 cm^{-1}) whereas spectra displayed on the right column (b, d, f) were performed on O-H vibration frequency region (3100-3800 cm^{-1}) of olivine, pyroxene and garnet, respectively.

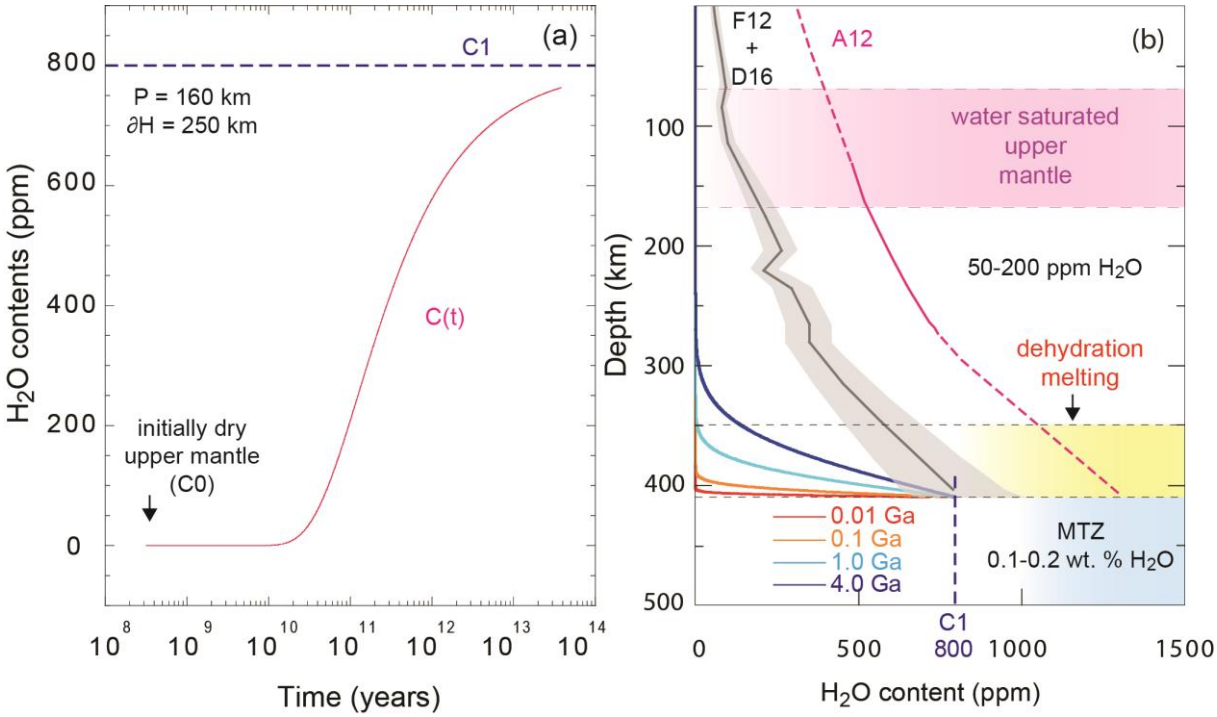

Figure V.S7 Water diffusion calculations for the hydration of Earth's upper mantle. (a). Water concentration profiles as a function of time at depth of 160 km (250 km of diffusion length). The diffusion profile is calculated for an initially dry upper mantle (C_0 = 0 ppm) and considering an olivine peridotite in contact with hydrous melt at 410-km discontinuity with a constant, sustained water concentration C1 = 800 ppm wt. The calculations are based on the diffusion coefficient of 7.89×10^{-9} m^2/s (Novella et al., 2017) at 1723 K (b) Water concentration profiles in the upper mantle for different times of diffusion (0.01 to 4 Ga) for an initially dry upper mantle and 800 ppm wt. olivine peridotite in equilibrium with hydrous melt at the top of the MTZ. The water saturation curves are for peridotite without considering garnet (F12+D16) (Demouchy and Bolfan-Casanova, 2016; Férot and Bolfan-Casanova, 2012) and with considering water partition between olivine and garnet (0.9) (A12) (Ardia et al., 2012). The diffusion profiles even for Earth's time scale can't reach the saturation curve. Diffusion is able to keep large gradients of water concentration in Earth's upper mantle over geological times.

4) Notes and additional information

Additional data that have not been inserted in published work will be provided and commented in this section. This will help to precise the technical aspects of this work as well as results on textural analyses, electrical conductivity results and Raman analyses. Additional discussions on melt and solid chemistry have been made in Freitas, 2016 (M2R thesis) but were not included in this manuscript. They are available upon request (freitas.damien@yahoo.com/Researchgate).

a) Additional experimental data

Table V.1 Sample length and diameter. Samples initial length and diameters were used for electrical conductivity and acoustic wave velocities measurements but were recalculated taking in account both elastic and thermal expansion behavior as explained in chapter III. Size after experiments is provided, however the author did not used this data because decompression cracks can significantly affect the sample as well as polishing issues (possible tilt to sample cylinder axis, cut made on the edges and not center as for M425 and M668 etc.). The % reduction when sample was nicely observed in the recovered run is very close to the original size (up to few %). Experiments without diameter data were not used for EC measurements (failures of SV only).

Sample	Initial length (µm)	Initial diameter (µm)	Estimated length at max T (µm)	Size after experiment (µm)	% variation
M412-7%	963.7	1250.0	938.2	944.2	2.02
M421-0%	763.5	1402.5	748.0	756.7	0.89
M425-2%	1081.0	-	1061.0	878.2	18.80
M456-3.5%	631.0	1100.0	619.1	641.7	1.70
M490-25%	552.5	-	542.7	574.1	3.91
M492-0%	826.8	-	809.2	843.4	2.00
M667-3.6%	504.5	1283.9	501.5	524.3	3.92
M668-6.7%	1222.0	1331.6	1315.4	993.7	18.68

b) Textural information for 6 and 9 GPa experiments

Our previous work (Freitas et al., 2019, Chapter III) highlighted the crucial importance of melt and solid micro-textures for a precise and proper quantification of electrical properties of the material. For these reasons, we performed similar textural analyses as made in our previous works.

In this section, we thus provide more information on texture with additional BSE images and high resolution FEG-SEM BSE microphotographs (appendix B). These images were treated with adapted software to provide binary (squeletonized) images. These images then can be analyzed via FOAMS to provide quantitative data on the textural parameters of each phase. 2D phase proportion can also be retrieved and extrapolated to 3D in cases of favorable phase aspect (Sahagian and Prousievitch, 1998). These results, given in table V.2, are also compared with more simple standard methods such as intercept method to get the average sample grain size.

Table V.2 Textural parameters and modal proportions of starting materials and experiments at 6 and 9 GPa. Each sample texture is quantified using image analysis and FOAMS software on BSE microphotographs, see Freitas et al. (2019), Chapter III for details. % refers to the modal proportion. EqDi corresponds to each phase equivalent diameter (circle of equivalent area) which is for rounded grains a good estimation grain size. Area perimeter long and short axis describes grain aspects (all of these are in mm). Orientation quantify if the angle of long axis with vertical direction (sample cylinder axis). Eccentricity, elongation, aspect ratio and regularity are textural parameters that quantify the geometrical aspects of each phase. N is the number of grains analyzed (on 3-10 images). Avg Gs to the average grain size of the sample obtained by intercept method. On some samples BSE contrast was not good enough to separate Cpx and garnets; they have been treated together in these cases. Each averaged data is followed by the associated standard deviation.

M665 6 GPa starting material													
Olivine	%	EqDi	Area	Perimeter	Long-axis	Short-axis	Orientation	eccentricity	elongation	aspect ratio	regularity	N	AVG GS
AVG	70.22	0.00258	7.06E-06	0.00988	0.00352	0.00215	91.03	0.75	0.24	0.63	0.89	845.00	6.06
STD	4.08	0.00152	9.56E-06	0.00651	0.00208	0.00131	50.46	0.14	0.12	0.16	0.08		0.99
CPX + GT	%	EqDi	Area	Perimeter	Long-axis	Short-axis	Orientation	eccentricity	elongation	aspect ratio	regularity	N	
AVG	29.78	0.00257	7.16E-06	0.00932	0.00344	0.00212	84.85	0.74	0.23	0.64	0.93	312.00	
STD	4.08	0.00158	9.78E-06	0.00656	0.00222	0.00132	51.58	0.14	0.12	0.15	0.06		
M667 6 GPa													
Olivine	%	EqDi	Area	Perimeter	Long-axis	Short-axis	Orientation	eccentricity	elongation	aspect ratio	regularity	N	AVG GS
AVG	69.97	0.00202	4.25E-06	0.00775	0.00270	0.00167	91.60	0.76	0.24	0.62	0.92	442.00	3.11
STD	2.33	0.00112	5.00E-06	0.00458	0.00149	0.00098	46.51	0.13	0.11	0.15	0.06		0.46
CPX	%	EqDi	Area	Perimeter	Long-axis	Short-axis	Orientation	eccentricity	elongation	aspect ratio	regularity	N	
AVG	13.44	0.00150	2.20E-06	0.00568	0.00207	0.00122	88.20	0.76	0.25	0.61	0.91	225.00	
STD	1.26	0.00072	2.45E-06	0.00309	0.00106	0.00061	51.03	0.13	0.13	0.16	0.07		
GT	%	EqDi	Area	Perimeter	Long-axis	Short-axis	Orientation	eccentricity	elongation	aspect ratio	regularity	N	
AVG	13.44	0.00129	1.55E-06	0.00464	0.00171	0.00106	88.96	0.74	0.23	0.64	0.93	300.00	
STD	1.26	0.00056	1.46E-06	0.00220	0.00078	0.00049	44.50	0.15	0.12	0.15	0.06		

Melt	%	EqDi	Area	Perimeter	Long-axis	Short-axis	Orientation	eccentricity	elongation	aspect ratio	regularity	N	
AVG	3.68	0.00057	3.14E-03	0.00521	0.00181	43.03752	50.26	0.87	0.42	0.43	0.61	255.00	
STD	1.86	0.00037	2.63E-03	0.00472	0.00122	23.25648	20.26	0.11	0.18	0.19	0.25		
M666 9 GPa starting material													
Olivine	%	EqDi	Area	Perimeter	Long-axis	Short-axis	Orientation	eccentricity	elongation	aspect ratio	regularity	N	AVG GS
AVG	70.38	0.00281	7.47E-06	0.01057	0.00406	0.00229	91.71	0.78	0.27	0.59	0.88	1848.00	3.24
STD	5.93	0.00127	7.72E-06	0.00579	0.00197	0.00113	43.40	0.14	0.14	0.17	0.08		0.43
CPX + GT	%	EqDi	Area	Perimeter	Long-axis	Short-axis	Orientation	eccentricity	elongation	aspect ratio	regularity	N	
AVG	29.62	0.00215	4.42E-06	0.00744	0.00304	0.00174	95.10	0.77	0.26	0.60	0.90	1841.00	
STD	5.93	0.00100	5.14E-06	0.00413	0.00151	0.00087	42.39	0.14	0.13	0.17	0.07		
M668 9 GPa													
Olivine	%	EqDi	Area	Perimeter	Long-axis	Short-axis	Orientation	eccentricity	elongation	aspect ratio	regularity	N	AVG GS
AVG	64.31	0.00238	5.98E-06	0.00924	0.00320	0.00197	93.03	0.75	0.24	0.62	0.91	471.00	3.47
STD	9.73	0.00136	6.95E-06	0.00563	0.00182	0.00118	45.21	0.15	0.13	0.16	0.08		0.68
CPX + GT	%	EqDi	Area	Perimeter	Long-axis	Short-axis	Orientation	eccentricity	elongation	aspect ratio	regularity	N	
AVG	29.36	0.00143	2.00E-06	0.00494	0.00178	0.00123	88.34	0.66	0.17	0.72	0.95	489.00	
STD	12.82	0.00069	2.05E-06	0.00263	0.00093	0.00060	48.53	0.16	0.10	0.14	0.05		
Melt	%	EqDi	Area	Perimeter	Long-axis	Short-axis	Orientation	eccentricity	elongation	aspect ratio	regularity	N	
AVG	6.33	0.00118	1.78E-06	0.00859	0.00288	0.00122	91.32	0.84	0.39	0.48	0.68	199.00	
STD	1.01	0.00092	4.26E-06	0.01285	0.00291	0.00155	55.21	0.15	0.22	0.23	0.27		

c) Electrical conductivity and conduction processes

i) Results

Electrical conductivity measurements were performed on hydrous (M412, M456, M667 and M668) and dry peridotite (M421) samples. At the desired pressure, i.e. 6, 9 and 12 GPa, the samples were kept at 500 K for more than 12 hours. While maintaining at 500 K, the electrical resistance of each sample was measured along regular intervals and the next heating cycle started once the sample resistance reached a steady value, which is often 1-2 orders of magnitude higher than initial one (Figure V.7). This procedure prevents diffusion of absorbed moisture into the sample at higher temperatures (Manthilake et al., 2009). Sample resistance was measured in several heating-cooling cycles with steps of 50-100 K until the trends were reproducible. This procedure minimizes the uncertainty of impedance measurements.

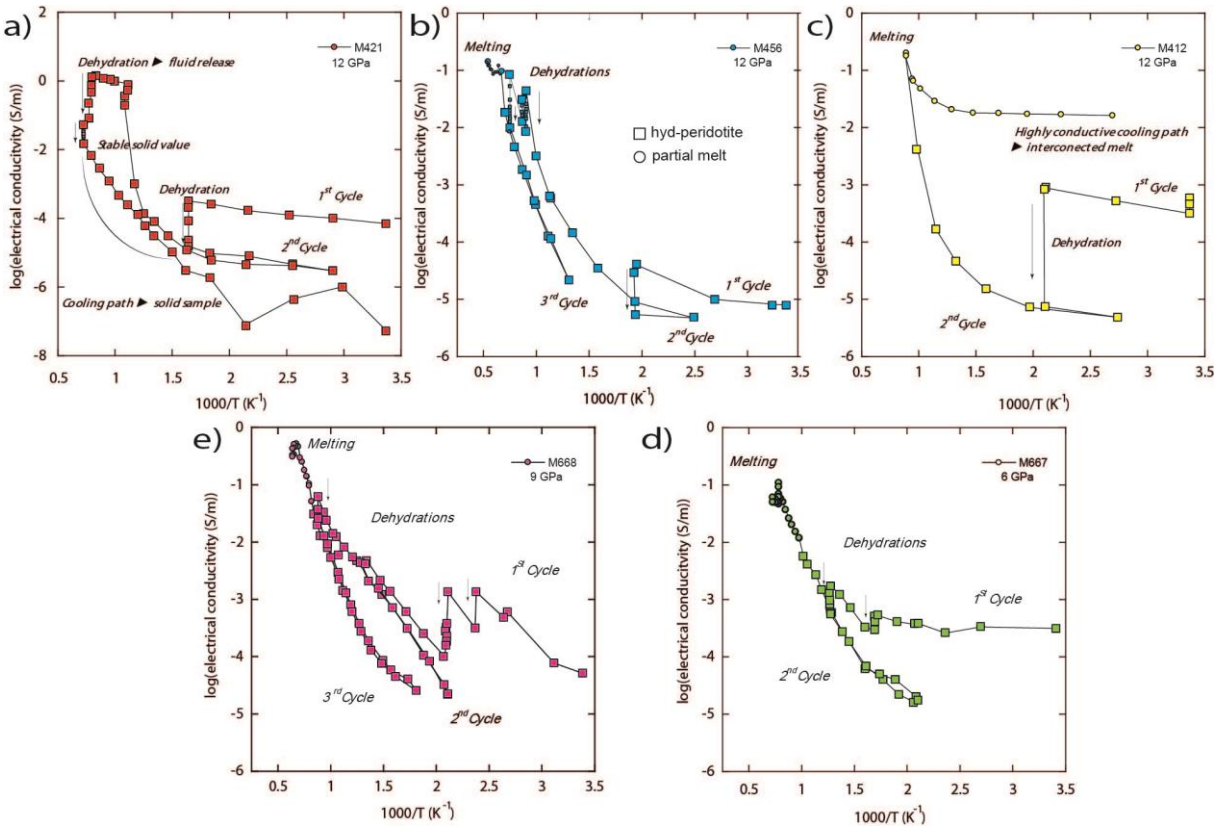

Figure V.7 Complete electrical conductivity data with dehydration cycles. Data measured on solid samples are represented with squared and partially molten samples with filed circles.

Examples of impedance spectra are shown in supplementary materials figure V.S3. Solid peridotite sample Argand diagram presented in figure V.S3 a) illustrate the common behavior of all of our samples between low and their melting temperatures after moisture removal. The nice semi-circular shape of the measurements can be explained with a simple R/CPE equivalent circuit with grains interiors sampled as resistances. The estimated resistance is

obtained with intercept of the circular fit with the abscissa axis. During the first cycles, at low temperature, our impedance spectra show a significant deviation from circular shape with a long persistence of high imaginary values toward low frequencies (figure V.S3 b). This shape of impedance spectra is interpreted as the presence of adsorbed moisture during the preparation of the run. Moisture can also be brought by the surrounding ceramics such as MgO which is known to have a high porosity and can store significant quantity of water (despite prior firing at 1373K). Such Argand diagrams are interpreted as a sum of R/CPE circuit disposed in parallel. Moisture removal process at low temperature is highlighted by a significant decrease of this "shoulder" toward perfectly circular impedance spectra.

When samples were brought to higher temperature, prior reaching their melting point, a new deviation of recovered impedance spectra from semi-circular shape was observed. The high temperatures and the previous reproducible electrical conductivity values at lower temperatures cannot imply adsorbed moisture as a source of the observed pattern (figure V.S3 c) and d). The impedance spectra shows a classical semicircle as observed in the "solid" sample (figure V.S3 a) with a long "tail" at constant impedance value. Such impedance spectra can be explained using a sum of R/CPE equivalent circuit disposed in parallel. This feature can be explained by fluid release of the sample made during the back transformation of wadsleyite into olivine. This transition generates high electrical conductivity values, which can be as high as melting values, but is characterized by a shape similar to "solid" spectra whereas partially molten sample usually provides no clear semicircular shape. The main difference observed with partially molten sample impedance spectra is time varying impedance spectra while keeping at constant temperature, with a strong increase of resistance with time toward solid values. This behavior can be interpreted as the progressive transformation of wadsleyite to olivine which might require some time, given that kinetics are not very high at temperatures slightly above 1000 K. Decreasing and increasing temperature in a new cycle after dehydration provides reproducible "solid" values as highlighted by figure V.S3 b) and c), these impedance spectra must be obtained in the absence of moisture onto a fully back transform sample equilibrated at 12 GPa (Figs. V.7 and V.8).

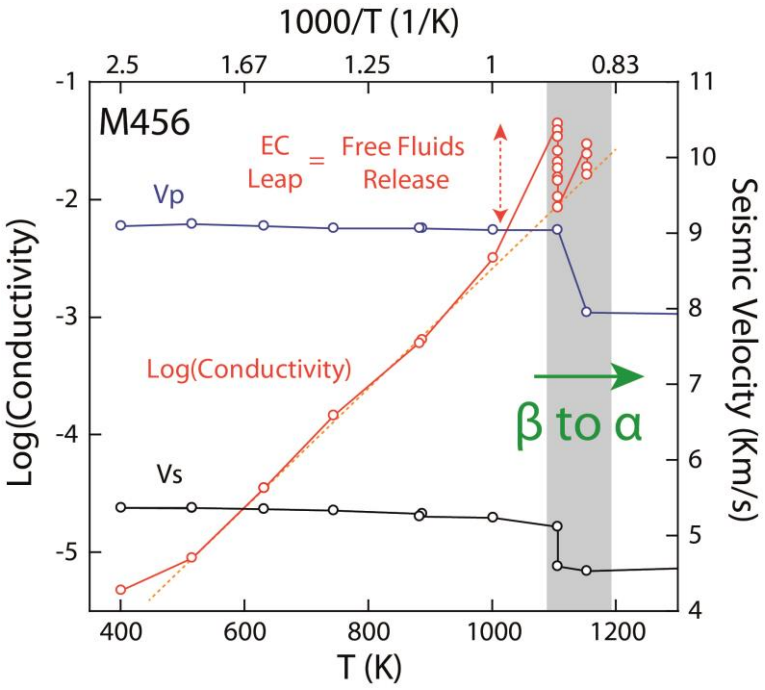

Figure V.8 Electrical conductivity and acoustic wave velocity during phase transformation of wadsleyite into olivine in our experiments (M456) at 12 GPa. EC increase due to fluid release can be easily interpreted as the result of phase transition as highlighted by the seismic velocity decrease.

Once the electrical conductivity along heating and cooling paths became reproducible, the samples were heated until their melting point. The conductivity abrupt increase by an order of magnitude, in hydrous samples, can be attributed to the onset of melting of the sample. The shape of impedance spectra recorded is typical of partially molten systems with a non-circular pattern with a really low resistance. The corresponding equivalent circuit to partially molten system is a bypass circuit with R/CPE circuit, the two resistances corresponding to the grain interior and the fluid/melt respectively. The electrode resistance which can also be seen on some spectra with an increase of values at low frequencies can be modeled as a separated R/CPE circuit connected in parallel to the main bypass circuit (see Fig. V.S3 d). The highest water content exhibits the highest electrical conductivity (Fig. V.7). Nominally dry sample does not have such abrupt conductivity increase. The values before melting vary between -1.73 and -2.3 in logarithmic scale, whereas the partially molten system shows values between -0.72 and -1.00. The melting temperature is accurately monitored by measuring electrical conductivity. It decreases by increasing the water content, and can be as low as 1300 K for few thousands ppm of water.

Such observations are consistent with the observed seismic velocities, where a first seismic velocity drop was observed in the sample between 1000 and 1200 K yielding wadsleyite bearing peridotite velocities to olivine bearing peridotites values. This event

coincides with the electrical conductivity pattern interpreted as fluid release during the transformation. Furthermore, electrical conductivity appears to be a more suitable tool to observe and monitor such kind of transition with a high variation of values in a short time interval. The observed progressive increase of sample resistance allows a fine monitoring of the transition whereas sound velocity does not gave transitional values and shows a more abrupt wd-dominant to ol-dominant transition (Fig. V.8). The dehydration/fluid release pattern observed in the dry sample does not correspond to a melting event due to the absence of any seismic velocity drop and the time varying measured resistance (increase of resistance while keeping at constant temperature). Partial melting occurrence in the hydrous samples, detected with the sudden electrical conductivity increase, is also compatible with the observed sound velocity drop over the probed range of temperature.

ii) Interpretation and conduction mechanism

Most silicate minerals act as insulators at room temperature, but behave at mantle conditions, as semiconductors (Chapter I). In each experiment, Arrhrenian behavior of electrical conductivity were observed in our solid samples (e.g. linear variation of ln(σ) vs 1/T). The slope of the Arrhenius plot (activation enthalpy) changes with increasing temperature, which can be calculated using:

$$\sigma = \sigma_0 e^{\left(\frac{-\Delta H}{kT}\right)}$$

Where σ_0 is the pre-exponential factor, ΔH is the activation enthalpy, k is the Boltzmann constant, and T is the absolute temperature. The fitting parameters for each sample are given in the table V.3. The changes of activation enthalpy indicate a change into the type of conduction mechanism. Below 600 K conductivity values are small and with a very weak activation enthalpy, this suggests that the adsorbed moisture controls the conductivity at low temperatures. At higher temperatures, between 700 K and 1400 K, the activation enthalpy is significantly higher, and the higher activation enthalpy, close to 1 eV, suggests different conduction mechanism, such as protons and small polaron conductions (electron hopping between Fe^{2+} and $Fe^{3+)}$. The effect of water has been proven to have a non-negligible effect on the electrical conductivity of solid compound. Literature data have reported a non-negligible effect of water present in Nominally Anhydrous Minerals (NAM's) for electrical conduction. (Yoshino, 2006) The presence of water should affect mainly proton conduction and has only minor effect on both small polaron and ionic conduction mechanisms as water is less or not involved in the physical process. This effect has been shown for both olivine polymorphs (Poe

et al., 2010; Yoshino, 2010; Manthilake et al., 2009), with a significant increase of EC with increasing water content and also other phases such as pyroxene (Yang, 2012). The presence of water and its effect on the conduction process would be characterized by a lower activation enthalpy.

Table V.3 Sum up of activation enthalpy of solid and partially molten samples.

Run #	M421	M456	M412	M667	M668
P (GPa)	12	12	12	6	9
	Solid EC				
T°range (K)	670-1385	765-1440	630-1131	690-1195	720-1225
DH (kJ/mol)	78.50	92.56	73.65	74.41	85.31
log S_0	0.99	1.51	1.29	2.24	1.82
	Partially molten				
T°range (K)	-	1680-1872	1068-1142	1248-1278	1255-1493
DH (kJ/mol)	-	70.14	139.28	127.39	110.37
log S_0	-	1.11	5.96	4.09	3.59

We can note that our activation enthalpies for our hydrous samples in olivine stability field are similar to values estimated by Dai and Karato (2009). Indeed, they reported water independent activation enthalpy of 88 kJ/mol for their hydrous wadsleyite samples corresponding to proton conduction. Our samples, with different initial water content have very similar activation enthalpies ranging between 74 to 92 kJ/mol. These values are probably too small for small polaron process and somewhat compatible with proton values given by Dai and Karato (2009). The various water content and pressure support the idea of independence activation enthalpy to the absolute water content (bulk from few hundreds to more than 3000 ppm) reinforcing Dai and Karato's conclusions against dependence reported by Yoshino et al. (2008) and Manthilake et al. (2009) probably due to the measurement method and charge build-up at electrodes. The pressure effect seems to be also negligible for water bearing olivine peridotite as no significant different was observed for 6, 9 and 12 GPa experiments.

Melts and partially molten systems are considered as ionically conducting materials. While absolute electrical conductivity was measured at melting temperature for our samples, the temperature dependence of electrical conductivity was not determined. Increase of temperature over a wide range above sample solidus, as commonly performed in EC dedicated studies (Tyburcy and Waff, 1983; Ni et al., 2011), would imply a significant change of melt fraction. Such temperature variation will also lead to an important chemical change

for incompatible elements such as alkalis and water. By consequence, the non Arrhenian behavior of silicate melts observed at low pressure (Khitarov et al., 1970; Presnall et al., 1972; Murase and McBirney, 1973; Waff and Weill, 1975; Tyburczy and Waff, 1983; Ni et al, 2011) can't be confirmed at high pressure. However, the shape of the natural logarithm of electrical conductivity curves in function of temperature does not seem to follow a linear law between values at just prior melting, at melting and just after sample "freezing".

Melt electrical properties are controlled by ions transports in the silicate liquid in particular light alkalis transport, which was demonstrated to be the dominating mechanism (Gaillard and Iacono Marziano, 2005; Ni et al., 2011). Na diffusivity activation energy in basaltic system (Lowry et al., 1982) is roughly equal to activation enthalpies of dry and hydrous basaltic melts. The value of 160 kJ/mol proposed by Lowry et al. (1982) as Na diffusivity activation energy is similar to observed values for both dry and hydrous basaltic systems 120-150 kJ/mol (Tyburcy and Waff, 1983; Ni et al., 2011).

We tried to estimate the values for our partially molten systems. However, because we did not increase the temperature after the onset of melting, the estimation was difficult. The obtained values are provided in the table V.3. Our samples behave nevertheless similarly with a constant slope before melting. Sudden electrical conductivity jumps occurred at melting and reach electrical conductivities higher than 0.1 S/m. At melting, the slope clearly changed and EC is pretty constant at melting temperature. One can see that estimates of activation enthalpies for M456 (~70 kJ/mol) are probably biased by the low number of data points. The values of M412 (thanks to the first "frozen" cooling point), M667 and M668 are more reliable due to the higher number of data points and compatible activation enthalpies were recovered: 139, 127 and 110 kJ/mol. The non-Arrhenian behavior of the system and the absence of measured temperature dependence should mitigate the obtained values that must be considered as a "compatible" to Na activation (above 110 kJ/mol) energy instead of a precise value.

The observed conductivities in our systems are not significantly different than basaltic values despite a significant deviation in major element composition and a much higher volatile content (up to 12% H_2O). Comparison of EC between different melts is not an easy task mainly due to several factors impacting the estimated conductivities: temperature, oxygen fugacity, melt chemistry and its volatile content. The conductivity usually increases by 4 to 5 times for basaltic melt between dry and hydrous melt (4% H_2O) (Ni et al., 2011) and

was reported to be 2-3 times higher for differentiated melt (Gaillard and Marziano, 2005; Pommier et al., 2008; Ni et al., 2011). Our partially molten system isn't comparable to these systems in terms of pressure range and composition, and our current data is probably more affected by the effect of difference of temperatures, pressure, melt fractions and melt chemical composition to see any clear effect of water. However, if electrical conduction is carried by Na diffusion in the melt, other components such as H_2O have a moderate impact at melting temperatures for a binary system. The measured values are compatible with basaltic systems because Na contents in our melts are lower than basaltic melts: average content in MORB have been reported to be 2.80% (Galer and O'Nions, 1986) whereas our melts have reached a maximum of 1.6%. These values encompass several uncertainties as Na measurements with EMP is difficult (migration and diffusion under the electron beam) and is much more difficult to estimate in melt pockets smaller than 20 microns. Similarly with our data, we don't see any significant correlation of pressure with activation enthalpies, this would suggest that the Na diffusivity process in silicate melt should be similar for the whole upper mantle range.

At its melting point, the partially molten peridotite follows an evolution of its texture toward a 3D interconnected melt network. This, evolution is possible to monitor by measuring electrical conductivity at regular intervals since the beginning of fusion (Freitas et al., 2019). The time required to achieve textural maturity is in the order of ten's of minutes. Dihedral angle close to 0 implies complete grain boundary wetting even at really low melt fraction. We observed steady state melt conductivity value in less than fifteen minutes after reaching the melting point suggesting safe observations and obtained values close to equilibrated ones.

The electrical properties of partially molten systems can be modeled using a series of theoretical and empirical laws. The commonly used laws are the Archie's law (Watanabe, 1993) and the Hashin-Shtrikman upper bound or Maxwell model (Waff, 1974) (Chapter I). The equations (chapter I) can be reverted to link the effective conductivity to the ones of solid and liquid with the melt fraction.

$$\sigma_t = \sigma_m + \frac{1 - X_m}{\frac{1}{\sigma_s - \sigma_m} + \frac{X_m}{3\sigma_m}}$$

Where σ_t is the effective conductivity (bulk), σ_s and σ_m solid and liquid conductivities and X_m the melt fraction. Both HS+ and Archie's law are commonly used to calculate, from separate phase, the effective conductivity of the resulting mixture sample (Fig. V.9). Here, knowing the effective conductivity of the sample (measured) and conductivity of the remaining solid,

melt intrinsic conductivity can be estimated. We used the maximum measured electrical conductivity of our samples as the effective conductivity, the melt fraction was chosen in a plausible range for the simulation. The conductivity of the solid was estimated using dry solid sample value (M421) estimated prior melting.

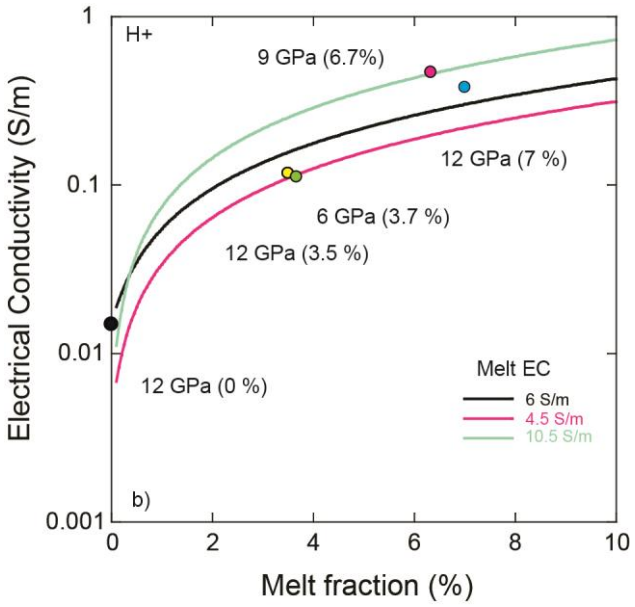

Figure V.9 Electrical conductivity of our samples represented as a function of melt fraction. Our different samples are represented with the color circles. Models of Hashin-Shtrikman upper bound are represented using different assumed melt conductivities σ_m (colors). Solid sample values used are M421 measurements (melt free sample), the values observed from molten samples are in good agreement with melt conductivities between 4.5 and 6S/m for both theoretical laws. Our molten samples are not aligned on the same trend due to the variation of melt chemistry while increasing the melt fraction and pressure effects. Realistic melt fraction implied in the LVZ will produce higher electrical conductivity melts (> 6S/m)

The results of this inversion are given in the figures V.9 and V.10. The values obtained for melt conductivities range between 3 to 5 S/m, which is compatible with dry basaltic melt and hydrous differentiated but much less than hydrous basalt. The commonly estimated high pressure melt conductivities of 6 S/m for numerical modeling can be verified (Toffelmier and Tyburczy, 2007).

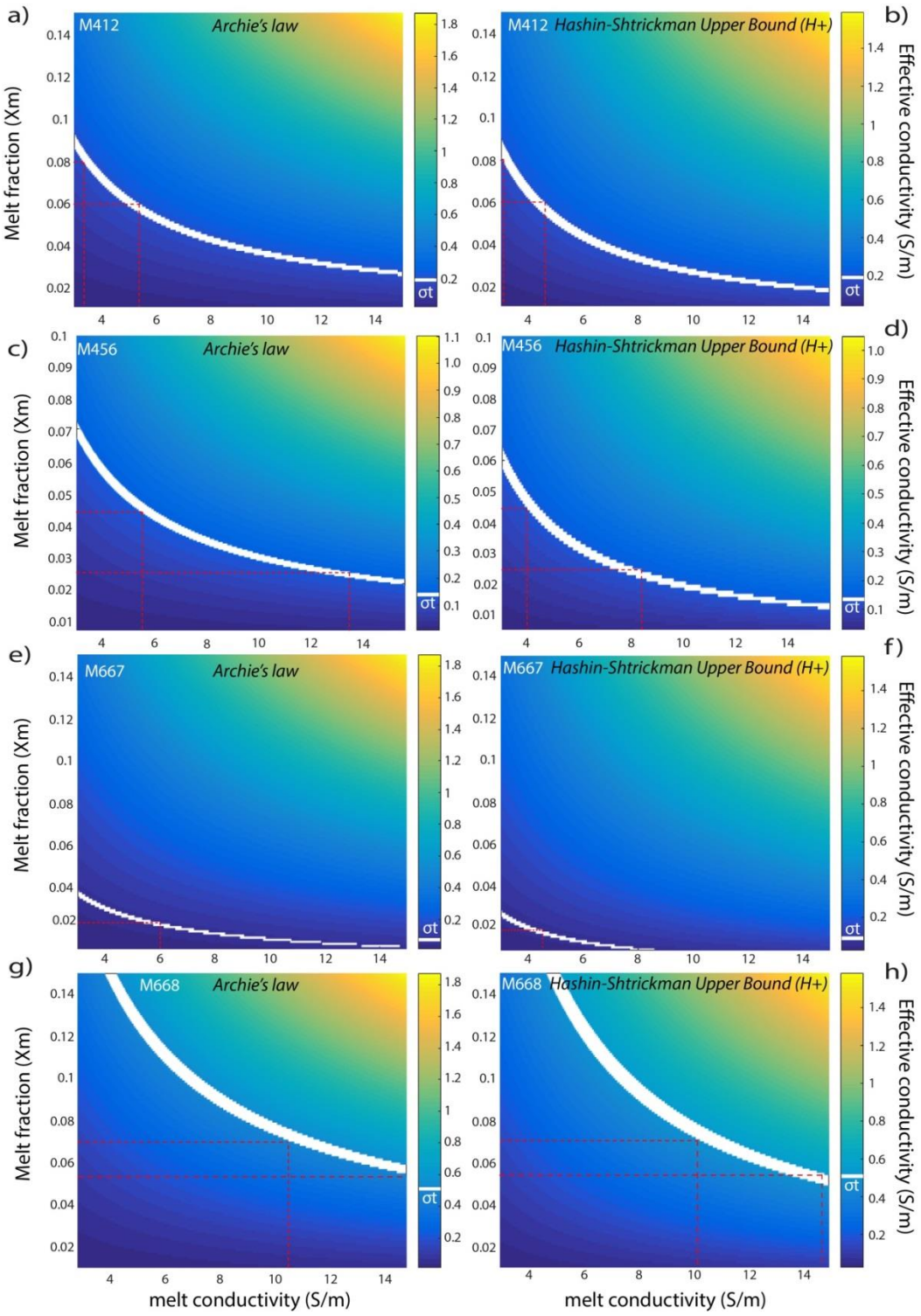

Figure V.10 Calculated (bulk) effective's conductivities for varying melt fraction and melt conductivity based on two different models: the Archie's law (left column) and Hashin-Shtrikman upper bound (H+) (right column). The color bar represents the effective conductivity for the different melt fractions and melts conductivities. The white area corresponds to the effective (bulk) conductivities measured on 12GPa samples: M412 (a and b), M456 (right frames); 6 Gpa sample (M667, e and f) and 9 GPa sample (M668, g and h) within an error of 5%. The values of measured effective conductivity (σ_t) are also represented in the color bar. The red dash lines represent the possible range of melt conductivities inferred from measured melt fractions in our recovered samples. The values are calculated considering the maximum and minimum possible melt fractions for each sample (measured value in %) ± 1%).

d) Electrodes reactions and oxygen fugacity

We checked possible electrodes reactions with our samples with SEM apparatus and doing chemical maps. Most of our samples do not have any reactions with electrodes (Fig V.11 a and b) molybdenum or rhenium staying metallic, without strong diffusion of other elements into them due to the restricted time spent at high temperature. Only experiments at very high temperature show limited reaction with electrodes, forming MoO_2 or ReO_2 (c and d). This reaction might happen at the highest temperatures and associated melting. No significant disturbance of electrical conductivity signal with time was observed (during the limited time spent at high temperatures << 1h).

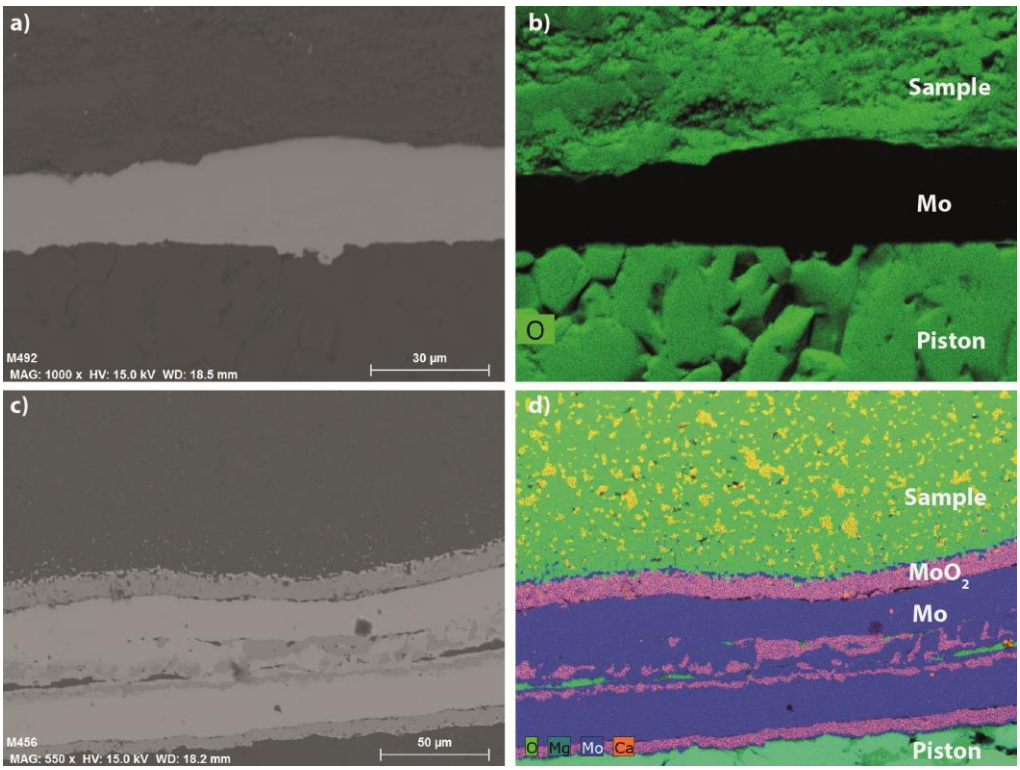

Figure V.11 Electrodes with SEM apparatus and doing chemical maps. Most of our samples do not have any reactions with electrodes (a and b). Only experiments with large melt fractions display limited reaction with electrodes forming MoO_2 or ReO_2 electrodes (c and d).

The electrode state is also a good constrain for oxygen fugacity in our samples with values lower than or at Mo-MoO_2 and Re-ReO_2 buffers. The oxygen fugacity cannot be controlled in our open capsule experiments. However, the absence of reaction (or moderate) indicates conditions that are not too oxidizing which may be compatible with upper mantle values around NNO buffer because Re-ReO_2 is considered as slightly higher than NNO (Xiong and Wood, 1999) and Mo-MoO_2 located between CCO and IW (Sokol et al., 2010). Using experimental calibrations and their pressure and temperature dependence via polynomial fits,

we calculated the most common buffers at 10 GPa as a function of temperature (Fig V.12). The upper mantle with temperature between 1300 and 1500 K was estimated to have oxygen fugacity's lower than FMQ buffer (around FMQ-2 for oceanic mantle at 1 GPa and lower with increasing depths) and absolutes log values between -2 and -5. Our experiments are below or at Re-ReO2 and Mo- (-2 to -10) and then are coherent with the bottom of upper mantle quite reducing values.

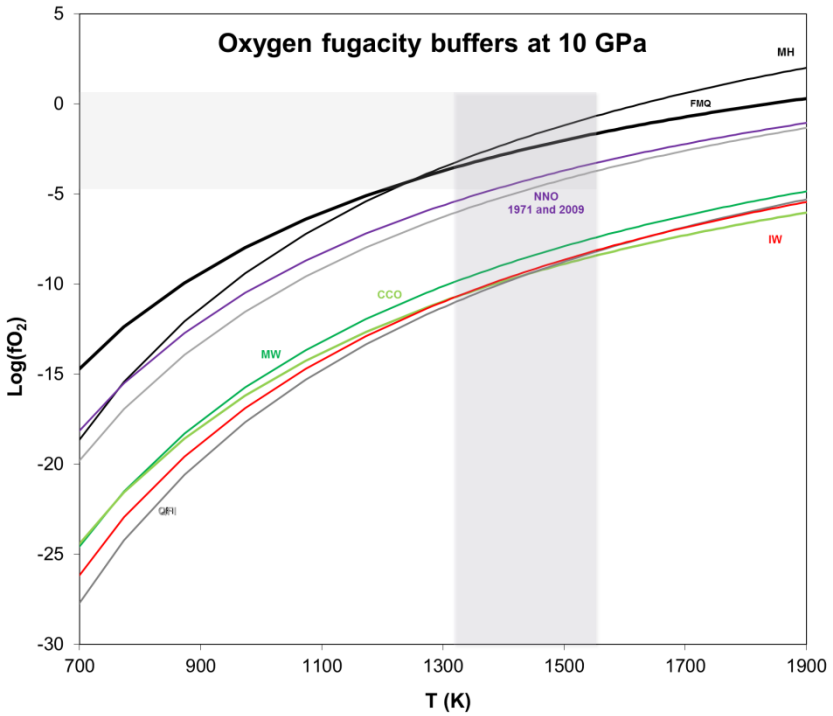

Figure V.12 Oxygen fugacity buffers at 10 GPa. Values were calculated only for most representative buffers with known pressures and temperatures parametrizations. IW (red) corresponds to Fe-Feo buffer (Hübner, 1971), MW for magnetite (Fe_3O_4)-wustite (FeO) buffer (Hübner, 1971), MH to magnetite (Fe_3O_4) hematite (Fe_2O_3) CCO to C-CO-CO_2 buffer, NNO to Ni-NiO buffer (Hübner, 1971 and Campbell et al., 2009), FMQ to quartz-Fayalite-Magnetite buffer (Hübner, 1971) and QFI for Quartz-Iron-Fayalite buffer (O'Neil and Wall., 1987).

e) Raman analyses and water contents estimations

In the published work, Raman spectra of low melting rate melts and their water quantification was given. In this section other useful details on the analysis performed on recovered runs, syntheses and EC/SV experiments are provided. Most of our Raman analyses would not have been possible without the significant contribution of F. Schiavi.

i) Starting materials: analyses of 14 GPa syntheses

Analyses on hydrous and "dry" starting materials (M410 & M482) composed of wadsleyite, majorite and clinopyroxene were performed by micro Raman. As wadsleyite was only the water bearing phase for which we got standards, only this phase was quantified.

Majorite and Clinopyroxene were not quantified due to the lack of appropriate standards. Thus, the water bearing phase for peridotites composition at 14 GPa is wadsleyite, mainly due to its very high solubility (Kohlstedt et al., 1996) and its major proportion (60% minimum).

The results after baseline correction and counting time normalization demonstrated that, despite the theoretically low anisotropy of the wadsleyite, water and silicate spectra are varying importantly according to grain orientation (Martinek and Bolfan Casanova, submitted). The indexed silicate peaks are in good agreement with the literature even if some peaks at 410, 471, 1004 and 1015 cm^{-1} are not described. 471 cm^{-1} seems to be due to the Neon light. The other peaks are not well documented especially above 920 cm^{-1}.

The water quantification was realized with the external calibration method similar to Bolfan-Casanova et al. (2014) with known wadsleyite standards (FTIR, ERDA and/or SIMS) kindly provided by N. Bolfan-Casanova. Once the OH/Si ratio was determined for each grain, the calibration was applied with respect to standard values. The data were treated with two methods, the first one on the raw data and the second one by adding a Fourier transform before doing the baseline correction with similar results. We considered for quantifications the average of the two values. The standard deviation of our final value is important (> 10%), but we consider this as a proof for our data-set to probe several grain orientations. This ensure a good statistics, and, by consequence, a value of water content closer to the real one.

The water content of wadsleyite in the starting martial (M410) was estimated to be 5445.76 ± 660 ppm wt (Fig. V.13, Appendix Table A.8). The bulk water content of the starting material can be calculated by assuming that the assembly at 14 GPa is made of 60% wadsleyite and 40% Cpx + majorite, and that the Cpx + majorite mixture is moderately hydrous (500 ppm). The calculated bulk water content is 3467 ppm wt. with an uncertainty in the order of 1000 ppm wt. given that majorite and Cpx water contents are unknown.

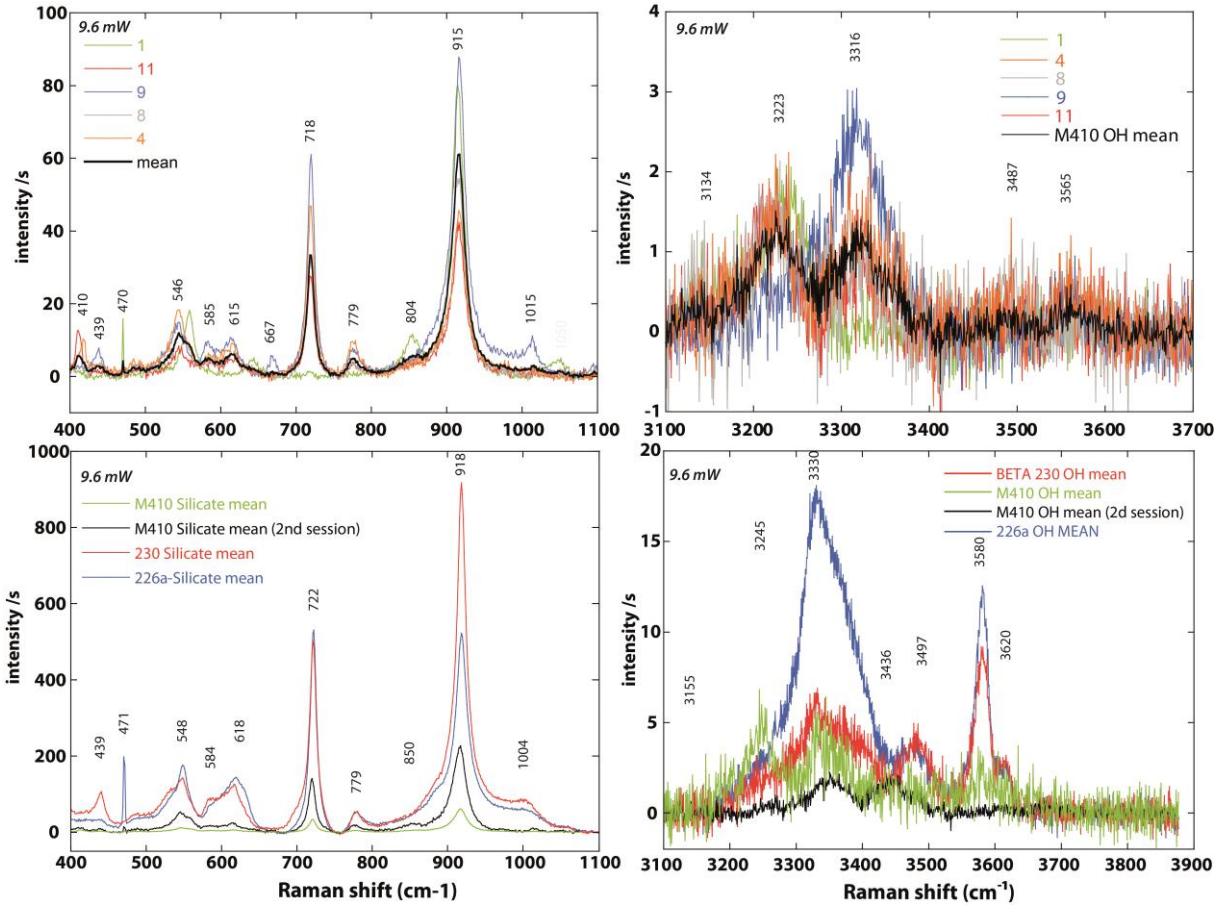

Figure V.13 Raman spectra of the wadsleyite of our starting material synthesized at 14 GPa (M410). A & B) Graphs showing silicate (A) and OH (B) stretching vibrations for multiple grains (in color) and their average spectrum (thick black line). C & D) Comparison graphs for Si and OH regions between the M410 averaged spectra from our first (black) and second (green) session of analyses and the two averaged standards spectra: 230 (red) having 0.10 wt.% H_2O and 226a (blue) having 0.42 wt.% H_2O.

This value is important compared to the initial amount of structural water provided by the starting powders. It highlights that the control of the water content is not trivial.

The dry wadsleyite sample was synthesized in two steps. In a first run, at low pressure, the "dry" sample was synthesized into rhenium capsule in olivine field at 2 GPa to ensure a low water solubility (M481). The recovered sample was inserted in a second run at wadsleyite stability field at 14 GPa in Au-Pd capsule with a Si metal buffer to lower the oxygen fugacity and water incorporation. The finally synthesized samples was recovered and analyzed with Raman spectroscopy. The estimated water content of wadsleyite was: 773 ± 537 ppm of water (Table A.9, Figure A.4). This can be translated to 500 - 700 ppm considering the other phases are between 0 and 400 ppm.

ii) Analyses of recovered runs at 12 GPa

Crystalline phases were analyzed to ensure their structures, chemistry as well as estimating qualitatively their water content. Representative spectra of the crystalline phases are shown in supplementary figures V.S4, V.S5 and V.S6. For each phase, both Raman spectra of water-bearing and water-free grains are reported for comparison. For olivine, the silicate spectra are similar with small variations due to the anisotropy. The peaks observed are in agreement with the literature even if the peaks between 300 and 500 cm^{-1} and above 900 cm^{-1} are usually not documented. Peaks in the OH region are consistent with observations of Bolfan-Casanova et al. (2014): 3579 and 3471 cm^{-1}. The water bearing samples were those which did not underwent partial melting. This observation is coherent with water loss into the melt due to a favorable partition coefficient.

The analyzed pyroxenes were trending from diopsidic to enstatitic compositions. Their silicate spectra indicate that the crystals have kept their Clinopyroxene structure but were depleted in their incompatible elements (clino-enstatite). All the residual pyroxenes were close to clino-enstatite with the exception for Cpx in the samples that did not melt. For OH bands, clear spectra with peaks at: 3250, 3401, 3517 and 3733 cm^{-1} were observed.

The silicate region of garnets is similar for all the samples, whereas the water content is variable with significant intensities only in the starting materials and unmolten samples. The peaks observed in the OH regions are shifted to higher values compared to the literature, with peaks at: 3617, 3745 and 3821 cm^{-1}.

The samples which underwent partial melting had high initial water contents. Raman spectra of the residual crystalline phases of recovered runs (olivine, pyroxene and garnet) indicate low water content, if not dry. This attests the loss of the defect/structural water from the crystalline phases upon melting. At the opposite, the initially “dry” samples, which did not melt during EC/SV runs, kept hydrous NAM phases (M421 and M492, Figs. V.S6 and A.5). The initial water content was too low to enhance dehydration melting during the phase transition.

Based on the method of Bolfan-Casanova et al. (2014), we tried to quantify the water content in our olivines with micro-Raman. Because the Raman apparatus used in this reference is different than LMV’s apparatus, the calibration curve has to be re-made (Martinek, 2019). To do that, a sample with high water content was provided by N. Bolfan-

Casaonova, quantified by ERDA, and used as a calibration curve with origin point (Figs. A.5 and A6). The OH/Si ratio vs. water content relationship must be linear. The recent work of Martinek (2019) helped improving the method and reducing the error bars by considering anisotropic effects. For time reasons and apparatus availability, such detailed study has not been made on our samples. However, we used some insights from this work, each sample analysis is an average of at least 5 to 10 grains both in silicate and OH frequency region, measurements in 2 perpendicular directions were made to statistically probe all the orientations and provide averaged values. We did not subtract the effect of anisotropy, this is why our errors are pretty large as a results of anisotropy (Ishibashi et al., 2008), the real errors, coming for apparatus (random errors, fluorescence perturbations) and spectra treatments (standardized baselines), are usually less than 20 %. Samples: M412, M425 and M456 had flat spectra in OH frequency regions and so were not directly quantified. The water contents of olivines in these samples are then probably inferior to 250 ppm (~detection limit). Problems associated to very small grain size (~5µm) were also observed with theses samples, where we used high confocality and low laser power (5% - 8 mW) setting for optimal analyses.

M421, ”dry” sample synthesized in the olivine field at 5 GPa and measured at 12 GPa, contains, after the two experiments, 751 ± 289 ppm. M492 the “dry” sample, synthesized in wadsleyite field at 14 GPa and characterized at 12 GPa, kept a low water content with 397 ± 140 ppm after the experiments.

For sample with large initial water content, such as M490 (~25% melt), the water content of olivine varies importantly (large error bar) and was estimated to have 1042 ± 450 ppm of water. This value is high considering water should partition into the melt (probably contamination).

The Raman estimations on olivine can be further used to give a rough budget of total water content of an experiment. Using water content estimated in olivine and mineral/mineral and mineral/melt water partition coefficient of hydrous systems at high pressure (Novella et al., 2014) and the modal proportion (surface analyses), the bulk water content can be estimated. In reality, the errors on estimated water content in olivine are large, and prevent a proper comparison for bulk water contents. For partially molten samples, the budget is usually bad when melt water content has not been measured. The results are given in the Appendix A (tables A.10 and A.11). The un-molten samples bulk contents estimated are coherent with

under saturated values whereas partially molten ones (samples with quantified melts) have content close to starting material estimations (~3000 ppm).

iii) Analyses on starting materials and recovered runs at 6 and 9 GPa:

For syntheses at lower pressures, 6 and 9 GPa, similar analyses were realized. Both synthesized and recovered runs spectra are provided in figures V.S4 and V.S5. The water contents in olivine are similar between 6 and 9 GPa syntheses. After the HP/HT experiments, these contents are way lower (Fig. A.6), due to the onset of melting during the EC/SV runs. However, the associated errors are very large. This can be explained by anisotropy effect and fitting errors, but they can only explain ~half of the observed dispersion (Martinek and Bolfan-Casanova, submitted). It appears that our starting samples are not fully homogenized in terms of water distribution after 1 to 2h at modest temperatures (~1000 K). Important variations can also be due to the small grain size (< 5 µm both before and after) which makes the Raman analysis difficult. M668 seems to have less water in olivine than M667, which is coherent with the higher melt fraction (Fig. A.6).

Water budget analysis was made using estimated olivine contents for both starting and recovered runs. For partially molten samples, the budget is usually bad because melt water content has not been measured and there are important errors in olivine estimations (table A.12).

iv) Melts

The melt water content was estimated successfully via micro-Raman for some of our samples (M412, M425 and M490) (Chapter IV). Their water content was calibrated against the water content of basaltic glass standards. Due to differences in compositions and structures between samples and standards, they may be affected by large errors. The treatment procedure and calibration is given in the published articles (Freitas et al., 2017; Schiavi et al., 2018). A complete study on melt water characterization is nicely described by Schiavi et al. (2018).

For larger melt fraction samples M412 (7%) and M490 (25%), several peaks were observed. They are mainly due to quench crystallization of pyroxenes and olivine. The silicate region of the remaining glass is very similar to pyroxene but peaks are broader. In the water frequency region, the peaks are very large. In addition, we observed presence of both melt and pyroxene peaks. For these sample, we preferred to absolute OH intensity of the water band

area as calibration because silicate spectra is polluted by pyroxene peaks, however, the OH/Si method gave similar results.

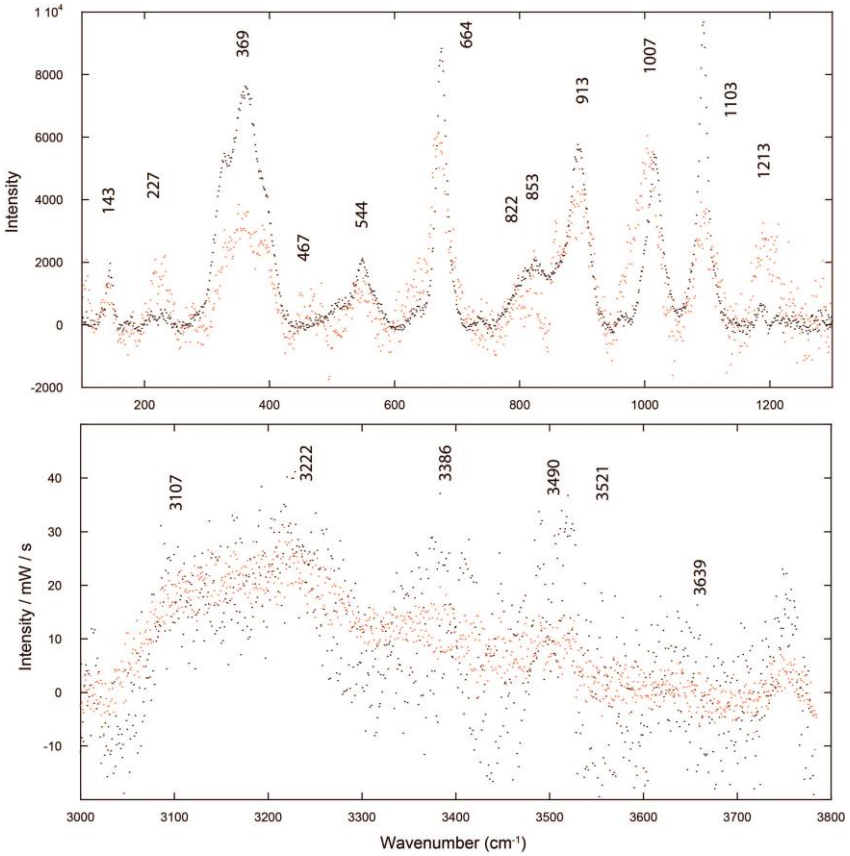

Figure V.14 Raman spectra collected in the residual melt (+ quench crystals) of M412 for both silicate frequency region (top) and OH region (bottom).

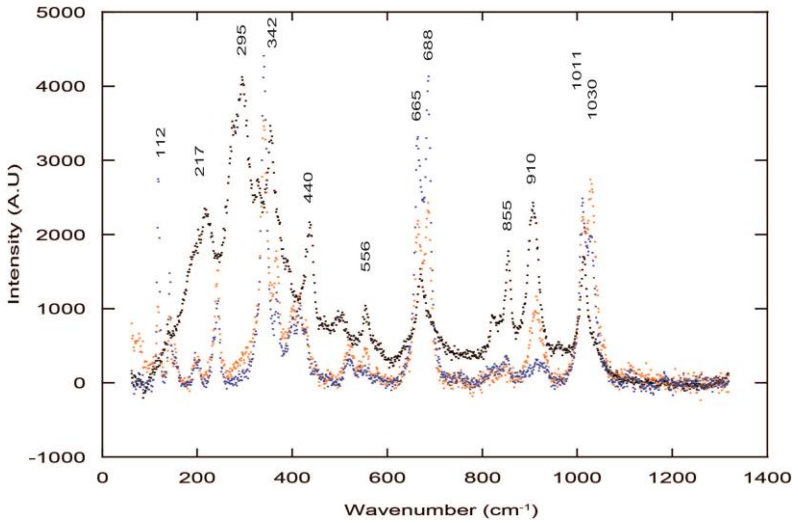

Figure V.15 Raman spectra collected on the residual melt and quenched crystals of M490 (olivine and pyroxene mainly) for silicate frequency region.

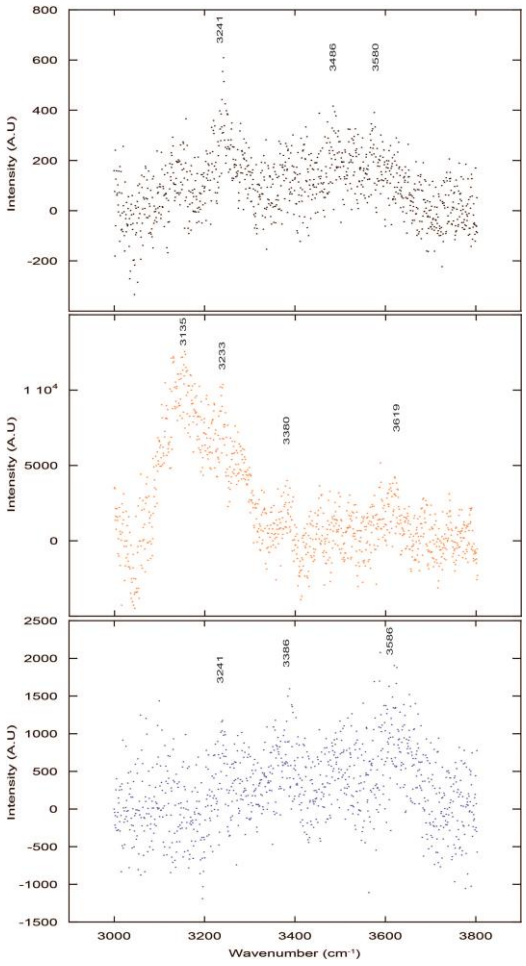

Figure V.16 Raman spectra collected on the residual melt and quenched crystals of M490 (olivine and pyroxene mainly) for OH bands frequency region.

f) Geochemical implications

The presence of a global melt layer above the mantle transition at a somewhat global scale should have a strong impact on our understanding of the mantle dynamics as well as its differentiation. In fact, as highlighted by Bercovici and Karato (2003) and Karato et al. (2006), some simple calculations can be performed to test if the chemical differentiation of the mantle can be reconciled with single convection cell. In this discussion, only trace elements will be discussed, further implications for isotopic ratios can be found in the above cited references and Hofmann (2003).

The geochemistry of OIB and MORB components are significantly different in term of trace elements, with an enrichment of highly incompatible in OIB compared to relatively depleted MORB. This variation comes from the depleted mantle source of the MORB in comparison with OIB's sources. Here, we performed simple calculations, using the melt fraction inferred from geophysical and experimental constrains, to create the depleted mantle

using the LVZ above the MTZ. Our estimation uses the following assumptions: 1) Earth's composition is chondritic. 2) The primitive mantle was affected by a partial melting and the extraction of the continental crust early in its history producing 0.6% of crust and resulting a depletion of almost 33.3% of the mantle (Workman and Hart, 2005). 3) The resulting mantle is composed of a depleted reservoir, which is the source of the MORB and so should be present at shallow depths. 4) At higher depths, a part of primitive/less depleted mantle is still preserved and is sampled via the OIB.

The "deep mantle" component will cross the MTZ via the passive upwelling and undergo between 0.4 to 3% partial melting (our estimation for observed ∂Vs between 2 and 9%; Revenaugh and Sipkin, 1994; Tauzin et al., 2010; Freitas et al., 2017; Freitas and Manthilake, 2019). Our calculations based on melt chemistry highlighted that the produced melts will be denser than the upper mantle. Thus, it will tend to be recycled back into the MTZ (Leahy and Bercovici, 2007) and only residues will passively upwell feeding the upper mantle in deep materials. The upper mantle is then progressively fed by this material. Such material is no more primitive due to the LVL action but not as "depleted" as MORB mantle due to the small melting ranges. However, the residual upwelling mantle will probably encounter the second important melting zone in the upper mantle the LVZ. Again the rocks will undergo partial melting for different possible reasons such as changes in appearance/disappearance of K-hollandite (Manthilake et al., in review), orthopyroxene structure (Mierdel et al., 2007) and induced water saturation (Freitas and Manthilake, 2019). This material will continue to ascend to produce MORB lavas and will be depleted in incompatible elements due to these several events of melting.

To realize this simulation, we used the primitive mantle values and N-MORB average from Hofmann (1988), DMM from Workman and Hart (2005), Hawaii, and MORB from Hofmann (1997), the partition coefficient from Hauri et al. (1994) and Alphamelt default values from McKenzie and O'Nions (1991), Blundy and Wood (2003), Wood and Blundy (1997) and the compatibility order from Hofmann (1997) and Karato et al. (2006). The bulk partition coefficients were calculated assuming the following modal proportion for the 350' LVL (60% Ol, 30% Gt, 10% Cpx) and for shallower LVZ (54% Ol, 28% Opx, 13% Cpx and 2% of Sp). The partition coefficients were only available for modest pressures and volatile poor systems. Despite the effect of pressure was shown to be modest (Taura et al., 1998) and similar to water effect (Wood and Blundy, 2002), partitions coefficients do not exist at the

pressures and conditions required for this 350 LVZ melting. We tried both batch and fractional melting with the 2 sets of partition coefficients (Fig. V.17).

The effect of 350 km LVL is to generate melts which are highly enriched in incompatibles and heat producing elements such as U, Th and Pb which will be stored at depth and removed from the residue. We can see that liquids produced are way more enriched than MORB lavas and have almost the same values than Hawaii lavas in magnitude. But our calculated lavas show a positive anomaly in Pb and higher incompatible elements concentrations than Hawaii OIB but also lower compatible values. To our knowledge, no melt from any hotspot/OIB shows these patterns. This suggests that no primitive mantle fusion, at low degree of melting from these depths, is directly sampled or it should be affected by ascending mixing/crystallization, etc. Residues produced have close values to MORB mantle for values around 3% of batch/fractional melting. Thus, it is possible to produce DMM mantle simply using the filter characteristics from a primitive material. This process is able to feed the upper part of the upper mantle in depleted materials via partial melting and segregation of the upwelling light residual mantle and sinking denser melt.

In the case of the asthenosphere LVZ, partial melting occurs with rates estimated to be 0.2 to 0.5% on the previous residue (made of olivine, Cpx, Opx and spinel). We choose to use fractional melting because it is the most plausible process given that the melt is buoyant at these depths. The drawback of this method implies that calculations for highly incompatible elements such as U, Th, and Pb with bulk $D < 10^{-2}$ are not calculable as the values tend to zero. We got a possible range with the melting at 0.2% of the less depleted residue, that previously undergone 0.4% of melting, which kept the higher incompatible trace elements concentration, and the most depleted composition with 0.5% melting of the residue previously affected by 3% of fusion. We can see that the ranges of the liquids produced are within the MORB composition and that residues are more depleted or close to the DMM. Both should show the Pb anomaly as highly incompatible elements depletion because they were mostly removed by the first fusion episode (Fig. V.17).

This calculation demonstrates that we are able to reproduce the MORB mantle with the estimated melt fraction starting from primitive preserved (OIB like source) mantle without requiring any solid layering of the mantle. The melt produced in depth is able to store incompatible elements as the heat producers and water and recycle it in the MTZ. If the residual DMM undergo fractional melting again at the shallower asthenosphere with really

low rates, MORB-like liquids can be generated as well as leaving a strongly depleted residual mantle. The 350 LVL is able to be a reservoir for highly incompatible elements explaining the noble gas paradox (He/Ar) (details in Karato et al. (2006) for isotopic consideration) and concentrate most of the Earth heat source element (U, Th, K) in the MTZ which can play an important role in the estimated bulk Earth thermal budget.

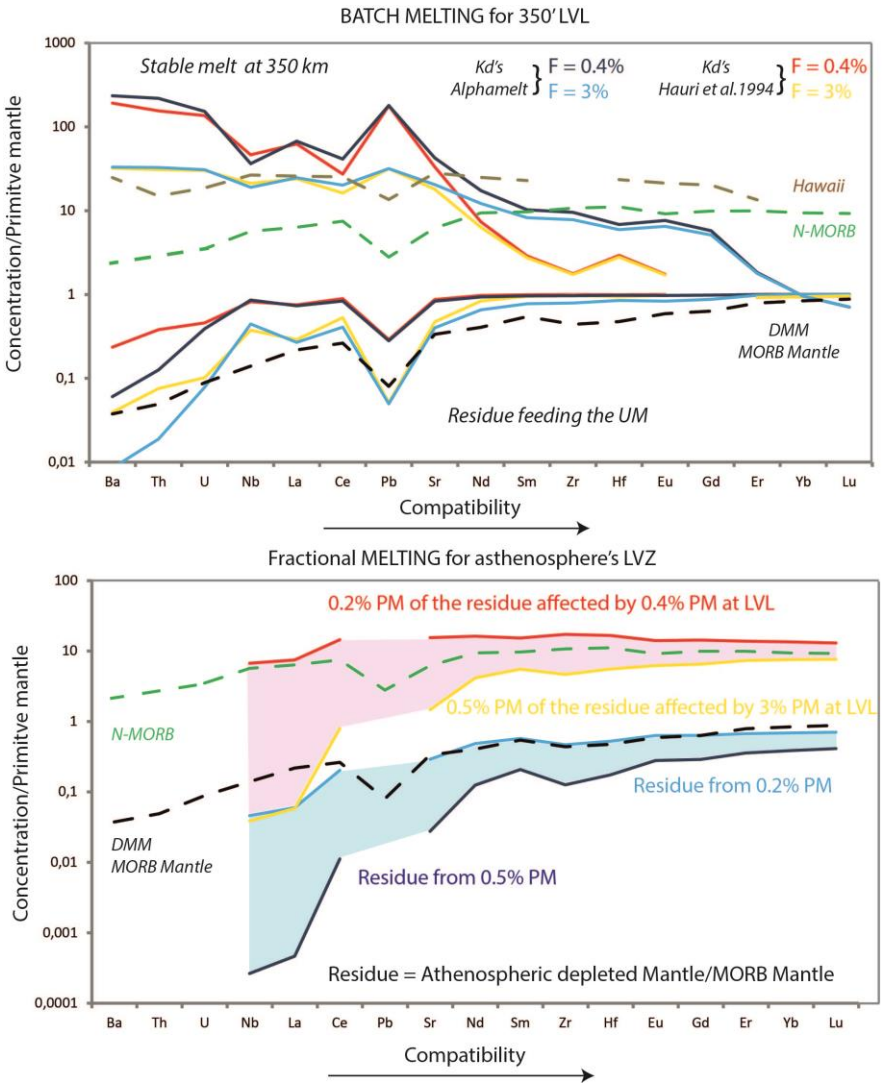

Figure V.17 A) Geochemical trace elements estimations for a batch partial melting at the LVL. Fractions between 0.4 - 3% were used, producing residual mantle close to DMM and liquids close to Hawaii OIB lavas (deep mantle source). We can note that no significant differences were found by choosing batch of fractional melting for this melting step. Thus, we chose batch melting representation for simplicity. ***1)*** *Melts spectra are visible in the part with concentrations > 1. The residues are the respective spectra by symmetry to the y=1 line (representing the primitive mantle, our starting material).* ***2)*** *0.4% and 3% of melting are represented by the red and yellow curves respectively, using Kd's from Hauri et al. (1994). The same melt fraction using Alphamelt default Kd's values (Blundy and Wood, 2003; McKenzie and O'Nions, 1991; Wood and Blundy, 1997) are shown in dark and light blue for 0.4 and 3% of melt fraction, respectively.* ***B)*** *The second figure represents fractional melting trace element spectra of the previous residues (from* ***A****) with the rates obtained the shallow asthenosphere LVZ (0.2 to 0.5%) (Freitas et al., 2019). The possible areas are shaded suggesting creation of MORB like liquids and more depleted or equivalent residual mantle. Calculated melt range is shown by pink shadowed area whereas residues ranges are by the blue one. Both areas are delimited by the most enriched liquid/residue and the most depleted ones due to the possible melt fractions of the two melting steps. For both* ***A)*** *and* ***B)*** *MORB and Hawaii trace concentrations are from Hofmann (1997) and DMM ones from Workman and Hart (2005).*

5) Summary

The interpretation of geomagnetic profiles of Earth's upper mantle requires experimental constrains due to the lack of natural samples. In this work, we measured electrical conductivity of peridotites and their partial melts in realistic melting process and compositions. Our experiments highlight that the upper mantle must be hydrous but remain unmolten except at two specific zones: low velocity zone between 75 and 150 km and the low velocity layer between 350 and 410 km deep.

The presence and the intensity of partial melting by dehydration during wadsleyite to olivine phase transition translate directly the water content of the MTZ. Geophysical observations are then coherent with moderately hydrated MTZ (1000 - 3000 ppm H_2O) whereas the uppermost mantle has been shown to have only 50 - 150 ppm. This difference motivated the development of bottom-up hydration model in which we investigated the possible mechanisms such as diffusion or upwelling and their consequence over geological times.

Our models are made using very large assumptions on both geodynamical parameters (subduction rate constant through geological time, age of the onset of modern tectonic plates etc.) and physical parameters (diffusion coefficient at 1723 K, constant concentration in the MTZ etc.), however their use in a constrained framework by natural observations, experiments and models highlight that realistic scenarios can be inferred. These scenarios imply a moderately hydrous MTZ (< 1500 ppm) and allow a stable LVL over times. Our calculation also shows that with a rather small diffusion compared to geological distances, large water gradients are expected both in MTZ and upper mantle with consequence of possible partial melting in localized areas in the upper mantle.

6) Perspectives

Perspectives on the melt layer located above the MTZ, its acoustic wave velocity characterization and chemical characteristics have been already discussed in the perspective of the previous chapter. Hence, in this section, we will try to give perspective more specific to electrical conductivity measurements and global water circulation model through geological times.

a) Electrical properties of melts and solids at high pressure

The electrical properties of melts are starting to be pretty well known for different types of composition, volatile content and ranges of pressure and temperatures (Tyburcy and Waff ,1989; Ni et al., 2011; Gaillard et al., 2008, Yoshino et al., 2010). These studies measured both silicate and carbonatite melts with a quite wide range of composition. In addition, this study shows that our melts, with somewhat different composition have conductivities that are compatible with previous estimations and that volatiles have important effect but never overcome the effects of changing from silicate to carbonatite melts.

A detailed characterization of electrical conductivity of melts at very high pressure with these extreme conditions would be of significant interest even if these experiments will be difficult (water rich melt are usually very aggressive for metallic electrodes, which can be a problem for 100% melt measurements). However, it would be very interesting to measure electrical conductivity of mixture of solids and melts for different melt fractions with a constant composition to check if Archie's law or HS+ models are still valid for these conditions. In fact, electrical conductivity of melt inferred here is an "averaged" or "integrated" value because both chemistry of melts and solids are function of the melt fraction. Thus, the inferred melt conductivity from fitting law based on physical models is an integration of the whole chemical range and conductivities explored in our experiments. This is why significant deviation from perfect fits was observed.

In addition, it seems that the pressure of melting will have a great effect on the phase contribution and so melt chemistry. A detailed study investigating the effect of pressure on the composition of the melts according the melt fraction and their electrical properties would be of a significant interest.

b) Water circulation models

Water distribution in the mantle both spatially and temporally is a very difficult question. Indeed, this topic requires a various number of constrains in which possible improvements are possible, among them we can cite:

- Mantle minerals volatile solubilities and contents: depends on intensive parameters such as pressure, temperature and oxygen fugacity. This work has been greatly studied by numerous researchers and groups (Demouschy and Bolfan-Casanova, 2018). However, only major phases have been constrained such as olivine, wadsleyite, ringwoodite, Cpx and Opx,

even if some works remain to do for oxygen fugacity effects. Important debates on phases such as garnet (Mookherjee et al., 2010; Adria et al., 2012) or accessory phases (alphabet phases, etc.) are still unresolved.

The stability of each major and accessory phase and its maximum solubility at the right pressure, temperature and oxygen fugacity conditions would be a significant constrain.

- Partition coefficients: the partition coefficients between minerals and melts are only available for a restrained P and T conditions and mineral assemblages. In fact, the partition coefficients are only usable in the determined phase's associations and can completely change with appearance of small accessory phases or presences of fluids. The elaboration of temperature, pressure, chemistry and oxygen fugacity dependence would be needed for solid-solid, solid-melt and fluids in order to better constrain the equilibrium and water content of residual solids.
- Diffusion coefficients: diffusion coefficients are one of the best constrained parameters as a function of P, T and FO_2. Olivine is by far the most studied minerals (Novella et al., 2017; Mackwell et al., 1990). However, robust studies have been made on other minerals such as wadsleyite (Hae et al., 2006). Diffusion coefficients at LVL conditions taking in account the presence of melt would be also of a significant interest to precise the models and the potential recycling of water into the MTZ or its leakage in upper mantle.
- Geophysical and geodynamical constrains: this section encompasses constrains from various domains. Constrains based on field evidences and modeling would help to precise the time of onset of subduction and its speed. Analysis of ophiolites through time is also providing clues on the amount of water carried to deep mantle and its variation in the past. Finally, actual seismic and magnetotelluric data must be refined in the LVL zone for a better quantification of both actual water content and melt fractions and their distribution along the MTZ-UM boundary.

Using these different constrains, a global model could be made using a much more sophisticated approach. This would be of significant interest but would require collaboration between researchers of different domains. It might also require important computational resources to build a time integrated model of water distribution in Earth's mantle.

Chapter VI

Thermal diffusivities measurements of geomaterials at high pressure and temperature using Angström method in multi-anvil apparatus

Chapter VI: Thermal diffusivities measurements of geomaterials at high pressure and temperature using Angström method in multi-anvil apparatus

1) General introduction

Thermal properties of Earth's materials have been investigated since the beginning of the 20th century with the pioneering work of Eucken (1911), Bridgman (1924), Birch and Clark (1940). However, despite significant increase of theoretical knowledge on heat transport mechanisms (Kellett 1952, 1953; Lubimova 1958; MacDonald, 1959), the first accurate measurements of geological materials were not performed before the mid-eighties and 2000's. First experiments were conducted at ambient conditions and limited ranges of temperature (Parker et al., 1961; Cape and Lehman, 1963; Kanamori et al., 1969) or moderated pressures but at room temperature (Kanamori et al., 1969; Dzhavadov, 1975). The increasing interest for thermal parameters at relevant mantle conditions led to significant technical developments to reach higher pressure and temperature ranges. It initially consisted to perform measurements in piston cylinder and multi-anvil apparatus (Fujisawa et al., 1968; Kanamori et al., 1969; Katsura, 1993) to characterize upper mantle phases and was recently adapted to diamond anvil cell (Ohta, 2010; Goncharov et al., 2008; Konopkova et al., 2016).

The variety of techniques used to estimate thermal properties translates the difficulty to obtain reliable and consistent measurements. Two major types of techniques were developed, with multiple contacts methods on one hand and contact free measurements on the other hands. Contact free techniques were developed to characterize material properties at ambient conditions. These techniques rely on propagation of heat wave induced by laser light pulse through a sample. This technique offers many advantages and the most accurate measurements at ambient pressures (Hofmeister et al., 2007). First, Laser Flash Analyses (LFA) were developed (Parker et al., 1961; Cape and Lehman, 1963) but more recent adaptations were realized (Chai et al., 1996), in particular for Diamond Anvil Cells (Konopkova et al., 2016; Ohta, 2010; Beck et al., 2007; Goncharov et al., 2009, 2010, 2015; McWilliams et al., 2015). Complementary, multiple contacts methods are defined to involve one or several thermocouples to estimate temperature evolution at both ends of a sample, these techniques are common in the high pressure studies due to the difficulty to access, physically and optically to the sample during the *in situ* measurement. Several types of contact methods exist and were then derived and adapted to experimental set up and constrains brought by high pressure apparatus. Among them, Angström method is the main

technique used in high pressure experiments, because it can be easily adapted for cylinders and so for multi-anvil and piston-cylinder apparatus (Fujisawa et al., 1968; Kanamori et al., 1969; Katsura, 1993; Xu et al., 2004; Manthilake et al., 2011). This technique also offers the possibility to infer directly thermal diffusivity from measurements, using the analytical solutions developed in Carslaw and Jaegger (1959) which do not require a complete system modeling. It worth adding that analytical solution for Angström method is direct and accurate if boundary conditions are respected. At the opposite to contact free techniques, such as LFA, that relies on graphic extrapolations, such as the relation between dimensionless parameters during temperature history (Parker et al., 1961). Graphical extrapolations are still used nowadays or have been improved (Heckman, 1973; Josell et al., 1995; Blumm and Lemarchand, 2002).

Knowledge of thermal parameters of Earth's mantle major components is a key prerequisite to understand its actual and past behavior and dynamics (see Chapter I). Temperature dependence of thermal conductivity will affect profoundly mantle thermal structure due to the presence of regional variations related to geodynamical contexts: cold or hot geotherms corresponding to subduction or ridges, rifts and hot spots regions. Because olivine is the most abundant phase in the Earth's upper mantle, and must be interconnected, this mineral was extensively studied by various techniques. These studies provide the largest database for a geological material (Kanamori et al., 1968; Kobayashi, 1974; Chai et al., 1996; Osako et al., 2004; Xu et al. 2004; Gibert et al., 2005; Petermann and Hofmesiter, 2006). Data on other major phases such as garnets (Kanamori et al., 1968; Chai et al., 1996; Osako et al., 2004; Hofmesiter , 2006) and pyroxenes (Kobayashi, 1974; Chai et al., 1996, Hofmesiter and Yuen, 2007) are available even if large compositional possibilities exist. At the opposite, minor phases, rocks, glasses and melts are however, very scarce in experiments at mantle pressures and temperatures (Blumm et al., 1997; Petermann and Hofmeister, 2006; Hofmeister et al., 2009; Romine et al., 2012).

However, even with this impressive number of studies on olivine, the results are significantly scattered (Xu et al., 2004). Differences up to 50% of thermal diffusivity have been reported for olivine at ambient conditions and up to 700K (Hofmeister, 2007; Hofmeister and Branlund, 2015). These discrepancies have been commonly explained by two major points: the technique employed and the lack of understanding of thermal transports (Hofmeister, 2007).

A significant progress has been made by recognition of new mechanisms: lattice components with acoustic models (Liebfried 1954; Dugdale and MacDonald 1955; Julian 1965; Roufosse and Klemens, 1973) or damped harmonic insulator model (Hofmeister et al., 1999, 2001 and 2007; Giesting et al., 2004), radiative components with ballistic, direct and diffusive radiative transfers (Hofmeister and Brandlund, 2015; Goncharov et al., 2008). In addition some recent hybrid components have been found: diffusive-radiative transfer in IR region that infers and increase phonon scattering (Hofmeister et al., 2014). However, our understanding of theses mechanisms dependence on P and T and environment conditions is still scarce. Photon mean free paths are also a crucial topic which is not perfectly understood (Shankland et al., 1979; Gibert et al., 2005). However, optical thickness considerations have been a key argument against some studies where low thermal conductivity values were found (Hofmeister et al., 2007) (See appendix E). Optically thin sample will lead to the presence of direct radiative transfer that crosses the middle without any participation of it, as well as presence of ballistic photons (if high thermal gradients). Presence of direct radiative photons at all relevant or several wavelengths will lead to underestimation of bulk sample thermal conductivity. At the opposite, ballistic photons can directly warm thermocouple leading to an overestimation. Still, reach optically thick or opaque condition is a challenging task combining experimental size limitation and optical transparency on the IR frequency range of mantle minerals. This aspect is particularly true for single crystals, therefore, effects on polycrystalline middle haven't been quantified yet (e.g. grain boundaries, impurities).

A consequent debate is also present on the ability of given method to estimate correctly thermal diffusivity. Indeed, it has been widely recognized that contact methods can underestimate thermal diffusivity due to thermal contact resistance and differential thermal expansion between the thermocouples and the sample (Hofmeister et al., 2007; Hofmesiter and Brandlund, 2015). This problem can't be avoided and would lead to an underestimation in the order of 20%. Such value was obtained by a comparison between literature thermal conductivities versus number of contacts involved in the measurement (Hofmeister and Branlund, 2015). Contact free techniques offer a great precision in thermal parameters estimation (within 2% for LFA), but are limited to room pressure. Some recent developments allowed contact free techniques in DAC allowing characterization of material to very high pressures (Ohta, 2010 and 2012; Konopkova et al., 2016; Goncharov et al., 2008 and 2009). However, it is well known that diamond anvil cell can't be as robust as multi-anvil apparatus for control of hydrostatic pressure and thermal gradients. As well, large sample size available

in multi-anvil experiments should allow a good simulation of polycrystalline material and be closer to optically thick conditions with the abundances of grain boundaries and impurities in larger samples. Multiple contact techniques are still of a significant interest to characterize upper mantle material and by improvement experimental protocols and data processing. With effort both on the experimental protocol and data processing, they should be able to reduce the potential effect of thermal contacts.

This chapter aims to explain and details the technical developments realized on LMV 1500 ton multi-anvil apparatus to allow thermal diffusivity and conductivity measurements using Angström method. The completely new treatment procedure elaborated for data processing and error characterizations will be explained as it represents a significant aspect of this work. Applications via thermal diffusivity measurements of single crystal and polycrystalline olivine and periclase, peridotites and various glass/melt samples for a total of 23 experiments will be given. The discussion will be shortened due to the lack of time to finish this study. However, the first results interpretations and expected development for a short term submission for publication will be given and detailed in perspectives section.

2) Materials and methods

This section aims to present the technical parts of this chapter with a presentation of the selected samples, their preparation as well as experimental methods.

a) Starting material selection and description
   i) *Glasses and melts*

In this study, we explored the thermal properties of glasses and melts. Both natural and synthetic compositions were used to analyze various compositions and potentially maximize the variation of the signals obtained, as melts and glasses remained poorly studied. We selected glasses from different locations and geological settings. The selection of these samples was made upon different criteria: sample quality, phenocrysts/quench crystals presence, color of the glass (for radiative heat transfer component), the locality and the associated documentation of the samples. Samples obtained were selected thanks to the contribution of several LMV researchers: N. Cluzel for Güney Dag, ATHO glassess, D. Laporte for haplobasalt, D. Andrault for MORB glass and A. Gougaud for MAPCO samples.

(1) Güney Dag obsidian (GD)

This obsidian was sampled from the Güney Dag rhyolitic dome (Turkey). This volcano belongs to the Acigöl complex located in the central Anotolia in Turkey. This complex is composed of quaternary volcanoes settled on the floor of a wide caldera. The eruption products of Güney Dag are mainly made of ash and pumices deposits with addition of juvenile obsidian blocks. The eruption took place into a maar crater between 16 and 20 ka (Bigazzi et al., 1993; Druitt et al., 1995). The obsidian samples were selected by F. Maciéjac and J-L Froger.

The Güney Dag obsidian is a massive glassy rock. Its color is dark going from black for massive sample to gray depending on the thickness. Microlites only represent a minor fraction and can be visible using microscope or imaging veins with SEM (Fig. B.33). Cluzel (2007) found evidences of potassic feldspar, plagioclase, amphibole, ilmenite, magnetite, biotite and zircons. Microlites are present in scarce beds (up to several mm in thickness) or local aggregates. The chemical composition (table VI.1) indicate a richness in silica (>7 6%) and alkaline elements (Na and K) and significant depletion in Ca and Fe. The volatile contents (table VI.2) are elevated because the sample was collected in the tuff ring. At the opposite of dome obsidians, obsidians of the tuff ring were ejected in the first phreatomagmatic phases. Thus, the moderate volatile content can be explained by absence of degassing.

Table VI.1 Major elements analyses our of glass samples, by inductive coupled plasma atomic emission spectrometer (ICP AES): Güney Dag (Druitt et al., 1995), ATHO (Cluzel, 2007), and EPMA: Haplobasalt (Hardiagon). For Güney Dag, the relative errors given in the reference are between 0.5% and 2%. The errors of 2% have been calculated and displayed in the second column of the table. For ATHO, iron is entirely reported as Fe_2O_3. The errors given are two standard deviations estimated on an average of 7 ICP analyses. Chemical composition of Hawaii glass (quenched melt from Pele's hairs from a gas mixing furnace at NNO fugacity buffer) were performed by EMP such as Haplobasalt.

	GD	2% STD	ATHO	STD 2σ	Haplobasalt	STD 2σ
SiO_2	76.51	1.53	74.97	0.44	49.25	0.46
Al_2O_3	15.56	0.31	11.86	0.57	19.41	0.25
FeO	0.08	0.00	3.66	0.11		
MgO	0.01	0.00	0.10	0.03	16.40	0.25
CaO	0.25	0.01	1.61	0.17	12.83	0.25
Na_2O	4.47	0.09	4.20	0.20	2.11	0.12
K_2O	4.24	0.08	2.54	0.08		
TiO_2	0.03	0.00	0.24	0.01		
MnO	0.07	0.00	0.10	0.00		
P_2O_5	-	-	0.03	0.00		
total	98.92	1.98	99.30	1.13	100	0.68

Additional Raman analyses were performed in order to check the volatile content of the melt with an independent method and are provided in the appendix A (Fig. A.7 and table A.13).

Table VI.2 Volatiles elements analyses on two samples of Güney Dag obsidian and ATHO. The sample A was analyzed by Mourtarda and Laporte (2002). The H_2O content of this sample was estimated by loss on ignition, CO_2 and S by colorimetric titration, Cl by colorimetry and F by specific electrode potentiometer. The sample B and ATHO were measured by Cluzel (2007). H_2O and CO_2 were measured by FTIR and Electron microprobe (EMP) for S, F and Cl.

	GD a	GD b	ATHO
H_2O (%.wt)	1.39	1.10	0.07
CO_2 (ppm)	200.00	5.00	4.00
S (ppm)	<100	14.00	11.00
Cl (ppm)	634.00	669.00	684.00
F (ppm)	710.00	577.00	745.00

(2) ATHO obsidian

ATHO obsidian is rhyolitic lava emplaced in the caldera of the Krafla complex in the Hrafntinnuhryggur formation. Located in the North-East of Iceland and precisely set on the medio-oceanic ridge. The formation is composed of an elongated dome of 2.5 km long for a volume of 0.05 km3. The formation was emplaced during an eruption under an icy shell during the last quaternary glaciation (50 ka). The ATHO obsidians were sampled by O. Sigmarsson and given to N. Cluzel for experimental purposes.

The ATHO obsidian is a massive glassy rock. The color is deep black and opaque at every thickness. The texture is aphyric and microlites are minor (< 1%) (Fig. B.34). Microlites of titano-magnetite measuring one to few microns are homogeneously distributed.

The chemistry (tables VI.1 and VI.2) was observed to be similar to Güney dag, the glass is very rich in silica (75%) but is much richer in Fe and Ca. Iron enrichment is a particularity of Icelandic rhyolites. The volatile content was found to be almost null for H_2O and CO_2 and is explained by an important degassing during emplacement. Complementary Raman analyses were also performed (table A.13 and Fig. A.7). The spectra in OH region are flat, which confirms the dry ICPAES composition.

(3) Haplobasalt

The haplobasalt is a synthetic glass made by Schott for D. Laporte and M. Hardiagon. Made from regent oxide powder, it has been molten in a furnace at 1 atmosphere and cast in a mold before quenched in water. The ingot is perfectly quenched. The composition is basaltic from which iron was removed. The absence of iron is then translated by very different optical properties of the glass, which is transparent and slightly yellow/gold colored (Figs. B35 and 36). The Raman analyses are given in the figure A.7 and table A.13. The spectrum on silicate is typical of basaltic melts. On OH regions, the spectra are completely flat confirming the absence of water.

Previous experiments were performed by M. Hardiagon in piston cylinder apparatus. The liquidus of this glass was found to be between 1475 and 1500°C at 2 GPa with CO_2 in excess. pMelts calculations indicated liquidus temperature, at such pressure without CO_2, between 1500 and 1550°C, which was confirmed experimentally at 1425°C showing around 75% of crystallization. Crystalline phases observed at 2 GPa and 1425°C were orthopyroxene, clinopyroxene, spinel, garnet and sapphirine.

(4) MORB powder (EPR MORB)

A MORB sample was also used for thermal diffusivity experiments. We used the same MORB powder as the study at 2.5 GPa (Chapter III, Freitas et al. 2019). The volatile content was estimated to be 2730 (± 140) ppm wt. H_2O and 165 (± 40) ppm wt. CO_2 by Fourier Transform Infrared Spectroscopy (FTIR) (Andrault et al., 2014). This MORB powder was filled directly in the assembly and hand packed. The complete experimental procedure is details in the following section.

(5) MAPCO samples

Facing difficulties with powder as starting materials, some solid basaltic samples were selected allowing required the machining steps. We found in LMV rock collection MORB samples from the MAPCO I and II campaigns (1979), in which dredges were realized along the North Atlantic ridge. These samples were kindly given by Alain Gourdaud.

The MAPCO cruises were French oceanographic campaigns realized between 1978 and 1980. The cruises were performed on an IFREMER ship (Jean Charcot) and represent a total of 16788 km of Seabeam profile and magnetism, 3704 km of sediment profiler and a total of 22 dredges. The objective was to study the heterogeneity of the oceanic crust and upper

mantle between FAMOUS zone (36°N) and KANE Fracture zone (24°N). The cruises aimed to better map the Atlantic medio-oceanic ridge and sample "zero age" basalts to perform chemical (major + trace elements) analyses (Bougault and Treuil, 1980).

On board, the samples were recovered, washed, sorted and photographed before being cut for thin section and analyzed. Analyses were realized on board with an x-ray fluorescence unit (accuracy of 1 % on major elements and 2 ppm on traces). Most of samples were pillow lava basalts with different amount of crystallinity and vesicularity. The sample freshness and the good preservation of the samples was a key point for their selection. The presence of plagioclase is very common in phenocrysts but can also be found in xenocrists. Olivine (quench/euhedral) is also visible at microscopic scale, as well as pyroxenes and oxides in few samples.

(a) DR07

Dredge 07 is located at the 33th segment of the middle Atlantic ridge. Recovered dredged material is composed of aphyric and sub-aphyric basalts, most of them are pillow lavas fragments. The global alteration of the rocks is low (Figs. B.37 and B.38).

The selected fragment is DR07-201. This sample is a fragment of pillow lava that was quenched by contact with water, as some traces of shellfish are visible on sample surface (Fig. B.38).This sample is labeled as sub-aphyric basalt but it was similar in terms of texture and crystal presence to aphyric ones. Size of sample, the absence of vesicles (<2%), abundance of glassy matrix and the low alteration (less than 2 mm in surface) were satisfying criteria for its selection. The lava is dark (opaque at every thickness) and massive.

Microphotographs revealed the presence of microcrystals (up to 300 μm size), with euhedral olivines (frequently squeletal) and fine aggregates of microlites. These microlites are quench crystals of plagioclase and minor olivine. At somewhat larger scale, some rounded and elongated objects composed extremely fine microcrystals aggregates coming either from quench or devitrification were identified (variolitic texture) (Fig. B.38).

The major elements compositions (table VI.3) between the different rocks samples from the dredges are very similar, indicating microcrystals are due to basalt cooling crystallization. The chemistry is similar to our EPR MORB from IODP core drilling, confirming sample freshness.

The volatiles content was estimated using Raman spectroscopy (Fig. A.8, Table A.15). Silicate spectra were observed to be contaminated with olivine. On OH frequency region, the peak of water is well visible. Since, olivine quenched crystals are dry, the glass is moderately hydrated. The presence of water together with the absence of vesicle indicates that the MORB didn't undergo extensive degassing. Values of 0.26 - 0.29 wt.% are minimum water content.

Table VI.3 Petrological and chemical information of DR07-201 and DR-11-201 (202 is reported for chemical composition). The abbreviation in the table are given here: A B: Aphyric basalt, sub A B Pg Ol: olivine and plagioclase bearing sub-aphyric basalt, pg: plagioclase, ol : olivine, pillow vac: vacuolar pillow lava. Major elements analyses are given in weight percent whereas trace elements are given in ppm. Al iron is given in Fe_2O_3 form.

Dredge N°	DR07	DR11		
Sample N°	201	201	202	Glass
Localization	32°17'2N-40°11'2W	30°41'3N-41°48'9W and 30°40'9N-41°47'3W and 30°40'0N-41°49'8W		
Depth	3000-3380 m	3640-3500 m		
Thin section	Yes	Yes	No	No
Phases	pg ol	ol pl	ol pl	None
Abondance	2%	rare	rare	None
Macroscopic name	pillow	pillow vac	pillow vac	Glass
Rock Name	sub A B pg	sub A B pg ol	sub A B pg ol	Glass
Composition				
SiO_2	49.03		49.28	49.4
Al_2O_3	14.41		14.34	14.18
Fe_2O_3	11.6		11.62	11.18
MgO	8.36		8.35	8.61
MnO	0.2		0.19	0.19
CaO	11.3		11.03	11.16
Na_2O				
K_2O	0.08		0.09	0.07
TiO_2	1.37		1.59	1.43
P_2O_5				
Total	96.35		96.59	96.22
Sr	86			92
Y	35			36
Zr	85			95
Nb	2.5			1

(b) DR11

Dredge 11 is located on 54th segment of the middle Atlantic ridge. The recovered material of dredges is composed of aphyirc and sub-aphyric basalts: pillow lavas fragments (Fig. B.40) the global alteration of the rocks is low.

Sub-aphyric basalt, DR11-201, was selected (Fig. B.41). This sample is a pillow lava fragment, with visible glassy crust. On cuts, the sample is really fresh, dark (opaque at every thickness), massive and the abundance of microcrystals is low. At microscopic scale, DR11-201 is much more crystallized than DR07-201. Microphotographs (Fig B.42) revealed the presence of euhedral olivine with sizes ranging up to 500 micrometers abundant quenched crystals (tabular plagioclases and oxides).

The chemical analyses (table VI.3) highlighted a very close composition to EPR MORB and DR11. Volatile content was estimated by Raman spectroscopy (Figs. A.9, 10 and table A.16). Silicate spectra showed mixture of glass, plagioclase and pyroxene signals ± olivine. On OH frequency region, the peak of water is well visible. Since, all quenched crystals are nearly dry, the glass is moderately hydrated. The presence of water peak together with the quasi-absence of vesicle means that the MORB didn't undergo extensive/complete degassing. The OH/Si ratio can't be used here as quench crystal contamination is too important. Water content of 0.33 - 0.37 wt.% were estimated.

ii) Solids (ceramics & rocks), single-crystal and polycrystalline samples

Angström measurements were first performed on solid materials. Characterization of known materials such as MgO helped to calibrate the heating software and processing codes.

(1) KLB-1 peridotite

KLB-1 peridotite composition was studied with Angström method. We used the "dry" KLB-1 powders that were prepared for the study at 6, 9 and 12/14 GPa (Freitas et al., 2017; Freitas and Manthilake, 2019). See details of preparation in the chapter IV. The starting powder was filled directly in the assembly and hand packed.

(2) Ray-Pic peridotite

Facing difficulties using powders as starting material, we have searched for fresh, fertile and fine grain sized peridotites, which will allow machining steps. We found that peridotites

nodules from Ray Pic in Ardèche are good candidates for experimental purposes (samples provided by D. Laporte).

The maar of Ray Pic is situated at 6 km north from Burzet, Ardèche in the French central massif. Emplaced in a crustal basement (granite, gneiss and migmatite), the quaternary volcanism is characterized by starting phreatomagmatic phases followed by strombolian and effusive activities. The phreatomagmatic eruption notches the basement to form the present maar of Ray Pic and the following strombolian activity built the "égueulé" cone with a crater of 1.2 by 1.5 km. The lava flow of Ray Pic is one of the longest lava flow in metropolitan France with 21 km. The lava flow is dated between 80000 years by thermoluminescence on plagioclases (Guérin, 1993) and > 35000 yr. by C14 (Berger, 1973, 1981; Berger et al., 1975).

The lava flow of a thickness of about 25 - 30 meters is basaltic with an almost aphyric texture (some olivine phenocrysts). These lavas are alkalis rich and the phenocrysts are mainly diopsides (Wo 45-47 En 41-45 Fs 9-12), olivines (Fo 80-85) and plogiclases (Ab 37-44). The liquidus temperature was estimated to be around 1220°C (Bambier et al., 1985) and crystallization pressure of 2.5 - 3.5 kb. The particularity of these lava is that they directly ascent from the mantle without any magma storage in the crust, allowing the entrainment of a significant amount of mantle enclaves.

The Ray Pic lava flow is famous for its extreme richness in peridotite enclaves. The enclaves are composed of 90% of lherzolites (peridotites) and 10 % of pyroxenites. Most of lherzolite/peridotites have a classical mineralogy of spinel equilibrated facies with olivine, clino (Cr rich) and ortho pyroxenes and spinels. In addition, a great variety of textures are presents (Mercier, 1972; Mercier and Nicolas, 1975; Harte, 1977) with a continuum representation of facies between isotropic to intense deformations. Most of lherzolites have a protogranular coarse grain structure (grains > 1 mm). Their texture is isotropic and no deformation is visible, grains contacts are curved or polygonal, indicating a sampling of tectonic inactive mantle under central massif of France (melting depths between 30 and 70 km). Few enclaves are very deformed, showing a pyroclastic texture with a clear foliation of olivine and lineation of spinels and pyroxenes. The average grain size is usually much thinner (> 0.5mm). These enclaves highlight the presence of intensely deformed zones in the sampled upper mantle. Finally, a last minority of enclaves have an equigranular texture with rather homogeneous and fine grains size (~0.5 mm) which is due to recrystallization. These enclaves also come from tectonic active zones.

The chemical analyses carried by Berger (1981) demonstrated that most of these enclaves in spinel facies are lherzolites, rare harzburgite and dunites with equilibrium temperature between 950-1250°C (Fig. VI.1).

Our selected sample is a large peridotite enclave from the large grain facies but showing a somewhat finer grain size (0.5 - 1mm) and a very low apparent porosity. The bulk chemistry was not available for this sample. However, its very fresh aspect and the abundance of Cpx and spinel indicate it must lie close to the fertile pole of lherzolite (Fig. VI.1). Texture is homogeneous through the overall enclave, the texture isotropic (no deformation observed) excepts a small possible lineation visible thanks to spinels and no reaction rim or infiltration with the surrounding basalt was observed (Fig. B.43).

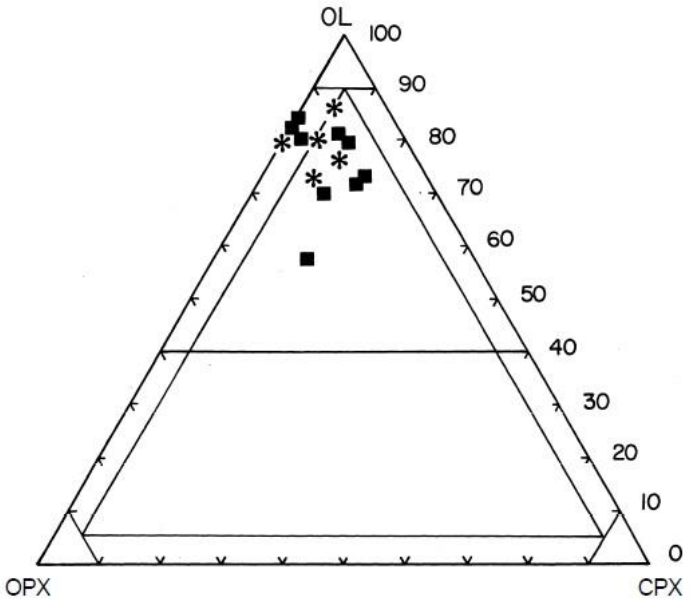

Figure VI.1Modal analysis of Vestide du Pal (nearby locality) mantle enclaves. Squares are forcoarse grains facies whereas stars are for other facies (equigranular and porphyroclastic). Figure from Berger (1981).

The chemical composition estimation via ICPAES and detailed petrological analysis will be realized in the autumn 2019 (mainly due lack of time and instruments shut-down during summer 2019).

Micro-Raman analysis was performed on olivine and pyroxenes grains (Figs. A.11, 12 and table A.17). The recovered spectra highlight a good chemical homogeneity. The OH frequency region was almost flat for olivine and shows some peaks for Cpx. However, the high fluorescence made difficult the baseline and evaluation of water. Water content of olivine was found to be 267± 153 ppm. Assuming, we have 60 % of olivine, 5% of dry spinel and a roughly equal proportion of Cpx and Opx as given in the literature (Berger et al., 1981),

with partition coefficient (Novella et al., 2014), the water content can be roughly estimated to 370 ± 140 ppm (Table A.17).

(3) Periclase (MgO)

Periclase samples were used to calibrate our heating software and performed the first Angström measurements in MAA. This compound is a simple oxide and has been extensively studied (Manthilake et al., 2011; Hofmeister et al., 2014). We used two types of MgO, for these experiments. First, single synthetic MgO crystals in wafers supplied by SPI were used. These synthetic crystals are fully transparent in visible and the crystal standard orientation is along (100) plane (Fig. B.44). We also used a synthetic polycrystalline MgO. High quality and fine grain size ceramic was bought from Goodfellow. The sintered MgO ceramic appears massive, dense and homogeneous. Compared to large grain size MgO, this ceramic has a soft touch and so a much smaller porosity which provides better condition for machining steps. Optically, the sample is white due to the small grain size.

(4) Olivine

The olivine samples were cylinders prepared by core drilling San Carlos or Pakistan's single crystals. Fine San Carlos olivine powder was used for small grain size samples.

(a) San Carlos polycrystalline samples

Fine polycrystalline samples were made from San Carlos olivine. The transparent green selected grains, inclusions free, were hand-picked and rinsed with acid to remove any surface impurities. The grains were crushed in ethanol in an automatic agate mortar pre-contaminated with lower quality grains. Recovered powder was sieved with metallic sieves (Mesh Fabric) between 40 and 36 μm to remove large grains and reduce the quantity of very fine grains. The recovered powder was rinsed with ethanol and was light green indicating that thinner particles (< 1 μm) were removed. However, due to hydrostatic effects forming aggregates, recovered grains are much smaller than 36 microns but their size was homogeneous and with a reduced dispersion. The starting powder size and grains parameters are given in the figure B.45.

(b) Single crystal

The selected olivine single crystal is transparent green and looked crack free with only minor impurities such as spinel inclusions. The olivine single crystals originating from San Carlos or Pakistan were provided by G. Manthilake.

The crystal was cut along crystallographic directions and was oriented with Raman spectroscopy (thanks to L. Martinek). Each face averaged spectrum was estimated from spectra taken at regular angles to the polarization direction. Each face spectrum was found to be typical of one crystallographic plan and was labeled according measurements from Ishibashi et al. (2008). (Fig VI.2). For both practical reasons and known variations of lattice thermal diffusivity along crystallographic directions the cylinders were drilled perpendicular to 001 plan. The cylinder then is randomly disposed between 100 and 010 (1 plan is probed between the 2 thermocouples). These two plans were selected due to the maximization of the dispersion of thermal diffusivity highlighted by Hofmeister et al. (2007), on forsterite single crystal. The recrystallization, under HP-HT during the experiment, was anticipated to produce values in between this observed range, due to random orientation of the newly created crystals (confirmed by EBSD analyses, see hereafter, appendix B). The cored cylinder size was adjusted with sandpaper and was drilled in the center with WC drill bit of 300 micron diameter according the procedure described below.

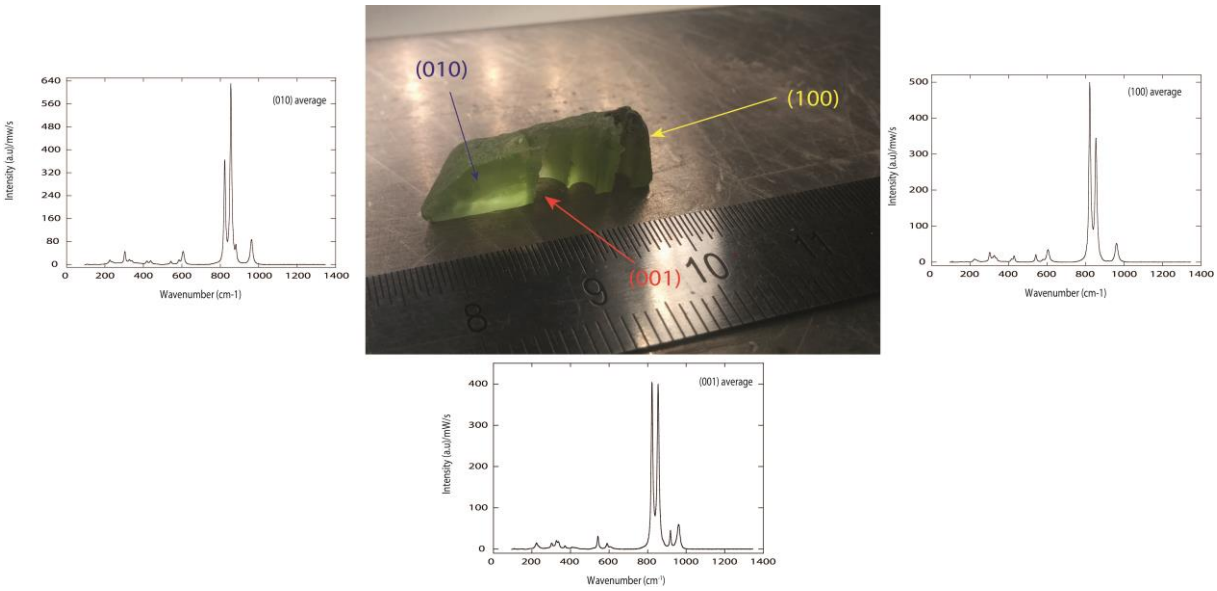

Figure VI.2 Olivine single crystal orientation and preparation with respective faces Raman analyses. The core drills are visible on the right side of the crystal and perpendicular to (001).

iii) *Sample preparation and machining*

The selected rock samples were prepared and machined in order to obtain samples satisfying the special requirements of thermal diffusivity measurements.

First, the rocks were cut (wheel saw, wire saw or diamond blades) in order to remove any weathering surface. Slabs with a thickness between 5 and 10 cm were prepared to fit under drilling machine. The drilling is made at high speed > 250 rotations per minute (RPM) and

lubricate by water injection at the center of the tool. The samples were cored with a Cincinnati Milacron apparatus and diamond drilling barrel (5 cm long). We used a tool with inner diameter of 5 mm and outer diameter of 6.5 mm for 4 mm sample diameter.

Ultrasonic drilling was also performed for sample preparation. A 4.5 mm inner diameter aluminum cylinder was used to obtain 4 to 3.5 mm diameter samples. For drilling, an ultrasonic vibration (around 19 kHz) is applied while a water and silicon carbide powder stream is added. The projection of water plus silicon carbide grains cuts the sample. No strength has to be applied on the sample and the drilling is very precise. For small samples, we found that inserting the sample in epoxy resin allows stable drilling. The ultrasonic drills were realized using LUD ultrasonic machine.

After some ultrasonic cleaning in ethanol, the sample is then cut from the starting material cylinder with diamond blades or diamond wire saw and adjusted to the good length and diameters with silicon carbide sandpapers and diamond piles.

The central hole required for the thermocouple was drilled in a final step. The samples were drilled with diamond burs for glasses and tungsten carbide drill bits. Only dental diamond burs allowed finding diameters lower than 1 mm (0.8 mm for ball and flat cylinder shapes and 0.6 mm with WC). Glass is very hard and can only be drilled using diamond burs. At the opposite, tungsten carbide drill bits allowed doing holes down to 300 microns in solids crystalline materials. Starting the drill is the most crucial point because diamond burs can break or bend. To prevent this effect, the glass is first abraded with a centre-drill made of tungsten carbide at low speed (50 RPM). Then, the diamond bur/WC drill is performed using high rotation speed (2000-2500 RPM) applying a low pressure on the bur. Water is used as lubricant to reduce friction and heating. During the drilling, pecking is necessary every 50 - 100 microns approximately. A complete drilling of 3.5 -4 mm depth requires at least 15 min per sample in order to preserve the diamond bur and minimize sample break. For solid samples, the main problem is to finish the drill as the material tends to pack and become harder at the bottom. In this case, it can be useful to use diamond or tungsten carbide burs to finish the drill from the other side. Recovered sample are rinsed in ethanol in ultrasonic baths and kept in oven before their insertions in the MAA assembly (Fig. B.46).

b) Experimental methods

i) *High pressure assemblies*

(1) Assembly's parts

High-pressure and high-temperature experiments were performed using a 1500 ton Kawai type multi-anvil apparatus at LMV. For experiments conducted between 0.5 and 4 GPa (mainly 2 GPa), we used octahedral pressure media with full length edges composed of MgO and Cr_2O_3 (5 wt.%) in an 25/17 multi-anvil configuration (octahedron edge length / anvil truncation edge length) (Fig. VI.3). Our assembly was designed to accommodate the geometrical requirements for measurements of thermal conductivity in a single high pressure cell for large samples (4 mm long for 4 - 3.5 mm diameter). Steeped graphite furnace with molybdenum electrodes were used to keep furnace geometry under compression and reduce thermal gradients. Pressure medium and cubes were thermally insulated via a thick zircona (ZrO_2) sleeve that helped to reduce thermal loss as well as gradients in the sample zone. Sample and wires were electrically insulated from the furnace with MgO sleeves that were thicker around the sample to ensure homogeneous heat repartition and respect boundaries conditions. Two tungsten-rhenium ($W_{95}Re_5$-$W_{74}Re_{26}$) thermocouples were used to measure temperature oscillations at the center and the edge of the sample. The junction of the two was made in a parallel plan at the center of the sample. The thermocouples were placed thanks to a 300 μm hole drilled in the sample cylinder and thin grew made by diamond coated wire on the MgO sleeve for outer thermocouple. After accurate measurement of inserted wire length, thermocouples were fixed by inserting fluid alumina cement, prepared with mortar, in the two Alumina rods above and under the sample. No alumina cement was found in the sample after experiments. The restricted size of thermocouple (300 μm versus 2 wires of 125/75 μm + bending thickness) holes allows reducing significantly the creation of pore and additional resistance. All ceramic parts of the cell assembly, including the pressure media, were fired at 1373 K prior assembling in order to remove the absorbed moisture. Oxygen fugacity of the sample was not controlled during the experiments but is expected to be in reduced conditions by the presence of the graphite furnace.

In this study, we used 75 microns thick (0.003 inches) type C thermocouples supplied from Goodfellow. These thermocouples are easier to insert in the thermocouple holes, easier to fix in the octahedron edges and allow using thinner coils.

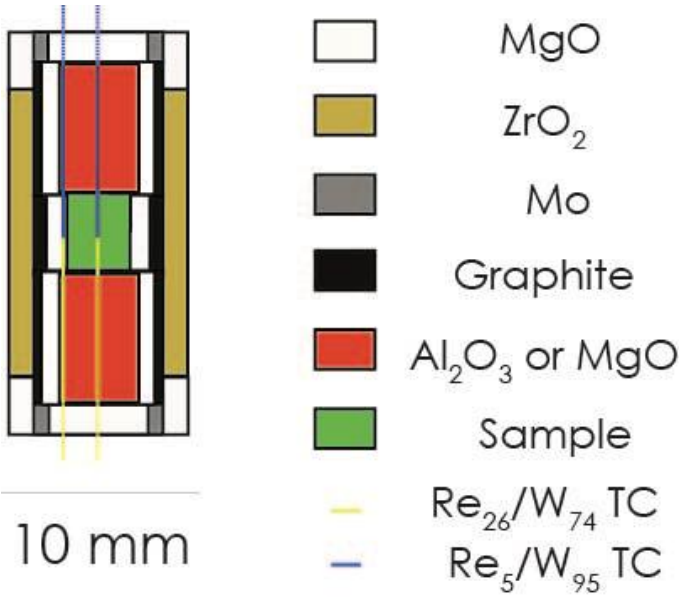

Figure VI.3 Schematic of the 25/17 assembly used for Angström method in multi anvil press

(2) Assembly preparation tips

These assemblies are particularly difficult to assemble despite their large size. The main problem came for the thermocouples as they are crossing the assembly from side to side and are not fixed. The thin thermocouples are fragile and the junctions are easily broken if pulled by hand. The position of the junction itself, which is adjusted under binocular with color marks, can move easily through the assembly if pulled.

In addition, for all the wire passes in the sample, MgO sleeves or alumina parts have to be manually precisely adjusted prior to assemble, in order to avoid too many manipulations which increase the risk of rupture. After many experiments, the author found easier to assemble the inner parts from sample to furnace outside the assembly and insert the whole together at the end and cement everything (Fig. VI.4).

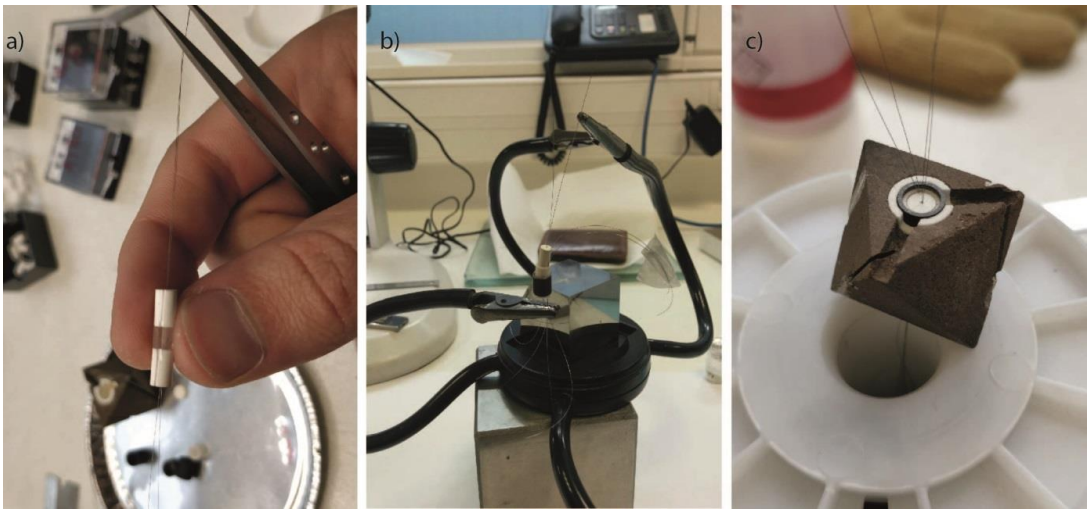

Figure VI.4 Examples of assemblies in realization. a) Haplobasalt sample M836, b) assembly with four free wires, the usefulness of second hand c) assembly with powder sample M851.

(3) Adaptation for glasses and melts

To measure melts and glasses, the risk of thermocouple short circuit, when the sample is molten, is great because melts, even dry, are good electrical conductors (see chapters III and V). To overcome this issue, several ideas were tested during this PhD work.

The first one was to use an olivine single crystal capsule (Fig. VI.5). Olivine cylinder is prepared from large single crystal, using a core drilling machine and wire saw apparatus. Then a toroidal cavity is drilled into olivine cylinder and a final central hole in the capsule center has to be drilled to pass the center thermocouple. The two first steps were realized successfully by G. Manthilake. However, the drilling of a central hole remained a significant problem. The author tried to drill the hole with 300 µm WC drill bits without success. We also tried to make the central hole with femtosecond laser ablation at UCA, institute of chemistry with the collaboration of N. Batisse without a complete success. First, it appears that olivine is almost transparent to 1030 nm laser, even at maximum power. It imposed a very fine focus working with 10.6 mm working distance which causes problems for the hole shape. Due to the large thickness of drilling almost 4 mm, the resulting hole shape is almost conical and irregular. Such ablation method did not give satisfying results.

To overcome the short circuit effect and keep the thermocouple alive at melting point, we propose a new insulation technique which consists into the use of alumina tubes. To do this, we used thin commercial alumina tubes of 0.6 mm diameter and 170 µm wall thickness. The thin thermocouples fit exactly into them and their outer diameter can be drilled in glass samples with dental diamond burs of 0.6 and/or 0.7 mm diameter. The tube length was taken

to be slightly longer than the sample to be inserted in the alumina rods above and below. This tip protects the thermocouples more efficiently and prevents melt leakage on sample/ alumina rods interfaces. The use of the alumina tube also helps maintaining the junction centered because small amounts of cement can be used to block the wires on each tube end. The tubes are also much stronger than free wires, helping the assembling of the experiments and reducing the thermocouple rupture due to rotational or pulling movements.

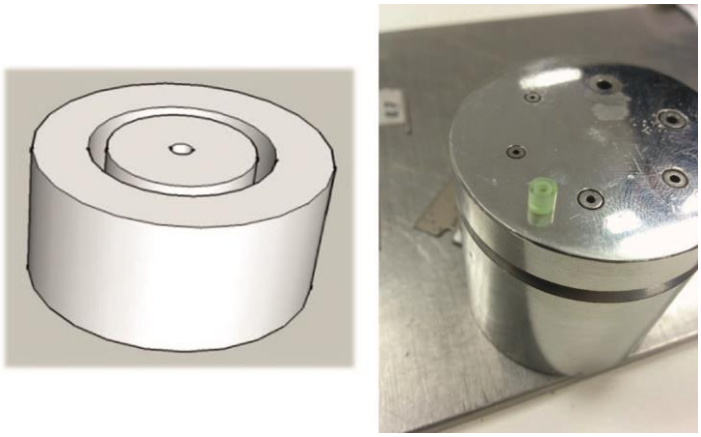

Figure VI.5 Olivine capsules schematic (left) and real views (right). Note that olivine capsule on the right frame has no central hole.

Our first experiments with these tips show almost no reaction with melts or samples and good resistance of these tubes to cold compression. Their efficiency against melt is good but some leakages for basaltic melts still have been found. Their presence must be taken in account and corrected for thermal diffusivity estimations (given after).

ii) Technical adaptation of heating systems for Angström method

This aspect is mainly described in the chapter II. The Angström method is based on heat wave propagation in permanent sinusoidal regime. The press heating system must be modulated to produce the required signal and two thermocouples channels are needed to measure the heat wave propagation in the sample. Our homemade heating system (described in chapter II) supplies alternative current. An Agilent wave function modulator was inserted to modulate the sent signals. Hence, the whole system is piloted from a LabView interface which allows selecting the form of the signal, its amplitude and frequency. Once the signal is set, a dedicated interface allows visualizing and recording the thermocouple signals. Signals are saved in .txt form with only three columns time and temperatures from both thermocouples. While the heating system in our 1500 T MAA is working well, the Angström

system however, was only tested in one experiment performed by G. Manthilake, on chlorite sample.

This study is the first complete study performed with this Angström system. This implied the possibilities of important issues in the first experiments (see results part) and required the establishment of a complete experimental procedure.

iii) *Experimental procedure*

Experimental procedure is, as other *in situ* experiments, typical to this experiment and was elaborated and improved by the authors during this study.

Usually, as these assemblies are very long to prepare (about 1 week per experiment considering sample preparation and machining), our experiments are prepared and assembled few days prior their insertion on the press. They are kept in ovens above 120°C to prevent moisture contamination and dry the alumina cement. The assembly is settled on the secondary anvils just prior inserting in the MAA. To not increase the risk of thermocouple failure, connection were check prior and during the cold compression, and smooth compression profiles were set (> 2 h to reach 83 bars (2 GPa) + 30 minutes only for the first 10 bars).

The heating and cooling procedure was elaborated to provide an important number of data and explore the different sample states (see figure VI.6 and appendix D for each experiment). The procedure is adapted during the experiment according the requirements and its progress.

For our solid samples, at least two heating and cooling cycles were performed. In the first cycle, the temperature is increased first above 500°C by 50°C steps and decreased to 150°C by 50° or 100°C steps to remove moisture and save some data in case the thermocouple fails during the second heating at high temperatures. The data quality is often better in the cooling cycle, once sample has been equilibrated and moisture removed. In the second cycle, temperature is increased up to the desired temperature and cooled down to room temperature by 100°C steps.

For glass and melt samples the procedure is more elaborated, with 3 cycles. A first cycle is made on glassy samples (depends on the natural/initial state), similar to solids for moisture removal by 50°C steps. The second cycle is made up to glass transition (Tg) by 100°C steps. Tg varies according to the rock composition and its water content (Giodano et al., 2005). However, because our samples are almost dry, the temperature of 800°C was considered to be above the Tg for all our compositions. Taking in account measurement time and that glass

transition temperature is surpassed by 10's of degree, the sample is kept almost 1 hour above glass transition to crystallize. The temperature then is decreased down to 150°C by 100°C steps. In the last cycle, the partially crystallized sample is heated up to its melting temperature by 100°C steps. Near its melting point, steps of 50°C are usually performed. The sample is not kept for long above its melting point (< 1 hour), to avoid sample leakage and chemical reaction with the surrounding parts. The sample is then "frozen" by applying a brutal temperature decrease in less than few seconds from melting temperature to 600°C - 550°C. This step must keep sample glassy but allow measurements at low temperature of 100% glass sample.

Using such procedure, the author aimed to probe samples at different states to see if differences can be seen and provide in a single experiment the thermal diffusivities of natural quenched glass, partially crystallized melts, molten samples and glassy experimentally quenched samples.

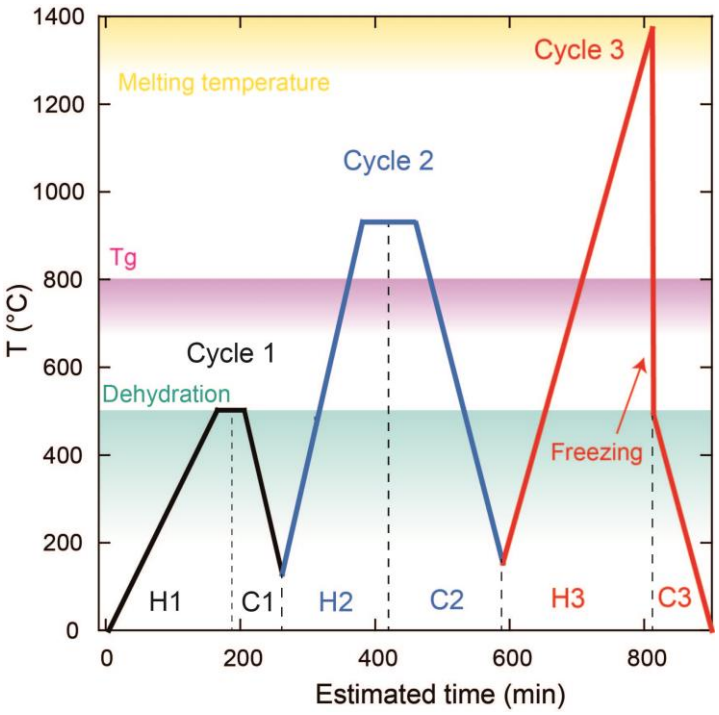

Figure VI.6 Experimental procedure of thermal diffusivity experiments for melts and solid samples (two first cycles only, until desired temperature). Each cycle is given in a color: black, blue and red for cycles 1, 2 and 3 respectively. Heating and cooling parts are separated by black dashed lines and labeled H and C with the cycle number (for example H1: 1st cycle heating). Approximated temperatures and duration are given with the experimental procedure. Theoretical zones for dehydration (until ~500°C), glass transition temperature and melting are given in shaded colors: green, pink and yellow respectively.

Thermocouples temperature oscillations were measured at each step for both heating and cooling paths. At each temperature step signals frequencies of 0.05, 0.1, 0.2, 0.3, 0.4, 0.5, 0.6,

0.7, 0.8 and 1 Hz before system modification and then 0.2, 0.3, 0.4, 0.5, 0.7, 0.85, 1.0, 1.2, 1.4, 1.5 Hz after (see results). The measurements are performed after at least 2 min of equilibration of temperature to reach a stable regime at each frequency (the smaller is the frequency, the longer is the required equilibration time). Temperature evolution with time was recorded for each thermocouple for 1 to 2 minutes or at least 10 periods when temperature was variable. Each temperature step associated with its ten measurements at different frequencies takes between 20 to 30 minutes to perform. Thus, each experiment heating duration exceeds easily 700 min (> 12h), this heating procedure can't be automatized as human vigilance, intuition and choices can't be replaced in real time.

The thermocouples values are saved by the software in .txt format and require then a significant amount of data processing.

c) Data processing and software development

The recorded data is a temperature evolution with time, drawing sinusoids of the input frequency. However, from this raw data to thermal diffusivity or conductivity final result, several (time consuming) steps of data processing are required. Because such measurements were not performed before at the LMV, I have developed a fully dedicated and improved (compared to literature) data processing sequence. The data sequence fitting has been made with Matlab® codes which will be provided in this manuscript (appendix C). For time reasons, the author did not made a user friendly interface. Thus, the program was only designed to fit and invert author's data. Using such program on different materials might require some adaptations, which can be made upon request.

Several parts of this program have been inspired from the CondFit software developed by J. D. Clemens. However, this previous program with user friendly interface was only available with executable version on Matlab 2012, which can't be used anymore on recent versions. The data processing was found to have errors and be very simple inducing several errors on the data inversion and a much restrained target zone.

In this section I will detail each data processing step, together with the appropriate code, to provide to the future users, the keys to use this work for their own data.

i) Raw signal fitting

The raw data is saved thanks to our LabVIEW interface in a simple file format: three columns, with time, temperature on TC1 and TC2 respectively. From this data, the sinusoidal

oscillation must be fitted to obtain both phase and amplitude values on each thermocouple to allow the data inversion.

Data treatment to estimate both phase lag and amplitude ratio was performed on Matlab® (2016b) software. The code first opens the desired file and allows selecting the fitting zone (Fig VI.7). Fitting zone selection is useful in the case of important temperature variations occurred during the recording. Then a non-disturbed zone can be selected, this ensures a much better fitting and lower associated errors. After this step, the program asks the input frequency to the user. We do not retrieve frequency by fitting for two reasons: first, frequency is stable and is not changed by the diffusion through the sample (no deviation was ever observed even for records of > 100 periods). Second, the precision of the inversion on phase and amplitude is much better if no degree of freedom exists on the frequency.

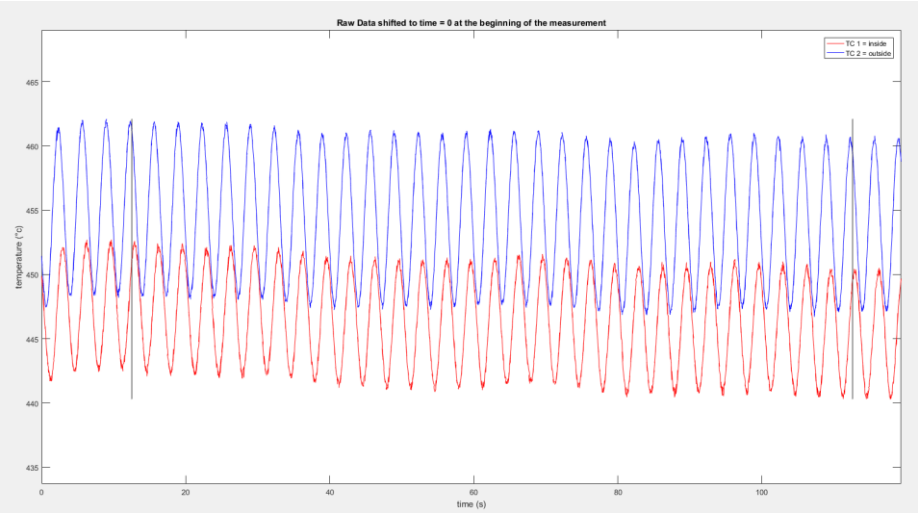

Figure VI.7 Example of raw data visualization window. The selected zone for the fit is situated between the two vertical black lines.

The first fitting step of the recorded waves on each thermocouple with a nonlinear least square (lsqcurvefit using Levenberg-Marquardt algorithm) solver was realized using the following equation:

$$T = A_0 + A_1 t + A_2 sin\left(2\pi A_3 t + \frac{A_4 \pi}{180}\right)$$

These fitting allowed inverting, for a temperature variation (T) during time (t), parametersA_0, A_1, A_2, A_3, A_4 corresponding respectively to initial/average temperature, baseline temperature, amplitude, frequency and phase of the recorded wave. The parameters are evaluated in a plausible range (given by the user) and the stopping criteria were reached using a very low

tolerance (10^{-20}). Errors were quantified recovering the residue on the non-linear curve fitting and using the *nlparci* function which computes from the residues the two standard deviations with 95% of confidence interval (2σ). This treatment was then integrated in our fitting code to perform proper error propagations (see result section).

The program then displays the fitting results and compares raw data with fits in dedicated figures. The user has a little time, which is tunable, to decide whether or not to save the fitted values (Fig VI.8).

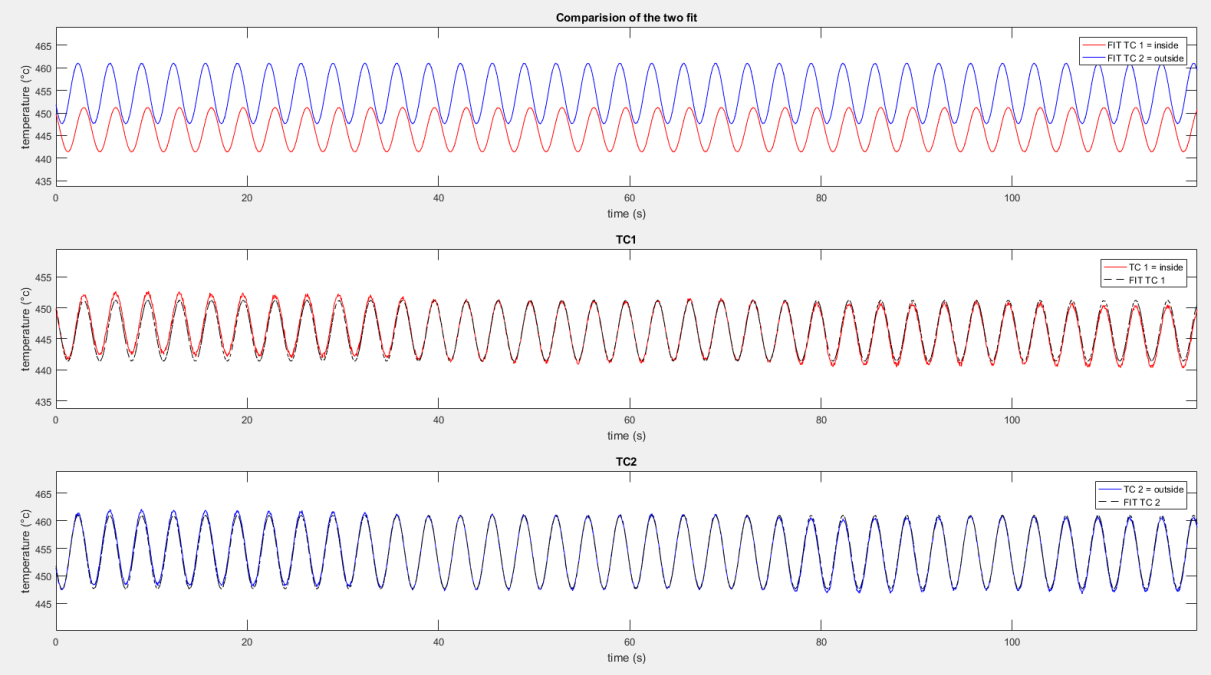

Figure VI.8 Example of data visualization after fitting step. The two fits are compared to estimate the phase shift in the first subplot, the second and third window are comparison of each measured signal and its fit.

If the user accepts the fitting after the visual checks, the program saves the fitting parameters for each thermocouple (A_0 to A_4), associated fitting errors on phase and amplitude and a header section in which the significance of each saved value is reminded. These parameters are saved in excel file of the same name into the experiment folder.

This manual step has to be done for each individual recorded file. It can't be automatized because abrupt temperature variations or manual errors (changing sinusoidal frequency) while saving are present in some files. In order to ensure maximum retrieved information from the experiment, this step has to be manual. In addition, the visualization of the signal, the quality of the fit is an important point to estimate the intrinsic quality of an experiment. This is also very important to see if the phase shift becomes larger than 1 period, which is a limitation of this technique. Each individual fitting takes about 1 minute per file

and thus for an average of 400 - 500 files saved during a successful experiment, the total treatment time is often a full day of work. In this PhD a total of 7606 files for 23 experiments were acquired and treated.

ii) Data checking/manuals steps and file stacking

Once the individual file fitting step has been realized, the files are manually sorted in folders corresponding to their heating and cooling cycles. This step is not necessary and the whole files can be stacked together, however, in this case the information coming from different cycles does not appear in the files. These files will be later mixed by Matlab (which uses its own ordering).

The excel sheets generated after fitting steps are simple, there are composed of 12 lines of header parts (fitting parameters explanation, etc.) and two lines in which the fitted parameters such as average temperature, amplitude, frequency and phase are given. Each line corresponds to one thermocouple. For data treatment, it is not convenient to load each file individually, Matlab is slow to do such task for 400 files, thus I created a stacking program to do this step and create a single file for each cycle of the assembly. This helps also the data pre-visualization which can be made in a single document and excel sheet.

This code simply reads the whole excels files in the folder and stack their data into a single file. In our experiment, we also set the convention that thermocouple N°1 is the centered one, and side thermocouple is thermocouple N°2. If the thermocouple order has been reversed during the experiment, which can happen for different reasons, the program proposes to invert their order. Thus the centered thermocouple will be first and the side in second, as it is required in the following treatment codes. The program also offers the possibility to correct the phase. Indeed phase is arbitrary fixed by Matlab and can be higher than 360° with ± 2π as it is an angle. The program can retrieve the phase between 0 and 360° which should be used.

After this step the program saves a single excel file in which the whole cycle/or experiment data is available.

iii) Phase and amplitude corrections before inversions

Before the step of data inversion, the data stacked in a single excel files can be visualized and corrected when needed before the final treatment step. With this file, the author used to do a manual pre-treatment to see if the phase shift estimated and amplitudes information are correct and that they can be correctly read and used by the inversion program.

This step is important and necessary as it ensures the inversion will work correctly. It also saves time as the inversion has to be completely repeated if an error has been detected afterward. In the case of thermocouples issues with temperature reading (see results part), temperature must also be corrected in this step.

In this step, the stacked file is duplicated, to not overwrite the original, and phase and amplitude are corrected if necessary. In a first step, the absolute value of amplitude of each thermocouple is taken. If it was negative, 180° are added to the phase, and the amplitude ratio between amplitudes of the two thermocouples can be then calculated. Phase is manually corrected to be between -360 and 360°, if not corrected in the previous step. The phase shift (phase difference between second and first thermocouple) must be negative, as the phase increase when shifting the wave to the smaller time (X axis) values. Thus, sometimes the phase of the first thermocouple must be negative when the phase of the second is low or when phase shift is important. In such case a special attention must be given, because if phase shift exceeds one period and is not seen during the data fitting, the corrected phase shift will be only between 0 and 360°. This step also allows seeing if the experiment worked properly, with coherent values evolution with temperature and frequencies (see appendix D).

Temperature, if thermocouple issues were encountered, must be corrected in this step. If the remaining thermocouple was working properly, the parameter A0 (average temperature parameter) of the remaining thermocouple is used to replace the bad temperature. When both temperature estimations are bad, a calibration curve in function of input power is used. It is mandatory to correct thermocouple values when issues happened because the final temperature of the analysis is calculated as the average of the average temperature of each thermocouple.

For melt and glass experiments, in which alumina tubes are used to protect the thermocouples, the effect of alumina tube on both phase and amplitude on the recorded signal must be corrected. The effect of these tubes is highlighted in the figure VI.9. The calculated correction indicates that the phase shift induced by the alumina must be accounted twice and that its effect on amplitude is even much greater. However, small size of the alumina wall thickness (170 µm) only implies modest corrections.

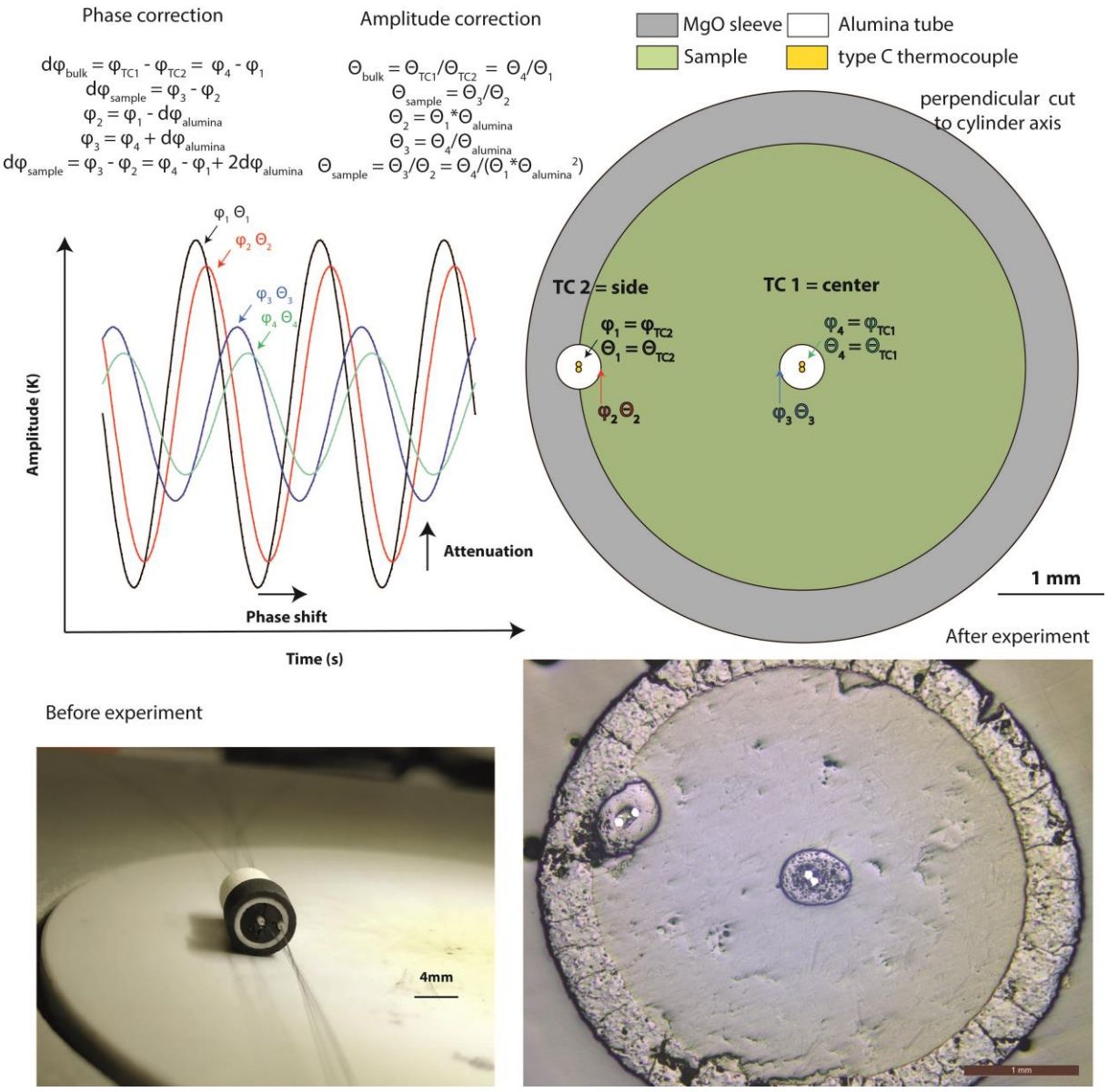

Figure VI.9 The alumina tube effect on phase and amplitude. The theoretical effect of the tube is detailed on the first part of the figure with effect on the recorded wave with the position on the schematic view of the sample. The theoretical effect and calculation is given above. The accuracy of the high pressure assembly scheme is confirmed with two microphotographs perpendicular to sample cylinder axis before and after the high pressure experiment.

The theoretical correction is made into a dedicated Matlab code built for this purpose. In this code, the corrected data (after temperature, amplitude and phase correction) is inserted as an input matrix. The calculation steps, given in the figure VI.9, are made to correct phase and amplitude of the first and second thermocouple. The effect of the alumina was calculated using the radial heat diffusion equations in their forward direction. The alumina wall thickness is fixed to 170 µm at RP and RT, which is perfectly reproducible as a commercial consumable, and is corrected in function of the P and T conditions. We used thermal expansion values from supplier (Goodfellow): $8e^{-6}$ K^{-1} between 20-1000 K and RP - RT bulk

modulus from Matweb (203 GPa). The thermal diffusivity values used for predictions are taken from Hofmeister and Brandlund (2015) (figure 12, alumina 0% porosity) at RP which hold until 1900 K (Fig. VI.10).

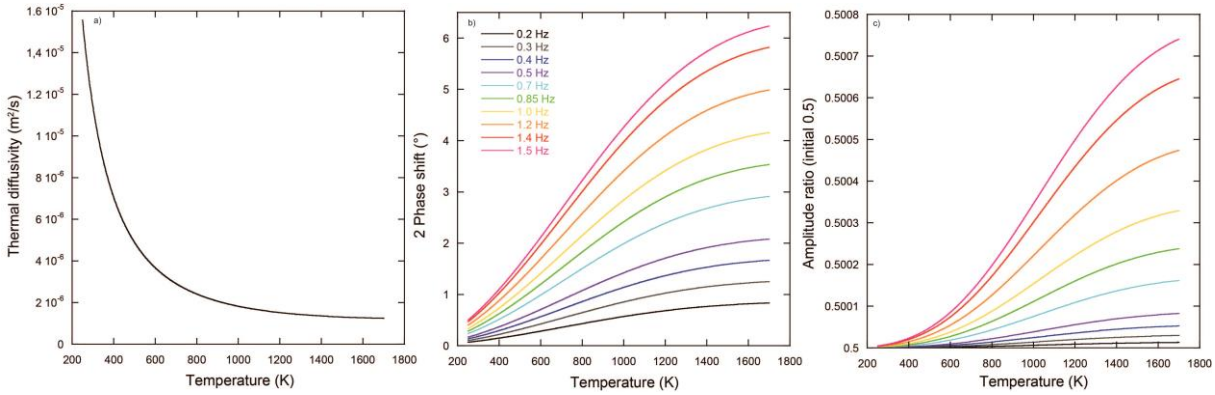

Figure VI.10 Alumina tube correction. A) thermal diffusivity of alumina in function of temperature (Hofmeister and Brandlund, 2015). B) 2 phases shits correction in fiction of temperature, correction is modest up to high frequencies (>6°). C). Corrected amplitude ratio as a function of temperature for an initial amplitude ratio of 0.5.

An additional correction step on amplitude can be made before treatment, as thermocouple issues are frequent. The thermocouples, while oscillating, display a lower temperature than the real one and so the estimated amplitude is not correct (see result section). The resulting amplitude ratio is higher than 1 if thermocouple 2 (side) failed, or very low (< 0.1) if thermocouple 1 suffered from this issue (center). However, we observed that the evolution of the amplitude and the amplitude ratio is similar in shape in "failed" and correct experiments. For these reasons, when the evolution of amplitude ratio with respect to temperatures and frequencies are similar to good experiments, the amplitude was normalized to have values between 0 and 1. This correction is empirical and might be subjected to careful interpretation. As amplitude ratio is never 1, even at really low frequency, we arbitrary selected to set 1 to the first round value above the maximum amplitude ratio measured at 0.2 Hz for the lowest temperature (for 1 cycle and used for all the others), this values can be better adjusted if first cycles were good and failure occurred after. The validity of such correction is limited but will allow interpreting properly the evolution of the thermal properties instead of the accurate absolute value.

All of these corrections would imply some error prorogation on the corrected values. However, given that most of the corrections are small, the original uncertainties coming from data fitting and sample length are usually much greater than these minor corrections. As results, we kept the original errors estimated after the fitting step as final errors after

corrections. Please, note that most of our corrections, such as removing n times 360° to the phase, are not subject to error prorogation.

A final file, in which corrected amplitude, phase and temperature, is created. This file used the template of the stacked file previously made where corrected values are pasted in their respective columns.

iv) Data inversion and Monte-Carlo simulations to recover thermal conductivities/diffusivities

This part is the major step to convert phase shifts and amplitude ratio into thermal properties of the studied sample. This code is much more complex and requires the use of several functions. Its operating conditions will be described in this part. The codes are given in the appendix C.

Thermal diffusivity is estimated via the minimization, with Monte Carlo simulation and neighborhood algorithm (Sambridge, 2002), of a generated diffusivity values and experimental data. The procedure is simple, artificial diffusivities are set, values of *u* (solution of the heat equation) can be then estimated. Theoretical phase shift and amplitude ratio can then be generated from Bessel functions. The minimization of the difference (misfit) between theoretical phase shift and amplitude ratio and the experimental measurements allows retrieving the best thermal diffusivity value.

Our program, named D_Fit, first reads the data form the excel files prepared in the previous steps. It also checks if the lines have some empty cell to ensure a correct input matrix is used for the calculations. Phase and amplitude are then corrected (if not done in the previous steps), to have only positive amplitudes and phases between -360° and +360°.

In this program, the user has to preliminary insert several important parameters. First, the sample length at RP/RT has to be given. This length can be the one measured before or after the high pressure runs, even if plastic deformation or decompression cracks can occur in each case respectively. If none of these problems is encountered, the sample length prior and after should be similar. The accurate sample length at each P and T step is recalculated using:

$$d(P,T) = d_0 * \left(1 - \alpha(T - 298) + \frac{P}{K}\right)^{-1/3}$$

Where d_0 is the sample length at room pressure (P) and temperature (T). α is the thermal expansion and K the bulk modulus of the sample.

In addition to sample length, the sample density and specific heat capacity are inserted manually in the program because there are mandatory to calculate thermal conductivity from thermal diffusivity. Because these parameters are function of P and T, literature data for similar samples is usually used, often extrapolated to get P or T dependences, to estimate these parameters the most accurately possible at each set of conditions. Thus, we use empirical equations to estimate each parameter's at each temperature and pressure.

For olivine and peridotites:

Thermal expansion was only used in function of temperature (no pressure dependence found) with the values of Bouhifd et al. (1996) on forsterite. Values are obtained from volume data for averaged samples along the three crystallographic axes in the 300-2000 K temperature range. The following equation was used:

$$\alpha_i = \alpha_{i0} + \alpha_{i1}T \leftrightarrow 2.832 * 10^{-5} + 0.758 * 10^{-8} * T$$

The bulk modulus is estimated at each P and T using values on forsterite provided by Li et al. (2007) in agreement with Gillet et al. (1991). The digitized curves from Gillet et al. were fitted by an order 2 polynomial law ($R^2 > 0.985$) for each represented pressure. Pressure dependence was estimated assuming a linear increase of *K* with increasing pressure which is a constant value for the pressure range 0 to 20 GPa (constant value of dK/DP).

The equation used is:

$$K(P,T) = 1.41 * 10^{-6} * T^2 - 1.79 * 10^{-2} * T + 139 + 4.2 * P$$

With *T* in K and *P* in GPa. The standard deviation of *K* values is not given the here mentioned studies. However, the good agreement between theoretical (Li et al., 2007) and experimental determinations (Gillet al., 1991) can let us considering 5% (1σ) uncertainty as a reasonable approximation.

The heat capacity was derived from Richet et al. (1991) and Watanabe et al. (1983), where pressure effect was not quantified. The equation used is:

$$Cp(T) = \frac{\left(205.99 - \frac{959.8}{T^{0.5}} - 30.137\frac{10^5 * 1}{T^2}\right) * 1}{0.14069} = J/K/kg$$

The density was estimated from data on forsterite from Li et al. (2007) with both P and T dependence: σ_ρ is estimated to be within 5%, the density is estimated using forsterite unit cell volume in function of P and T given by first principle modeling. Unit cell volume is translated to the density using:

$$\rho = \frac{\frac{N}{Na}M}{V}$$

$$\rho(P,T) = -0.2017P^2 + 25.019P + 3225.5 - 0.11749T$$

Where N is the number of atom in the formula unit, Na is the Avogadro number, M is the molar mass, and V the unit cell volume. Errors on N, Na and M can be considered as negligible. Errors on volume are not given by the authors but should be lower than 5%, as shown by the very good agreement between theoretical and experimental data on forsterite. Estimation of density at each P and T is made using a polynomial fitting at the order 2 of the volume data ($R^2 = 0.9998$) on Volume vs Pressure curves and Temperature correction is made assuming a linear dependence of ρ with temperature.

For MgO samples:

Thermal expansion is estimated in function of P and T using the work of Chopelas et al. (1996), the used equation is:

$$\alpha = 2.53 * 10^{-14} * T^3 - 6.83 * 10^{-11} * T^2 + 7.19 * 10^{-8} * T + 1.32 * 10^{-5} - 3 * 10^{-7} * P$$

The bulk modulus was estimated from Kumar et al. (2000) in function of temperature only:

$$K(T) = -0.0269 * T + 169.95$$

The heat capacity was estimated with the data from Richet al. (1991), for temperature only:

$$Cp(T) = (2.53 * 10^{-9} * T^3 - 1.16 * 10^{-5} * T^2 + 2.14 * 10^{-2} * T + 34)/40.3 * 10^{-3} = J/K/kg$$

The density was estimated for P and T effects from Speziale et al. (2001):

$$\rho(P,T) = (1.216 * 10^{-11} * T^3 - 5.5844 * 10^{-8} * T^2 - 7.569 * 10^{-5} * T + 3.6522) * 1000 + 19.07815 * P^{-2}$$

For basaltic/MORB glass and melts:

For MORB and rhyolite, the main problem comes from the fact that most of variables change importantly above glass transition and melting temperatures. However, the best solution would be taking solid calibration at low temperatures and melt data above melting

point (Romine et al., 2012). The second problem is that these data are not always available for solids and melts in function of P and T, this is particularly true for rhyolites that are usually not studied at such depths.

For MORB, solid calibrations were only used:

Density was estimated in function of P and T with the data of Bajgain et al. (2015):

$$\rho(P,T) = \left(-3.79 * 10^{-8} * P^4 + 1.14 * 10^{-5} * P^3 - 1.29 * 10^{-3} * P^2 + 7.863 * 10^{-2} * P + 2.750 - 6.1 * 10^{-4} * (T - 2200)\right) * 1000$$

Thermal expansion was only found at room pressure with the data from Hartlieb (2015).

$$\alpha(T) = 6.651 * (T - 273.15)^{-0.6438}$$

Bulk modulus was estimated only as function of pressure with data from MatWeb and a pressure derivative of 3.6 (Bajgain et al., 2015).

$$K = 23 + 3.6 * P$$

The heat capacity was estimated in function of temperature only (Bajgain et al., 2015):

$$Cp = (0.1312 * ln(T) + 0.2427) * 1000$$

Haplobasalt physical characteristics are not well known for our composition, so the parameters of MORB will be used for this sample.

For rhyolitic glass and melts:

For rhyolitic compositions, we used data obtained on glasses rather than data on melts as finding a complete data set was difficult. Pressure effect is only little compared to temperature.

Density was estimated in function of P and T with the data from Spera et al. (2000).

$$\rho(P,T) = -0.072 * T + 2621 + 180.60 * (P - 1)$$

Thermal expansion studies were not found, data from Universalism academic website at room pressure and temperature was used.

$$\alpha = 8 * 10^{-6} \pm 3 * 10^{-6}$$

Heat capacity was inferred from data of Neuville et al. (1993) converted into J/kg/K using a molar mass of 66.02 g/mol estimated from our ATHO composition. Pressure dependence is unknown.

$$Cp(T) = -1.75 * 10^{-4} * T^2 + 0.381 * T + 162$$

Bulk modulus was estimated from Malfait et al. (2014) with both P and T dependences.

$$K(P,T) = 11.5 + 6.5 * P - 0.0016 * T$$

From the inserted values and data from read files, D_Fit estimates phase shift and amplitude ratio values for each couple of data (TC1 and TC2) and calculates their associated errors (see appendix C). Then, the minimization part is done in a separate function for convenience. In this function, the input: measured phase shift and amplitude ratio, are compared to artificially generated ones and their differences are minimized to retrieve the good thermal diffusivity because heat diffusion equation does not allow a simple forward estimation.

One of the most important, and neglected part, in the literature, is that phase shifts are involving angles. These angles are strictly equal if they are multiples of 360° (2π) and so the equation would yield to the same exact result every 360°. Thus, all the solutions that we are trying to minimize are mathematically equivalent. An automatic search of the "good minimum" by just exploring linearly the diffusivity space would induce errors due to selection of a "bad" minimum (literature inversions). Then, the estimation of the phase shift is limited to 1 period of phase shift (360°), if larger phase shifts are not seen during the fitting step (such differences can be seen while switching on/off the modulation or with temperature perturbations). This is a quite important limitation for very insulating materials or materials over a too large distance. The second important point is that the user should have a pretty good a priori on the thermal diffusivity of the analyzed material. For geological materials, such as oxides and silicates, most of the diffusivities are between 10^{-5} and 10^{-7} m²/s but if this program is used on metallic samples or very insulating materials on similar dimensions, this point has to be carefully checked.

For amplitude ratio, a Monte Carlo iterative process using a neighborhood algorithm is used (Sambridge, 2002). A first homogeneous (in log space) draft of artificial data in large

diffusivity space is made (Fig. VI.11). The difference between the measured and calculated data (called misfit) is estimated and is near zero for good thermal diffusivities values every 2 Pi. Our program selects the four smaller misfits and proceeds to another draw in a more restricted zone around the selected values and a thinner step value. This iteration is made 9 times until the programs stops with the "most" correct minimum to misfit function. Accuracy, correctness and errors associated to this procedure are given in the following sections.

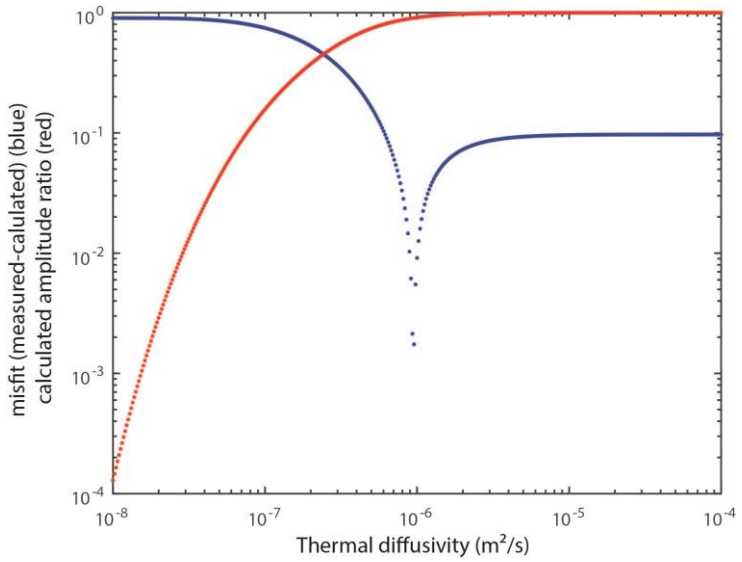

Figure VI.11 Representation of misfit and calculated amplitude ratio as a function of drawn thermal diffusivity for the first draft of the Monte Carlo inversion. Sample M651,H2- 0.2 Hz.

For phase shift, the author preferred to do this step manually due to the presence of more local minima (which does not occur in amplitude ratio). The presence of local minima increases while increasing frequency (Figs. VI.12 and 13). It first allows seeing and checking where the potential minima are and offers the possibility to manually select the zone for a second draw. Then, similarly to amplitude, the second draw is made in the specified zone with more precision. Again, the user selects the minimum point. Our tests on the code showed that most of the time, the good value is retrieved from the second iteration with acceptable misfit values (10^{-5} - 10^{-6}). This is why for time consideration, I limited this selection to two steps (it takes approximatively 20 min for 50 inversions). Finally, the function sends back the best diffusivities determined during the inversion to the main program which can compute the thermal diffusivities and thermal diffusivities values. Graphical representations of the obtained data are proposed to the user with amplitude ratio and phase shift determination of thermal conductivity and diffusivity. After little time, the code asks to the user whether these data should be saved or not. If yes, the data are saved in a new excel sheet of the same name with Dfit_results concatenated to the original title. In this file, all the important data is saved

such as measured phase shift and amplitude ratio, their closest computed values and their associated diffusivities with their respective errors and misfits.

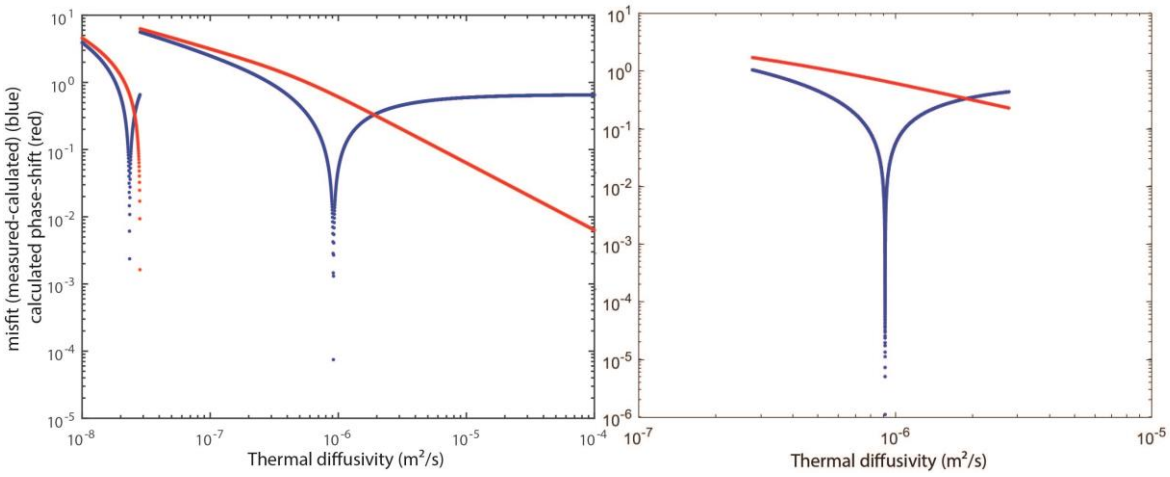

Figure VI.12 Representation of misfit and calculated phase shift as a function of drawn thermal diffusivity for the first draw of the inversion on the left and the second draw on the right. Sample M651, H2- 0.2 Hz.

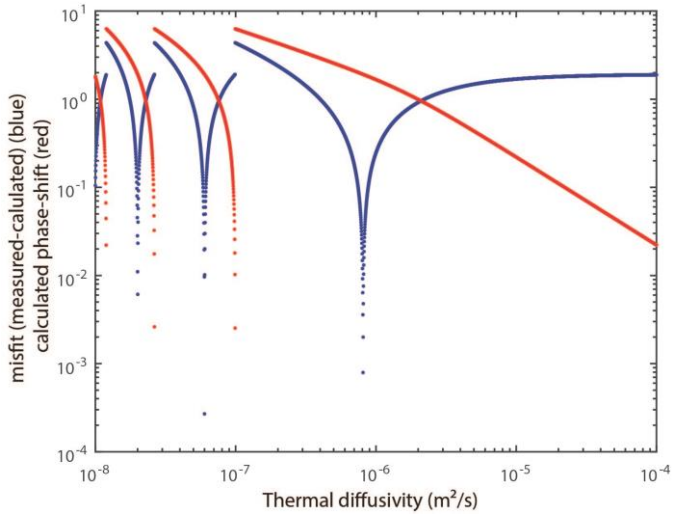

Figure VI.13 Representation of misfit and calculated phase shift as a function of drawn thermal diffusivity for the first draw of the inversion. Sample M651, H2- 1.2 Hz. Note the presence of several local minima at high frequencies which corresponds to every 2π in the calculated function. These solution are mathematically equivalent and an a priori is required to select the good diffusivity (here 10^{-6} m²/s).

NB: Please note that this inversion procedure in not made with user friendly interface, thus, the program does not allow doing anything else than the treatment. If mistakes are made or errors in the choice of the minima, the program has to be shut down and restarted. Due to the use of functions, the data can't be retrieved in case of failure. For convenience, it is recommended to do a "close all" (to close remaining figures) before re-starting the program.

3) Results and discussions

We have, for thermal diffusivity measurements by Angström method, performed a total of 23 experiments on various chemical compositions. The sum up of each experiment is given in the following table VI.6. This results/discussions section will be different from a simple explanation of results as experimental failures, system issues and technical modifications were required to yield correct results. This section details the experimental issues and their resolutions. Then, upgrades to the programs for uncertainty propagation are provided. Then a results description is provided with thermal diffusivity data and their interpretation. Sample chemical and textural analyses on olivine samples will be addressed. Due to lack of time (these experiments were performed during July-August 2019) the discussion will not be pushed for geological implications, hence planned works are given in the perspectives.

a) Experimental and thermocouple issues

Thermal diffusivity measurements by Angström method in MAA is a difficult task. The fact of using two thermocouples increases dramatically the risk of failures. With our 1500-ton MAA, such experiments can only be made on large assemblies, limiting the studied pressure range to 5 GPa. However, due to a weak pressure dependence of thermal parameters (Hofmeister and Brandlund, 2015) performing the measurement at moderate pressure (2 GPa) is not a problem for upper mantle purposes.

Upon the series of experiment carried during this PhD project, two main issues were encountered. First issues were observed during our experiments with the thermocouples. Second ones were associated to the experimental setup. Their explanation and resolution will be succinctly explained in this section.

First, we often observed, during the HP-HT experiment, the deviation of one of the two thermocouples from the power-temperature calibration curve (appendix D for M617, M619, M661 etc.). The deviant thermocouple followed a power/temperature line characterized by a smaller slope than calibration. However, the thermocouple was found to react perfectly to heating and cooling but in much lower magnitude (displayed temperature between 50 and 400°C instead of 50 and > 1400°C) (Fig VI.14). The thermocouple was also observed to react very well to oscillations made by heating modulation. The oscillations are well visible, had smaller amplitude than working thermocouple and were slightly noisier. However, they were able to be fitted properly (Fig VI.14).

Table VI.4: Sum up of Angström experimental compositions, conditions and important associated parameters.

Run#	M517	M525	M525-2	M617	M618	M619	M661	M662	M770	M773	M774	M802
Sample name	MgO SC	Ol SC	Ol SC	olivine poly	MORB powder	MgO	Peridotite	EPR-MORB	MgO polycryst	MgO polycryst	MgO SC	MgO polycryst
Composition	MgO	Olivine	Olivine	olivine poly	EPR MORB	MgO	Peridotite	MORB	MgO	MgO	MgO	MgO
Pressure (GPa)	0.5	2	4	2	2	2	2	2	2	2	2	2
lenght before (um)	1700	1700	1700	1700	1700	1700	1700	1400	1645	1645	1700	1645
length after	1658.301	1688.337	1688.337	1744.334	-	-	1603.927	1334.214	1967.564	1480.913	1840.827	1623.905
expected Melting T° (K)	>3100	>2000	>2000	>2000	>2000	>3100	>1523	>1600	>3100	>3100	>3100	>3100
Max T (K)	879	1538	1925	1464	FAILED	1392	1280	1614	1249	1357	1568	1471
Run duration (min)	238	382	466	259	FAILED	248	405	544	637	318	567+477	688

Run#	M804	M807	M808	M833	M836	M843	M844	M846	M847	M848	M850	M851
Sample name	RP4-S2	DR07-S2	GD-S1	Ol-SC	Haplo S1	ATHO-S1	DR11-S1	DR11-S2	RP4-S3	ATHO-S2	GD-S2	Olvine poly - 2
Composition	Peridotite	MORB	Rhyolite	olivine	haplobasalt	Rhyolite	MORB	MORB	Peridotite	Rhyolite	Rhyolite	olivine polycryst
Pressure (GPa)	2	2	2	2	2	2	2	2	2	2	2	2
lenght before (um)	1771.198	1061.943	1098.817	1361.3	1124.6	1541.89	1141.33	1048.2	1652.934	1045.068	1336.402	1400
length after	1780.004	-	1462.731	1659.386	1213.209	1666.07	1287.564	1324.891	1643.637	1309.103	1287.409	1424.907
expected Melting T° (K)	>1523	>1600	>1173	>2000	>1723	>1173	>1600	>1600	>1523	>1173	>1173	>2000
Max T (K)	1681	1612	1146	1676	1769	1219	1609	1284	1573	1325	1073	1383
Run duration (min)	1089	953	480	478	832	800	834	439	767	761	610	894

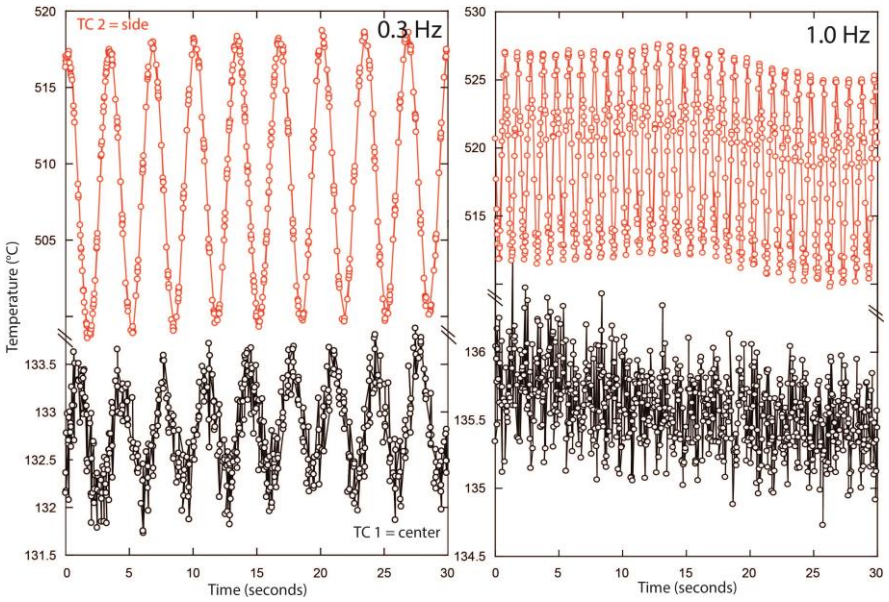

Figure VI.14 Example of thermocouple issue where the first thermocouple (black) displays a lower temperature than the correct thermocouple (in red). However, oscillations are still well visible even if noisier at higher frequencies (see the right panel at 1Hz). These data were taken at 520W of heating power.

Samples, in which such issue was observed, were check after the experiments. The wires inside the assemblies were still in correct position, in contact with each other and no sign of inner failure was observed (Appendix D). Signals with open thermocouple and short circuit with MAA were acquired and could not explain our observation. Finally, the source was found to be due to a double contact of the thermocouple wires and secondary WC anvil. Indeed in 4 wires experiment, the thermocouples exits on the octahedron share a common cube (which is isolated from the MAA). When the two wires of the same thermocouple touch the cube, they could short-circuit the junction present in the assembly.

We tried to solve the problem using thinner thermocouple copper coils and drilled the gaskets in the center. However, such issue was still found to occur in several experiments.

To determine if the oscillation measured can be used to infer thermal properties via phase shift (and amplitude, if corrected), the principle of thermocouple temperature has to be considered (see Chapter II).

A thermocouple relies on Seebeck effect to determine accurately temperature between a "hot-junction", located in the assembly, and "cold-junctions" at multi-meter holders. Cold junctions are usually at room temperature in the multi-meter device. Voltage in the loop is a function of the temperature gradient between hot and cold/reference junctions (Fig. VI.15):

$$\Delta V = \int_{Tref}^{Thot} S_{ab}(\theta) d\theta$$

Where S_{ab} is the Seebeck coefficient of the metal couple a-b ($S_{ab} = S_b - S_a$). To determine accurately the hot junction temperature, the cold junction temperature must be measured near the multi-meter by an independent system, usually a platinum pt100 or pt1000 thermo-resistance. In real case, the electromotive force (EMF) is used instead of Seebeck coefficient (see chapter II) with known polynomial calibration using a reference temperature of 0°C. By consequence, the system (at RT) must have a cold junction correction. The wires in the multi-meter (copper) have no effect when the two connections are at the same temperature.

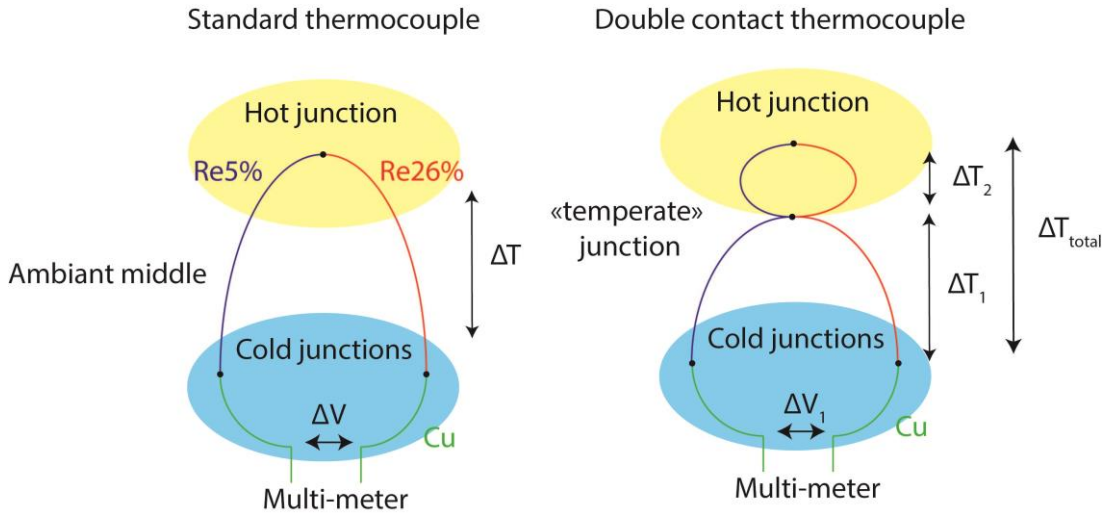

Figure VI.15 Thermocouple theoretical operation and double contact cases.

In our case, the thermocouple seems to have a second "temperate" junction on the external part of the assembly and/or secondary anvil (Fig. VI.15). This junction prevents knowing the real electromagnetic force because the second loop must have a lower EMF (lower temperature). This hypothesis is confirmed by the lower observed temperature. Temperature correction according working thermocouple temperature can be foreseen.

Potential difference as a function of the gradient of temperature in each loop can be expressed (labeled 1 for cold to temperate junctions and 2 between temperate and hot junctions).

$$\Delta V_{total} = \Delta V_1 + \Delta V_2$$

$$\Delta V_{total} = \int_{Tref}^{Thot} S_{ab}(\theta)d\theta = \int_{Tref}^{Ttemperate} S_{ab}(\theta)d\theta + \int_{Ttemperate}^{Thot} S_{ab}(\theta)d\theta$$

However, this correction cannot be made after the experiment because cold junction temperature is not saved in our files, neither the measured EMF. The output data is only temperature and time. Such correction, can however be considered in a near future.

The main point of thermocouple operation is that having two cold junctions has no effect, if they are at the same temperature. Thus, the temperature variations observed, when oscillations are set, occur in the hot junction regions. They are not perturbed because the cold junction temperature is constant during these times. We can consider the same effect for the "temperate" region. Its average temperature varies according to the temperature in the assembly. As no oscillations can reach outside the octahedron (attenuated before), we can consider that during the time of measurement, the "temperate" temperature is constant. Thus any observed EMF perturbation must be due to variations occurring in the hot loop, modulating slightly the bulk signal. This point would indicate that sinusoidal oscillation observed could be used for phase shift estimation as they are coming from the desired zone of analysis. Such argument is validated by comparison between phases shifts observed between a perfectly working experiment and experiment with thermocouple issues (appendix D).

A second type of issues was observed in our first series of experiment (M517-M770) experiment. Our second thermocouple was observed to be noisier than the first one (despite identical reading channel) and positive phase shifts (instead of negative) were observed.

The source of the problem was due to the heating system and our LabVIEW interface. After several tests, we observed that significant phase shifts (up to 35°!) and amplitude variations were generated by our apparatus. The issue was due to a bad affectation of our time variables inducing a misplacement of our second thermocouple measurements.

We also found that the correct time could not be retrieved after experiments. The effect was observed to variable for each data point and so no global correction can be applied. As a consequence, the data from experiments made prior these tests can't be considered as correct (before M770). Due to possible underestimations of phases shifts and overestimation of amplitude ratio, the measured data would indicate maximum thermal diffusivities for phase shifts estimations and a minimum for amplitudes one. The "good point" of our previous experiments is that they were made at low frequencies (0.05 to 1 Hz) which limits greatly the impact on amplitude introducing much less uncertainty for its use.

In front of these issues, a corrected program was made by A. Mathieu, in which TC1 and TC2 are read simultaneously at the very beginning of the loop in a data table. The read time is then fixed and absolute for the two thermocouples (no TC2 reading after TC1). Tests performed with modified programs were indicated perfect signal estimation.

We also took this modification step as a possibility to increase the sampling rate of our apparatus. Thanks to optimization of computing time and computer resource utilization via modification of the LabVIEW interface, we increase our sampling rate by a factor 3. The interval between data points is not constant anymore (depends on the execution speed) but sampling rate was increased up to almost one point every 40 ms instead of 140 ms previously.

These modifications allowed obtaining reliable data for both phase and amplitude. The second important point is that we have increased the sample rate by an order of 3, which allows extending the studied range up to 1.5 Hz, which is similar to other Misasa/Bayreuth devices and increased the quality of the data measured with our setup. Finally, the data on all the previously made experiments (prior M770) should be considered with caution as potential strong issues on phase shifts and amplitude ratio may be expected.

b) Error and uncertainty treatment implementation in the fitting and inversion programs

The literature on thermal diffusivity measurements is very elusive onto errors propagations and their consideration. In this work, we have developed a much robust procedure to estimate thermal properties via the inversion of phase shift and amplitude ratio using Monte Carlo inversion or neighborhood methods (Sambridge, 2002). The errors (deviation to the real value) and uncertainties (interval of confidence around the measured value) on each step are estimated. The complete development is given in the appendix C with the Matlab codes which incorporate this uncertainty treatment procedure.

c) Thermal diffusivity results and data processing

i) Phase shifts and amplitude ratio

Our measured values of phase shifts, amplitude ratio and inferred thermal diffusivities depend on the sample size, modulation frequency and temperatures.

A representative example of data obtained after processing are displayed in the figure VI.16. The (absolute) phase shifts are drawing trends while plotted as a function of frequency and temperature. At constant frequency, the phase shift usually decreases with increasing temperature (lower diffusivity at HT) and frequency. A constant temperature, the phase shift

increases while increasing excitation frequency. The amplitude ratio is decreasing with increasing frequency and temperature, again behaving coherently with decreasing thermal diffusivities at high temperatures (1/T behavior).

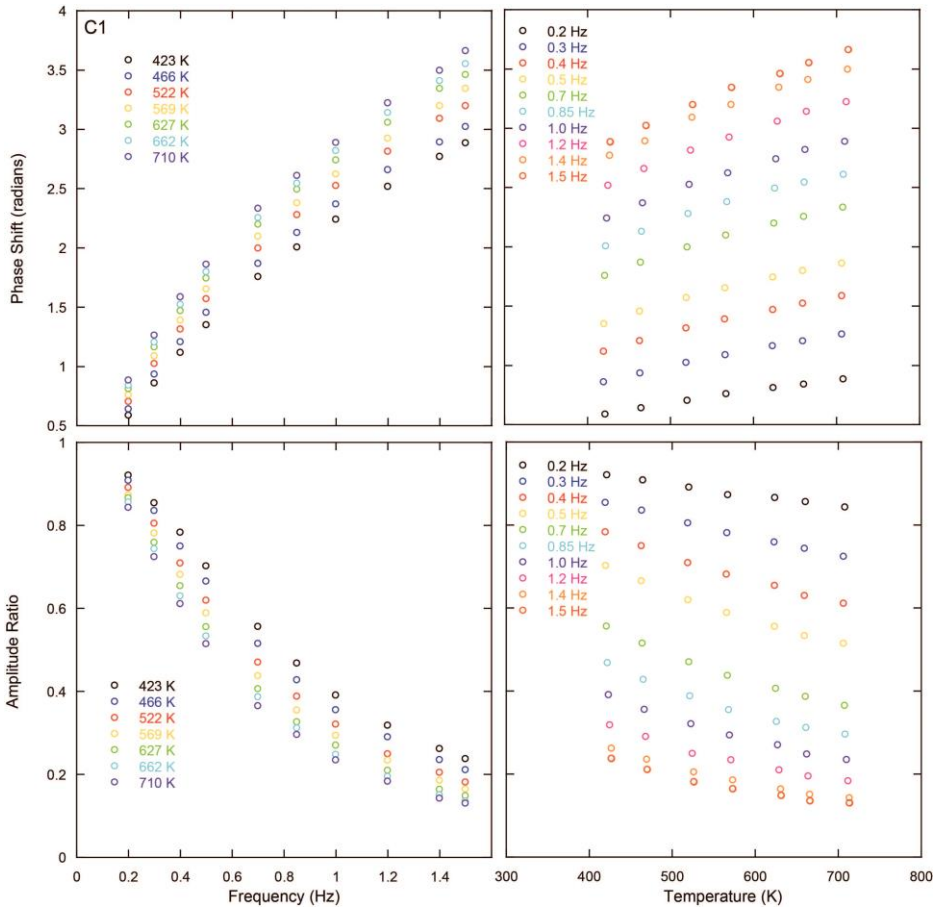

Figure VI.16 Phase shift and amplitude ratio results obtained after inversion as a function of frequency and temperature. Sample M851, Cycle C1.

ii) Thermal diffusivity estimation and fitting

From these values, thermal diffusivities and conductivities inferred from phase shifts and amplitude ratio are given for a representative example at different cycles (Fig. VI.17, appendix D). Hence, we can see that for a single experiment, a large range of possible diffusivities were estimated at a constant temperature and that estimations coming from different frequencies are not strictly equal and showing some important deviations. In previous literature measurements of Xu et al. (2004) or Manthilake et al. (2011), these differences have been explained by invoking deviation from infinite long sample cylinder hypothesis formulated for the mathematical simplification of heat diffusion equation. This effect should be more present at low frequencies (Bhandari and Rowe, 1998; Xu et al., 2004). These studies chose to fit the diffusivity versus frequency curves to obtain infinite frequency asymptote. While Manthilake et al. (2011) used:

$$D = D_\infty + A_0 exp\,(A_1 * f)$$

Xu et al. (2004) preferred the following formulas:

$$D = D_\infty + A_0 exp(-xf)(1) \wedge D = D_\infty + A_0 exp\left(\frac{-f}{f_0}\right)(2)$$

Where D_∞, A_n and f_0 are inverted parameters. In case of no systematic dependence to frequency, the average value between all the frequencies was considered. With this step, only one diffusivity values for phase and amplitude is obtained at each temperature step.

We tried to fit our data by taking in account the procedure reported above and results are provided hereafter (Figure VI.18, figures for each experiment in appendix D). For each temperature step, we calculated the average, the uncertainty (via error propagation), maximum and minimum values and also fitted the data. We used the Signal Processing Toolbox of Matlab to fit using the equation 1 (but fixing x = 1) and 2 of Xu et al. (2004). In addition, we took in account errors on diffusivities as weights for the inversion and recovered the errors on final parameters due to the fitting step. Error on average is:

$$\sigma_{AVG} = \sqrt{\left(\frac{1}{n}\right)^2 * \sum_{1:n} {\sigma_D}^2}$$

We saw that this propagation was inferior to the average of uncertainties on the averaged diffusivities (between a factor 2 and 3).

For our data, the selection between fitted values and averaged ones is not very obvious and systematic (see discussion). Thus, we preferred the averaged values of thermal diffusivities, as fitted ones do not seem to be very reliable and have a wider uncertainty.

Globally, our experiments show similar patterns in the thermal diffusivity evolution with temperature and frequencies (appendix D). The magnitude of phase shift and amplitude ratio changed between the samples according their thicknesses and their thermal properties. Thus, the largest phase shifts and smaller amplitude ratio were observed at high temperature and for basaltic and rhyolitic glasses/melts. Our samples measured before software correction, have data with a clearly worst quality (amplitude ratio trends were found to be nicer, see above). Our values are coherent with previous literature estimations for both solid and glasses. Partial melting effect was observed in few experiments and is translated by a drop of the thermal diffusivity. The intensity of the drop was found to be much greater in solids (our molten

peridotites) than glasses (where the drop is not very clear) due to more contrasted properties. Similar observations were made by Hofmeister et al. (2009) and Romine et al. (2012). Experimental failures are also easily visible, with a loss of trends at the failure temperature and scattered values.

For each experiment, diffusivities values, with both average and fitting method for all the cycles, are given in the appendix D. The thermal diffusivity obtained ranges from very conductive materials such as MgO, to intermediate (olivine, peridotite) and very insulating ones with glasses and melts. Even if important refinements must be made on our data (precise estimation of sample size etc.) absolute values of diffusivities can be given at 2 GPa.

Our MgO samples gave good values between $7e^{-6}$ and $1e^{-6}$ m²/s between 320 and 1800 K. Values inferred are slightly high for single crystals.

Olivine is less conductive than periclase. Our single crystals characterization gave values between $4e^{-6}$ m²/s and $0.8e^{-6}$ m²/s from 300 K to 1900 K. Dunites samples with smaller grain size had low values between $1e^{-6}$ and $5e^{-7}$ m²/s which are pretty compatibles with our peridotites samples : $1.5e^{-6}$ and $5e^{-7}$ m²/s from RT to 1600K. At partial melting our peridotites samples had a much lower thermal diffusivities with absolute values that are varying (according to solid one) between $2e^{-7}$ m²/s and $5e^{-7}$ m²/s. Melting is characterized by a drop of 0.1 to $0.3e^{-7}$ m²/s compared to solid values (may depend on melt fraction). Crossing Tg is often visible with lower estimated diffusivities above it and a change in slope. Difference between cycles are also visible, D seems to increase after recrystallization cycle, and must be investigated more in details.

For basaltic glasses and melts, the diffusivity values are much lower. The diffusivities ranges from $5e^{-7}$ to $2e^{-7}$ from RT to melting temperature and values for melts are characterized by a drop of 2 to $3e^{-7}$ m²/s. At melting, the absolute values were observed to be around 1 to $1.5e^{-7}$ m/s (M807 is too high but sample diameter is not well known).

For silica rich melts such as our rhyolite samples, thermal diffusivities trends were more flat than basalts. Variations were observed to be between $6e^{-7}$ and $3e^{-7}$ m²/s. Melting is not very clear with measured values under $4e^{-7}$ m²/s which are similar to previous glass measurements.

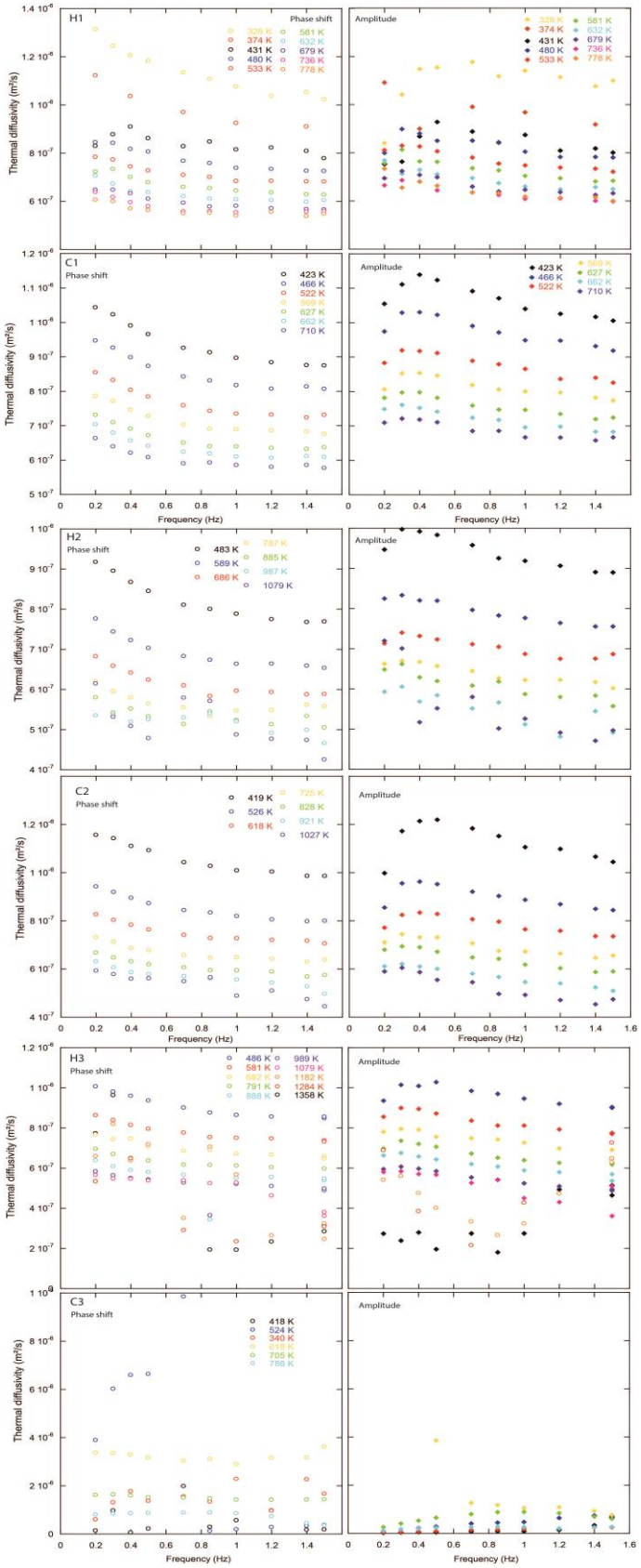

Figure VI.17 Phase shift and amplitude ratio inverted thermal diffusivities as a function of frequency and temperature for M851 for all the cycles.

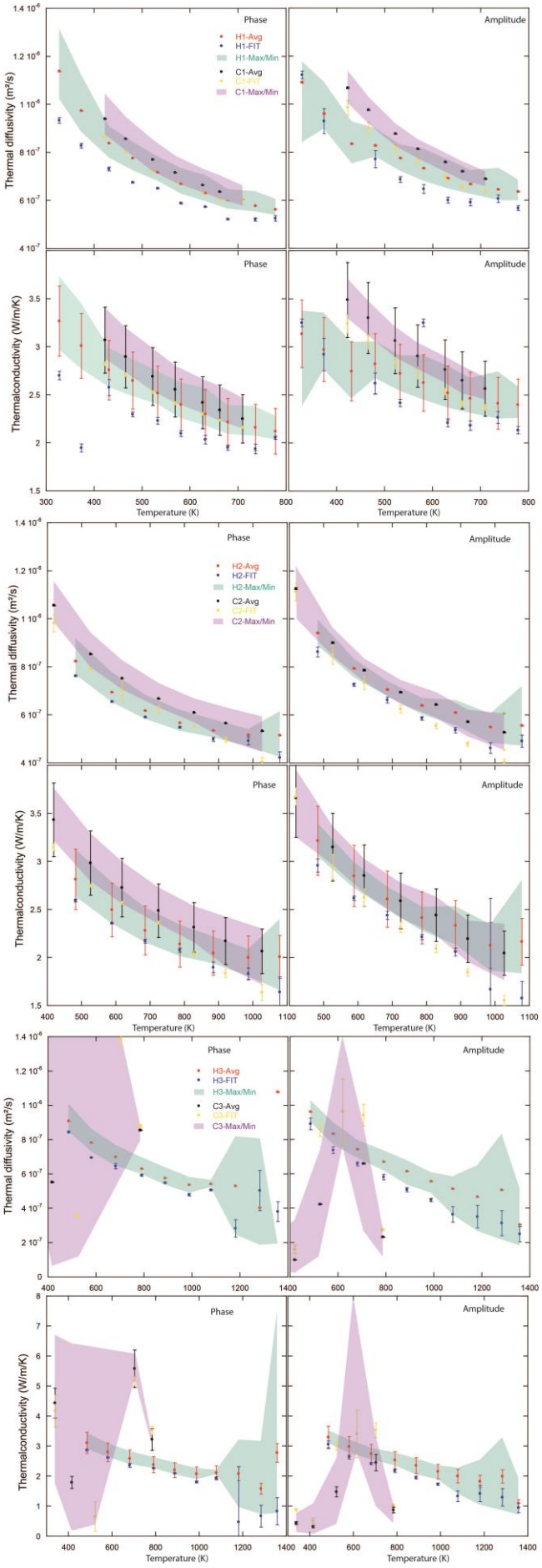

Figure VI.18 Comparison of thermal diffusivities and conductivities estimations for different methods (average and fit) for each cycle of M851.Left panels are for phase and right panels for amplitudes. The colored intervals represent data range between maximum and minimum values of diffusivities from the different frequencies (green and purple for average and fitting methods respectively). Values for average are displayed in red and blue for average and fitted diffusivities for heating cycle and black and yellow for cooling one. We can see that cooling cycle always displays values slightly higher then heating ones.

iii) Thermal conductivity estimations

Thermal conductivities were computed from thermal diffusivity results using heat capacity and density which were computed at each step at the correct P-T conditions (see above, Appendix C).

The computed values are much more uncertain than inferred diffusivities because external values such as density and heat capacity have to be calibrated and extrapolated for dedicated studies. Our obtained values are coherent with literature estimates for MgO, olivine, peridotites and various glasses and melts (Figs. VI.19 and 20) with values ranging from 20 to 2 W/m/K for MgO sample, 10 and 1 W/m/K for olivine and peridotite ones and values between 5 and 0.1 W/m/K for glasses an melts.

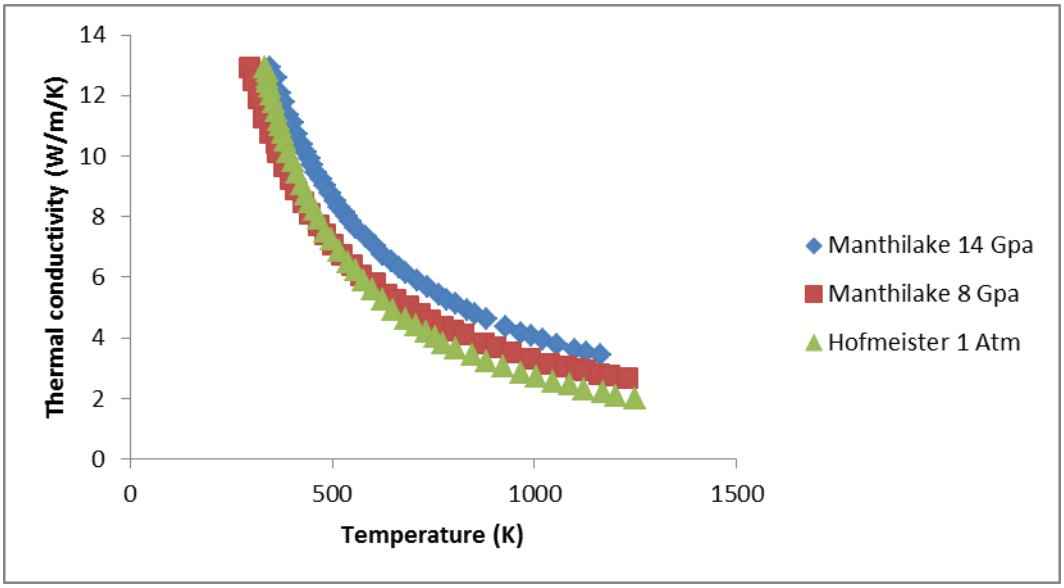

Figure VI.19 Thermal conductivity of periclase as a function of temperature according different literature studies (Manthilake et al., 2011; Hofmeister and Brandlund, 2015).

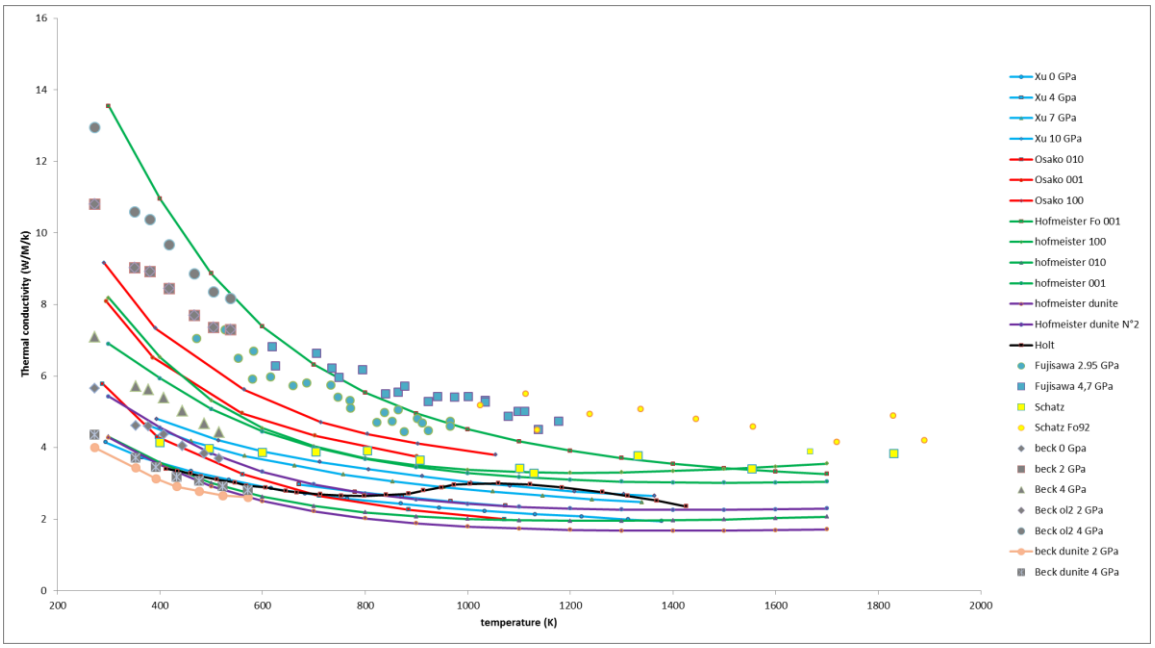

Figure VI.20 Thermal conductivity of olivine as a function of temperature according different literature studies (Xu et al., 2004; Fujisawa et al., 1968; Osako et al., 2004; Beck, 1978; Schatz and Simmons, 1972; Holt, 1975; Hofmeister and Brandlund, 2015).

The comparison with low pressure data from other techniques such as LFA is interesting because it helps to understand the pressure effects as well as evaluate the contribution from lattice and radiative components.

Thermal conductivities and diffusivities have to be further processed to achieve final "polished" results. Hence, here we provided raw results and important data analyses for the choice between fitted or averaged values. With final polished values of thermal conductivity, fits will be realized using the equation provided in Manthilake et al. (2011):

$$k = k_{ref} * \left(\frac{T_{ref}}{T}\right)^{a} \left(\frac{\rho}{\rho_{ref}}\right)^{g}$$

Such equation will allow understanding if significant deviation for 1/T behavior is present and will permit extrapolation from our data set for modeling purposes and precise geological implications (perspectives)

iv) Discussion

(1) Observations and comments on data processing and fitting methods

While the data processing of our experiment was realized several observations were found important for comparisons of values with other methods. First, we observed that patterns depicted by these former studies on phase shift (higher diffusivities at low

frequencies) and amplitude ratio (lower diffusivities at low frequencies) are not systematically observed in our experiments (Appendix D, Fig VI.17). We also observed numerous cases (on perfectly working experiments), where the data does not show any clear asymptotic behavior, fits values can't be used in such case. We observed that the equation used by Manthilake et al., does not allow good fitting with our software, this is why it was ruled out for our data processing. We found that equation 1 of Xu et al. (2004) (see above) worked properly most of the time and that equation 2 was working particularly well when asymptotic patterns were observed. The resulting errors are usually smaller using equation 1 because, with x value fixed to 1, less degrees of freedom exists for inversion. We also found that fitting errors are always more important than ones obtained by average method. The error estimations is also completely omitted in previous works (Katsura, 1993; Xu et al., 2004) or estimated roughly. Manthilake et al. (2011) considered errors on their estimation. However, they used as uncertainty a constant value for each data point (see appendix of their paper) and no propagations of errors were realized during the fittings steps (or not mentioned). This is however crucial when comparison, extrapolations and evaluation of absolute thermal properties are needed. Underestimation of uncertainties is thus probable in these mentioned studies.

We must also note that the precision of the fit and associated error is directly a function of the number of data points. By consequence, using data measured between 3-5 different frequencies such has Manthilake et al. (2011), or 6 frequencies such has Xu et al. (2004) would provide higher uncertainties than our procedure with 11 measurements ranging from 0.2 to 1.5 Hz.

The results inferred from average and fitted methods are given in the figure VI.18 and in appendix D for fit and average methods. We can clearly see that the inferred values by different methods are significantly different and most of the time not overlapping, even considering the uncertainties. Thus, the proposed procedure by Xu to take the fitted values when fits are correct and averaged ones when fits are bad would results in a significant difference. For our data, differences high than 25 % between the two estimations have been found. For M851 the fitted values are lower than average ones, but the reverse order was also observed in some of our experiments (appendix D). At melting the fitted and averaged values were very different yielding to difficulties into the data interpretation.

Finally, results are coherent within a given technique and so relative variations must be correct. We observed that data obtained during the cooling cycles seems always higher than values estimated during the heating ones, probably due to a better thermal equilibration of the sample and good thermal contacts.

To sum up, both fitting methods and associated uncertainties, heating/cooling paths used and phase or amplitude choice have a profound impact on the final thermal diffusivity trend given in literature experiments. Then, arguments used by Hofmeister et al. (2007), against contact methods, for which large variations of results and underestimations compared to other techniques such as LFA were reported, may also be due to such issues. Thermal resistance due to contact methods probably exist, however, many other sources of data dispersion are present, and given their magnitude, they could explain significant amount of the observed discrepancies. In addition, there is no point to quantify the effect of thermal resistance on measured diffusivities to discredit contact methods, as commonly made by Hofmeister et al., as variations observed are due to several parameters and not only the presence of contact resistances.

(2) Heat transfer processes: conduction, radiation and convection?

Previous studies show that radiative conduction mechanism can contribute significantly to the recovered signals. However, only few experiments have typical shapes translating the presence of radiative transfer at high temperature. Thermal conductivity increase at high temperature are scarce in our samples and no clear experimental evidences of these transfer were found, even if optical properties changed dramatically from one sample to another (opaque basalts to transparent MgO). Ballistic photons may occur, however simulation of thermal gradients in our assembly made in chapter II, indicate that the gradients our samples are moderates (~15 K).

Optical absorption is an important factor controlling the presence of radiative transfer, such consideration are discussed in the appendix E. Our samples are thick, 4 mm diameter, which indicates that, for optically dark samples such as basalts, rhyolite and samples with fine grain size, optically thick conditions are reached. Such radiative transfer suppression has also been discussed by Xu et al. (2004) for similar samples. Similarly, Kanamori et al. (1969) showed that diffusivities estimated from amplitude ratio are more subjected to radiative perturbation than phase shifts estimations in case of low optical density. However, our phase

shifts and amplitude ratio data are not significantly different confirming that radiative transfer might be restricted in our experiments.

For partially and fully molten samples at high pressure and temperature, measured thermal diffusivities/conductivities are usually decreasing at melting. This indicates that melts are more insulating than rocks and to a lesser extent than glasses. Most of our glasses are opaque (except hapobasalt), thus radiative transfer must not be significant. In addition, for melts, a possible convective transfer can occur in the high pressure assembly. This type of transfer is efficient and must be translated by way higher "apparent conductivity" with low phase shift and high amplitude ratio. We estimated Rayleigh number for our experiments to be around $5e^{-2}$ (using a viscosity of 10 Pa.s, temperature gradient of 15 K, thermal diffusivity of $5e^{-7}$ m^2/s and characteristic length of 4 mm). This Rayleigh number which is clearly lower than the threshold of 1700 indicating convection is unlikely in our experiments as suggested by our *in situ* observations.

d) Chemical and textural analyses

Chemical analyses were performed on both our olivine starting materials and experimental products. Because most of our experiments were conducted in summer 2019, the analyses on the last series of experiment will be performed afterward (see perspectives). Only the olivine samples of the first experiments were analyzed. Despite these experiments results are lapsed due to technical issues described above, insights are good for the overall understating of our assembly behavior as conditions were similar for all the experiments.

i) *Analytical techniques*

Chemical composition for major elements was measured using the Cameca SX100 electron probe micro analyzer at the LMV (Chapter I). The apparatus was calibrated against olivine standards prior our analysis. Electron beams of 20 micrometers were used to cancel grain boundaries effects on the analysis quality.

Raman spectroscopy was used to estimate the water contents of our olivine, starting peridotites and glasses samples (see above). A Renishaw InVia confocal Raman micro spectrometer was used. Such apparatus and working conditions are described in chapters I, IV and V.

Micro-textures of the samples were observed with a Scanning Electron Microscope (SEM) JEOL Jeol JSM-5910 LV at the LVM. For imaging, an accelerating voltage of 15 kV and

working distance of 11.4mm were used. Electron Back Scattered Diffraction (EBSD) analyses were performed with this apparatus with an accelerating voltage of 15 kV and exposure time between 10-16 ms. Because our analyzed samples are chemically homogeneous and composed of olivine only, the band detection was compared to two standards (Fo and Fo0.9 olivines) for pattern recognition and orientation estimation. Zero solutions pixels varied between 10 to 30%, higher rates are mostly due to the presence of holes resulting of grains removal during polishing.

Textural analyzes were binarized from EBSD and BSE images, grain boundaries were evidenced by zones of zero solution between two domains of different misorientation (Figs. B.47, 48, 49, 50, 51, 52 and 53). The grain size of our samples was estimated using different techniques described in our Chapter III.

ii) *Petrological descriptions of samples and textural analyses*

Due to the great variety of compositions studied in this study and the different experimental procedures, a pretty wide variety of textures were observed. We will first describe solid samples and then glasses and molten ones on a second step. The available photographs or BSE microphotographs are provided in this section or individual experiment in the appendixes B and D.

The recovered samples have been cut parallel and perpendicular to the assembly to observe the thermocouples emplacement within the assembly and measured sample radius accurately (perpendicular) and sample cross section for imaging and analysis (vertical). Samples were polished with a particular attention to catch the plane where the two thermocouples junction are visible. However, the wire thickness (2*125 or mostly 2*75 µm) does not allow seeing the complete junction on one plane.

For our solid samples, both single crystal and polycrystalline samples were studied for olivine, MgO and peridotites. In most of our experiments, our samples seemed to have recrystallized moderately due to the high pressure and temperature experimental conditions. The resulting sample texture was often close to the initial sample, even for small grain size which indicates that our protocol is appropriate for in-depth studies on grain size effect on thermal parameters. For polycrystalline samples, the observed texture is homogeneous for the whole samples and the texture looks equigranular for mono-mineralic samples. Olivine samples appeared chemically homogeneous in BSE images with no variations within sample

location neither inside the constitutive grains, no other minerals were found in the samples (Figs. B.47, 48 and 49). Their textures seemed to be close to equilibrium with nicely connected grains of similar size, with 120° tipple junctions. Single crystal samples have behaved differently according their experimental path. Our MgO samples (M517 and M774) seemed to stay at single crystal state because their spent time above > 1000°C is very limited (< 1h). The olivine sample, M833, stayed at single crystal state even if large domains could have recrystallized (>> 100 μm), at the opposite M525, for which very high temperature were explored (> 1900K), the sample has partially recrystallized. This sample should represent polycrystalline olivine aggregate with coarse grain size (> 50 μm).

EBSD analyses were performed on M525 and M617, two olivine bearing samples with different grain size. First, it allowed checking if samples have recrystallized, and obtaining information on grain geometries and size. The EBSD analyses also ensured that our assembly is near hydrostaticity and that the grains, even if recrystallization occurs, would be oriented randomly. The new grains are well visible both in FSE clichés and EBSD maps and are oriented randomly in all spatial direction (see FSE and pole figures Figs. B48, 49, 50 and 51). However, the distribution of orientation seems to be more represented on median misorientation angles (around 90°). These analyses indicate that our experimental assembly will provide, for both single crystals and polycrystalline samples, suitable conditions to obtain randomly orientated samples and near hydrostatic conditions.

Table VI.5 Textural parameters obtained from our textural analyses for M525 and M617 samples. Average grain size can be constrained using equivalent diameter, mode of the distribution obtained by fitting (labeled Fit), value obtained by EBSD software, average grain size from FOAMS. Then textural parameters obtained from grain shapes by FOAMS are given.

	M525											
	EqDi	Fit	EBSD soft	AVG GS	Long-axis	Short-axis	Orientation	eccentricity	elongation	aspect ratio	regularity	N
AVG	34.57	36.8	87.88	63.63	55.66	25.29	100.88	0.88	0.43	0.42	0.87	607.00
STD (1σ)	39.81	58.2	48.8	27.69	60.60	31.55	66.62	0.11	0.18	0.18	0.10	
	M617											
DEV	8.28	8.40	10.54	9.46	11.64	6.66	81.77	0.78	0.27	0.59	0.91	1149.00
STD	5.33	6.17	2.29	1.56	7.66	4.50	54.21	0.14	0.13	0.16	0.08	

The grain morphological parameters were inferred from FOAMS (area, perimeter, shape from 2D ellipse with a long and short axis, aspect ratio and elongation). Histograms of equivalent diameter were also represented and fitted with a log normal distribution, which provided excellent fits (Fig. B.53). Results of the textural analyses are provided in table VI.5. Our samples have a log-normal distribution with a strong unimodal grain size.

For our glassy and melt samples, the resulting textures are different according their experimental paths. Indeed starting material are more or less glassy (see starting material section) and the experimental procedure consists into their crystallization in the second cycle while going above their glass transition temperature (> 800°C, for 1h or more). Our experiments stopped at this point, show very nice partially crystallized textures. In these samples of different chemistry, the crystallized phases are different probably olivine and pyroxenes in our basaltic melts (M846) and pyroxenes or oxides in our rhyolites (M808). This procedure did not perfectly worked for all our samples as M850 which appears glassy even after 1h above its glass transition temperature. This sample was probably above its melting point.

For samples that have undergone the complete procedure and went above their melting point, the "freezing" step worked pretty well (even if less quick than a conventional quench). Some of our samples are perfectly quenched (M662, M807, M844) and some of them have suffered from quench crystallization (M843, M848) probably due to a slightly longer quench, higher water contents or compositional effect such as in haplobasalt, which is mostly crystallized (M836).

In our partially molten peridotite sample (M847), it is possible to see abundant presence of melt which seem to have migrated on a corner. The quenched was not very efficient as large dendritic crystals are present. The estimation of the melt fraction could be however, only possible with BSE or chemical map information.

iii) *Chemical analyses results*

Chemical analyses have been performed on olivine samples starting material and recovered experimental products. Major elements (Table VI.6) of our olivine samples remain constant before and after experimental run. No significant losses or gains were observed and variations are fully covered by the range of analytical uncertainties.

Volatile content of the samples were also analyzed via Raman spectroscopy. No peaks from CO_2 were observed but peaks from OH bands. A great variation was found in our samples indicating grains of very different orientation were probed, which is confirmed by their EBSD analyses. However, the absolute intensity of OH peaks remained weak indicating a low amount of water in both samples (Figs. A.13, 14 and 15). Values similar were found for our two samples with 286 ± 199 ppm H_2O for M525 (coarse grain sample) and 268 ± 221

ppm H_2O for M617 (small grain sample). The low measured water content associated with the important error (up to 80% relative) indicates that the sample are mostly dry and water incorporation was really limited during the experiment.

Table VI.6 Chemical analysis of starting material and recovered samples. Analyses were performed with electron microprobe (EMP) for starting material and final products. Numbers in parenthesis represent the standard deviation (2σ) given by the EMP apparatus.

	Starting material	**M619 Final**	**M525 Final**
SiO_2	41.97 (0.8)	40.19 (0.45)	40.47 (0.45)
TiO_2	0.06 (0.02)	0.01 (0.05)	0.01 (0.03)
Al_2O_3	0.1 (0.03)	0.04 (0.03)	0.04 (0.03)
FeO	9.3 (0.3)	9.62 (0.25)	9.41 (0.24)
MnO	0.11 (0.03)	0.17 (0.05)	0.18 (0.06)
MgO	48.65 (0.9)	49.23 (0.57)	49.44 (0.57)
CaO	0.23 (0.1)	0.10 (0.04)	0.03 (0.03)
NiO	-	0.44 (0.08)	0.35 (0.07)
Na_2O	<0.01	-	-
K_2O	<0.01	-	-
Cr_2O_3	-	0.02 (0.06)	0.01 (0.02)
Total	**100.4 (0.2)**	**99.82**	**99.93**

The chemical analyses performed on both starting material and recovered products highlight that chemical composition of the studied samples is almost constant during the experiment both considering major and volatile elements. The variation observed on geophysical signal cannot be supported by chemical variation.

4) Conclusions

This chapter aimed to provide new geological material thermal characterizations via the realization of *in situ* Angstrom method at mantle P and T conditions using multi-anvil apparatus. The improvement of existing technique for characterization of various solid, partially molten and molten samples is a significant interest to both provide new constrains on mantle thermal state in specific zones (partially molten layer, magma percolation, thermal anomalies such as plumes or slabs). It can also help to confirm the theoretical constrains on heat transfers mechanisms.

After solving several important and structural technical issues on LMV 1500 T multi-anvil apparatus and heating system, we were able to realize accurate and precise operation of the Angstrom method. To infer thermal parameters such as thermal diffusivity or conductivity

from temperature oscillations, we developed a new, complete and improved treatment procedure that is given and explained in this manuscript. In this software, the inversion of thermal parameters is realized via a Monte Carlo inversion using neighborhood algorithm. A complete treatment of uncertainties and errors has been implemented in our program to ensure their propagation for input to outputs.

Thermal diffusivity measurements of solid single crystals and polycrystalline samples made of olivine, periclase and polycrystalline rocks such as peridotites were performed at mantle pressures and over a wide range of temperatures. A special adaptation of the assembly was realized allowing the characterization of glassy, partially molten and molten samples. The preservation of thermocouples at high temperature was permitted by the use of alumina tubes and their effects on thermal signals were modeled and subtracted to ensure correct estimations. Using a novel "cycle" approach of the experimental procedure by performing heating and cooling cycles, samples at different physical states were also characterized. In this chapter, we thus successfully report the measurement of thermal conductivity of different glasses and liquids with distinct compositions (rhyolites, basalts etc.) at mantle conditions for the first time. In addition, the first *in situ* characterization of partially molten peridotite has been realized. The numerous applications and detailed chemical and textural analyses were not realized yet, due to the lack of time however, the incoming steps are detailed in the next perspective sections.

5) Perspectives

The perspectives implied by this work are numerous. Several steps have to be made in order to finish of our study on melts and possibly on solids. In addition, the newly operating system and treatment procedure can provide important ideas for more experiments in a near future as well as new ideas of implications and associated modeling. Thus, I will first describe short terms perspectives that are required to finish this study and write a scientific paper(s). In a second time, we will see the more long term perspectives and potential studies allowed by the realization of this work.

a) Short term perspectives to finish the work and submit for publication

To complete this work, it first appears important to perform SEM analyses both on starting materials and recovered runs. Indeed, BSE images and chemical maps would be of a great interest to better interpret the geophysical data. With these maps we will be able to

understand if chemical reactions appeared with alumina tubes and if these data are able to be translated to geological implications. These maps will also allow performing textural analyses as we previously did for most of our experimental products as texture is important information for geophysical interpretations.

After SEM BSE analyses a session of EMP can be made to have good chemical composition estimations for our glass and solids. Partially molten peridotite seems to be large enough for conventional measurements. The new EMP apparatus of the LMV will also permit high resolution imaging.

After major elements, volatile content could be estimated by Raman spectroscopy. It will be useful to check if our melts have lost their volatiles during the HP-HT experiment which has influence for the exact characterization of their melting temperature (which is seen during our experiment by a drop of thermal properties) as well as estimation of glass transition temperature and physical parameters estimations.

Finally, for solid samples, EBSD maps could be realized to check the random orientation of the grains. This aspect is important if a proper comparison between single and polycrystalline sample must be made. The idea behind the FEG-SEM analyses is also to quantify the grain size and the amount of grain boundaries. This would be of significant interest to quantify the effect of grain boundary density on thermal properties as grain boundaries act as a sum of little thermal resistances. Such effect is not considered in the theoretical works and might be investigated (or ruled out?). The role of grain boundaries and grain size in optical thickness consideration is also crucial, and such data would help to decipher if theoretical indications provided by Hofmeister et al., are correct for polycrystalline samples.

After these analyses, the thermal diffusivity data could be re-analyzed and refined. More adapted treatment can be performed as well as diffusivities selection. Indeed, we saw that frequency fitting procedure is much less reliable than told in the previous literature.

The geological implications of the recovered data have also to be formulated with various possible axes. For the publication of this work I will try to estimate via mixing laws the effect of melt and extrapolate these results to realistic and small melt fractions typical of LVZ and LVL (with pressure dependence correction) layers for example. Geological implications have

been poorly developed in the previous works (Hofmeister et al., 2009) and would provide a good added value to our data for publication.

b) Long term perspectives

Several "long term" perspectives are raised by this work. First, the establishment of a correct device and treatment procedure allow the future characterization of different types of materials. The successful use of the alumina tubes to protect the thermocouple will also allow the characterization of materials which can't be studied in standard configuration. Thus, it would be very interesting to measure more glasses and fully molten samples as experimental issues are numerous. In addition, we could imagine characterization of samples with controlled melt fraction (Morb+olivine), as performed in our previous studies. Such samples must be synthesized in prior piston cylinder to have large samples allowing machining steps. With our alumina tubes, we could characterize exotic materials such as metals or mixture of metals and silicate for early Earth and solar system implications. If the materials can be characterized, not so conductive in front of alumina tubes effect, it would help to under check the validity of the Wiedemann & Franz law which is currently use to infer thermal properties of Earth's core.

The data obtained in this study, as well as suggested experiments, can be inserted in models to simulate different thermal properties of various geological settings. As conventional models usually uses a constant thermal diffusivity value, we could imagine building new models with calibrated temperature evolution and more interestingly include the effect of melting as observed by drops of thermal conductivity. Modeling of mantle heat fluxes can be foreseen and quantification of LVZ and LVL effects on the upper mantle thermal structure realized. The data obtained on melt with various chemistry could be further used to models smaller processes, such as magma chambers. Indeed, data at P-T conditions are valuable insights for complex thermal problems.

Finally, I observed while making the state of art on thermal conduction process that several semi-empirical models are used to described lattice thermal conductivity. Among these, the acoustic models of lattice heat transport and damped harmonic oscillator (DHO) are interesting because, they both link thermal properties to acoustic velocities of the considered materials. We performed in our previous chapters III and IV measurement of acoustic velocities of partially molten samples at various pressures, thus it could be of significant

interest to convert them into thermal properties to verify the theoretical formulations and provide an independent way to quantify them.

I already started to consider this study which has not been further investigated due to several data gaps which could be filled realizing new quantifications (and obviously the time required to do them). Among the whole formula available, acoustic model of Dugdale and Macdonald (1955) was preferred:

$$k_{lat} = \frac{B}{T} = \frac{C_v * u * a}{3\alpha * \gamma_{th} * T} = \frac{V * K_T * u * a}{3 * {\gamma_{th}}^2 * T}$$

Where *Cv* is the heat capacity at constant volume, a^3 is the volume of the unit cell, α is the thermal expansivity, *V* is the molar volume, γ is the thermal Gruneisen parameter (equal to αVK/Cv), *Kt* is the bulk modulus and *u* is the bulk sound speed. These different parameters have then to be parameterized for our sample at the right P and T conditions.

For the DHO model used by Hofmesiter et al. (2007), thermal parameters are expressed as:

$$K_{lat} = \frac{\rho}{3ZM} C_v \langle u \rangle^2 \tau = \frac{\rho}{3ZM} \frac{C_v \langle u \rangle^2}{2\pi \langle FWHM \rangle}$$

Where $FWHM$ is the full width at half maximum from the individual peaks from dielectric function from IR reflectivity or Raman. $\langle u \rangle$ is the bulk sound speed (average of longitudinal and transverse mode). τ is the life time of the mode. And if *Cp* is assumed to be equal to *Cv*:

$$D_{lat}(T) = \frac{\langle u(T) \rangle \Lambda(T)}{3Z} = \frac{\langle u(T) \rangle^2}{6\pi Z \langle FWHM(T) \rangle}$$

Where Λ is the mean free path, equal to $u*\tau$. Thermal properties can also be extracted from these formulas via the sound velocity. However, the FWHM is fairly difficult to obtain at the right P and T conditions. Thus, some Raman analyses could be foreseen using a LH-DAC device to estimate more precisely theses parameters. Such quantifications will be performed in a near future.

Chapter VII

Development of thermal diffusivity measurements at high pressure and temperature with a pulse heating apparatus

Chapter VII: Development of thermal diffusivity measurements at high pressure and temperature with a pulse heating apparatus

1) Introduction and objectives

a) General introduction

In this chapter, the development of a pulse heating apparatus for thermal diffusivity measurements at high pressure and temperature with multi-anvil apparatus is described. The objectives of the development are given together with technical descriptions. The technical development was based on the pulse heating apparatus of Osako et al. (2004). Author emphasizes the importance of technical parts, as literature on this type of apparatus is scarce and more than elusive on technical details.

A significant modeling development will be presented in order to predict and quantify thermal properties from temperature evolution recorded during HP-HT experiments with our newly built apparatus.

Finally, this chapter will intend to explain the apparatus operation and the results of the several tests performed at ambient and HP-HT conditions. The geological applications were limited (mainly due to lack of time and technical issues). However, this development represents a significant part of this PhD work and will allow a full set of material characterization in a very near future.

This chapter was made in collaboration with J. Monteux, who gave a significant contribution to our modeling part and A. Mathieu who helped on the design, building of the apparatus and its adaptation to multi-anvil apparatus

b) Objectives of the development

Among transport properties of materials, heat transfer is one of the most important process governing the movement and evolution of planets and their different reservoirs. The precise quantification of thermal parameters, such as thermal conductivity, thermal diffusivity, thermal expansion etc., are thus needed to better understand heat propagation in solids, melts and fluids and may be incorporated in various geological models.

However, thermal diffusivity measurements are far from being easily measured. Different techniques were developed (Chapter II) to evaluate these properties with respect to influencing variables such as temperature, pressure, oxygen fugacity etc. In order to perform thermal diffusivity measurements at high pressure, the number of available techniques is

limited. Most of solid pressure apparatus (except diamond anvil cell) can't use optical methods to determine material responses to thermal excitations because compression is made in opaque middles (metals or ceramics). For these reasons contact methods (involving at least 1 thermocouple) are usually used in solid pressure apparatus.

Angström method (see chapters II and VI) is from far the most used technique in multi-anvil apparatus. However, the presence of 2 thermocouples is a significant drawback of the technique, which is technically difficult to realize, fragile to high pressure (more chances of failures) and not easily adaptable for small presses (low tonnage). The increasing number of contact sensors such as thermocouples was shown to increase the underestimation of the real thermal diffusivity by the presence of resistant interfaces with imperfect contacts (Hofmeister et al., 2007) (Chapter II). In addition, such technique uses permanent regimes (sinusoidal oscillations) to simplify the heat conduction equation and allows a simple estimation of diffusivity, without considering the whole propagation of the signal but only its final observation.

The pulse heating technique came from the Laser Flash Analysis (LFA) technique developed by Parker et al. (1961) and later Dhzahadov (1975). It offers the possibility to study and monitor the reaction of a material to a transient heat wave. Such experimental characterization can be adapted to high pressure apparatus and only 1 thermocouple is required, minimizing a potential underestimation due to contact resistances. However, the equation of heat conduction is then not simplified and can't be resolved directly (Chapter I). Such dispositive requires a significant part of modeling to reproduce the experimental signal. The inferred thermal diffusivities are then obtained by comparison and bracketing with models. Such technique has not been extensively used in geological high pressure research (Osako et al., 2004) as Angström method was often preferred (Fujisawa et al., 1968; Kanomori et al., 1968, 1969; Katsura et al., 1993; Manthilake et al., 2011).

However, the motivation to develop again such kind of apparatus came from the need to adapt thermal diffusivity measurements to synchrotron experiments, which could allow a wide range of possible and innovative studies. The objective was to build a new portable pulse heating apparatus for thermal diffusivities characterization at high pressure and temperature for experiments performed at both LMV and synchrotrons. Indeed, for classical thermal diffusivity measurements methods, an especially dedicated apparatus is mandatory. For example, determination in LH-DAC requires an optical bench and dedicated

spectrometers (Goncharov et al., 2009; Otha et al., 2010). Similarly, Angström method requires a special heating system adaptation with signal modulation parts. All these technical adaptations are often home-made, adapted to a given apparatus and can't be transferred easily from the host laboratory to synchrotron for *in situ* measurements. As a result, perform thermal conductivity measurements in synchrotron is not possible in "standard" MAA configuration.

For these reasons, we wanted to develop a portable apparatus that will allow, similarly to ultrasonic interferometry apparatus, measurements in high pressure devices and realizing on-line experiments at synchrotron radiation facilities. However, the lack of technical details available in the literature implied a complete development of this apparatus to satisfy the new specific requirements.

One of the aims of this study is also to confirm the quality of the Angström method by realizing similar thermal diffusivity measurement on the same sample at similar conditions using another experimental technique. This is not an easy task as most of other reliable techniques, such as LFA or other radiation techniques, are usually only available at room pressure or in diamond anvil cells in which such pressure range is difficult to achieve and sample size is very limited. Only the existing technique pulse heating apparatus adapted to multi-anvil such as designed by Osako et al. (2004) would permit such systematic comparison.

The very interesting aspect of this comparison also relies on the better understanding of heat carriers in materials at extreme conditions and potentially removes the experimental unwanted effects such as the presence of ballistic photons or radiative transfers.

2) Description of the technique and theoretical considerations

The thermal properties of materials, rocks or minerals govern their behavior from microscopic to macroscopic scale (Chapter I). Heat transport is mainly diffusive in the Earth's mantle. To determine a thermal state of geological problems as well as experimental ones, the equation of heat diffusion (Chapter I) should be solved:

$$\Delta T + \frac{1}{\kappa}\frac{d\kappa}{dt}\left(\overrightarrow{gradT}\right)^2 + \frac{Pe}{\kappa} = \frac{Cp\rho}{\kappa}\frac{dT}{dt} = \frac{1}{\alpha}\frac{dT}{dt}$$

Where t is the time, T is the temperature, Pe is the internal heat production and α is the thermal expansion. Thermal conductivity is κ, *h*eat capacity (C_p) and density (ρ).The internal heat production Pe can be considered as null in the absence of internal heat sources. In

addition, in the case of heating by short pulses of temperatures the term $\frac{d\kappa}{dt}$ can be neglected because the pulse is only increasing few degrees. Considering one dimensional heat flow, the equation can be simplified in:

$$\frac{dT^2}{d^2z} = \frac{Cp\rho}{\kappa}\frac{dT}{dt} = \frac{1}{\alpha}\frac{dT}{dt}$$

No simple and forward solutions to the heat conduction equation are available in the case of 1D transient heat perturbation. As a result, modeling approaches can be used to determine the temperature repartition at a given instant. However, they require external inputs such as thermal diffusivity, its temperature derivation, heat capacity and sample density.

The technical description of existing pulse heating apparatus is given in the chapter II (Parker et al., 1961; Dhzahadov, 1975; Osako et al., 2004).

3) Methods : development of a portable pulse heating apparatus for multi anvil experiments

a) Pulse heating apparatus

The designed pulse heating system was built to send a short electrical pulse during a given time to the additional furnace, which is inserted nearby the sample in a high pressure assembly and insulated from the main heater. This system should be able to trigger the volt-meter to record the signal instantaneously.

Our pulse heating system composed of two distinct loops: the first one to send the electrical pulse to the metal resistance and the second one to record the signal obtained via the thermocouple (Fig. VII.1).

The first loop is composed of a DC generator (ISO-TECH DC power supply IPS 3303S) which delivers a pulse of current between 20-40W (20 V and 1-2 A) of power. This generator is activated via a push button connected to the DC generator via a Panasonic (LT4H) digital timer. The timer controls the time of the current delivery to the loop after pressing the push-button. This high accuracy timer can control the pulse duration up to 1 ms but good precision is really achieved above 5 ms. The timer, which acts as switch, will let the current pass during the fixed duration. The function produced is close to square, at $t = 0$ the current increases up to the maximum power, remains at this value during the closing time of the loop and decreases to 0 when the timer opens again at $t = \tau$ (pulse duration). The channels of the timer were selected to have better resolution on short pulses times. The current is sent via shielded

wires of few meters long to the high pressure assembly. The wires are connected to 5% Re/W wires, used for their mechanical resistance, outside the multi-anvil press and insulated from upper and lower ram with Teflon tape. The wires were mechanically connected during compression to the additional metal resistance furnace (impulse heater) placed beneath the sample. The additional metal resistance is a rhenium foil which was cut with LMV laser cutting system with a photo-etched pattern ("radiator type") (Fig. VII.2). This special type of cut allows increasing the metal resistance length and surface for a higher resistance and a more efficient pulse. The configuration of the sample cell into the multi-anvil press assembly ensures a mostly 1 D heat flow from the heater surface to the sample (Osako et al., 2004). Our heater photo-etched pattern is less fine than Osako et al. ones because rhenium is difficult to cut very precisely. Finer designs we tried were often fragile and broke when emplaced in the assembly. The two bands on the side of the heater are bent along the piston to make the connection with the wires in similar manner to our donuts used in electrical conductivity experiments (Chapter III, IV and V).

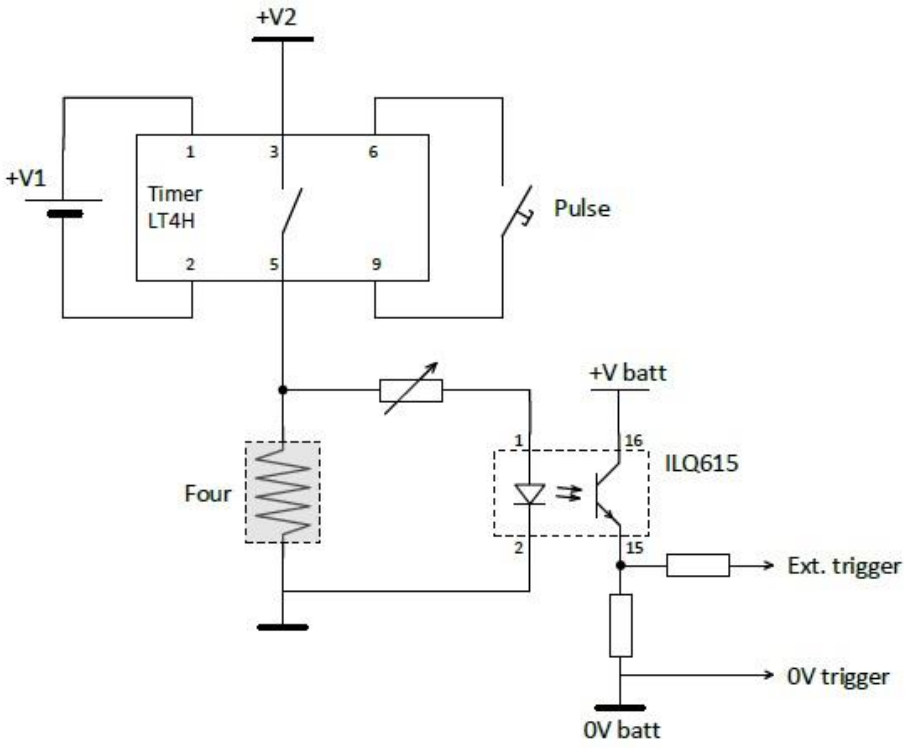

Figure VII.1 Electrical scheme of our pulse heating apparatus. Pulse sending loop is on the top part, analysis and trigger one on the lower right part (see text for complete description).

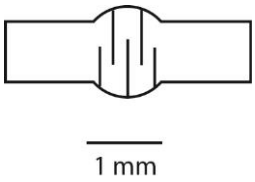

Figure VII.2 Photo-etched slot Rhenium pulse heater

The first loop (power sending) is connected to the second loop (signal recording) due to the necessity to trigger the data acquisition. The trigger system was home built by A. Mathieu. It consists into the use of a diode connected to the first loop, which will shine when the loop is closed, placed in front of a photo-transistor. The transistor will be activated when receiving diode light. This device offers a faster response and ensures there is no electrical contact between the two loops. The photo-transistor in "on" mode closes the second loop in which a 9 V standard battery was included to send current to the digital multimeter and activate the recording of thermocouple tension. The digital multimeter used is an Agilent 34410A, the trigger function allows to record 50000 points per acquisition and resolution of 1 point every 100 microseconds. Thus resolution is enough to probe fast variations of sample temperature. The temperature wave generated by the impulse heater travels across the sample and was monitored on the opposite side with a type C thermocouple. This thermocouple was connected to an amplifier in order to increase resolution on temperature increase as few degrees results in micro volt augmentation of the potential. The amplifier used was built and designed at the LMV and is a low noise tension amplifier, which is particularly helpful in this case. The amplifier gain is 1000 and was recalibrated before included in the pulse heating system. The amplifier was alimented by a second DC generator (ISO-TECH DC power supply IPS 3303S) used in symmetrical mode (+14/-14V). The value of the gain also tightly depends on the DC current applied to the amplifier (between 12 and 15 V).

The signal from the amplifier was checked via an oscilloscope at the beginning of each experiment and then recorded by the digital multimeter. The data are saved in non-volatile memory during data acquisition and then loaded in PC computer via the internal web server of the Agilent multimeter. This server works with a Java 5 runtime application and a special network card must be used for connection to a laptop.

The components for the trigger were fixed and welded on an electronic card. All the components were inserted in a plastic case and so almost fixed between each other and offer an apparatus close to a "ready to plug system". Only power supply, amplifier and multimeter

have to be plugged separately which is resulting into a user friendly apparatus. The wires, amplifier, multimeter and components fixed in the case easily fit into a small luggage allowing its transportation by airplane which can be of significant interest for synchrotron facilities. Only power generators have to be found on site, which is usually fairly easy as this type of alimentation are commonly used by electrical and electronic engineers for tests and component reparation (Fig. VII.3).

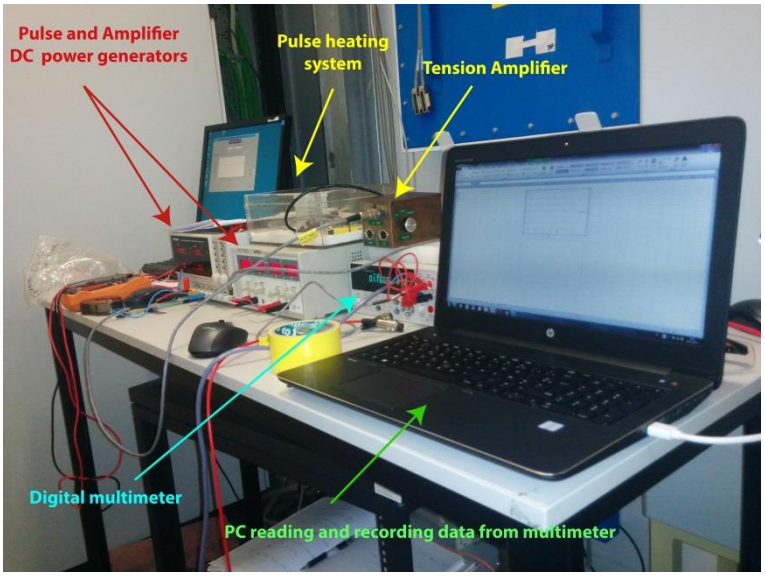

Figure VII.3 Pulse heating system while installed at PSICHE beamline

b) Resolution of the recording system

Our measurements made at LMV and during the synchrotron session at SOLEIL highlighted that our resolution in voltage is good enough to measure small variation of temperature (< 1 mV after the amplifier). Such precision is not possible with thermocouple reading channels, where the uncertainty is close to few degrees (no amplification).

The resolution of the multimeter is indicated to be 0.003% of the measurement for DC circuit by Agilent. For signals without amplification the theoretical type C thermocouples have tabulated increases between 0 and 20 mV which should ranges between 0 and 20V at a factor 1000 of amplification. However, our amplifier is “rail to rail” and only tensions up to the input ones (12-15V) can be achieved. This effect is not problematic, when going to modest temperature but can be important above 800°C (Fig. VII.4). In any case, the accurate measurement of temperature cannot be easily made directly with our system using the average measured voltage corrected by amplifying factor. Indeed, the amplifier is manually adjusted prior the experiments using an oscilloscope, its multiplication factor is not perfectly 1000, 100

or 10. Then variations of a factor 10 in "1000" amplification are small but will be translated to pretty large uncertainties while trying to recover the temperature. Accurate measurement of average temperature rather requires plugging the thermocouple on a conventional reading system for estimation at each step prior a pulse recording. The variations recorded during a pulse translatable in temperature variation as the type C thermocouple variation is almost linear on small temperature ranges (up to 10°).

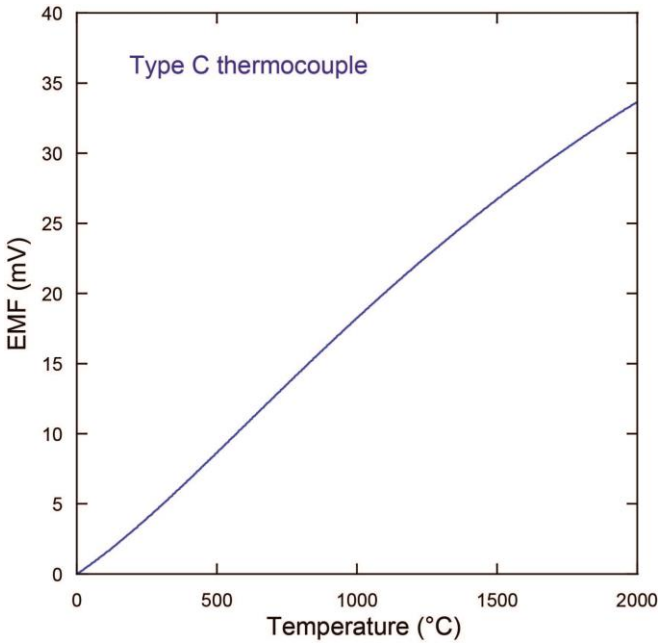

Figure VII.4 EMF of type C thermocouple as a function of temperature. EMF calculated using 5th order polynomial fits from Annual Book of ASTM Standards.

If we take a TC increase of 2V at the end of the amplifier, the error of the multimeter is 60 µV, as the apparatus is able to see real variations up to 0.06 µV without amplifier. Assuming quasi linear variation of tension, type C thermocouple table indicates a variation of 13 µV for 1°C increase. Thus, an increase of 0.06 µV (detection limit) will result in a temperature increase of 0.005°C. Temperature variations < 0.005 °C can't be measured. It limits the material nature or size that can be characterized (see modeling part hereafter).

c) Multi-anvil assemblies

Different types of assemblies were used for multi-anvil tests of our apparatus. We used 18-11 geometry for experiments at fairly low pressure (~2 GPa) at LMV. This assembly is inspired from EC/SV assemblies (Chapter III) (Fig. VII.5).

The assemblies were using an octahedron of 18 mm truncation composed of MgO + 5% Cr_2O_3. The temperature was provided by a rhenium 25 µm thick foil cut by laser cutting system. The thermal insulation was assured by a ZrO_2 sleeve. The inner part of the assembly

was composed of MgO sleeves to electrically insulate the sample, thermocouple and pulse wires. The sample is surrounded by two MgO single crystals discs in case of melting experiment. In case of solid samples, the sample will be directly in contact with the pulse heater made of rhenium atop and the thermocouple below. The pulse heater is connected to the generating loop via two 5% Re/W wires conducted along a MgO piston with passes made with diamond wire prior we assemble the parts. Thermocouple was inserted at the opposite side using 4 holes Al_2O_3 or mullite tubes. A metallic disc can be inserted between the thermocouple junction and the sample for a better contact and homogeneous temperature measurement.

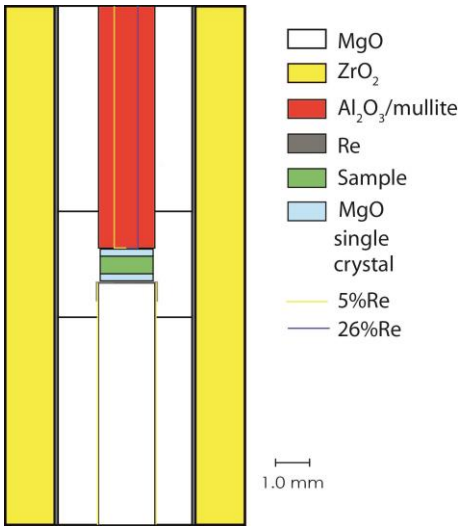

Figure VII.5 Cross section of the 18/11 assemblies used for LMV experiments with all the parts labeled on the side.

A second 10/4 multi-anvil assembly was used for higher pressure purposes and associated tests performed in PSICHE beamline at SOLEIL Synchrotron. Thus, this assembly is composed of X-ray transparent materials suitable for dedicated *in situ* measurements (imaging, diffractions, etc.)

We used a MgO + 5% Cr_2O_3 octahedron. The main temperature was set up by using the TiB_2 + BN furnace. This furnace was a new ceramic which was kindly provided by A. Thomson and first tested in SOLEIL for this session. The connection to the WC cubes was made using a topping electrode of the same material. A layer of HBN (hexagonal boron nitride) was inserted between the furnace and the octahedron to insulate electrically the sample from the main furnace, thus it also helps to homogenize heat around the sample. We did not use ZrO_2 insulation sleeve to maximize the sample size and because it was found to react with TiB_2. The associated drawback is that heat loss is important. This configuration is

fine for low pressure experiments but can be problematic if temperatures are above 1500°C. The pulse heating was made by "photo-etched" rhenium furnaces miniaturized for 10/4 assembly (Fig. VII.7).

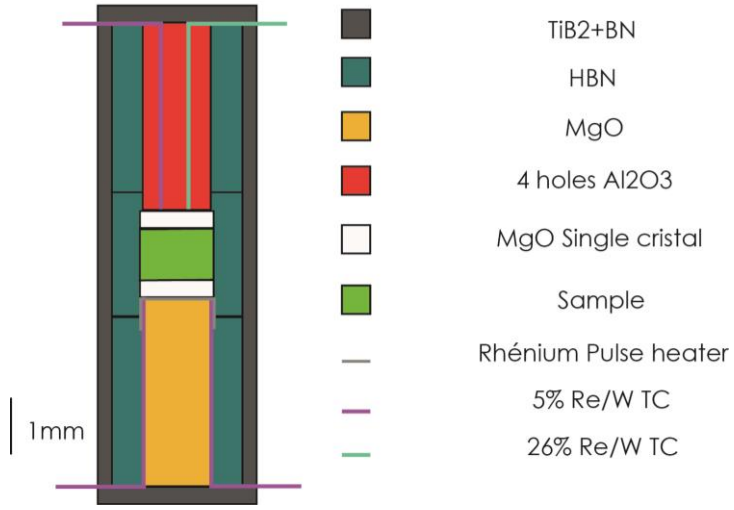

Figure VII.6 Cross section of the 10/4 assemblies used for synchrotron experiments with all the parts labeled on the side.

We placed two MgO single crystals disks at top and bottom of the sample to protect the system from short circuit during partial melting experiments. Indeed, as melt is a good electrical conductor, with a pulse of 20 W (20 V for 1A) the amplifier could undergo overvoltage (amplify 1000* a tension of 20 V). It also helped into keeping the melt inside the center of the assembly as it can escape easily. We have chosen MgO because its thermal properties are well known and will have little effect in term of thermal resistance compared to very insulating sample (thermal diffusivity around 10 times higher than melts).

At pressure, and high temperature, the mechanical contact is almost perfect and was confirmed by X-ray imaging at HP/HT. Thus, it must be acceptable to say that thermal contacts are perfect between the MgO and the sample and assume that no thermal resistance and no thermal boundary layers are present in our assembly.

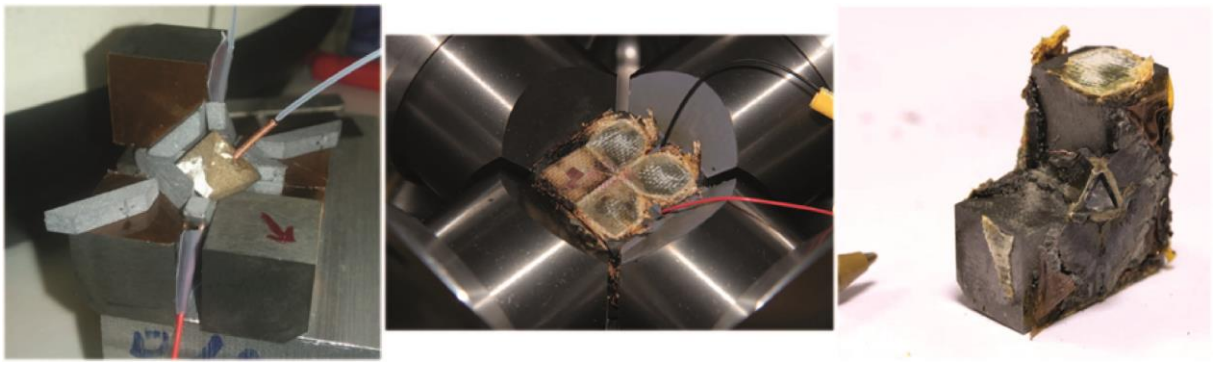

Figure VII.7 (left) 10/4 Assembly with secondary anvils, Capton tape was used as insulation in between the anvils. The red arrow marks the X-ray path. (center) Experiment in the DIA module right after the decompression. (Right) Octaedron recovered after the experiment. No reaction with TiB_2 furnace is observed. The burned epoxy sheets indicate that temperatures above 150°C were reached on the cubes while sample's temperature was above 1300°C. Photographs were kindly provided by L. Martinek.

4) Modeling of thermal transfers in the high-pressure cell assembly

a) Modeling and software development

Modeling is a direct consequence of the impossibility to solve directly equation of heat propagation. Models must be used to predict and constrain values of thermal conductivity with confrontation to the experimental records.

For these reasons, we adapted a FORTRAN code developed by J. Monteux in axisymmetric cylindrical geometry to simulate impacts of asteroids on a planetary body and estimate associated heat propagation (Monteux, 2009). This code was adapted to miniature dimensions and was, at each step, refined toward our assembly geometry and experimental constrains. The aim of the model is to be able to send a pulse of heat during a given time and monitor its propagation through the sample as a function of time, in order to reproduce perfectly our experimental situation.

Several parameters are difficult to establish as they rely on several assumptions:

- No flux conditions imposed
- Temperature freely evolves in all points after the pulse delivery
- The temperature is homogeneous before the pulse = T_o (step) and returns after pulse propagation to T_o. The additional heat is not conserved in the middle.
- The heat wave is transient (e.g. no steady state or equilibrium). Initial and final state are equal and at equilibrium.

i) Description of the program

The program is coded in FORTRAN 90 and requires a compiler to be used on a PC. We performed test using LINUX system using G Fortran compiler with appropriate libraries, the figures were made using GMT program and representation of generated data was done using XMGRACE. The program was improved to be more user- friendly with dedicated sections, in which thicknesses of the parts can be written and the thermal properties of each compound can be inserted.

The program is then easy to compile with an .exe file that lunches the different steps and the code, named ViscoVcyl2b.f90, contains the calculation and modeling part. User should use command window, go to the desired current directory and then lunch the executable file (./exe).

The description of the program is given in J.Monteux (PhD thesis, 2009), in particular in their appendix A. The code was originally built to calculate temperature increase due to meteoritic impact on a planetary body. The model proposes to calculate thermo-mechanical readjustment after the impact. The code is based on dynamical equation of continuous media. The dynamic part of the initial code (e.g. convection) was removed for our case, where sample is mostly solid on all measurements.

Three main equations were used:

Mass conservation:

$$\frac{d\rho}{dt} + \nabla.\rho\vec{v} = 0$$

Transport of movement quantity:

$$\rho\frac{D\vec{v}}{Dt} = -\nabla P + \nabla.\vec{\tau} + p\vec{g}$$

Transport of internal energy:

$$\rho Cp\frac{DT}{Dt} - \nabla.(K\nabla T) = \alpha T\frac{DP}{Dt} + \vec{\tau}:\nabla\vec{v} + \rho H$$

On these equations only the third one was used for our case, as only energy travels through the sample assembly. The equations were adimensioned using characteristic length, temperature and time of the model and several approximations (Boussinesq) were formulated

in order to simplify the calculations. The numerical simulation resolves the equations with finite differences method and using a second order precision. Equations were adapted with axis symmetrical geometry and heat equation is resolved by alternate direction implicit (ADI) method.

During the following descriptions, we aimed to reproduce the typical signals recorded in our tests made at LMV and PSICHE (see test section), such as the one given in the figure VII.8. Results of models presented in the following section can be compared with this example.

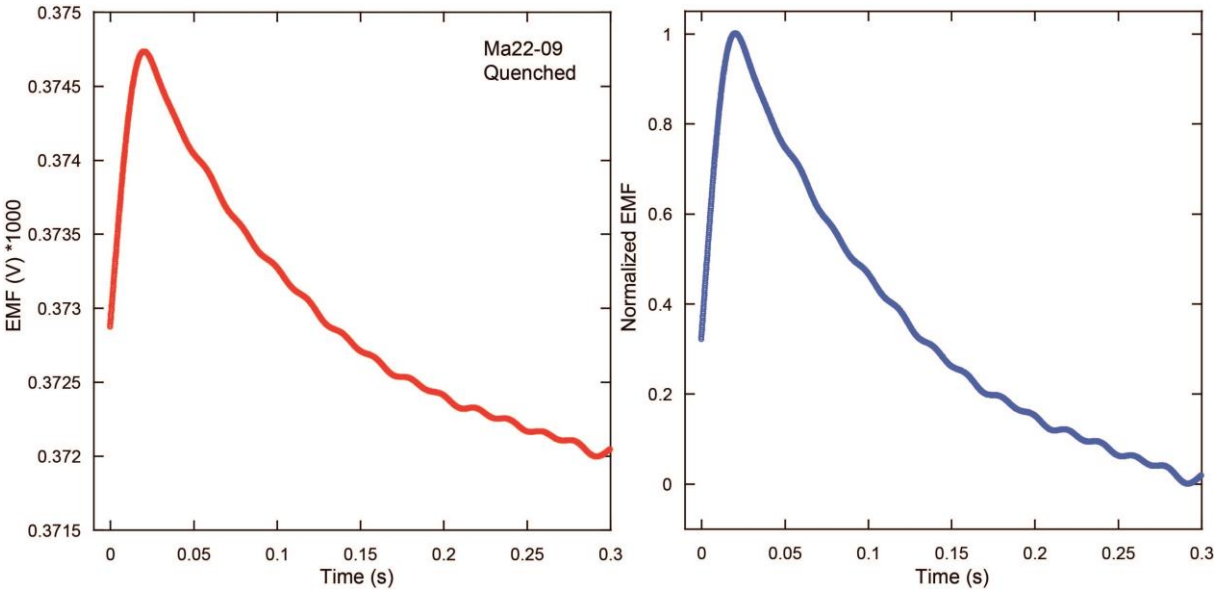

Figure VII.8 Time evolution of the EMF (V) in response to pulse heating (0 corresponds the beginning of pulse). Raw data is given on the left panel and was normalized to maximum tension increase on the right panel.

ii) Homogeneous models

First modeling tests were made to validate our approach and tune our numerical code to be compatible with the assembly geometry. The first axisymmetric cylindrical model used is composed of a single layer of material where the heat pulse is generated (Fig. VII.9). The "thermocouples" can be virtually placed at different distances from the temperature source.

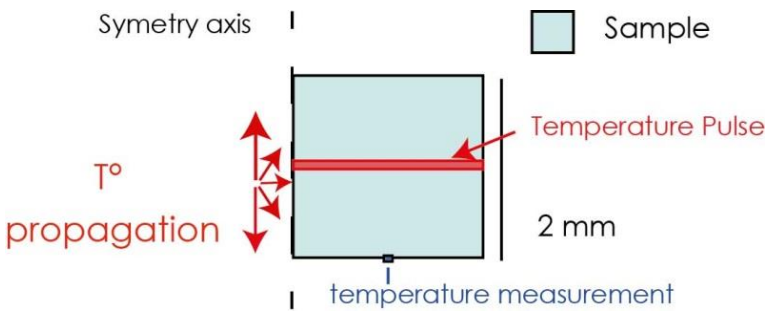

Figure VII.9 Scheme of model geometry for the first and homogeneous version

First results of homogeneous models are presented here (Figs. VII.10, 11 and 12). The temperature evolution with time is modeled in 2D across the sample and surrounding materials. Temperature evolution with time is represented for a single material assembly with a thickness of 1 mm (Fig. VII.10). The intensity of the pulse is set to +100 K. The three curves show different temporal evolutions at 3 positions along Z axis. Black line represents temperature at 0.33 mm of the pulse, red at 0.5 mm, and green curve at 1mm of the base of the domain (values of thermal conductivity used for calculations are 130 W/m/K).

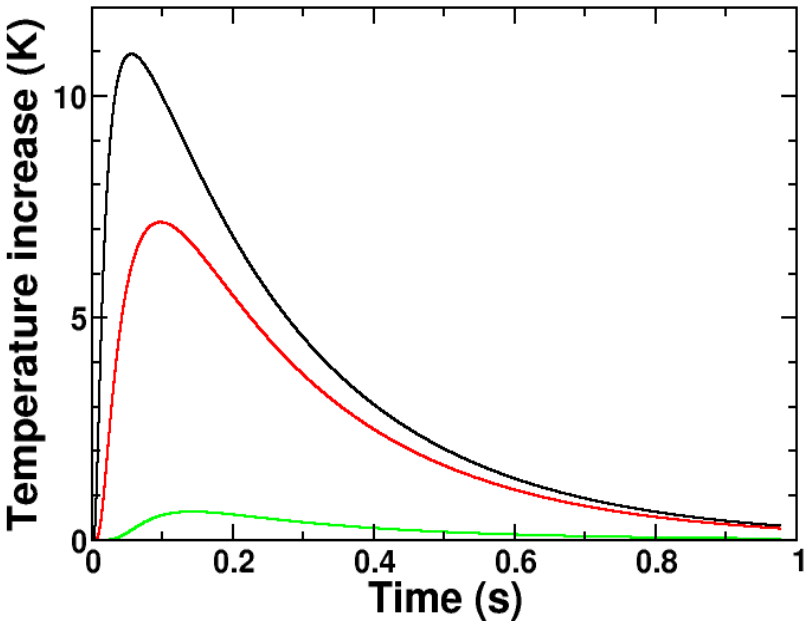

Figure VII.10 Time evolution of temperature at different distances from the pulse computed from our numerical model: black = 0.33mm red = 0.5mm and green = 1mm.

The influences of thermal parameters are shown on second figure (VII.12), where arrival times for a simple geometry can vary over 2 orders of magnitude: from 0.01s and few seconds with varying thermal conductivities on plausible ranges. Values of thermal conductivities for silicates commonly varies between 0.1 and 40 W/m/K at low and high

temperature and so expected heat wave arrival times for such material should be within the range shown here.

However, this model is very simplistic and surrounding sample materials must be taken in account (due to their different thermal properties) to better represent our experimental setup, in particular for boundary conditions.

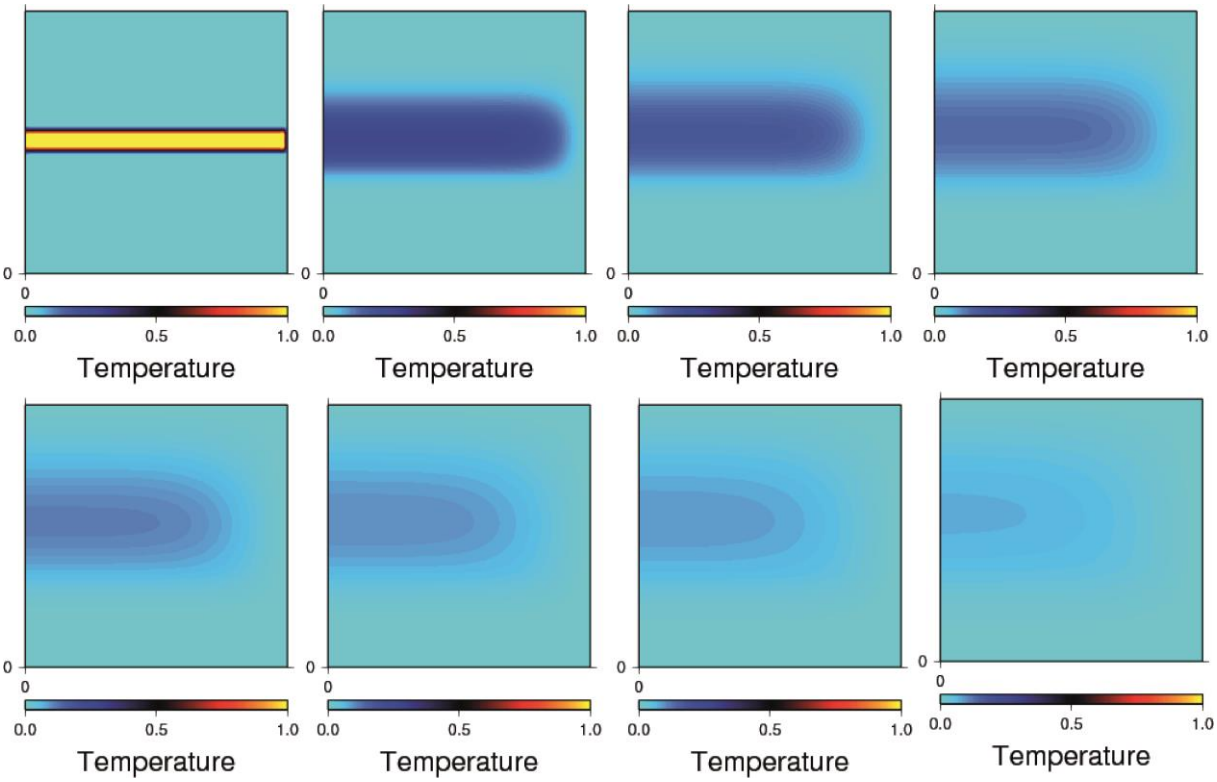

Figure VII.11 Temperature evolution computed for different times since pulse emission (from left to right, top to bottom) of the assembly at high temperature (sample 1 mm, MgO 400 micron). The temperature is normalized by the initial maximum temperature increase (0 to 1). The top part (above the initial pulse) is composed of MgO, the bottom one is a succession of MgO layers and sample (same geometry as given in figure VII.21). The temperature wave mostly diffuses upward and only little toward sample on the bottom part.

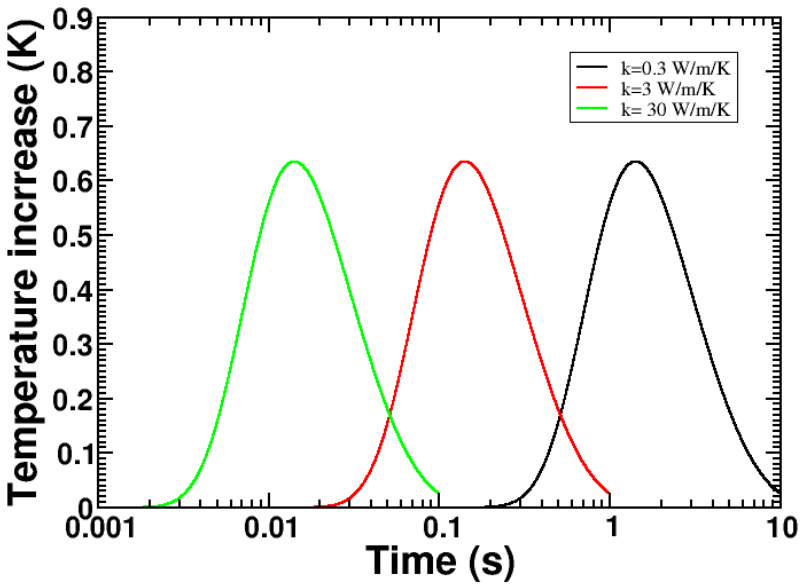

Figure VII.12 Time evolution of temperature at the rear face of the sample computed from our model with varying sample thermal conductivity.

iii) Multi-layer model

As the sample cell is much more complex than a simple single material cylinder, the succession of different material such as the two MgO layers has been inserted at sample ends. The figure VII.13 reminds the complexity of high pressure assembly which must be approximated in our model.

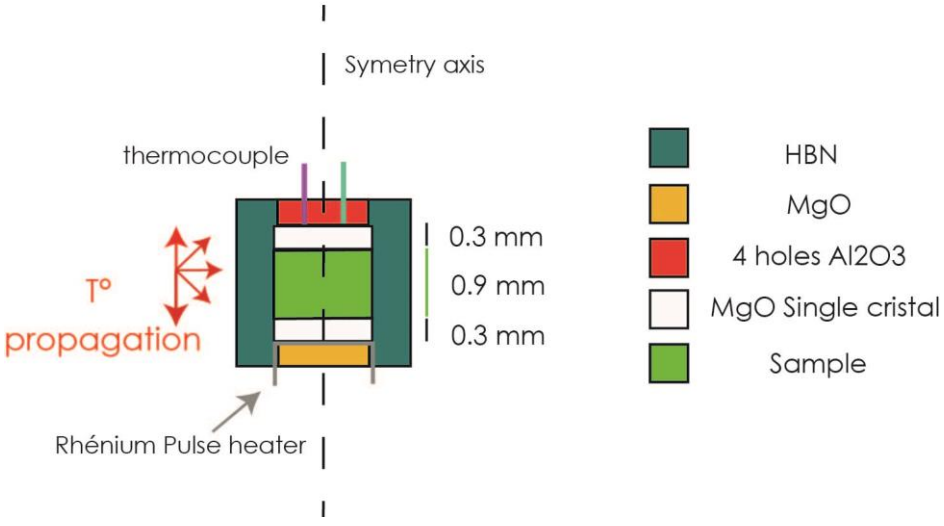

Figure VII.13 Assembly's ideal geometry for modeling to match our synchrotron assemblies

A first improvement was made taking in account the two MgO layers which can be independently tuned in the model in terms of thickness and thermal conductivity. The layer

atop the pulse heating location was also replaced by MgO layer instead of sample material (Fig. VII.13).

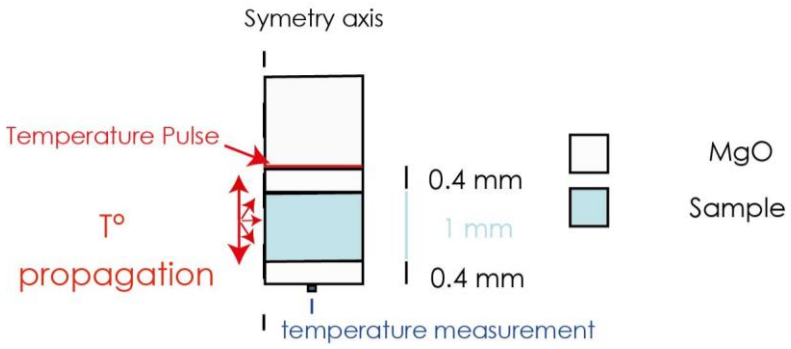

Figure VII.14 Scheme of model geometry, for the second "multi-layer" version

Table VII.1 Sum up of the conditions and parameters used for "multi-layer" modeling

Name	Condition	MgO	MgO thickness (µm)	K MgO (W/m/K)	Sample thickness (µm)	K sample (W/m/K)
essai	TEST Julien	yes	328	14	1119	1400
Essai-1	LT-400 K	yes	400	37.5	1000	5.2
Essai-2	MT-800 K	yes	400	16	1000	3.4
Essai-3	HT-1200 K	yes	400	10.4	1000	3
Essai-4	BN parameters low	no	0	0	1800	50
Essai-5	BN parameters high	no	0	0	1800	300

Several runs were performed in order to test the role of MgO and sample on signal shape at different temperatures (table VII.1). The run Essai-1, 2 and 3 represent the assembly with MgO and sample with realistic size. The values of thermal conductivity of MgO were taken from Hofmeister (1999) and olivine values from Xu et al. (2004) were considered. The results of these models are represented in the figure VII.15. The main information visible in this plot is the change of shape induced by the presence of MgO. The temperature peaks are much broader than previous models (Fig. VII.15). Their broadness increases while increasing K_{sample}/K_{MgO} ratio. The temperature increase is always lower at low temperature/ high thermal conductivity and is a constant observation through all the models we have lunched, due to the efficient release of heat. This figure also shows that the difference between time arrivals of the temperature peak is significant between low and high temperature data. The time arrival for these data is in the order of 0.25 to 0.75 seconds.

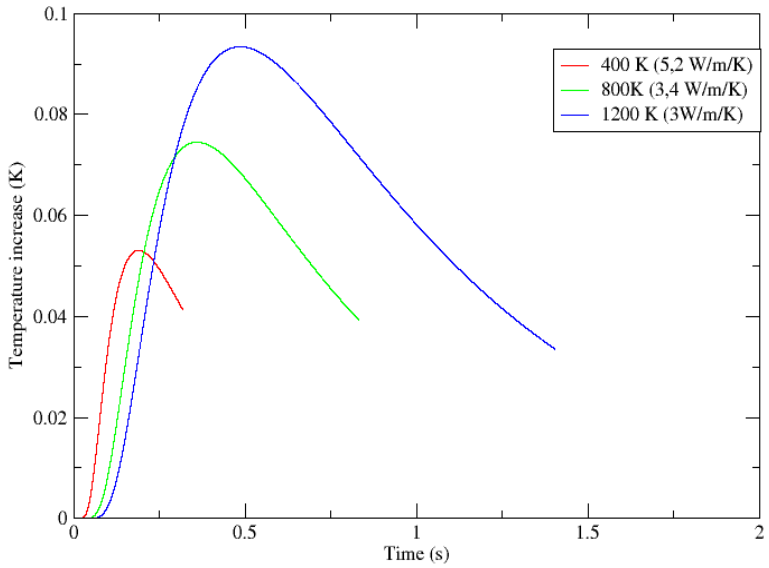

Figure VII.15 Time evolution of temperature increase for signal modeled various temperatures (and conductivities) for realistic assembly geometry.

iv) BN sleeve effect?

Our multi-layer model highlighted that presence of surrounding materials, with thermal properties significantly different than sample ones, have a profound effect on the recovered temperature pattern with important changes in signal shape, amplitude and arrival times. Hence, the presence of the HBN sleeve in our 10/4 assembly should be taken in account.

Values of thermal conductivities of HBN are not known at HP and HT conditions. Given its graphite-like structure; the orientation of the ceramic is crucial, as it can vary by orders while taking values perpendicular or parallel. Values available in literature are scarce and vary importantly with conductivities between 20 and 300 W/m/K. Our fine polycrystalline HBN was supplied by Goodfellow, the technical description provides values between 20 and 60 W/m/K only.

To account these possible differences, we have improved our model to create a lateral domain representing assembly insulation sleeve in which distinct thermal properties can be set. The value of thickness and thermal conductivity of the layer is able to be tuned (Fig. VII.16).

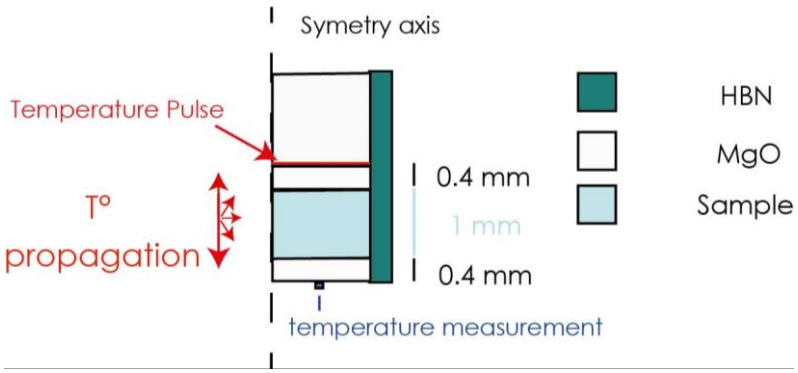

Figure VII.16 Scheme of assembly geometry in the model including the BN lateral sleeve

The runs "Essai 6","7" and "8" were made to test the influence of HBN insulating sleeve on the side of the sample (table VII.2). Essai-6 and 7 were done using 50 W/m/K BN thermal conductivity whereas Essai-8 was made using high bound of 125 W/m/K.

Table VII.2 Sum up of the runs made considering the BN layer and runs considering only photon and phonons conductivities (see text).

Name	Condition	K BN (250 µm)	MgO thickness (µm)	K MgO (W/m/K)	Sample thickness (µm)	K sample (W/m/K)
Essai-6	LT	50	400	37.5	1000	5.2
Essai-7	HT	50	400	10.4	1000	3
Essai-8	LT	125	400	37.5	1000	5.2
Olivine HT	HT	50	0	0	1800	3
Olivine BT	LT	50	0	0	1800	5.2
Phonon Ol BT	LT	50	0	0	1800	5.33
Phonon Ol HT	HT	50	0	0	1800	2.33
Photon Ol BT	LT	50	0	0	1800	0.14
Photon Ol HT	HT	50	0	0	1800	4.9
Assembly Phonon BT	LT	50	400	37.5	1000	5.33
Assembly Phonon HT	HT	50	400	10.4	1000	2.33
Assembly Photon BT	LT	0	0	5	1000	0.14
Assembly Photon HT	HT	0	0	5	1000	4.9

The figure VII.17 shows the 3 models calculated with the presence of BN layer. The previous simulation without BN layer for low temperatures, medium temperatures and high temperatures (LT, MT and HT) are shown for comparison. We can see that adding the BN layer will have only slight difference on temperature curve, it increases the amplitude of the curve but only changes slightly the position of the curve on time axis, the shape of the curve remains unchanged. Thus changes in thermal conductivity of BN will not have a strong effect on our recorded data.

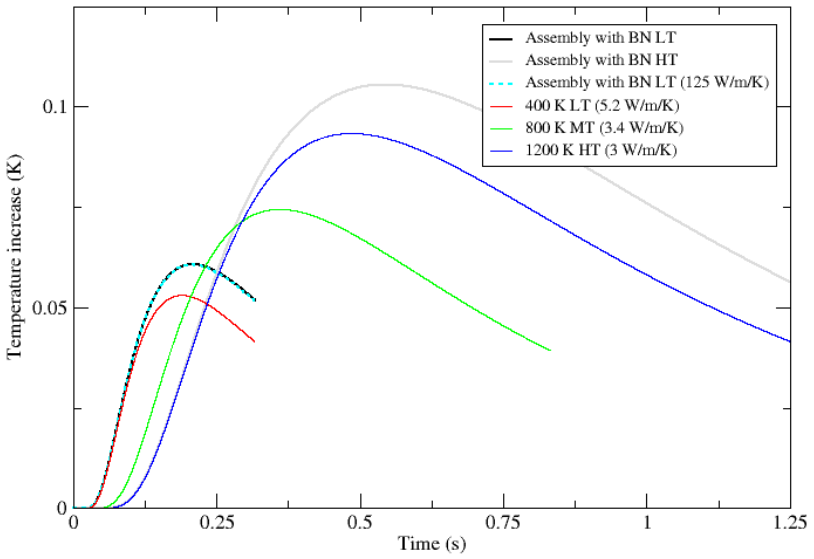

Figure VII.17 Time evolution of temperature computed for runs 6 (black), 7 (grey), 8 (dotted) including BN sleeve at different temperatures compared computed evolution for assembly without BN lateral layer

v) Radiative and ballistic contributions

In addition to heat diffusion, possible other thermal transfers have been described by previous studies and summarized by Hofmeister and Brandlund (2015) and our Chapter I.

In case of thin samples, our samples are ~1 mm thickness, other types of heat transfer must be considered. Indeed three types of heat transfer occur in a semi-transparent middle such as olivine (conduction, radiation and ballistic) and periclase. It first depends on the optical conditions for the presence of radiative or ballistic transfers. Thus radiative and ballistic transfers must be considered. Optical thicknesses estimations for our samples are given in the appendix E.

The first possibility is the presence of ballistic photons. They are emitted from the source, pass through the sample without any interaction and warm the thermocouple. These photons should arrive instantaneously as they travel at speed of light in the crystal without any participation of the middle.

For radiative transfers, two types are competing in the sample. If sample is optically thin, the photons will cross the sample without strongly interacting with it. The increase at the rear side of the sample should be almost instantaneous. If sample is not considered as optically thin, photons can be emitted and reabsorbed with a grain to grain process. This process is called radiative diffusive transfer (Hofmeister, 1999). In our samples, as it should be both optically thin and thick depending photon frequencies, a mixing of diffusive and direct

process is expected (appendix E). Due to the lack of HP data on absorption spectra, the calculations made are qualitative.

Different groups (Gibert et al., 2005; Goncharov et al., 2008) have been trying to separate signals coming from photons and phonons for years without a complete success. In fact, theoretical considerations are not perfectly understood yet. Moreover, experimental devices have problems to rule out direct and ballistic transfer from photons due to huge thermal gradients (that are not existing in the mantle) and samples lengths below the mean free paths of the photons.

Gibert et al. (2005) tried to separate the effect from phonons and photons during experimental determination of thermal conductivity. Even if this publication uses inappropriate equations to determine radiative part values (e.g. Hofmeister, 2007), the inferred values of *D* for phonons (diffusive) and photons (radiative diffusive), were used to simulate signals and arrival times. The values obtained were inserted in our program blindly. Our model will not provide relative contribution of the two, neither try to combine the different contributions. It will just provide their position in time axis as two different runs with different "diffusivities".

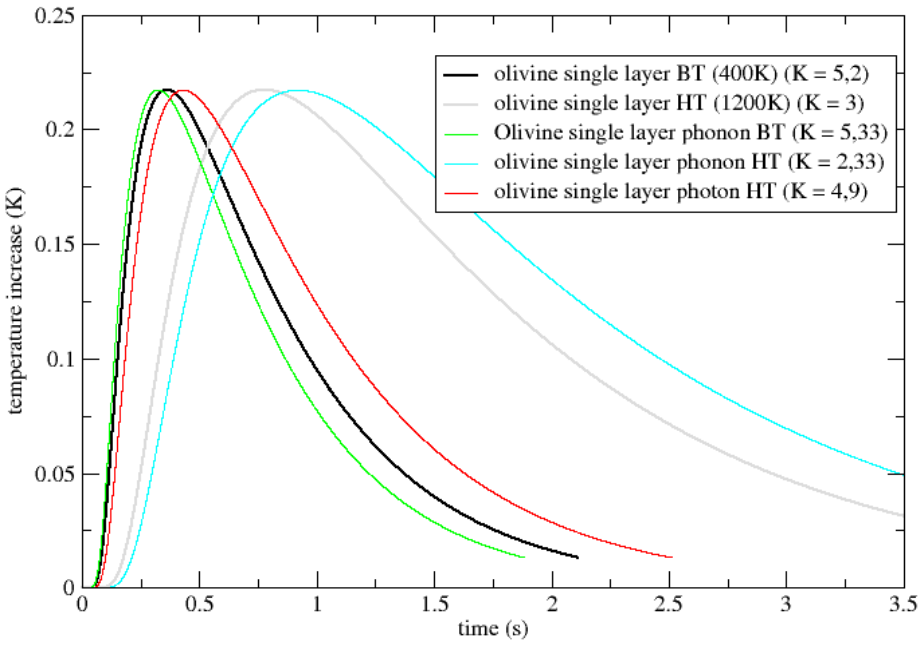

Figure VII.18 Time evolution of temperature from simulations separating phonons and photons contributions. The inferred K for each process was selected from Gibert et al. (2005) and Hofmeister et al. (1999). Photon contribution is very low at low temperature and does not fit in the window (> 5s).

The figure VII.18 gives estimation of olivine with bulk conductivity estimated in the literature at different temperatures (black and grey curves). The other curves represent

calculations using D for each component, photons and phonons extracted from Gibert et al. (2005). D_{photon} and D_{phonon} were then calculated in function of temperature and simulations were lunched using the inferred values at low and high temperature. Calculations were performed using assembly's configuration, composed of an olivine sample and two MgO layers, the lateral layer of BN was also inserted. MgO single crystal is completely transparent to visible light and as it is really thin (< 400 µm) photons should only be ballistic/without absorption-reemission through it. For these reasons, we did not put MgO on calculation for photons, since there is no radiative-diffusive transport through it. At the opposite, on phonons calculations (diffusive) MgO was incorporated with bulk values (MgO D_{phonon} was not constrained in Gibert et al. (2005)).

Behind these simulations, the idea of splitting the signal merges. In fact, if MgO is optically thin, it does not participate to the diffusive radiative transfer, but instead participating to the lattice component of heat diffusion. It might be possible, with the MgO single crystals, to separate more distinctly the time arrival of radiative and lattice components. This assembly configuration could favor the observation, distinction and quantification of both mechanisms.

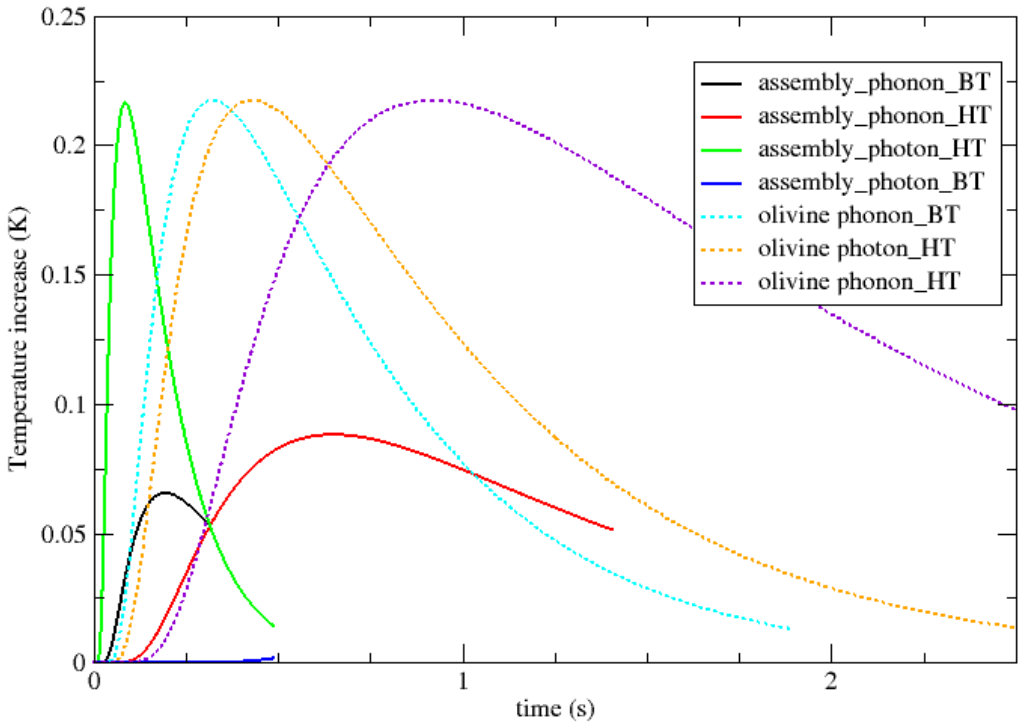

Figure VII.19 Time evolution of temperature increase from computed models using thermal diffusivity inferred from photons and phonons for the whole assembly (MgO+Sample+surroundings). Comparison with previous simulations results using single material: olivine

The resulting signals from simulations with the assembly are not similar to the first simulations with only olivine (Fig. VII.19). In fact, because diffusive radiative heat transport does not occur in the MgO, recovered signal is less attenuated. Signal for photons at low temperature is quasi null. The difference between signal from the assembly and signal from single olivine layer of same size is the intensity of the recovered peak. Peak position also appears earlier in the assembly because MgO layers have a much higher conductivity than olivine and so phonons propagate faster. At the opposite, the values from photons at high temperature are really different. We can clearly see that olivine photon values are slightly before HT phonons curve but with same intensity whereas for assembly, photons are way before the HT phonons assembly curve and significantly higher in intensity. The peak is also much sharper than the previous simulation (as it crosses less material).This effect is really interesting and must be tested experimentally; investigation on this direction will be detailed in the perspective section.

Finally, estimation of radiative-diffusive transfer is difficult as it can't be really calculated like phonon's diffusion. However, approximations made by Gibert et al. (2005) allow seeing that these grain to grain processes are similar to standards diffusion in terms of signal shape and arrival time. They highlight possible interesting behavior of the system while combining optically thin and thick materials.

vi) Pulse heating apparatus limitations

Another main concern of the previous simulations realized is that predicted signals display very low amplitudes while we used a temperature increase during the current pulse artificially set to + 100 K.

We have seen in the technical part that our analytical limit is set to be 0.005 K. However, we found that realistic pulse power delivered is between 20 and 40 W. We have estimated independently the temperature increase for 20 W over duration of 10 ms. Using the temperature power calibration of rhenium furnaces, a temperature increase about 40 K is expected. Using heat capacity of Rhenium, the temperature increase was found to be around 40 K equally.

News simulations were lunch taking in account this realistic pulse temperature increase. The simulations were lunched considering the whole assembly and potential phonon-photon behaviors (explained above). During these simulations we also varied sample and MgO

thicknesses and used thermal properties at low and high temperature (table VII.3 and Fig. VII.20).

The associated results, once using realistic pulse power, are important. The limit of 0.005°C is never reached except for sample size lower than 500 µm.

Table VII.3 Summary of simulations lunched with the model using pulse thickness and realistic temperature increase.

Name	Condition	K BN (250 µm) (W/m/K)	MgO thickness (µm)	K MgO (W/m/K)	Sample thickness (µm)	K sample (W/m/K)
1000 µm BT	LT	50	400	37.5	1000	5.2
1000 µm HT	HT	50	400	10.3	1000	3
1500 µm BT	LT	50	400	37.5	1500	5.2
1500 µm HT	HT	50	400	10.3	1500	3
400 µm BT	LT	50	400	37.5	400	5.2
400 µm HT	HT	50	400	10.3	400	3
850 µm BT	LT	50	300	37.5	850	5.2
850 µm HT	HT	50	300	10.3	850	3

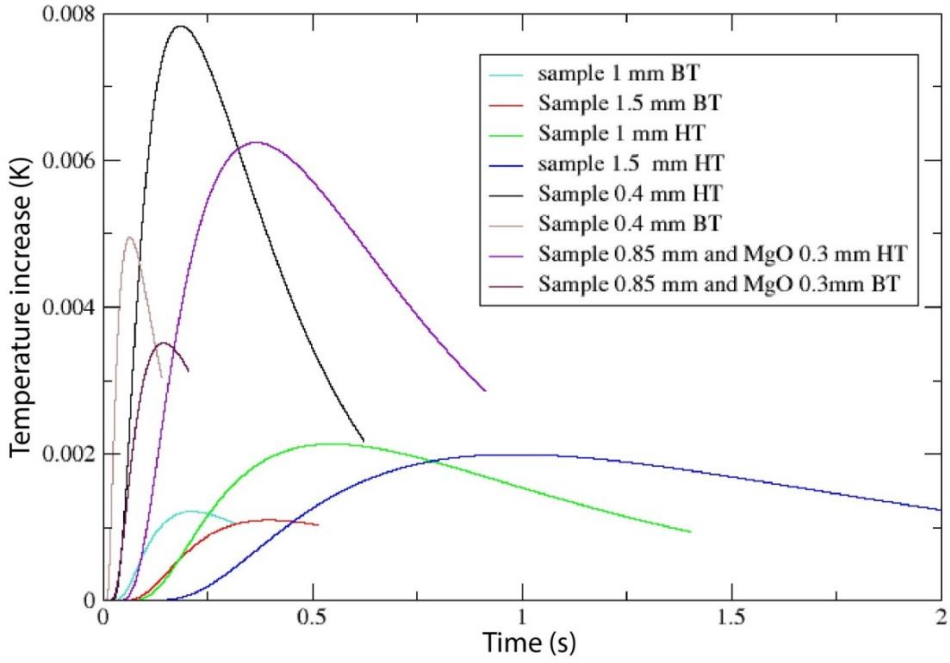

Figure VII.20 Time evolution of temperature increase computed for various samples thicknesses and two temperatures.

Following the idea on tool limitations, we thus explored conditions which will maximize the record signal intensity in order to improve heat wave detection and their signal to noise ratio. To do that, there are few options that can be considered:

- Reduce sample and MgO size. The previous simulations have shown that the size of the sample greatly affects the shape and the intensity of the recorded signal. The simulation shows that intensity does not evolve linearly with sample thickness and decreasing by twice

the sample size will only result in a small increase of intensity recorded. Furthermore, reducing sample size smaller than 1 mm will also ensure its optically thinness.

- Increase temperature pulse: the power delivered to the additional metal resistance is already close to the maximum our rhenium furnace can accept. Several options can be tested: increase the number of cuts in the photo etched pattern of the sample, it will increase metal length crossed by the current and by consequence resistance of the furnace. Or changing the metal for a material with higher heat capacity to better convert power delivery into temperature. Comparison between different metals yields to the following observation: Rhenium which has a quite low heat capacity (0.13 J/kg/K) can be replaced by molybdenum (0.25 J/kg/K), copper (0.38 J/kg/K), iron (0.44 J/kg/K), nickel (0.44 J/kg/K), or titanium (0.52 J/kg/K). Using Nickel would be fairly easy as it can be cut with our laser cutting system and available in thin foils for moderate cost.
- Change assembly geometry/components: change assembly geometry is difficult. Parts surrounding the sample play an important role in the heat dissipation. The parts used in our assembly are for most of them good heat conductors compared to studied samples. The observation of temperature repartition in a cross section of the model shows clearly that temperature increases much faster in upper part (that is modeled as MgO) than in the sample (Fig. VII.11). Then, heat is mostly evacuated, dissipated in assembly part and does not cross the sample. The idea could be a replacement of the 4 holes alumina tube for insulating ceramic.

Again, we have improved our model by inserting important modifications: thermal conductivity of the layer above pulse heater can be tuned manually and does not depend on MgO conductivity anymore (Fig. VII.21). This high resolution model needs much more calculations and iterations to achieve this resolution. The time required for a simulation increased to more than 4 hours.

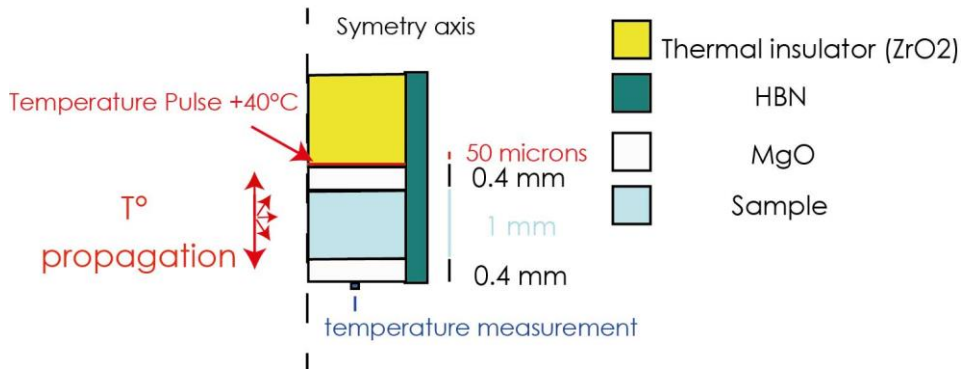

Figure VII.21 Assembly geometry in last version of modeling program considering an insulator placed above the sample.

We tried to perform calculations using the standard assembly configuration with a sample of 1 mm and two MgO plates of 400 microns. In this model, we replaced MgO top layer by a layer of zirconia which is considered as one of the best thermal insulator (thermal conductivity of 2.5 W/m/K). Two runs were performed to simulate assembly at high temperature and low temperature to explore the experimental range.

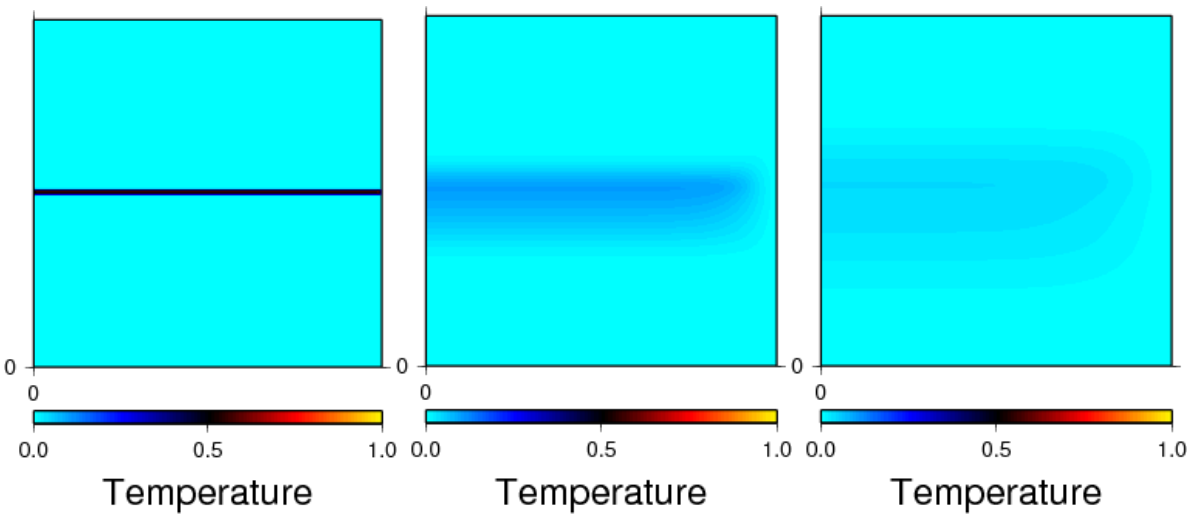

Figure VII.22 Temperature evolution for different times (left to right) since pulse emission considering a thermal insulator in the top part (above the pulse). The temperature is normalized by the initial maximum temperature increase (0 to 1). Heat mainly goes across the sample, downwards.

The figures VII.23 and 24, highlight clearly that using insulating material above the sample increases the temperature recovered at the rear face of the sample. The magnitude of the increase is really important and needs to be taken in account for further experiments. Also, the position of the maximum of temperature increase curve is slightly shifted in such case.

Instead of zirconia, further simulations were made using mullite and pyrophyllite which can be used in 4 holes for thermocouple. This provides a good alternative as it is a good

thermal and electrical insulator. The main difference between first and second simulations (table VII.4, Figs. VII.23 and VII.24), is the layer above pulse heater. In fact, first tests were run with pyrophyllite thermal conductivity (2 W/m/k) whereas second runs were performed with mullite. In fact, 4 holes TC tubes are made of mullite with thermal conductivity around 6 W/m/K.

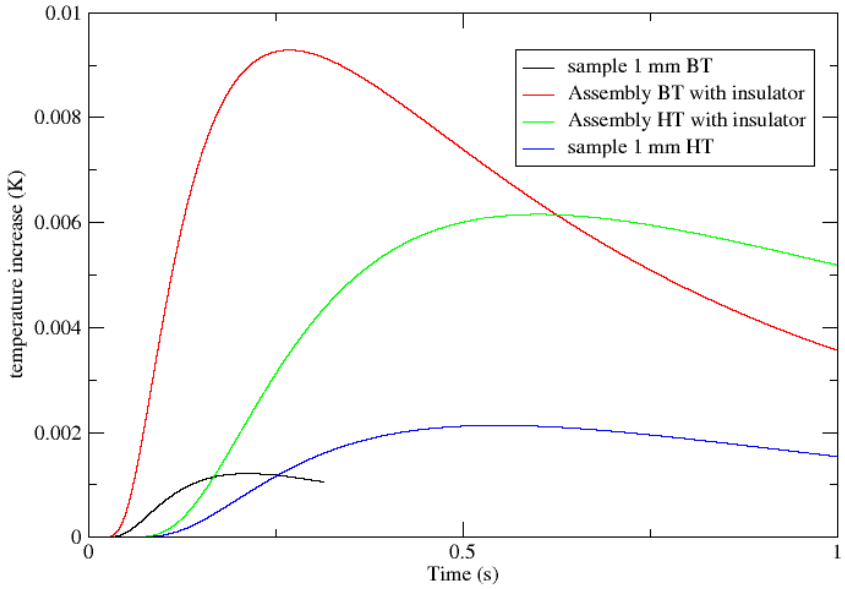

Figure VII.23 Time evolution of temperature computed using an insulating layer or MgO atop the sample and its comparison with previous simulations.

Table VII.4 Summary of last simulations performed using pyrophyllite and mullite insulator above the sample and no MgO layer.

Name	Condition	K BN (250 µm)	MgO thickness (µm)	K MgO (W/m/K)	Sample thickness (µm)	K sample (W/m/K)
MgO BT	LT	50	0	37.5	500	37.5
MgO HT	HT	50	0	10.3	500	10.3
ol BT	LT	50	0	5.2	500	5.2
ol HT	HT	50	0	3	500	3
MGO BT V2	LT	50	0	37.5	500	37.5
MGO HT V2	HT	50	0	10.3	500	10.3
OLIVINE BT V2	LT	50	0	5.2	500	5.2
OLIVINE HT V2	HT	50	0	3	500	3

Finally a last simulation was made to predict further tests made at the LMV (Fig. VII.24) detailed in the next section.

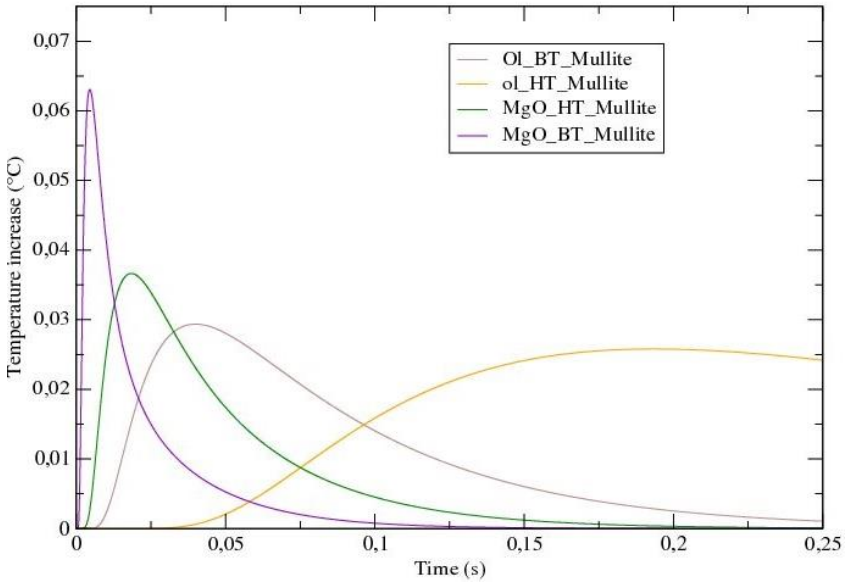

Figure VII.24 Time evolution of temperature computed using a mullite layer above MgO and olivine samples (see the temperature increase of a factor 10 above detection limit).

5) Tests and experiments results and discussions

Together with the realization of modeling and predictive parts described above, a series of different tests were performed at the LMV and PSICHE beamline in SOLEIL. These tests were performed at various conditions from ambient to high pressure and temperature in multi-anvil experiments.

These experiments were made to test our modeling software and verify our newly built pulse heating apparatus. First ambient conditions clamp tests will be described and will be followed by results of multi-anvil experiments.

a) Room pressure/Clamp tests

Several tests were made at room pressure and temperature using a Clamp to maintain the experimental configuration. The main reason of these tests is the accurate and visual control of the sample, pulse heater and thermocouple configuration. Such test allowed fixing issues on our pulse heating apparatus and understanding its working conditions. We preferred to realize such test prior to the multi-anvil ones because in HP-HT experiments sources of failures are numerous and the sample state can't be checked visually during the experiment.

These measurements are not made aiming retrieving the exact thermal parameters as contacts can be imperfect due to ambient conditions. However, it must highlight the simple

behavior of the apparatus and its ability to measure transient heat waves (test its resolution, etc.).

Our system was adapted to perform measurements without pressure, which is not very straightforward. The pulse heater was welded with tin onto two copper wires and connected to our pulse system. The thermocouples were welded by arc solder with argon. The samples used were different commercial silica glasses and polycrystalline MgO ceramic of various thickness. The sample was mechanically connected to the thermocouple and pulse heater while placed in large clamp. The sample, pulse heater and thermocouple were slightly compressed between large rods of MgO (see Fig. VII.25). The mechanical contact was kept perfectly perpendicular thanks to rubber bands located on each clamp side.

We use two types of samples: commercial silica glass with thicknesses of 160 and 1600 µm and polycrystalline MgO bought from Goodfellow of 431 and 745 µm.

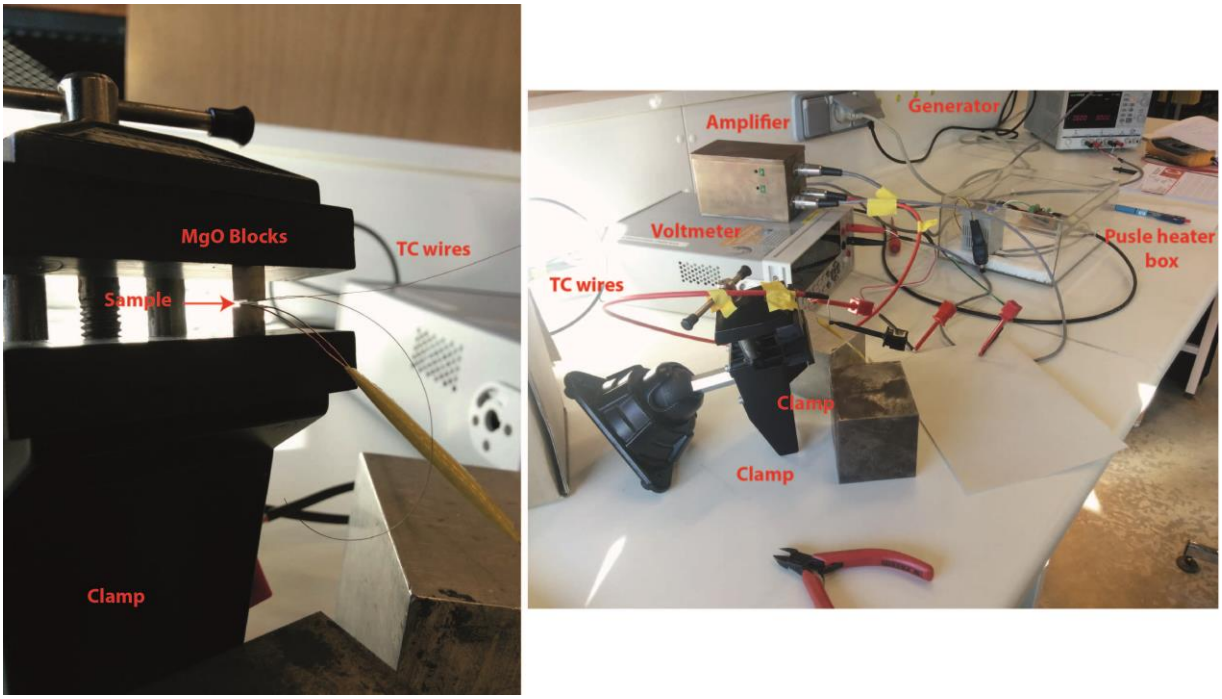

Figure VII.25 Illustration on RP-RT tests made using clamp to put mechanically in contact, the different parts for pulse heating characterization

During these tests, different pulse heating measurements while varying the sample nature, sample size, length of pulse duration and intensity of the sent current (temperature increase) were performed. The resulting signals were quantified with the time of pulse arrival and absolute amplitude of the signal which will help to find suitable conditions for successful analyses.

In a first step, the recorded data were plotted and the quality of the recovered pattern was checked in order to identify appropriate conditions. Our overall experiments highlight several and significant points:

- The quality of the data depends on the amplification factor, indeed we have seen that *100 and *1000 gave better signal/noise ratios. Hence, the use of *1000 channel must be favored. The recovered amplitude tensions are similar when data are normalized with multiplication factors. This indicates a quasi linear behavior of our amplifier.
- The quality of the data increases with pulse duration. Larger pulses (up to two seconds) usually yield much greater temperature increases with large amplitudes and so decreasing the signal noise-ratio. A factor 10 of amplitude increase was observed between short pulse duration (5 - 10 ms) and longer ones (1 - 2 s).
- The sample thickness plays a crucial role into the recovered signal quality. We saw that thin MgO and glasses signals were of better quality than respective thicker samples.
- The pulse power has an important effect on the quality of the recovered signals. Indeed, we have observed with tests at 30 W and 60 W that the quality of the recovered signal also increases with increasing pulse power. In fact, the temperature increase is greater and so, recovered signal have greater amplitude (almost a factor 10!) and a high signal/noise ratio.
- The chemical compositions of the samples and their associated thermal properties seem to have an effect, as our glass samples (even if thinner than “thin MgO”) display worse pattern over a wider range of pulse duration indicating a more insulating behavior. Such behavior is expected as MgO is at least 40 times more conductive than silica glass at RP-RT conditions.
- The data of poor/bad quality with low signal to noise ratio yields to a bad estimation of the “peak position” (maximum temperature) of the signal.
- Finally, no clear differences in recorded signals were found while using optically thin samples (glass is transparent) and optically intermediate/thick samples such has fine polycrystalline MgO.

We paid attention to the electrical state of the tests and no short circuits were observed. This is translated by low voltage observed on recovered signal (see comparison with press measurements with short circuits in the following part). The arrival time of temperature maximum (peaks) is far from the end of pulse duration as highlighted by the figure VII.26. This indicates diffusive case has been reached for these tests, despite the transparency of the glass sample would suggest the presence of radiative photons. The peak position of the

recovered signals was found to change with the pulse duration, with the largest observed deviations to 1:1 line for low pulse duration. In fact, at larger pulse duration, the trends shown in all of our experiments for different arrival time are going closer to the 1:1 line. The amplitude of the recovered signal was also fitted to estimate the correctness of our amplifier apparatus (Fig. VII.27).We can see that the recovered signals display very similar trends at different amplification and that a factor 10 of difference between each case is well respected. The final measured amplitude is varying from 10^{-4} to almost 1 V indicating signals are well above detection limit for this RP-RT case. The signal recorded are corresponding to thermocouple tension increase between 0.1 and 0.001 mV which can be translated by 0.1 to 10°C of increase at the rear side of the sample.

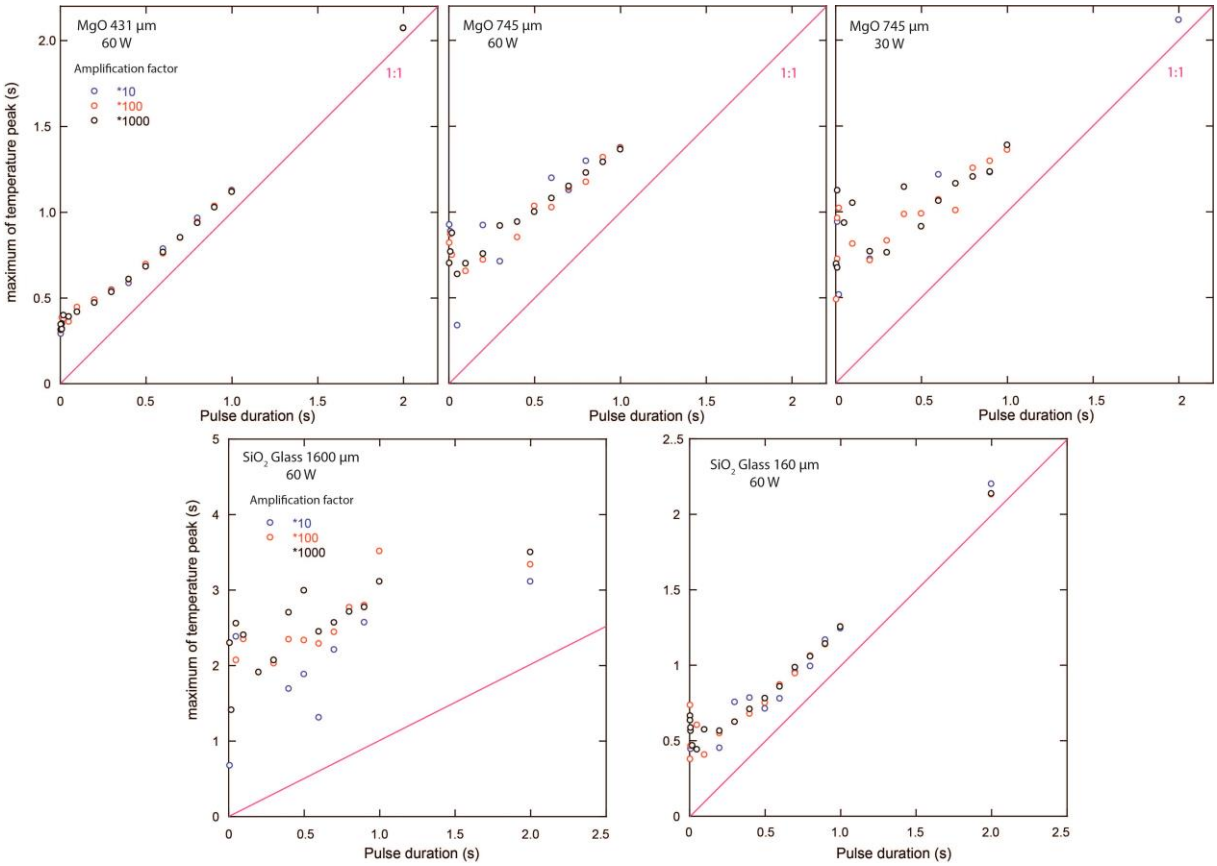

Figure VII.26 "peak" maximum temperature position as a function of pulse duration. Significant deviation from 1:1 line is observed. Thin samples display much better reproducible patterns for all amplification factors. Low amplification data quality is less good than higher ones as highlighted by the nice lines drawn by 1000 points*

We also tried to model the resulting signals for MgO samples (Fig. VII.28). Again the shape obtained is pretty correct even if our sample temperature decrease is less fast than predictions. However, the corresponding thermal conductivity is very low, with estimated values of 0.3 and 0.5 W/m/K. The computed conductivities are close for both MgO samples and the peak position is coherent with different thicknesses. However, the computed thermal

conductivity is low compared to expected ones (> 30 W/m/K) which be easily explained by imperfect thermal contacts due to the room pressure test.

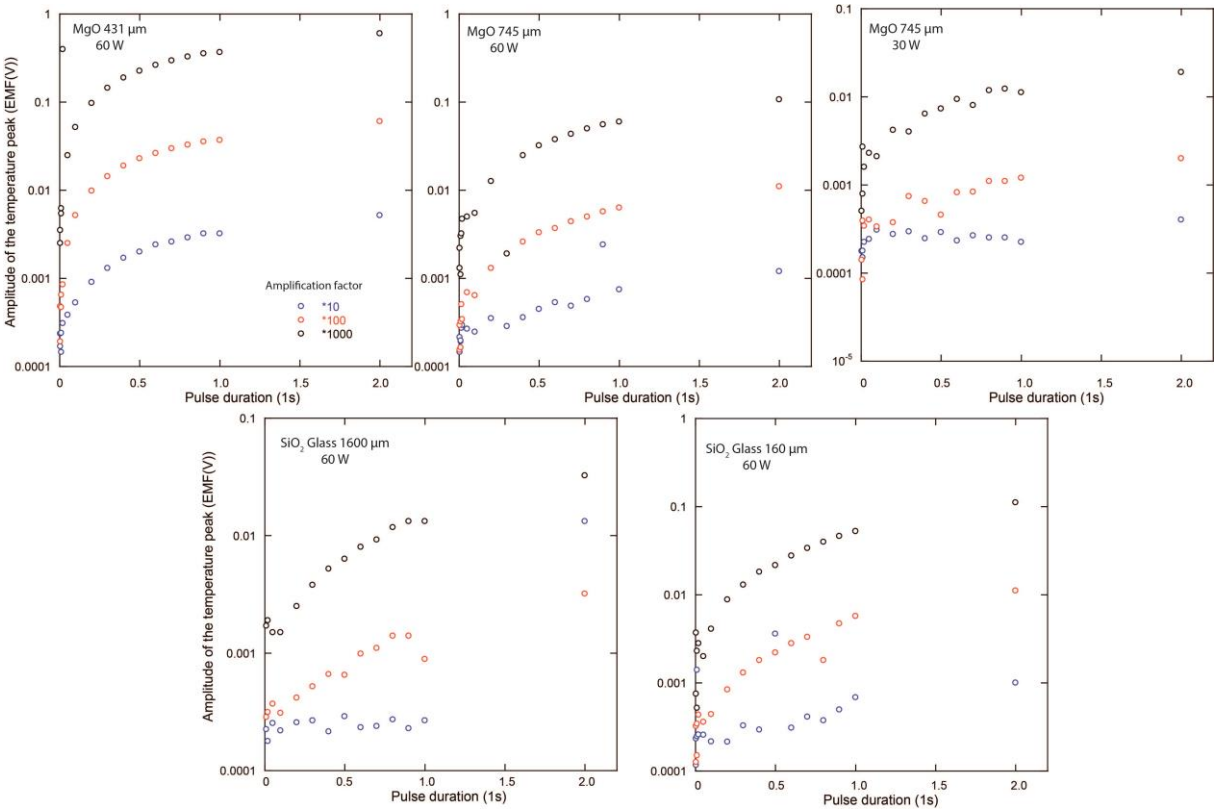

Figure VII.27 Amplitude at temperature maximum of the measured signals as a function of the pulse duration for our different samples.

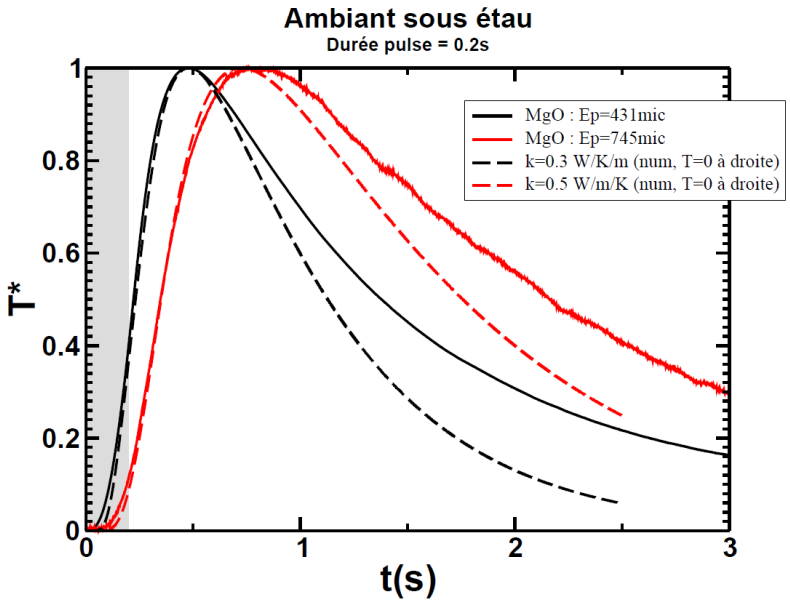

Figure VII.28 Comparison of our two MgO samples measurements normalized to maximum temperature increase with modeled signals (also normalized by maximum increase) in dashed lines for 20 ms pulse duration (grey zone).

Nevertheless, these tests were precious to estimate the conditions suitable for good data analyses. We have shown that increase of pulse power and using thin samples will maximize the quality of the recovered signals. Similarly, we saw that increase pulse power will provide better signals and that samples with higher thermal conductivities are easier to measure. However, the simulations performed do not allow retrieving the good thermal parameters. Despite data quality seems good, the quality of thermal contact during this RP and RT test does not allow deciphering between software issues and experimental underestimation of thermal properties. Thus tests, with good thermal contacts in multi-anvil apparatus, are then required.

b) Multi-anvil tests

Several tests were made with high pressure and temperature experiments using 1500 Tons MAA at the LMV and the 1200 tons MAA present at PSICHE beamline. These experiments were realized using 18/11 (at the LMV) and 10/4 (at PSICHE) assemblies described in the previous parts

Among the different experiments, we have encountered several issues and failures with short circuit between pulse heaters and furnaces during LMV tests, whereas the system seems to work properly during PSICHE experiments.

i) *LMV tests*

For the tests made at the LMV, the encountered issues were first heater failure at HT and short circuits (M626) and pulse heater rupture during compression (M660).

M626 (2 GPa) was performed on an olivine sample (500 µm thick) (Fig. VII.29). the resistance between the pulse and TC wires was only 16 ohm indicating a probable short circuit. Still few measurements were performed to understand the effect of short circuit on the measure signals (can be useful to understand further experiments).

The recorded signal has a nice shape even if the signal was observed to be reversed (going from positive to negative while plugged correctly). The measured EMF was near 2 V at 100*, which translated into temperature, yield to 1100°C of increase. Such increase is not possible and might be due to short circuit with an attenuation of the sent signal (16 ohm resistance). The peak position was observed to vary while changing pulse duration and was very close to it (~8 ms for 5 ms pulse, ~14 for 10 ms and 22 for ~10 ms). Hence, the signal observed is

direct analysis of the sent pulse. For these reasons, the data from this experiment was not further used.

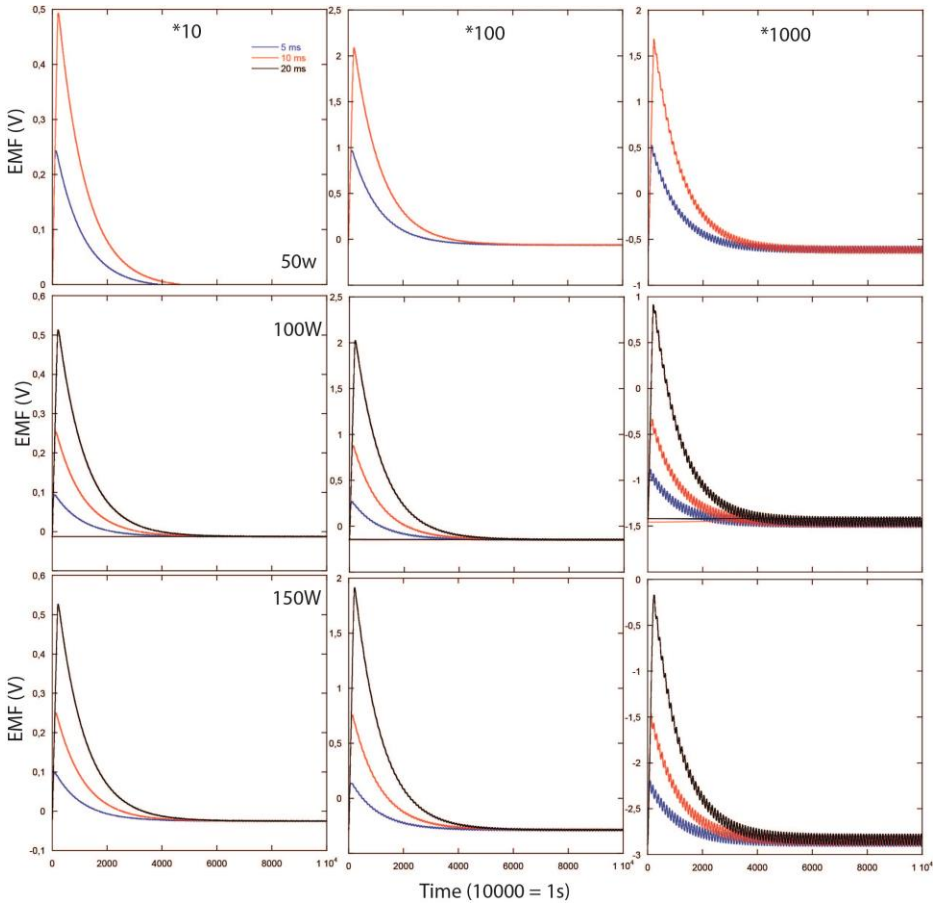

Figure VII.29 Example of time evolution of EMF measured on thermocouple during M626 for 50, 100 and 150W heating power (other temperatures are similar) and various amplifications.

A second experiment was performed at 2 GPa for an olivine sample (M660; 610 µm thick). In this run, a rhenium disk was inserted on the thermocouple side to stop the ballistic or radiative photons. A strong issue occurred during the compression with the loss of electrical contact with the pulse heater. However, the data measured at room pressure and temperature prior compression can be analyzed (Fig. VII.30). We realized different heating durations with a constant amplification factor (1000*). The normalized profiles and computed peaks are displayed in the figures VII.30 and 31.

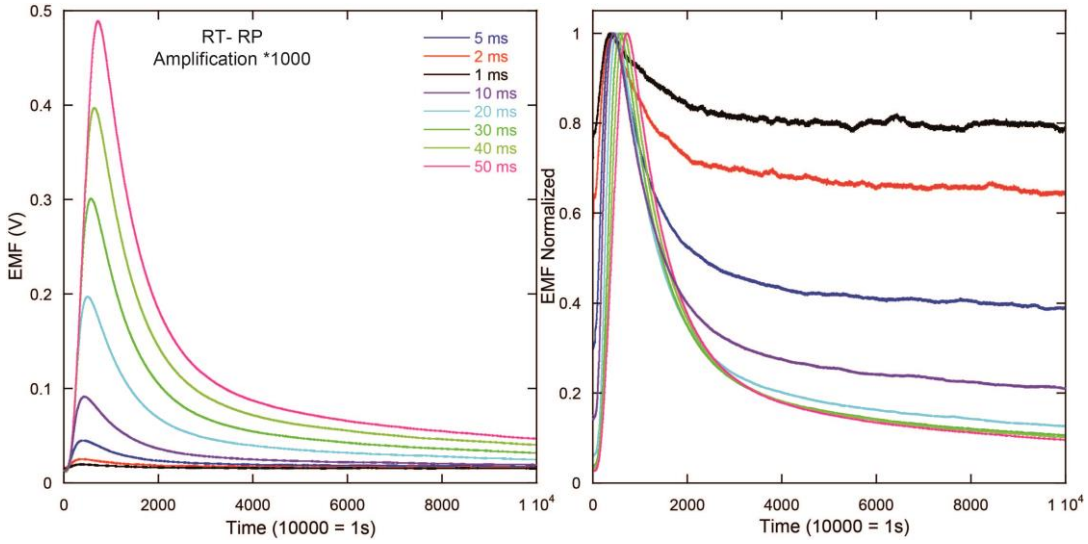

Figure VII.30 Time evolution of EMF measured on thermocouple from M660 at RP and RT conditions for different heating times. This data is normalized to maximum increase in the right panel to see the relative increase of signal noise ratio for higher pulse times (same color code).

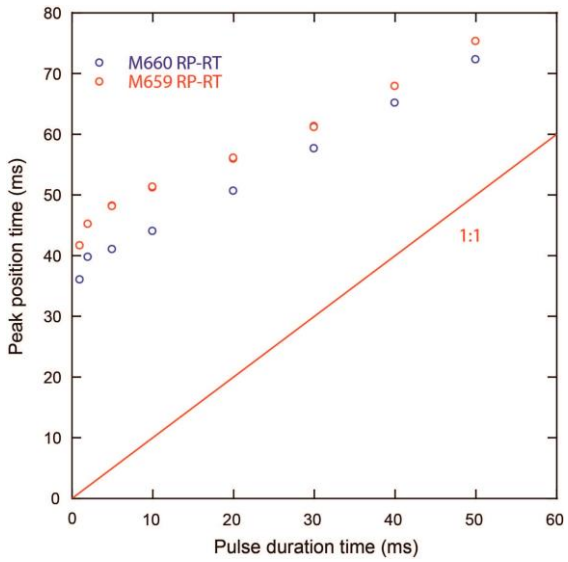

Figure VII.31 M660 and M659 "peak positions" of EMF as a function of pulse duration.

A third experiment was performed at 2 GPa for a MgO sample (M659) (547 µm thick). A rhenium disk was also inserted at thermocouple side in this experiment. The experiment suffered from the same issue than M626, low resistance between pulse and thermocouple loops was observed. For similar reasons to previous test only RT and RP data were used. Data recovered during two sessions of analyses are given in the figure VII.32. The shape of the observed signal is similar to signals observed in the previous experiments and clamp tests. Time position of temperature peak was also measured as a function of pulse duration in the figure VII.32 and is comparable to the data of M660.

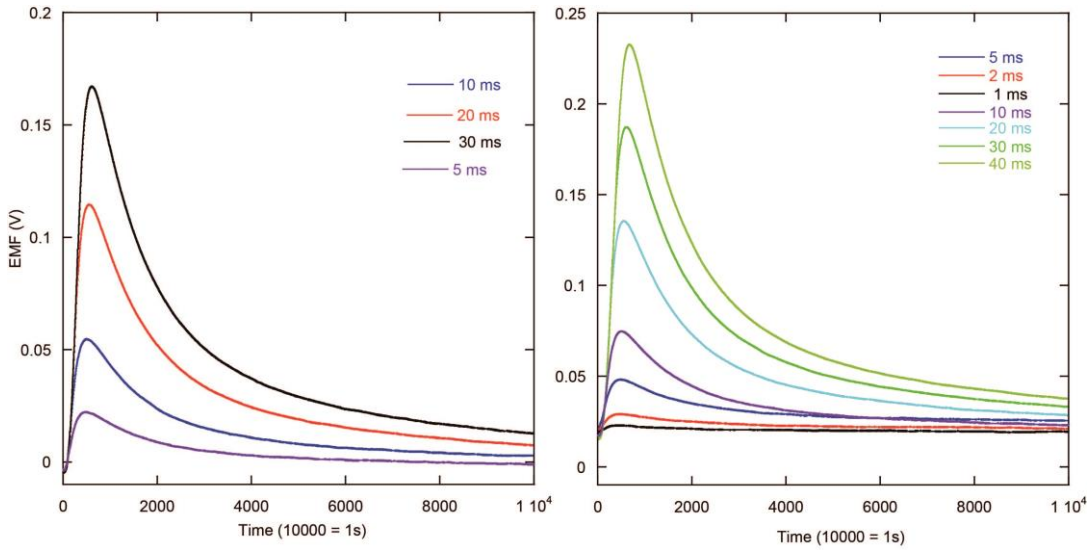

Figure VII.32 Time evolution of EMF of M659 at RP and RT conditions for different heating times. Each panel represent a distinct sessions of analyses. Measured temperature evolutions are comparable for similar pulse duration.

Once normalized to the maximum temperature increase, these data have been compared to modeled signals in the figure VII.33. We can see that the observed shape is very good for 20 ms pulse duration and matches very well with our calculations. The signals between olivine and MgO are somewhat similar even if MgO signal seems to stay at high temperature for longer time. The inferred thermal conductivities are, however, very different than real ones with 0.4 W/m/K for MgO and 0.5 W/m/K for olivine. These values are very low compared to expected thermal conductivities of 37.5 W/m/K and 5.2 W/m/K for MgO and olivine respectively. Such low values can be explained by the very bad contact between sample, pulse heater and thermocouple at room pressure and by the presence of imperfect thermal contacts (similar to clamp results).

These tests highlight the correct operation of our pulse heating apparatus. The results obtained in high pressure assemblies are similar to previous results obtained during the clamp tests. The signal shape is coherent with our modeling. However, the absolute conductivities cannot be estimated due to imperfect thermal contacts.

Thus, more experiments are then required to find a good assembly configuration which could present such short circuit failures. The realization of such experiments will be detailed in the perspectives.

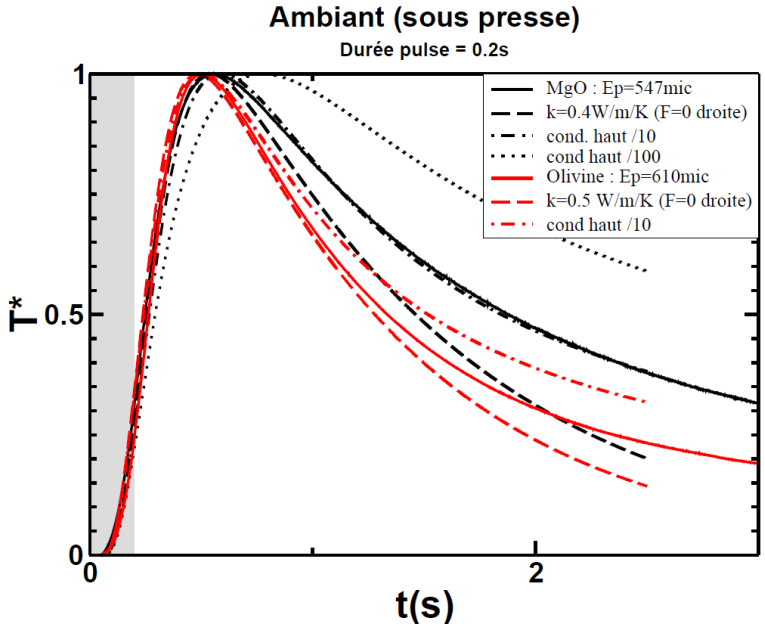

Figure VII.33 Time evolution of normalized temperature of M659 and M660 (solid lines) compared with modeled signals for corresponding assembly (dashed lines). Data with 20 ms pulse duration were selected for MgO (M659) and olivine (M660) samples. Different types of models were used according boundary conditions. Large dashed lines correspond to the assembly modeling in standard conditions, dotted lines were made using lateral flux condition of F = 0. Then different conductivities were used with respect to MgO conductivities labeled "cond haut/10" or "cond haut/100".

ii) *PSICHE tests*

Finally, several tests were conducted at PSICHE beamline in SOLEIL synchrotron facility. These tests were performed to check the adaptability of our portable pulse heating apparatus to synchrotron setups, find the proper operating conditions and perform thermal diffusivity measurements.

During this session, we have performed a total of 6 pulse heating runs. The samples analyzed were mixture of San Carlos Olivine and MORB glasses (0, 0.5, 2 and 100% of MORB). We used the powders prepared for the study made in the chapter III. The powders were synthesized in a preliminary HP-HT runs using MAA in 25/17 configuration at 2 GPa, in rhenium capsules and at temperatures of ~1000 K for 4 hours. The analyzed samples were prepared from cores of the large synthesized ones and were polish top and bottom to have flat surfaces to ensure good mechanical contacts. MgO single crystal discs were prepared similarly from large synthetic single crystals (see chapter VI). The 10/4 assembly used is described in the method section of this chapter.

The adaptation of our pulse heating system was very simple and required only few hours for successful installation (including safety checks). The main difficulty was to pass the wires

into the experimental hutch. The tool, which is controlled manually during the experiment, must be located outside the hutch for evident safety reasons.

Thanks to synchrotron X-ray beam several *in situ* analyses were obtained during the experimental runs, making its use of a very great interest to understand our experiments.

The assembly configuration, as well as sample size was checked at each temperature step by high contrast X-ray imaging (Figs. VII.34 and 35). Changes in sample length, due to thermal expansion or sample contraction during the cold compression, are important because they will change the arrival time of the measured temperature wave. Moreover, for modeling purpose and data interpretation, the thickness of each part can be estimated at each temperature step which would yield to a much better precision. The high contrasts of the X-ray images allowed separating the different parts of the assembly: sample and the two MgO thin cylinders inserted top and bottom. The contrast is really good at RP/RT but decreases with increasing P and T.

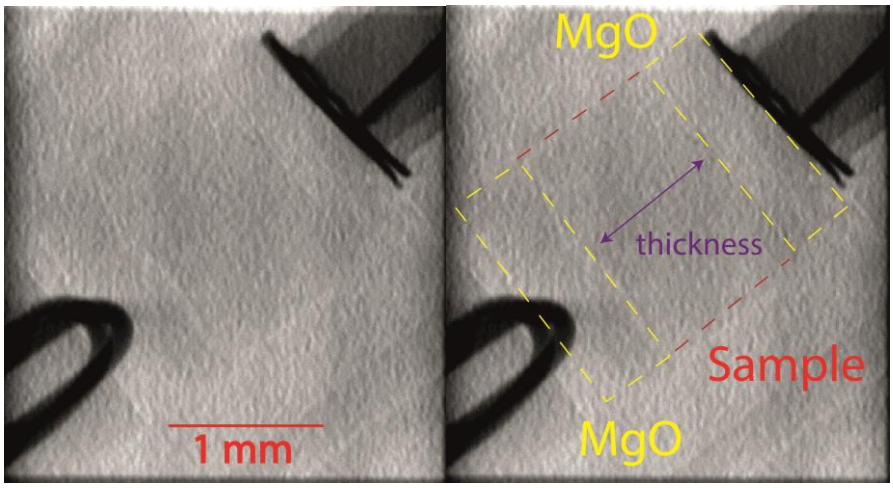

Figure VII.34 X- ray absorption image of the sample cell before compression. Black wires are the TC on the bottom left and the pulse heater on top right

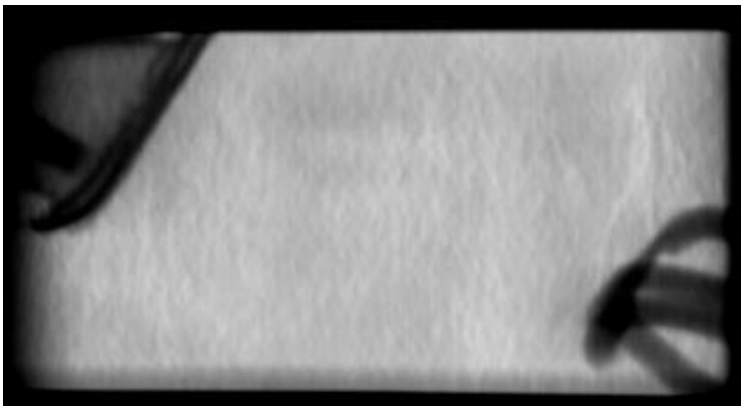

Figure VII.35 Example of X-ray absorption image of the sample cell at HT and HP

X-ray diffraction clichés were made to control the pressure in the in cell assembly (BN was used as a pressure marker, Le Godec et al., 2000). Diffraction measurements were also made at sample's center to check its physical state. While approaching melting point of the binary system, time scans were acquire to follow quick changes in sample structure. At solid state, time scans resulted into a fixed picture of diffraction peaks. At the opposite, onset of melting showed different patterns with peak positions varying with time (peaks disappearing and appearing quickly) and large variations of intensities due to grain rotation and spinning due to the presence of thin melt films between grains (Andrault et al., 2018; Pesce, 2016). Partial melting is also marked by the apparition of a broad diffusive background due to the structure of the melt (Figs. VII.36 and 37).

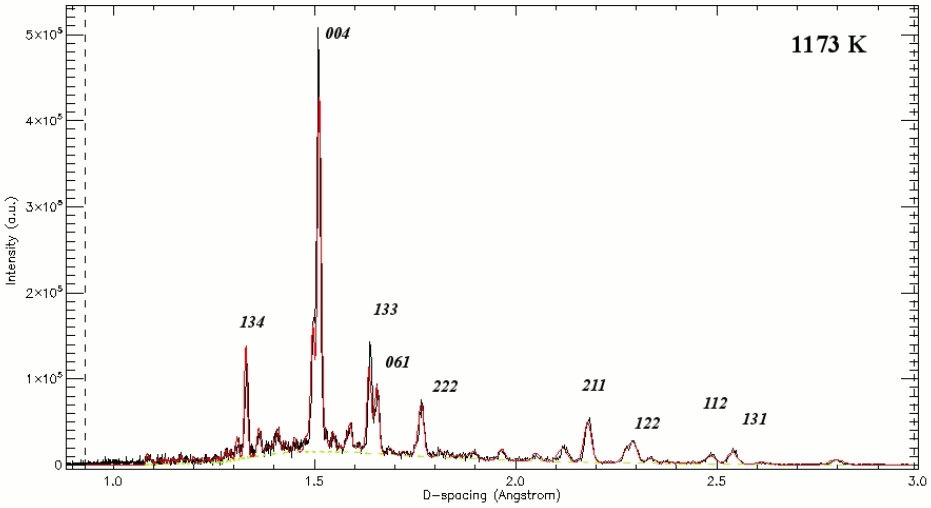

Figure VII.36 X-ray diffraction of Ma22-08 ol+Morb sample at subsolidus temperature of 1173 K , showing some olivine peaks

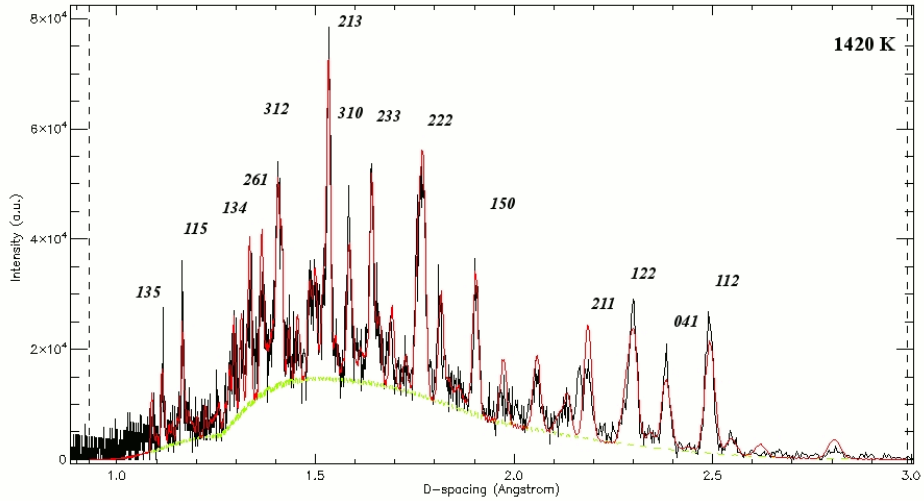

Figure VII.37 X-ray diffraction of Ma22-08 ol+Morb sample above solidus, temperature of 1420 K , showing some olivine peaks and large diffusive back ground due to partial melting.

During the HP and HT experiments performed at PSICHE beamline, we were able to successfully send and receive heat pulses via our newly developed apparatus. The behavior of the electronic part was similar to our prior tests made at the LMV.

The recorded signals (Fig. VII.38) were found to have important electrical noise due to the equipment of the beamline (electrical wires inside and outside the hutch) and press heating system. Two frequencies of noise were found corresponding to the standard French electrical current: 50 Hz and press heating system: 1khz. This effect may be due to the common path of thermocouple wires and other cables. A signal processing program was developed for the noise removal on Matlab®, the following steps are realized:

- The raw signal is smoothed with smoothing spline
- The spline is subtracted to the raw signal is order to get the "noise" component
- The resulting "noise" is Fourier transformed to extract frequencies of the real noise a superposition of 50 Hz and 1 kHz.
- The maximum frequency to remove is then chosen manually. All the frequencies below this choice will be equal to 0. This will only keep the noise frequencies and remove the DC component from the noise.
- The resulting part of the noise is IFFT (inverse fast Fourier transform) to reconstruct only pure noise signal.
- The real noise is then subtracted to the raw data to retrieve the pure DC component.

Once the signal has been processed and filtered from this background noise (Fig. VII.38b), the tension increase indicates the temperature rise of the rear face of the sample.

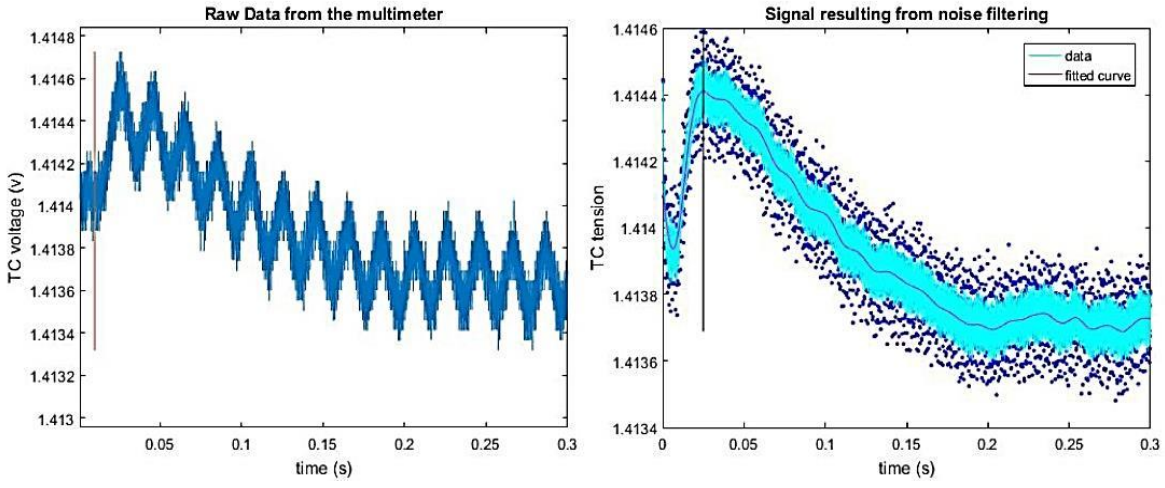

Figure VII.38 (a) Example of raw EMF data time evolution recorded by the multimeter (b) Same EMF data after noise filtering (dots) and data smoothing (light blue and purple curve)

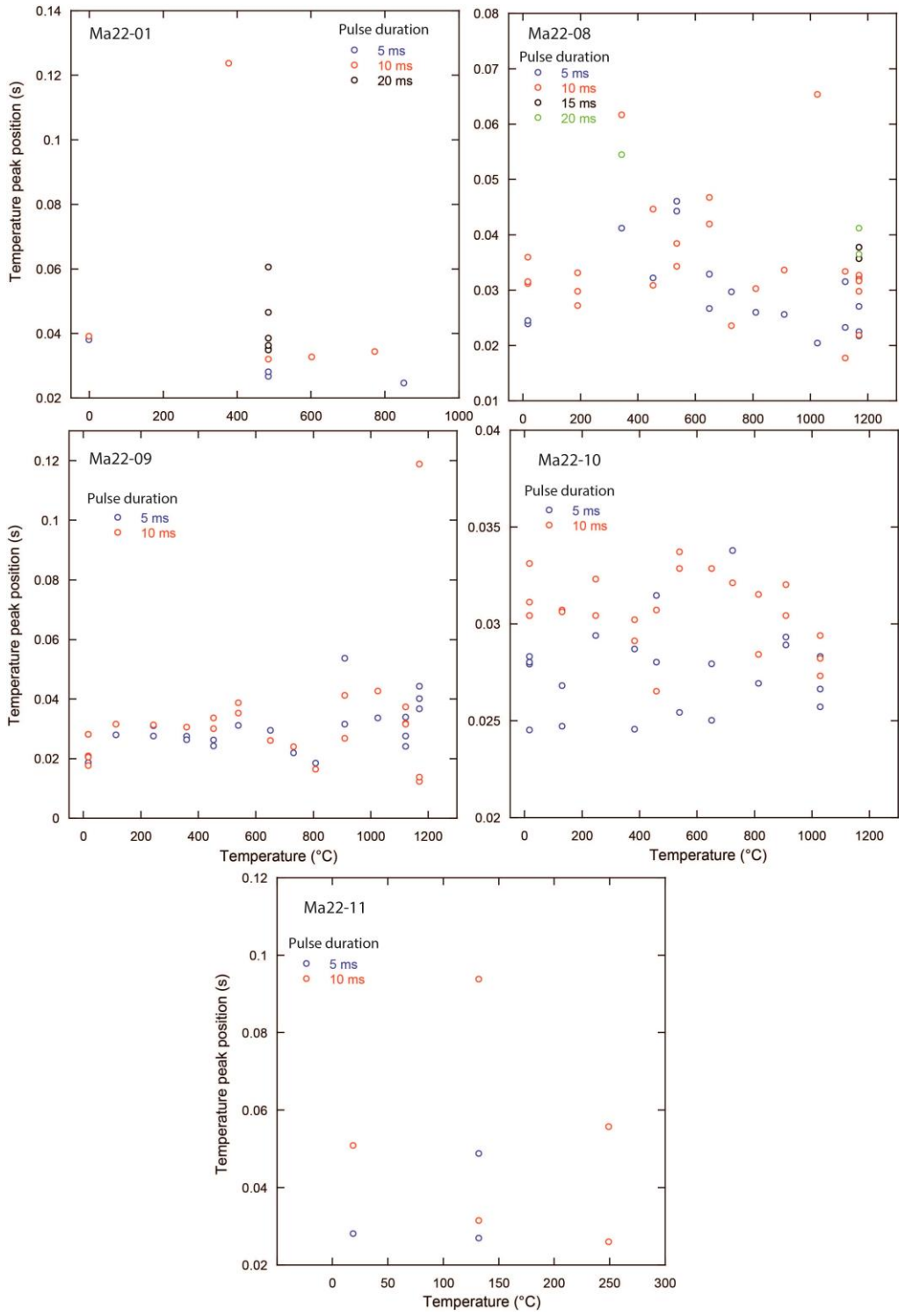

Figure VII.39 Peak position in function of temperature for Ma22-01 Sc Ol, Ma22-08 Sc Ol +0.5% Morb, Ma22-09 Sc Ol +2% Morb, Ma22-10 100% MORB and Ma22-11 Sc Ol+0.5% MORB.

The pulse heating data recovered on our experiments is difficult to interpret whereas the shape, once filtered, is coherent with modeled signals. Our data is very similar at all temperatures and between the different samples, the position of temperature peak at low and melting temperature was measured between 0.02 and 0.035 second. The position of the peak, with varying pulse durations, of our different experiments is given in the figure VII.39. While

peak position is expected to change with variation in thermal conductivity, it stayed similar for all of our experiments. In addition, it does not seem to depend on sample size and composition.

Peak positions observed can't be explained by our predictive modeling (see previous figures). The very short arrival time after the onset of pulse could only be obtained invoking short circuit (which has not observed and recorded signals different from our previous short-circuit LMV run M626), or other heat transfer processes such as radiation or ballistic photons. As our MORB sample was opaque, without significant differences with other samples, this explanation is unlikely.

Moreover, Osako's recordings (2004) indicated the presence of induction in their recorded signal. Such effect is possible to explain the observed signal. The presence of important noise, probably due to the common path of the thermocouple, pulse and numerous other wires to enter the experimental hutch, reinforces this hypothesis.

Such observation indicates that thermal conductivity could not be retrieved from measurements performed during this session. However, this study allowed validating our experimental strategy, assembly and the correct operating of the pulse heating apparatus. More experiments while taking in account these noises induced by the surrounding wires (which were never observed at LMV) can be conceivable.

6) Conclusions

In this chapter, we detailed the construction steps of a portable pulse heating apparatus for thermal diffusivity characterization, modeling of its effective operation and associated experimental tests.

The construction of the apparatus and its associated objectives are first given in order to provide a reliable explanation of our development sequence. These descriptions are important because we found, during our tentative to reproduce Osako et al. pulse heating apparatus, that literature is more than elusive on these technical, but crucial, details.

An important modeling sequence was then developed in collaboration with J. Monteux in order to model and predicts the temperature evolution recorded at the rear face of a sample in our multi anvil assemblies. We build a series of different types of models to suit and explain

the possible recorded signals while taking in account the surrounding environment of the sample, the types of heat transfers and the experimental limitations.

Several tests were performed afterward at the LMV in different conditions. First tests at RP - RT in a clamp allowed checking the correct operation of the pulse heating tool and provide qualitative information on instrument setting. Experiments performed with multi-anvil apparatus were much complicated with important experimental failures observed. These experiments only allowed characterizations at RT and RP conditions. Both Clamp and multi-anvil tests gave signal shapes that were coherent with modeled signals. However, the thermal properties inferred from models are not coherent with literature results indicating that our measurements were not precise due to imperfect thermal contacts.

Additional tests made at PSICHE beamline with this system, together with further tests and experiments have been reported. Discussions and resolutions of the different experimental, numerical and methodological issues have been proposed to the light of the different possible thermal transfer processes and their modeling. The results were however found to be inoperable.

This work clearly showed that our developed apparatus works efficiently and is adapted for *in situ* measurements in high-pressure apparatus (or other) in addition to a good portability of the system for synchrotron studies. The problem resides more into instruments and cell assembly settings (pulse duration, sample size etc.) which were found to be critical parameters for successful data acquisitions.

The whole performed tests and modeling represent a real progression toward the establishment of routine pulse heating measurement in high-pressure apparatus. The perspectives of such works are numerous and worth some further dedication.

7) Perspectives

The perspectives of the studies performed here are numerous as the work performed is not achieved and geological implications were not explored. More than perspectives, some points are just continuation of the started work which was not achieved mostly due to the lack of time. Here are some directions suggested by the previous work:

a) High pressure tests and standard materials characterization

Further multi-anvil tests must be performed to ensure the complete correctness of our instrumental setup, high pressure assembly and our modeling program. Indeed, our previous data does not allow confirming all of these aspects. The targeted samples must be simple such as known standards and only one variable should be explored at the same time.

First, known samples should be characterized such as polycrystalline MgO and olivine samples with two different thicknesses (500 and 1000 μm) in order to check if the program is working properly. An optically opaque sample must also be tested with samples such as MORB glass or pyroxene or a given crystal with carbon coating. Metals can also be considered but should be electrically insulated. In addition, in all these runs, a metal plate (rhenium, molybdenum etc.) should also be inserted between sample and thermocouple in order to block the path of ballistic and radiative photons if present. This would allow their detection in the recorded signal (never seen yet).

After successful tests on known materials and good agreement with model predictions for these samples, unknown geological material can be characterized. As proposed initially, it would be of a great interest to repeat MORB+olivine experiments to check if various proportions of partially molten materials in a solid matrix significantly affect the bulk thermal properties.

If the MgO single crystal discs technique offers the possibility to split the different contribution, such technique should be explored in depth. Indeed, it may offer a unique possibility to better constrain the different components and verify the processes described at ambient conditions from Hoffmeister's group. If MgO discs insulate well the samples, as shown in our synchrotron study, their use to characterize largely molten samples and electrical conductors is very precious. Indeed measured thermal properties of these materials are delicate with other techniques such as Angström method. It would be particularly

interesting to measure thermal properties of metals and molten metals or metal/silicate mixtures to provide better constraints on CMB heat flow or early Earth dynamics.

b) Modeling program improvement… toward a complete physically based model

Our modeling program allows the prediction of temperature evolution in a high pressure assembly in response to short pulse of heat. The models, however, failed to obtain comparable signals for the different tests with coherent thermal parameters. This issue may be due to the presence of imperfect thermal contacts. However, issues with modeling software can't be ruled out and the realization of the tests suggested in the first point will allow verifying the agreement between predicted and measured signals.

In addition, the program developed can be significantly improved. The current code is blind to the physical process involved and just computes the temperature evolution considering a given conductivity/diffusivity. Insertion of the distinct physical processes and their competition would be of a significant importance when radiative transfers are also a part of the total heat transfer. Such program, would first establish which type of process is involved in the heat transfer. To make the decision, the optical absorption spectra (obtained with FTIR) of the different materials have to be inserted in the program and calibrated in function of P and T. With material properties and sample thickness, the $A(v)d$ product can be estimated and so, optical conditions can be defined (see appendix E). With them, the program will be able to choose if optical conditions are opaques (no radiative transfer), thin (direct radiative transfer), thick at all explored frequencies (radiative diffusive only) or mixed (mix of diffusive radiative or direct transfers).

The frequencies of photons in the experiments can be calculated using Wien's law and the optical conditions can be estimated at each step:

- opaque ($A(v)d > 7$) at covered frequencies: no radiative transfer, no radiative infrared transfer and no ballistic photons. Lattice thermal conductivity can be simulated using the method presented in the current code.
- If thick ($A(v)d > 2$) at covered frequencies: no ballistic photons. Lattice thermal conductivity is simulated with current code. In addition, radiative infrared enhanced lattice thermal conductivity and radiative thermal conductivities must be estimated using models provided by Hofmeister et al. (1999 and 2015).

- If thin ($A(v)d < 1$) at covered frequencies. Lattice thermal conductivity is simulated with current code. Direct radiative, ballistic and infrared conversion must be estimated using different models from Mehling et al. (1998) and Hofmeister et al. (1999 and 2015).

Such programs will be able to propose a physical model of heat conduction at each sample's conditions. The main limitation is the poor quantification of the different parameters required at HP and HT. Finally, the main remaining problem is the effect of the grain size as it is poorly defined in the theoretical approaches and crucial into optical thickness characterization. Such theoretical considerations worth also significant exploration due to their importance in geological processes.

c) Pushing further to the comparisons with Angström data

The second main aim of this study was the comparisons of thermal diffusivities data obtained on similar samples and experimental conditions between transient and steady state techniques. Such comparisons could be possible in a very near future with our correction and improvement of Angström method and the development of these pulse heating apparatus.

The comparisons of the different technique might help to decipher if thermal transfer by radiative ways are present in the experiments and compare methods involving two and one thermal contacts to ensure argumentation of Hofmeister et al. (1999) against contact methods is correct.

In a further way, we could imagine using our pulse heating generator to make sinusoidal signal and compare recorded signal to models (which can also be adapted for that) and ensure Angström mathematical solutions are perfectly correct. In such program, the forward calculation of Angström experiments signals would be made without using the solution provided in Carslaw and Jaegger (1959), and would provide another robust constraint on obtained signal (no inversion needed but bracketing).

General conclusions

The aim of this study was to better constrain Earth's mantle geophysical observables and in particular to provide a viable explanation of the global electrical and seismological anomalies detected such as the LVZ and the LVL. To answer this research problem, we have developed a series of new techniques under the common theme of *in situ* measurements for transport properties experimental characterizations. Indeed, new high pressures devices development allowed the first combination of different *in situ* techniques such as MHz ultrasonic interferometry and electrical impedance characterizations. Their adaptation to multi-anvil apparatus as well as the renovation of the classical thermal diffusivity measurement devices (Angström and pulse heating methods) allowed investigations of materials under various conditions for up-to-date geological implications. The experimental results obtained on different realistic, solid and partially molten systems were of significant interest to constrain and quantify upper mantle geophysical anomalies and refine to small scale our idea of Earth's upper mantle.

Presence of partial melting in the upper mantle: localization, melting processes and physico-chemical quantifications.

The Earth's mantle is known to have several major discontinuities thanks to seismological and electromagnetic investigations. Associated to these major changes, small zones, recently investigated with a much greater resolution, highlighted the presence of several low seismic velocities and high electrical conductivities anomalies. These anomalies were not located randomly, but appeared to be situated in focused zones such as the so-called low velocity zone, between 70 and 200 km depths, and the low velocity layer, the "350" discontinuity between 350 and 410 km deep. The nature of these zones remained unclear, in particular for the LVL, until the very recent advances in seismological investigation led by Tauzin et al., (Tauzin et al., 2010; Hier-Majumder and Tauzin, 2014 and 2017, etc.). The reported anomalies could be explained via different scenario, including partial melting, but were however, difficult to translate in terms quantifications and induced geological implications. Thanks to the coupled *in situ* measurements of electrical conductivity and acoustic wave velocity during high pressure and temperature multi-anvil experiments, we were able to investigate the parameters influencing the partially molten system geophysical properties and quantified the melt fractions potentially implied into these anomalies.

LVZ anomalies were first investigated. Our experiments underlined the importance of textural equilibration of partially molten rocks to compare laboratory estimations of electrical conductivities. Thus, the long debate between conflicting estimations of the LVZ melt fractions by electrical conductivities calibrations and acoustic wave velocities have been reconciled with 0.3 - 0.8 vol.% of partial melting.

Moreover, such experimental development allowed the first experimental simulation of hydrous material ascent from the mantle transition zone to the upper mantle. In this case, not only the physical properties are investigated but the melting process itself by dehydration melting enhanced via fluid release during transformation of hydrous wadsleyite into olivine (from 14 to 12 GPa). The measurements of acoustic wave velocities during the partial melting of our sample allowed the calibration of the S wave velocity drop as a function of melt fraction. Melt fractions implied in the LVL anomalies have been evaluated to be < 2 vol.%. The consequences of melt presence in these upper mantle anomalous zones were also explored for different aspects. The chemical analyses revealed the extreme nature of these low melt fraction magmas, which were found to be much enriched in volatiles and incompatible elements suggesting that the melting process can create a filter between upper and lower mantle. The density of such melt layer located above the MTZ was confirmed to be neutrally buoyant, confirming the stability of such features through geological times. The density dependence to volatile and iron contents confirmed the possibilities to generate instabilities forming upper mantle plumes. The association of these data with modeling of water diffusion and transfers allowed estimating the volatile budget of the mantle transition zone and upper mantle. Indeed, with the present constraints on water content in the upper mantle (Hirschmann, 2009) and the estimated solubility profile (Férot and Bolfan-Casanova, 2012), a bottom-up hydration process of the upper mantle has been proposed. Diffusion in crystals was found to be negligible in front of material circulation thanks to passive/active convection, bringing deep water-rich materials to shallower mantle parts and produce extensive partial melting. This shallow melting due to water saturation also corresponds to LVZ depths providing a potential mechanism for its genesis. We found such process matching current observations with only moderate MTZ water content (< 1500 ppm).

Thermal properties estimations: improved tools for new applications.

During this PhD work, a significant development was performed on methods for thermal diffusivity measurements in HP-HT apparatus. We adapted and improved previous

designs of Angström (steady state temperature oscillations) and pulse heating methods for new innovative purposes such as adaptation to synchrotron experiments and characterization of partially/fully molten systems.

For Angström method, a significant improvement of the heating system of our multi-anvil apparatus allowed accurate measurements with an increased resolution (wider frequency range). A complete treatment procedure and treating codes were also created while taking in account the error propagation, which was not described in any previous literature studies. The adaptation of the device for glasses and melts characterization allowed the conduction of the first successful measurement of different types of melts in high-pressure devices. Similarly different sets of geologically relevant materials such as periclase, olivine (single crystals and polycrystalline samples) and natural peridotite samples were investigated. Despite numerous experimental difficulties, we manage to successfully measure glasses, mixture of glass and crystals, while going above the glass transitions, and melts. We also reported the first natural peridotite partial melting thermal characterizations. These measurements have important implications for both melting in the mantle and understanding of the thermal conduction process in mineral/melt mixtures.

For pulse heating apparatus, an innovative and portable system was built allowing simple operation during multi-anvil (and synchrotron) experiments. Numerical models were developed and adapted to understand and quantified obtained experimental results. Different set of tests were performed in order to better understand the apparatus allowing successful geological materials characterizations in a very near future.

General bibliography

A

Abbott, D., Burgess, L., Longhi, J., (1994). An empirical thermal history of the Earth ' s upper mantle. J. Geophys. Res. B Solid Earth 99, 835–850. doi:10.1029/94JB00112.

Afonso, J.C., Schutt, D.L., (2012). The effects of polybaric partial melting on density and seismic velocities of mantle restites. Lithos 134–135, 289–303. doi:10.1016/j.lithos.2012.01.009.

Agee, C.B., (2008). Compressibility of water in magma and the prediction of density crossovers in mantle differentiation. Philos. Trans. A. Math. Phys. Eng. Sci. 366, 4239–52. doi:10.1098/rsta.2008.0071

Akimoto, S., Fujisawa, I., (1968). Olivine-Spinel Solid Solution Equilibria in the System. J. Geophys. Res. 73.

Akins, J. A., Luo, S. N., Asimow, P. D., & Ahrens, T. J., (2004). Shock-induced melting of MgSiO3 perovskite and implications for melts in Earth's lowermost mantle. Geophysical Research Letters, 31(14).

Anderson D., Sammis C., (1970) Partial melting in the upper mantle. Phys Earth Planet Inter 3:41–50.

Andrault, D., Bolfan-Casanova, N., Nigro, G. L., Bouhifd, M. A., Garbarino, G., & Mezouar, M., (2011). Solidus and liquidus profiles of chondritic mantle: Implication for melting of the Earth across its history. Earth and planetary science letters, 304(1-2), 251-259.

Andrault, D., Pesce, G., Bouhifd, M.A., Bolfan-Casanova, N., Hénot, J.-M., Mezouar, M., (2014). Melting of subducted basalt at the core-mantle boundary. Science 344, 892–5. doi:10.1126/science.1250466

Andrault, D., Monteux, J., Le, M., Samuel, H., (2016). The deep Earth may not be cooling down. Earth Planet. Sci. Lett. 443, 195–203. doi:10.1016/j.epsl.2016.03.020.

Andrault D., Monteux J., LeBars M., Samuel H., (2016b). The deep Earth may not be cooling down. Earth and Planetary Science Letters vol.443, p.195-203, DOI:10.1016/j.epsl.2016.03.020.

Andrault, D., Pesce, G., Manthilake, G., Monteux, J., Bolfan-casanova, N., Chantel, J., Novella, D., Guignot, N., King, A., Itié, J., Hennet, L., (2018). Deep and persistent melt layer in the Archaean mantle. doi:10.1038/s41561-017-0053-9

Andrault, D., Muñoz, M., Pesce, G., Cerantola, V., Chumakov, A., Kantor, I., Hennet, L. (2018). Large oxygen excess in the primitive mantle could be the source of the Great Oxygenation Event. Geochemical Perspectives Letters, 6, 5-10.

Andrault, D., (2019). Thermodynamical constraints on the crystallization of a deep magma-ocean on Earth. Comptes rendus - Geosci. 351, 221–228. doi:10.1016/j.crte.2018.06.003

Ardia, P., Hirschmann, M.M., Withers, A.C., Tenner, T.J., (2012). H2O storage capacity of olivine at 5-8GPa and consequences for dehydration partial melting of the upper mantle. Earth Planet. Sci. Lett. 345–348, 104–116. doi:10.1016/j.epsl.2012.05.038.

Asheghi, M., Kurabayashi, K., Kasnavi, R., & Goodson, K. E. (2002). Thermal conduction in doped single-crystal silicon films. Journal of applied physics, 91(8), 5079-5088.

Auer, L., Boschi, L., Becker, T.W., Giardini, D., (2014). Journal of Geophysical Research : Solid Earth Savani : A variable resolution whole-mantle model of anisotropic shear velocity variations based 3006–3034. doi:10.1002/2013JB010773.

B

Baba, K., Utada, H., Goto, T.N., Kasaya, T., Shimizu, H., Tada, N., (2010). Electrical conductivity imaging of the Philippine Sea upper mantle using seafloor magnetotelluric data. Phys. Earth Planet. Inter. 183, 44–62. doi:10.1016/j.pepi.2010.09.010.

Bajgain, S., Ghosh, D.B., Karki, B.B., (2015). Structure and density of basaltic melts at mantle conditions from first-principles simulations. Nat. Commun. 6, 1–7. doi:10.1038/ncomms9578.

Bambier, A., Berger, E., Mergoil, J., Valadas, B., Veyret, Y., Weisbord, A., (1985). Carte géologique de la France à 1/50 000 (n 840), Burzet: Des sources de l'Ardèche aux sources de la Loire. Carte et notice explicative.

Beck A.E., Darbha D.M., Schloessin, H.H., (1978) Lattice conductivities of single-crystal and polycrystalline materials at mantle pressures and temperatures. Phys. Earth Planet. Inter. 17:35–53. doi: 10.1016/0031-9201(78)90008-0.

Beck, P., Goncharov, A.F., Struzhkin, V., Militzer, B., Mao, HK., Hemley ,R.J., (2007) Measurement of thermal diffusivity at high pressure using a transient heating technique Measurement of thermal diffusivity at high pressure using a transient heating technique. Applied Physics Letters. 181914:9–12. doi: 10.1063/1.2799243

Becker, T.W., Kellogg, J.B., O' Connell, R.J., (1999). Thermal constraints on the survival of primitive blobs in the lower mantle. Earth Planet. Sci. Lett. 171, 351–365. doi:10.1016/S0012-821X(99)00160-0

Bercovici, D., Karato, S.-I., (2003). Whole-mantle convection and the transition-zone water filter. Nature 425,

39–44. doi:10.1038/nature01918.
Berger, E., (1973). Le volcanisme récent de l'Ardèche. Thèse, Orsay, 402 p.
Berger, E., Forette, M. C., (1975). Réactions de basaltes alcalins des Causses, du Vivarais et du Velay (France) avec les xénocristaux et les minéraux des enclaves homoéogènes. Bulletin de Minéralogie, 98(6), 366-373.
Berger, E., (1981). Enclaves ultramafiques, mégacristaux et leurs basaltes-hôtes en contexte océanique (Pacifique Sud) et continental (Massif Central Français). Thèse d'État, Université de Paris-Sud, Orsay, 470 p.
Bigazzi, G., Yegingil, Z., Ercan, T., Oddone, M., Özdogan, M., (1993). Fission track dating obsidians in Central and Northern Anatolia. Bulletin of Volcanology, 55(8), 588-595.
Birch, A. F., Clark. H., (1940). No The thermal conductivity of rocks and its dependence upon temperature and composition. Am. J. Sci. 238:529–558.
Bhandari, C.M., Rowe, D., (1998). Thermal Conduction in Semi- conductors. Wiley, New York, pp. 13–34.
Blumm, J., Henderson, J. B., Nilsson, O., Fricke, J., (1997). Laser flash measurement of the phononic thermal diffusivity of glasses in the presence of ballistic radiative transfer. High Temperatures. High Pressures, 29(5), 555-560.
Blumm, J., Lemarchand, S., (2002). Influence of test conditions on the accuracy of laser flash measurements. High Temp. Press. 34:523–528.
Blundy, J., Wood, B., (2003). Partitioning of trace elements between crystals and melts. Earth Planet. Sci. Lett. 210, 383–397. doi:10.1016/S0012-821X(03)00129-8
Boehler, R., (2000). High-pressure experiments and the phase diagram of lower mantle and core materials. Reviews of Geophysics, 38(2), 221-245.
Bolfan-Casanova, N., Keppler, H., Rubie, D.C., (2000). Water partitioning between nominally anhydrous minerals in the MgO-SiO2-H2O system up to 24 GPa: Implications for the distribution of water in the Earth's mantle. Earth Planet. Sci. Lett. 182, 209–221. doi:10.1016/S0012-821X(00)00244-2.
Bolfan-Casanova, N., Montagnac, G., Reynard, B., (2014). Measurement of water contents in olivine using Raman spectroscopy. Am. Mineral. 99:149–156. doi: 10.2138/am.2014.4444.
Bolfan-casanova, N., Schiavi, F., Novella, D., Bureau, H., Raepsaet, C., Khodja, H., Demouchy, S., (2018). Examination of Water Quantification and Incorporation in Transition Zone Minerals : Wadsleyite, Ringwoodite and Phase D Using ERDA (Elastic Recoil Detection Analysis). Frontiers in Earth Sciences. 6:75. doi: 10.3389/feart.2018.00075.
Bougault, H., Treuil, M., (1980). Mid-Atlantic Ridge: zero-age geochemical variations between Azores and 22 N. Nature, 286(5770), 209.
Bouhifd, M.A., Andrault, D., Fiquet, G., Richet, P., (1996). Thermal expansion of forsterite up to the melting point. Geophys. Res. Lett. 23:1143–1146.
Boulard, E., King, A., Guignot, N., Deslandes, J.-P., Le Godec, Y., Perrillat, J.P., Clark, A.N., Morard, G., Itié, J.-P., (2018). High-speed tomography under extreme conditions at the PSICHE beamline of the SOLEIL Synchrotron research papers. J. Synchrotron Radiat. 25, 1–8. doi:10.1107/S1600577518004861
Bridgman, P. W., (1924). The thermal conductivity and compressibility of several rocks under high pressures. Am. J. Sci. 7:81–102. doi: 10.2475/ajs.s5-7.38.81.
Brunet, F., Andrault, D., Chazot, G., (2007). La Terre interne: roches et matériaux en conditions extrêmes. Soc. géologique de France: Vuibert.
Buffett, B. A., (2002). Estimates of heat flow in the deep mantle based on the power requirements for the geodynamo. Geophysical Research Letters, 29(12), 7-1.
Buffett, B., (2003). The thermal state of Earth's core. Science (80). 299, 1675–1677. doi:10.1126/science.1081518.
Buffett, B.A., (2007). Core–Mantle Interactions. Treatise Geophys. 8–12.
Bussod, G.Y., Christie, J.M., (1991). Textural development and melt topology in spinel lherzolite experimentally deformed at hypersolidus conditions. J. Petrol. 2:17–39.
Byrnes, S. J., (2008). Basic theory and phenomenology of polarons. Department of Physics, University of California at Berkeley, Berkeley, CA, 94720.

C

Cagniard, L., (1953). "Basic theory of the magneto-telluric method of geophysical prospecting". Geophysics. 18 (3): 605–635. doi:10.1190/1.1437915.
Cahill, D. G., Watson, S. K., & Pohl, R. O., (1992). Lower limit to the thermal conductivity of disordered crystals. Physical Review B, 46(10), 6131.

Campbell, A.J., Danielson, L., Righter, K., Seagle, C.T., Wang, Y., Prakapenka, V.B., (2009). High pressure effects on the iron-iron oxide and nickel-nickel oxide oxygen fugacity buffers. Earth Planet. Sci. Lett. 286, 556–564. doi:10.1016/j.epsl.2009.07.022.

Canup, R. M., (2012). Forming a Moon with an Earth-like composition via a giant impact. Science, 338(6110), 1052-1055.

Cape, J., Lehman G., (1963). Temperature and Finite Pulse-Time Effects in the Flash Method for Measuring Thermal Diffusivity. Journal of Applied physics.

Caricchi, L., Gaillard, F., Mecklenburgh, J., Le Trong, E., (2011). Experimental determination of electrical conductivity during deformation of melt-bearing olivine aggregates: implications for electrical anisotropy in the oceanic low velocity zone. Earth Planet. Sci. Lett. 302(1–2):81–94. https ://doi.org/10.1016/j.epsl.2010.11.041.

Carslaw, H., Jaegger, J., (1959). Conduction of heat in solids, OXFORD.

Cartigny, P., Pineau, F., Aubaud, C., Javoy, M., (2008). Towards a consistent mantle carbon flux estimate: insights from volatile systematics (H2O/Ce, δD, CO2/ Nb) in the North Atlantic mantle (14°N and 34°N). Earth Planet. Sci. Lett. 265(3–4):672–685. https ://doi. org/10.1016/j.epsl.2007.11.011.

Chai, M., Brown, J.M., Slutsky, L.J., (1996). Thermal diffusivity of mantle minerals. Phys. Chem. Miner. 23:470–475. doi: 10.1007/BF00202033.

Chang, Y.-Y., Jacobsen, S. D., Bina, C. R., Thomas, S. M., Smyth, J. R., Frost, D. J., (2015). Comparative compressibility of hydrous wadsleyite and ringwoodite: effect of H2O and implications for detecting water in the transition zone. J. Geophys. Res. Solid Earth 120, 259–8280.

Chantel, J., (2012). PhD Thesis. Measurement of elastic properties of silicates at realistic mantle pressures.

Chantel, J., Manthilake, G., Andrault, D., Novella, D., Yu, T., Wang, Y., (2016). Experimental evidence supports mantle partial melting in the asthenosphere. Sci. Adv. 2(5):e1600246. https ://doi.org/10.1126/ sciadv.16002 46.

Chopelas, A., (1996). Thermal expansivity of lower mantle phases MgO and MgSiO3 perovskite at high pressure derived from vibrational spectroscopy. Phys. Earth Planet. Inter. 98, 3–15. doi:10.2138/am-2000-2-301.

Cluzel, N., (2007). Thèse, Simulation expérimentale de l'ascension et de la vésiculation des magmas rhyolitiques. Sciences de la Terre. Université Blaise Pascal - Clermont-Ferrand II, Français. <NNT : 2007CLF21749>. <tel-00717870>.

Cmíral, M., Fitz Gerald, J.D., Faul, U.H., Green, D. H., (1998). A close look at dihedral angles and melt geometry in olivine-basalt aggregates: a TEM study. Contrib. Mineral. Petrol. 130(3–4):336–345. https :// doi.org/10.1007/s0041 00050 369.

Constable, S., (2006). SEO3: a new model of olivine electrical conductivity. Geophys. J. Int. 166(1):435–437. https ://doi.org/10.1111/j.1365- 246X.2006.03041 .x.

Constable, S., Constable, C., (2004). Observing geomagnetic induction in magnetic satellite measurements and associated implications for mantle conductivity. Geochemistry, Geophysics, Geosystems, 5(1).

Cooper, R. F., Kohlstedt, D. L., (1984). Sintering of olivine and olivine basalt aggregates. Phys. Chem. Miner. 11:5–16. https ://doi.org/10.1007/ BF003 09372.

Crank, J., (1975). The mathematics of diffusion. Clarendon Press, Oxford.

D

Dai, L., Karato, S.n, (2009). Electrical conductivity of wadsleyite at high temperatures and high pressures. Earth Planet. Sci. Lett. 287, 277–283. doi:10.2138/am.2011.3796.

Dai, L., Li, H., Hu, H., Shan, S., Jiang, J., Hui, K., (2012). The effect of chemical composition and oxygen fugacity on the electrical conductivity of dry and hydrous garnet at high temperatures and pressures. Contributions to Mineralogy and Petrology, 163(4), 689-700.

Dai, L., Li, H., Hu, H., Jiang, J., Hui, K., Shan, S., (2013). Electrical conductivity of Alm82Py15Grs3 almandine-rich garnet determined by impedance spectroscopy at high temperatures and high pressures. Tectonophysics, 608, 1086-1093.

Dai, L., Karato, S., (2014). High and highly anisotropic electrical conductivity of the asthenosphere due to hydrogen diffusion in olivine. Earth Planet. Sci. Lett. 408, 79–86. doi:10.1016/j.epsl.2014.10.003.

Dasgupta, R., Hirschmann, M. M., (2006). Melting in the Earth's deep upper mantle caused by carbon dioxide. Nature 440(7084):659–662.

Dasgupta, R., Hirschmann, M. M., (2007). Effect of variable carbonate concentration on the solidus of mantle peridotite. Am Mineral 92:370–379. https ://doi.org/10.2138/Am.2007.2201.

Davies, G. F., O'Connell, R. J., (1977). Transducer and bond phase shifts inultrasonics and their effects on measured pressure derivatives of elastic moduli. In: Manghnani, M., Akimoto, S., (eds) High pressure research: application in geophysics. Academic Press, New York, pp 533–562.

Davies, G.F., (2009). Effect of plate bending on the Urey ratio and the thermal evolution of the mantle. Earth Planet. Sci. Lett. 287, 513–518. doi:10.1016/j.epsl.2009.08.038.
Debye, P., (1912). Zur theorie der spezifischen wärmen. Annalen der Physik, 344(14), 789-839.
Debye, P. P., Conwell, E. M., (1954). Electrical properties of n-type germanium. Physical Review, 93(4), 693.
Demouchy, S., Bolfan-Casanova, N., (2016). Distribution and transport of hydrogen in the lithospheric mantle: A review. Lithos 240–243, 402–425. doi:10.1016/j.lithos.2015.11.012.
Devreese, J. T. (1996). Polarons. Encycl. Appl. Phys., 14(cond-mat/0004497), 383-409.
Dixon, J.E., Leist, L., Langmuir, C., Schilling, J., (2002). Recycled dehydrated lithosphere observed in plume-influenced mid-ocean-ridge basalt. Nature 420, 385–389.
Dobson, D. P., Richmond, N. C., Brodholt, J. P., (1997). A high-temperature electrical conduction mechanism in the lower mantle phase (Mg, Fe) 1− xO. Science, 275(5307), 1779-1781.
Dobson, D. P., Brodholt, J. P., (2000). The electrical conductivity of the lower mantle phase magnesiowüstite at high temperatures and pressures. Journal of Geophysical Research: Solid Earth, 105(B1), 531-538.
Druitt, T. H., Brenchley, P. J., Gökten, Y. E., Francaviglia, V., (1995). Late Quaternary rhyolitic eruptions from the Acigöl Complex, central Turkey. Journal of the Geological Society, 152(4), 655-667.
Du Frane, W. L., Roberts, J. J., Toffelmier, D. A., & Tyburczy, J. A., (2005). Anisotropy of electrical conductivity in dry olivine. Geophysical research letters, 32(24).
Dugdale, J., MacDonald, DK., (1955). Lattice thermal conductivity, Phys. Rev. 58-1751.
Dzhavadov, L., (1975). Measurement of thermophysical properties of dielectrics under pressure. High Temp. Press. 7:49–54.

E

Eucken, A., (1911). Über die Temperaturabhängigkeit der Wärmeleitfähigkeit fester Nichtmetalle. Ann Phys. doi: 10.1002/andp.19113390202.

F

Faul, U.H., Toomey, D.R., Waff, H.S., (1994). Intergranular basaltic melt is distributed in thin, elongated inclusions. Geophys. Res. Lett. 21(1):29–32.
Faul, U.H., Fitz Gerald, J.D., Jackson, I., (2004). Shear wave attenuation and dispersion in melt-bearing olivine polycrystals: 2. Microstructural interpretation and seismological implications. J. Geophys. Res. B. Solid Earth 109:1–20. https ://doi.org/10.1029/2003J B0024 07.
Farla, R. J., Peach, C. J., & Ten Grotenhuis, S. M., (2010). Electrical conductivity of synthetic iron-bearing olivine. Physics and Chemistry of Minerals, 37(3), 167-178.
Fei, H., Yamazaki, D., Sakurai, M., Miyajima, N., Ohfuji, H., Katsura, T., Yamamoto, T., (2017). A nearly water-saturated mantle transition zone inferred from mineral viscosity. Sci. Adv. 3, 1–8.
Fei, H., (2018) EMPG XVI. Talk. Ionic conductivity in natural olivine. Clermont-Ferrand, France.
Férot, A., Bolfan-Casanova, N., (2012). Water storage capacity in olivine and pyroxene to 14GPa: Implications for the water content of the Earth's upper mantle and nature of seismic discontinuities. Earth Planet. Sci. Lett. 349–350, 218–230. doi:10.1016/j.epsl.2012.06.022.
Fischer, K.M., Ford, H.A., Abt, D.L., Rychert, C.A., (2010). The lithosphere– asthenosphere boundary. Annu Rev Earth Planet Sci 38(1):551– 575. https ://doi.org/10.1146/annur ev-earth -04080 9-15243 8.
Fourier, J., (1820). Extrait d'une mémoire sur le refroidissement séculaire du globe terrestre. Bulletin des Sciences par la Société Philomathique de Paris, April 1820, 58-70.
Freitas, D., Manthilake, G., Schiavi, F., Chantel, J., Bolfan-Casanova, N., Bouhifd, M.A., Andrault, D., (2017). Experimental evidence supporting a global melt layer at the base of the Earth's upper mantle. Nat. Commun. 8:2186. https ://doi.org/10.1038/s4146 7-017-02275 -9.
Freitas, D., Manthilake, G., Chantel, J., Bouhfid, M.., Andrault, D., (2019). Simultaneous measurements of electrical conductivity and seismic velocity of partially molten geological materials: Implications for melt fraction in the upper mantle. Phys. Chem. Miner. 0, 0. doi:10.1007/s00269-019-01021-5.
Freitas, D., Manthilake, G., (2019). Electrical conductivity of hydrous silicate melts : Implications for the bottom-up hydration of Earth ' s upper mantle EPSL 523, 1–9. doi:10.1016/j.epsl.2019.115712.
French, S.W., Romanowicz, B., (2015). Broad plumes rooted at the base of the Earth's mantle beneath major hotspots. Nature. doi:10.1038/nature14876.
Frost, D.J., Poe, B.T., Trønnes, R.G., Liebske, C., Duba, A., Rubie, D.C., (2004). A new large-volume multianvil system 507–514. doi:10.1016/j.pepi.2004.03.003.
Fujisawa, H., Fujii, N., Mizutani, H., Kanmori, H., Akimoto, S., (1968) Thermal Diffusivity of Mg2SiO4, Fe2SiO4, and NaCl at High Pressures and Temperatures. J. Geophys. Res. 73:4727.

G

Gaillard, F., (2004). Laboratory measurements of electrical conductivity of hydrous and dry silicic melts under pressure. Earth Planet. Sci. Lett. 218, 215–228. doi:10.1016/S0012-821X(03)00639-3.

Gaillard, F., Marziano, G.I., (2005). Electrical conductivity of magma in the course of crystallization controlled by their residual liquid composition. J. Geophys. Res. Solid Earth. https ://doi.org/10.1029/2004J B0032 82.

Gaillard, F., Malki, M., Iacono-Marziano, G., Pichavant, M., Scaillet, B. (2008). Carbonatite melts and electrical conductivity in the asthenosphere. Science 322(5906):1363–1365. https ://doi.org/10.1126/ science.11644 46.

Galer, S.J.G., O'Nions, R.K., (1986). Magmagenesis and the mapping of chemical and isotopic variations in the mantle. Chem Geol 56(1):45–61. https ://doi.org/10.1016/0009-2541(86)90109 -9.

Gardes, E., Laumonier, M., Massuyeau, M., Gaillard, F., n.d. Melt interconnection in the low velocity zone of Earth's upper mantle.

Gasparik, T., (1989). Transformation of enstatite — diopside — jadeite pyroxenes to garnet. Contrib. to Mineral. Petrol. 389–405.

Getting, I.C., Kennedy, G.C., (1970). Effect of Pressure on the emf of ChromelAlumel and PlatinumPlatinum 10% Rhodium Thermocouples 4552. doi:10.1063/1.1658495.

Gibert, B., Schilling, F.R., Gratz, K., Tommasi, A., (2005) Thermal diffusivity of olivine single crystals and a dunite at high temperature: Evidence for heat transfer by radiation in the upper mantle. Phys. Earth. Planet. Inter. 151:129–141. doi: 10.1016/j.pepi.2005.02.003.

Giesting, P. A., Hofmeister, A. M., Wopenka, B., Gwanmesia, G. D., Jolliff, B. L., (2004). Thermal conductivity and thermodynamics of majoritic garnets: implications for the transition zone. Earth and Planetary Science Letters, 218(1-2), 45-56.

Gillet, P., Richet, P., Guyot, F., Fiquet, G., (1991). High-temperature thermodynamic properties of forsterite. J. Geophys. Res. B96:11805–11816.

Glover, P., Ross, R. G., Jolly, H., (1990). The measurement of saturated rock electrical conductivity at lower crustal temperatures and high pressures. High Pressure Science and Technology, 5(1-6), 705-707.

Goetze, C. (1977). A brief summary of our present day understanding of the effect of volatiles and partial melt on the mechanical properties of the upper mantle. In: Manghnani MH, Akimoto S-I (eds) High-pressure research, applications in geophysics. Academic Press, New York, pp 3–23.

Goncharov, A. F., Struzhkin, V. V., Jacobsen, S. D., (2006). Reduced radiative conductivity of low-spin (Mg, Fe) O in the lower mantle. Science, 312(5777), 1205-1208.

Goncharov, A.F., Haugen, B.D., Struzhkin, V. V., Beck, P., Jacobsen, S.D., (2008). Radiative conductivity in the Earth's lower mantle. Nature 456, 231–4. doi:10.1038/nature07412.

Goncharov, A.F., Beck, P., Struzhkin, V., Haugen, B. D., Jacobsen, S.D., (2009) Thermal conductivity of lower-mantle minerals. Phys. Earth. Planet. Inter .174:24–32. doi: 10.1016/j.pepi.2008.07.033.

Goncharov, A.F., Struzhkin, V. V., Montoya, J.A., Kharlamova, S., Kundargi, R., Siebert, J., Badro, J., Antonangeli, D., Ryerson, F.J., Mao, W., (2010) Effect of composition, structure, and spin state on the thermal conductivity of the Earth's lower mantle. Phys. Earth. Planet. Inter. 180:148–153. doi: 10.1016/j.pepi.2010.02.002.

Goncharov, A.F., Lobanov, S.S., Tan, X., Hohensee, G.T, Cahill, D.G., Lin, J.F., Thomas, S.M., Okuchi, T., Tomioka, N., (2015) Experimental study of thermal conductivity at high pressures: Implications for the deep Earth's interior. Phys. Earth. Planet. Inter. 247:11–16. doi: 10.1016/j.pepi.2015.02.004.

Gordon, G., (1995a). Plate motions , crustal and lithospheric mobility, and paleomagnetism : Prospective viewpoint. J. Geophys. Res. 100, 24367–24392.

Gordon, G., (1995b). Global Earth Physics: A Handbook of Physical Constants, AGU Washin. ed.

Grant, F. S., West, G. F., (1965). Interpretation theory in applied geophysics. 583 pp., McGraw-Hill Book Co., New York.

Grayver, A. V., Munch, F.D., Kuvshinov, A. V., Khan, A., Sabaka, T.J., Tøffner-Clausen, L., (2017). Joint inversion of satellite-detected tidal and magnetospheric signals constrains electrical conductivity and water content of the upper mantle and transition zone. Geophys. Res. Lett. 44, 6074–6081. doi:10.1002/2017GL073446.

Grotenhuis, S.M., Drury, M.R., Spiers, C.J., Peach, C.J. (2005). Melt distribution in olivine rocks based on electrical conductivity measurements 110, 1–11. doi:10.1029/2004JB003462.

Grotzinger, J., Jordan, T. H., & Press, F., (2010). Understanding earth. Macmillan.

Guillot, B., Sator, N., (2007). A computer simulation study of natural silicate melts. Part II: High pressure properties. Geochim. Cosmochim. Acta 71, 4538–4556. doi:10.1016/j.gca.2007.05.029.

H

Hae, R., Ohtani, E., Kubo, T., Koyama, T., Utada, H. (2006). Hydrogen diffusivity in wadsleyite and water distribution in the mantle transition zone. Earth Planet. Sci. Lett. 243, 141–148. doi:10.1016/j.epsl.2005.12.035.

Hall, H.T., (1958). Some high-pressure, high-temperature apparatus design considerations – Equipment for use at 100000 atmospheres and 3000◦C, Rev. Sci. Instrum. 29(4), pp. 267–275.

Hall, H.T., (1962). Anvil guide device for multiple-anvil high pressure apparatus, Rev. Sci. Instrum. 33(11), pp. 1278–1280.

Hall, H.T., (1967). High pressure apparatus – Ram-in-tie-bar multianvil presses, Rev. Phys. Chem. Jpn. 37(2), pp. 63–7.

Hammond, W.C., Humphreys, E.D., (2000). Upper mantle seismic wave attenuation: effects of realistic partial melt distribution. J. Geophys. Res. 105(B5):10987–10999. https ://doi.org/10.1029/2000jb9000 42.

Hansen, R.T.J., Bostock, M.G., Christensen, N.I., (2012). Nature of the low velocity zone in Cascadia from receiver function waveform inversion. Earth Planet. Sci. Lett. 337–338:25–38. https ://doi. org/10.1016/j.epsl.2012.05.031.

Harte, B., (1977). Rock nomenclature with particular relation to deformation and recrystallisation textures in olivine-bearing xenoliths. The Journal of Geology, 85(3), 279-288.

Hartlieb, P., Toifl, M., Kuchar, F., Meisels, R., Antretter, T., (2015). Thermo-physical properties of selected hard rocks and their relation to microwave-assisted comminution. Min. Eng. doi:10.1016/j.mineng.2015.11.008.

Hauri, E.H., Wagner, T.P., Grove, T.L., (1994). Experimental and natural partitioning of Th, U, Pb and other trace elements between garnet, clinopyroxene and basaltic melts. Chem. Geol. 117, 149–166. doi:10.1016/0009-2541(94)90126-0.

Heckman, H., (1973). Finite pulse-time and heat-loss effects in pulse thermal diffusivity measurements. Journal of applied physics. 44-4.

Hernlund, J., Einenweber, K., Locke, D., Tyburczy, J., (2006). A numerical model for steady-state temperature distributions in solid-medium high-pressure cell assemblies. Am. Min. 91, 295–305. doi:10.2138/am.2006.1938.

Herzberg, C., Asimow, P.D., Arndt, N., Niu, Y., Lesher, C.M., Fitton, J.G., Cheadle, M.J., Saunders, A.D., (2007). Temperatures in ambient mantle and plumes: Constraints from basalts, picrites, and komatiites. Geochemistry, Geophys. Geosystems 8. doi:10.1029/2006GC001390.

Herzberg, C., Condie, K., Korenaga, J., (2010). Thermal history of the Earth and its petrological expression. Earth Planet. Sci. Lett. 292, 79–88. doi:10.1016/j.epsl.2010.01.022.

Hier-Majumder, S., (2008). Influence of contiguity on seismic velocities of partially molten aggregates. J Geophys Res Solid Earth 113(12):1–14. https ://doi.org/10.1029/2008J B0056 62.

Hier-Majumder, S., Keel, E.B., Courtier, A.M., (2014). The influence of temperature, bulk composition, and melting on the seismic signature of the low-velocity layer above the transition zone. J. Geophys. Res. Solid Earth 119, 971–983. doi:10.1002/2013JB010314.

Hier-majumder, S., Tauzin, B., (2017). Pervasive upper mantle melting beneath the western US. Earth Planet. Sci. Lett. 463, 25–35. doi:10.1016/j.epsl.2016.12.041.

Hirano, N., Takahashi, E., Yamamoto, J., Abe, N., Ingle, S., Kaneoka, I., Hirata, T., Kimura, J-I., Ishii, T., Ogawa, Y., Machida, S., Suyehiro, K., (2006). Volcanism in response to plate flexure. Science 313(5792):1426–1428. https ://doi.org/10.1126/scien ce.11282 35.

Hirayama, M., (1934). On the relations between the variations of earth potential gradient and terrestrial mechanism.

Hirsch, L. M., Shankland, T. J., Duba, A. G., (1993). Electrical conduction and polaron mobility in Fe-bearing olivine. Geophysical Journal International, 114(1), 36-44.

Hirschmann, M.M., Aubaud, C., Withers, A.C., (2005). Storage capacity of H2O in nominally anhydrous minerals in the upper mantle. Earth Planet. Sci. Lett. 236, 167–181. doi:10.1016/j.epsl.2005.04.022.

Hirschmann, M.M. (2006). Water, melting, and the deep Earth H2O cycle. Annu. Rev. Earth Planet. Sci. 34, 629–653. doi:10.1146/annurev.earth.34.031405.125211.

Hirschmann, M.M., Tenner, T., Aubaud, C., Withers, A.C. (2009). Dehydration melting of nominally anhydrous mantle: The primacy of partitioning. Phys. Earth Planet. Inter. 176, 54–68. doi:10.1016/j.pepi.2009.04.001

Hirth, G., Kohlstedt, D.L., (1995). Experimental constraints on the dynamics of the partially molten upper mantle: Deformation in the diffusion creep regime. J. Geophys. Res. Solid Earth 100, 1981–2001. doi:10.1029/94JB02128.

Höfer, M., (2002). Heat transfer in quartz, orthoclase, and sanidine at elevated temperature. Physics and Chemistry of Minerals, 29(9), 571-584.

Hofmann, A.W., (1988). Chemical differentiation of the Earth: the relationship between mantle, continental

crust, and oceanic crust. Earth Planet. Sci. Lett. 90, 297–314. doi:10.1016/0012-821X(88)90132-X.
Hofmann, A.W., (1997). Mantle geochemistry: the message from oceanic volcanism. Nature 385, 219–229.
Hofmann, A.W., (2003). Just add water. Nature 425, 24–25. doi:10.1029/2001GL014064.
Hofmeister, A.M., (1999). Mantle Values of Thermal Conductivity and the Geotherm from Phonon Lifetimes. Science (80-.). 283, 1699–1706. doi:10.1126/science.283.5408.1699.
Hofmeister, A.M., (2001). Thermal conductivity of spinels and olivines from vibrational spectroscopy: Ambient conditions. Am. Mineral. 86, 1188–1208.
Hofmeister, A.M., (2005). Dependence of diffusive radiative transfer on grain-size, temperature, and Fe-content : Implications for mantle processes. Journal of Geodynamics. 40, 51–72. doi:10.1016/j.jog.2005.06.001.
Hofmeister, A.M., (2007a). Pressure dependence of thermal transport properties. Proc. Natl. Acad. Sci. USA 104:9192–7. doi: 10.1073/pnas.0610734104.
Hofmeister, A.M., Yuen, D.A., (2007b). Critical phenomena in thermal conductivity: Implications for lower mantle dynamics. J. Geodyn. 44, 186–199. doi:10.1016/j.jog.2007.03.002.
Hofmeister, A.M., (2008). Inference of high thermal transport in the lower mantle from laser-flash experiments and the damped harmonic oscillator model. Phys. Earth Planet. Inter. 170, 201–206. doi:10.1016/j.pepi.2008.06.034.
Hofmeister, A. M., Whittington, A. G., Pertermann, M., (2009). Transport properties of high albite crystals, near-endmember feldspar and pyroxene glasses, and their melts to high temperature. Contributions to Mineralogy and Petrology, 158(3), 381.
Hofmeister, A.M., (2010a). Scale aspects of heat transport in the diamond anvil cell, in spectroscopic modeling, and in Earth's mantle: Implications for secular cooling. Phys. Earth Planet. Inter. 180, 138–147. doi:10.1016/j.pepi.2009.12.006.
Hofmeister, A.M., (2010b). Thermal diffusivity of oxide perovskite compounds at elevated temperature. J. Appl. Phys. 107, 1–20. doi:10.1063/1.3371815.
Hofmeister, A., (2014). Thermodynamic and optical thickness correction to diffusive radiative transfer formulations with applications to planetary interiors. Geophys. Res. Lett. 1, 1–7. doi:10.1002/2014GL059833.
Hofmeister, A.M., (2014a). Thermal diffusivity and thermal conductivity of single - crystal MgO and Al 2 O 3 and related compounds as a function of temperature. Phys. Chem. Min. 361–371. doi:10.1007/s00269-014-0655-3.
Hofmeister, A.M., Dong, J., Branlund, J.M., (2014b). Thermal diffusivity of electrical insulators at high temperatures: Evidence for diffusion of bulk phonon-polaritons at infrared frequencies augmenting phonon heat conduction. J. Appl. Phys. 115. doi:10.1063/1.4873295.
Hofmeister, A.M., Sehlke, A., Whittington, A.G., (2014c). Thermal diffusivity of Fe-rich pyroxene glasses and their melts. Chem. Geol. 384, 1–9. doi:10.1016/j.chemgeo.2014.06.018.
Hofmeister, A.M., Whittington, A.G., Goldsand, J., Criss, R.A.G., (2014d). Effects of chemical composition and temperature on transport properties of silica-rich glasses and melts. Am. Mineral. 99, 564–577. doi:10.2138/am.2014.4683.
Hofmeister, A.M., Branlund, J.M., (2015). Thermal Conductivity of the Earth. Treatise of geophysics, 583-608.
Holland, K. G., Ahrens, T. J. (1997). Melting of (Mg, Fe) 2SiO4 at the core-mantle boundary of the Earth. Science, 275(5306), 1623-1625.
Hosseini, K., Matthews, K.J., (2018). SubMachine : Web - based tools for exploring seismic tomography and other models of Earth ' s deep interior. G^3. doi:10.1029/2018GC007431
Hsieh, W.P., Chen, B., Li, J., Keblinski, P., Cahill, D.G., (2009). Pressure tuning of the thermal conductivity of the layered muscovite crystal. Phys. Rev. B - Condens. Matter Mater. Phys. 80. doi:10.1103/PhysRevB.80.180302.
Huang, X., Xu, Y., Karato, S., (2005). Water content in the transition zone from electrical conductivity of wadsleyite and ringwoodite. Nature 434, 746–749. doi:10.1038/nature03426.

I

Inoue, T., (1994). Effect of water on melting phase relations and melt composition in the system Mg2SiO4MgSiO3H2O up to 15 GPa. Phys. Earth Planet. Inter. 85, 237–263. doi:10.1016/0031-9201(94)90116-3/.
Inoue, T.,Weidner, D. J., Northrup, P. A., Parise, J. B., (1998). Elastic properties of hydrous ringwoodite (?-phase) in Mg2SiO4. Earth Planet. Sci. Lett. 160, 107–113. doi: 10.1016/S0012-821X(98)00077-6.
Ishibashi, H., Arakawa, M., Ohi, S., Yamamoto, J., Miyake, A., Kagi, H., Wiley, J., (2008). Relationship between Raman spectral pattern and crystallographic orientation of a rock-forming mineral : a case study of Fo 89 Fa 11 olivine. J. Ram. Spec. 1653–1659. doi:10.1002/jrs.

J

Jackson, I., Niesler, H., Weidner, D.J., (1981). Explicit correction of ultrasonically determined elastic wave velocities for transducer-bond phase shift. J. Geophys. Res. 86:3736–3748.

Jackson, I., Gerald, J.D.F., Faul, U.H., Tan, B.H., (2002). Grain-size-sensitive seismic wave attenuation in polycrystalline olivine. J. Geophys. Res. 107:1–16. https ://doi.org/10.1029/2001J B0012 25.

Jackson, I., Faul, U.H., Fitz Gerald, J.D., Tan, B.H., (2004). Shear wave attenuation and dispersion in melt-bearing olivine polycrystals: 1. Specimen fabrication and mechanical testing. J. Geophys. Res. B Solid Earth 109:1–20. https ://doi.org/10.1029/2003J B0024 07.

Jacobsen, S.D., Smyth, J.R., Spetzler, H.A., Holl, C.A., Frost, D.J., (2004). Sound velocities and elastic constants of iron-bearing hydrous ringwoodite. Phys. Earth Planet. Interiors 143–144, 47-56.

Jing, Z., Karato, S. I., (2008). Compositional effect on the pressure derivatives of bulk modulus of silicate melts. Earth Planet. Sci. Lett. 272, 429–436. doi:10.1016/j.epsl.2008.05.013.

Jing, Z., Karato, S. I., (2012). Effect of H2O on the density of silicate melts at high pressures: Static experiments and the application of a modified hard-sphere model of equation of state. Geochim. Cosmochim. Acta 85, 357–372. doi:10.1016/j.gca.2012.03.001.

Josell, D., Warren, J., Cezairliyan, A., (1995). Comment on "'Analysis for determining thermal diffusivity from thermal pulse experiments."".

Julian, C.L., (1965). Theory of heat conduction in rare-Gas crystal. Physical review, 137.

K

Kaminsky, F., (2012). Earth-Science Reviews Mineralogy of the lower mantle : A review of 'super-deep ' mineral inclusions in diamond. Earth Sci. Rev. 110, 127–147. doi:10.1016/j.earscirev.2011.10.005.

Kanamori H., Mizutani, H., Fujii, N., (1969). Method of thermal diffusivity measurement. J. Phys. Earth. 17:43–53.

Kanamori, I., Fujii, X., Mizutani, I., (1968). Thermal diffusivity measurement fo rock-forming minerals from 300° to 1100° K. J. Geophys. Res. 73.

Kantor, A.P., Jacobsen, S.D., Kantor, I.Y., Dubrovinsky, L.S., Mccammon, C.A., Reichmann, H.J., Goncharenko, I.N., (2004). Pressure-Induced Magnetization in FeO : Evidence from Elasticity ¨ ssbauer Spectroscopy and Mo 19–22. doi:10.1103/PhysRevLett.93.215502.

Karato, S., (1990). The role of hydrogen in the electrical conductivity of the upper mantle. Nature 347:183–187. https ://doi.org/10.1038/34618 3a0.

Karato, S., (1993). Importance of anelasticity in the interpretation of seismic tomography. Geophys. Res. Lett. 20:1623–1626.

Karato, S., Bercovici, D., Leahy, G., Richard, G., Jing, Z. (2006). The Transition-Zone Water Filter Model for Global Material Circulation : Where Do We Stand ? Earth's Deep Water Cycle 289–313. doi:10.1029/168GM22.

Karato, S.I. (2011). Water distribution across the mantle transition zone and its implications for global material circulation. Earth Planet. Sci. Lett. 301, 413–423. doi:10.1016/j.epsl.2010.11.038.

Karato, S., (2014). Does partial melting explain geophysical anomalies? Phys Earth Planet Inter 228:300–306. https ://doi.org/10.1016/j. pepi.2013.08.006.

Katayama, I., Nakashima, S., (2003). Hydroxyl in clinopyroxene from the deep subducted crust : Evidence for H2O transport into the mantle. Am. Mineral. 88, 229–234.

Katsura, T., (1993). Thermal diffusivity of silica glass at pressures up to 9 GPa. Phys Chem Miner 20:201–208. doi: 10.1007/BF00200122.

Katsura, T., (1997). Thermal diffusivity of periclase at high temperatures and high pressures. Physics of the earth and planetary interiors, 101(1-2), 73-77.

Katsura, T., Sato, K., Ito, E., (1998). Electrical conductivity of silicate perovskite at lower-mantle conditions. Nature 395:493–495.

Katsura, T., Yoshino, T., Manthilake, G., Matsuzaki, T., (2009). Electrical conductivity of the major upper mantle minerals: a review. Russ. Geol. Geophys. 50, 1139–1145. doi:10.1016/j.rgg.2009.11.012.

Katsura, T., Yoneda, A., Yamazaki, D., Yoshino, T., Ito, E., Suetsugu, D., Bina, C., Inoue, T., Wiens, D., Jellinek, M., (2010). Adiabatic temperature profile in the mantle. Phys. Earth Planet. Inter. 183, 212–218. doi:10.1016/j.pepi.2010.07.001.

Kawai, N., Endo, S., (1970). Generation of ultra-high hydrostatic pressures by a split sphere apparatus, Rev. Sci. Instrum. 41(8), pp. 1178–1181.

Kawakatsu, H., Kumar, P., Takei, Y., Shinohara, M., Kanazawa, T., Araki, E., Suyehir,o K. (2009). Seismic evidence for sharp boundaries of oceanic plates. Science 324(5926):499–502.
Kellett, B. (1952). Transmission of radiation through glass in tank furnace. J Soc Glas Technol 36:115–123.
Kellett, B. (1953). Correction to the paper in the 1952 issue. J. Soc. Glas. Technol 37:268.
Kellogg, L. H., Hager, B. H., Van Der Hilst, R. D., (1999). Compositional stratification in the deep mantle. Science, 283(5409), 1881-1884.
Kelvin, W. T. B., (1897). On the age of the earth. Victoria Institute.
Kennett, B.L.N., Engdah, E.R., (1991). Traveltimes for global earthquake location and phase identification 429–465.
Kennett, B.L.N., Engdahl, E.R., Buland, R. (1995). Constraints on seismic velocities in the Earth from traveltimes. Geophys J Int 122:108–124. https ://doi.org/10.1111/j.1365-246X.1995.tb035 40.x.
Khitarov, N. I., Slutsky, A. B., Pugin, V. A., (1970). Electrical conductivity of basalts at high TP and phase transitions under upper mantle conditions. Physics of the Earth and Planetary Interiors, 3, 334-342.
Klemens, P. G., (1958). Thermal conductivity and lattice vibrational modes. In Solid state physics (Vol. 7, pp. 1-98). Academic press.
Knibbe, J.S., Luginbühl, S.M., Stoevelaar, R., Plas, W. Van Der, Harlingen, D.M. Van, Rai, N., Steenstra, E.S., (2018). Calibration of a multi-anvil high-pressure apparatus to simulate planetary interior conditions, EPJ Techniques and instrumentation. 5:5 https://doi.org/10.1140/epjti/s40485-018-0047-z
Kobayashi, Y. (1974). Anisotropy of thermal diffusivity in olivine, pyroxene and dunite. Journal of Physics of the Earth, 22(3), 359-373.
Kohlstedt, D.L., (1992). Structure, rheology and permeability of partially molten rocks at low melt fractions. In: Phipps-Morgan J, Blackman DK, Sinton JM (eds) Mantle flow and melt generation at mid-ocean ridges. American Geophysical Union, Washington, DC, pp 103–121.
Kohlstedt, D.L., Keppler, H., Rubie, D.C., (1996). Solubility of water in the α, β and γ phases of (Mg,Fe)2SiO4. Contrib. to Mineral. Petrol. 123, 345–357. doi:10.1007/s004100050161.
Kono, Y., Park, C., Sakamaki, T., Kenny-Benson, C., Shen, G., Wang, Y. (2012). Simultaneous structure and elastic wave velocity measurement of SiO2 glass at high pressures and high temperatures in a Paris–Edinburgh cell. Rev. Sci. Instrum. 83(3):33905. https ://doi.org/10.1063/1.36980 00.
Konôpková, Z., McWilliams, R.S., Gómez-Pérez, N., Goncharov, A.F., (2016). Direct measurement of thermal conductivity in solid iron at planetary core conditions. Nature 534, 99–101. doi:10.1038/nature18009.
Korenaga, J., (2008). Urey Ratio and the Structure and Evolution of Earth ' S Mantle. Am. Geophys. Union 1–32. doi:10.1029/2007RG000241.1.
Kumar, M., (2000). Equation of state and bulk modulus under the effect of high pressure–high temperature. Physics and Chemistry of Minerals, 27(9), 650-655.
Kung, J., Li, B., Uchida, T., Wang, Y., (2005). In-situ elasticity measurement for the unquenchable high-pressure clinopyroxene phase : Implication for the upper mantle 32, 2–5. doi:10.1029/2004GL021661.
Kunimoto, T., Irifune, T., (2010). Pressure generation to 125 GPa using 6-8-2 type multianvil apparatus with nano- polycrystalline diamond anvils, J. Phys.: Conf. Ser. 215(1), p. 012190.
Kuvshinov, A., Utada, H., Avdeev, D., Koyama, T., (2005). 3-D modelling and analysis of Dst C-responses in the North Pacific Ocean region, revisited. Geophys. J. Int. 160, 505–526. doi:10.1111/j.1365-246X.2005.02477.x.
Kuvshinov, A., Olsen, N., (2006). A global model of mantle conductivity derived from 5 years of CHAMP, ??rsted, and SAC-C magnetic data. Geophys. Res. Lett. 33, 1–5. doi:10.1029/2006GL027083.
Kuvshinov, A. V., (2008). 3-D Global Induction in the Oceans and Solid Earth : Recent Progress in Modeling Magnetic and Electric and Oceanic Origin 139–186. doi:10.1007/s10712-008-9045-z.

L

Labrosse, S., Poirier, J. P., Le Mouël, J. L., (2001). The age of the inner core. Earth and Planetary Science Letters, 190(3-4), 111-123.
Labrosse, S., Hernlund, J.W., Coltice, N., (2007). A crystallizing dense magma ocean at the base of the Earth's mantle. Nature 450, 866–869. doi:10.1038/nature06355.
Labrosse, S., Jaupart, C., (2007). Thermal evolution of the Earth: Secular changes and fluctuations of plate characteristics. Earth Planet. Sci. Lett. 260, 465–481. doi:10.1016/j.epsl.2007.05.046.
Landau, L. D., Lifshitz, E. M., (1965). Quantum mechanics, vol. 3. Course of theoretical physics, 3.
Laporte, D., Rapaille, C., Provost, A., (1997). Wetting angles, equilibrium melt geometry, and the permeability threshold of partially molten crustal protoliths BT. In: Bouchez JL, Hutton DHW, Stephens WE (eds) Granite: from segregation of melt to emplacement fabrics. Springer Netherlands, Dordrecht, pp 31–54.

Laporte, D., Provost, A., (2000). The grain-scale distribution of silicate, carbonate and metallosulfide partial melts: a review of theory and experiments. In: Bagdassarov N, Laporte D, Thompson AB (eds) Physics and chemistry of partially molten rocks. Kluwer Academic, Norwell, pp 93–140.

Laporte, D., Toplis, M.J., Seyler, M., Devidal, J.L., (2004). A new experimental technique for extracting liquids from peridotite at very low degrees of melting: Application to partial melting of depleted peridotite. Contrib. to Mineral. Petrol. 146, 463–484. doi:10.1007/s00410-003-0509-3.

Laske, G., Markee, A., Orcutt, J.A., Wolfe, C.J., Collins, J.A., Solomon, S.C., Detrick, R.S., Bercovici, D., Hauri E.H., (2011). Asymmetric shallow mantle structure beneath the Hawaiian Swell-evidence from Rayleigh waves recorded by the PLUME network. Geophys J Int 187(3):1725–1742. https ://doi.org/10.1111/j.1365-246X.2011.05238 .x.

Laumonier, M., Farla, R., Frost, D. J., Katsura, T., Marquardt, K., Bouvier, A-S., Baumgartner, L.P., (2017). Experimental determination of melt interconnectivity and electrical conductivity in the upper mantle. Earth Planet Sci Lett 463(Supplement C):286–297. https ://doi.org/10.1016/j.epsl.2017.01.037.

Lay, T., (2007). Deep Earth Structure – Lower Mantle and D 0. Treatise Geophys. 1–18.

Lay, T., Hernlund, J., Buffett, B., (2008). Core – mantle boundary heat flow. Nat. Geosci. 1, 13–15. doi:10.1038/ngeo.2007.44.

Leahy, G.M., Bercovici, D. (2007). On the dynamics of a hydrous melt layer above the transition zone. J. Geophys. Res. Solid Earth 112, 1–14. doi:10.1029/2006JB004631.

Leahy, G.M., Bercovici, D.; (2010). Reactive infiltration of hydrous melt above the mantle transition zone. J. Geophys. Res. Solid Earth 115, 1–17. doi:10.1029/2009JB006757.

Le Godec, Y. Le, Martinez-Garcia, D., Mezouar, M., Syfosse, G., Itié, J.-P., Besson, J.-M., (2000). Thermoelastic behaviour of hexagonal graphite-like boron nitride. High Press. Res. 17, 35–46. doi:10.1080/08957950008200304.

Leinenweber, K.D., Tyburczy, J.A., Sharp, T.G., Soignard, E., Diedrich, T., Petuskey, W.B., Wang, W.Y., Mosenfelder, J.L., (2012). Cell assemblies for reproducible multi-anvil experiments (the COMPRES assemblies) 97, 353–368.

Lekic, V., Romanowicz, B., (2011). Inferring upper-mantle structure by full waveform tomography with the spectral element method 799–831. doi:10.1111/j.1365-246X.2011.04969.x.

Lesher C.E, UC Davis, (2005) COMPRES workshop

Li, B., Liebermann, R. C., Weidner, D. J., (2001). P-V-Vp-Vs-T measurements on wadsleyite to 7 GPa and 873 K: Implications for the 410-km seismic discontinuity. Journal of Geophysical Research: Solid Earth, 106(B12), 30579-30591.

Li, B., Kung, J., Liebermann, R.C. (2004). Modern techniques in measuring elasticity of Earth materials at high pressure and high temperature using ultrasonic interferometry in conjunction with synchrotron X-radiation in multi-anvil apparatus. Phys. Earth Planet. Inter. 143, 559–574. doi:10.1016/j.pepi.2003.09.020

Li, B., Liebermann, R.C., (2007). Indoor seismology by probing the Earth's interior by using sound velocity measurements at high pressures and temperatures. PNAS. 104:9145–9150.

Li, L., Weidner, D., Raterron, P., Chen, J., Vaughan, M., (2004). Stress measurements of deforming olivine at high pressure, Phys. Earth Planet. Inter. 143, pp. 357–367.

Li, L., Wentzcovitch, R.M,. Weidner, D.J., Da Silva, C.R.S., (2007). Vibrational and thermodynamic properties of forsterite at mantle conditions. J. Geophys. Res. Solid Earth. doi: 10.1029/2006JB004546.

Liebermann, R.C., (2011). Multi-anvil , high pressure apparatus : a half-century of development and progress High Pressure Research. 31, 493–532.

Liebfried, (1954). Warmleitund in elektrische isolierenden Kristallen. Nachrichten aus Gesundheitswesen Wissenschaften Goettingen Mathematik und Physik.

Liu, W., Kung, J., Li, B., (2005). Elasticity of San Carlos olivine to 8 GPa and 1073 K. Geophysical Research Letters, 32(16).

Lizarralde, D., Chave, A., Hirth, G., Schultz, A., (1995). Northeastern Pacific mantle conductivity profile from long-period magnetotelluric sounding using Hawaii-to-California submarine cable data. Journal of Geophysical Research: Solid Earth, 100(B9), 17837-17854.

Lobanov, S.S., Holtgrewe, N., Goncharov, A.F., (2016). Reduced radiative conductivity of low spin FeO6-octahedra in FeCO3 at high pressure and temperature. Earth Planet. Sci. Lett. 449, 20–25. doi:10.1016/j.epsl.2016.05.028.

Love, A. E. H., (1927). A Treatise on the Mathematical Theory of Elasticity, Cambridge Univ. Pres, Cambridge, 104.

Lowry, R.K., Henderson, P., Nolan, J., (1982). Mineralogy and Tracer Diffusion of Some Alkali , Alkaline-Earth and Transition Element Ions in a Basaltic and an Andesitic Melt, and the Implications Concerning Melt Structure. Contrib. Mineral. Petrol. 80: 254–261.

Lubimova, H., (1958). Variable Thermal Conductivity of its Mantle. Geophys. J. R. Astron. Soc. I:115–134.

M

MacDonald, G.J., (1959). Calculations on the Thermal History of the Earth.

Malfait, W. J., Seifert, R., Petitgirard, S., Mezouar, M., Sanchez-Valle, C., (2014). The density of andesitic melts and the compressibility of dissolved water in silicate melts at crustal and upper mantle conditions. Earth and Planetary Science Letters, 393, 31-38.

Manthilake, M.A.G.M., Matsuzaki, T., Yoshino, T., Yamashita, S., Ito, E., Katsura, T., (2009). Electrical conductivity of wadsleyite as a function of temperature and water content. Phys. Earth. Planet. Inter. 174(1– 4):10–18. https ://doi.org/10.1016/j.pepi.2008.06.001.

Manthilake, G.M., de Koker, N., Frost, D.J., McCammon, C.A., (2011). Lattice thermal conductivity of lower mantle minerals and heat flux from Earth's core. Proc Natl Acad Sci 108:17901–17904. doi: 10.1073/pnas.1110594108.

Manthilake, G., Mookherjee, M., Bolfan-Casanova, N., Andrault, D., (2015). Electrical conductivity of lawsonite and dehydrating fluids at high pressures and temperatures. Geophys. Res. Lett. 42, 7398–7405.

Manthilake, G., Bolfan-Casanova, N., Novella, D., Mookherjee, M., Andrault, D., (2016). Dehydration of chlorite explains anomalously high electrical conductivity in the mantle wedges. Sci. Adv. 2.

Manthilake, G., Chantel, J., Monteux, J., Andrault, D., Bouhifd, M. A., Bolfan Casanova, N., Itie, J. P., (2019). Thermal conductivity of FeS and its implications for Mercury's long sustaining magnetic field. Journal of Geophysical Research: Planets.

Martinek, L., (2019) Thèse. Effet de la fugacité d'oxygene sur le stockage des fluids C et H dans le manteaux terrestre.

Martinek, L., and Bolfan-Casanova N., (submitted), Water quantification in olivine and wadsleyite by Raman spectroscopy and study of errors and uncertainties. American Mineralogist.

Martinez Moreno, F.J., (2015). PhD Thesis. Detection and characterization pf kartstic caves: integration of geological and geophysical techniques.

Mason, W.P., Mcskimin, H.J., (1947). attenuation and scattering of high frequency sound waves in metals and glasses. J. Acous. 19.

Matsukage, K.N., Jing, Z., Karato, S., (2005). Density of hydrous silicate melt at the conditions of Earth's deep upper mantle. Nature 438, 488–91. doi:10.1038/nature04241.

Maumus, J., Bagdassarov, N., Schmeling, H., (2005). Electrical conductivity and partial melting of mafic rocks under pressure. Geochemica Cosmochimica Acta 69:4703–4178. https ://doi.org/10.1016/j. gca.2005.05.010.

Mavko, G., Kjartansson, E., Winkler, K. (1979). Seismic wave atteuation in rocks. Rev. Geophys. Sp. physicse 17, 1155–1164.

Mavko, G. (1980). Velocity and attenuation in partially molten rocks. J Geophys Res 85:5173–5189.

McKenzie, D., Bickle M. J., (1988). The Volume and Composition of Melt Generated by Extension of the Lithosphere. J. Petrol. 29, 625–679.

McKenzie, D., O'Nions, R.K., (1991). Partial melt distribution from inversion of rare earth element concentrations. J. Petrol. 32, 1021–1091.

McSkimin, H. J. (1950). Ultrasonic measurement techniques applicable to small solid specimens. The Journal of the Acoustical Society of America, 22(4), 413-418.

McWilliams, R.S., Konôpková, Z., Goncharov, A.F., (2015). A flash heating method for measuring thermal conductivity at high pressure and temperature: Application to Pt. Phys. Earth Planet. Inter. 247:17–26. doi: 10.1016/j.pepi.2015.06.002.

Médard, E., Grove, T.L. (2008). The effect of H2O on the olivine liquidus of basaltic melts: Experiments and thermodynamic models. Contrib. to Mineral. Petrol. 155, 417–432. doi:10.1007/s00410-007-0250-4.

Médard, E., McCammon, C.A., Barr, J.A., Grove, T.L., (2008). Oxygen fugacity, temperature reproducibility, and H2O contents of nominally anhydrous piston-cylinder experiments using graphite capsules. Am. Mineral. 93, 1838–1844. doi:10.2138/am.2008.2842.

Mehling, H., Hautzinger, G., Nilsson, O., Fricke, J., Hofmann, R., Hahn, O. (1998). Thermal diffusivity of semitransparent materials determined by the laser-flash method applying a new analytical model. International Journal of Thermophysics, 19(3), 941-949.

Mercier, J.-C.C., (1972). Structure des péridotites en enclaves dans quelques basaltes d'Europe et d'Hawaii. Regards sur la constitution du manteau supérieur. Thèse 3e cycle, Nantes, France, 229 p.

Mercier, J. C., Nicolas, A., (1975). Textures and fabrics of upper-mantle peridotites as illustrated by xenoliths from basalts. Journal of Petrology, 16(1), 454-487.

Mercier, M., Muro, A. Di, Métrich, N., Giordano, D., Belhadj, O., Mandeville, C.W., (2010). Spectroscopic analysis (FTIR, Raman) of water in mafic and intermediate glasses and glass inclusions. Geochim. Cosmochim. Acta 74, 5641–5656. doi:10.1016/j.gca.2010.06.020.

Merriman, J. D., Whittington, A. G., Hofmeister, A. M., Nabelek, P. I., Benn, K., (2013). Thermal transport properties of major Archean rock types to high temperature and implications for cratonic geotherms. Precambrian Research, 233, 358-372.
Mibe, K., Fujii, T., Yasuda, A., (1998). Connectivity of aqueous fluid in the Earth's upper mantle. Geo. Res. Lett. 25, 1233–1236.
Mibe, K., Fujii, T., Yasuda, A., (1999). Control of the location of the volcanic front in island arcs by aqueous fluid connectivity in the mantle wedge. Nature 401, 259–262. doi:10.1038/45762.
Michael, P.J., (1988). The concentration, behavior and storage of H20 in the suboceanic upper mantle: Implications for mantle metasomatism. Geochim. Cosmochim. Acta 52, 555–566.
Mierdel, K., Keppler, H., Smyth, J.R., Langenhorst, F., (2007). Water Solubility in Aluminous Orthopyroxene and the Origin of Earth's Asthenosphere. Science (80). 315, 364–368. doi:10.1126/science.1135422.
Minarik, W.G., Watson, E.B., (1995). Interconnectivity of carbonate melt at low melt fraction. Earth. Planet. Sci. Lett 133(3–4):423–437. https://doi.org/10.1016/0012-821X(95)00085 –Q.
Mookherjee, M., Stixrude, L., Karki, B., (2008). Hydrous silicate melt at high pressure. Nature 452, 983–986. doi:10.1038/nature06918.
Mookherjee, M., Karato, S., (2010). Solubility of water in pyrope-rich garnet at high pressures and temperature. Geophys. Res. Lett. 37, 1–5. doi:10.1029/2009GL041289.
Montagner, J., Kennett, B.L.N., (1996). How to reconcile body-wave and normal-mode reference earth models Geophys. J. Int. (1996) 125, 229-248.
Monteux, J., (2009). Thèse. Modélisation numerique de la formation du noyau terrestre: contribution des impacts météoritiques.
Morgan, J.P., Morgan, W.J., (1999). Two-stage melting and the geochemical evolution of the mantle : a recipe for mantle plum-pudding. Earth Planet. Sci. Lett. 170, 215–239.
Mourtada-Bonnefoi, C. C., Laporte, D., (2002). Homogeneous bubble nucleation in rhyolitic magmas: an experimental study of the effect of H2O and CO2. Journal of Geophysical Research: Solid Earth, 107(B4), ECV-2.
Murakami, M., Goncharov, A.F., Hirao, N., Masuda, R., Mitsui, T., Thomas, S.-M., Bina, C.R., (2014). High-pressure radiative conductivity of dense silicate glasses with potential implications for dark magmas. Nat. Commun. 5, 5428. doi:10.1038/ncomms6428.
Murase, T., Mcbirney, A.R., (1973). Properties of Some Common Igneous Rocks and Their Melts Properties of Some Common Igneous Rocks and Their Melts at High Temperatures. Geological Society of America Bulletin 1973;84, 11;3563-3592. doi:10.1130/0016-7606(1973)84<3563.
Murch, G. E., (1982). The Haven ratio in fast ionic conductors. Solid State Ionics, 7(3), 177-198.

N

Naumov, V.B., Dorofeeva, V.A., Girnis, A.V., Yarmolyuk, V.V., (2014). Comparison of major, volatile, and trace element contents in the melts of mid-ocean ridges on the basis of data on inclusions in minerals and quenched glasses of rocks. Geochem. Int. 52(5):347–364. https://doi.org/10.1134/S0016 70291 40500 73.
Neal, S., Mackie, R.L., Larsen, J.C., Schultz, A., (2000). Variations in the electrical conductivity of the upper mantle beneath North America and the Pacific Ocean 105, 8229–8242.
Neuville, D.R., Courtial, P., Dingwell, D.B., Richet, P., (1993). Thermodynamic and rheological properties of rhyolite and andesite melts 572–581.
Ni, H., Keppler, H., Behrens, H., (2011). Electrical conductivity of hydrous basaltic melts: implications for partial melting in the upper mantle. Contrib. Mineral. Petrol. 162(3):637–650. https ://doi.org/10.1007/ s0041 0-011-0617-4.
Nielser, H., Jackson, I., (1989). Pressure derivatives of elastic wave velocities from ultrasonic interferometric measurements on jacketed polycrystals. J. Acoust. Soc. Am. 86:1573–1585.
Nishi, M., Irifune, T., Tsuchiya, J., Tange, Y., Nishihara, Y., Fujino, K., Higo, Y., (2014). Stability of hydrous silicate at high pressures and water transport to the deep lower mantle. Nature. doi:10.1038/NGEO2074.
Nishihara, Y., MAtsukage, K.N., Karato, S., (2006). Effects of metal protection coils on thermocouple EMF in multi-anvil high-pressure experiments. Am. Mineral. 91, 111–114. doi:10.2138/am.2006.1883.
Nolet, G., Karato, S. I., Montelli, R., (2006). Plume fluxes from seismic tomography. Earth and Planetary Science Letters, 248(3-4), 685-699.
Novella, D., Frost, D.J., (2014). The composition of hydrous partial melts of garnet peridotite at 6GPa: Implications for the origin of group II Kimberlites. J. Petrol. 55, 2097–2124. doi:10.1093/petrology/egu051.
Novella, D., Frost, D.J., Hauri, E.H., Bureau, H., Raepsaet, C., Roberge, M., (2014). The distribution of H2O between silicate melt and nominally anhydrous peridotite and the onset of hydrous melting in the deep upper mantle. Earth Planet Sci Lett 400:1–13. https ://doi. org/10.1016/j.epsl.2014.05.006.

Novella, D., Dolejš, D., Myhill, R., Pamato, M.G., Manthilake, G., Frost, D.J., (2017a). Melting phase relations in the systems Mg2SiO4–H2O and MgSiO3–H2O and the formation of hydrous melts in the upper mantle. Geochim. Cosmochim. Acta 204, 68–82. doi:10.1016/j.gca.2016.12.042.

Novella, D., Jacobsen, B., Weber, P.K., Tyburczy, J.A., Ryerson, F.J., Du Frane, W.L., (2017b). Hydrogen self-diffusion in single crystal olivine and electrical conductivity of the Earth's mantle. Sci. Rep. 7, 1–10. doi:10.1038/s41598-017-05113-6.

O

O'Connell, R.J., Budiansky, B., (1974). Seismic velocities in dry and saturated cracked solids. J. Geophys. Res. 79(35):5412–5426. https ://doi.org/10.1029/JB079 i035p 05412.

O'Neil, H. st C., Wall, V.J., (1987). The Olivine-Orthopyroxene-Spinel Oxygen Geobarometer , the Nickel Precipitation Curve , and the Oxygen Fugacity of the Earth ' s Upper Mantle. J. Petrol. 28, 1169–1191.

O'Reilly, S.Y., Griffin, W.L., (2010). The continental lithosphere-asthenosphere boundary: Can we sample it? Lithos 120, 1–13. doi:10.1016/j.lithos.2010.03.016.

O'Rourke, J. G., Stevenson, D. J., (2016). Powering Earth's dynamo with magnesium precipitation from the core. Nature, 529(7586), 387.

O'Rourke, J.G.O., Korenaga, J., Stevenson, D.J., (2017). Thermal evolution of Earth with magnesium precipitation in the core. Earth Planet. Sci. Lett. 458, 263–272. doi:10.1016/j.epsl.2016.10.057.

Ochs III, F. A., Lange, R. A., (1997). The partial molar volume, thermal expansivity, and compressibility of H 2 O in NaAlSi 3 O 8 liquid: new measurements and an internally consistent model. Contributions to Mineralogy and Petrology, 129(2-3), 155-165.

Ochs, F.A., Lange, R.A., (1999). The Density of Hydrous Magmatic Liquids. Science (80-.). 283, 1314–1317. doi:10.1126/science.283.5406.1314.

Ohta, K., (2010). Electrical and thermal conductivity of the Earth ' s lower mantle.

Ohta, K., Yagi, T., Taketoshi, N., Hirose, K., Komabayashi, T., Baba, T., Ohishi, Y., Hernlund, J., (2012). Lattice thermal conductivity of MgSiO3 perovskite and post-perovskite at the core–mantle boundary. Earth Planet. Sci. Lett. 349–350, 109–115. doi:10.1016/j.epsl.2012.06.043.

Ohtani,A, Onodera, A.and N. Kawai, (1979). Pressure apparatus of split-octahedron type for X-ray-diffraction studies, Rev. Sci. Instrum. 50(3), pp. 308–315.

Ohtani, E., Nagata, Y., Suzuki, A., Kato, T., (1995). Melting relations of peridotite and the density crossover in planetary mantles. Chem. Geol. 120, 207–221. doi:10.1016/0009-2541(94)00139-Y.

Ohtani, E., Litasov, K., Hosoya, T., Kubo, T., Kondo, T., (2004). Water transport into the deep mantle and formation of a hydrous transition zone. Phys. Earth Planet. Inter. 143, 255–269. doi:10.1016/j.pepi.2003.09.015.

Okumura, S., Hirano, N., (2013). Carbon dioxide emission to earth's surface by deep-sea volcanism. Geology 41(11):1167–1170. https ://doi.org/10.1130/G3462 0.1.010.

Olsen, N., (1998). The electrical conductivity of the mantle beneath Europe derived from C-responses from 3 to 270 hr. R. Astron. Soc. 133, 298–308. doi:10.1017/CBO9781107415324.004.

Olsen, N., (1999). Long-period (30 days–1 year) electromagnetic sounding and the electrical conductivity of the lower mantle beneath Europe. Geophysical Journal International, 138(1), 179-187.

Omura, K., (1991). Change of electrical conductivity of olivine associated with the olivine-spinel transition. Physics of the Earth and Planetary Interiors, 65(3-5), 292-307.

Osako, M., Ito, E., Yoneda, A., (2004). Simultaneous measurements of thermal conductivity and thermal diffusivity for garnet and olivine under high pressure. Phys. Earth Planet. Inter. 143, 311–320. doi:10.1016/j.pepi.2003.10.

P

Pamato, M.G., Myhill, R., Boffa Ballaran, T., Frost, D.J., Heidelbach, F., Miyajima, N., (2014). Lower-mantle water reservoir implied by the extreme stability of a hydrous aluminosilicate. Nat. Geosci. 8, 75–79. doi:10.1038/NGEO2306.

Papadakis, E. P., (1990). The measurement of ultrasonic velocity. Physical acoustics, 19, 81-106.

Parker, W., Jenkins, R., Butler, C., Abbott, G., (1961). Flash Method of determining thermal diffusivity, heat capacity, and thermal conductivity. J. Appl. Phys. 32:1679–1684.

Pearson, D.G., Brenker, F.E., Nestola, F., McNeill, J., Nasdala, L., Hutchison, M.T., Matveev, S., Mather, K., Silversmit, G., Schmitz, S., Vekemans, B., Vincze, L., (2014). Hydrous mantle transition zone indicated by ringwoodite included within diamond. Nature 507, 221–224.

Peierls, R. (1929). Zur kinetischen theorie der wärmeleitung in kristallen. Annalen der Physik, 395(8), 1055-1101.

Peierls, R., (1929). Zur theorie der galvanomagnetischen effekte. Zeitschrift für Physik, 53(3-4), 255-266.
Pesce, G., (2016). PhD Thesis. Experimental investingation of deep earth's mantle melting properties.
Petermann, M., Hofmeister, A.M., (2006). Thermal diffusivity of olivine-group minerals. American Mineralogist 91: 1747–1760.
Pfeiffer, T., (1998). Viscosities and electrical conductivities of oxidic glass-forming melts. Solid State Ion 105(1):277–287. https ://doi.org/10.1016/S0167 -2738(97)00475 –X.
Planck, M., (1914). The theory of radiation. Blakiston's Son and Co., Philadelphia, Pa.
Plank, T., Langmuir, C.H., (1992). Effects of the melting regime on the composition of the oceanic crust. J Geophys. Res. 97(B13):19749–19770. https ://doi.org/10.1029/92jb0 1769.
Poe, B.T., Romano, C., Nestola, F., Smyth, J.R., (2010). Electrical conductivity anisotropy of dry and hydrous olivine at 8GPa. Phys. Earth Planet. Inter. 181, 103–111. doi:10.1016/j.pepi.2010.05.003.
Pommier, A., Gaillard, F., Pichavant, M., Scaillet, B., (2008). Laboratory measurements of electrical conductivities of hydrous and dry Mount Vesuvius melts under pressure. Journal of Geophysical Research. 113, 1–16. doi:10.1029/2007JB005269.
Pommier, A., Garnero, E.J., (2014). Petrology-based modeling of mantle melt electrical conductivity and joint interpretation of electromagnetic and seismic results. J. Geophys. Res. Solid. Earth 119:4001–4016. https ://doi.org/10.1002/2014J B0115 67.
Pommier, A., Leinenweber, K., Kohlstedt, D.L., Qi, C., Garnero, E.J., Mackwell, S.J., Tyburczy, J.A., (2015) Experimental constraints on the electrical anisotropy of the lithosphere-asthenosphere system. Nature 522(7555):202–206.
Presnall, D.C., Simmons, C.L., Porath, H., (1972). Changes in electrical conductivity of a synthetic basalt during melting. J. Geophys. Res. 77(29):5665. https ://doi.org/10.1029/JB077 i029p 05665.
Püthe, C., Kuvshinov, A., Khan, A., Olsen, N. (2015). A new model of Earth's radial conductivity structure derived from over 10 yr of satellite and observatory magnetic data. Geophysical Supplements to the Monthly Notices of the Royal Astronomical Society, 203(3), 1864-1872.

R

Reichmann, H., Jacobsen, S., (2004). High-pressure elasticity of a natural magnetite crystal. Am. Mineral. 89, 1061–1066.
Revenaugh, J., Sipkin, S., (1994). Seismic evidance for silicate melt atop the 410-km mantle discontinuity. Nature 369, 474–476.
Richard, G., Bercovici, D., Karato, S., (2006). Slab dehydration in the Earth's mantle transition zone. EPSL. 251, 156–167. doi:10.1016/j.epsl.2006.09.006.
Richet, P., Fiquet, G., (1991). High-Temperature Heat Capacity and Premelting of Minerals in the System MgO-CaO-A1203-SiO2. J. Geophys. Res. 96:445–456. doi: 10.1029/90JB02172.
Rigden, S., Ahrens, J., Stolper, E.M., (1988). Shock compression of molten silicate results for a model basaltic composition. J. Geophys. Res. 93, 367–382.
Rikitake, T., (1948). Note on the electromagnetic induction within the Earth. Bull. Earthq. Res, Inst., Univ, Tokyo, 24,1-9.
Rikitake, T., (1951) Electromagnetic induction within the Earth and its relation to the electrical state of the earth's interior part I-IV Bull. Earthq. Res, Inst., Univ, Tokyo, 28-29.
Ringwood, A. E., (1975). Composition and Petrology of the Earth's Mantle. MacGraw-Hill, 618.
Ringwood, A.E., (1991). Phase transformations and their bearing on the constitution and dynamics of the mantle. Geochim. Cosmochim. Acta 55.
Rivers, M.L., Carmichael, I.S.E., (1987). Ultrasonic studies of silicate melts. J. Geophys. Res. 92:9247–9270.
Roberts, J.J., Tyburczy, J.A., (1999). Partial-melt electrical conductivity: influence of melt composition. J. Geophys. Res. 104(B4):7055. https://doi.org/10.1029/1998J B9001 11.
Romano, C., Poe, B.T., Kreidie, N., McCammon, C.A., (2006). Electrical conductivities of pyrope-almandine garnets up to 19 GPa and 1700°C. Am. Mineral. 91, 1371–1377. doi:10.2138/am.2006.1983.
Romanowicz, B., (1995). A global tomographic model of shear attenuationin the upper mantle. J. Geophys. Res. 100(B7):12375. https ://doi.org/10.1029/95JB0 0957.
Romine, W.L., Whittington, A.G., Nabelek, P.I., Hofmeister, A.M., (2012). Thermal diffusivity of rhyolitic glasses and melts : effects of temperature, crystals and dissolved water. Bull. Volcanol. 2273–2287. doi:10.1007/s00445-012-0661-6.
Ross, R. G., Andersson, P., Sundqvist, B., Backstrom, G., (1984). Thermal conductivity of solids and liquids under pressure. Reports on Progress in Physics, 47(10), 1347.
Roufosse, M., Klemens, P.G., (1973). Thermal Conductivity of Complex Dielectric Crystals. Physical Review B - Condensed Matter and Materials Physics. 7.
Rüpke, L., Morgan, J.P., Dixon, J.E., (2006). Implications of Subduction Rehydration for Earth ' s Deep Water

Cycle, in: Jacobsen, S.D., Van Der Lee, S. (Eds.), Earth's Deep Water Cycle. American Geophysical Union, pp. 263–276.

S

Saal, A.E., Hauri, E.H., Langmuir, C.H., Perfit, M.R., (2002). Vapour under saturation in primitive mid-ocean-ridge basalt and the volatile contentof Earth's upper mantle. Nature 419(6906):451–455. https ://doi.org/10.1038/nature0107 3.

Sæmundsson, K., (1991). Geology of the Krafla system (in Icelandic). In Náttúra Mývatns (The Natural History of Lake Mývatn) (pp. 24-95). The Icelandic Natural History Society Reykjavík.

Sahagian, D.L., Proussevitch, A.A., (1998). 3D particle size distributionsfrom 2D observations: stereology for natural applications. J.Volcanol. Geotherm Res 84(3):173–196. https ://doi.org/10.1016/S0377 -0273(98)00043 -2.

Sakamaki, T., Suzuki, A., Ohtani, E., (2006). Stability of hydrous melt at the base of the Earth's upper mantle. Nature 439, 192–194. doi:10.1038/nature04352.

Sakamaki, T., Ohtani, E., Urakawa, S., Suzuki, A., Katayama, Y., (2009). Measurement of hydrous peridotite magma density at high pressure using the X-ray absorption method. Earth Planet. Sci. Lett. 287, 293–297. doi:10.1016/j.epsl.2009.07.030.

Sakamaki, T., Ohtani, E., Urakawa, S., Suzuki, A., Katayama, Y., (2010). Density of dry peridotite magma at high pressure using an X-ray absorption method. Am. Mineral. 95, 144–147. doi:10.2138/am.2010.3143

Salters VJM, Hart SR (1989) The hafnium paradox and the role of garnet in the source of mid-ocean-ridge basalts. Nature 342:420.

Sambridge, M., Mosegaard, K., (2002). Monte Carlo methods in geophysical inverse problems. Reviews of Geophysics, 40(3), 3-1.

Sato, H., Sacks, I.S., Murase, T., Muncill, G., Fukuyama, H. (1989). Qp-melting temperature relation in peridotite at high pressure and temperature: attenuation mechanism and implications for the mechanical properties of the upper mantle. J. Geophys. Res. 94(B8):10647. https ://doi.org/10.1029/JB094 iB08p 10647.

Schaeffer, A.J., Bostock, M.G., (2010). A low-velocity zone atop the transition zone in northwestern Canada. J. Geophys. Res. 115:B06302. https ://doi.org/10.1029/2009J B0068 56.

Schärmeli, G. H., (1982). Anisotropy of olivine thermal conductivity at 2.5 GPa and up to 1500°K measured on opticammy non-thick samples.

Schiavi, F., Bolfan-casanova, N., Withers, A.C., Médard, E., Laumonier, M., Laporte, D., Flaherty, T., Gómez-ulla, A., (2018). Water quanti fi cation in silicate glasses by Raman spectroscopy : Correcting for the e ff ects of confocality , density and ferric iron. J. Chem. Geo. doi:10.1016/j.chemgeo.2018.02.036.

Schmandt, B., Jacobsen, S.D., Becker, T.W., Liu, zhenxian, Dueker, K., (2014). Dehydration melting at the top of the lower mantle. Science. 344, 1265–1268.

Schmeling, H., (1986). Numerical models on the influence of partial melton elastic, anelastic and electrical properties of rocks. Part II: electrical conductivity. Phys. Earth Planet. Inter. 43(2):123–136. https ://doi.org/10.1016/0031-9201(86)90080 -4.

Schmerr, N., (2012). The Gutenberg discontinuity: melt at the lithosphere- asthenosphere boundary. Science 335(6075):1480–1483. https ://doi.org/10.1126/science.12154 33.

Schock, R. N., Duba, A. G., Shankland, T. J., (1989). Electrical conduction in olivine. Journal of Geophysical Research: Solid Earth, 94(B5), 5829-5839.

Sempolinski, D. R., Kingery, W. D., (1980). Ionic conductivity and magnesium vacancy mobility in magnesium oxide. Journal of the American Ceramic Society, 63(11-12), 664-669.

Shankland, T.J., Waff, H.S., (1977). Partial melting and electrical conductivity anomalies in the upper mantle. J. Geophys. Res; 82(33):5409–5417.

Shankland, T. J., Nitsan, U., Duba, A. G., (1979). Optical absorption and radiative heat transport in olivine at high temperature. Journal of Geophysical Research: Solid Earth, 84(B4), 1603-1610.

Shaw, H. R. (1963). Obsidian-H2O viscosities at 1000 and 2000 bars in the temperature range 700° to 900° C. Journal of Geophysical Research, 68(23), 6337-6343.

Shea, T., Houghton, B.F., Gurioli, L., Cashman, K.V., Hammer, J.E., Hobden, B.J., (2010). Textural studies of vesicles in volcanic rocks: an integrated methodology. J. Volcanol. Geotherm. Res; 190(3–4):271–289. https ://doi.org/10.1016/j.jvolg eores .2009.12.003

Shearer, P.M., (1996). Transition zone velocity gradients and the 520-km discontinuity. J Geo. Res. 101, 3053–3066.

Shimizu, H., Utada, H., Baba, K., Koyama, T., Obayashi, M., Fukao, Y., (2010). Three-dimensional imaging of electrical conductivity in the mantle transition zone beneath the North Pacific Ocean by a semi-global induction study. Physics of the Earth and Planetary Interiors, 183(1-2), 252-269.

Sifré, D., Gardés, E., Massuyeau, M., Hashim, L., Hier-Majumder, S,. Gaillard, F., (2014). Electrical conductivity during incipient melting in the oceanic low-velocity zone. Nature. 509(7498):81–85. https ://doi.org/10.1038/natur e1324 5.

Silaeva, O. I., Shamina, O. G.; (1958). Propagation of elastic pulses in cylindrical specimens. Izv. Akad. Nauk SSSR, Ser. Geofiz, 1, 32-35.

Simmons, N.A., Forte, A.M., Boschi, L., Grand, S.P., (2010). GyPSuM : A joint tomographic model of mantle density and seismic wave speeds 115, 1–24. doi:10.1029/2010JB007631

Simons, K., Dixon, J., Schilling, J.-G., Kingsley, R., Poreda, R., (2002). Volatiles in basaltic glasses from the Easter-Salas y Gomez Seamount Chain and Easter Microplate: Implications for geochemical cycling of volatile elements. Geochemistry, Geophys. Geosystems 3, 1–29. doi:10.1029/2001GC000173.

Sisson, T.W., Grove, T.L., (1993). Experimental investigations of the role of H_2O in calc-alkaline differentiation and subduction zone magmatism. Contrib. to Mineral. Petrol. 113, 143–166. doi:10.1007/BF00283225.

Slack, G. A., (1962). Thermal Conductivity of MgO, Al 2 O 3, Mg Al 2 O 4, and Fe 3 O 4 Crystals from 3° to 300° K. Physical Review, 126(2), 427.

Slack, G. A., Oliver, D. W., (1971). Thermal conductivity of garnets and phonon scattering by rare-earth ions. Physical Review B, 4(2), 592.

Smyth, J.R., Jacobsen, S.D., (2006). Nominally Anhydrous Minerals and Earth's Deep Water Cycle, in: Jacobsen, S.D., Van Der Lee, S. (Eds.), Earth's Deep Water Cycle, Geophysical Monograph Series. American Geophysical Union. doi:doi:10.1029/168GM02

Sokol, A.G., Palyanov, Y.N., Kupriyanov, I.N., (2010). Effect of oxygen fugacity on the H 2 O storage capacity of forsterite in the carbon-saturated systems. Geochim. Cosmochim. Acta 74, 4793–4806. doi:10.1016/j.gca.2010.05.032.

Song, A. T.-R., Helmberger, D. V, Grand, S.P., (2004). Low-velocity zone atop the 410-km seismic discontinuity in the northwestern United States. Nature 427, 530–533. doi:10.1038/nature02231.

Soustelle, V., Manthilake, G., (2017). Deformation of olivine-orthopyroxene aggregates at high pressure and temperature: implications for the seismic properties of the asthenosphere. Tectonophysics 694:385–399. https ://doi.org/10.1016/j.tecto .2016.11.020.

Spera,, F., J., (2000). Physical properties of magma. Encyclopedia on Volcanoes.

Speziale, S., Zha, C. S., Duffy, T. S., Hemley, R. J., Mao, H. K. ,(2001). Quasi-hydrostatic compression of magnesium oxide to 52 GPa: Implications for the pressure-volume-temperature equation of state. Journal of Geophysical Research: Solid Earth, 106(B1), 515-528.

Stixrude, L., Lithgow-Bertelloni, C., (2005). Mineralogy and elasticity of the oceanic upper mantle: origin of the low-velocity zone. J. Geophys. Res. B Solid Earth 110(3):1–16. https ://doi.org/10.1029/2004J B0029 65.

Suzuki, A., Ohtani, E., Kato, T., (1998). Density and thermal expansion of a peridotite melt at high pressure. Phys. Earth Planet. Inter. 107, 53–61. doi:10.1016/s0031-9201(97)00123-4.

Suzuki, A., Ohtani, E., (2003). Density of peridotite melts at high pressure. Phys. Chem. Miner. 30, 449–456. doi:10.1007/s00269-003-0322-6.

T

Takei, Y. (1998). Constitutive mechanical relations of solid–liquid composites in terms of grain-boundary contiguity. J. Geophys. Res. 103(B8):18183–18203.

Takei, Y., (2000). Acoustic properties of partially molten media studied on a simple binary system with a controllable dihedral angle. J. Geophys. Res; 105(B7):16665. https ://doi.org/10.1029/2000J B9001 24.

Takei, Y., (2002). Effect of pore geometry on *V*P/*V*S: from equilibrium geometry to crack. J. Geophys. Res. 107(B2):2043. https ://doi.org/10.1029/2001J B0005 22.

Tarits, P., (2004). Water in the mantle: Results from electrical conductivity beneath the French Alps. Geophys. Res. Lett. 31, 749–752. doi:10.1029/2003GL019277.

Taura, H., Yurimoto, H., Kurita, K., Sueno, S., (1998). Pressure dependence on partition coefficients for trace elements between olivine and the coexisting melts. Phys. Chem. Miner. 25, 469–484. doi:10.1007/s002690050138.

Tauzin, B., Debayle, E., Wittlinger, G., (2010). Seismic evidence for a global low-velocity layer within the Earth's upper mantle. Nat. Geosci. 3, 718–721. doi:10.1038/ngeo969.

Tauzin, B., van der Hilst, R.D., Wittlinger, G., Ricard, Y., (2013). Multiple transition zone seismic discontinuities and low velocity layers below western United States. J. Geophys. Res. Solid Earth 118, 2307–2322. doi:10.1002/jgrb.50182.

Ten Grotenhuis, S.M., Drury, M.R., Spiers, C.J., Peach, C.J., (2005). Melt distribution in olivine rocks based on electrical conductivity measurements. J. Geophys. Res. Solid Earth 110(12):1–11. https ://doi.org/10.1029/2004J B0034 62.

Tenner, T.J., Hirschmann, M.M., Withers, A.C., Hervig, R.L., (2009). Hydrogen partitioning between nominally anhydrous upper mantle minerals and melt between 3 and 5 GPa and applications to hydrous peridotite partial melting. Chem. Geol. 262, 42–56. doi:10.1016/j.chemgeo.2008.12.006.

Tenner, T.J., Hirschmann, M.M., Withers, A.C., Ardia, P., (2012). H2O storage capacity of olivine and low-Ca pyroxene from 10 to 13 GPa: Consequences for dehydration melting above the transition zone. Contrib. to Mineral. Petrol. 163, 297–316. doi:10.1007/s00410-011-0675-7.

Thomas, C., Kendall, J., Lowman, J., (2004). Lower-mantle seismic discontinuities and the thermal morphology of subducted slabs 225, 105–113. EPSL. doi:10.1016/j.epsl.2004.05.038.

Tikhonov, A.N., (1950). in 1953 On determining electrical characteristics of the deep layers of the Earth's crust, Doklady, 73, 295-297.

Toffelmier, D.A., Tyburczy, J.A., (2007). Electromagnetic detection of a 410-km-deep melt layer in the southwestern United States. Nature 447, 991–994. doi:10.1038/nature05922.

Toomey, D.R., Wilcock, W.S.D, Solomon, S.C., Hammond, W.C., Orcutt, J.A., (1998). Mantle seismic structure beneath the MELT region of the East Pacific Rise from P and S wave tomography mantle seismic structure beneath the MELT region of the East Pacific Rise from P and S wave tomography the primary ocean bottom seismometer. Science (80-) 280:1224–1227. https ://doi.org/10.1126/science.280.5367.1224.

Toomey, D.R., Jousselin, D., Dunn, R., Wilcock, W.S.D., Detrick, R.S. (2007). Skew of mantle upwelling beneath the East Pacific Rise governs segmentation. Nature 446(7134):409–414. https ://doi.org/10.1038/natur e0567 9.

Tu, L.T., Brennan, J.., Sauer, J.., (1955). Dispersion of Ultrasonic Pulse Velocity in Cylindrical Rods. J. Acoust. Soc. Am. 27, 550–555.

Tyburczy, J.A., Waff, H.S, (1983). Electrical conductivity of molten basalt and andesite to 25 kilobars pressure: geophysical significance and implications for charge transport and melt structure. J. Geophys. Res. 88(2):2413–2430. https ://doi.org/10.1029/JB088 iB03p 02413.

U

Utada, H., Koyama, T., Shimizu, H., Chave, A. D., (2003). A semi-global reference model for electrical conductivity in the mid-mantle beneath the north Pacific region. Geophysical Research Letters, 30(4).

V

Van der Hilst, R. D., De Hoop, M. V., Wang, P., Shim, S. H., Ma, P., Tenorio, L., (2007). Seismostratigraphy and thermal structure of Earth's core-mantle boundary region. Science, 315(5820), 1813-1817.

Von Bargen, N., Waff, H.S., (1986). Permeabilities, interfacial areas and curvatures of partially molten systems: results of numerical computations of equilibrium microstructures. J. Geophys. Res. 91:9261–9276.

Vinnik, L., Farra, V., (2007). Low S velocity atop the 410-km discontinuity and mantle plumes. Earth Planet. Sci. Lett. 262, 398–412. doi:10.1016/j.epsl.2007.07.051.

W

Waff, H.S., (1974). Theoretical consideration of electrical conductivity in a partially molten mantle and implications for geothermometry. J. Geophys. Res. 79(26):4003–4010.

Waff, H.S., Weill, D., 1975. Electical conductivity of magmatic liquids: effects of temperature, oxygen fugacity and composition. Earth Planet. Sci. Lett. 28, 254–260.

Waff, H.S., Blau, J.R. (1982). Experimental determination of near equilibrium textures in partially molten silicates at high pressures. In: Akimoto S, Manghnani MH (eds) High pressure research in geophysics. Center for Academic Publication, Tokyo, pp 229–236.

Waff, H.S., Faul, U.H., (1992). Effects of crystalline anisotropy on fluid distribution in ultramafic partial melts. J. Geophys. Res. 97(B6):9003. https ://doi.org/10.1029/92JB0 0066.

Wagner, L., Forsyth, D.W., Fouch, M.J., James, D.E., (2010). Detailed three-dimensional shear wave velocity structure of the northwestern United States from Rayleigh wave tomography. Earth Planet. Sci. Lett. 299(3–4):273–284. https ://doi.org/10.1016/j.epsl.2010.09.005.

Wakatsuki, M., Ichinose, K., Aoki T., (1971), Characteristics of link-type cubic anvil, high pressure-high temperature apparatus, Jpn. J. Appl. Phys. 10(3) pp. 357–366.

Wakatsuki, M., Ichinose, K., (1982). A wedge-type cubic anvil high-pressure apparatus and its application to materials synthesis research, in High-Pressure Research in Geophysics, S. Akimoto and M.H. Manghnani, Ed.,Center for Academic Publications/D. Reidel, Tokyo/Dordrecht, , pp. 13–26.

Walker, D., Carpenter, M.A., aC.M. Hitch, (1990). Some simplifications to multianvil devices for high-pressure experiments, Am. Mineral. 75(9–10), pp. 1020–1028.

Walker D., (1991), Lubrication, gasketing, and precision in multianvil experiments, Am. Mineral. 76(7–8) pp. 1092–1100.
Walter, M.J., (1998). Melting of Garnet Peridotite and the Origin of Komatiite and Depleted Lithosphere. J. Petrol. 39, 29–60.
Wanamaker, B. J., Duba, A. G., (1993). Electrical conductivity of San Carlos olivine along [100] under oxygen- and pyroxene-buffered conditions and implications for defect equilibria. Journal of Geophysical Research: Solid Earth, 98(B1), 489-500.
Wanamaker, B. J., Duba, A. G., (1993). Electrical conductivity of polycrystalline olivine containing a silicate glass. Geophysical research letters, 20(19), 2107-2110.
Wang, D., Mookherjee, M., Xu, Y., Karato, S. I., (2006). The effect of water on the electrical conductivity of olivine. Nature, 443(7114), 977.
Wang, W., Takahashi, E., (2000). Subsolidus and melting experiments of K-doped peridotite KLB-1 to 27 GPa: Its geophysical and geochemical implications. J. Geophys. Res. 105, 2855–2868.
Watanabe, T., (1993). Effects of water and melt on seismic velocities and their application to characterization of seismic reflectors. Geophys. Res. Lett. 20, 2933. doi:10.1029/93GL03170
Watanabe, T., Kurita, K. (1993). The relationship between electrical conductivity and melt fraction in a partially molten simple system: Archie's law behavior. Physics of the earth and planetary interiors, 78(1-2), 9-17.
Watson, E. B., (1979). Zircon saturation in felsic liquids: experimental results and applications to trace element geochemistry. Contributions to Mineralogy and Petrology, 70(4), 407-419.
Watson, E.B., Brenan, J.M., Baker, D.R., (1991). Continental Mantle. Oxford Univeristy Press.
Widmer, R., Masters, G., Gilbert., F., (1991). Spherically symmetric attenuation within the Earth from normal mode data. Geophys. J. Int ;104(3):541–553. https ://doi.org/10.1111/j.1365-246X.1991.tb05700.x.
Wood, B.J., Blundy, J.D., (1997). A predictive model for rare earth element partitioning between clinopyroxene and anhydrous silicate melt. Contrib. to Mineral. Petrol. 129, 166–181. doi:10.1007/s004100050330
Wood, B.J., Blundy, J.D., (2002). The effect of H2O on crystal-melt partitioning of trace elements. Geochim. Cosmochim. Acta 66, 3647–3656. doi:10.1016/S0016-7037(02)00935-3.
Workman, R.K., Hart, S.R., (2005). Major and trace element composition of the depleted MORB mantle (DMM). Earth Planet. Sci. Lett. 231, 53–72. doi:10.1016/j.epsl.2004.12.005.

X

Xiong, Y., Wood, S.A., (1999). Experimental determination of the solubility of ReO 2 and the dominant oxidation state of rhenium in hydrothermal solutions. Chemical Geology. 158 245–256.
Xu, Y., Poe, B. T., Shankland, T. J., Rubie, D. C., (1998). Electrical conductivity of olivine, wadsleyite, and ringwoodite under upper-mantle conditions. Science, 280(5368), 1415-1418.
Xu, Y., Shankland, T. J., (1999). Electrical conductivity of orthopyroxene and its high pressure phases. Geophysical Research Letters, 26(17), 2645-2648.
Xu, Y., Shankland, T.J., Linhardt, S., Rubie, D.C., Lagnenhorst, F., Kalinski, K., (2004) .Thermal diffusivity and conductivity of olivine, wadsleyite and ringwoodite to 20 GPa and 1373 K. Phys Earth Planet Inter 143–144:321–336. doi: 10.1016/j.pepi.2004.03.005.

Y

Yagi, T., Ida Y., Sato Y., and S. Akimoto, (1975) Effect of hydrostatic pressure on the lattice parameters ofFe2SiO4 olivine up to 70 kbar, Phys. Earth Planet. Inter. 10, pp. 348–354.
Yamazaki, D., Ito, E., Yoshino, T., Tsujino, N., Yoneda, A., Guo, X., Xu, F., Higo, Y., Funakoshi, K., (2014). Over 1Mbar generation in the Kawai-type multianvil apparatus and its application to compression of (Mg0.92Fe0.08)SiO3 perovskite and stishovite. Phys. Earth Planet. Inter. 228, 262–267. doi:10.1016/j.pepi.2014.01.013.
Yan, B., Graham, E.., Furlong, K., (1989). Lateral variations in upper mantle thermal structure inferred from three-dimentional seismic inversion models. Geophys. Res. Lett. 16, 449–452.
Yang, X., Keppler, H., McCammon, C., Ni, H., Xia, Q., & Fan, Q. (2011). Effect of water on the electrical conductivity of lower crustal clinopyroxene. Journal of Geophysical Research: Solid Earth, 116(B4).
Yang, X., (2012). Orientation-related electrical conductivity of hydrous olivine, clinopyroxene and plagioclase and implications for the structure of the lower continental crust and uppermost mantle. Earth Planet. Sci. Lett. 317–318, 241–250. doi:10.1016/j.epsl.2011.11.011.
Yoshino, T., Walter, M. J., Katsura, T. (2004). Connectivity of molten Fe alloy in peridotite based on in situ electrical conductivity measurements: implications for core formation in terrestrial planets. Earth and Planetary Science Letters, 222(2), 625-643.

Yoshino, T., Takei, Y., Wark, D.A;, Watson, E.B., (2005). Grain boundary wetness of texturally equilibrated rocks, with implications for seismic properties of the upper mantle. J. Geophys. Res. B Solid Earth 110(8):1–16. https ://doi.org/10.1029/2004J B0035 44.

Yoshino, T., Matsuzaki, T., Yamashita, S., Katsura, T., (2006). Hydrous olivine unable to account for conductivity anomaly at the top of the asthenosphere. Nature, 443(7114), 973.

Yoshino, T., Nishihara, Y., Karato, S.I., (2007). Complete wetting of olivine grain boundaries by a hydrous melt near the mantle transition zone. Earth Planet. Sci. Lett. 256(3–4):466–472. https ://doi.org/10.1016/j.epsl.2007.02.002.

Yoshino, T., Manthilake, G., Matsuzaki, T., Katsura, T., (2008). Dry mantle transition zone inferred from the conductivity of wadsleyite and ringwoodite 451, 1–4. doi:10.1038/nature06427.

Yoshino, T., Katsura, T., (2009). Effect of iron content on electrical conductivity of ringwoodite, with implications for electrical structure in the transition zone. Physics of the Earth and Planetary Interiors, 174(1-4), 3-9.

Yoshino, T., Yamazaki, D., Mibe, K., (2009). Well-wetted olivine grain boundaries in partially molten peridotite in the asthenosphere. Earth Planet. Sci. Lett. 283(1–4):167–173. https ://doi.org/10.1016/j.epsl.2009.04.007.

Yoshino, T., Laumonier, M., McIsaac, E., Katsura, T., (2010). Electrical conductivity of basaltic and carbonatite melt-bearing peridotites at high pressures: implications for melt distribution and melt fraction in the upper mantle. Earth Planet. Sci. Lett. 295(3–4):593–602.https ://doi.org/10.1016/j.epsl.2010.04.050.

Yoshino, T., (2010). Laboratory Electrical Conductivity Measurement of Mantle Minerals. Surv. Geophys. 31, 163–206. doi:10.1007/s10712-009-9084-0.

Yoshino, T., and Katsura, T., (2012). Re-evaluation of electrical conductivity of anhydrous and hydrous wadsleyite. Earth Planet. Sci. Lett. 337, 56–67. doi: 10.1016/j.epsl.2012.05.023.

Young, C. J., Lay, T., (1989). The core shadow zone boundary and lateral variations of the P velocity structure of the lowermost mantle. Physics of the earth and planetary interiors, 54(1-2), 64-81.

Z

Zeitlin, A., Brayman, J., (1963). Ultra-high-pressure calibration: Influence of cubic workpiece configuration,in High Pressure Measurement, A.A. Giardini and E.C. Lloyd, Ed., Butterworths, Washington, , pp. 301–320.

Zhang, B., Yoshino, T., Yamazaki, D., Manthilake, G., Katsura, T., (2014). Electrical conductivity anisotropy in partially molten peridotite under shear deformation. Earth Planet. Sci. Lett. 05:98–109. https://doi.org/10.1016/j.epsl.2014.08.018.

Zhang, Y., Ni, H., Chen, Y., (2010). Diffusion data in silicate melts. Reviews in Mineralogy and Geochemistry, 72(1), 311-408.

Zhao, D., (2004). Global tomographic images of mantle plumes and subducting slabs : insight into deep Earth dynamics 146, 3–34. doi:10.1016/j.pepi.2003.07.032.

Appendix A

Additional Raman data tables, water content estimations and reproducibility tests

Appendix A: Additional Raman data tables, water content estimations and reproducibility tests

During this PhD work, Raman spectroscopy was intensively used because of the importance of volatiles in the studied fields and the accessibility of the apparatus. Additional data tables and records of the tests (made to check the impact of the user while doing baselines) will be given in this appendix.

Several tests were made by the author to point out the effect due to the user on the estimated water content. Results with calibrations for basaltic and differentiated glasses are given in this section.

In the first two tables, the data obtained for glass calibration are given here under (table A.1 and 2). Table A.1 presents the values obtained on silicate regions for calibration glasses of Médard and Grove (2008). The data normalized to power and counting time. Data on water frequency region are given in the second table A.2 and also normalized to power and counting time. FTIR or SIMS estimation of water content is given in the last columns with the OH/Si ratio. Water content of unknown glasses can be obtained using the straight line made by these standards for OH/Si ratio, normalized intensity and high depending on the similarity of the unknown glass to standard ones.

Table A.1 Raman analyses and quantification of basaltic standard glasses from Médard and Grove (2008). Data on measured intensity and height of the highest peaks are given and normalized for the Silicate frequency region.

Sample		Silicate frequency region (300-1220 cm^{-1})				
Reference glasses	Power (mW)	Time (s)	Intensity (height)	Intensity (area)	Normalized height	Normalized area
7	8	90	13100.00	3471587.00	18.19	4821.65
9	8	90	13400.00	3594004.10	18.61	4991.67
10	8	90	15000.00	4134852.50	20.83	5742.85
19	8	90	15200.00	4093487.50	21.11	5685.40
22	8	90	14800.00	4104985.00	20.56	5701.37

Table A.2 Raman analyses and quantification of basaltic standard glasses from Médard and Grove (2008). Data on measured intensity and height of the highest peaks are given and normalized for the Water frequency region. Values of standard water content are given (FTIR or SIMS estimations) in %wt. The ratio of normalized intensities of water and silicate frequency region (OH/Si) is given in the last column.

Sample	Water frequency region (3000-3800 cm^{-1})					FTIR/SIMS		
Reference glasses	Time (s)	Intensity (height)	Intensity (area)	Normalized height	Normalized area	H_2O	error	OH/Si
7	180	23000.00	5351122.90	15.97	3716.06	3.03	0.25	0.77
9	180	15900.00	3581936.60	11.04	2487.46	2.28	0.13	0.50
10	180	9080.00	1994118.80	6.31	1384.80	1.39	0.08	0.24
19	180	4100.00	866740.19	2.85	601.90	0.58	0.05	0.11
22	180	602.00	52967.70	0.42	36.78	0	0	0.01

Unknown glasses used in the chapters IV, V, VI and VII are quantified using one or both of the calibration curves given in the three next figures (Figs A.1, A.2, A.3). We can see for both of the calibration curve: OH maximum intensity, OH frequency region area and OH/Si ratio that the relation to water content is linear. This linear behavior is well proven by the different fitting curves where R values are always above 0.99.

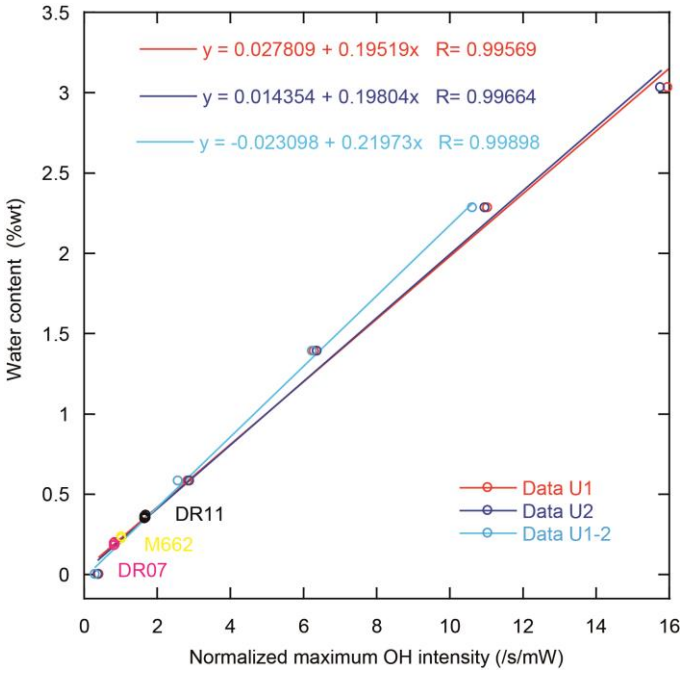

Figure A.1 OH maximum intensity as a function of water content of the basaltic glasses. The highest OH intensity is normalized to power and counting time. Calibration curve using glasses standard are displayed in red, blue and cyan. Their respective linear fits and equations are in the same color. Red is calibration based on author fits, Blue based on F.Schiavi fits and cyan are fits performed by the author after a full session (apparatus drift). Values of unknown water content glass are reported on each calibration curve (several circle of each color): DR11 in black, M662 in yellow and DR07 in magenta (see Chapter VI).

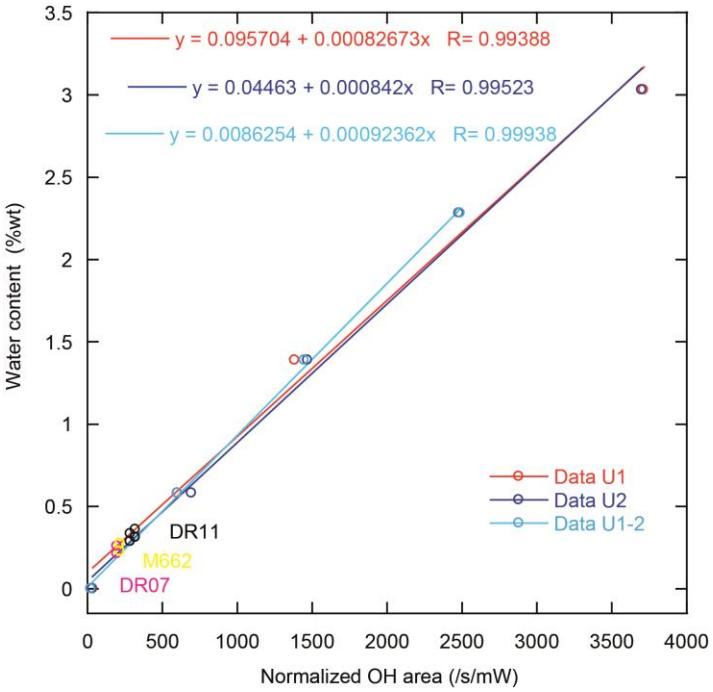

Figure A.2 OH frequency region area intensity as a function of water content of the basaltic glasses. The integrated area is normalized to laser power and counting time. Calibration curve using glasses standard are displayed in red, blue and cyan. Their respective linear fits and equations are in the same color. Red is calibration based on author fits, Blue based on F.Schiavi fits and cyan are fits performed by the author after a full session (apparatus drift). Values of unknown water content glass are reported on each calibration curve (several circle of each color): DR11 in black, M662 in yellow and DR07 in magenta.

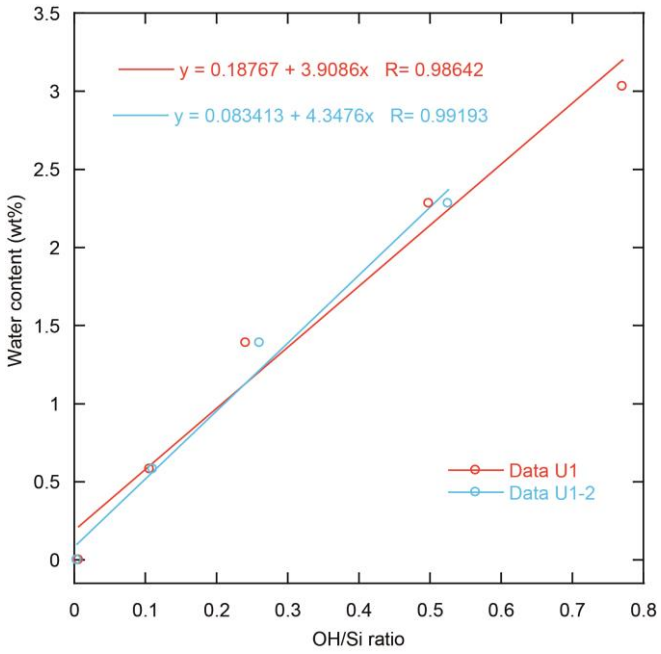

Figure A.3 OH/Si integrated areas as a function of water content of the basaltic glasses. The integrated areas are normalized to laser power and counting time, the ratio is dimensionless. Calibration curve using glasses standard are displayed in red and cyan. Their respective linear fits and equations are in the same color. Red is calibration based on author fits and cyan fits are performed by the author after a full session (apparatus drift).

To test the reproducibility of our fitting method and the influence of the user, the author and F. Schiavi fitted the same data using the method described in Schiavi et al. (2018). The baselines were realized under Peakfit software and were non parametric fit with 2 anchor point around 300 cm^{-1}, 2 anchor points at 1210 ± 5 cm^{-1} and integrating between 300 and 1220 cm^{-1} for silicate region. For OH frequency regions, the fits used were cubic with anchor points continuous from start (2800 cm^{-1} or higher) of the analysis to 3000 cm^{-1} and between 3700 cm^{-1} to the end (3800 cm^{-1}). The zone taken for the integral was between 3000 and 3800 cm^{-1}. The difference between one user to another, using the same data and method, are visible in the 3 precedent figures and quantifications are available in the next tables (Tables A.3, A.4, A.5, A.6, A.7 and A.8). The differences seem to be moderate on graphic representation (between blue and red data and fits) with deviations observed to be less than 5%. However, the data of less good quality (cosmic ray, instrumental deviation etc.) can induce much greater difference as fitting becomes less obvious and subtle adaptations of the method are required.

The effect of instrumental drift during a daily session has also been studied with the repetition of the glass standard analyses at the end of the session. The analyses which were baselined and fitted by the author are represented by the cyan data in the graphs and labeled as glass N° -- 2 in the tables. We can observe that the experimental drift is greater than fitting difference due to the user and deviation can be significant, around 5% but sometimes up to 15% (table A.4). We can observe that the most important relative variation, both for user fit and baseline is obtained for lowest water contents. This simply translates that baseline fitting is a bit more difficult and uncertain at these low contents (low signal to noise ratio). Relative variation seems important, however, it only slightly affects the fitting curve because the values (intensity and area) are very low and close to 0. The user impact has been quantified from calibrating glasses as well as two unknown MORB glasses used in chapter VI: DR11 and DR07 (see Tables A.6 and A.7).

Table A.3 Influence of user baseline on OH Intensity and Area of the OH frequency region for our set of calibration glasses. Values obtained after baselining are given and normalized. Variation between the two users results are given in %. U1 : author, U2 :F.Schiavi. Water content of SIMS/FTIR analyses are given in wt.%.

		Water frequency region (3000-3800 cm^{-1})					FTIR/SIMS	
Reference glasses	Power (mW)	Time (s)	Intensity (height)	Intensity (area)	Normalized height	Normalized area	**OH**	error
7-U1	8	180	23000.00	5351122.90	15.97	3716.06	3.03	0.25
7-U2	8	180	22700.00	5328412.10	15.76	3700.29	3.03	0.25
% variation			1.30	0.42	1.30	0.42		
9-U1	8	180	15900.00	3581936.60	11.04	2487.46	2.28	0.13
9-U2	8	180	15800.00	3574825.60	10.97	2482.52	2.28	0.13
% variation			0.63	0.20	0.63	0.20		
10-U1	8	180	9080.00	1994118.80	6.31	1384.80	1.39	0.08
10-U2	8	180	9190.00	2116154.30	6.38	1469.55	1.39	0.08
% variation			1.20	5.77	1.20	5.77		
19-U1	8	180	4100.00	866740.19	2.85	601.90	0.58	0.05
19-U2	8	180	4170.00	999979.29	2.90	694.43	0.58	0.05
% variation			1.68	13.32	1.68	13.32		
22-U1	8	180	602.00	52967.70	0.42	36.78	0	0
22-U2	8	180	554.00	49290.45	0.38	34.23	0	0
% variation			7.97	6.94	7.97	6.94		

Table A.4 Influence of instrumental drift during a day of analyses for silicate frequency region. The analyses performed at the beginning of the session are labeled by their number and analyses performed at the end of the session are labeled as –2. Variations are given in %. Variations are moderate (around 5%).

		Silicate frequency region (300-1220 cm^{-1})				
Reference glasses	Power (mW)	Time (s)	Intensity (height)	Intensity (area)	Normalized height	Normalized area
7	8	90	13100.00	3471587.00	18.19	4821.65
7--2	8	90	13100.00	3445931.30	18.19	4786.02
% variation			0.00	0.74	0.00	0.74
9	8	90	13400.00	3594004.10	18.61	4991.67
9--2	8	90	12700.00	3411232.80	17.64	4737.82
% variation			5.22	5.09	5.22	5.09
10	8	90	15000.00	4134852.50	20.83	5742.85
10--2	8	90	14500.00	3997906.50	20.14	5552.65
% variation			3.33	3.31	3.33	3.31
19	8	90	15200.00	4093487.50	21.11	5685.40
19--2	8	90	14300.00	3927908.80	19.86	5455.43
% variation			5.92	4.04	5.92	4.04
22	8	90	14800.00	4104985.00	20.56	5701.37
22--2	8	90	15200.00	4217013.20	21.11	5856.96
% variation			2.63	2.66	2.63	2.66

Table A.5 Influence of instrumental drift (beginning/ end of the analytical session) of analyses for water frequency region. The analyses at the end of the day are labeled as –2. Variations are given in %. Variations are moderate (around 5%) except for low water content probably comes from fitting uncertainties due to low signal to noise ratio.

		Water frequency region (3000-3800 cm^{-1})				FTIR/SIMS		
Reference glasses	Time (s)	Intensity (height)	Intensity (area)	Normalized height	Normalized area	H_2O	error	OH/Si
7	180	23000.00	5351122.90	15.97	3716.06	3.03	0.25	0.77
7--2	180	22700.00	5328412.10	15.76	3700.29	3.03	0.25	0.77
% variation		1.30	0.42	1.30	0.42			0.32
9	180	15900.00	3581936.60	11.04	2487.46	2.28	0.13	0.50
9--2	180	15300.00	3585058.80	10.63	2489.62	2.28	0.13	0.53
% variation		3.77	0.09	3.77	0.09			5.17
10	180	9080.00	1994118.80	6.31	1384.80	1.39	0.08	0.24
10--2	180	8990.00	2086865.00	6.24	1449.21	1.39	0.08	0.26
% variation		0.99	4.44	0.99	4.44			7.61
19	180	4100.00	866740.19	2.85	601.90	0.58	0.05	0.11
19--2	180	3720.00	868862.63	2.58	603.38	0.58	0.05	0.11
% variation		9.27	0.24	9.27	0.24			4.28
22	180	602.00	52967.70	0.42	36.78	0	0	0.01
22--2	180	447.50	31497.75	0.31	21.87	0	0	0.00
% variation		25.66	40.53	25.66	40.53			42.11

Table A.6 Raman analyses and quantification of DR11-201(MAPCO II, see starting material section), MORB. For this sample, only OH frequency region spectrum was used as (quench) crystals prevent the use of silicate region spectra (no OH/Si possible). U1 and U2 refers to user 1 and user 2 (the author and F.Schiavi) for two independent baseline fittings (on lines). The variation in % of the value is given for each analysis. Water contents inferred from normalized intensity and area values are given for the two user fits based on their analysis on the standard glasses. Water contents inferred are given in wt.%.

		Water frequency region (3000-3800 cm^{-1})					OH AREA		OH MAX INT	
Sample	Power (mW)	Time (s)	Intensity (height)	Intensity (area)	Normalized height	Normalized area	OH calc U2 fit	OH calc U1 fit	OH calc U2 fit	OH calc U1 fit
DR11-04-U1	8	180	1940.00	277372.82	1.35	192.62	0.21	0.25	0.28	0.30
DR11-04-U2	8	180	1520.00	240896.77	1.06	167.29	0.19	0.23	0.22	0.24
% variation			21.65	13.15	21.65	13.15	10.31	8.22	20.54	19.61
DR11-05-U1	8	180	2600.00	534307.05	1.81	371.05	0.36	0.40	0.37	0.39
DR11-05-U2	8	180	2700.00	410623.97	1.88	285.16	0.28	0.33	0.39	0.40
% variation			3.70	23.15	3.70	23.15	20.26	17.65	3.57	3.45
DR11-07-U1	8	180	1230.00	205061.00	0.85	142.40	0.16	0.21	0.18	0.20
DR11-07-U2	8	180	1190.00	222414.93	0.83	154.45	0.17	0.22	0.18	0.19
% variation			3.25	7.80	3.25	7.80	5.81	4.46	3.00	2.79
DR11-08-U1	8	180	2350.00	441071.07	1.63	306.30	0.30	0.35	0.34	0.35
DR11-08-U2	8	180	2360.00	443456.62	1.64	307.96	0.30	0.35	0.34	0.35
% variation			0.42	0.54	0.42	0.54	0.46	0.39	0.41	0.39
DR11-09-U1	8	180	3780.00	644649.18	2.63	447.67	0.42	0.47	0.53	0.55
DR11-09-U2	8	180	3810.00	740726.00	2.65	514.39	0.48	0.52	0.54	0.55
% variation			0.79	12.97	0.79	12.97	11.76	10.59	0.77	0.75
DR11-10-U1	8	180	4080.00	683019.68	2.83	474.32	0.44	0.49	0.58	0.59
DR11-10-U2	8	180	4320.00	814111.95	3.00	565.36	0.52	0.56	0.61	0.62
% variation			5.56	16.10	5.56	16.10	14.72	13.37	5.42	5.31
DR11-11-U1	8	180	1120.00	232535.49	0.78	161.48	0.18	0.23	0.17	0.18
DR11-11-U2	8	180	1040.00	212833.84	0.72	147.80	0.17	0.22	0.16	0.17
% variation			7.14	8.47	7.14	8.47	6.38	4.94	6.53	6.05
AVG-U1			2442.86	431145.18	1.70	299.41	0.29	0.33	0.35	0.37
STD-U1			1152.92	197472.12	0.80	137.13	0.11	0.11	0.16	0.16
AVG-U2			2420.00	440723.44	1.68	306.06	0.31	0.36	0.35	0.36
STD-U2			1281.37	248279.73	0.89	172.42	0.14	0.14	0.17	0.17
% variation on AVG			0.94	2.17	0.94	2.17	8.40	7.19	2.01	1.93

Table A.7 Raman analyses and quantification of DR07-201(MAPCO II, see starting material section), MORB. For this sample, only OH frequency region spectrum was used as (quench) crystals prevent the use of silicate region spectra (no OH/Si possible). U1 and U2 refers to user 1 and user 2 (the author and F.Schiavi) for two independent baseline fittings (on lines). The variation in % of the value is given for each analysis. Water contents inferred from normalized intensity and area values are given for the two user fits based on their analysis on the standard glasses. Water contents inferred are given in wt.%.

		Water frequency region (3000-3800 cm^{-1})					OH AREA		OH MAX INT	
Sample	Power (mW)	Time (s)	Intensity (height)	Intensity (area)	Normalized height	Normalized area	OH calc U2 fit	OH calc U1 fit	OH calc U2 fit	OH calc U1 fit
DR07-01-U1	8	180	1120.00	266414.84	0.78	185.01	0.20	0.25	0.17	0.18
DR07-01-U2	8	180	1060.00	256521.23	0.74	178.14	0.19	0.24	0.16	0.17
% variation			5.36	3.71	5.36	3.71	2.89	2.28	4.90	4.54
DR07-02-U1	8	180	1170.00	281394.45	0.81	195.41	0.21	0.26	0.18	0.19
DR07-02-U2	8	180	1230.00	305894.98	0.85	212.43	0.22	0.27	0.18	0.20
% variation			4.88	8.01	4.88	8.01	6.41	5.18	4.50	4.19
DR07-03-U1	8	180	1160.00	285187.66	0.81	198.05	0.21	0.26	0.17	0.19
DR07-03-U2	8	180	1240.00	371008.34	0.86	257.64	0.26	0.31	0.18	0.20
% variation			6.45	23.13	6.45	23.13	19.19	15.96	5.95	5.55
DR07-04-U1	8	180	1120.00	279976.38	0.78	194.43	0.21	0.26	0.17	0.18
DR07-04-U2	8	180	1220.00	366751.15	0.85	254.69	0.26	0.31	0.18	0.20
% variation			8.20	23.66	8.20	23.66	19.59	16.27	7.55	7.03
DR07-05-U1	8	180	1340.00	312905.26	0.93	217.30	0.23	0.28	0.20	0.21
DR07-05-U2	8	180	1290.00	271399.87	0.90	188.47	0.20	0.25	0.19	0.21
% variation			3.73	13.26	3.73	13.26	10.66	8.66	3.46	3.24
DR07-06-U1	8	180	1260.00	289322.09	0.88	200.92	0.21	0.26	0.19	0.20
DR07-06-U2	8	180	1330.00	307076.94	0.92	213.25	0.22	0.27	0.20	0.21
% variation			5.26	5.78	5.26	5.78	4.63	3.75	4.88	4.57
AVG-U1			1195.00	285866.78	0.83	198.52	0.21	0.26	0.18	0.19
STD-U1			87.58	15339.86	0.06	10.65	0.01	0.01	0.01	0.01
AVG-U2			1228.33	313108.75	0.85	217.44	0.23	0.28	0.18	0.20
STD-U2			92.39	47455.39	0.06	32.96	0.03	0.02	0.01	0.01
% variation on AVG			2.71	8.70	2.71	8.70	7.00	5.68	2.50	2.33

For solid samples recovered from experiments at 6, 9 and 12 GPa water content estimation, calibration curves and data tables are given in this section.

Calibration curve and data table are also given for wadsleyite water content estimations in synthesized runs at 14 GPa: Figure A.4 and tables A.8 and A9.

Calibration curve and data tables are then provided for olivine samples with data on 12 GPa experiments first, and 6 and 9 GPa in second. This data is followed by bulk sample water budget estimations. All of them are discussed in the chapter V.

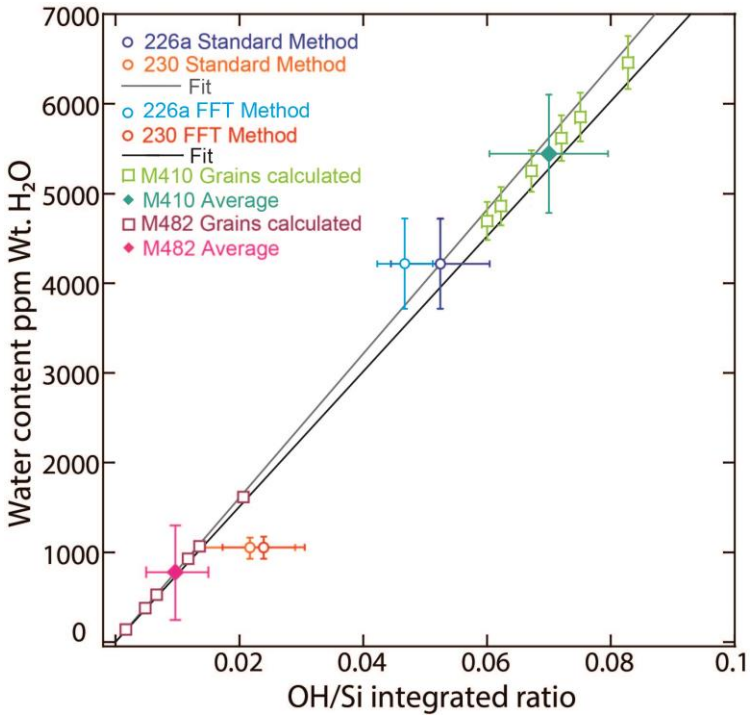

Figure A.4 Water content vs. OH/Si ratio of our dry and hydrous wadsleyite samples M482 & M410 respectively. The standards 226a and 230 (Bolfan-Casanova) were quantified for water content by ERDA with 12% maximum of error. Results are given for two standards, each treated by two different methods: the first based on raw spectra in purple (226a) and orange (230), the second based on Fourier-transformed data in blue (226a) and red (230). The two fits of the standards are represented in black and grey and have similar values. Single measurements in grains of the starting material (M410) are reported in light green, as well as their average value (green diamond).

Table A.8 Summary of the Raman spectra inferred values on integration parameters, and estimation of the water content of our hydrous wadsleyite starting material.

M410 Wadsleyite	1st Session	2nd Session				
Point N°	13	1	4	8	9	11
OH	Integrated range = 3200-3700 cm^{-1} / power = 9.5mW / Counting time 150s					
Area/time/power	21.15	22.88	37.72	27.26	3.48	23.97
Silicate	Integrated range = 400-1100 cm^{-1} / power = 9.5mW / Counting time 50s					
Area/time/power	293.45	339.93	604.56	362.36	606.48	289.30
OH/Si	0.072	0.0673	0.0624	0.0752	0.0601	0.0829
Water content calculated ppm wt.						
Low estimation	5432.08	5071.84	4701.39	5668.98	4532.20	6244.32
High estimation	5783.49	5399.95	5005.52	6035.72	4825.39	6648.27
Average	5607.79	5235.89	4853.46	5852.35	4678.79	6446.29
Standard Deviation	248.48	232.00	215.06	259.32	207.32	285.64
Total mean (ppm) H_2O		**5445.76**				
Standard Deviation		**659.66**				

Table A.9 Summary of the Raman spectra inferred values on integration parameters, and estimation of the water content of our dry wadsleyite starting material.

M482 Wadsleyite	Standard confocality 5% power								high confocality 10% power					
Point N°	1	2	3	5	6	7	8	9	1	2	3	4	7	8
OH	Integrated range = 3200-3700 cm^{-1} / power = 9.5mW / Counting time 250s								Integrated range = 3200-3700 cm^{-1} / power = 16.8 mW / Counting time 400s					
Area/time/power	20.06	95.71	40.55	60.60	91.45	100.98	93.89	102.52	7.46	1.56	29.07	5.25	19.91	22.48
Silicate	Integrated range = 400-1100 cm^{-1} / power = 9.5mW / Counting time 50s								Integrated range = 400-1100 cm^{-1} / power = 16.8mW / Counting time 40s					
Area/time/power	6133	4157	3627	4810	3926	5759	5423	5749	1110	897	2445	1084	1459	1084
OH/Si	0.00	0.02	0.01	0.01	0.02	0.02	0.02	0.02	0.01	0.00	0.01	0.00	0.01	0.02
Water content calculated ppm wt.	254.44	1791.05	869.90	980.24	1812.21	1364.15	1346.91	1387.37	522.51	135.67	924.70	376.58	1061.47	1614.09
	Integrated range = 0-1045 cm^{-1} / power = 9.5mW / Counting time 50s								Integrated range = 1-1045 cm^{-1} / power = 16.8mW / Counting time 40s					
Water content calculated ppm wt.	156.49	1101.58	535.03	602.90	1114.60	839.02	828.42	853.30	321.37	83.44	568.74	231.62	652.85	992.74
Total mean (ppm) H_2O	**400-1100 cm^{-1}** 1225.78				**0-1045 cm^{-1}** 753.92				**400-1100 cm^{-1}** 772.50			**0-1045 cm^{-1}** 475.13		
Standard Deviation	514.62				316.51				536.61			330.04		

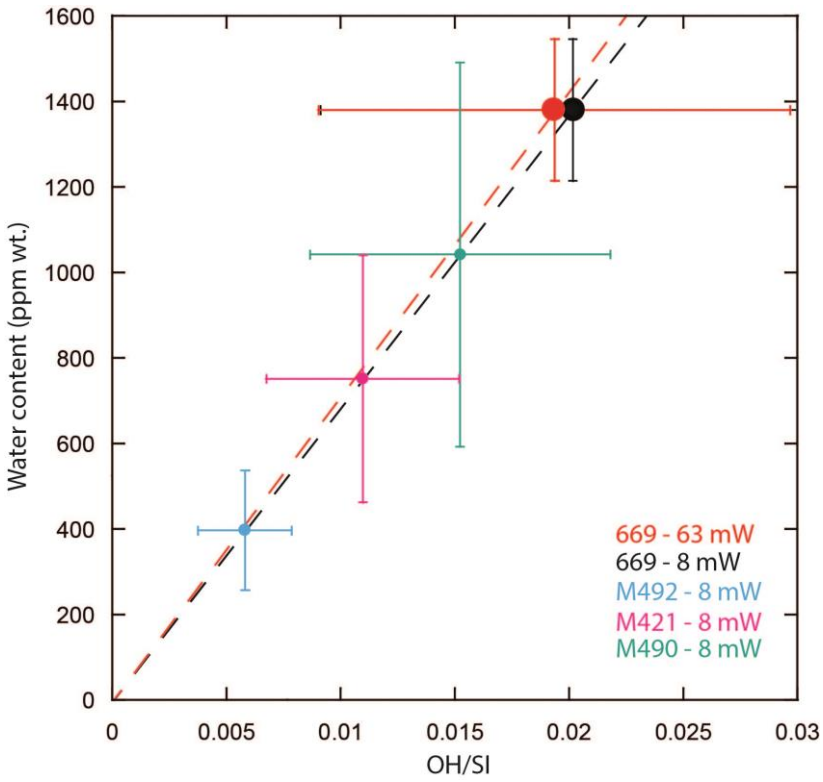

Figure A.5 Water content as a function of OH/Si ratio of olivine in our recovered samples. 669 is the olivine standard provided by N. Bolfan Casanova with 1380 ± 166 ppm and associated calibration lines for different laser power. Our samples water contents are calculated via the OH/SI ratio measured, the large errors (1 σ) are due to combination of anisotropy and errors from apparatus and treatment.

Table A.10 Water budget estimation for our experimental runs products at 12 GPa for moderate water content samples (M421 and M492). Water content of olivine was estimated via Raman analyses (Bolfan-Casanova et al., 2014). Water concentrations of other phases were estimated with partition coefficients of Novella et al. (2014). Errors are 1 Standard deviation. Values in blue were measured, values in green were calculated.

M421					
Minerals	Olivine	CPX	gt	CPX+GT	bulk
Proportion	0.615	0.193	0.193	0.385	
STD prop	0.014	0.007	0.007	0.014	
Water content (ppm)	751.213	2159.736	600.970		993.557
STD (ppm)	288.513	939.824	289.780		260.231
M492					
Minerals	Olivine	CPX	gt	CPX+GT	Bulk
Proportion (%)	0.722	0.139	0.139	0.278	
STD prop	0.035	0.017	0.017	0.035	
Water content (ppm)	397.033	1141.470	317.627		489.506
STD (ppm)	140.128	465.661	145.404		124.313

Table A.11 Water budget estimation for our experimental runs products at 12 GPa for partially molten samples (M412, M425 and M490). Water content of olivine was estimated via Raman analyses (Bolfan-Casanova et al., 2014). Water concentrations of other phases were estimated with partition coefficients of Novella et al. (2014). Melt water content were quantified with Raman spectroscopy Freitas et al. (2017), Schiavi et al. (2018). Errors are 1 Standard deviation. Values in blue were measured, values in green were calculated.

M412						
Minerals	Olivine	CPX	gt	CPX+GT	Melt	bulk with melt
Proportion	0.662	0.076	0.076	0.151	0.070	
STD prop	0.018	0.009	0.009	0.018	0.020	
Water content (ppm)	168.000	483.000	134.400		42000.000	3097.777
STD (ppm)	27.141	73.183	73.183		2520.000	858.5622

M425					
Minerals	Olivine	CPX	gt	Melt	bulk with melt
Proportion	0.615	0.169	0.169	0.020	
STD prop	0.040	0.0199	0.020	0.005	
Water content (ppm)	480.000	1380.000	384.000	120000.000	3030.1968
STD (ppm)	77.546	209.093	209.093	7200.000	627.19674

M490						
Minerals	Olivine	CPX	gt	CPX+GT	Melt	bulk with melt
Proportion	0.640	0.052	0.052	0.103	0.257	
STD prop	0.040	0.014	0.014	0.029	0.025	
Water content of the phase (ppm)	1042.075	2995.967	833.660		3000.000	1634.524
STD (ppm)	449.589	1430.537	434.094		180.000	316.6307

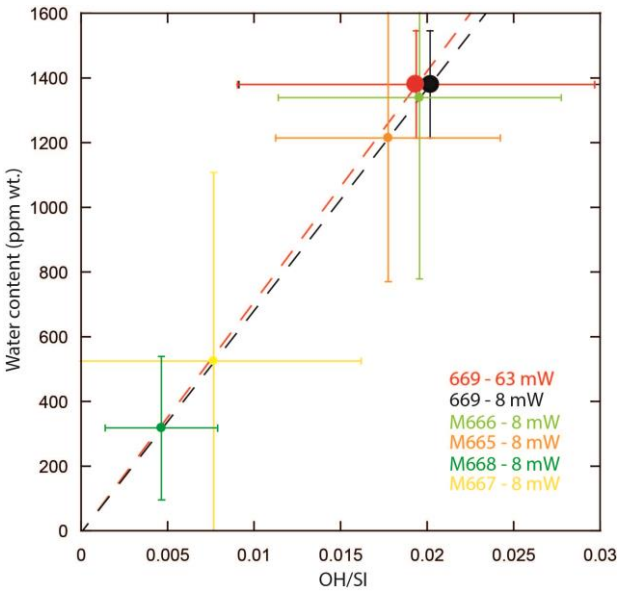

Figure A.6 Water content as a function of OH/Si ratio of olivine in our recovered samples at 6 (yellow) and 9 (green) GPa. 669 is the olivine standard provided by N. Bolfan Casanova with 1380 ± 166 ppm and associated calibration lines for different laser power. Our samples water contents are calculated via the OH/SI ratio measured, the large errors (1 σ) are due to combination of anisotropy and errors from apparatus and treatment.

Table A.12 Water content estimation for our starting materials and experimental runs products at 6 and 9 GPa. Water content of olivine was estimated via Raman analyses (Bolfan-Casanova et al., 2014). Water concentrations of other phases were estimated with partition coefficients of Novella et al. (2014). The high bulk content estimated from experimental runs comes from the big uncertainty on olivine water content for these experiments, due to small water content and anisotropy effects. These imply large water content into the melt fraction that heavily depends on olivine estimated content. Errors are 1 Standard deviation. Values in blue were measured, values in green were calculated.

	M665 6 GPa starting material				M667 6 GPa				
Minerals	Olivine	CPX+GT	CPX	GT	Olivine	CPX+GT	CPX	GT	Melt
Proportion (%)	70.22	29.78	14.89	14.89	69.97	26.88	13.44	13.44	3.68
STD prop	4.08	4.08	2.04	2.04	2.33	2.52	1.26	1.26	1.86
Water content (ppm)	1264.18		3634.51	1011.34	524.30		1507.35	419.44	131074.07
STD (ppm)	461.99		1522.20	472.80	583.28		1705.06	482.38	147140.16
Bulk water	1579.45				5449.96				
STD bulk	412.49				5956.96				
	M666 9 GPa starting material				M668 9 GPa				
Minerals	Olivine	CPX+GT	CPX	GT	Olivine	CPX+GT	CPX	GT	Melt
Proportion (%)	70.38	29.62	14.81	14.81	64.31	29.36	14.68	14.68	6.33
STD prop	5.93	5.93	2.96	2.96	9.73	12.82	6.41	6.41	1.01
Water content (ppm)	1394.06		4007.93	1115.25	330.89		951.32	264.72	82723.44
STD on water	582.49		1864.63	568.22	230.93		691.87	200.22	59051.80
Bulk water	1739.84				5629.41				
STD bulk	522.91				3837.28				

Raman quantification of starting materials for Angström method characterizations is provided in the next tables and figures. Calibration curves are also given in this section.

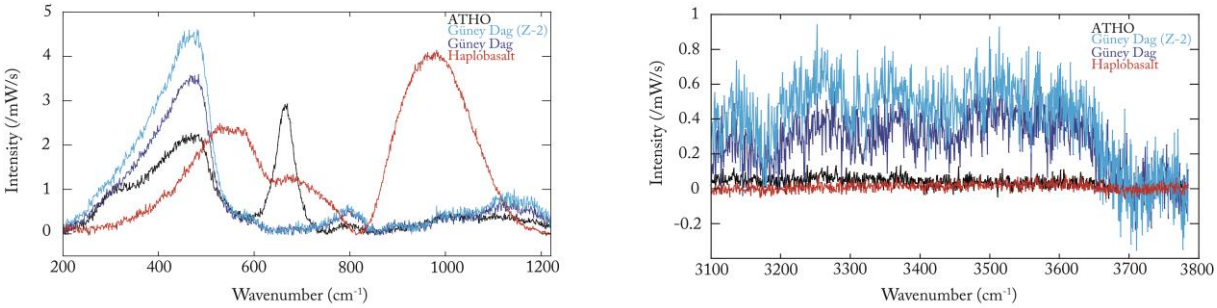

Figure A.7 Raman Spectra of Güney Dag, ATHO and haplobasalt samples. Left figure indicate spectra recorded in silicate region, right spectra in the OH region, the intensities are normalized to laser power and counting time. The color of the spectra is similar in the two panels meaning analyses have been carried on a single point in the sample. Güney Dag (Z-2) was measured doing the laser focus 2 mm under the sample surface in order to maximize the signal quality.

Table A.13 Quantification with Raman spectra made with spectra of figure A.7 The first part details the values obtained in silicate part (integration between 300 and 1220 cm^{-1}) with the intensity of the highest peak and the integrated area, these values are normalized to power and counting time in the two last columns. The second part details the values obtained with the water region (integration between 3000 and 3800 cm^{-1}). The intensity of the highest peak and the total area are given, and then normalized to counting time and power. OH/Si column indicates the ratio of the area of the water region divided by the area of the silicate region.

		Silicate frequency region (300-1220 cm^{-1})				
Sample	Power (mW)	Time (s)	Intensity (height)	Intensity (area)	Normalized height	Normalized area
ATHO	19.6	60	3450.00	8223325.90	2.93	6992.62
Gunedag	19.6	60	4220.00	913879.54	3.59	777.11
Gunedag Frag 2	19.6	60	5410.00	1161865.80	4.60	987.98
haplobasalt	19.6	60	4870.00	1603858.40	4.14	1363.83
		Water frequency region (3000-3800 cm^{-1})				
Sample	Time (s)	Intensity (height)	Intensity (area)	Normalized height	Normalized area	**OH/Si**
ATHO	180	470.67	101946.58	0.13	28.90	0.00
Gunedag	180	2270.00	660528.03	0.64	187.22	0.24
Gunedag Frag 2	180	3320.00	1007862.00	0.94	285.68	0.29
haplobasalt	180	305.00	27587.82	0.09	7.82	0.01

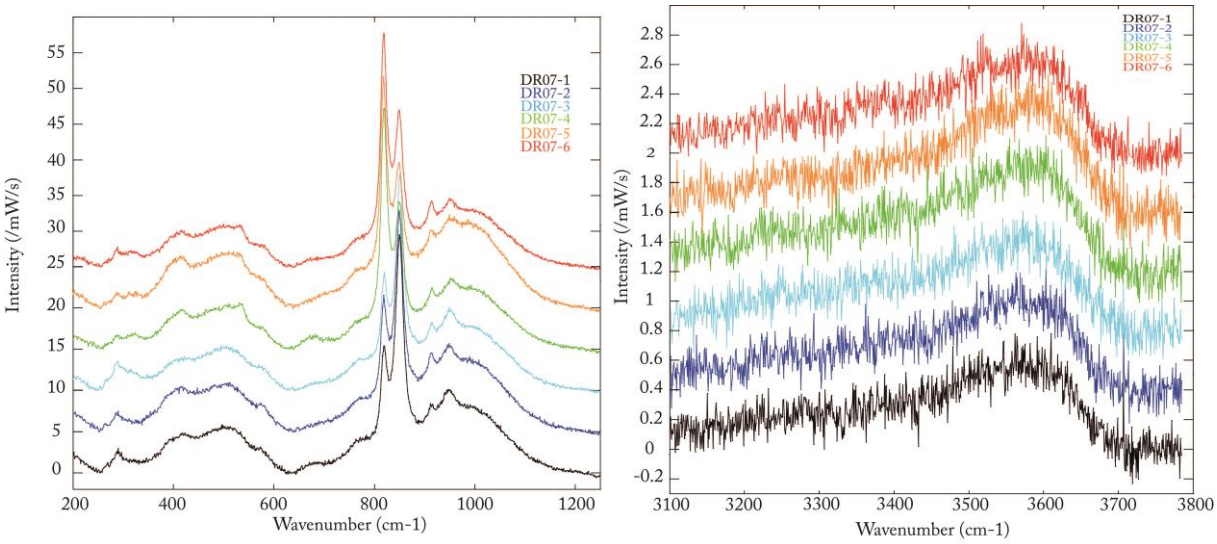

Figure A.8 Raman spectra of DR07-201 sample, the first graph is focused on silicate frequency region whereas the second is detailed on OH frequency regions. Spectra intensity is normalized to counting time and laser power. The different spectra were offset by 5 and 0.4 intensity units for silicate and OH regions respectively for visibility.

Table A.15 Quantification with Raman spectra of DR07-201 sample. The first table details the analyses on silicate region. The second table details the analyses made on OH region. Quantification of OH content of samples (in wt%) is proposed in the 3 last columns with values inferred from calibration on OH area, peaks intensity or OH/Si regions areas ratio, details on the method are given in the Raman section.

		Silicate frequency region (300-1220 cm^{-1}) + Olivine contamination				
Sample	Power (mW)	Time (s)	Intensity (height) at 1000 cm^{-1}	Intensity (area)	Normalized height	Normalized area
DR07-01	8	90	5845.00	2988762.30	8.12	4151.06
DR07-02	8	90	6230.00	3126739.20	8.65	4342.69
DR07-03	8	90	6430.00	3257422.60	8.93	4524.20
DR07-04	8	90	5934.00	3179633.90	8.24	4416.16
DR07-05	8	90	7250.00	3423404.40	10.07	4754.73
DR07-06	8	90	5617.00	3144293.10	7.80	4367.07
AVG			6217.67	3186709.25	8.64	4425.99
STD			581.57	145364.07	0.81	201.89

	Water frequency region (3000-3800 cm^{-1})						OH AREA	OH MAX INT	OH/SI ratio
Sample	Time (s)	Intensity (height)	Intensity (area)	Normalized height	Normalized area	**OH/Si**	OH calc	OH calc	OH calc
DR07-01	180	1120.00	266414.84	0.78	185.01	0.04	0.25	0.18	0.29
DR07-02	180	1170.00	281394.45	0.81	195.41	0.04	0.26	0.19	0.29
DR07-03	180	1160.00	285187.66	0.81	198.05	0.04	0.26	0.19	0.28
DR07-04	180	1120.00	279976.38	0.78	194.43	0.04	0.26	0.18	0.28
DR07-05	180	1340.00	312905.26	0.93	217.30	0.05	0.28	0.21	0.29
DR07-06	180	1260.00	289322.09	0.88	200.92	0.05	0.26	0.20	0.29
AVG		1195.00	285866.78	0.83	198.52	0.04	0.26	0.19	0.29
STD		87.58	15339.86	0.06	10.65	0.00	0.01	0.01	0.00

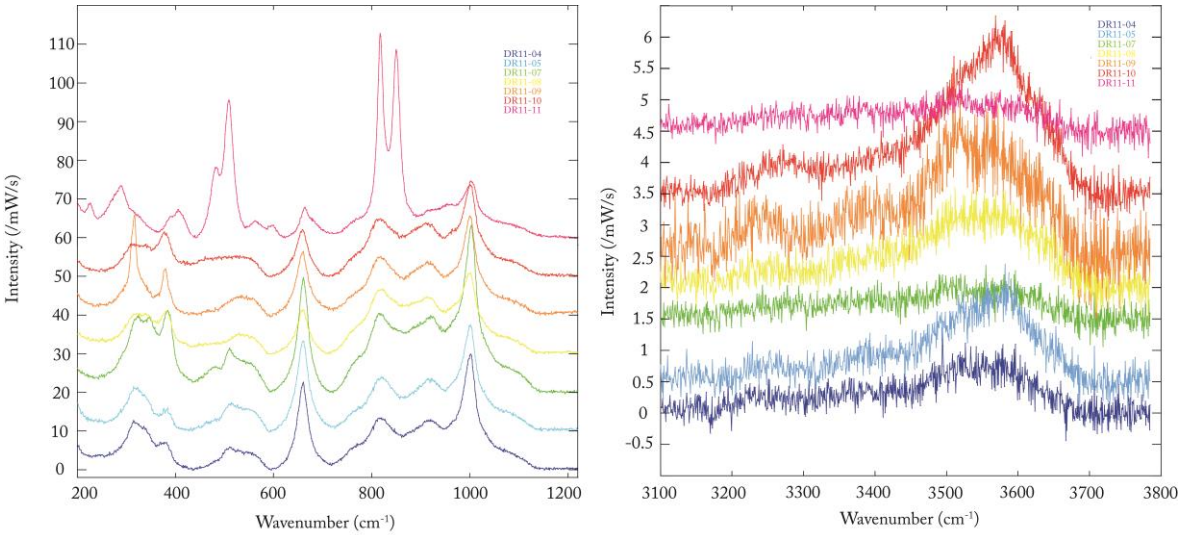

Figure A.9 Raman spectra of DR011-201 sample, the first graph is focused on silicate frequency region whereas the second is detailed on OH frequency regions. Spectra intensity is normalized to counting time and laser power. The different spectra were offset by 10 and 0.5 intensity units for silicate and OH regions respectively for visibility.

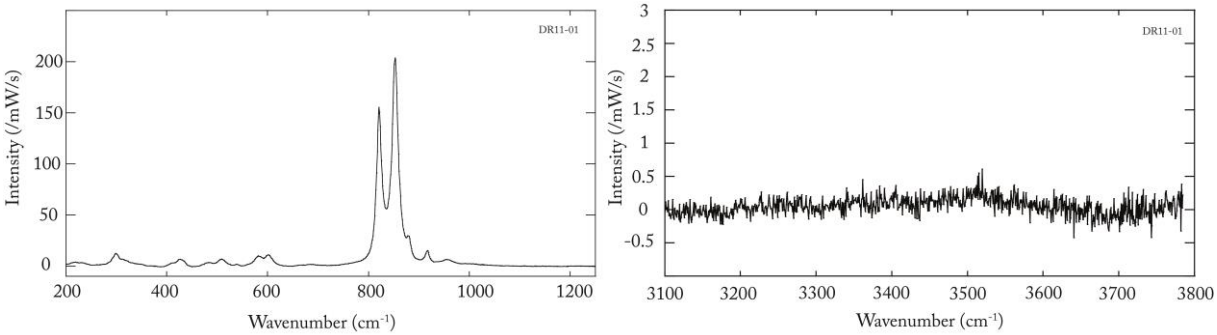

Figure A.10 Raman spectra on both silicate and OH region (left and right respectively) of a euhedral olivine crystal from DR11-201. The spectrum in OH region confirms the almost dry (little peaks at 3510 cm^{-1}) nature of olivines crystalized from the MORB melt.

Table A.16 Quantification with Raman spectra of DR11-201 sample. The table details the analyses made on OH region. Quantification of OH content of samples (in wt.%) is proposed in the 2 last columns with values inferred from calibration on OH area and peaks intensity.

		Water frequency region (3000-3800 cm^{-1})					OH AREA	OH MAX INT
Sample	Power (mW)	Time (s)	Intensity (height)	Intensity (area)	Normalized height	Normalized area	OH calc	OH calc
DR11-04	8	180.00	1940.00	277372.82	1.35	192.62	0.25	0.30
DR11-05	8	180.00	2700.00	410623.97	1.88	285.16	0.33	0.40
DR11-07	8	180.00	1230.00	205061.00	0.85	142.40	0.21	0.20
DR11-08	8	180.00	2350.00	441071.07	1.63	306.30	0.35	0.35
DR11-09	8	180.00	3780.00	644649.18	2.63	447.67	0.47	0.55
DR11-10	8	180.00	4080.00	683019.68	2.83	474.32	0.49	0.59
DR11-11	8	180.00	1120.00	232535.49	0.78	161.48	0.23	0.18
AVG			2457.14	413476.17	1.71	287.14	0.33	0.37
STD			1155.81	192165.21	0.80	133.45	0.11	0.16

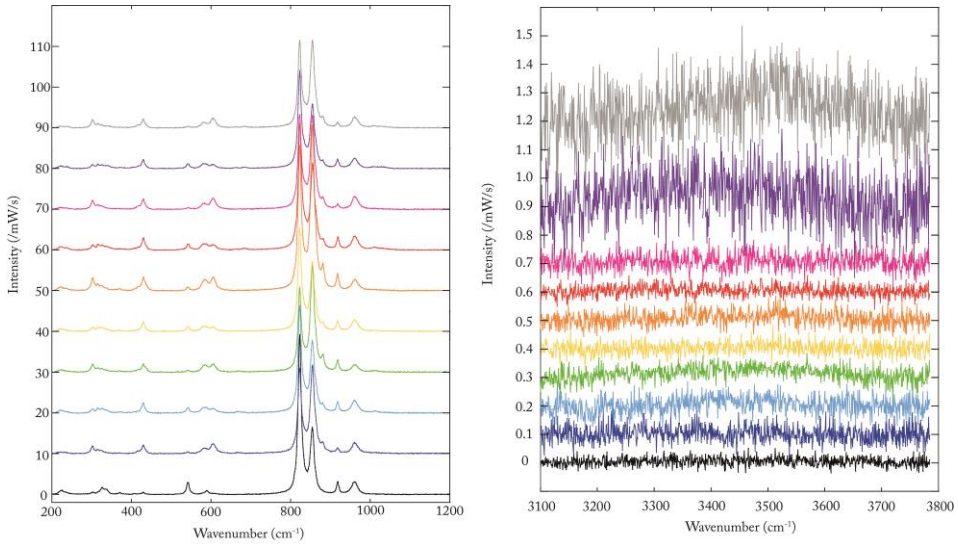

Figure A.11 Representative Raman spectra of RP4 olivines for silicate and volatile frequency regions. Our sample was shown to have almost dry olivines.

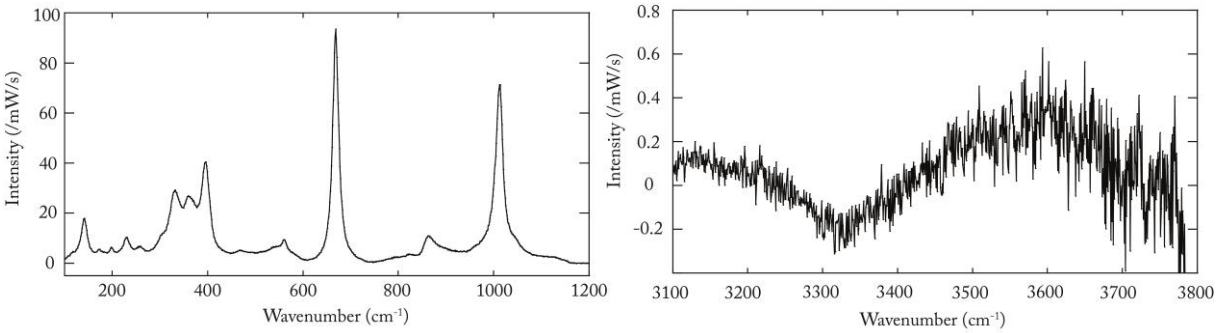

Figure A.12 representative Raman spectra of RP4 clinopyroxenes for silicate and volatile frequency regions. OH frequency region is very difficult to analyze due to the high Cr content of this phase inducing high fluorescence and difficult baseline

Table A.17 Estimated water content of RP4 sample with micro Raman estimated content on olivine. Proportions are estimated by eye and modal abundances reported by Berger (1981). Water content of other phases were estimated by mineral/mineral coefficient partition of Novella et al. (2014).

Minerals	Olivine	CPX	OPX	SP
Proportion (%)	0.60	0.18	0.18	0.05
STD prop	0.05	0.05	0,05	0.01
Water content of the phase	266.63	766.55	426.60	0.00
STD on water	153.20	467.55	254.74	0.00
Bulk water	368.78			
STD bulk	138.68			

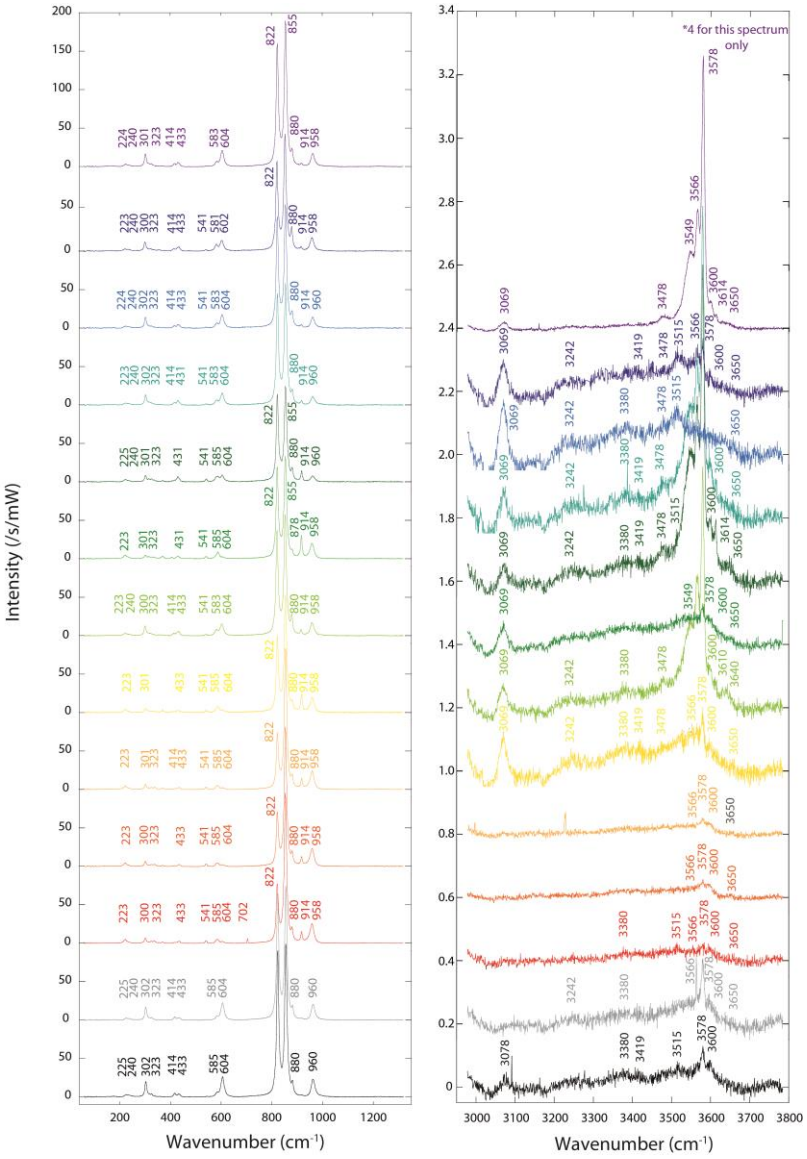

Figure A.13 Raman analyses of M525. On the left panel silicate region is represented. On the right panel the OH frequency region is given.

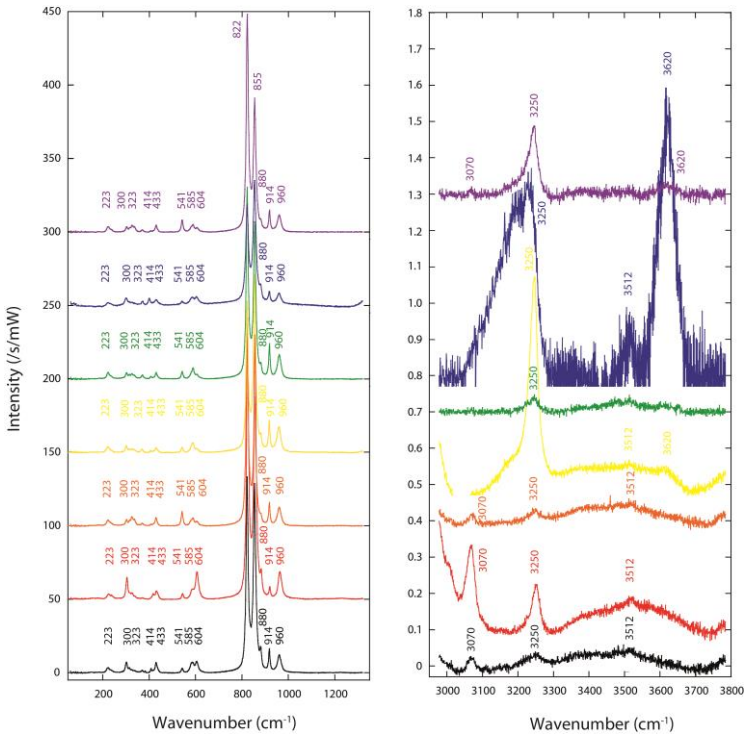

Figure A.14 Raman analyses of M617. On the left panel silicate region is represented. On the right panel the OH frequency region is given.

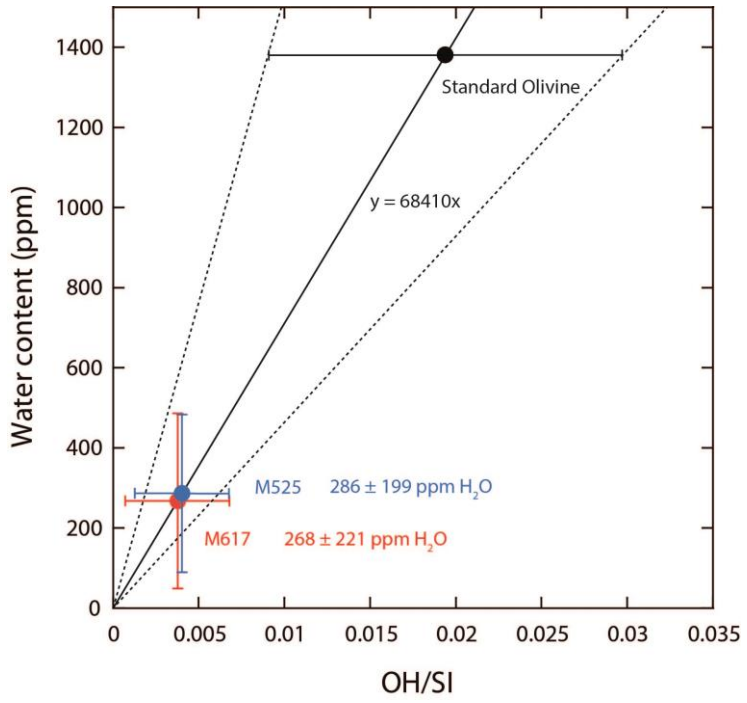

Figure A.15 Volatile analysis of the recovered olivine samples after Angström experiments (M525 and M617): estimation of the water content. Analyses were performed with Raman spectrometer. The OH/Si integrated ratio for silicate and water bands is proportional to the water content of the olivines. The standard sample water content was analyzed by SIMS. The standard deviation reported (1σ) represents the error from the technique and the variation due to crystal orientation. Each sample OH/Si is obtained from averaging at least 10 grains with different orientations.

Appendix B

Microphotographs and textural analyses

Appendix B: Microphotographs and textural analyses

During this PhD work, a significant amount of Scanning Electron Microscope clichés and optical images were obtained. These images were used to better constrain our samples to understand and interpret geophysical *in situ* measurements. These images were exploited for different cases such as melt fraction estimation, modal proportion estimate as well as obtain the different textural parameters details in our Chapter III and published work Freitas et al. 2019.

In this appendix, the additional information relative to macro and microphotographs, SEM images and textural analyses for the different sets of samples and studies are represented. These data were acquired in similar manner; this is why they are represented in a common section. They will be represented in subsection according each chapter to find them easily as the representations are similar.

Chapter III

Textural analyses in our chapter III have been mainly described and analyzed in our PCM paper. In this paper, results of textural analyses performed with FOAM software are given. In this section, we provide the binary images used to realize these analyses and histograms for grain size and grain orientation estimations.

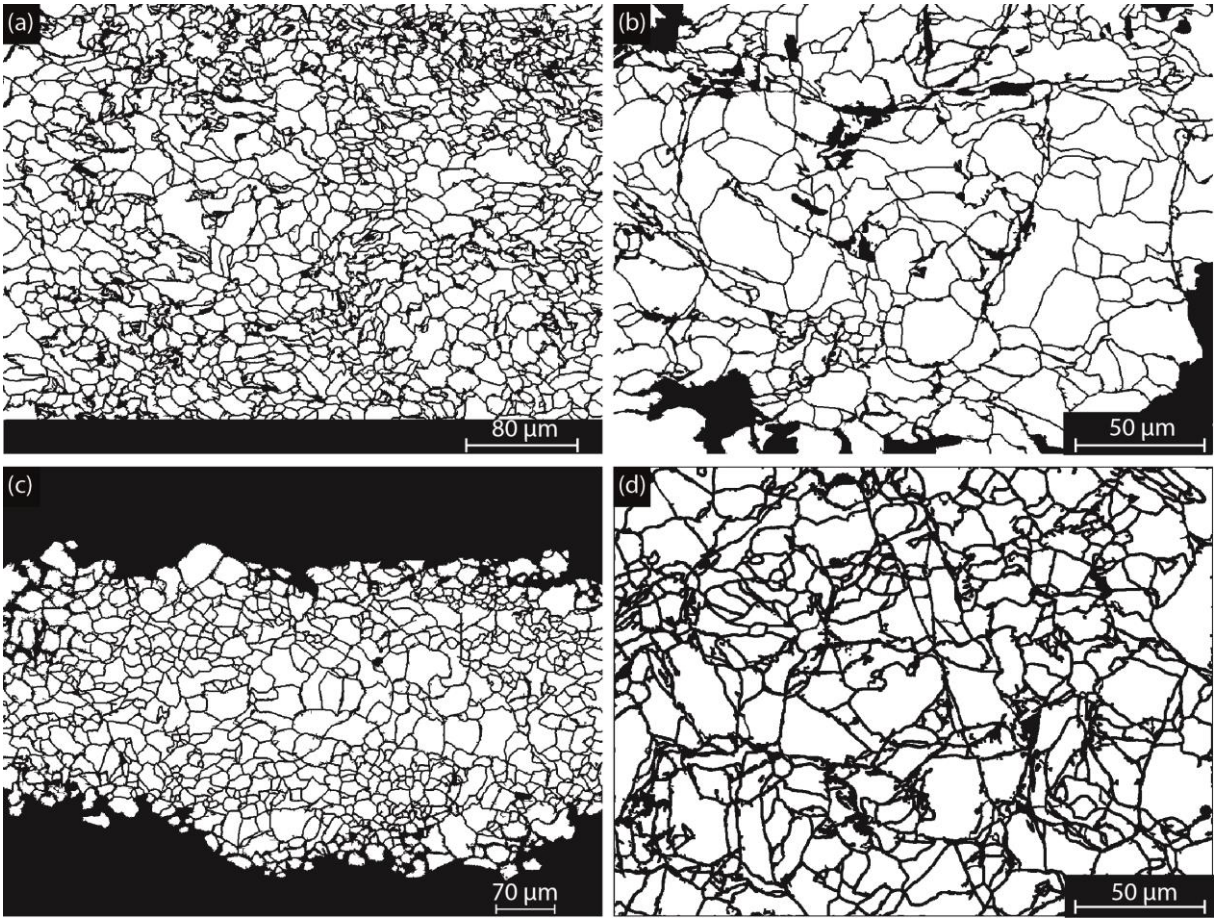

Figure B. 1 Binary or "squeletonized' images used for textural analyses and in particular FOAMS analyses. The binary images were made starting from high resolution BSE clichés, a color threshold was applied to discriminates holes, grains boundaries and melt pockets that were colored in black. Images were then improved manually to ensure boundaries are 2 pixels thick (mandatory for foam analysis). In addition, pictures must be only composed of 2 types of colors for a successful treatment, the images were manually checked to color the pixels that haven't been caught by the threshold. For a better accuracy grains with less than 5 pixels (<< 5 µm) were not considered, as their textural parameters will not be precise. Image processing was realized with GIMP and ImageJ. The result of FOAM processing of these images is given in table III.S1 in Freitas et al. (2019). (a) is 2% MORB sample (M324) (b) 1% MORB (M357) (c) 0.5% MORB (M343).

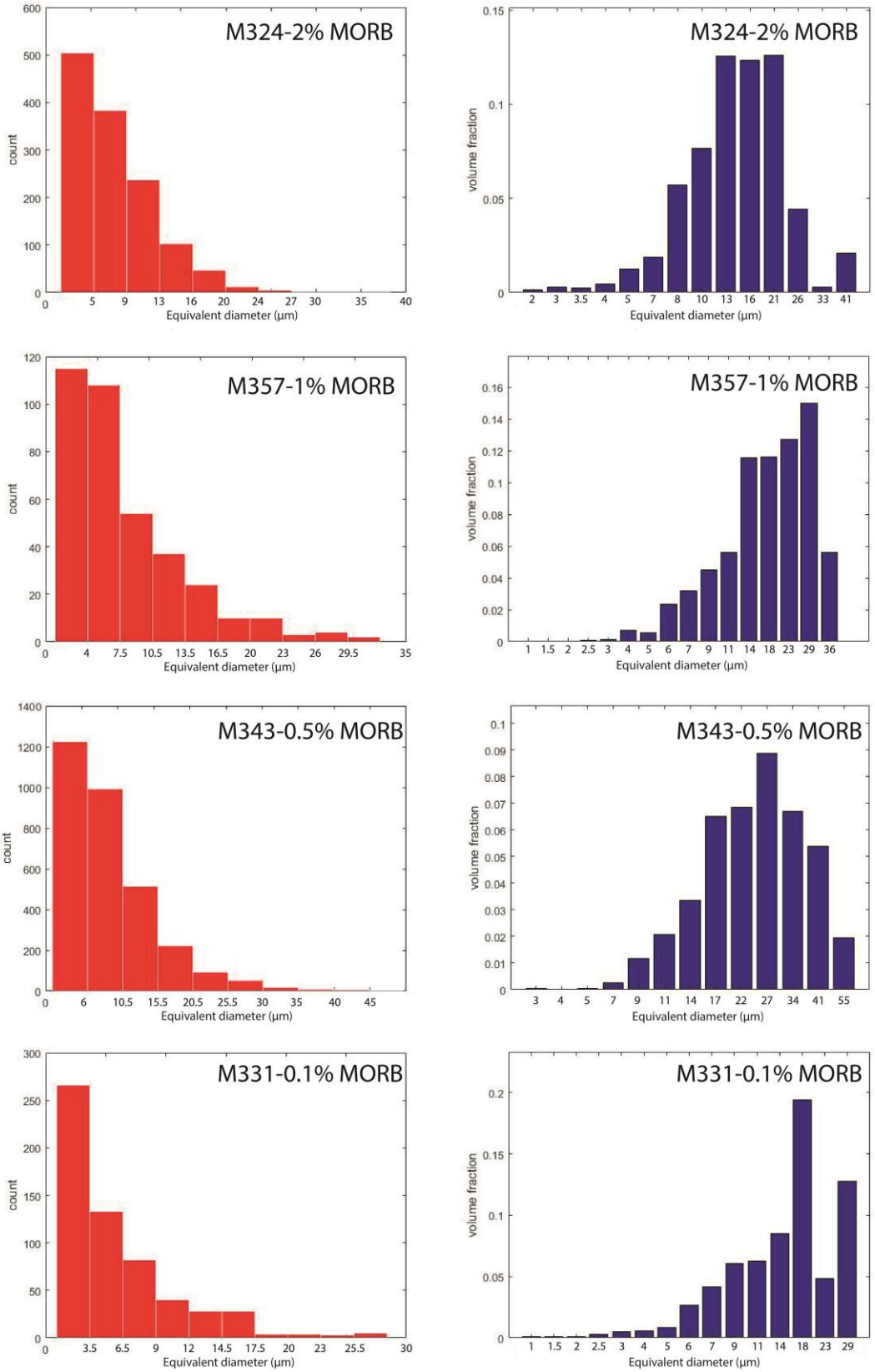

Figure B.2 Left frame (red histograms): grain size (equivalent diameter) frequency estimations are given for each sample. We observe a similar behavior with a log normal decreasing grain size for all of our samples. The majority of grains have equivalent diameter lower than 20 microns. The right frame shows the part of volume fraction of the sample represented by each bin size. The shape of the obtained curve is similar for each sample with a unimodal distribution with a maximum between 10 - 20 microns.

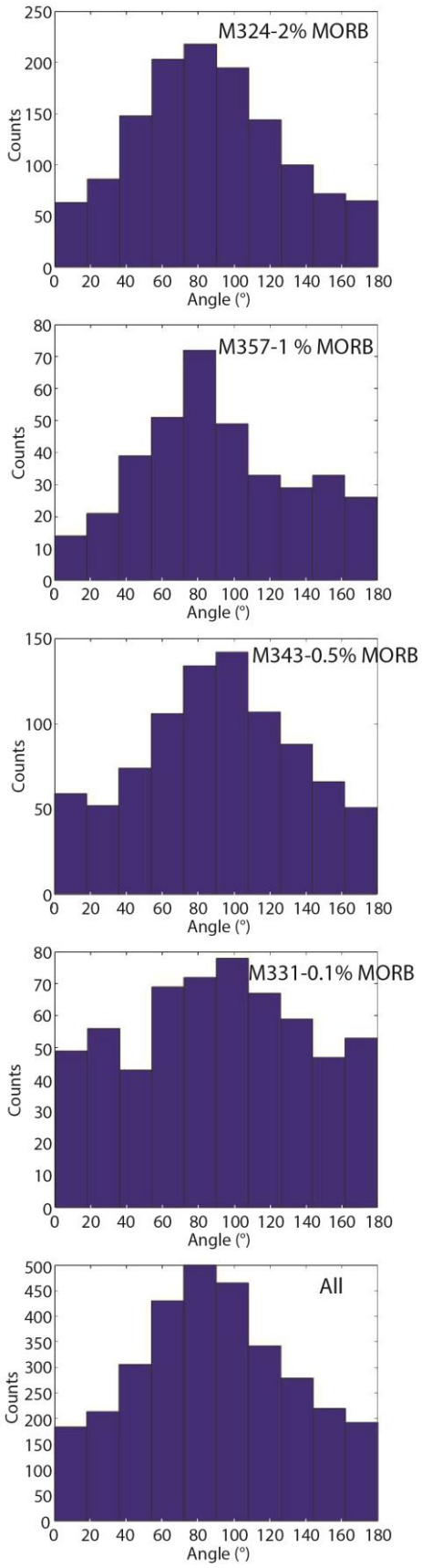

Figure B.3 Grain orientation (long axis of the best fitting ellipse of the grain surface) represented as a function of the number of counts for each 20° bin. The angle in degree is equal to 0 in the direction of cylinder/assembly axis (N-S or vertical) and 90° in the perpendicular direction to the sample cylinder axis (E-W or horizontal). The values highlight similar grain orientation/elongation in both our samples (2% MORB to 0.1%). All the histograms are showing similar pattern with curves showing one population of grains with a preferred orientation of 90°. This orientation of 90° is classical of multi anvil orientation because of pressure gradients existing in sample assembly brought by both pistons. However, the number of preferentially oriented grains in the 90° direction is not that significant with less than 3 times more grains oriented in this direction compare to 0° direction. This orientation estimation must be coupled with the elongation parameter of the grains. In fact, images highlight that our grains are mostly rounded as it is shown also by 2D shape parameters estimated in table III.S1 of Freitas et al. 2019.

Chapter IV

Textural analyses in our chapter IV for experiments at 12 GPa have been realized in a similar manner than those described in Freitas et al. (2019), Chapter III. In this section, we provide additional BSE images. The binary images used to realize these analyses are then given and histograms for grain size and grain orientation estimations are also provided.

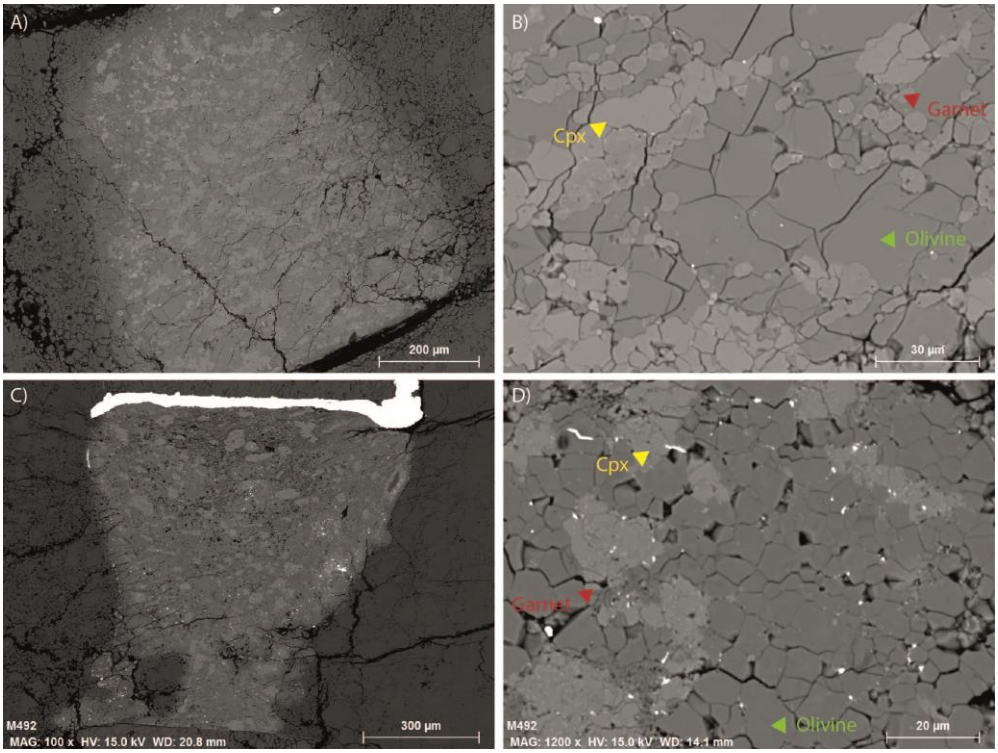

Figure B.4 BSE pictures for unmolten samples after EC/SV runs at 12 GPa. Top microphotographs are M421 (a,b), bottom ones are M492 (c,d). Left frames represent the whole sample view whereas right ones are zooms on the texture (phases labeled).

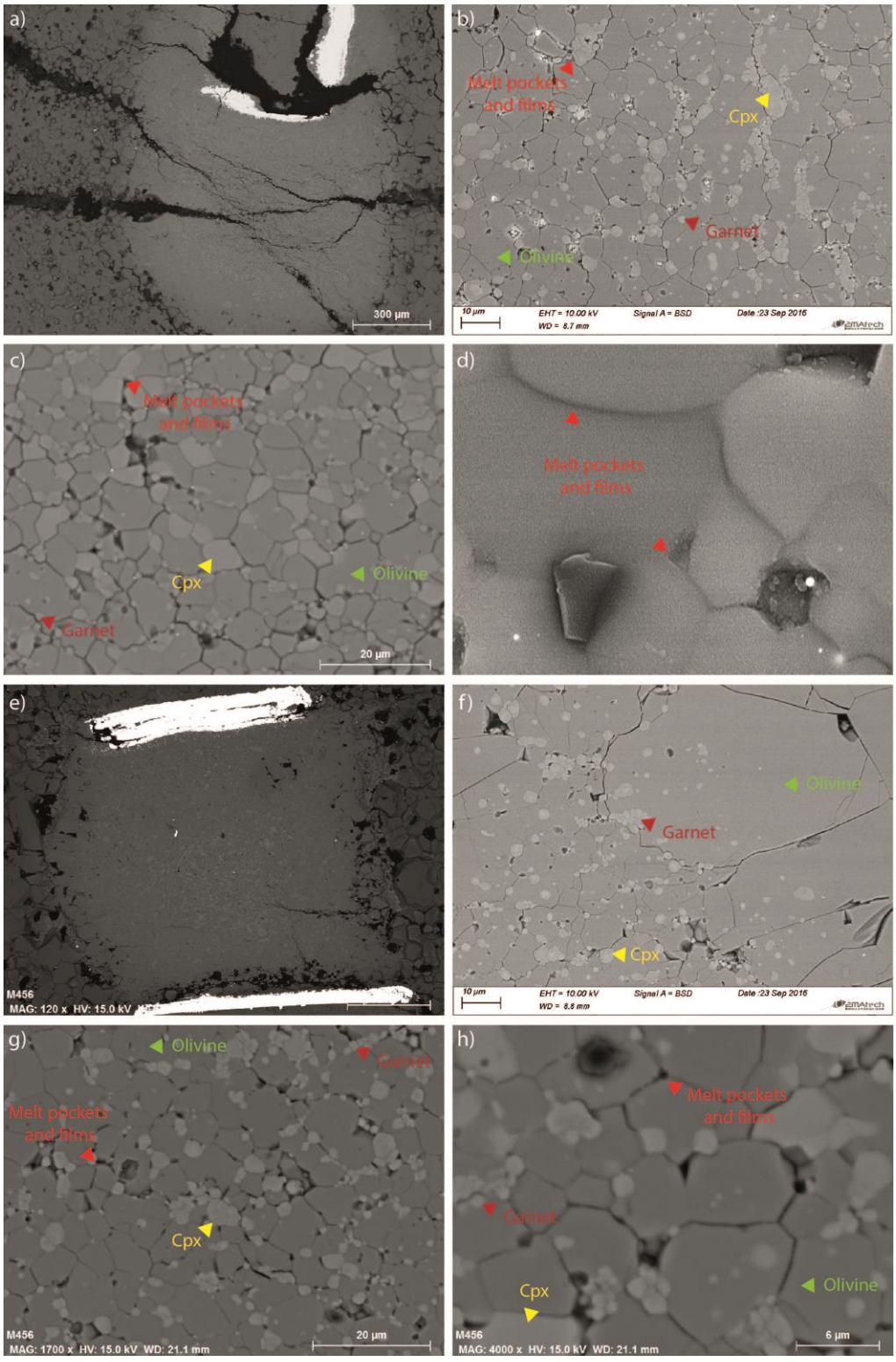

F*igure B.5 BSE pictures for molten samples with small melt fractions after EC/SV runs at 12 GPa. First microphotographs are M425 (a, b, c, d) with 2% of melt. Following microphotographs are M456 with 3.5% of melt (e, f, g, h). First frames (a, e) represent the large sample views whereas following ones are progressive zooms on the texture (phases labeled). Very high magnifications microphotographs were taken with FEG SEM. Samples phases are labeled in color.*

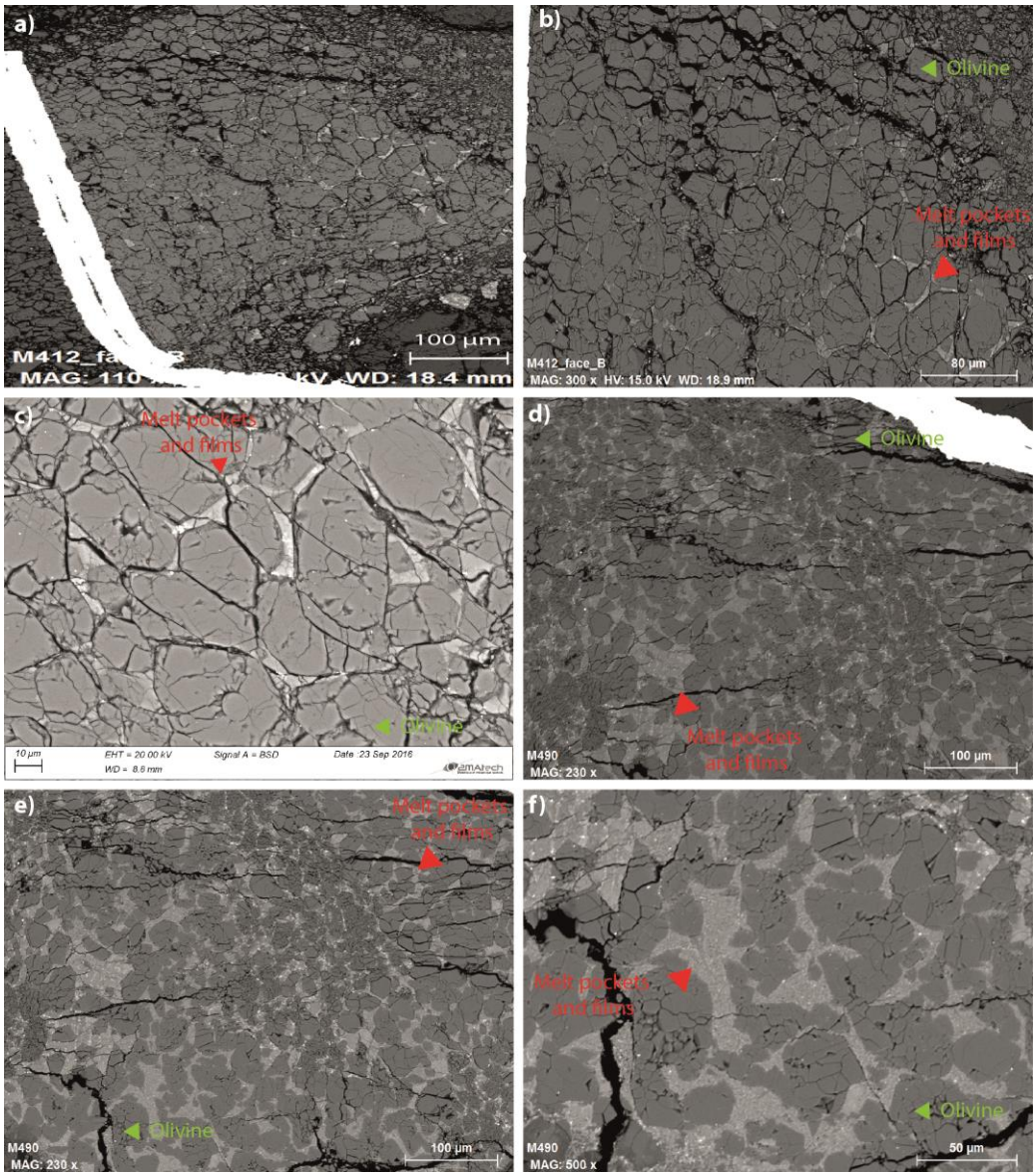

Figure B.6 BSE pictures for molten samples with large melt fractions after EC/SV runs at 12 GPa. First microphotographs are M412 (a, b, c) with 7% of melt, and bottom ones are M490 with 25% of melt (c, d, e). First frames (a, d) represent the large sample views whereas following ones are progressive zooms on the texture. Samples phases are labeled in color. Note: the bottom part of M412 was damaged and crushed by our hot epoxy molding machine which applies pressure and temperature for fast epoxy solidification (10 min), this machine was no longer used afterward to avoid sample damage when application of pressure.

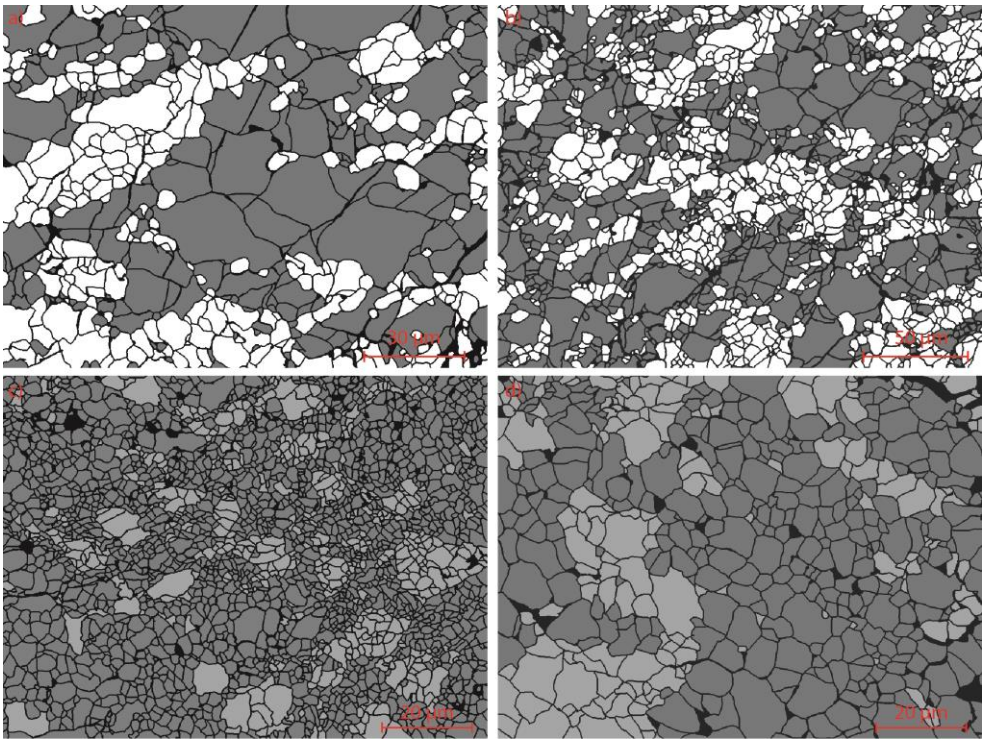

Figure B.7 Binary images from derived from BSE microphotograph for unmolten samples. a) and b) are examples made from M421 and c) and d) from M492. Grain boundaries and holes (from polishing, porosity at 12 GPa and high temperature is almost null) are drawn in black, olivine in dark grey and clinopyroxene and garnet are in white/light grey. BSE colors of Cpx and garnet are similar and difficult to distinguish; this is why they have been treated together.

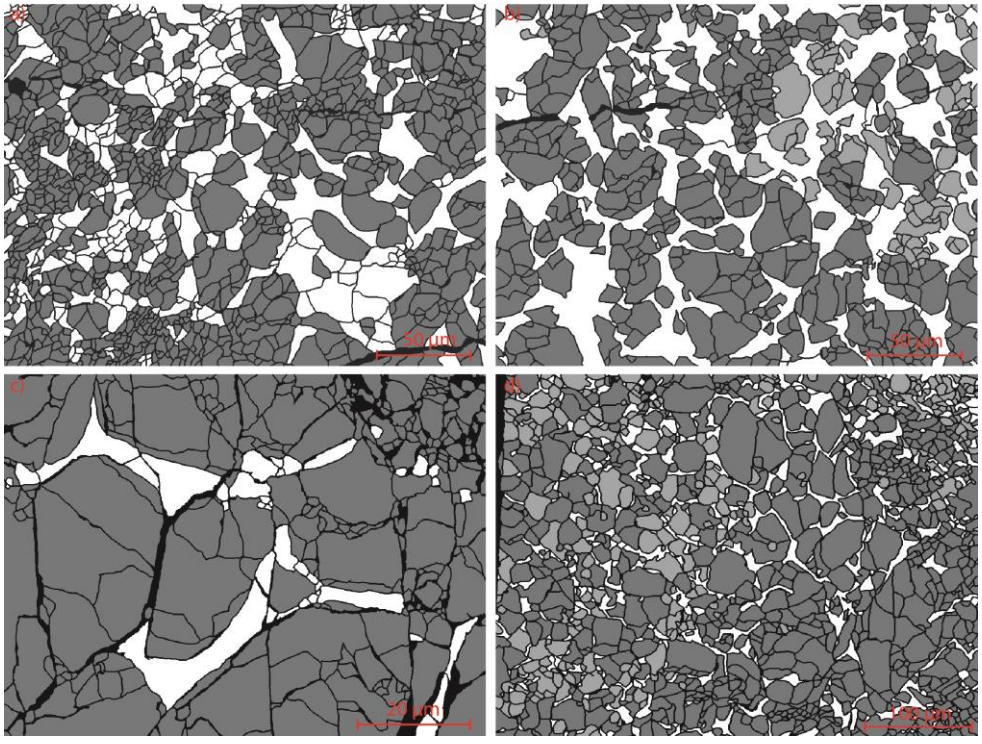

Figure B.8 Binary images derived from BSE microphotograph for large melt fraction samples. a), and b) are examples made from M490, 25% of melt and c), and d) from M412, 7% melt. Grain boundaries are drawn in black, melt is drawn in white, olivine in dark grey and clinopyroxene and garnet (when present) are in white/light grey.

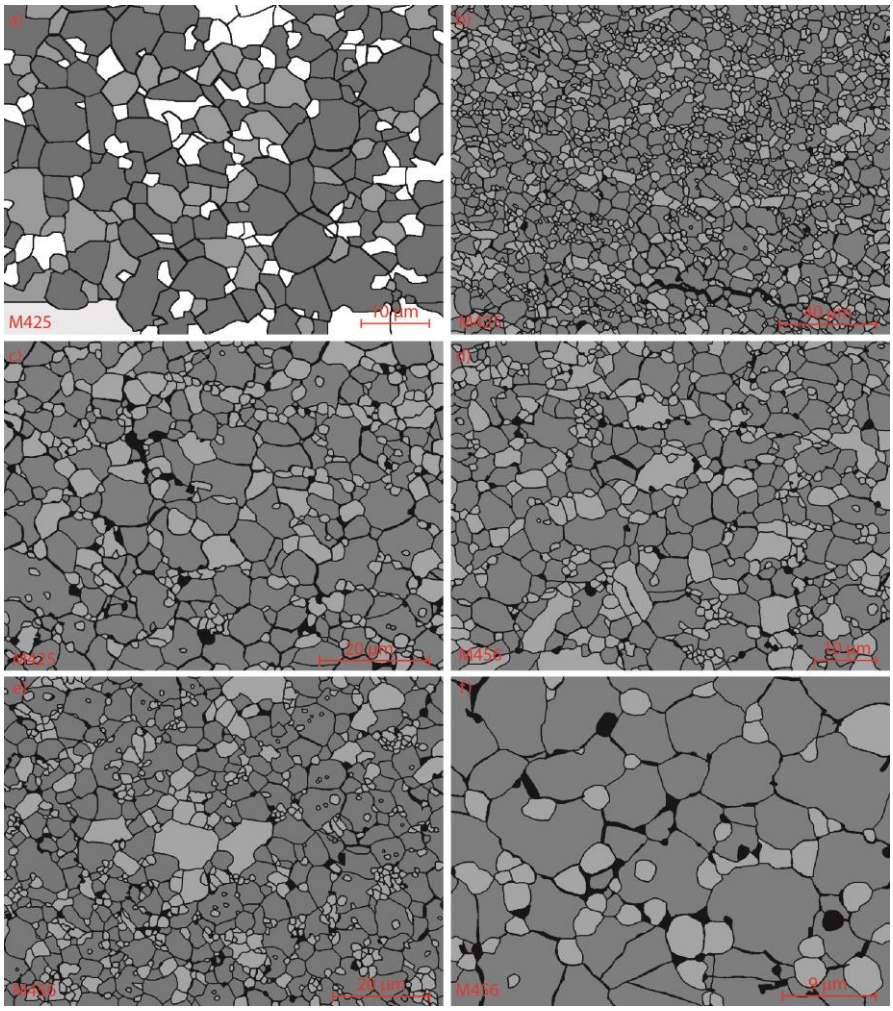

Figure B.9 Binary images from derived from BSE microphotograph for low melt fraction samples. a), b) and c) are examples made from M425, 2% melt and c), d) and e) from M456 (3.5% of melt). Grain boundaries and melt/holes (with completely wetting melt, we can assume that porosity is equal to the melt fraction) are drawn in black, olivine in dark grey and clinopyroxene and garnet are in white/light grey. BSE colors of Cpx and garnet are similar and difficult to distinguish; this is why they have been treated together expect from a) which is retrieved form a chemical map where Cpx is in light grey and garnet in white.

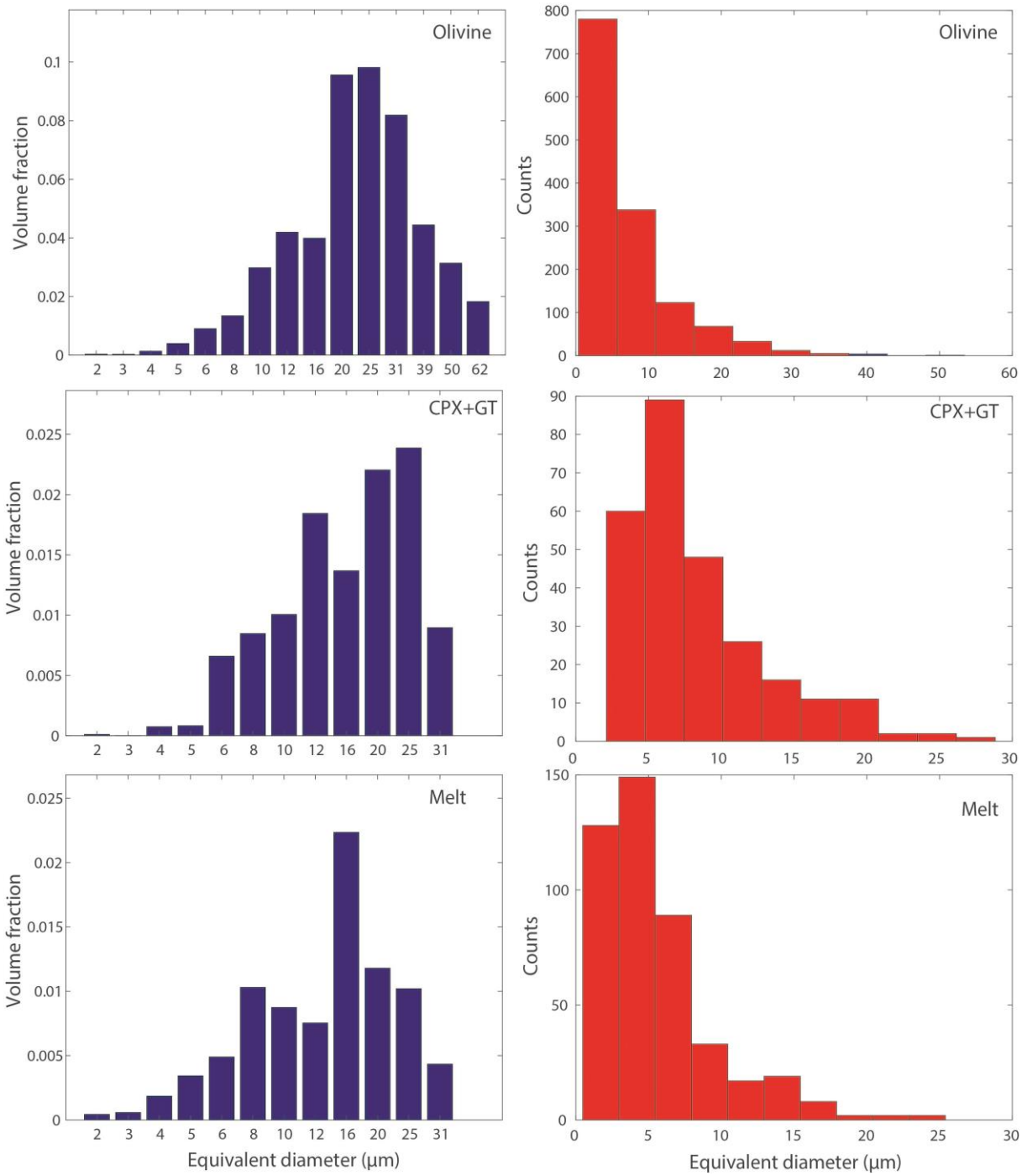

Figure B.10 Grain size and volume fraction as a function of grain equivalent diameter of all computed FOAMS images for each phase on M412. Cpx and Gt are treated together due to similar color in BSE microphotographs.

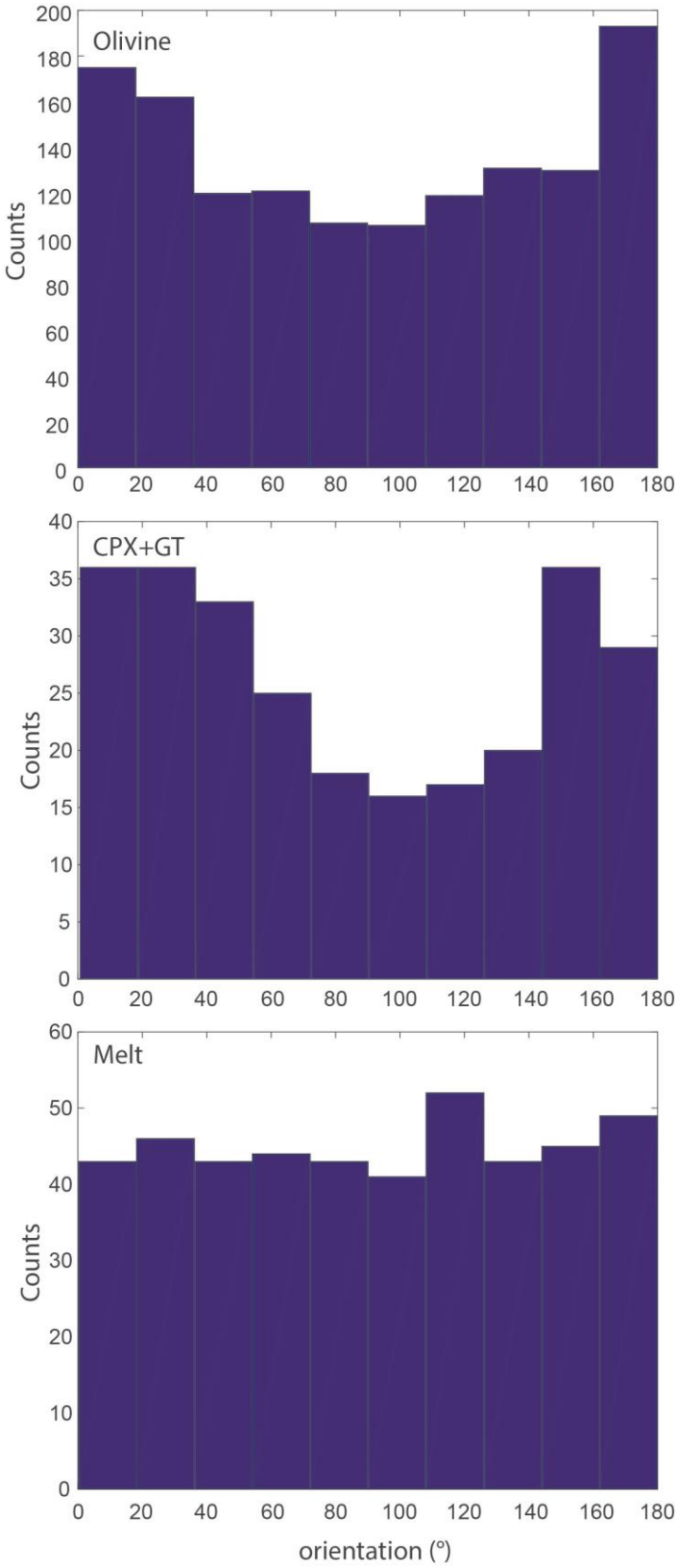

Figure B.11 Orientation of long axis for each phase derived from FOAMS analysis for M412. 90° correspond to the vertical axis of sample cylinder and 0° is perpendicular sample cylinder axis.

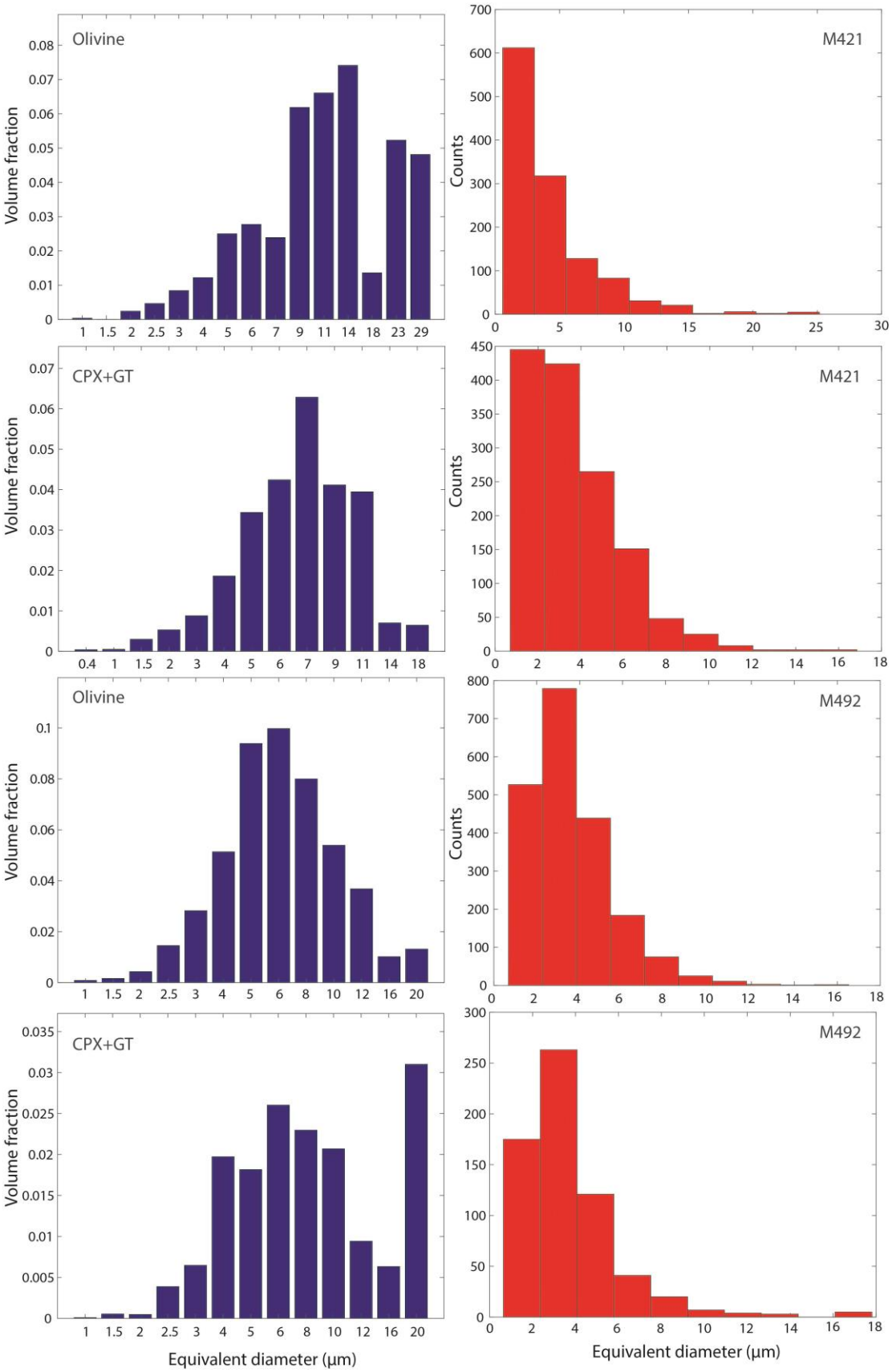

Figure B.12 Grain size and volume fraction as a function of grain equivalent diameter of all computed FOAMS images for each phase on M421 and M492, unmolten samples. Cpx and Gt are treated together due to similar color in BSE microphotographs.

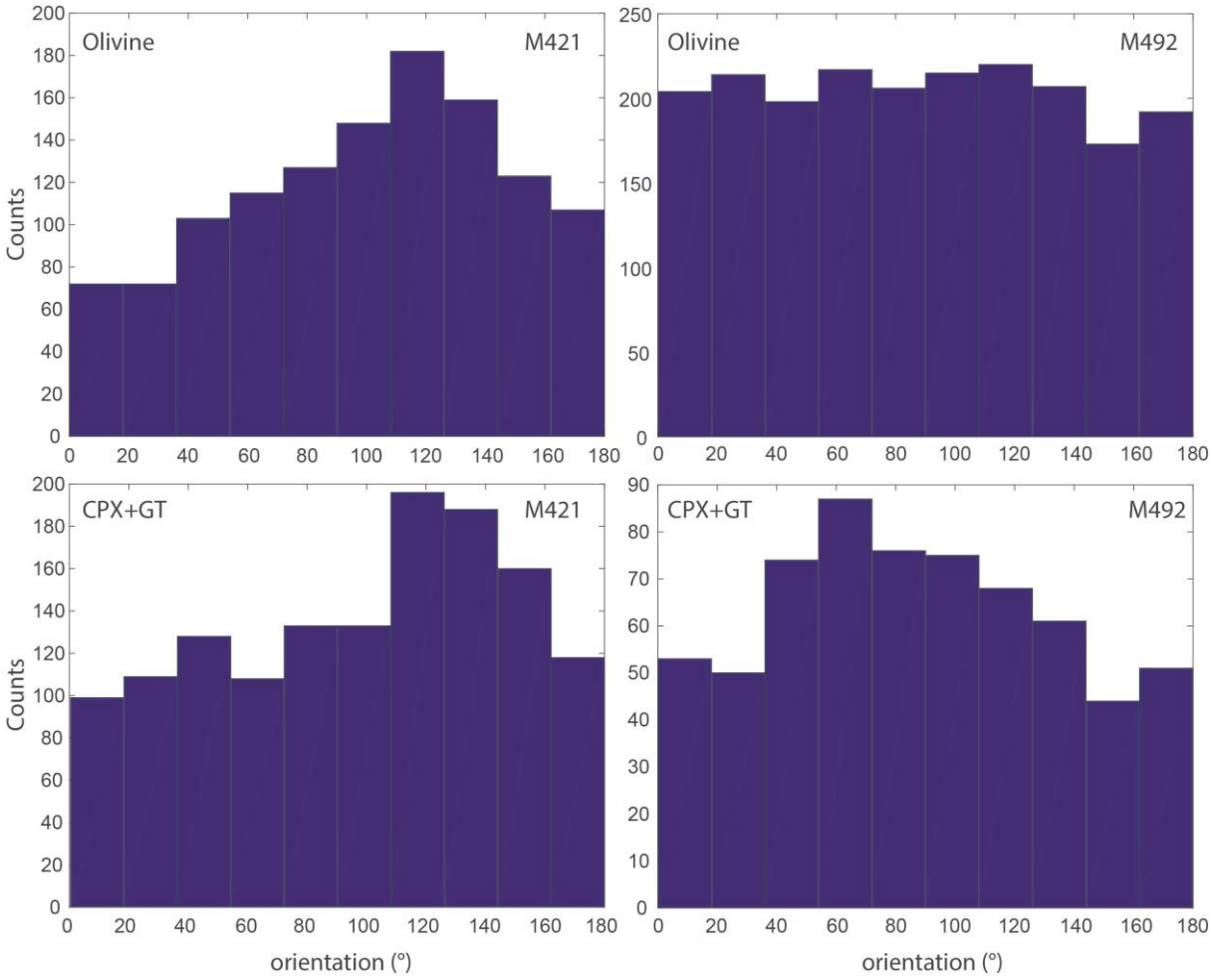

Figure B.13 Orientation of long axis for each phase derived from FOAMS analysis. 90° correspond to the vertical axis of sample cylinder and 0° is perpendicular sample cylinder axis. M421 is on left and M492 on right frames respectively

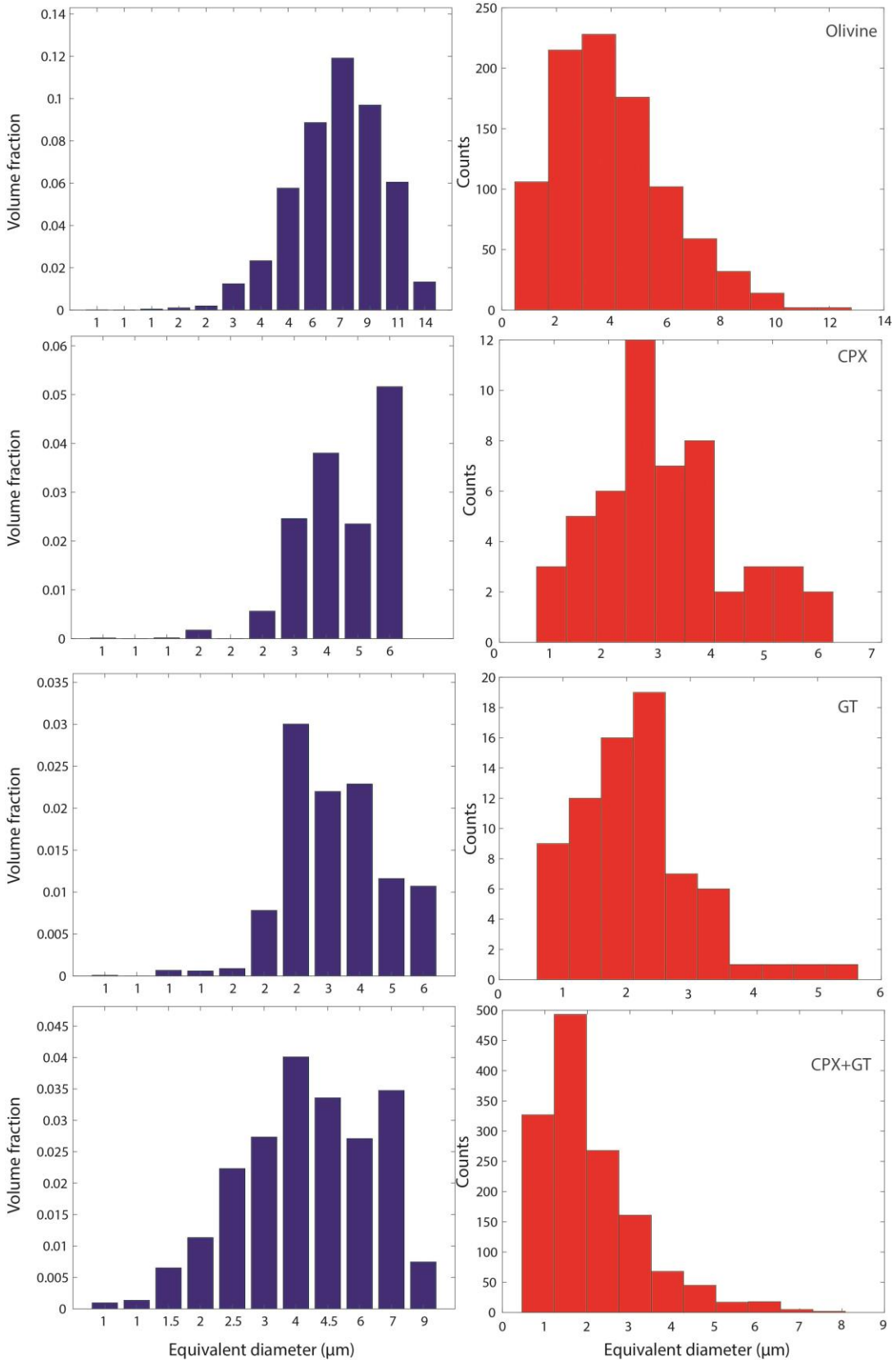

Figure B.14 Grain size and volume fraction as a function of grain equivalent diameter of all computed FOAMS images for each phase on M425. Cpx and Gt are treated together due to similar color in BSE microphotographs, however chemical maps allowed having individual phase information but with a lower number of analyzed grain. Melt has not been treated because it was only present at grain boundaries and needed high resolution images.

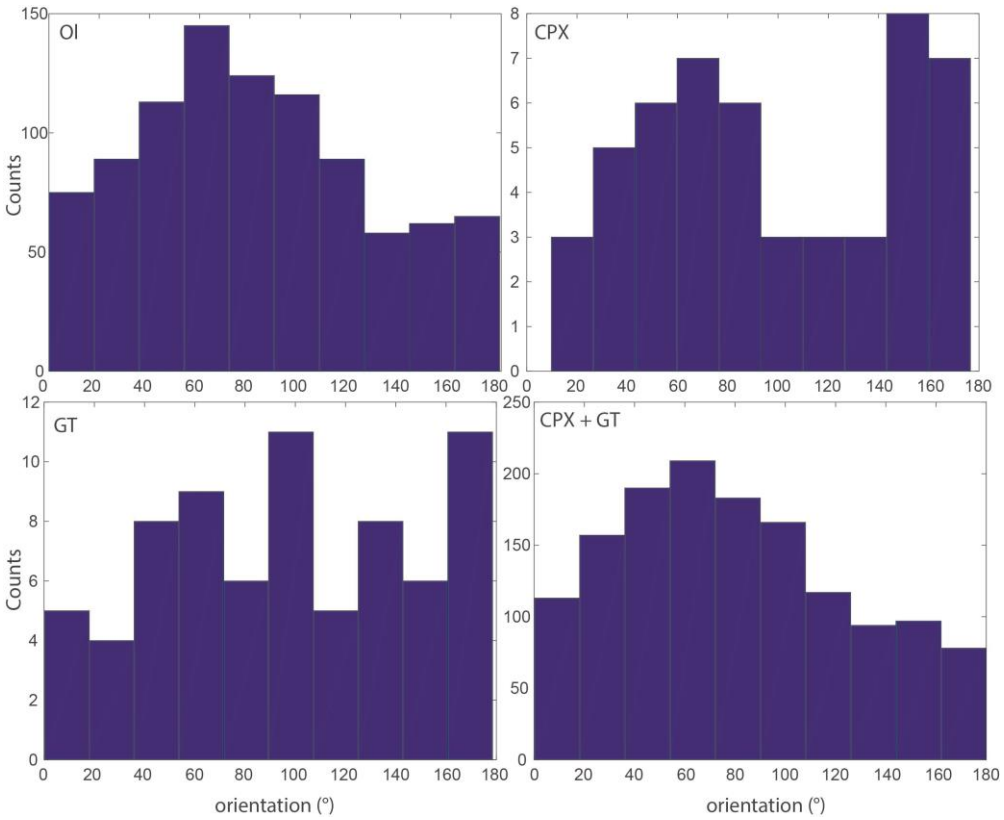

Figure B.15 Orientation of long axis for each phase derived from FOAMS analysis for M425. 90° correspond to the vertical axis of sample cylinder and 0° is perpendicular sample cylinder axis.

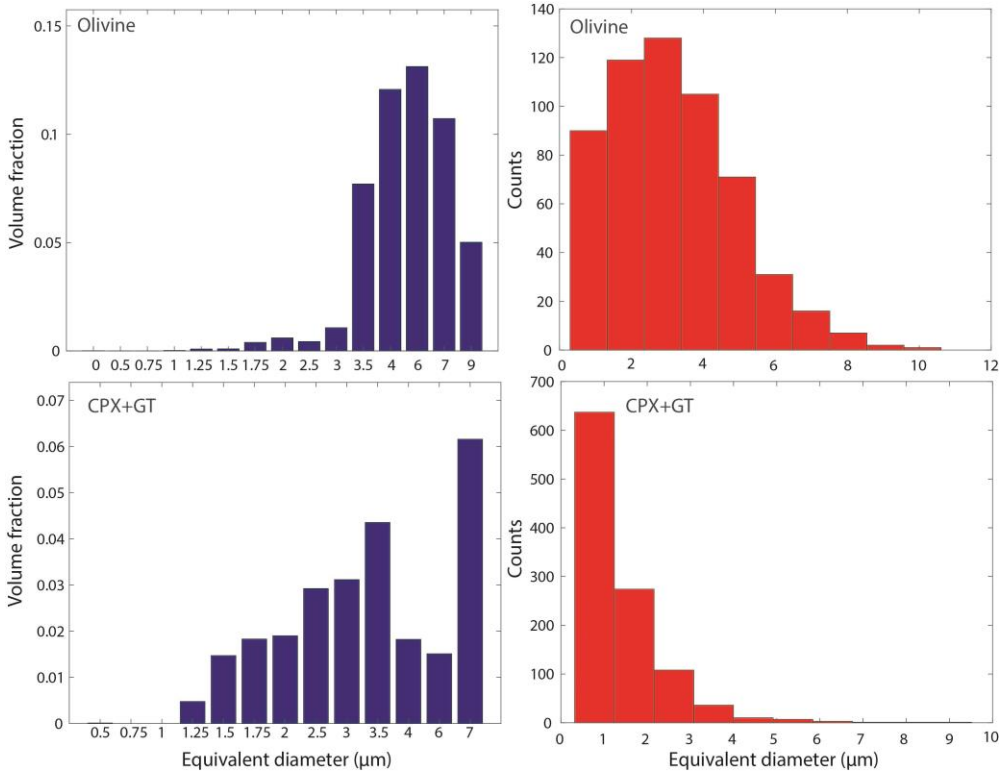

Figure B.16 Grain size and volume fraction as a function of grain equivalent diameter of all computed FOAMS images for each phase on M456. Cpx and Gt are treated together due to similar color in BSE microphotographs. Melt has not been treated because it was only present at grain boundaries and needed high resolution images.

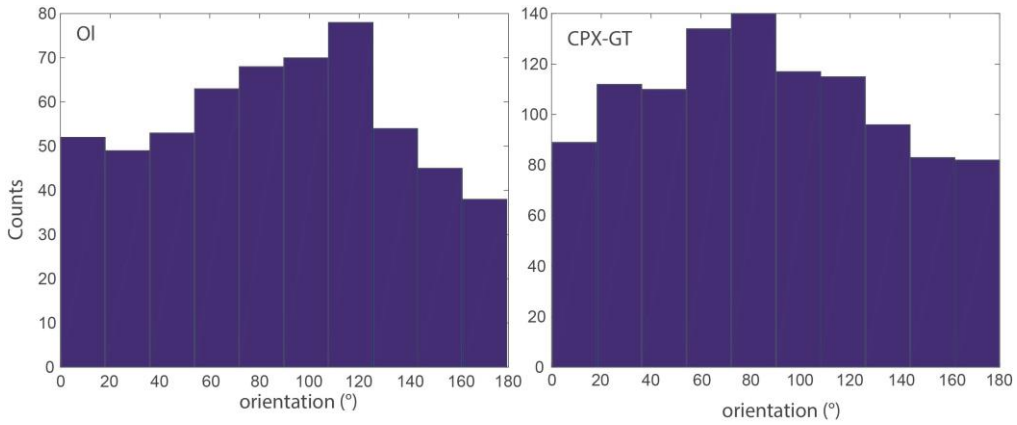

Figure B.17 Orientation of long axis for each phase derived from FOAMS analysis for M456. 90° correspond to the vertical axis of sample cylinder and 0° is perpendicular sample cylinder axis.

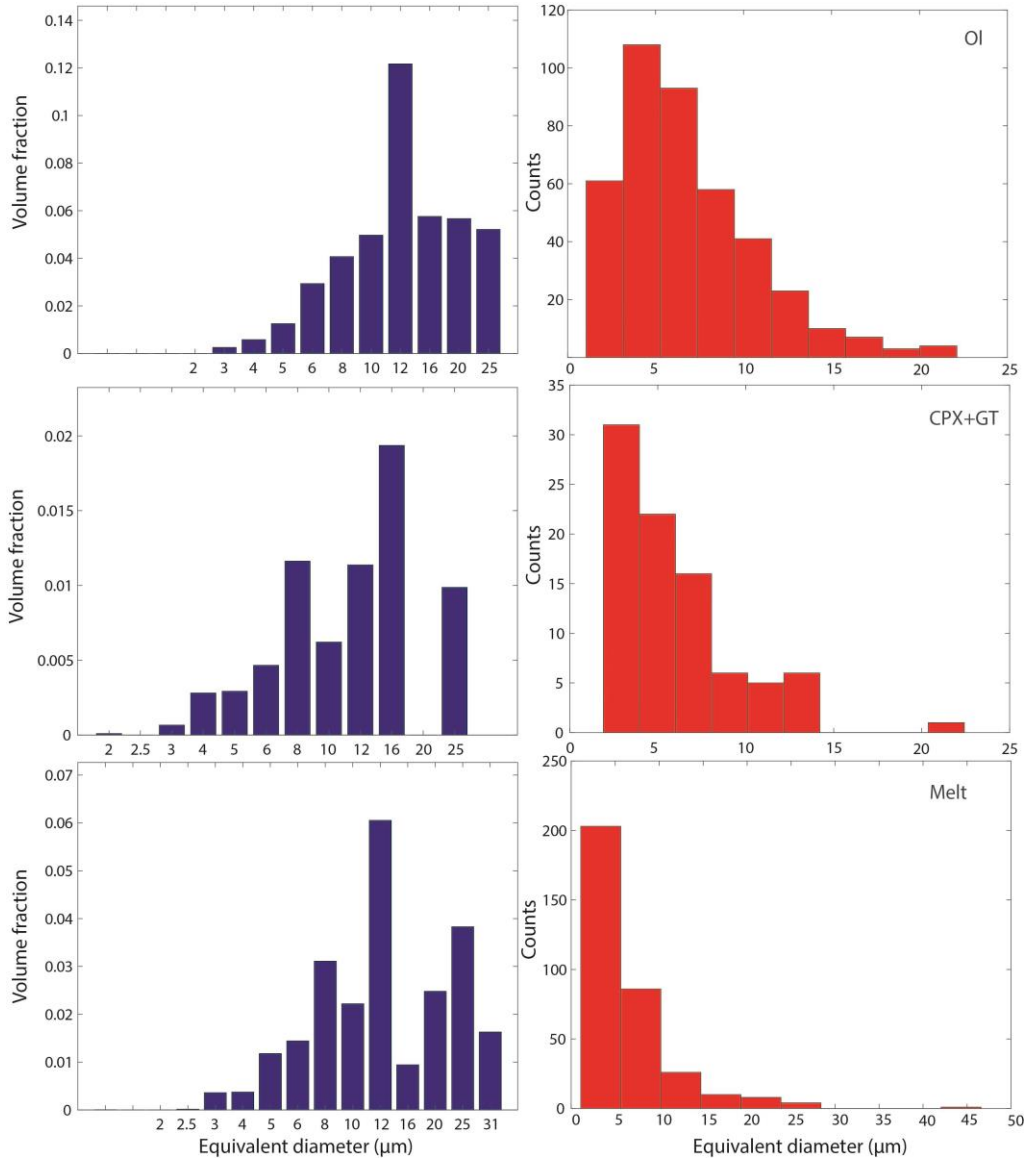

Figure B.18 Grain size and volume fraction as a function of grain equivalent diameter of all computed FOAMS images for each phase on M490. Cpx and Gt are treated together due to similar color in BSE microphotographs.

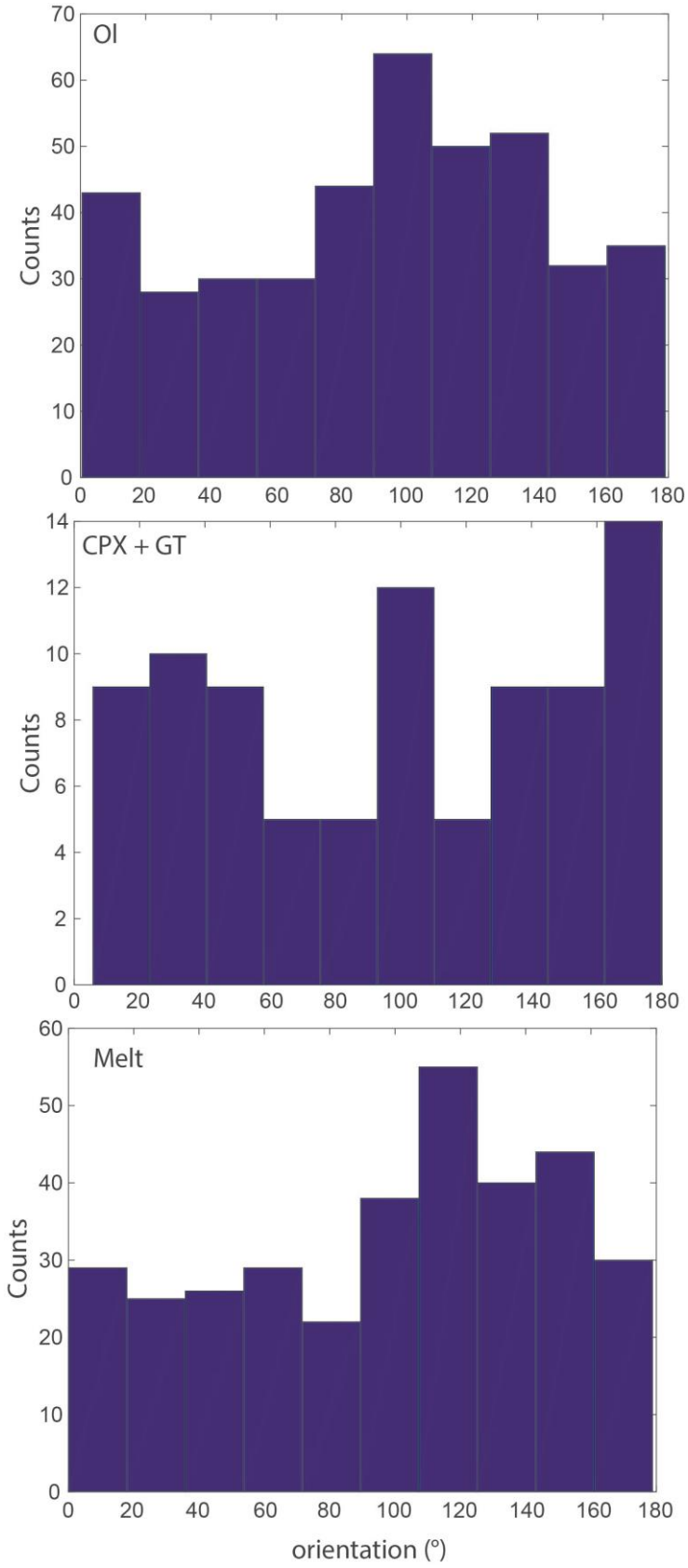

Figure B.19 Orientation of long axis for each phase derived from FOAMS analysis for M490. 90° correspond to the vertical axis of sample cylinder and 0° is perpendicular sample cylinder axis.

Chapter V

Textural analyses in our chapter V for experiments at 6 and 9 GPa have been realized in a similar manner than those described in Freitas et al., (2019), Chapter III. In this section, we provide additional BSE images. The binary images used to realize these analyses are then given and histograms for grain size and grain orientation estimations are also provided.

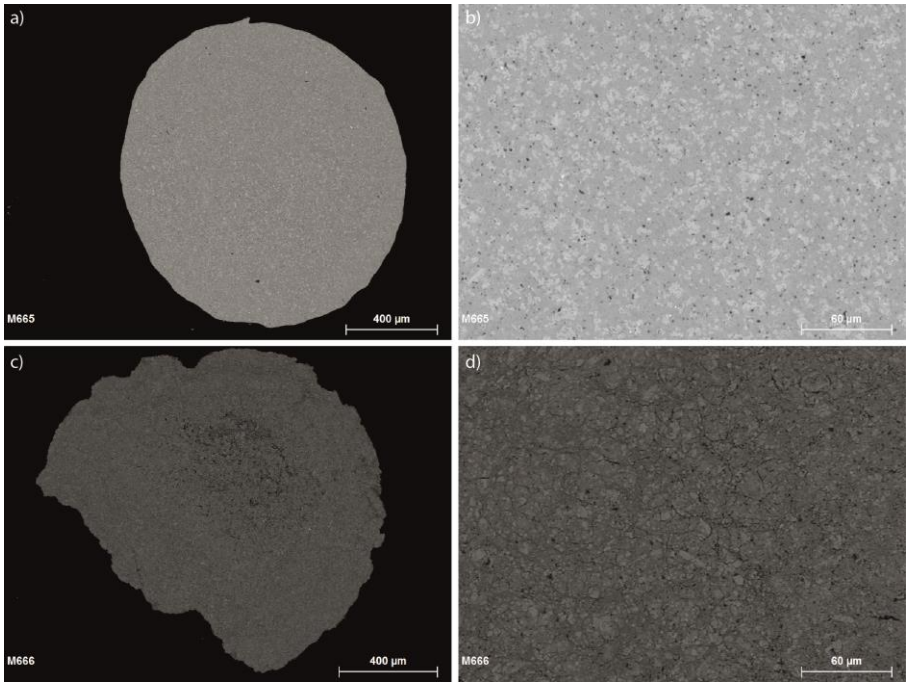

Figure B.20 BSE microphotographs of chips recovered on starting material samples after synthesis runs. a) and b) are M665 at 6 GPa and c) and d) M666 at 9 GPa. The images highlight a very homogeneous mineralogical composition and distribution throughout the sample. The grain size was found to be very small due to moderate temperatures of synthesis run in order to keep volatiles.

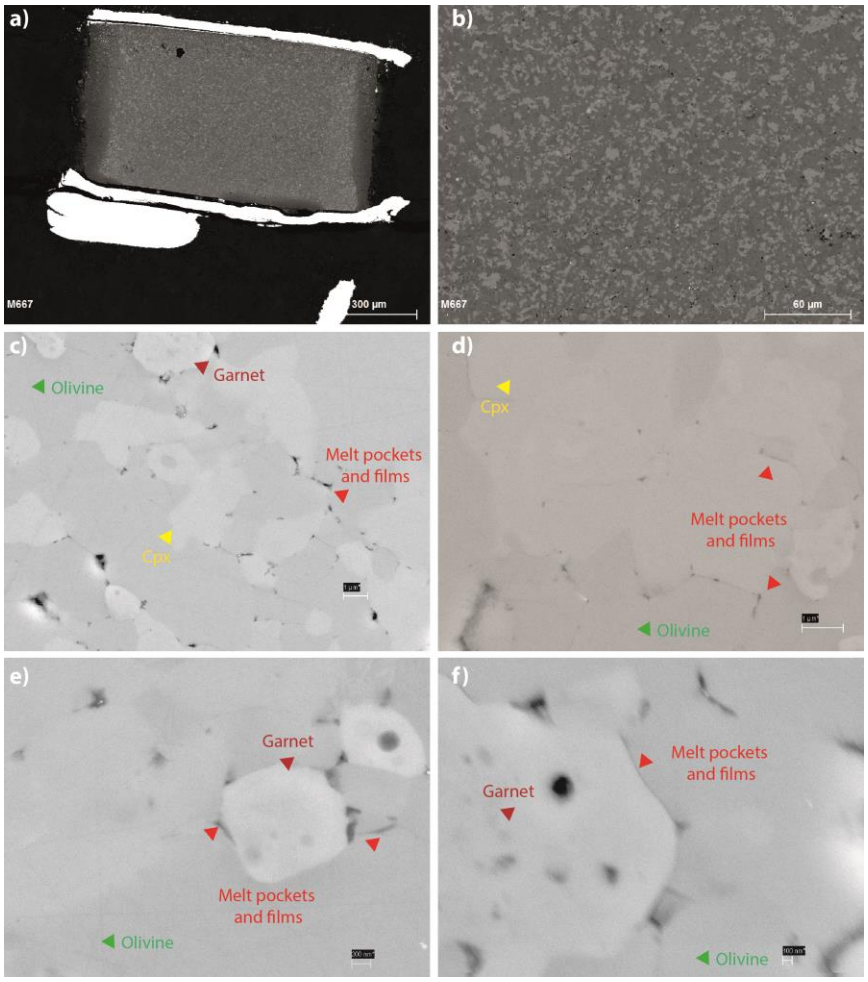

Figure B.21 BSE microphotographs of M667 recovered after EC experiment at 6 GPa. a) and b) are large scale images showing sample homogeneity. A little reaction on sample borders with MgO capsule is visible and is here visually enforced because this zone is covered by epoxy resin (softer during polishing, needed impregnation). c) , d), e) and f) are FEG SEM images for melt identification at grain boundaries.

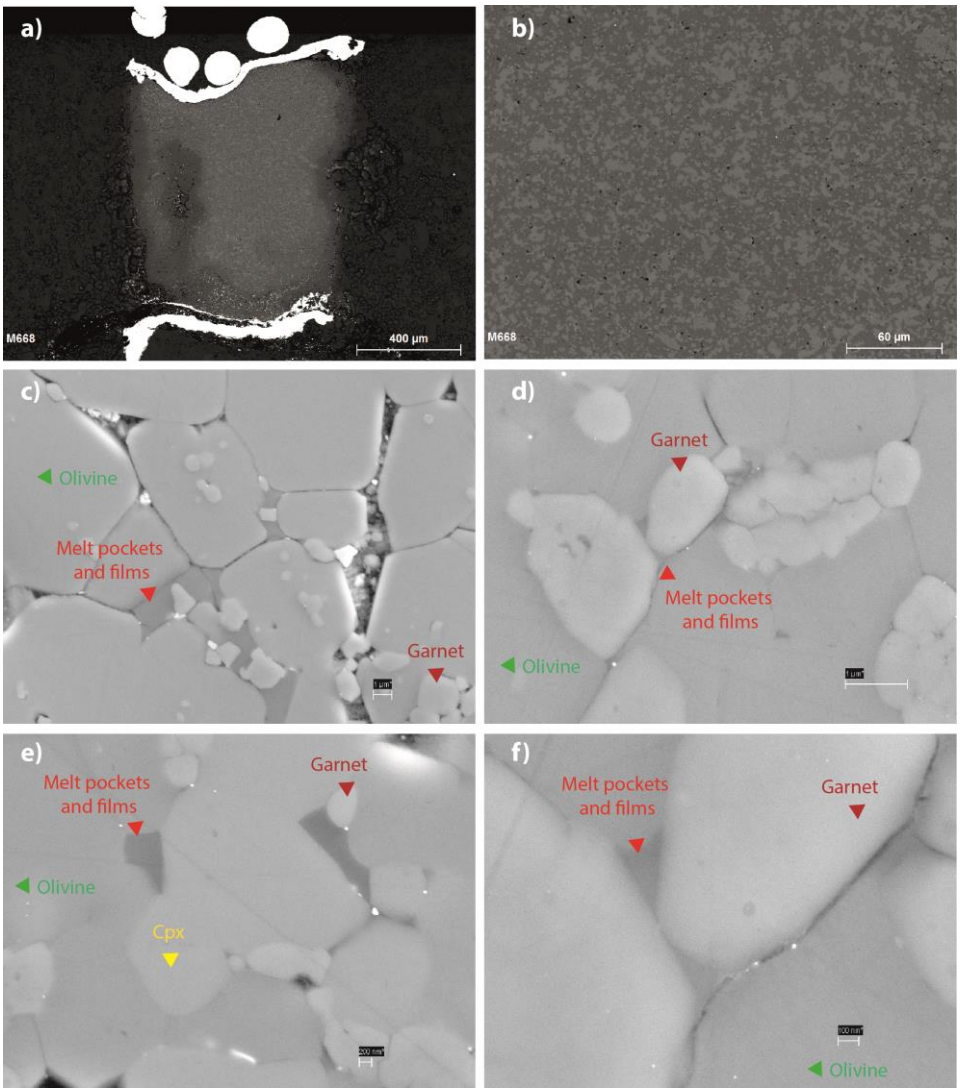

Figure B.22 BSE microphotographs of M668 recovered after EC experiment at 9 GPa. a) and b) are large scale images showing sample homogeneity. A little reaction on sample borders with MgO capsule is visible and is here visually enforced because this zone is covered by epoxy resin (softer during polishing, needed impregnation). A melt pool is visible at sample's center left indicating significant amount of melt was produced during this experiment. c) , d), e) and f) are FEG SEM images for melt identification at grain boundaries.

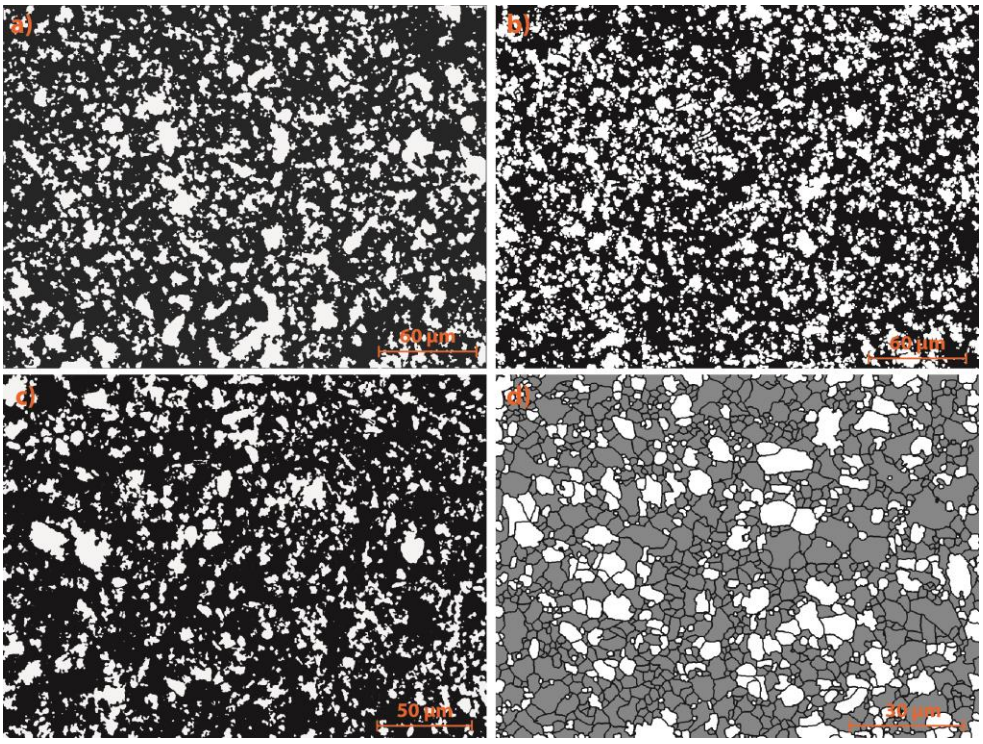

Figure B.23 Binary images derived from BSE microphotograph for starting material sample before EC/SV run at 6 GPa (M665). Clichés a), b) and c) served to get olivine (black) and pyroxene + garnet (white) proportions. Image d) is an example of binary image used in for FOAM's analysis (olivine in grey, pyroxenes + garnet in white, grain boundaries in black).

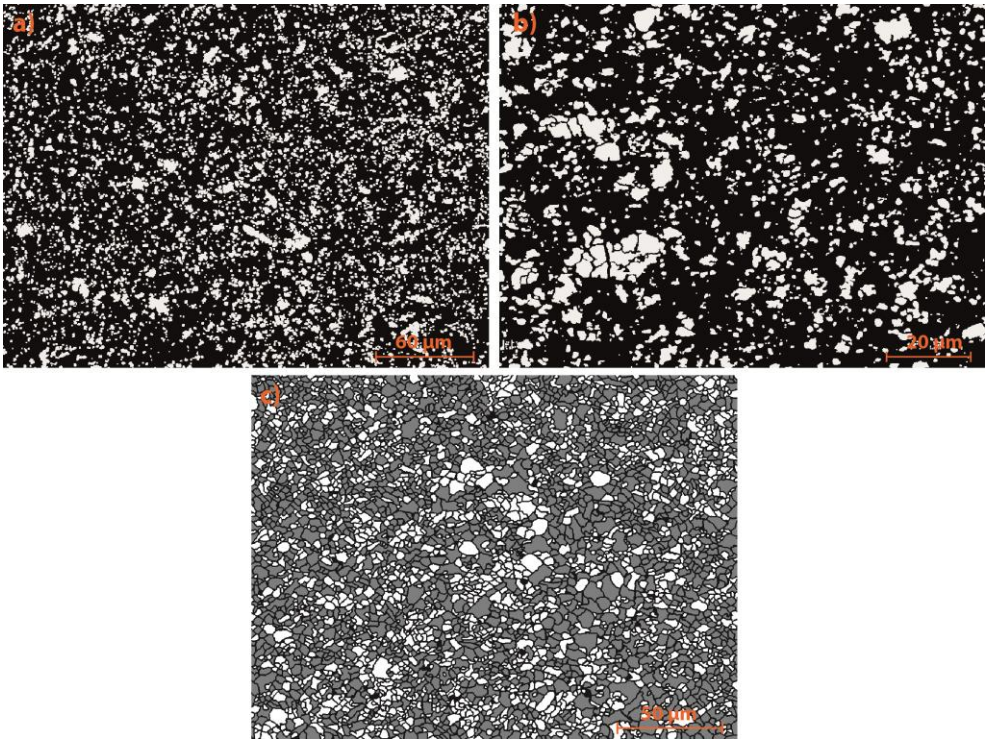

Figure B.24 Binary images derived from BSE microphotograph for starting material sample before EC/SV run at 9 GPa (M666). Images a) and b) served to get olivine (black) and pyroxene + garnet (white) proportions. Image c) is an example of binary image used in for FOAM's analysis (olivine in grey, pyroxenes + garnet in white, grain boundaries in black).

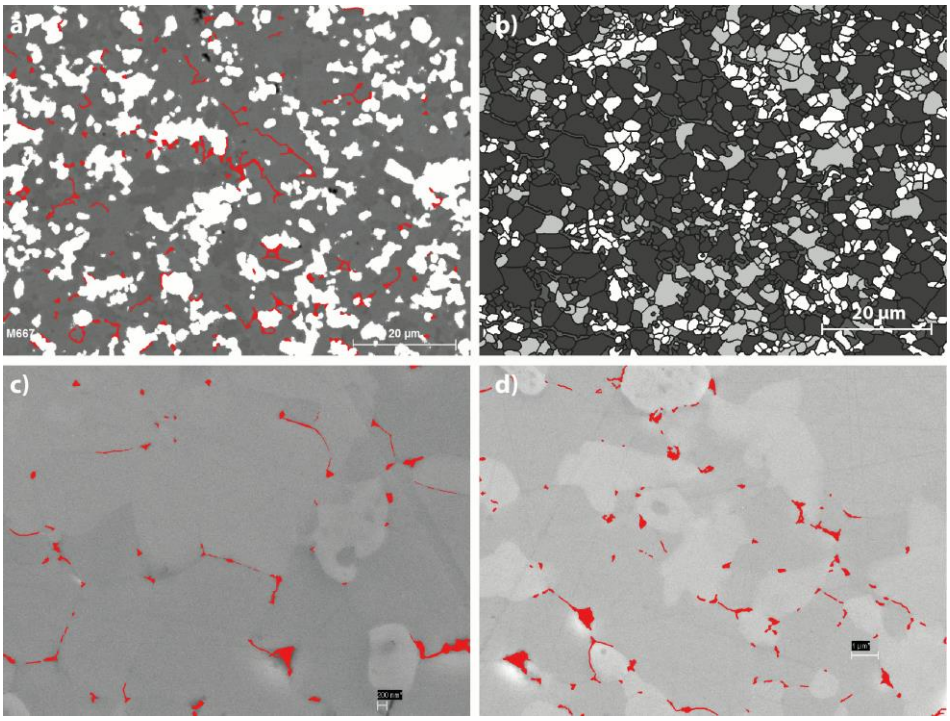

Figure B.25 Binary images derived from BSE microphotographs for the sample recovered after EC/SV run at 6 GPa (M667).Image a) served to get melt (red), olivine (dark grey) and pyroxene + garnet (white). Image b) is an example used to obtain textural parameters: olivine in dark grey, melt in grey, pyroxene in light grey and garnet in white. Images c), and d) FEG SEM microphotographs treated to get the melt fraction (in red). Each image is treated by hand because contrasts are usually too small to ensure an automatic perfect recognition of each phase.

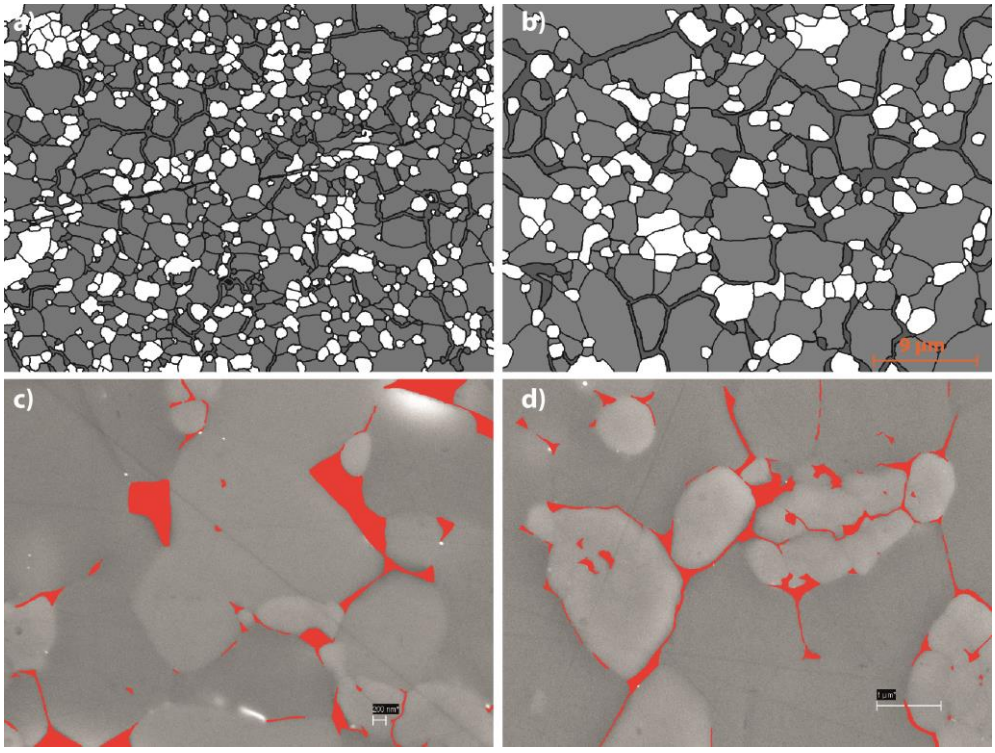

Figure B.26 Binary images derived from BSE microphotographs for the sample recovered after EC/SV run at 9GPa (M668).Images a) and b) are used to obtain textural parameters: olivine in grey, melt in dark grey, pyroxenes + garnet in white. Images c), and d) FEG SEM microphotographs treated to get the melt fraction (in red). Each image is treated by hand because contrasts are usually too small to ensure an automatic perfect recognition of each phase.

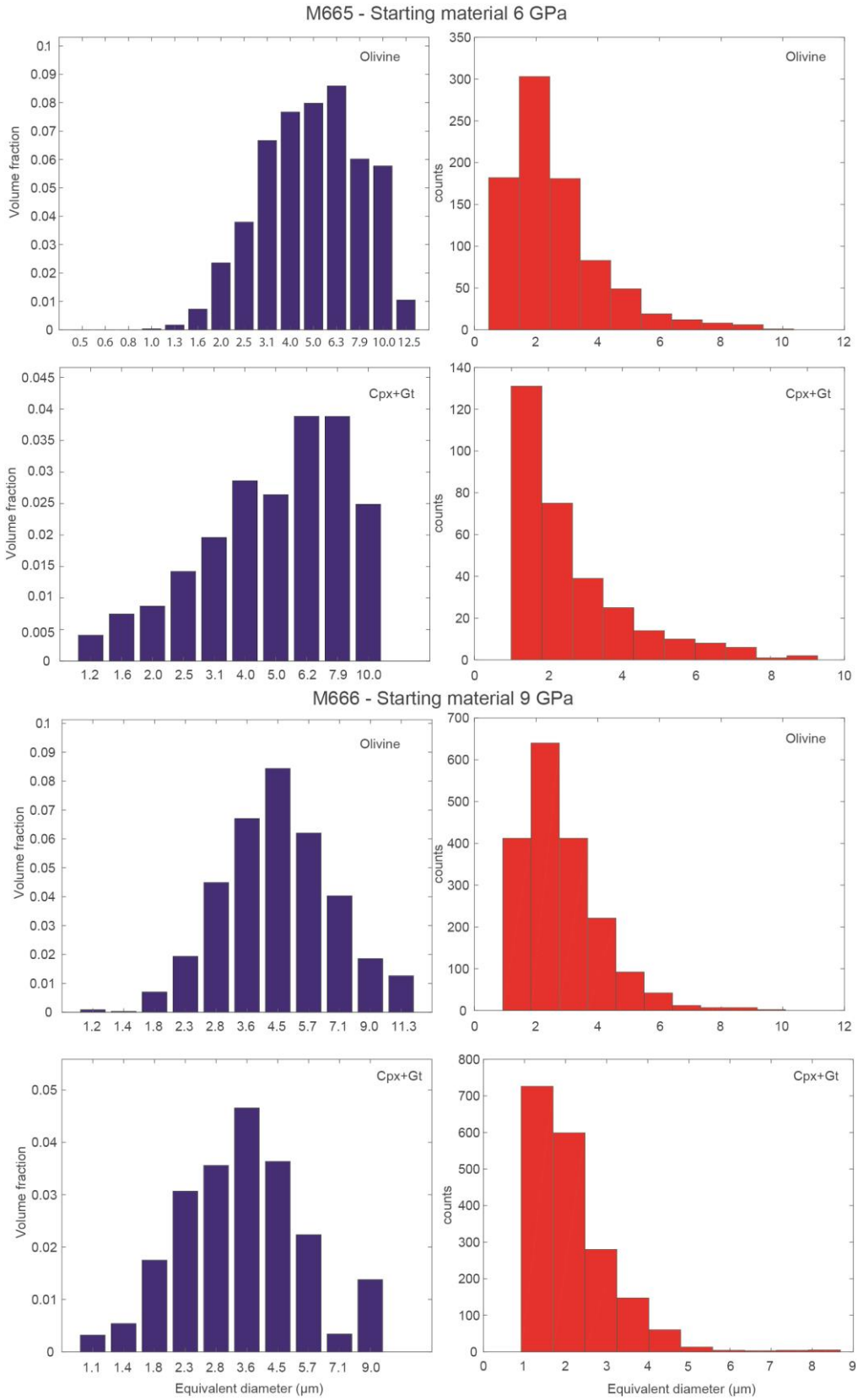

Figure B.27 Grain size and volume fraction as a function of grain equivalent diameter of all computed FOAMS images for each phase for M665 and M666 starting materials, unmolten samples. Cpx and Gt are treated together due to similar color in BSE microphotographs.

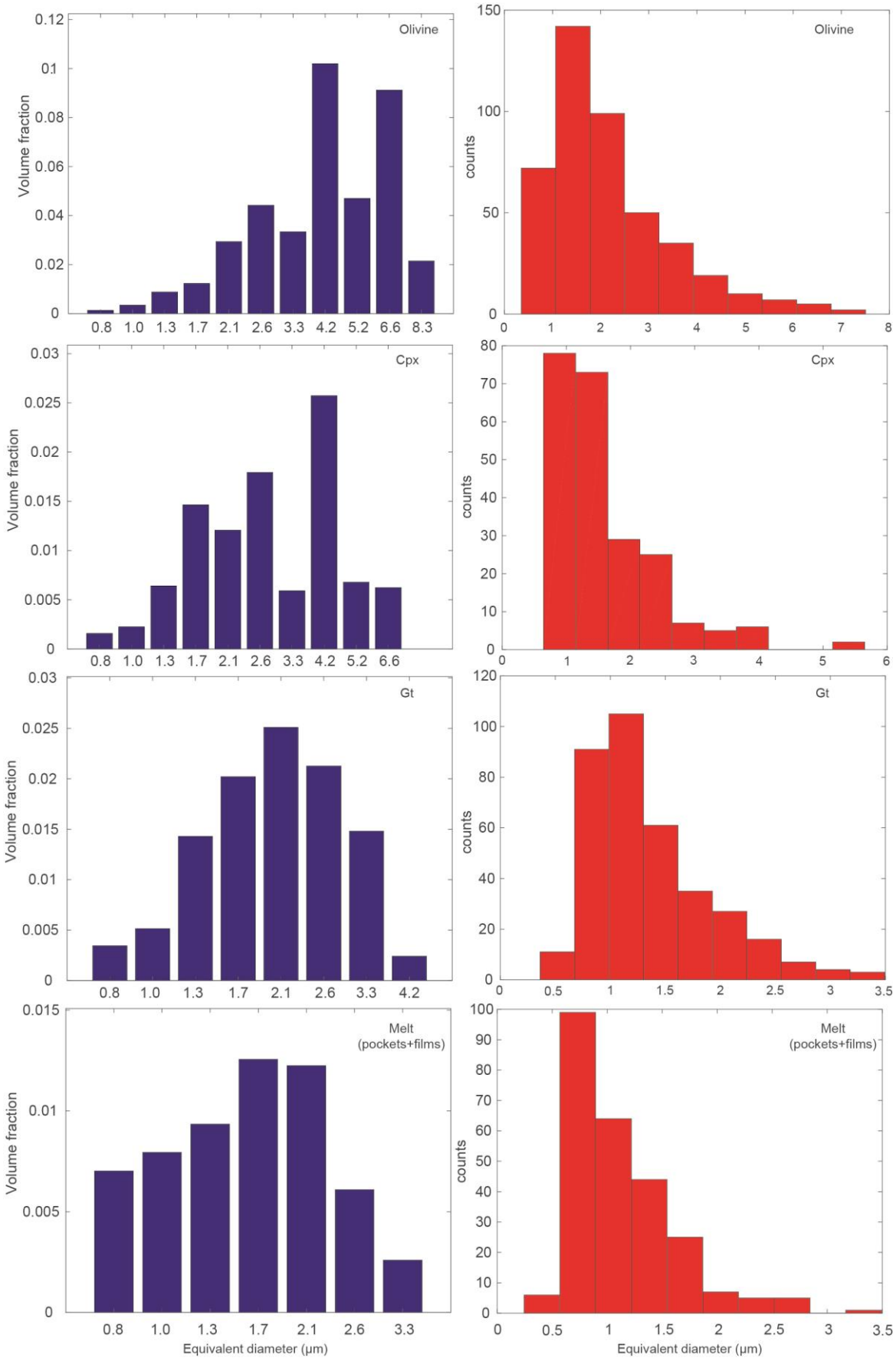

Figure B.28 Grain size and volume fraction as a function of grain equivalent diameter of all computed FOAMS images for each phase for M667.

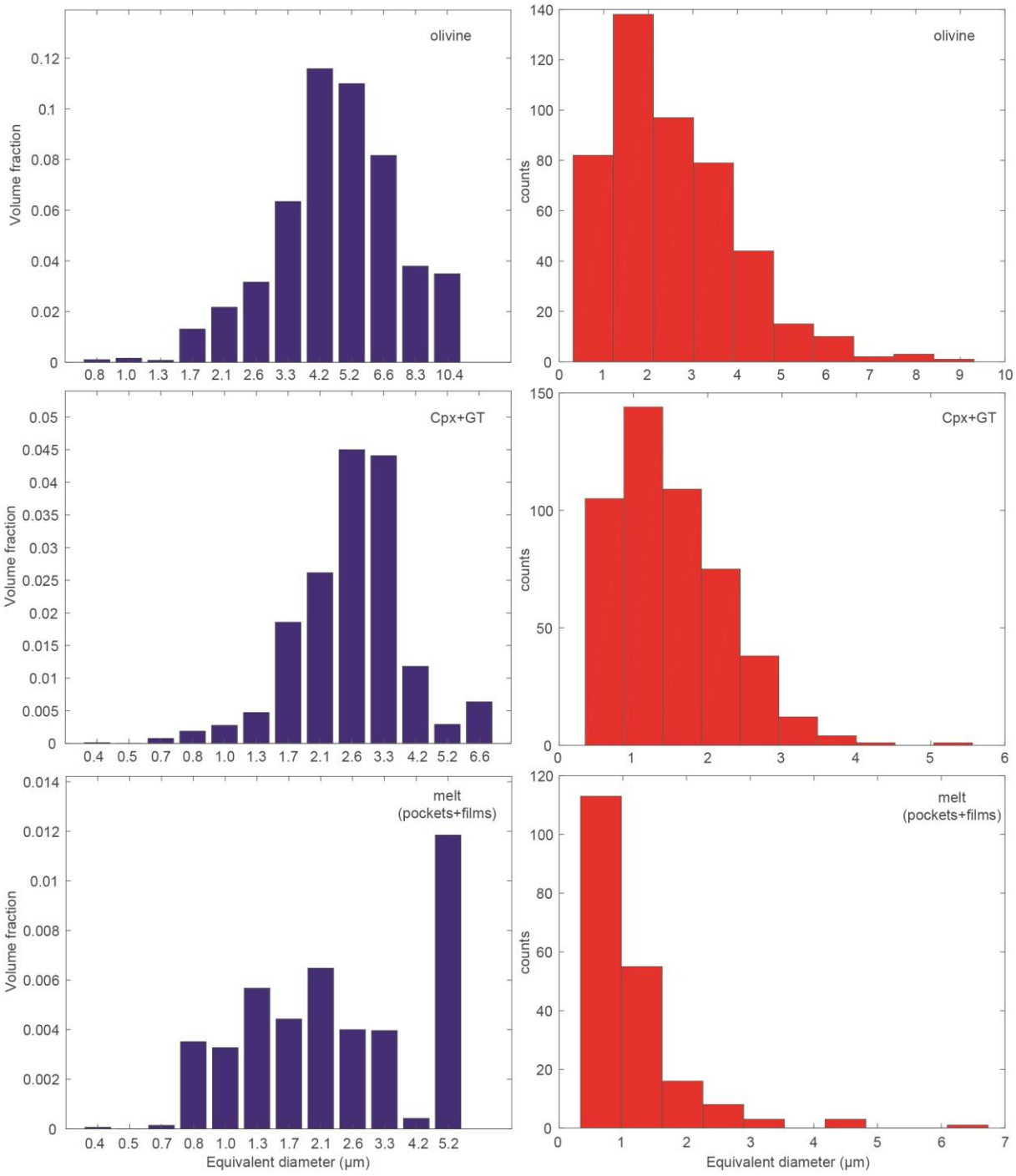

Figure B.29 Grain size and volume fraction as a function of grain equivalent diameter of all computed FOAMS images for each phase for M668, unmolten samples. Cpx and Gt are treated together due to similar color in BSE microphotographs.

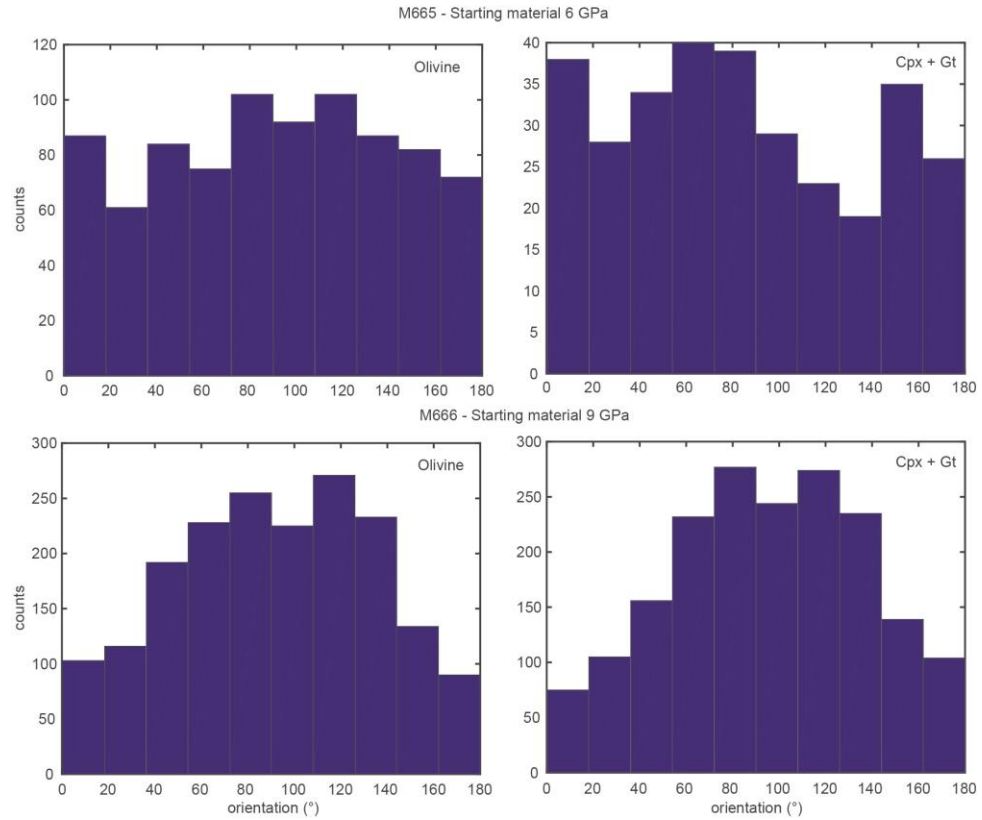

Figure B.30 Orientation of long axis for each phase derived from FOAMS analysis for M665 and M666, starting materials. 90° correspond to the vertical axis of sample cylinder and 0° is perpendicular sample cylinder axis.

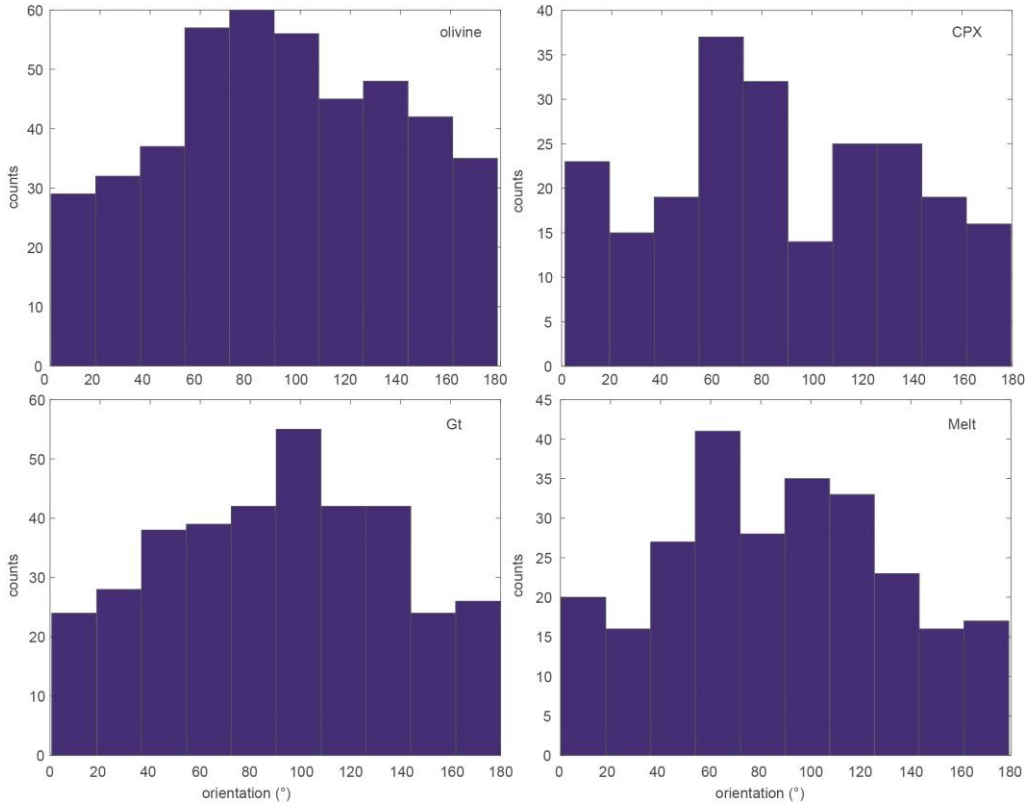

Figure B.31 Orientation of long axis for each phase derived from FOAMS analysis for M667. 90° correspond to the vertical axis of sample cylinder and 0° is perpendicular sample cylinder axis.

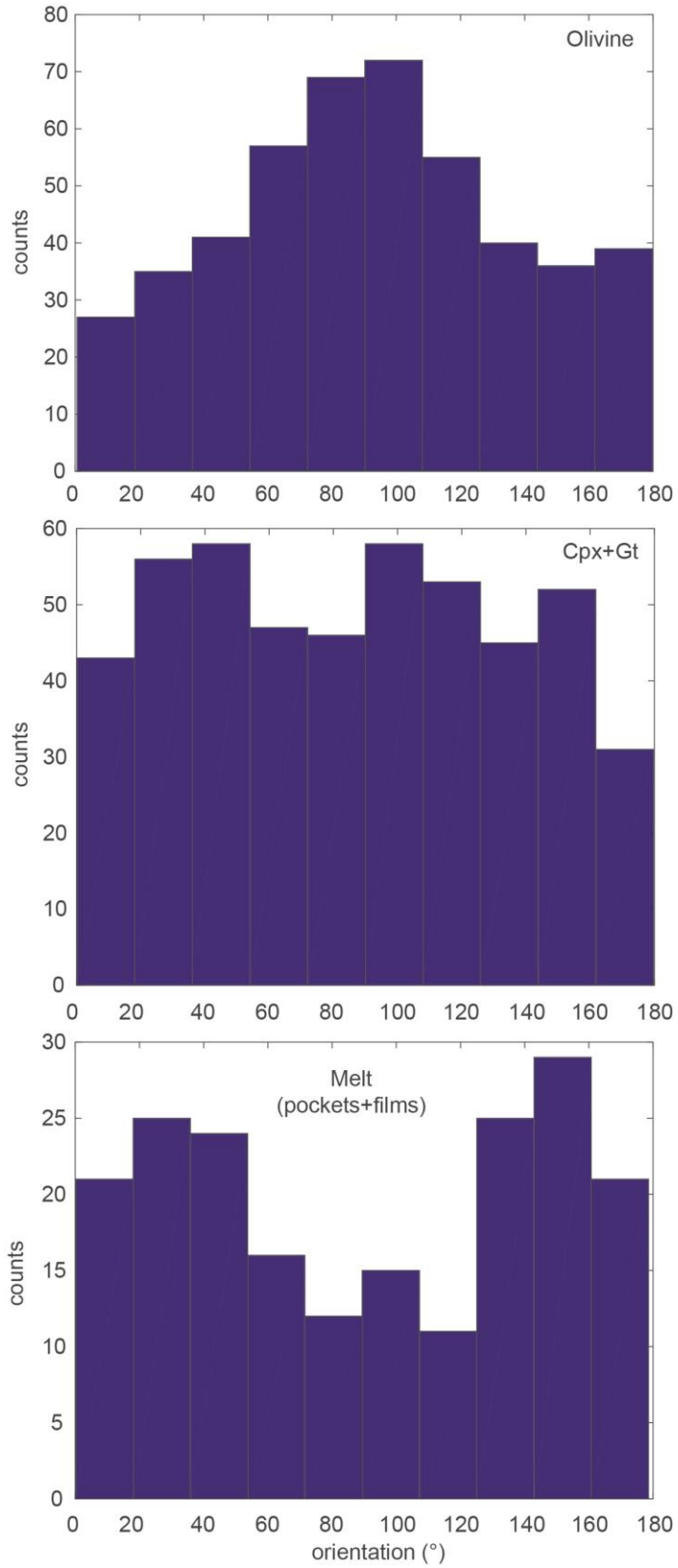

Figure B.32 Orientation of long axis for each phase derived from FOAMS analysis for M668. 90° correspond to the vertical axis of sample cylinder and 0° is perpendicular sample cylinder axis

Chapter VI

Microphotographs, BSE pictures, associated EBSD characterization and micro-Raman analyzes made on starting materials and olivine samples recovered after Angström experiments are provided in this subsection.

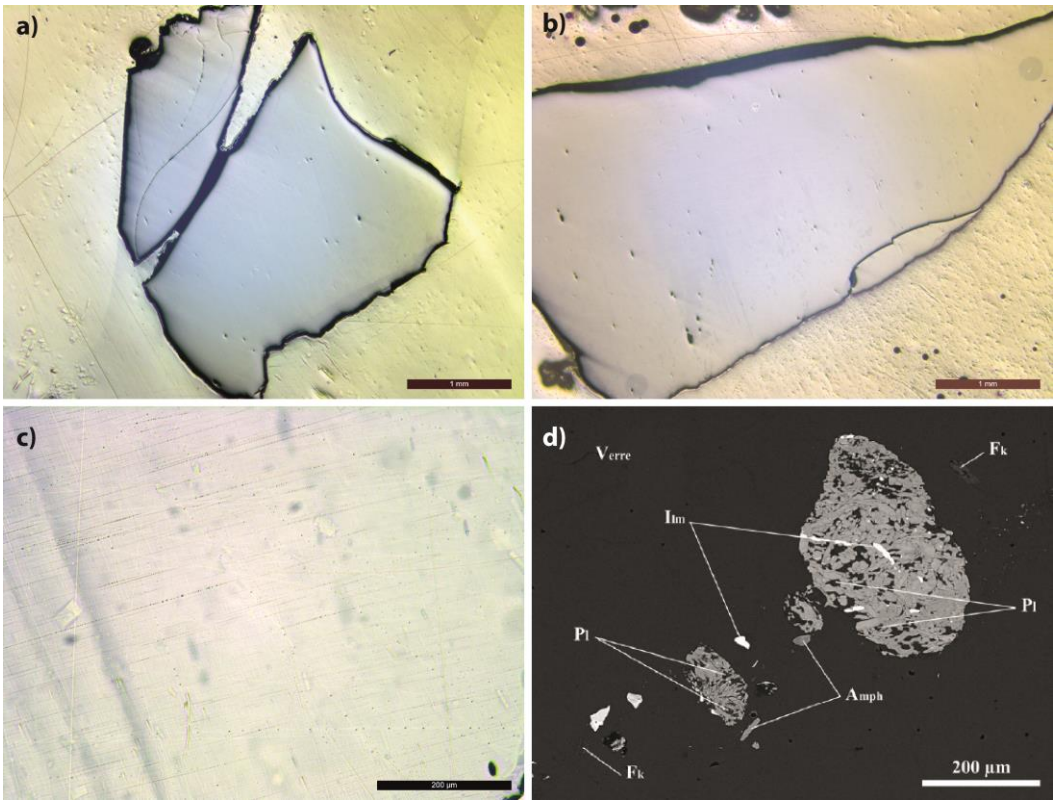

Figure B.33 a) b) and c) microphotographs of polished Güney Dag fragment using reflected light for a) and b) and transmitted light for c). Microphotograph c) shows the interior of the rhyolitic glass, the sample surface has polishing scratches. Inside the sample, scarce dark inclusions (ilmenite, amphibole) are present with elongated and tabular transparent crystals (plagioclase and orthose). Scales of microphotograph are 1 mm in a) and b) and 200 µm for c). d) is a backscattered electron (BSE) cliché taken with SEM by Cluzel (2007). This photograph is taken in a microlite vein into the obsidian. The identified phases were: orthose (FK), ilmenite (Ilm), plagioclase (Pl) and amphibole (Amph). The glass is the black matrix (Verre).

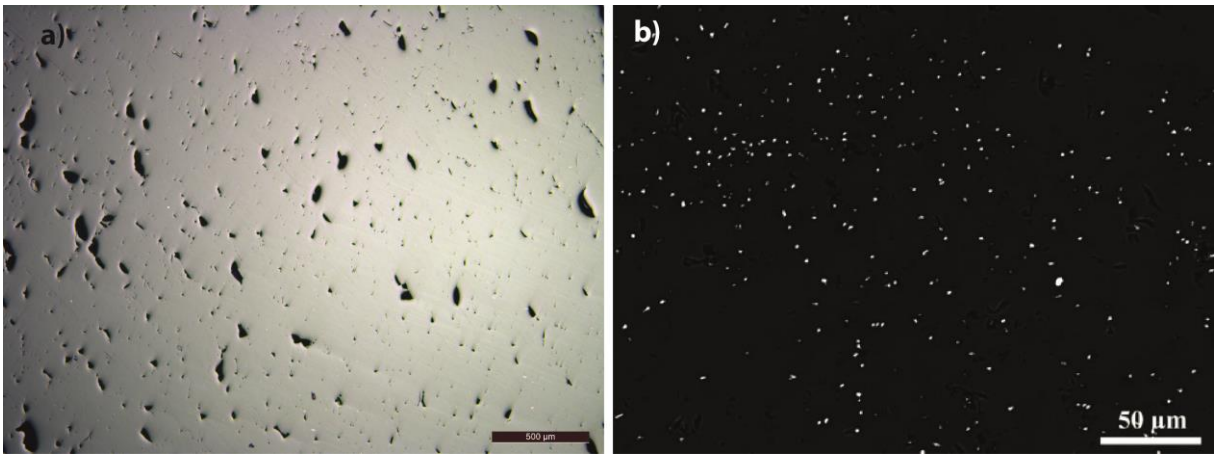

Figure B.34 a) Reflected light microphotograph of mirror polished ATHO obsidian sample. White and reflective part is the glassy ground mass and black dots are holes coming from polishing). Scale of microphotograph is 500 µm. b) BSE microphotograph. Black part is the glassy groundmass; bright spots are iron oxides of titano magnetite. Microlites are mostly homogeneously distributed. This image was taken from Cluzel (2007).

Figure B.35 Synthetic Haplobasalt ingot. The glass is slightly yellow tainted and transparent. Drilled holes for are visible in the left side of the ingot. The camera cap is given on the left side for scale.

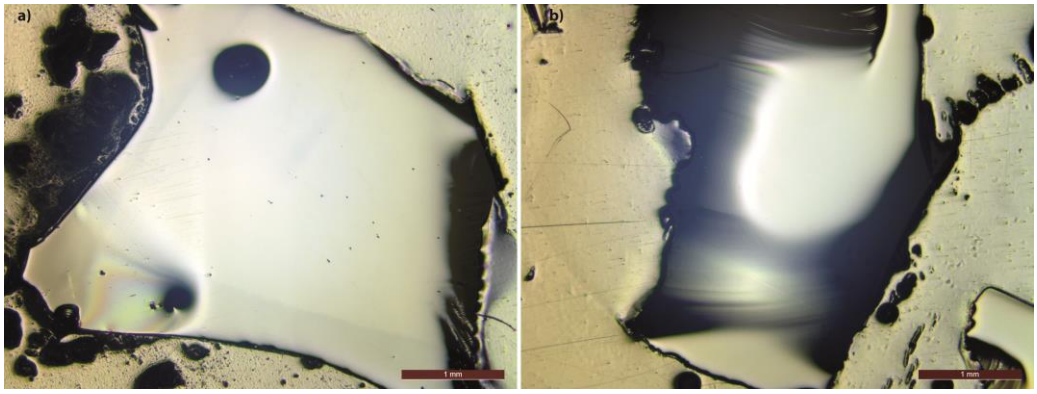

Figure B.36 Microphotograph of haplobasalt with reflected light under optic microscope. The sample is perfectly glassy and transparent but difficult to polish and photograph as it is visible in figure b.

Figure B.37Photograph taken on board with the samples from the dredge DR07. One can remark the important number of pillow lava fragments.

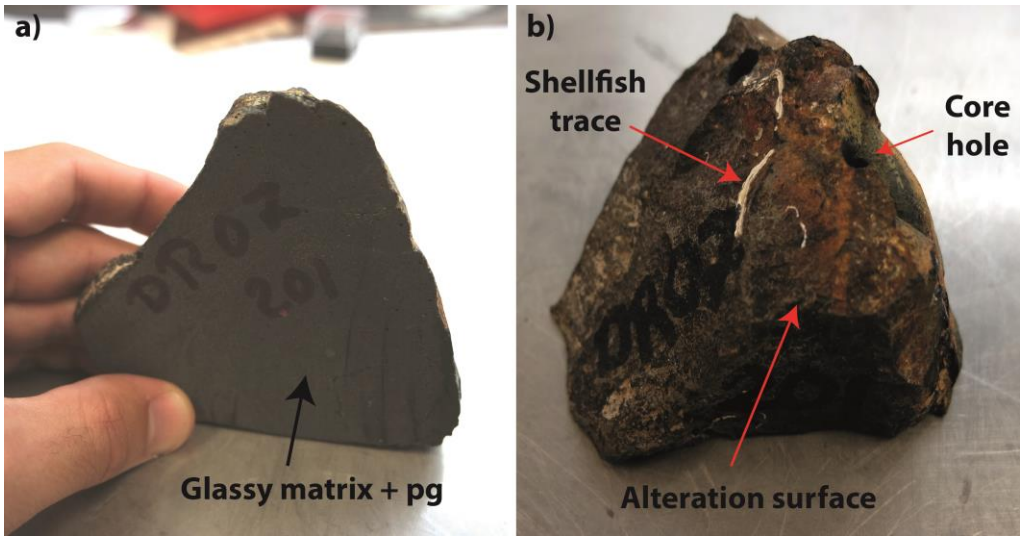

Figure B.38 Photograph of DR07-201 sample. The sample is a fragment of pillow lava, with the external surface (b) which was in contact with water and undergone little alteration (biologic activity traces). The cut of the fragment shows very homogeneous lava with sub-aphyric texture with no vesicle. Author fingers are given for scale.

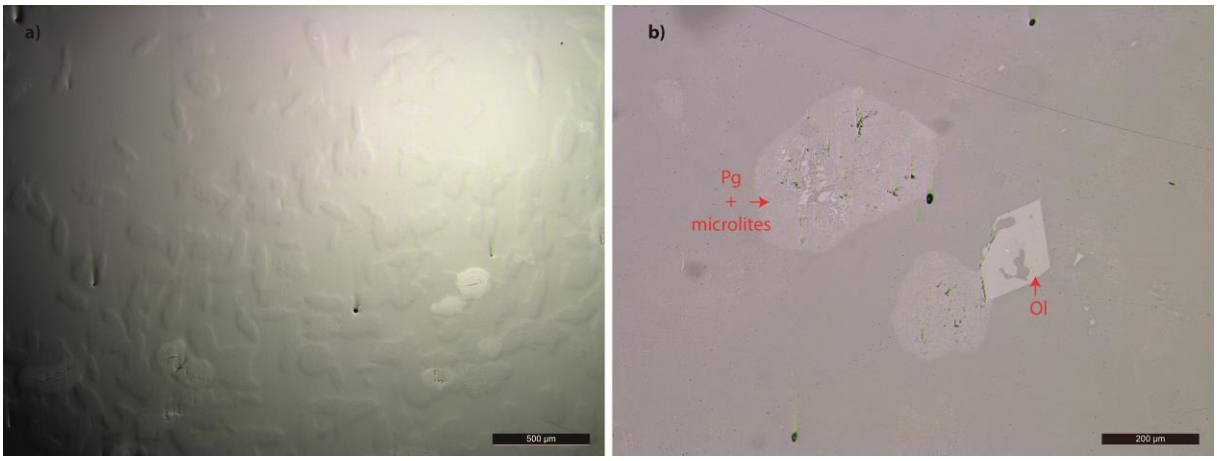

Figure B.39 Microphotographs of DR11-07-201 taken with reflected lights under optical microscope. Picture a) is a large view of the sample texture in which small bright crystals are visible and rounded/elongated shapes. These shapes are not single crystals but more a quench crystallization/devitrification texture with very thin microlites and possibly testify of variolitic texture, one can note the abundance of quenched glass remaining in the sample. Image b) is a more focused view where euhedral crystal of olivine is visible; the crystal is not fully grown with a skeletal-like shape and the presence of melt inclusions. Some darker microcrystal agglomerates are presents; there are mainly plagioclases but the very thin texture in those rounded aggregates (what eye appears as plagioclase) does not allow to fully distinguish the mineral species (ol+ pg probably).

Figure B.40 Photographs taken of DR11 dredge on board, with the full dredge on the top picture in which we can see important size of pillow lavas and lava fragments recovered as well as the important presence of glassy fragments. The 4 pictures are detailed view on recovered sample, sample on left column is a lava crust sample (view from top and bottom) and the sample on the right column is a pillow lava surface with the nicely quenched glassy surface on top.

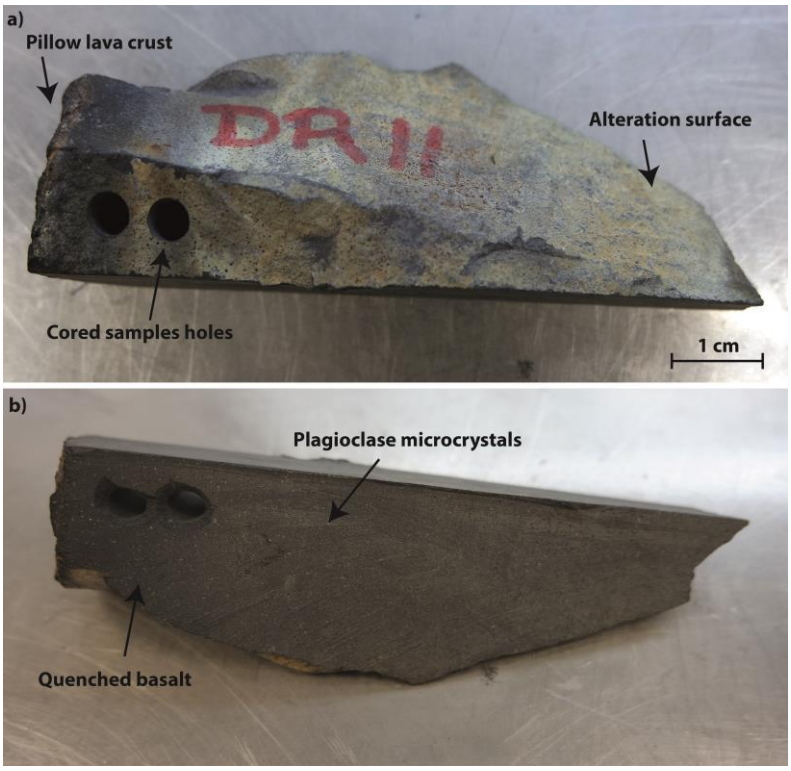

Figure B.41 DR11-201 sample. a) photograph taken on the altered side, with quenched glassy crust visible on the left side. Drilled holes performed for sampling are visible on the left.b) cuts of the sample showing massive lava without vesicles and presence of numerous plagioclase microcrystals.

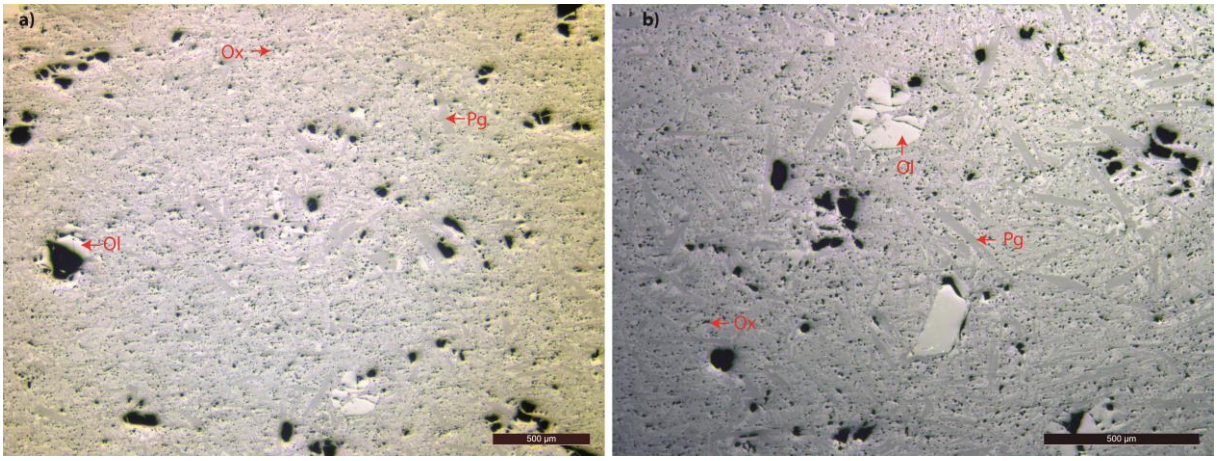

Figure B.42 Microphotographs of DR11-201 taken with reflected lights under optical microscope. Pictures a) and b) are view of the sample texture. The sample is more crystalized than DR07 with the presence of euhedral olivine crystals and a large amount of tabular plagioclase microlites, plus some oxide crystals. The black dots are not only oxides but also some holes from polishing and some might also be little vesicles.

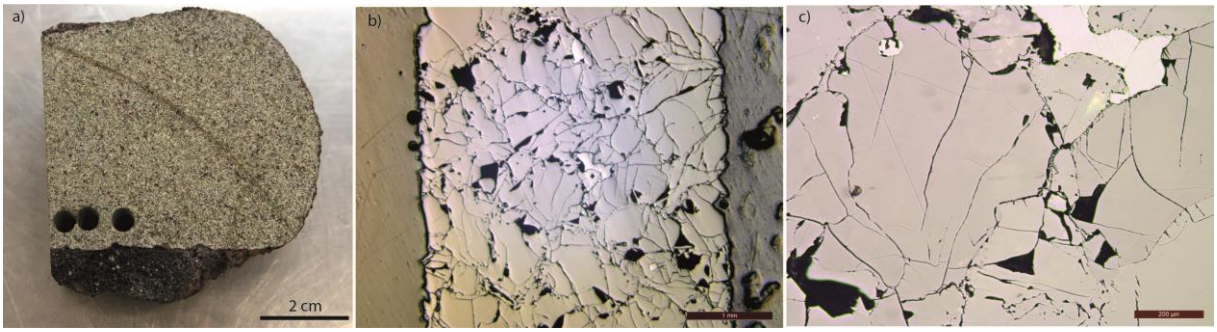

Figure B.43 RP4 sample. a) Large sample with isotropic texture, core holes are visible at the bottom of the sample. The richness in Cpx/spinel is highly visible. b) and c) Reflected light microphotographs on a cored polished section (parallel to the core cylinder long axis). Olivine and pyroxenes grains appear grey whereas spinel is highly visible in white.

Figure B.44 Examples of MgO wafers supplied by 2SPI. The wafers are single crystals with perfectly transparent optical properties. Figure from supplier website.

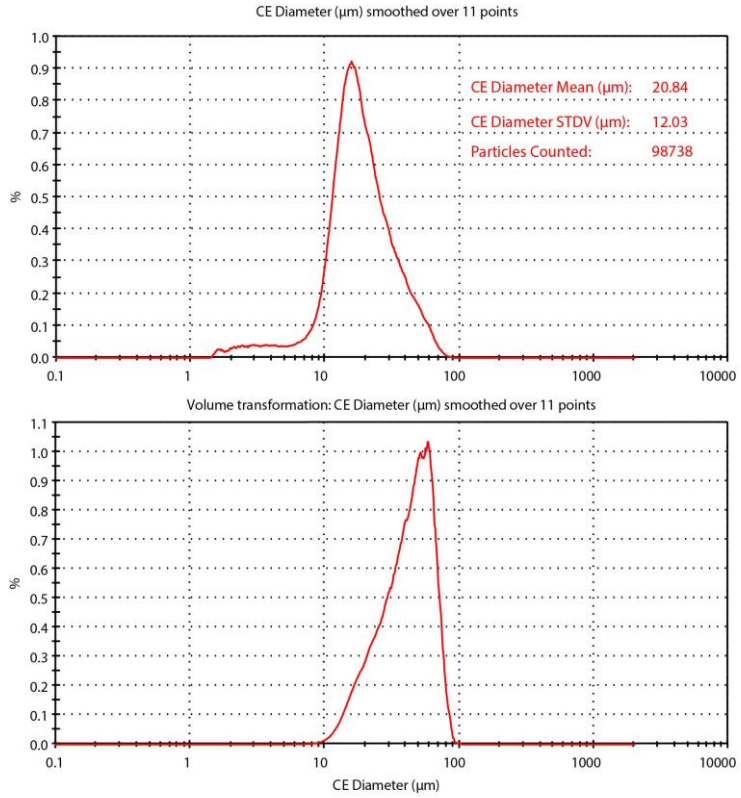

Figure B.45 Grain size distribution of our San Carlos olivine sieved powder made with Morphologi G3 apparatus

Figure B.46 Cores samples realized with the drilling machine at the LMV. Core samples of ATHO, Güney Dag, DR07-201, DR11-201, Haplobasalt and RP4 peridotite (from to left to bottom right respectively).

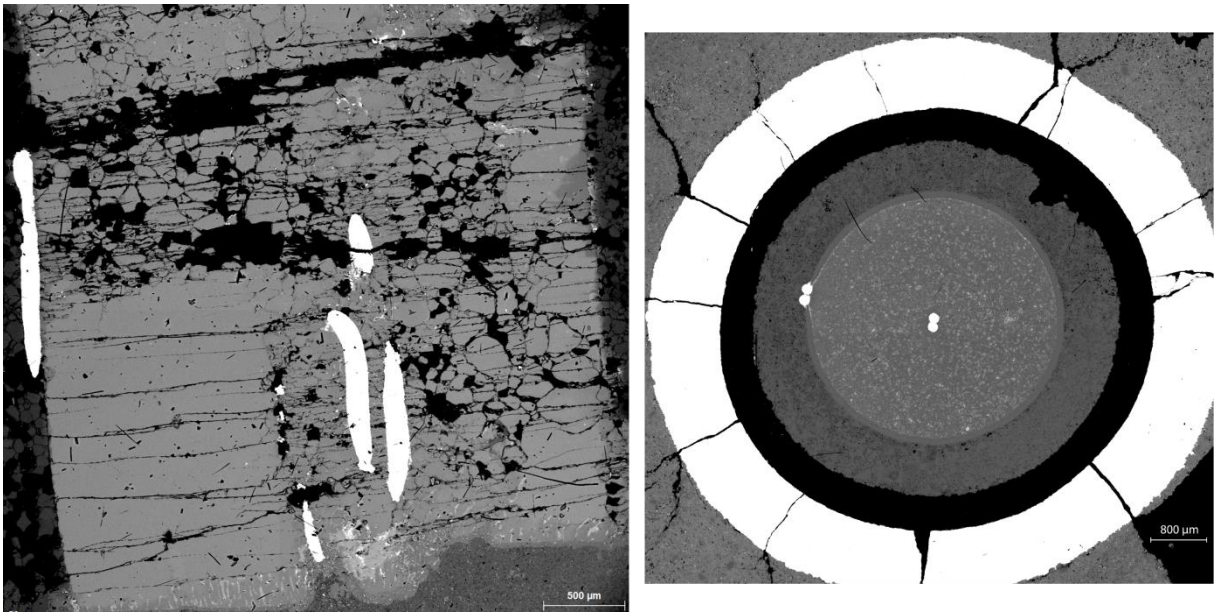

Figure B.47 BSE microphotographs taken on M525 showing cuts perpendicular and parallel to sample cylinder axis (right and left frames respectively). Recrystallization of the single crystal is visible with presence of coarse grains in between the thermocouples (analyzed region for thermal diffusivity).

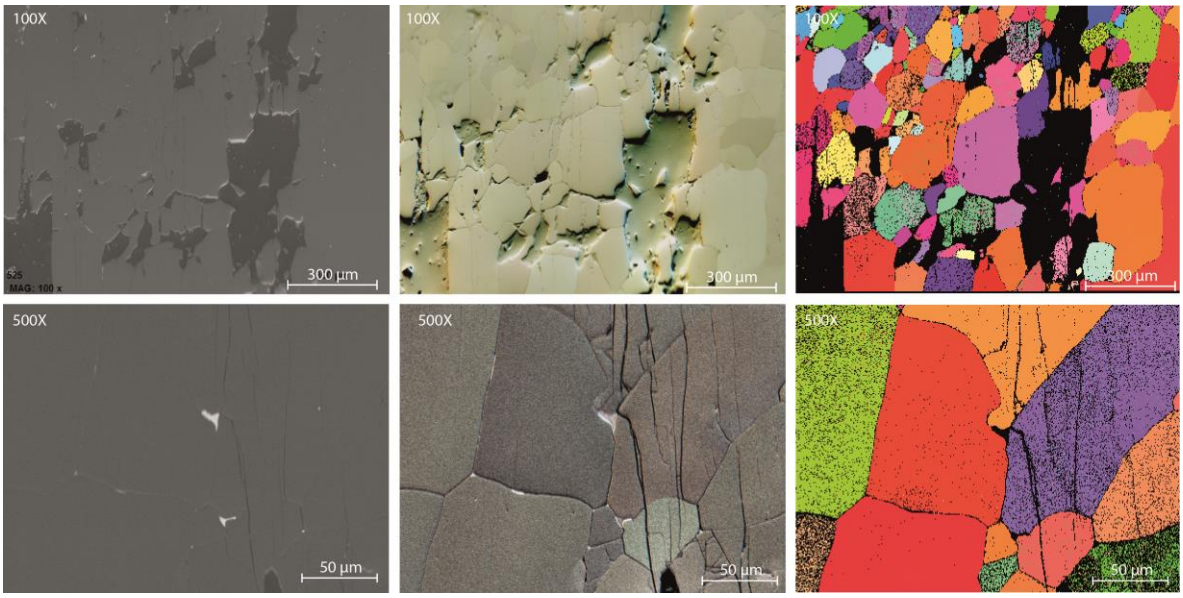

Figure B.48 EBSD analysis on M525 olivine sample after the experiment. Two different maps were made at different focus. The first column (left) correspond to BSE image showing a very good homogeneity of the sample (dark parts are holes). The second column is the FSE image on the sample zone and the last column correspond to the EBSD maps. The indexation is good with more than 80% of indexed pixel, which should be near 100 when removing holes due to grain removal during polishing.

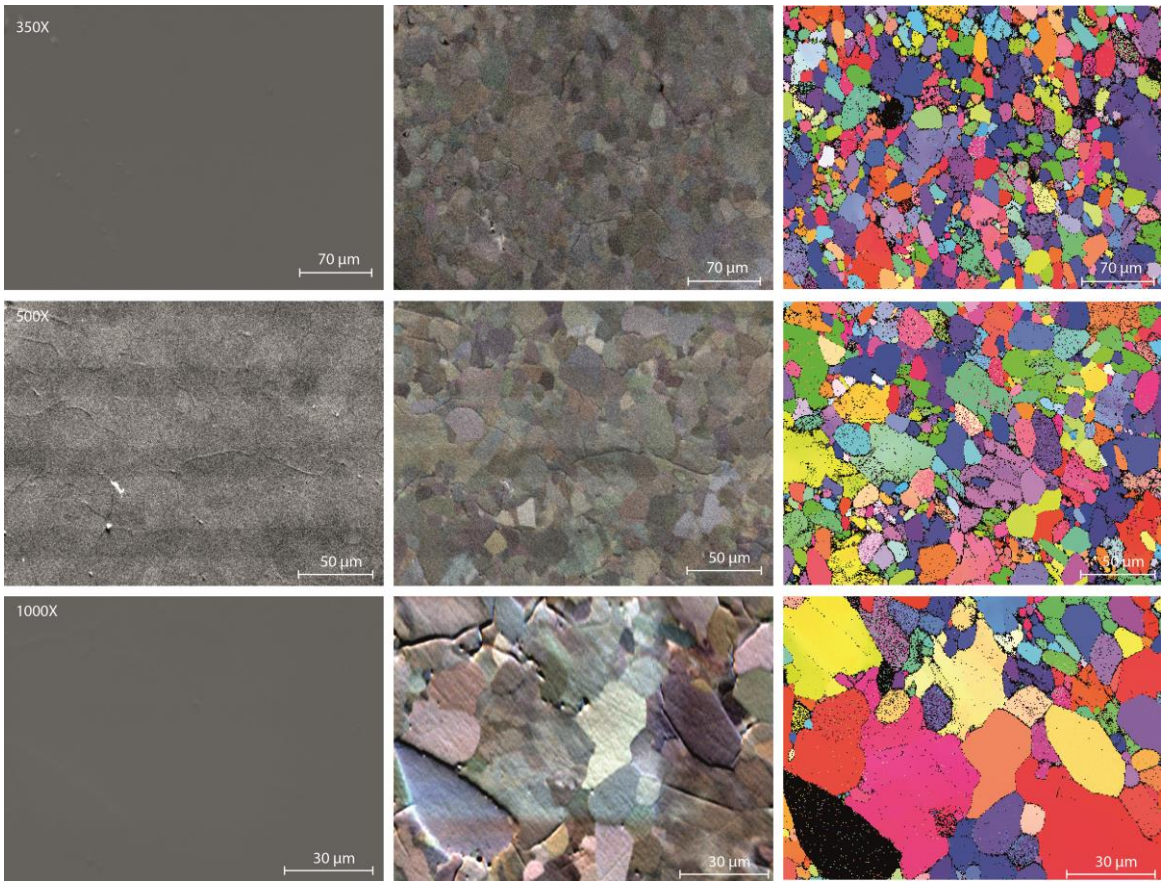

Figure B.49 EBSD analysis on M617 olivine sample after the experiment. Three different maps were made at different focus. The first column (left) correspond to BSE image showing a very good homogeneity of the sample (second picture bands are due to the EBSD analysis which damages sample's surface, see the horizontal analysis band of the raster mode). The second column is the FSE image on the sample zone and the last column correspond to the EBSD maps. The indexation is good with more than 80% of indexed pixel, which should be near 100% when removing holes due to grain removal during polishing.

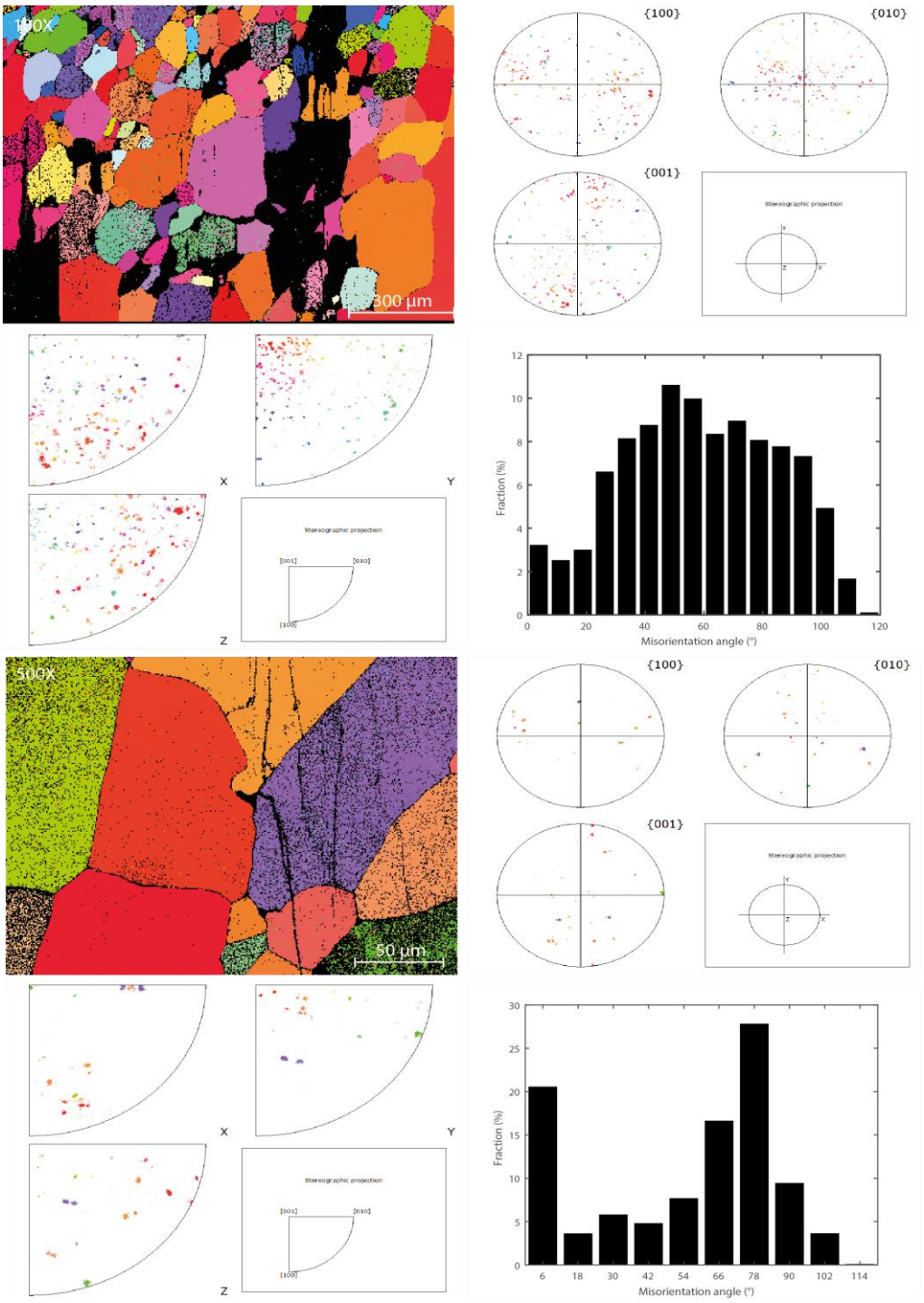

Figure B.50Polar figures for EBSD maps performed on M525. EBSD map is provided for the color code, the two common polar projections are also provided as well as the histogram of misorientation angle.

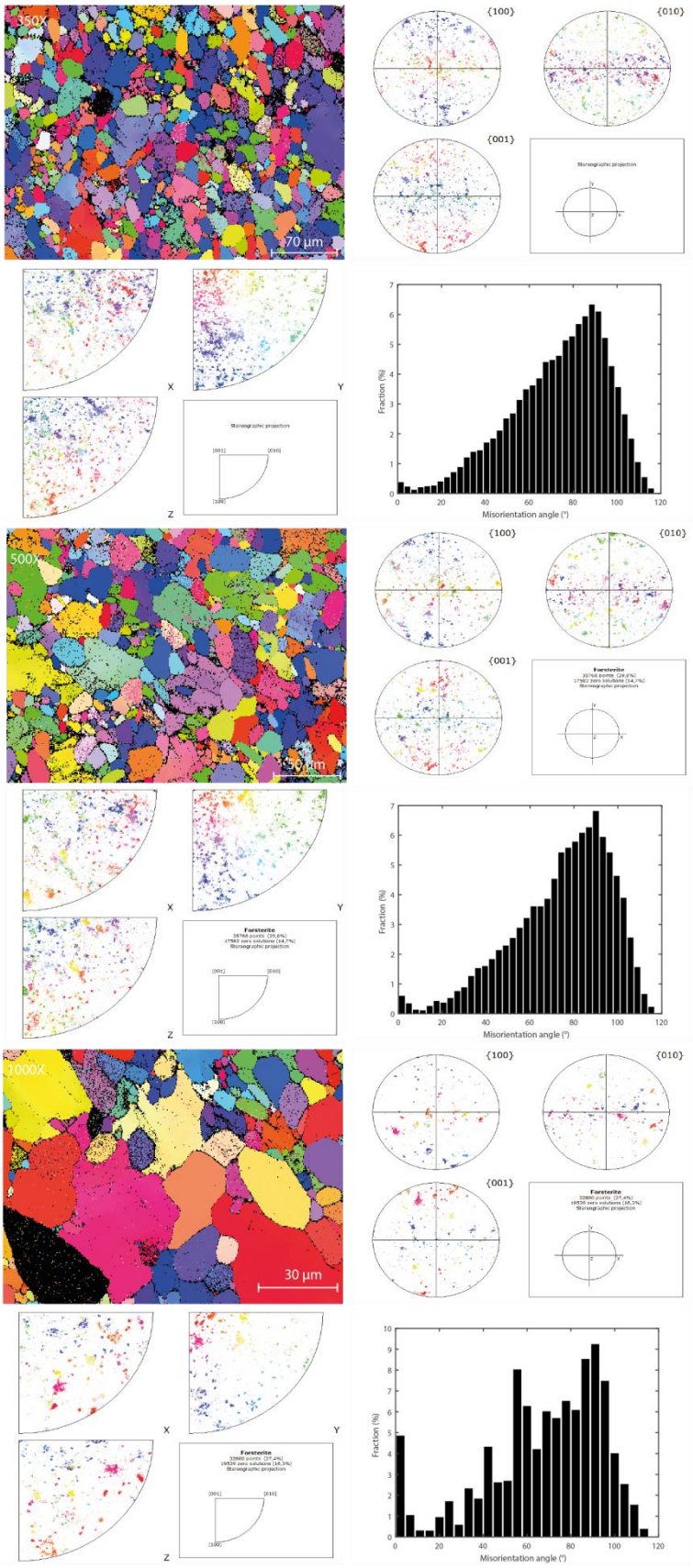

Figure B.51 Polar figures for EBSD maps performed on M617. EBSD map is provided for the color code, the two common polar projections are also provided as well as the histogram of misorientation angle.

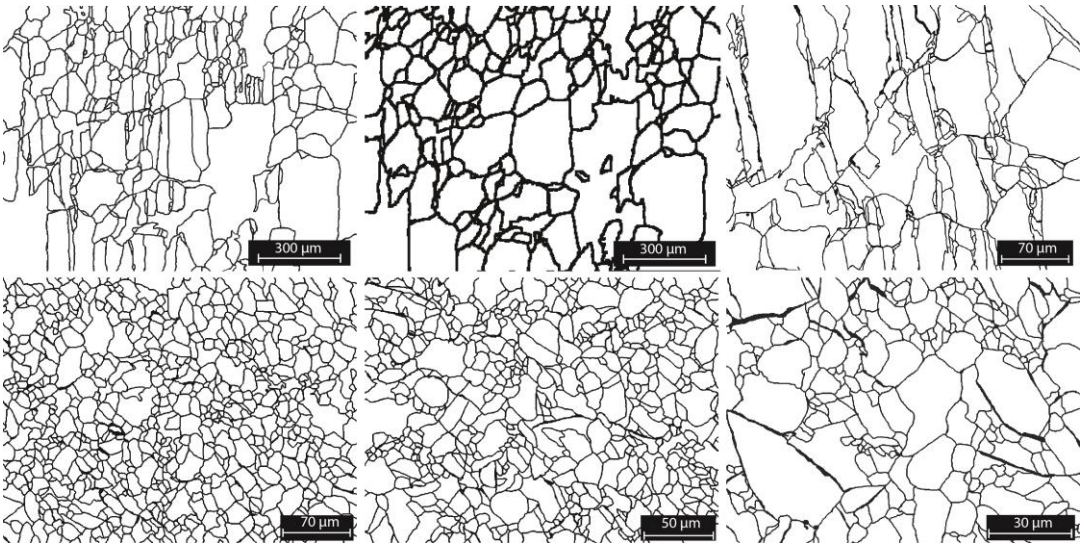

Figure B.52 Skeletonized/binarized pictures made from FSE or EBSD maps for M525 (on top) and M617 (bottom) samples.

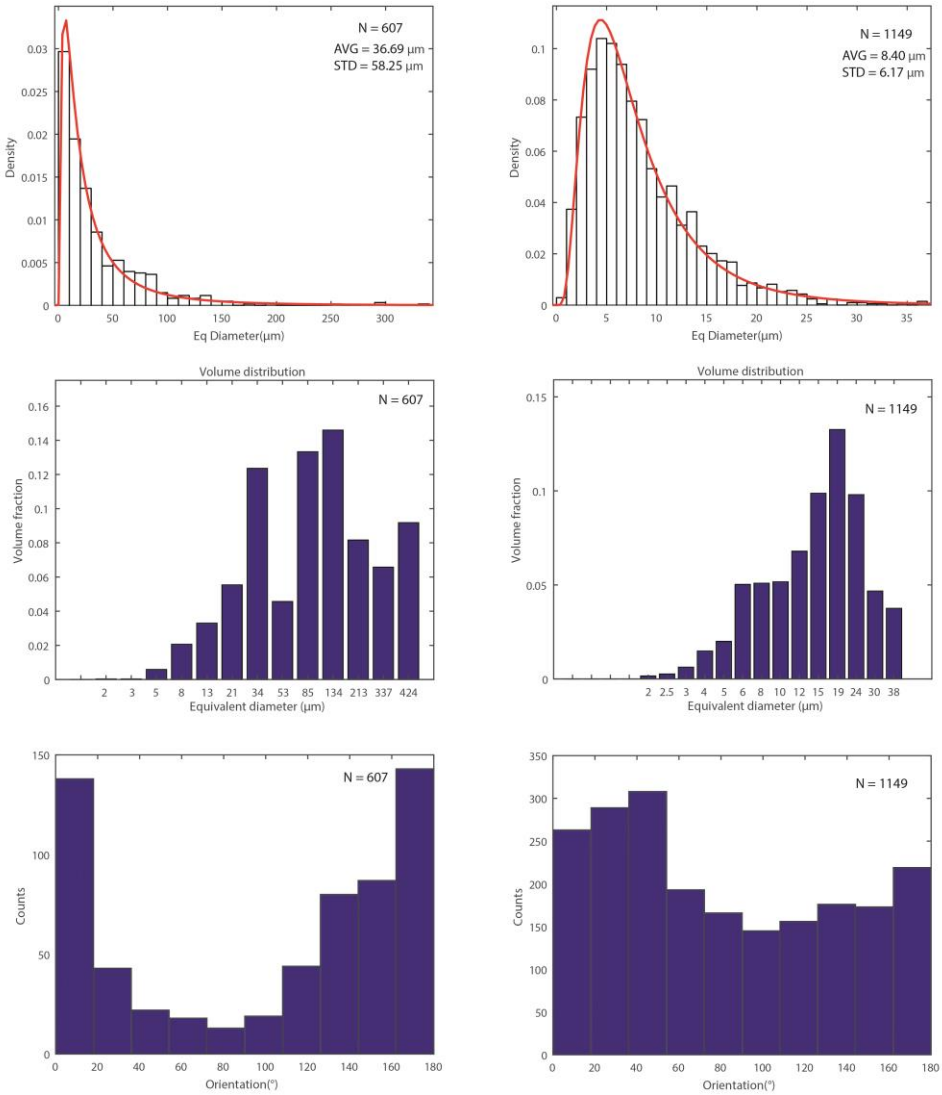

Figure B.53Textural information on the sum of all the textural parameters and analyses performed on M525 (left) and M617 (right) samples. First line represents the average grain size, the second volume fraction per equivalent diameter bins and orientation for each sample.

Appendix C

Codes for Ångström method data processing

Appendix C: Codes for Angström method data processing

The code presented is made in Matlab® language on Matlab R2016b version 9.1. It requires the use of Global Optimization Toolbox© (ver. 3.4.1), Curve Fitting Toolbox© (ver. 3.5.4) and Statistics and Machine Learning Toolbox© (ver. 11) for data fitting and inversion.

1) pre_D_fit_treatment

The pre_D_fit_treatment is made to fit the data recovered from heating software. The recovered data should have 3 data column, in the first column the time should be given in day format. This column is followed by two columns of temperature corresponding to TC1 and TC2. The data fitting procedure in described in the manuscript in the chapter VI. The code is given in the following lines:

```
% D . Freitas

% 22/02/2017

% If you are using this program please contact me at
% freitas.damien@yahoo.com /or on researchgate for any explanation.
% This program is a part of my
% PhD work, please cite it or contact me
% for co-authoring or acknowledgment

% cleaning trilogy
clear all
close all
clc

%% Part 1 Read the file

[fileID, filepath] = uigetfile({'*.*'},'pick a
file','E:\PhD\data_treatment\'); %select the file
fileadress = cat(2,filepath,fileID); %whole file address
fileopen = fopen(fileadress,'r+');% open it
filecell=textscan(fileopen,'%s %f %f'); %read it I tree columns time TC1 and
TC2
timecell = filecell{1};
time_char = datestr(timecell,'HH:MM:SS,FFF'); %in string
time_days = datenum(time_char,'HH:MM:SS,FFF');% in days since 1st jan 0
time_sec = time_days*24*60*60; % conversion in seconds

T1 = filecell{2};
T2 = filecell{3};

file= [time_sec,T1,T2]; % Final file ready for fitting
```

```
%% Part 2 Plot the read file

fig = figure; % plot raw data
        set(fig,'name','Raw Data','NumberTitle','off')
plot (file(:,1),file(:,2),'r',file(:,1),file(:,3),'b');
    xlabel('time (s)');
    ylabel('temperature (°c)');
    title('Raw Data from the heating software of the 1500 T press')
    legend('TC 1 = inside','TC 2 = outside')
    axis([min(file(:,1)) max(file(:,1)) min(min(file(:,2:3)))-
0.015*min(min(file(:,2:3)))
max(max(file(:,2:3)))+0.015*max(max(file(:,2:3)))]);

%restart time to 0
file(:,1)= file(:,1)-min(file(:,1));
fig2 = figure; %plot with the new time
    set(fig2,'name','Time shifted Data','NumberTitle','off')
plot (file(:,1),file(:,2),'r',file(:,1),file(:,3),'b');
    xlabel('time (s)');
    ylabel('temperature (°c)');
    title('Raw Data shifted to time = 0 at the beginning of the measurement')
    legend('TC 1 = inside','TC 2 = outside')
    axis([min(file(:,1)) max(file(:,1)) min(min(file(:,2:3)))-
0.015*min(min(file(:,2:3)))
max(max(file(:,2:3)))+0.015*max(max(file(:,2:3)))]);
hold on

%select the part of the curve that is able to be fitted
%it must be the same zone for the 2 TC for phase measurements as phase
%shift is relative.
%Of course the first clic muse be before the second clic in the time axis
disp('select the zone of interest with 2 clic')
t = [];
temp = [];
for i = 1 : 2
[ti,tempi]= ginput(1);
t=[t;ti];temp=[temp;tempi]; % take the g input each time and plot the line in
direct
hold on; p1 = plot([ti ti],[min(min(file(:,2:3))) max(max(file(:,2:3)))],'-
k'); hold off; drawnow; pause(0.5);
end
line =[max(max(file(:,2:3)))+2 min(min(file(:,2:3)))-2];
linex = [t(1) t(1)];
linex2 = [t(2) t(2)]; %draw the lines of selected area
ind = find(file(:,1)>t(1)&file(:,1)<t(2));

fig3 = figure; % plot both, and each thermocouple in a subplot for the
selected zone of fitting only
    set(fig3,'name','Treatment','NumberTitle','off')
subplot(3,1,1)
plot(file(:,1),file(:,2),'r',file(:,1),file(:,3),'b',linex,line,'k',linex2,lin
e,'k')
    xlabel('time (s)');
    ylabel('temperature (°c)');
    title('selected zone for fitting')
    legend('TC 1 = inside','TC 2 = outside')
```

```
    axis([min(file(:,1)) max(file(:,1)) min(min(file(:,2:3)))-
0.015*min(min(file(:,2:3)))
max(max(file(:,2:3)))+0.015*max(max(file(:,2:3)))]);
hold on

subplot (3,1,2)
plot(file(ind,1),file(ind,2),'r') %TC1
    xlabel('time (s)');
    ylabel('temperature (°c)');
    title('TC 1')
    legend('TC 1 = inside')
    axis([min(file(ind,1)) max(file(ind,1)) min(file(ind,2))-
0.015*min(file(ind,2)) max(file(ind,2))+0.015*max(file(ind,2)) ])
subplot(3,1,3)
plot(file(ind,1),file(ind,3),'b') %TC2
    xlabel('time (s)');
    ylabel('temperature (°c)');
    title('TC 2')
    legend('TC 2 = outside')
    axis([min(file(ind,1)) max(file(ind,1)) min(file(ind,3))-
0.015*min(file(ind,3)) max(file(ind,3))+0.015*max(file(ind,3)) ])

%% Part3 Fit the file

file2= file(ind,:);
a0TC1 = mean(file2(:,2));%Average of TC1 temperature
a0TC2 = mean(file2(:,3));%Average of TC2 temperature
a1TC1 = 0;% need the special box for correction
a1TC2 = 0;
a3TC1 = inputdlg('insert a frequency (in hertz)','Frequency', [1 50]);
a3TC1 = str2num(a3TC1{:});
a3TC2 = a3TC1; %f is the same for the two waves
xdata = file2(:,1); % redefine the good x

%calc for TC1
fun =
@(x,xdata)x(1)*sin(2*pi*a3TC1*xdata+((x(2)*pi)/(180)))+a0TC1+a1TC1*xdata; %
create the function to be fitted, with x 1 and 2 as unknown
x0=[-10 0]; % give a guessed minimal possible value of the parameters x1 and 2
options = optimoptions('lsqcurvefit','Algorithm','levenberg-
marquardt','TolFun',1e-20); % type of algorithm chosen
lb = []; %lower boundary
ub = []; %upper boundary

%error estimation
[beta, resnorm, resid, exitflag,output,lembda, T]=
lsqcurvefit(fun,x0,file2(:,1),file2(:,2),lb,ub,options); %non linear curve
fitting in the last square sense
x= beta
ci = nlparci(beta,resid,'jacobian',T)
ycal = a0TC1+a1TC1*file(:,1)+x(1)*sin(2*pi*a3TC1*file(:,1)+((x(2)*pi)/(180)));
% calculates with the inverted parameters TC1
ampTC1 = x(1);
errorampTC1 = abs(max(x(1)-ci(1,1),ci(1,2)-x(1)));% error on amplitude
phaseTC1 = x(2);
errorphaseTC1 = abs(max(x(2)-ci(2,1),ci(2,2)-x(2))); % error on phase
```

```
%calc for TC2
fun =
@(x,xdata)x(1)*sin(2*pi*a3TC2*xdata+((x(2)*pi)/(180)))+a0TC2+a1TC2*xdata; %
create the function to be fitted, with x 1 and 2 as unknown
x0=[-10 0]; % give a guessed minimal possible value of the parameters x 1 and
2
options = optimoptions('lsqcurvefit','Algorithm','levenberg-
marquardt','TolFun',1e-20); % type of algorithm chosen
lb = []; %lower boundary
ub = []; %upper boundary
[beta, resnorm, resid, exitflag,output,lembda, T]=
lsqcurvefit(fun,x0,file2(:,1),file2(:,3),lb,ub,options); %non linear curve
fitting in the last square sense
x= beta
ci = nlparci(beta,resid,'jacobian',T)
xdata = file2(:,1); % redefine the good x
ycal2 =
a0TC2+a1TC2*file(:,1)+x(1)*sin(2*pi*a3TC2*file(:,1)+((x(2)*pi)/(180))); %
calculates with the inverted parameters TC2
ampTC2 = x(1);
phaseTC2 = x(2);
errorampTC2 = abs(max(x(1)-ci(1,1),ci(1,2)-x(1))); %error on amplitude
errorphaseTC2 = abs(max(x(2)-ci(2,1),ci(2,2)-x(2))); % error on phase

%plot and representation of the data
fig3 = figure; % subplot with fits
    set(fig3,'name','Fitted values','NumberTitle','off')
subplot(3,1,1)
plot(file(:,1),ycal,'r',file(:,1),ycal2,'b');
    xlabel('time (s)');
    ylabel('temperature (°c)');
    title('Comparision of the two fit')
    legend('FIT TC 1 = inside','FIT TC 2 = outside')
    axis([min(file(:,1)) max(file(:,1)) min(min(file(:,2:3)))-
0.015*min(min(file(:,2:3)))
max(max(file(:,2:3)))+0.015*max(max(file(:,2:3)))]);
subplot(3,1,2)
plot (file(:,1),file(:,2),'r',file(:,1),ycal,'--k');
    xlabel('time (s)');
    ylabel('temperature (°c)');
    title('TC1')
    legend('TC 1 = inside','FIT TC 1')
    axis([min(file(:,1)) max(file(:,1)) min(file(:,2))-0.015*min(file(:,2))
max(file(:,2))+0.015*max(file(:,2))])
hold on;
subplot(3,1,3)
plot (file(:,1),file(:,3),'b',file(:,1),ycal2,'--k');
    xlabel('time (s)');
    ylabel('temperature (°c)');
    title('TC2')
    legend('TC 2 = outside','FIT TC 2')
    axis([min(file(:,1)) max(file(:,1)) min(file(:,3))-0.015*min(file(:,3))
max(file(:,3))+0.015*max(file(:,3))])
hold on;

% in a separate figure
```

```
fig5 = figure; % fits against data in separate plots with displays of fitted
values for better visual check
    set(fig5,'name','TC1 Fit','NumberTitle','off')
plot(file(:,1),ycal,'--b',file(:,1),file(:,2),'r');
    xlabel('time (s)');
    ylabel('temperature (°c)');
    title('TC1')
    legend('FIT TC 1','TC 1 = inside')
    axis([min(file(:,1)) max(file(:,1)) min(file(:,2))-0.015*min(file(:,2))
max(file(:,2))+0.015*max(file(:,2))])
    bh = 0.8*max(file(:,1)); % displays values of amplitude and phase on the
figure for more visibility
    bb = 0.99*min(file(:,2));
    text(bh,bb,sprintf(['Amplitude= ',num2str(ampTC1),'\nPhase=
',num2str(phaseTC1)]))

    fig6 = figure;
    set(fig6,'name','TC2 Fit','NumberTitle','off')
    plot(file(:,1),ycal2,'--b',file(:,1),file(:,3),'r');
    xlabel('time (s)');
    ylabel('temperature (°c)');
    title('TC2')
    legend('FIT TC 2','TC 2 = outside')
    axis([min(file(:,1)) max(file(:,1)) min(file(:,3))-0.015*min(file(:,3))
max(file(:,3))+0.015*max(file(:,3))])
    bbh = 0.8*max(file(:,1)); % displays values of amplitude and phase on the
figure for more visibility
    bbb = 0.99*min(file(:,3));
    text(bbh,bbb,sprintf(['Amplitude= ',num2str(ampTC2),'\nPhase=
',num2str(phaseTC2)]))


    %% Part4 save the result

    %create a excel file for this part (only this temperature)
    wait = 5; %usually put 10, depends on the time you need to check if the
fitting is good or not
    pause(wait)
    choice = questdlg('Would you save the fitted data?','Yes','No');%
Construct a questdlg with two options
    % Handle response
    switch choice
        case 'Yes'
            expname = fileID(1:4);
            compo = fileID(6:8);% need to be adapted according the name
            pressP = fileID(10:12);
            fittingeq = 'Fitting equation: Y =
A0+A1*x+A2*sin(2*pi*A3*x+((A4*pi)/(180)))';
            A0 ='A0=Temperature';
            A1 ='A1=baseline T';
            A2 ='A2=amplitude';
            A3 ='A3= frequency';
            A4 ='A4=phase';
            TC1 = 'Inner thermocouple';
            TC2 = 'outer thermocouple';
            SA2 = 'std dev Amp (2Sigma)';
            SA4 = 'std dev phase (2Sigma)';
```

```
            header1 = {expname;compo;fittingeq};
            header3 = {A0, A1, A2, A3, A4, SA2, SA4};
            header4 = {TC1, TC2};
            datalabel = {'Temperature (C)','Frequency (Hz)', 'A0', 'A1', 'A2',
'A3', 'A4', 'SA2', 'SA4'};
            finalfile = [a0TC1 a1TC1 ampTC1 a3TC1 phaseTC1 errorampTC1
errorphaseTC1; a0TC2 a1TC2 ampTC2 a3TC2 phaseTC2 errorampTC2 errorphaseTC2]; %
T T0 Amp f phi
            xlsfileadress = cat(2,fileID(1:end-4),'.xlsx'); %new file name
+extension
            sheet = 1;
            xlsrangeheader1 = 'C1';
            xlsrangeheader2 = 'F2';
            xlsrangeheader3 = 'A5';
            xlsrangeheader4 = 'A6';
            xlsrangedata = 'A12';
            xlsrange = 'C13';
            xlswrite(xlsfileadress, header1, sheet, xlsrangeheader1);
            xlswrite(xlsfileadress, pressP, sheet, xlsrangeheader2);
            xlswrite(xlsfileadress, header3, sheet, xlsrangeheader3);
            xlswrite(xlsfileadress, header4, sheet, xlsrangeheader4);
            xlswrite(xlsfileadress, datalabel, sheet, xlsrangedata);
            xlswrite(xlsfileadress, finalfile, sheet, xlsrange);
        case 'No'
            % this case not is just to get manually the phase, amplitude
            % will be taken from the fitting
            figure(fig2)
            disp('Fit is not working, select the two peaks with 2 clic')
            %select the peaks
            w = [];
            tempw = [];
            for i = 1 : 2
                [wi,tempj]= ginput(1);
                w=[w;wi];tempw=[tempw;tempj]; % take the g input each time and
plot the line in direct
                hold on; p1 = plot([wi wi],[min(min(file(:,2:3)))
max(max(file(:,2:3)))],'-g'); hold off; drawnow; pause(0.5);
            end
            line =[max(max(file(:,2:3)))+2 min(min(file(:,2:3)))-2];
            linex = [w(1) w(1)];
            linex2 = [w(2) w(2)]; %draw the lines of selected area

            dt = abs(w(1)-w(2))
            dphi = dt*360/(1/a3TC1)

            choice2 = questdlg('Would you save the calculated phase
shift?','Yes','No');% Construct a questdlg with two options
            % Handle response
            switch choice2
                case 'Yes'
                    expname = fileID(1:4);
                    compo = fileID(6:8);% need to be adapted according the
name
                    pressP = fileID(10:12);
                    fittingeq = 'Fitting equation: Y =
A0+A1*x+A2*sin(2*pi*A3*x+((A4*pi)/(180)))';
```

```
                    A0 ='A0=Temperature';
                    A1 ='A1=baseline T';
                    A2 ='A2=amplitude';
                    A3 ='A3= frequency';
                    A4 ='A4=phase';
                    TC1 = 'Inner thermocouple';
                    TC2 = 'outer thermocouple';

                    header1 = {expname;compo;fittingeq};
                    header3 = {A0, A1, A2, A3, A4};
                    header4 = {TC1, TC2};
                    datalabel = {'Temperature (C)','Frequency (Hz)', 'A0',
'A1', 'A2', 'A3', 'A4'};
                    finalfile = [a0TC1 a1TC1 ampTC1 a3TC1 0; a0TC2 a1TC2
ampTC2 a3TC2 dphi]; % T T0 Amp f phi
                    xlsfileadress = cat(2,fileID(1:end-4),'.xlsx'); %new file
name +extension
                    sheet = 1;
                    xlsrangeheader1 = 'C1';
                    xlsrangeheader2 = 'F2';
                    xlsrangeheader3 = 'A5';
                    xlsrangeheader4 = 'A6';
                    xlsrangedata = 'A12';
                    xlsrange = 'C13';
                    xlswrite(xlsfileadress, header1, sheet, xlsrangeheader1);
                    xlswrite(xlsfileadress, pressP, sheet, xlsrangeheader2);
                    xlswrite(xlsfileadress, header3, sheet, xlsrangeheader3);
                    xlswrite(xlsfileadress, header4, sheet, xlsrangeheader4);
                    xlswrite(xlsfileadress, datalabel, sheet, xlsrangedata);
                    xlswrite(xlsfileadress, finalfile, sheet, xlsrange);
                case 'No'

            end

    end
```

2) XLS file stacking

The program XLS file stacking, merges the fitted parameters obtained from the previous program in a single xls file.

```
%05/03/2017
% Freitas Damien

% If you are using this program please contact me at
% freitas.damien@yahoo.com /or on researchgate for any explanation.
% This program is a part of my
% PhD work, please cite it or contact me
% for co-authoring or acknowledgment

%cleaning trilogy
clear  all
close all
clc

%% part 1 read all the previous files

filefolder = inputdlg('experiment name/folder name','Directory input', [1
50]); % put the folder name starting for the current directory and end with
antislash ex: M802\C2\
filefolder = num2str(cell2mat(filefolder(1)));
filefolder2 = cat(2,'\',filefolder);
intial_cd = cd;
folder = cat(2,intial_cd,filefolder2);
cd (filefolder)

fnames = dir('*.xlsx');
numfids = length(fnames);
vals = cell(1,numfids);
for K = 1:numfids
    vals{K} = xlsread(fnames(K).name);
end


%% part 2 create the new file

finalfile = [];
valsmat = cell2mat (vals); %create the data matrix
for i = 1:1:size(valsmat,1)
    ind = isnan(valsmat(i,:));
    if ind == 0
        finalfile = [finalfile;valsmat(i,:)];
    end
end

choice = questdlg('Invert TC1 and TC 2?','Yes','No');% Construct a questdlg
with two options
% Handle response
switch choice
```

```
    case 'Yes'  %Tc1 must be centered one in all the treatment and TC2 the
side one. If they were reversed during the experiment, select yes
        finalfilei = [finalfile(2,:); finalfile(1,:)];
        step = 7;
        finalfile2 = [];
        for j = 1:step:size(finalfilei,2)
            finalfile2 = [finalfile2; finalfilei(:,j:j+step-1)];
        end

    case 'No' % if not select no
        step = 7;
        finalfile2 = [];
        for j = 1:step:size(finalfile,2)
            finalfile2 = [finalfile2; finalfile(:,j:j+step-1)];
        end
end

% Correct phi before
choice = questdlg('Would you correct phase before the condfit
treatment?','Yes','No');% phi can be corrected prior the data treatment eg
takig values between 0 and 2pi
% Handle response
switch choice
    case 'Yes'
        for i = 1:size(finalfile2,1);
            while finalfile2(i,5)>=360;
                finalfile2(i,5)= finalfile2(i,5)-360;
            end
            while finalfile2(i,5)<0;
                finalfile2(i,5)= finalfile2(i,5)+360;
            end
        end
    case 'No'
end

expname = fnames(1).name(1:4);
compo = fnames(1).name(6:8); % need to be adapted according to the name
pressP = fnames(1).name(10:12);
fittingeq = 'Fitting equation: Y = A0+A1*x+A2*sin(2*pi*A3*x+((A4*pi)/(180)))';
A0 ='A0=Temperature';
A1 ='A1=baseline T';
A2 ='A2=amplitude';
A3 ='A3= frequency';
A4 ='A4=phase';
SA2 = 'SA2 std dev Amp 2Sigma';
SA4 = 'SA4 std dev phase 2Sigma';
TC1 = 'Inner thermocouple';
TC2 = 'outer thermocouple';

header1 = {expname;compo;fittingeq};
header3 = {A0, A1, A2, A3, A4, SA2, SA4};
header4 = {TC1, TC2};
datalabel = {'Temperature (C)','Frequency (Hz)', 'A0', 'A1', 'A2', 'A3', 'A4',
'SA2', 'SA4'};
xlsfileadress = cat(2,expname,'.xlsx'); %new file name +extension
sheet = 1;
```

```
xlsrangeheader1 = 'C1';
xlsrangeheader2 = 'F2';
xlsrangeheader3 = 'A5';
xlsrangeheader4 = 'A6';
xlsrangedata = 'B12';
xlsrange = 'D13';
xlswrite(xlsfileadress, header1,sheet,xlsrangeheader1);
xlswrite(xlsfileadress, pressP,sheet,xlsrangeheader2);
xlswrite(xlsfileadress, header3,sheet,xlsrangeheader3);
xlswrite(xlsfileadress, header4,sheet,xlsrangeheader4);
xlswrite(xlsfileadress, datalabel,sheet,xlsrangedata);
xlswrite(xlsfileadress, finalfile2,sheet,xlsrange);
```

3) D_Fit

The D_Fit programs invert the fitted data from both thermocouple to calculate thermal diffusivity and conductivity. A single file of merged fitting parameters should be used. The programs treatment and operation are detailed in the chapter VI.

```
%D .Freitas 02/01/2018

% If you are using this program please contact me at
% freitas.damien@yahoo.com /or on researchgate for any explanation.
% This program is a part of my
% PhD work, please cite it or contact me
% for co-authoring or acknowledgment
The architecture of this code was inspired from Condfit from J.Clemens, but
this was completely build and adapted by D.Freitas to our experimental
purposes.

% Monte carlo regression taking in account the error propagations
% version with tunable CP, rho and alpha in function of P and T
% This depends on each mineral, empirical estimations
% values are given here for olivine

%cleaning the matlab
clear all

%%
% PART 1 Define the variables, to check before each run

d0= 0.001643637;% Sample length (m)
Sd0= 10*10^(-6); %error on sample length (1S)
P= 2; % pressure in Gpa
SP = P*0.05; %error on Pressure (1S)

%%
% PART 2 read the input file

[fileID, filepath]= uigetfile({'*.*'},'pick a file'); %select the file
fileadress= cat(2,filepath,fileID); %whole file adress
fileopen= fopen(fileadress,'r+');% open it
data=xlsread(fileadress); %load from excel file

%%
%PART 3
%search for empty lines in the excel spreadsheet and delete the adjacent line
which belongs to this line

inda=isnan(data(:,1)); %check if there is NaN if the file is complete no need
to search for them.TRUE=1
indb=find(inda==1);% If there is, indb will be different than []

if length(indb)== 0
    result=data(:,:);%if no gap take the whole xls file
```

```
else

    if max(indb)>12 %12 first lines header part
        if length(indb)>0 % if there is not indb=[] so length=0, if there is
length will be greater
            %first find the NaN lines
            ind=find(isnan(data(:,1)));

            %get if they are either the first or the second line of a
            %measurement
            unevenInd=find(mod(ind,2)~=0); % check if it is pair, modulus not
0 impair line and so 1st line of the same freq (A) ind= line before (ind-1)
            evenInd=find(mod(ind,2)==0); %modulus=0 pair line and so second
line of the same freq (B) ind = 2 line before (ind-2)

            %according to the position of the line calculate the indices
            %before a failed measurement
            ind(unevenInd)=ind(unevenInd)-1; % impair so first line ind= line
before (ind-1)
            ind(evenInd)=ind(evenInd)-2; % pair so second line ind = 2 line
before (ind-2)

            %now construct the array without the failed measurements
            %it is done by always by append from the original data from
            %calculated ind(k)+3 to the next ind(k+1)
            %additionally we need to handle the beginning an d the end of
            %the array
            if ind(1)>2
                result=data(1:ind(1),:); % if it is not the first two line
with NaN, take all the lines until the first data gap
            else
                result=[]; % esle do not take these lines
            end

            for k=1:length(ind)-1 % all the gap postions
                result=[result; data((ind(k)+3):ind(k+1),:)]; % 1st data after
the gap of two line or more(so +3)until the next one
            end

            if ind(end)+3<length(data)
                result=[result; data((ind(end)+3):length(data),:)];
            end

        else
            result=data(:,:);%if no gap take the whole xls file
        end
    else
        result = data(12:end,:);
    end
end


%% PART4
%first correct the phi and theta values. This should have been done
%manually in the previous manual step, in case it is repted here.
```

```
for l=1:size(result,1)
    %test if the amplitude is negative
    if result(l,3)<0
        result(l,3)=abs(result(l,3));
        %shift the phase by 180°
        result(l,5)=result(l,5)+180;
        if result(1,5)>360; %if phase bigger than 2 pi --> subtract 1 pi()
            result(1,5)=result(1,5)-360;
        end
    end
end

outputData = [];
for l=1:size(result,1)/2
    temperature=(result(2*l-1,1)+result(2*l,1))/2+273.15; %T average
    St = 5;% error on temperature (1S)

    SthetaTC1=result(2*l-1,6)/2;% error on theta from TC1 (1S)
    SthetaTC2=result(2*l,6)/2; %error on theta from TC2 (1S)
    theta=result(2*l-1,3)./result(2*l,3); %Theta1/theta2
    Stheta= sqrt((-result(2*l-
1,3)./(result(2*l,3)^2))^2*SthetaTC2^2+(1/(result(2*l,3)))^2*SthetaTC1^2);%std
dev on theta exp (1s)

    f=(result(2*l-1,4)+result(2*l,4))/2; %frequency average
    Sf = 1*10^(-6); %Error on frequency (1S)

    SphiTC1=result(2*l-1,7)/2;% error on phi from TC1 (1S)
    SphiTC2=result(2*l,7)/2; %error on phi from TC2 (1S)
    phi=correct_phi(result(2*l-1,5))-correct_phi(result(2*l,5));% phi1-phi2
%if some functions are missing, please contact D.Freitas
    Sphi=(sqrt(SphiTC1^2+SphiTC2^2))*pi()/180;% std on phi (1s)
    while phi<0 %important step to keep the phase shift
        phi=abs(phi);
    end

        % ALPHA, rho,K AND CP CALC
    rho = -0.2017*P^2+25.019*P+3225.5+temperature*(-0.11749); %calculated from
Li and Li 2007
    Srho= rho*0.05; % error on rho (1s)
    alpha= 2.825*10^-5+0.758*10^-8*temperature; %Sample thermal expension (K-
1) Bouhifd 1996, No P
    Salpha= alpha*0.05; % error on alpha (1s)
    cp = (205.99-959.8/(temperature^(0.5))-
(30.137*10^5)/(temperature^2))/0.14069; % heat capacity (J/K/kg) Richet 1991
No P
    Scp = 0.1*cp; % error on cp(1S)
    K = -1.41*10^-6*temperature^2-1.794*10^-2*temperature+130.8+4.2*P;
%calculated from Li 2007 and Gillet 1991
    SK = K*0.05; % error on K (1S)

    d=d0*(1-alpha*(temperature-298.15)+P/K)^(-1/3); %calculation of size
variations
    Sd = sqrt(((1-alpha*(temperature-298.15)+P/K)^(-1/3))^2*Sd0^2 ...
```

```
    +(-d0/3*(temperature-298)*(1-alpha*(temperature-298.15)+P/K)^(-
4/3))^2*Salpha^2 ...
    +(-d0/3*alpha*(1-alpha*(temperature-298.15)+P/K)^(-4/3))^2*St^2 ...
    +(-d0/(3*K)*(1-alpha*(temperature-298.15)+P/K)^(-4/3))^2*SP^2 ...
    +((d0*P)/(3*K^2)*(1-alpha*(temperature-298.15)+P/K)^(-4/3))^2*SK^2);%Error
on D (1s)

    [phi_calc, Sphi_calc, mis_phi, Smis_phi, theta_calc,
Stheta_calc,mis_theta, Smis_theta, D_theta,D_phi,SD_theta,SD_phi, D_theta_1st,
SD_theta_1st, D_phi_1st, SD_phi_1st]=
minimization_D_fit(d,f,phi,theta,Sd,Sf,Sphi,Stheta);

    %little correction needed on SDtheta --> equal to Sthetacal/thetacalc
    SD_theta = Stheta_calc/theta_calc*D_theta;
    %end of correction part

    cond_phi= D_phi*rho*cp;
    cond_phi_1st= D_phi_1st*rho*cp;
    Scond_phi=
sqrt((cp*D_phi)^2*Srho^2+(rho*D_phi)^2*Scp^2+(rho*cp)^2*SD_phi^2);
    Scond_phi_1st=
sqrt((cp*D_phi_1st)^2*Srho^2+(rho*D_phi)^2*Scp^2+(rho*cp)^2*SD_phi_1st^2);
    cond_theta= D_theta*rho*cp;
    cond_theta_1st= D_theta_1st*rho*cp;
    Scond_theta=
sqrt((cp*D_theta)^2*Srho^2+(rho*D_theta)^2*Scp^2+(rho*cp)^2*SD_theta^2);
    Scond_theta_1st=
sqrt((cp*D_theta_1st)^2*Srho^2+(rho*D_theta_1st)^2*Scp^2+(rho*cp)^2*SD_theta_1
st^2);
    %outputData =[outputData; [temperature f phi D_phi cond_phi D_theta
cond_theta Scond_phi Scond_theta D_phi_1st cond_phi_1st D_theta_1st
cond_theta_1st Scond_phi_1st Scond_theta_1st]];
    outputData =[outputData; [temperature f phi Sphi phi_calc Sphi_calc
mis_phi Smis_phi D_phi SD_phi cond_phi Scond_phi D_phi_1st SD_phi_1st
cond_phi_1st Scond_phi_1st...
     theta Stheta theta_calc Stheta_calc mis_theta Smis_theta D_theta SD_theta
cond_theta Scond_theta D_theta_1st SD_theta_1st cond_theta_1st
Scond_theta_1st]];
    % Temperature, phase sifht measured + error, phase shift calculated +
    % error,diffusivity phi + error, conductivity phi + error, diffusivity
    % 1st+ error, conductivity 1et +error --> idem for theta
end

%%
% PART5 %Data representation
figure;
hold on

plot(outputData(:,1), outputData(:,11),'b+');
xlabel('Temperature (K)');
ylabel('Thermal conductivity by phi (W/m.K)');
figure;
plot(outputData(:,1), outputData(:,25),'b+');
xlabel('Temperature (K)');
ylabel('Thermal conductivity by theta (W/m.K)');
hold on
```

```
figure;
hold on
plot(outputData(:,1), outputData(:,9),'b+');
xlabel('Temperature (K)');
ylabel('Thermal difusivity by phi (m2/s)');
hold on
figure;
plot(outputData(:,1), outputData(:,23),'b+');
xlabel('Temperature (K)');
ylabel('Thermal difusivity by theta (m2/s)');
hold on

%%
% Part 6 SAVE DATA

wait = 10;
pause(wait)
choice = questdlg('Would you save the fitted data?','Yes','No');% Construct a
questdlg with two options
% Handle response
switch choice
    case 'Yes'
        fileID2 = cat(2,fileID(1:end-5),'_D_fitresult');
        fileadress2= cat(2,filepath,fileID2); %whole file adress
        outputHeader={'T (°K)', 'f', 'phi measured', 'STD phi measured',
'phi_calculated', 'STD phi_calculated','misfit phi','STD misfit_phi', 'D phi',
'STD D phi','Cond Phi', 'STD cond phi', 'D phi 1st',
'Sd_phi_1st','cond_phi_1st','Scond_phi_1st', 'theta measured','STD theta
measured', 'thetacalc', 'S_theta_calc','misfit theta','STD misfit_theta', 'D
theta', 'STD dtheta', 'Cond Theta', 'Std Cond theta', 'D theta_1st', 'STD
Dtheta phi','condtheta_1st', 'Std Cond theta_1st'};
        xlswrite(fileadress2,outputHeader,'condFit results');
        xlswrite(fileadress2,outputData,'condFit results','A2');
    case 'No'
end
```

4) Minimization_D_fit

The D_Fit program requires the use of a crucial function, in which the Monte Carlo inversion by Neighborhood algorithm is made. The detail on the programs operating is given in the chapter VI.

```
function [phi_cc, Sphi_cc, mis_phi, Smis_phi theta_cc, Stheta_cc, mis_theta,
Smis_theta, D1, D2, SD1, SD2, D11ST, SD11ST, D21ST,
SD21ST]=minimization_D_fit(d,f, phi, theta, Sd, Sf, Sphi, Stheta)

%% function by Damien Freitas
%
% If you are using this program please contact me at
% Freitas.damien@yahoo.com /or on researchgate for any explanation.
% This program is a part of my
% PhD work, please cite it or contact me
% for co-authoring or acknowledgment

w=2.*pi.*f; % angular frequency
theta=abs(theta); % amplitude must positive (just a security)

%%
%Monte carlo N°1 THETA (amplitude ratio)
% 1st draft

y= 10.^[-8:0.01:-4]; % generate D over a wide possible range from 10-8 to 10-4
m2/s
u=d.*sqrt(w./y); %analytical solution to the heat diffusition calculation in
radial geometry
Su=sqrt(((2*pi()*f./y).^(1/2)).^2*Sd^2+(d*pi()./y.*(2*pi()*f./y).^(-
1/2)).^2*Sf^2); % error on the solution of the equation
J0=besselj(0,u.*1i^(3/2));
theta_calc= 1./(sqrt(real(J0).^2+imag(J0).^2)); %amplitude ratio calculated
with the generated diffusivities
stheta_calc= sqrt((-
imag(J0)./((real(J0).^2+imag(J0).^2).^(3/2))).^2.*(Su./u.*imag(J0)).^2+(-
real(J0)./((real(J0).^2+imag(J0).^2).^(3/2))).^2.*(Su./u.*real(J0)).^2);%error
on theta calc
res=abs(theta-1./(sqrt(real(J0).^2+imag(J0).^2))); % misfit
Sres = sqrt(stheta_calc.^2+Stheta.^2); %error on misfit (coming from error on
infered exp values and uncertainties calcuted on the generated D)

midx= [];
midy = [];
for j = 1:length(y)-1;
    % find the middle of the segments
    midx = [midx,(y(1,j+1)+y(1,j))/2];
    midy = [midy, (res(1,j+1)+res(1,j))/2];
end

%take the four best models (can be tuned)
m = (1:length(res))';
```

```
res=res';
res= [res m];
best = (sortrows(res,1))';
fourbest = best(1,1:4);

%Retrieve the indexes of the good Diffisivities
fourind = best(2,1:4);
for mm= 1:length(fourind)
    if fourind(1,mm) == length(y);
        disp('becarefull error on min, end of generated D, no midle possible')
% if the soft display this, thre is many chances that the amplitude ratio is
not between 1 and 0.
        fourind(1,mm) = fourind(1,mm)-1;
    end
end
ind = fourind;
bestD = y(1,ind);
SresofbestD = Sres(1,ind);
resup = fourbest+SresofbestD; %Values + upper error
resdown = fourbest-SresofbestD; %Values -lower error
SbestD = [];
for jjj = 1:length(fourbest)
    bfind = find(resup(1,jjj)>res); %Find the index of values lower than the
upper limit
    erd = y(1,min(bfind)); %calc
    Serror = abs(bestD(1,jjj)-erd); %Values of the error
    SbestD = [SbestD, Serror]; %Save into the matrix
end
D11ST = bestD(1,1);
SD11ST = SbestD(1,1);

%Find the bounds
bup = [];
bdown = [];
for jjj= 1:length(fourbest)
    if ind(1,jjj)<2
            ind(1,jjj)=2;
        end
    bup = [bup, midx(1,ind(1,jjj))];
    bdown = [bdown, midx(1,ind(1,jjj)-1)];
end

%%
%itterative part
% number of itteration
maxiter = 9;
iter = 1;
while iter < maxiter
    %succesive dafts
    % draft in between the bounds
    y2 = [];
    for i = 1:length(fourbest)
        y2= [y2,(bup(1,i)-bdown(1,i))*rand(1,1000)+bdown(1,i)];
    end

    %calculaion part
```

```
    u2=d.*sqrt(w./y2);
    Su2=sqrt(((2*pi()*f./y2).^(1/2)).^2*Sd^2+(d*pi()./y2.*(2*pi()*f./y2).^(-
1/2)).^2*Sf^2);
    J0=besselj(0,u2.*1i^(3/2));
    theta_calc2= 1./(sqrt(real(J0).^2+imag(J0).^2));
    stheta_calc2= sqrt((-
imag(J0)./((real(J0).^2+imag(J0).^2).^(3/2))).^2.*(Su2./u2.*imag(J0)).^2+(-
real(J0)./((real(J0).^2+imag(J0).^2).^(3/2))).^2.*(Su2./u2.*real(J0)).^2);%err
or on theta calc
    res2=abs(theta-1./(sqrt(real(J0).^2+imag(J0).^2))); % misfit
    Sres2 = sqrt(stheta_calc2.^2+Stheta.^2);

    %middle
    midx2= [];
    midy2 = [];
    for j = 1:length(y2)-1;
        % calculate the middle
        midx2 = [midx2,(y2(1,j+1)+y2(1,j))/2];
        midy2 = [midy2, (res2(1,j+1)+res2(1,j))/2];
    end

    %Take the four best models
    m = (1:length(res2))';
    res2=res2';
    res2= [res2 m];
    best = (sortrows(res2,1))';
    fourbest = best(1,1:4);

    %retrieve the good index
    fourind = best(2,1:4);
    for mm= 1:length(fourind)
        if fourind(1,mm) == length(y2);
            disp('becarefull error on min, end of generated D, no midle
possible')
            fourind(1,mm) = fourind(1,mm)-1;
        end
    end
    ind = fourind;
    bestD = y2(1,ind);
    if length(bestD)>4
        bestD = bestD(1,1:4);
    end
    SresofbestD = Sres2(1,ind);
    if length(SresofbestD)>4
        bestD = SresofbestD(1,1:4);
    end
    resup = fourbest+SresofbestD;
    resdown = fourbest-SresofbestD;
    SbestD = [];
    for jjj = 1:length(fourbest)
        bfind = find(resup(1,jjj)>res2);
        erd = y2(1,min(bfind));
        Serror = abs(bestD(1,jjj)-erd)
        SbestD = [SbestD, Serror];
    end
```

```
    %Find the bounds
    bup = [];
    bdown = [];
    for jjj= 1:length(fourbest)
        if ind(1,jjj)<2
            ind(1,jjj)=2;
        end
        bup = [bup, midx2(1,ind(1,jjj))];
        bdown = [bdown, midx2(1,ind(1,jjj)-1)];
    end

    iter = iter +1;
end

% When the number of iterations is reached
%Find back the good D
ind = [];
ind= fourind;
bestD = y2(1,ind);
SresofbestD = Sres2(1,ind);
bestmodels = bestD;
Sbestmodels = SresofbestD;

theta_cc = theta_calc2(1,ind(1,1)); % The good calculated theta, the good
error
Stheta_cc = stheta_calc2(1,ind(1,1));
mis_theta = res2(ind(1,1),1); % value of the good misfit
Smis_theta = Sres2(1,ind(1,1)); % error on the good misfit
D1 = bestD(1,1);
SD1 = stheta_calc2(1,ind(1,1))/theta_calc2(1,ind(1,1)); % error on % to give
an idea

%%
%calc N°2 PHI

% 1 draft
y= 10.^[-8:0.001:-4]; % generate D over a wide possible range from 10-8 to 10-
4 m2/s
u = d.*sqrt(w./y);
Su = sqrt(((2*pi()*f./y).^(1/2)).^2*Sd^2+(d*pi()./y.*(2*pi()*f./y).^(-
1/2)).^2*Sf^2);
J0 = besselj(0,u.*1i^(3/2));

phi_calc = atan2(imag(J0),real(J0)); % calculated phae shift
for i = 1:length(phi_calc)
if phi_calc(:,i)<0
    phi_calc(:,i)=phi_calc(:,i)+2*pi();
end
end

Sphi_calc =
sqrt((1./(real(J0).*((imag(J0).^2)./(real(J0).^2)+1))).^2.*(Su./u.*imag(J0)).^
2+(-
imag(J0)./(real(J0).^2.*((imag(J0).^2)./(real(J0).^2)+1))).^2.*(Su./u.*real(J0
)).^2);
res = abs(phi-phi_calc); % misfit
```

```
Sres = sqrt(Sphi_calc.^2+Sphi.^2); %error on the misfit

% For diverse reasons (see my PhD) no monte carlo were used for this
% version as phase is true problem and need to be manually checked

%Visualisation to get the good D
fig1 = figure;
loglog(y,res,'.b')
xlabel('D in m2/s')
ylabel('misfit (blue) and calc phase shift')
hold on
loglog(y,phi_calc,'.r')

% Find the good minima manually on, the figure. This require an a pirori on
% the diffusivity values (at least the order of magnitude).
[xi,yi] = getpts %manually get it
D21ST = xi;
SD21ST = 0; %no error with this method
%define the bounds
bdown = xi*0.3;
bup = xi*3;

%2nd draft, which should be much more precise both in the dissuvity range
%and a much thinner increment
y2 = bdown:xi/100000:bup;

%Calculation
u2=d.*sqrt(w./y2);
Su2=sqrt(((2*pi()*f./y2).^(1/2)).^2*Sd^2+(d*pi()./y2.*(2*pi()*f./y2).^(-
1/2)).^2*Sf^2);
J0=besselj(0,u2.*1i^(3/2));

phi_calc2 = atan2(imag(J0),real(J0));
for i = 1:length(phi_calc2)
if phi_calc2(:,i)<0
    phi_calc2(:,i)=phi_calc2(:,i)+2*pi();
end
end

Sphi_calc2 =
sqrt((1./(real(J0).*((imag(J0).^2)./(real(J0).^2)+1))).^2.*(Su2./u2.*imag(J0))
.^2+(-
imag(J0)./(real(J0).^2.*((imag(J0).^2)./(real(J0).^2)+1))).^2.*(Su2./u2.*real(
J0)).^2);
res2=abs(phi-phi_calc2); % misfit
Sres2 = sqrt(Sphi_calc2.^2+Sphi.^2);

%visulatisation
fig2 = figure;
loglog(y2,res2,'.b')
xlabel('D in m2/s')
ylabel('misfit (blue) and calc phase shift')
hold on
loglog(y2,phi_calc2,'.r')
```

```
%Find back the good D
[xi2,yi2] = getpts % Manually click
dt = delaunayTriangulation(y2',res2');
pid = [];
pid = nearestNeighbor(dt,[xi2,yi2]);
bestD = y2(1,pid);
SresofbestD = Sres2(1,pid);
bestmodels = bestD;
Sbestmodels = Sphi_calc2(1,pid);
D2 = bestD(1,1);
SD2 = D2 * Sphi_calc2(1,pid)/phi_calc2(1,pid);
phi_cc = phi_calc2(1,pid); % The good calculated theta, the good error
Sphi_cc = Sphi_calc2(1,pid);
mis_phi = res2(1,pid); % value of the good misfit
Smis_phi = Sres2(1,pid); % error on the good misfit
close(fig2)
close(fig1)

end
```

5) Errors and uncertainties treatment implementation in the fitting and inversion programs

In this section, we have developed a much robust procedure to estimate thermal properties via the inversion of phase shift and amplitude ratio using Monte Carlo inversion or neighborhood methods (Sambridge, 2002). The errors (deviation to the real value) and uncertainties (interval of confidence around the measured value) on each step are estimated. Such development is included in the codes given here-above.

Uncertainties on Phi (measured):

Phase information from Angström method is inferred from the phase shift measured between the two thermocouples:

$$\varphi = \varphi_A - \varphi_B$$

Uncertainties on the phase shift can be expressed as:

$$\sigma_\varphi = \sqrt{{\sigma_{\varphi_A}}^2 + {\sigma_{\varphi_B}}^2}$$

They are estimated to be majored by 1.5°, so up to 12.5% (1σ) of the phase value for noisy signals but commonly are below 5%.

Uncertainties on Theta (measured):

Amplitude ratio from Angström method is obtained from the ratio of the amplitude of the two thermocouples sinusoidal signals.

$$\theta = \frac{\theta_B}{\theta_A}$$

Where B is the signal from TC 1 (inner at $r= 0$) and A from TC 2 (outer at $r=d$)

Uncertainties can be expressed as:

$$\sigma_\theta = \sqrt{\left(\frac{-\theta_B}{{\theta_A}^2}\right)^2 * {\sigma_{\theta_A}}^2 + \left(\frac{1}{\theta_A}\right)^2 * {\sigma_{\theta_B}}^2}$$

They are estimated to be around 0.015 K, so up to 1.5% of the amplitude value (1 σ) (extreme case for a low amplitude value).

Comments on both phase and amplitude errors/uncertainties estimations

To check the uncertainties on both phase and amplitude inversions, we tested the fitting program with an artificial sine function, with known parameters, without instrumental noise. For a wave of frequency of 0.4 Hz, 60° of phase and amplitude of 0.5 K, the program (for several runs) find the exact value of both phase and amplitude with a very high accuracy. Maximum probability values of 60.0064° and 0.4999 K were reported by the software. The 95 % confidence interval (2σ) was observed to be symmetrical, and equal to 60.0064° ± 0.07° and 0.4999 K ± 0.007 K representing 0.12 % and 1.4 % of the values. The recovered values are very precise (low errors and uncertainties); however the instrumental noise influence is far from being negligible on the signal recorded during experiments.

We tested our code on several recorded waves, with unknown absolute values. The fit was visually good but noise presence induces a larger uncertainty in the fitted parameters. After several fitting, we observed the error on phase can be as high as 2°, which can represent up to 25 % (2σ) for low phase values (example 0 - 20°). The uncertainties depend on the signal quality and may be few degrees for all analyses, however if the angle is 0, 360 or 1800, the relative precision can change importantly. On amplitude, uncertainties were found to be smaller: around 0.03 K which corresponds to 3 % of the value (2σ).

a. Thermal diffusivity estimation: minimization algorithm

Uncertainties on thermal diffusivity:

Thermal diffusivity error/uncertainty using minimization algorithm, without Monte Carlo simulation with neighborhood algorithm, is associated to the precision of the step for thermal diffusivities generation. Our tests on the algorithm show that step of 10^{-10} m²/s is a good balance between calculation time and obtained values (no variation with lower step). We can consider this value as the standard deviation of our measurements. However, this procedure ignores the

potential effects of local minima which are a significant problem with this type of functions. The value measured is accurate but the result can be wrong if caught in the "bad" part of the function.

To solve this problem, we developed a Monte Carlo simulation using the neighborhood algorithm; the minimum is then constrained by iterative steps. The function performs a classical first run and then performs new draws near the previous estimated minima at each new iteration. The associated error to the inferred thermal diffusivity is a function of the number of iterations of the Monte Carlo simulation, the number of draws and the step interval of the first draw. The error associated with this procedure is very low. The program was calibrated to stop when measurement's and models are strictly equals (15 digits of precision in Matlab®), this occurs after more than 10 iterations. The error on inferred diffusivities should be $10^{-15/-16}$ m²/s.

However, the determination of *D*, also suffers from uncertainties injected in the calculation of *u* and calculated phase shift and amplitude ratio. *D* estimation is very accurate (low errors) but real standard deviation can be higher due to associated uncertainties.

Uncertainties on u

u is the solution of the heat equation (e.g Fujisawa 1968, Carslaw and Jaegger 1959, etc). It is calculated using the modeled *D,* but using also experimental parameters such as the angular frequency (*w*).

$$u = d(w/D)^{1/2} \leftrightarrow u = d(2\pi f/D)^{1/2}$$

$$\sigma_u = \sqrt{\frac{du}{dd}^2.{\sigma_d}^2 + \frac{du}{df}^2.{\sigma_f}^2 + \frac{du}{dD}^2.{\sigma_D}^2}$$

This can be expressed using partial derivative as:

$$\sigma_u = \sqrt{\left(\left(\frac{2\pi f}{D}\right)^{1/2}\right)^2.{\sigma_d}^2 + \left(\frac{\pi d}{D}.\left(\frac{2\pi f}{D}\right)^{-1/2}\right)^2.{\sigma_f}^2 + \left(\frac{d\pi f}{D^2} * \left(\frac{2\pi f}{D}\right)^{-1/2}\right)^2.{\sigma_D}^2}$$

Because *D* is generated artificially, we can consider its value is absolute: $\sigma_D = 0$, the expression reduces to:

$$\sigma_u = \sqrt{\left(\left(\frac{2\pi f}{D}\right)^{1/2}\right)^2 . {\sigma_d}^2 + \left(\frac{\pi d}{D} . \left(\frac{2\pi f}{D}\right)^{-1/2}\right)^2 . {\sigma_f}^2}$$

- The error on the frequency is due to the wave function generator. We used an Agilent 33500B Series with an uncertainty on the frequency of 1 µHz (1 σ).
- Uncertainty on the sample size estimation is from far, the biggest source of errors. Sample length is checked before and after the experiment. Before the experiment, we used a Mitutoyo digital high gauge, with a precision in the order of 1 µm (1 σ). After the experiment, sample diameter is measured on both vertical and horizontal cuts (using the thermocouples) using SEM or optical imaging with a precision less than 5 µm (1 σ). Sample length is recalculated at each P and T step (see above) with the following formula:

$$d(P,T) = d_0 * \left(1 - \alpha(T - 298) + \frac{P}{K}\right)^{-1/3}$$

Where d_0 is the sample length measured at ambient conditions, α the thermal expansion, T the temperature, P the pressure and K the bulk modulus. At each measurement performed at given P and T conditions the parameters α, K and d are calculated.

$$\sigma_d = \sqrt{\frac{dd}{dd_0}^2 . {\sigma_{d_0}}^2 + \frac{dd}{d\alpha}^2 . {\sigma_\alpha}^2 + \frac{dd}{dT}^2 . {\sigma_T}^2 + \frac{dd}{dP}^2 . {\sigma_P}^2 + \frac{dd}{dK}^2 . {\sigma_K}^2}$$

This can be written:

$$\sigma_d = \sqrt{\begin{aligned} &\left(\left(1-\alpha(T-298)+\frac{P}{K}\right)^{\frac{-1}{3}}\right)^2 . \sigma_{d_0}^2 \\ &+\left(\frac{-d_0}{3} * (T-298) * \left(1-\alpha(T-298)+\frac{P}{K}\right)^{\frac{-4}{3}}\right)^2 . \sigma_\alpha^2 \\ &+\left(\frac{-\alpha d_0}{3} * \left(1-\alpha(T-298)+\frac{P}{K}\right)^{\frac{-4}{3}}\right)^2 . {\sigma_T}^2 \\ &+\left(\frac{-d_0}{3K} * \left(1-\alpha(T-298)+\frac{P}{K}\right)^{\frac{-4}{3}}\right)^2 . \sigma_P^2 \\ &+\left(\frac{P d_0}{3K^2} * \left(1-\alpha(T-298)+\frac{P}{K}\right)^{\frac{-4}{3}}\right)^2 . {\sigma_K}^2 \end{aligned}}$$

- The standard deviation on the ambient condition length is 5 to 10 µm (1 σ) (see above).
- Standard deviation of temperature is related to the type C thermocouple. The standard deviation is usually considered within 5 K (1 σ) on the absolute value even if sinusoidal variations of 1 K or less are easily visible (good relative precision, absolute temperature more uncertain). Background noise on the recorded signals was observed to be between 1 or 2 orders lower (0.1 - 0.01 K).
- Standard deviation on pressure is inferred from our laboratory calibration, it is majored while taking 10 % of the value (2 σ).
- Thermal expansion, density, bulk modulus and heat capacity are estimated at each temperature and pressure step using literature estimations for each phase (see above). We found the errors are usually between 5 and 10 % of the value (1 σ).

Uncertainties on Phi (calculated):

The calculation of phase shift is made from calculated values of *u*:

$$\varphi = tan^{-1}\left(\frac{bei(u)}{ber(u)}\right)$$

Where *bei* and *ber* are the imaginary and real parts of the Bessel functions respectively. Bessel function used were from Matlab ® library, for simplicity, we consider that the uncertainty on *u* is

equal (in %) to the error on *ber(u)* and *bei(u)* (software is only inducing a very low additional uncertainty).

$$\sigma_\varphi = \sqrt{\left(\frac{1}{ber(u).\left(\frac{bei(u)^2}{ber(u)^2}+1\right)}\right)^2 * \left(\frac{\sigma_{(u)}}{u}.bei(u)\right)^2 + \left(\frac{-bei(u)}{ber(u)^2.\left(\frac{bei(u)^2}{ber(u)^2}+1\right)}\right)^2 * \left(\frac{\sigma_{(u)}}{u}.ber(u)\right)^2}$$

Because we consider standard deviation of both imaginary and real part equal to the relative one of u (in %), we can write:

$$\sigma_\varphi = \sqrt{\left(\left(\frac{ber(u)}{bei(u)^2+ber(u)^2}\right)^2 + \left(\frac{-bei(u)}{bei(u)^2+ber(u)^2}\right)^2\right).\sigma_{(u)}{}^2}$$

Uncertainties on Theta (calculated):

The calculation of phase shift is made from calculated values of *u*:

$$\theta = \frac{1}{\sqrt{bei(u)^2+ber(u)^2}}$$

Where *bei* and *ber* are the imaginary and real parts of the Bessel functions respectively. We consider for the same reasons that phase shift errors on Bessel function are equal to uncertainties on *u* (in %):

$$\frac{\sigma_{bei(u)}}{bei(u)} = \frac{\sigma_{ber(u)}}{ber(u)} = \frac{\sigma_{(u)}}{u}.$$

$$\sigma_\theta = \sqrt{\left(\frac{-bei(u)}{(bei(u)^2+ber(u)^2)^{3/2}}\right)^2.\sigma_{bei(u)}{}^2 + \left(\frac{-ber(u)}{(bei(u)^2+ber(u)^2)^{3/2}}\right)^2.\sigma_{ber(u)}{}^2}$$

This can be simplified in

$$\sigma_\theta = \sqrt{\left(\left(\frac{-bei(u)}{(bei(u)^2+ber(u)^2)^{3/2}}\right)^2.\left(\frac{\sigma_{(u)}}{u}.bei(u)\right)^2 + \left(\frac{-ber(u)}{(bei(u)^2+ber(u)^2)^{3/2}}\right)^2\right).\left(\frac{\sigma_{(u)}}{u}.ber(u)\right)^2}$$

Errors on the minimization and inferred diffusivities

The algorithm minimizes the difference between the experimental value and the calculated one, both for φ and θ. This misfit function is thus, submitted to the errors on experimentally determined values and must be propagated to the calculated one.

$$Misfit = \theta_{measured} - \theta_{calculated} \; or \; \varphi_{measured} - \varphi_{calculated}$$

The uncertainty associated to the misfit calculation is:

$$\sigma_{misfit} = \sqrt{{\sigma_{\theta_{measured}}}^2 + {\sigma_{\theta_{calculated}}}^2} \; or \; \sqrt{{\sigma_{\varphi_{measured}}}^2 + {\sigma_{\varphi_{calculated}}}^2}$$

The uncertainty coming for this part is the major problem. In fact, because the misfit tends to be close to zero for the best *D* values the relative uncertainties suddenly become very important. For example considering a θ measured equal to 2 ± 0.2 K (10% relative) and from which we subtract a calculated θ of 1.999 ± 0.2 K (10% relative error), the result of the misfit is 0.001 ± 0.28 and the relative uncertainty suddenly become 28280 %. This estimation signifies that the misfit can be really precise (low error; e.g really close to 0), however, the uncertainty on its value is significant because it lies in reality between 0 and 0.28 in this example (it can't be negative).

The best diffusivity is inferred from the lower misfit after the Monte Carlo simulation. The uncertainty of the best *D* was estimated retrieving all the diffusivities that can lead the value of the best misfit taking in account its uncertainty. This estimation works for the first draw, but can be performed in next draws because new generated diffusivities are only surrounding the minima on a limited but precise zone. The drawn diffusivities are discrete and on restricted zones, thus the value given by our program is decreasing significantly because the area probed is narrowing. The value given then by the program is decreasing toward Maltlab precision 10^{-15}. This represents the accuracy on the misfit value but the uncertainty must be somewhat larger, similar to the first draw because space is linearly covered for this first iteration.

b) Thermal conductivity calculation

Uncertainties on thermal conductivity:

Thermal conductivity is calculated by using the following formula:

$$D = \frac{K}{\rho Cp} \leftrightarrow K = \rho CpD$$

Where D is thermal diffusivity (m²/s), ρ density (kg/m3), Cp the heat capacity (J/kg.K) and K is the thermal conductivity (W/m/K)

Error propagation can be estimated to:

$$\sigma_K = \sqrt{\frac{dK}{d\rho}^2.{\sigma_\rho}^2 + \frac{dK}{dCp}^2.{\sigma_{Cp}}^2 + \frac{dK}{dD}^2.{\sigma_D}^2}$$

This can be expressed as:

$$\sigma_K = \sqrt{(CpD)^2.{\sigma_\rho}^2 + (\rho D)^2.{\sigma_{Cp}}^2 + (\rho Cp)^2.{\sigma_D}^2}$$

Where heat capacity and density are estimated for each sample at the right P and T thanks to literature calibrations. D and its uncertainty are provided by our fitting and calculation starting from experimental data.

Monte Carlo simulation: accuracy and errors/uncertainty

The value obtained on diffusivities errors after the Monte Carlo simulation are not the real uncertainty (see above) but the accuracy of the iterative process. As well, the accuracy of the iterative process can be seen using statistical information while lunching several times the same data to fit. To quantify these effects and the correctness of the diffusivity value, the program has been lunched 50 times for a single file (olivine, 2 GPa, 1165 K and 0.4 Hz) (table C.1). The results of the calculations were saved independently and statistics were made on the recovered results (tables C.1 (1 run) and C.2 (50 runs)). The minimization is very accurate (low errors) with standard deviation values few orders lower than the average. The uncertainties on thermal diffusivities are lower than the one obtained at the first iteration (which are more realistic) but it does not change that much the final results because uncertainties on final thermal conductivity is mainly due to uncertainties on other parameters such as density or heat capacity.

The shape of the histogram of solutions is also confirming correct estimated values by the program (Fig. C.1). The number of runs (50) is too low to perform more accurate analysis and at

least 10 times more data are needed to have a correct Gaussian like shape. The value of each bin is given above the histogram and the Gaussian fit of the data are given. The fit highlights that our data is probably more leptokurtic than Gaussian distribution with a more pronounced modal value and thinner shoulders. This indicate that the real accuracy of the data is even greater than the here determined standard deviation (which a Gaussian indicator). This aspect seems to be truer for theta than phi.

Table C.1 Example of error propagation for a standard inversion (1 run) an artificial function (0.4 Hz, phase and amplitude set to 0.5) and experimental signal taken at 1165 K with 0.4 Hz imposed temperature oscillation (all the errors are 1 σ).

	Artificial function		Experimental signal	
Parameter	Parameter values	Standard deviation (1 σ)	Parameter values	Standard deviation (1 σ)
d_o (m)	0.001	$5e^{-6}$	0.0017	$5e^{-6}$
P (GPa)	2	0.1	2	0.1
T (K)	423.147	5	1165.5	5
θTC_1 (K)	0.5	$1.9535e^{-4}$	2.98	0.0365
θTC_2(K)	0.5	$2.5966e^{-4}$	4.45	0.105
θ_{ratio}	1	$6.4996e^{-4}$	0.65	0.0174
F (Hz)	0.4	1e-6	0.4	1e-6
φTC_1 (°)	60.0027	0.0224	15.84	0.73
φTC_2(°)	9.0992	0.0299	30.25	1.355
Φ_{shift} (rad)	0.8727	$6.524e^{-4}$	6.0316	0.0269
P (kg/m^3)	3225	161.2508	3137.8	156.89
α (K^{-1})	$3.1457e^{-5}$	$1.5729e^{-6}$	3.7084e-5	1.8542e-6
Cp (J/kg/K)	$1.0129e^{3}$	101.2863	1248.5	124.8536
K (GPa)	131.35	6.5678	116.3766	5.8188
d (m)	$9.9626e^{-4}$	$4.9945e^{-6}$	0.0017	$5.1597e^{-5}$
1st Monte Carlo				
u	4.995 to 0.4995	0.025 to 0.0025	8.5655 to 0.9566	0.0259 to 0.0026
θ_{calc} (K)	0.161 to 0.999	1.36e-6 to 0.0013	0.017 to 0.9917	4.58e-11 to 0.0015
res ($\theta_{exp} - \theta_{calc}$) (K)	0.839 to 0.001	6.4996e-4 to 0.0014	0.6329 to $3.2781e^{-4}$	0.0174 to 0.0175
bestDθ (m^2/s)	$9.99e^{-6}$	$3.64e^{-6}$	$1.14e^{-6}$	$5e^{-8}$
Kθ 1st (W/m/K)	32.6323	12.43	4.4661	0.5364
φ_{calc} (rad)	-1.5446 to 1.5614	0.0025 to 0.0084	$1e^{-5}$ to 1.369	$4.3991e^{-4}$ to 0.0011
Res(φ_{exp} - φ_{calc}) (rad)	0.0032 to 2.4173	0.0026 to 0.0084	6.662 to 4.6374	0.0269 to 0.0273
BestDφ (rad)	$6.6e^{-7}$	$1.0e^{-8}$	$9.1e^{-7}$	$1e^{-8}$
$K\varphi^{1st}$ (W/m/K)	2.1559	0.2426	3.5651	0.3991
After all the iterations				
Dφ (m^2/s)	6.5786 e^{-7}	$9.1496e^{-13}$	$9.0579e^{-7}$	$3.206e^{-16}$
Dθ (m^2/s)	$9.9948e^{-6}$	$1.1191e^{-13}$	$1.1391e^{-6}$	$1.6736e^{-13}$
Kφ (W/m/K)	2.1489	0.2403	3.5486	0.3967
Kθ (W/m/K)	32.6479	3.651	4.4624	0.4989

The values obtained through the treatment shows that our minimization is correct and accurate (low error on known signals) and that uncertainties on the final diffusivities and conductivities are mostly controlled by uncertainties on the external parameters required such as sample length or density, thermal expansion, heat capacity and bulk moduli. The errors coming from the computational part are somewhat negligible given that the final results and are really similar to the obtained ones at the first draw. The overall errors are estimated to be around 10% (1σ) on the final diffusivities and conductivities.

Table C.2 Average value obtained from 50 inversions on the same input file for diffusivities and conductivities. The value and its standard deviation reported (1 σ) reflect the precision of the Monte Carlo simulation. The values given in the second raw are the ones returned by the program for 1 analysis.

		D_θ	D_φ	K_θ	K_φ
50 analysis	**Average value**	1.139E-06	9.057E-07	4.463	3.548
Monte Carlo only	**STD DEV**	1.455E-10	4.537E-10	5.701E-04	1.777E-03
Program error after 1 analysis	**Average value**	1.139E-06	9.058E-07	4.462	3.549
	STD DEV (calculated by propagation)	1.673E-13	3.206E-16	0.499	0.398

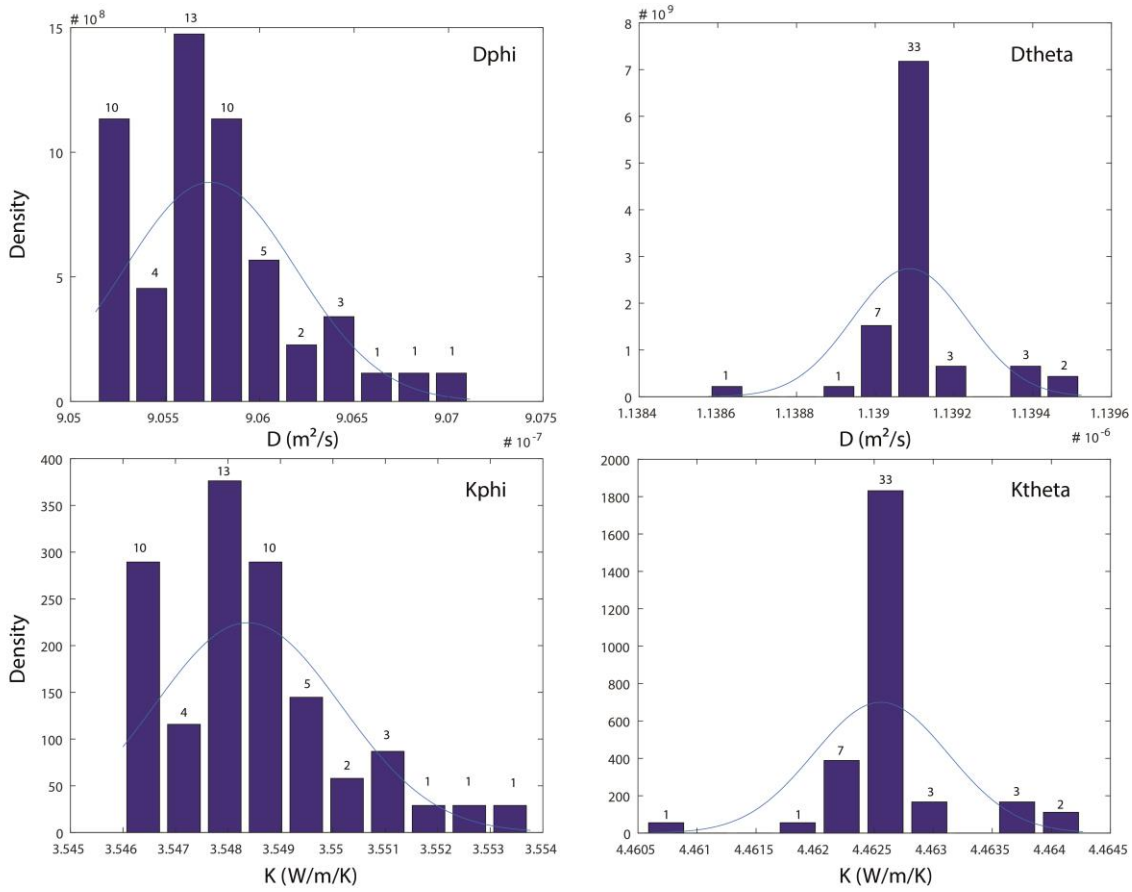

Figure C.1 Histograms of the computed thermal diffusivities and conductivities after 50 inversions. Gaussian fit was shown with the blue curve.

Appendix D

Sample information, phase shift and amplitude ratio data for thermal diffusivity estimations

Appendix D: Sample information, phase shift and amplitude ratio data for thermal diffusivity estimations

In this appendix, data on our thermal diffusivity experiments are provided. First, the experimental procedure and paths with the different cycles are represented. Optical microphotographs are also provided for each sample before and after the experiments, as SEM analyses have not been carried for all the samples. For each experiments phase shifts and amplitude ratio and associated inferred thermal diffusivities (raw data) have been represented for each cycle as a function of temperature and frequency. In these graphs, all the temperatures and frequencies are provided, resulting into a large amount of values. These values are then processed as indicated in the chapter VI to provide diffusivity final data.

M517

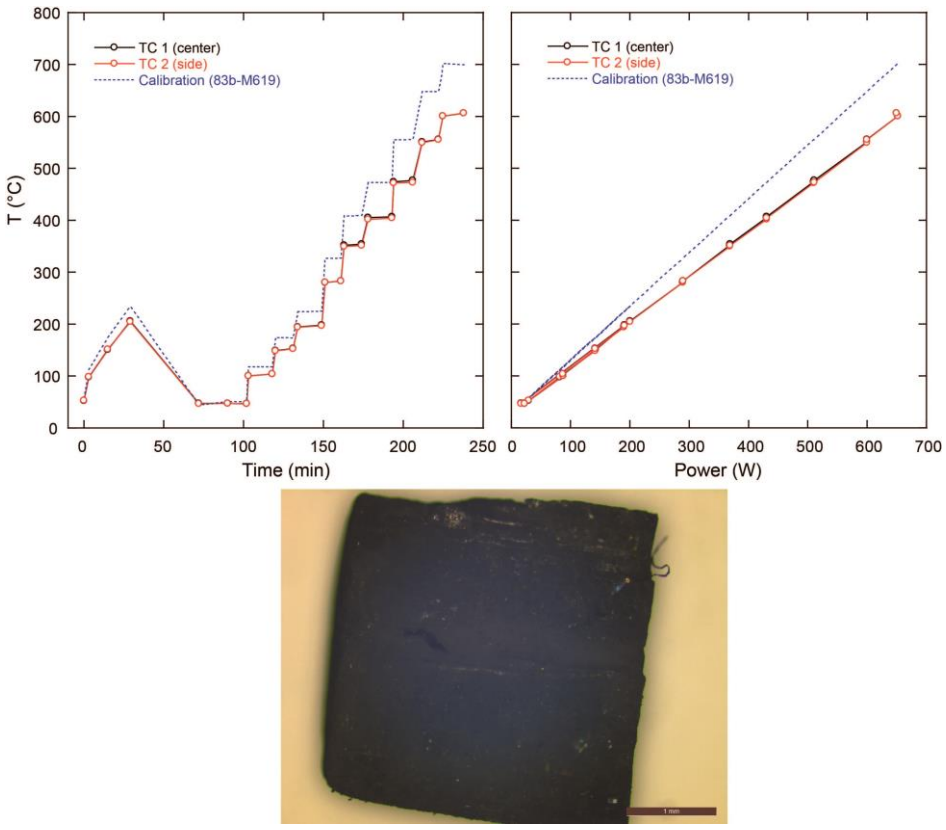

Figure D.1 M517 experimental procedure with temperature history with time, power/temperature calibration and recovered sample microphotograph.

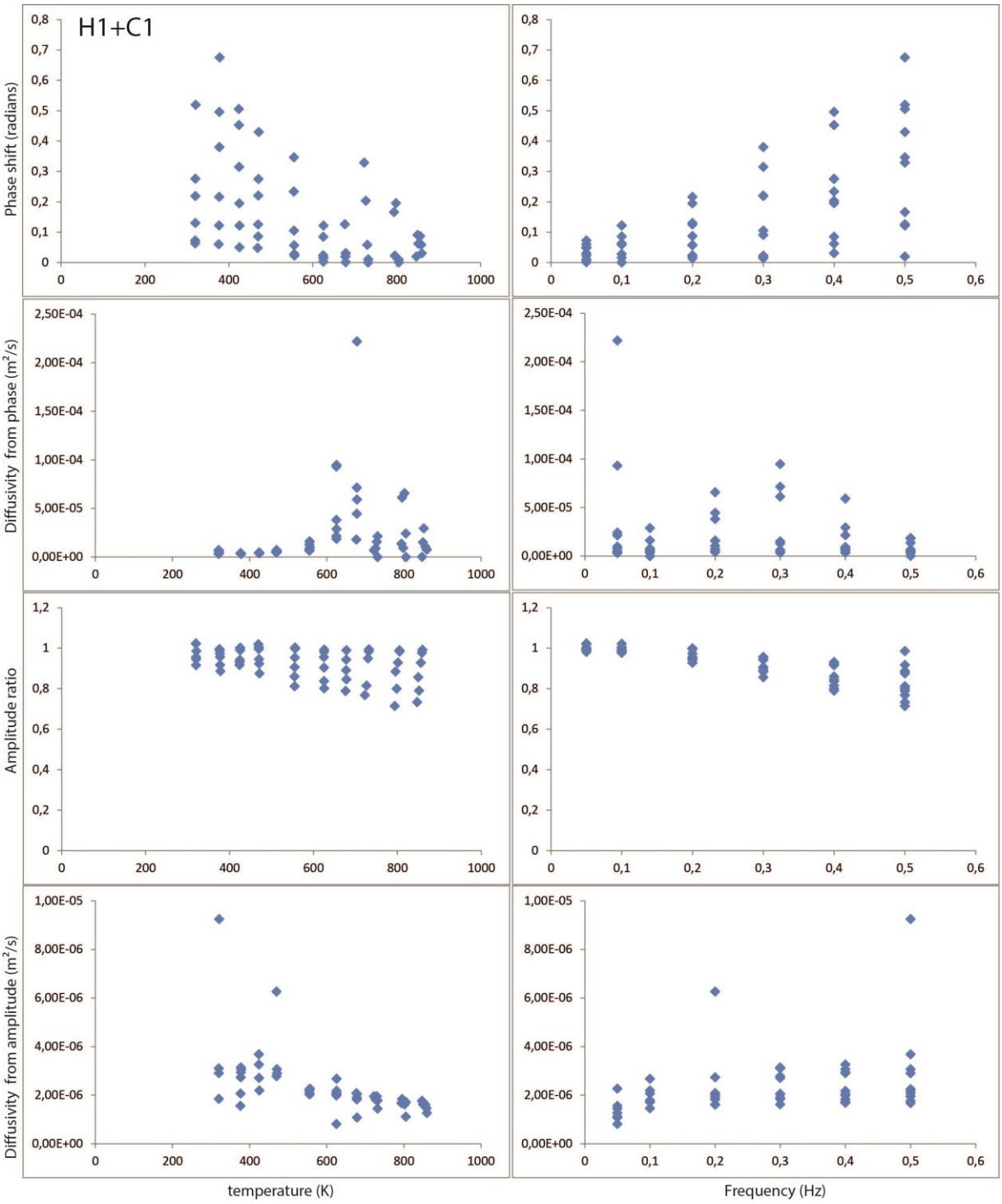

Figure D.2 M517 Experimental results for the first cycle. Phase shift (first raw), amplitude ratio (third raw) and inferred diffusivities (second and fourth raw respectively), are represented as function of temperature and frequency.

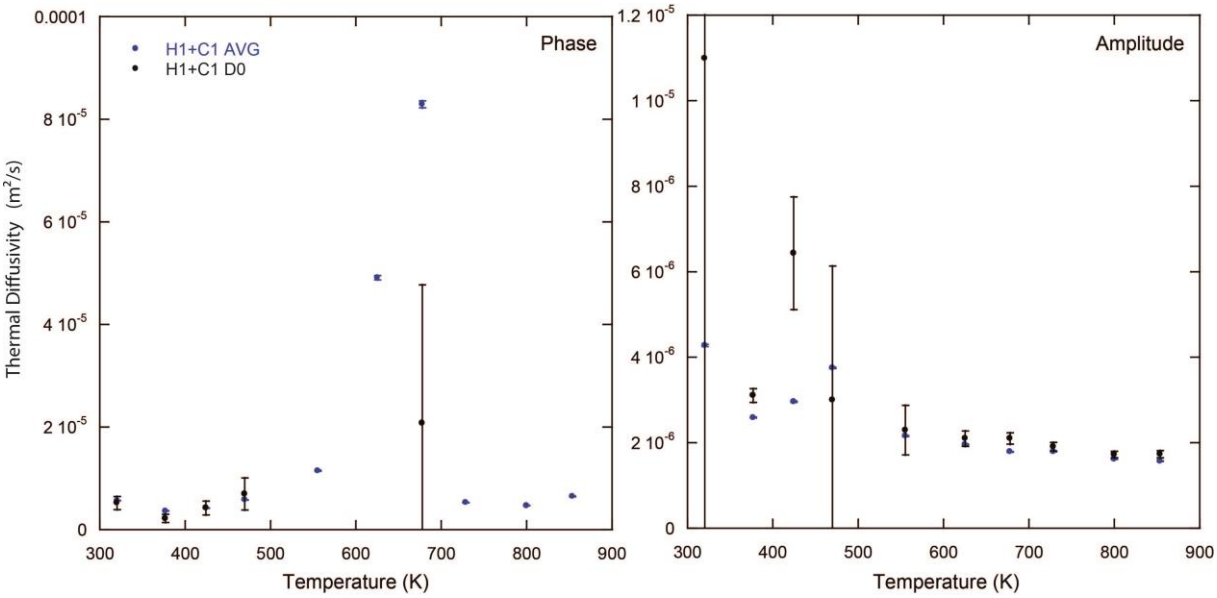

Figure D.3 M517 Thermal diffusivities obtained after fitting (D_0) and average (AVG) methods on diffusivities obtained at different frequencies at a fixed temperature. Phase and amplitude estimated are given in left and right panels respectively.

M525 - 83b

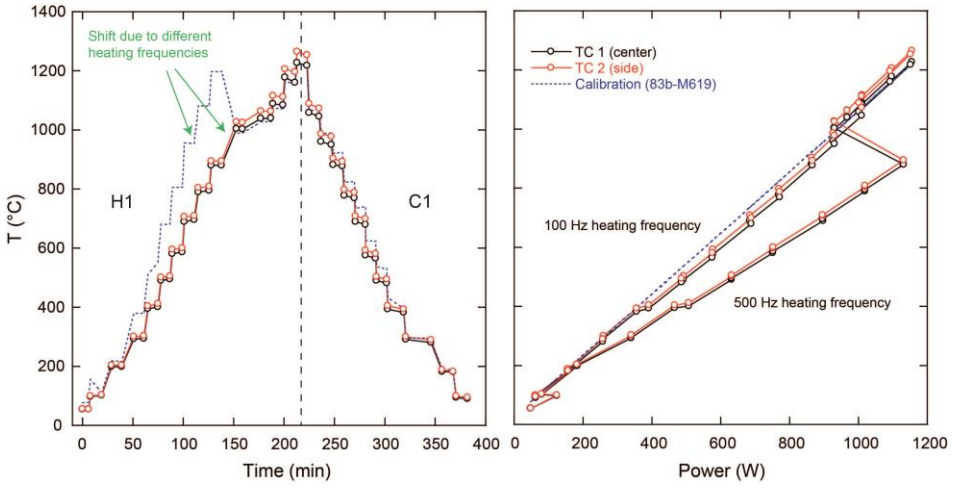

Figure D.4 M525 - 83b (2GPa) experimental procedure with temperature history with time and power/temperature calibration.

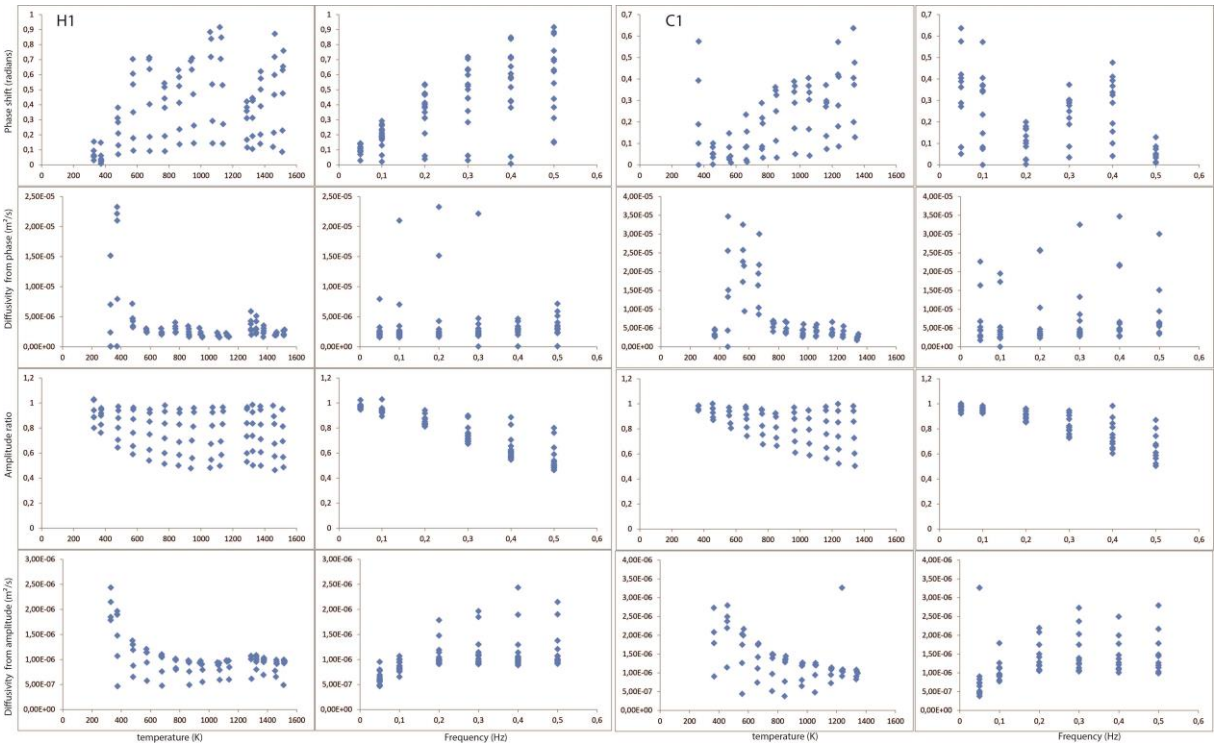

Figure D.5 M525 - 83b Experimental results for the first cycle. Phase shift (first raw), amplitude ratio (third raw) and inferred diffusivities (second and fourth raw respectively), are represented as function of temperature and frequency.

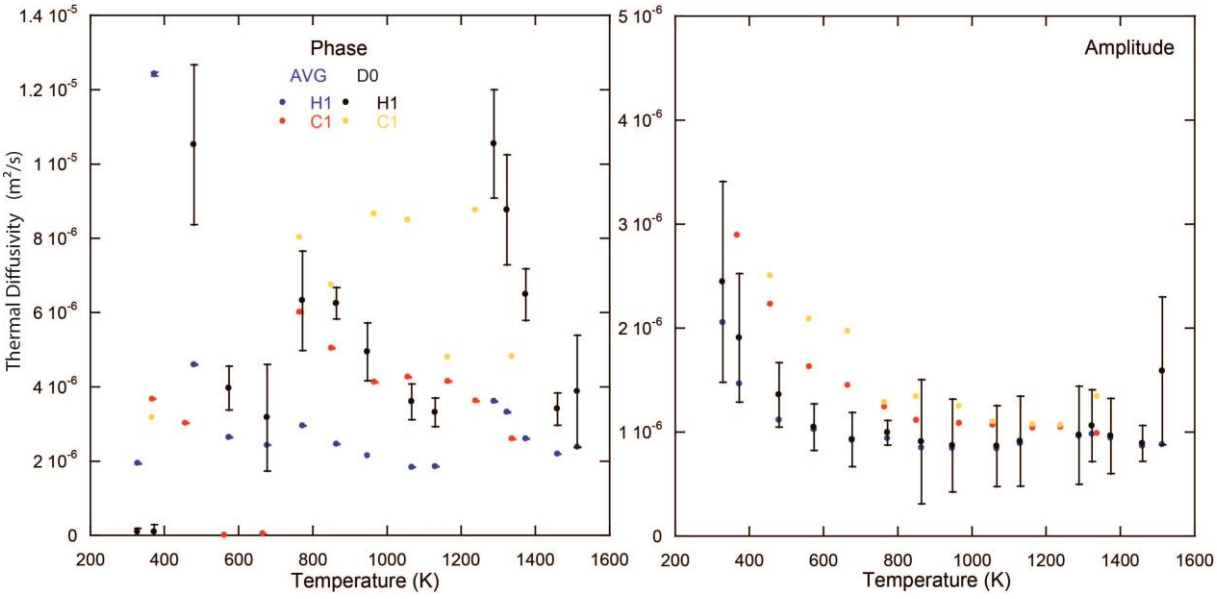

Figure D.6 M525 - 83b Thermal diffusivities obtained after fitting (D_0) and average (AVG) methods on diffusivities obtained at different frequencies at a fixed temperature. Phase and amplitude thermal diffusivity estimations are given in left and right panels respectively.

M525 - 166b

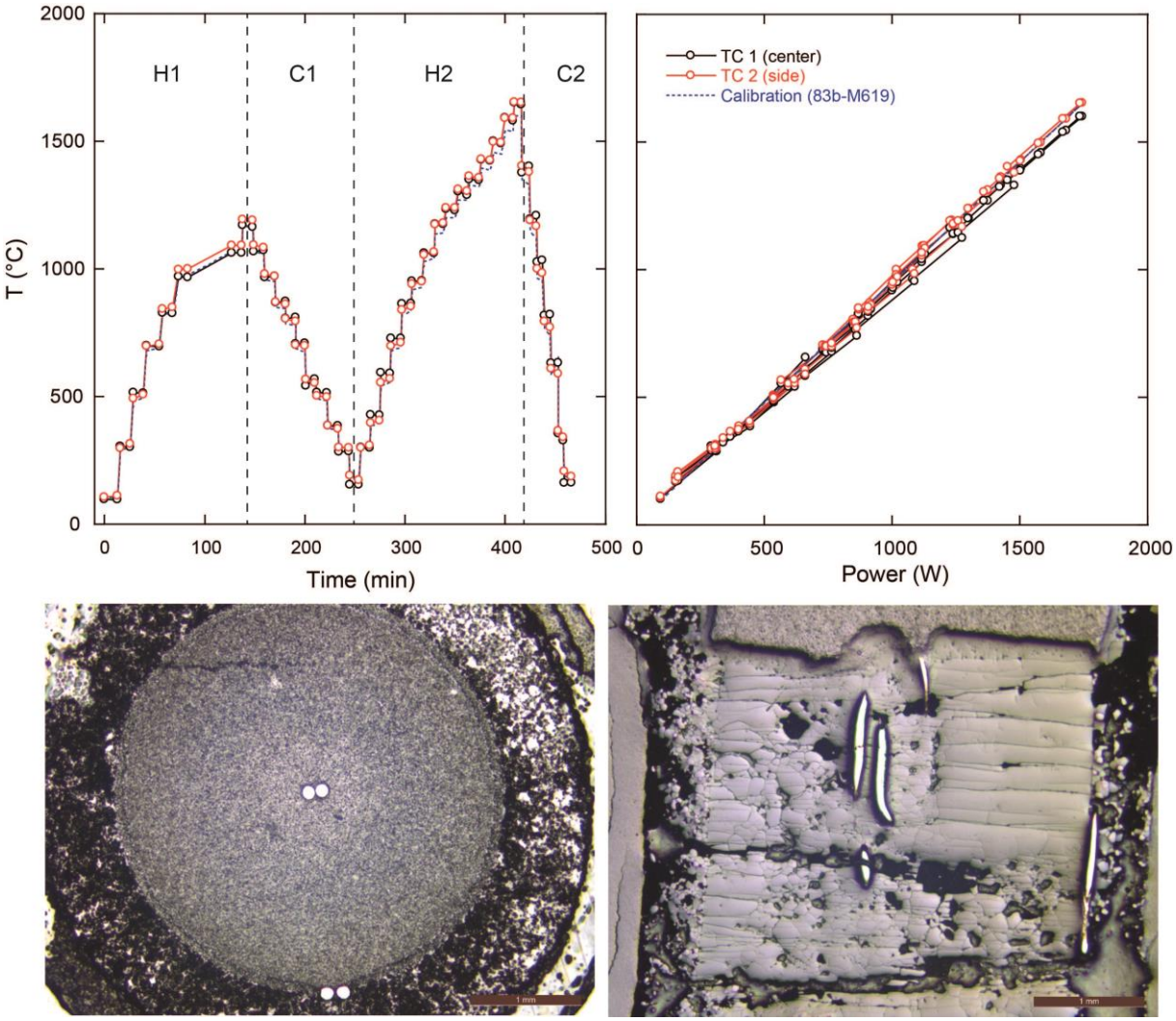

Figure D.7 M525 - 166b (4 GPa) experimental procedure with temperature history with time and power/temperature calibration. Microphotographs of recovered sample are provided perpendicular (left) and parallel (right) to sample cylinder axis.

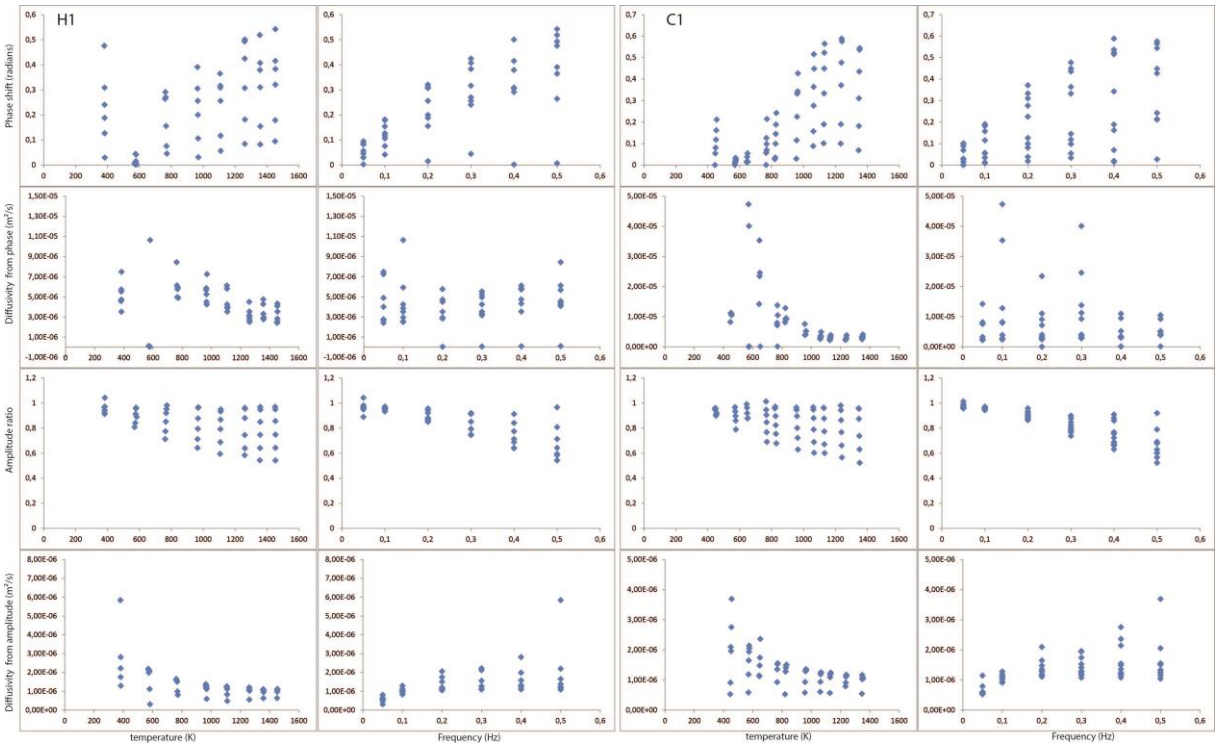

Figure D.8 M525 - 166b Experimental results for the first cycle. Phase shift (first raw), amplitude ratio (third raw) and inferred diffusivities (second and fourth raw respectively), are represented as function of temperature and frequency.

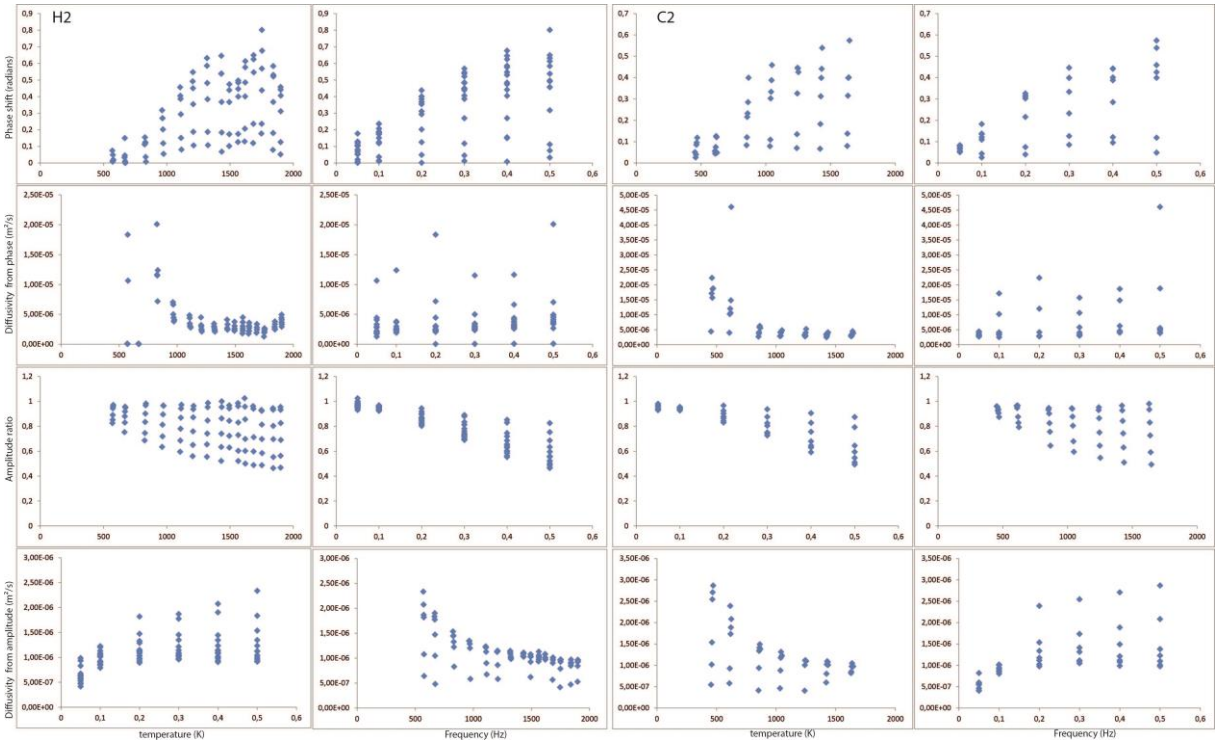

Figure D.9 M525 - 166b Experimental results for the second cycle. Phase shift (first raw), amplitude ratio (third raw) and inferred diffusivities (second and fourth raw respectively), are represented as function of temperature and frequency.

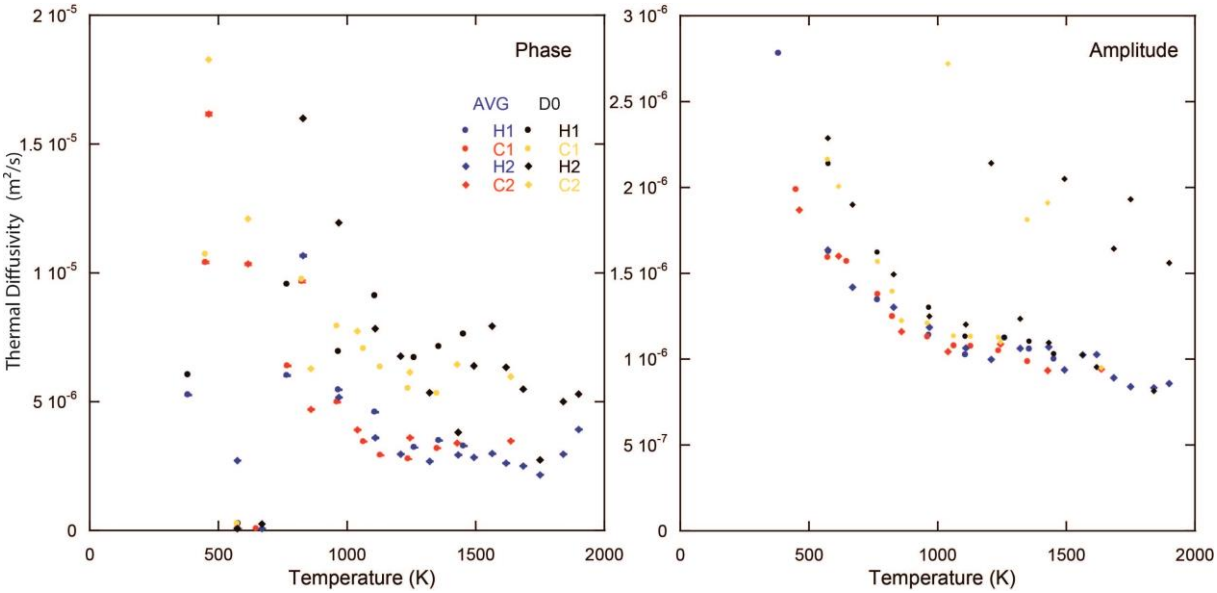

Figure D.10 M525 - 166b Thermal diffusivities obtained after fitting (D_0) and average (AVG) methods on diffusivities obtained at different frequencies at a fixed temperature. Phase and amplitude thermal diffusivity estimations are given in left and right panels respectively.

M617

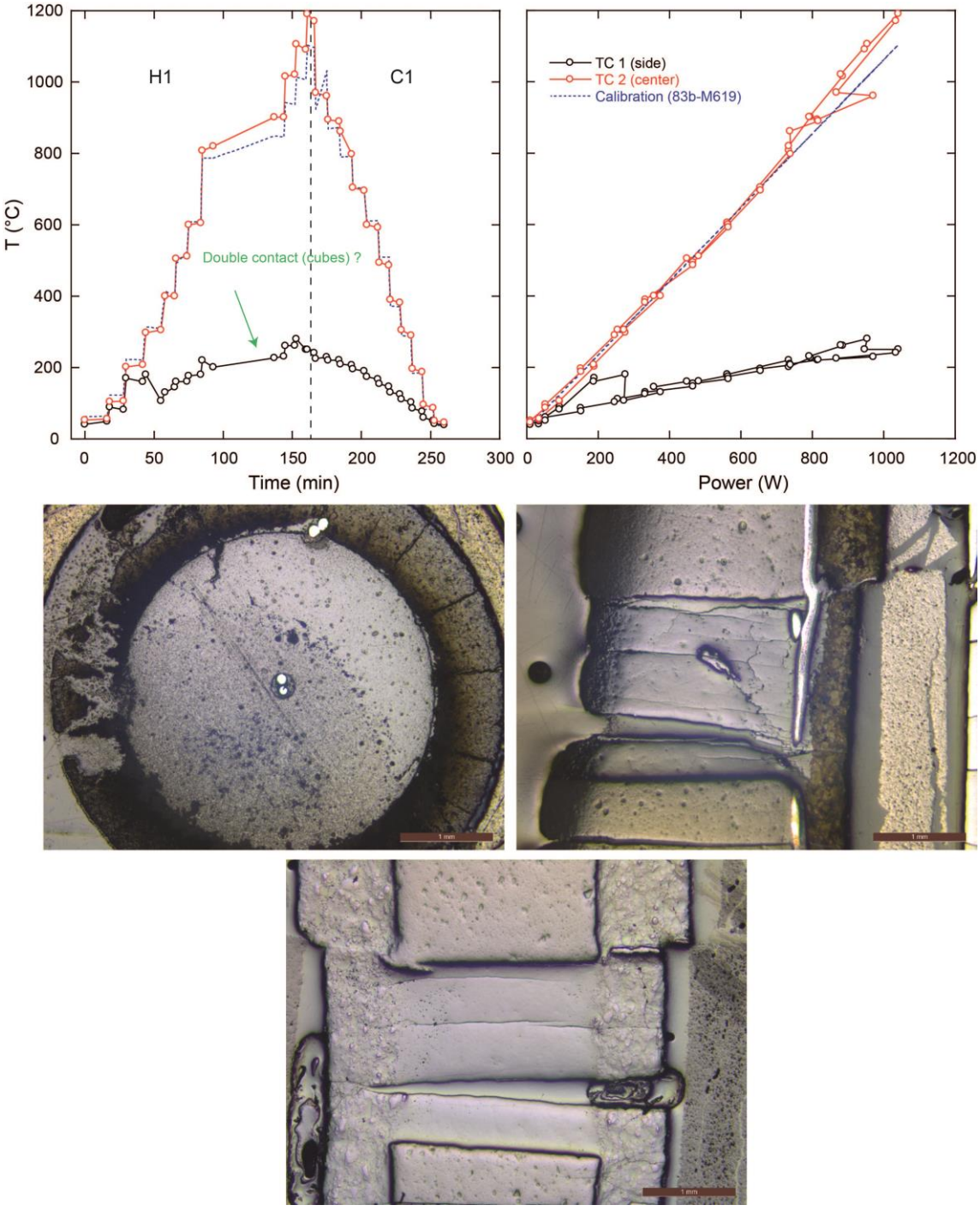

Figure D.11 M617 experimental procedure with temperature history with time and power/temperature calibration. Microphotographs of recovered sample are provided perpendicular (left) and parallel (right and bottom) to sample cylinder axis.

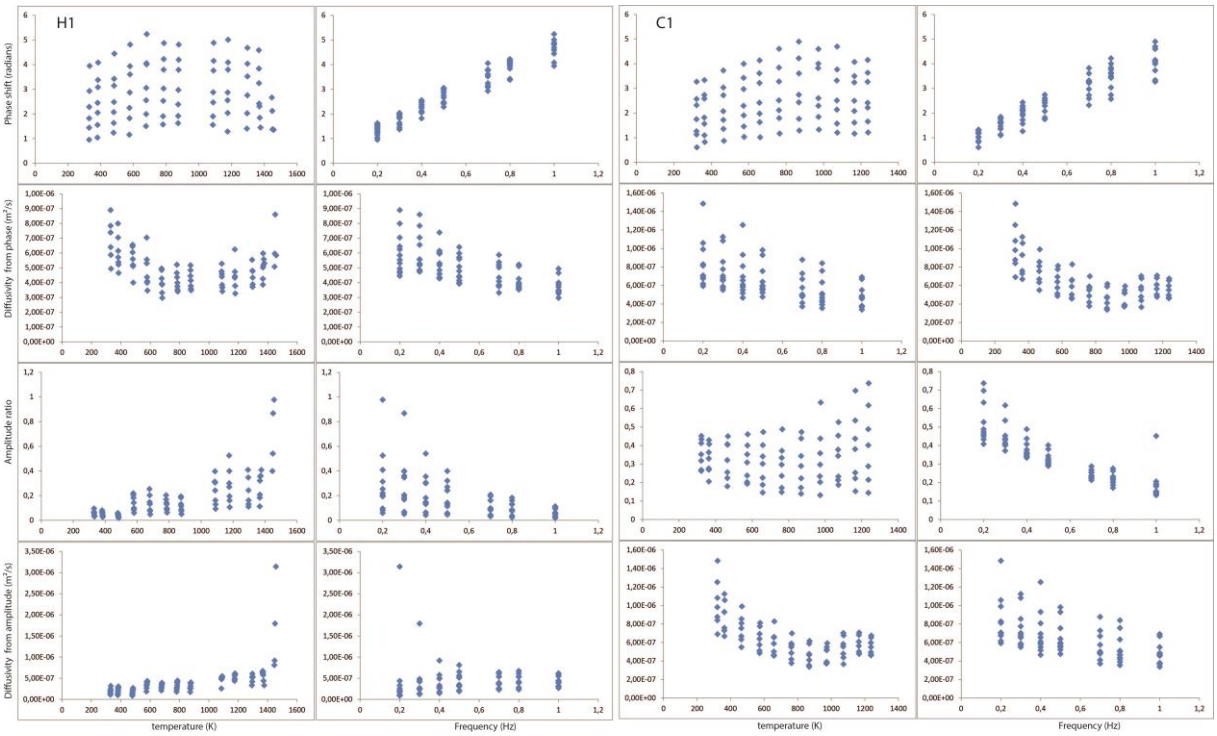

Figure D.12M617 Experimental results for the first cycle. Phase shift (first raw), amplitude ratio (third raw) and inferred diffusivities (second and fourth raw respectively), are represented as function of temperature and frequency.

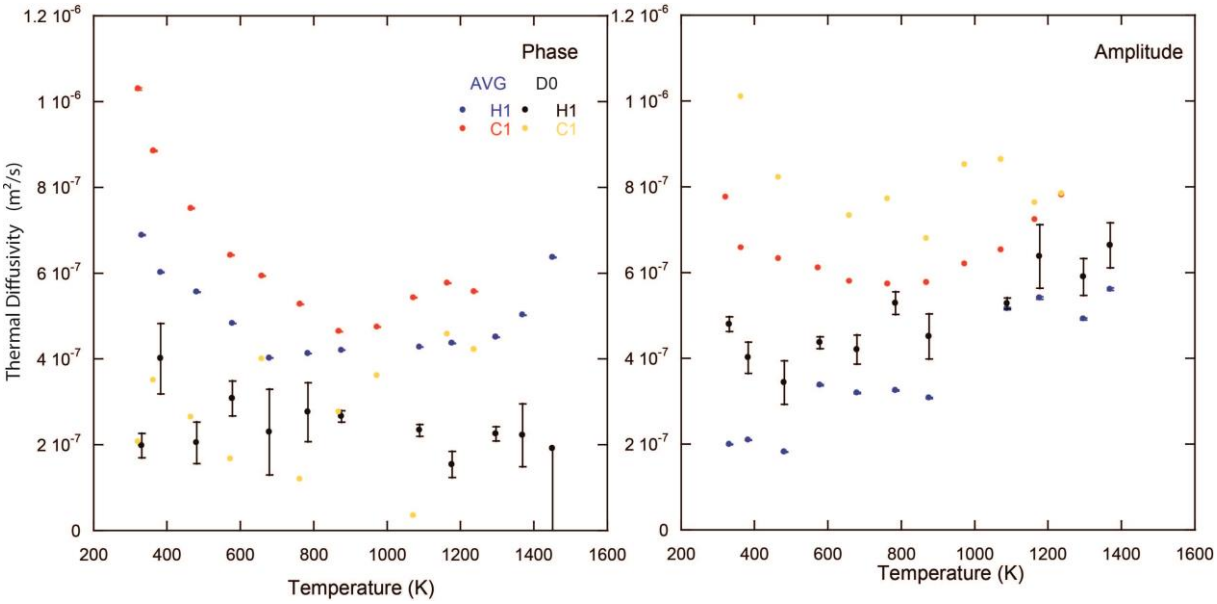

Figure D.13 M617 Thermal diffusivities obtained after fitting (D_0) and average (AVG) methods on diffusivities obtained at different frequencies at a fixed temperature. Phase and amplitude thermal diffusivity estimations are given in left and right panels respectively.

M619

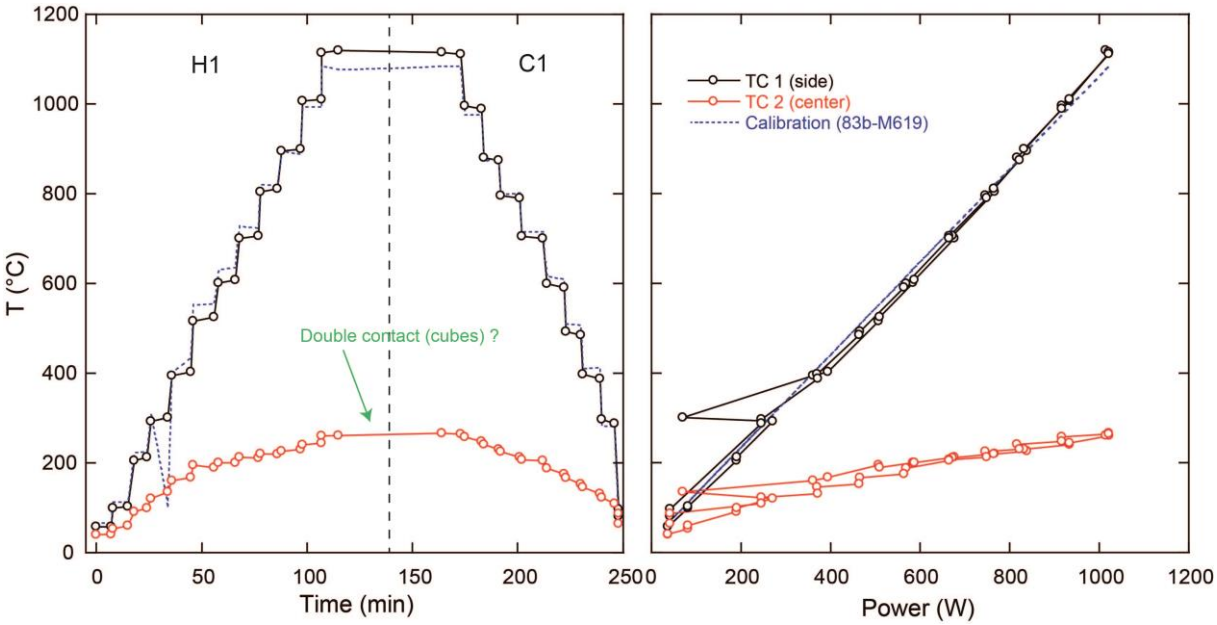

Figure D.14 M619 experimental procedure with temperature history with time and power/temperature calibration.

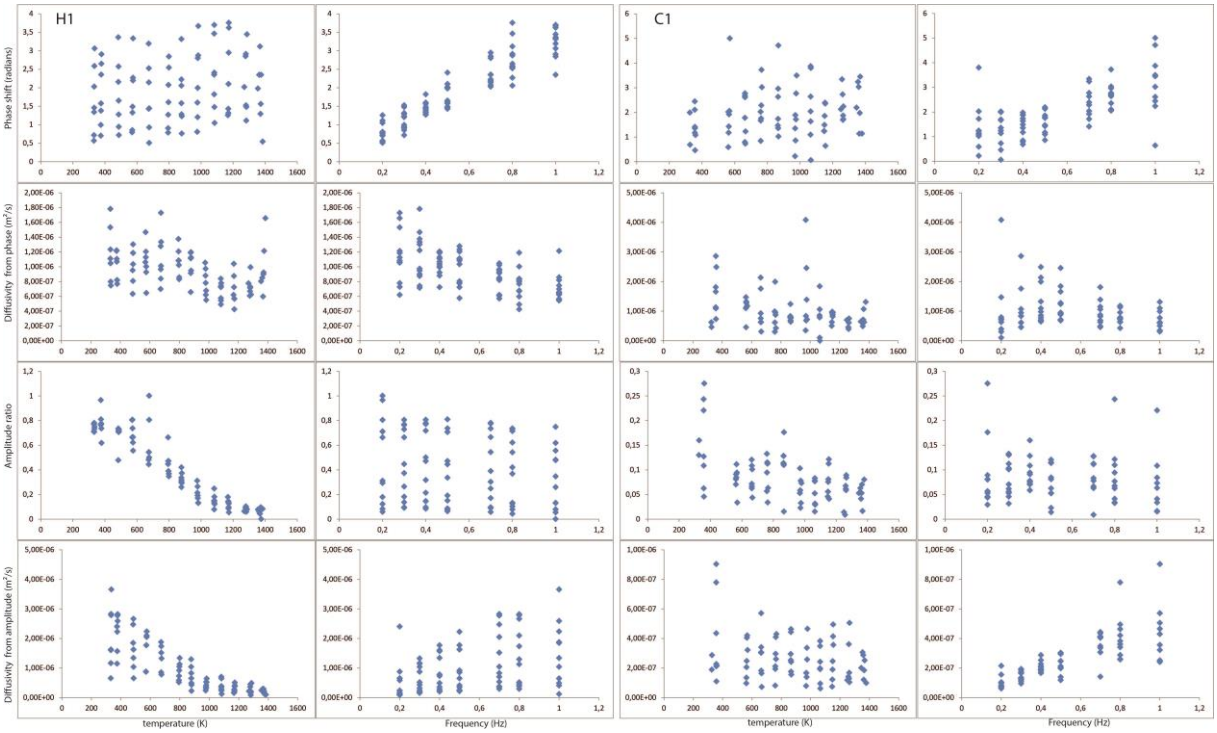

Figure D.15 M619 Experimental results for the first cycle. Phase shift (first raw), amplitude ratio (third raw) and inferred diffusivities (second and fourth raw respectively), are represented as function of temperature and frequency.

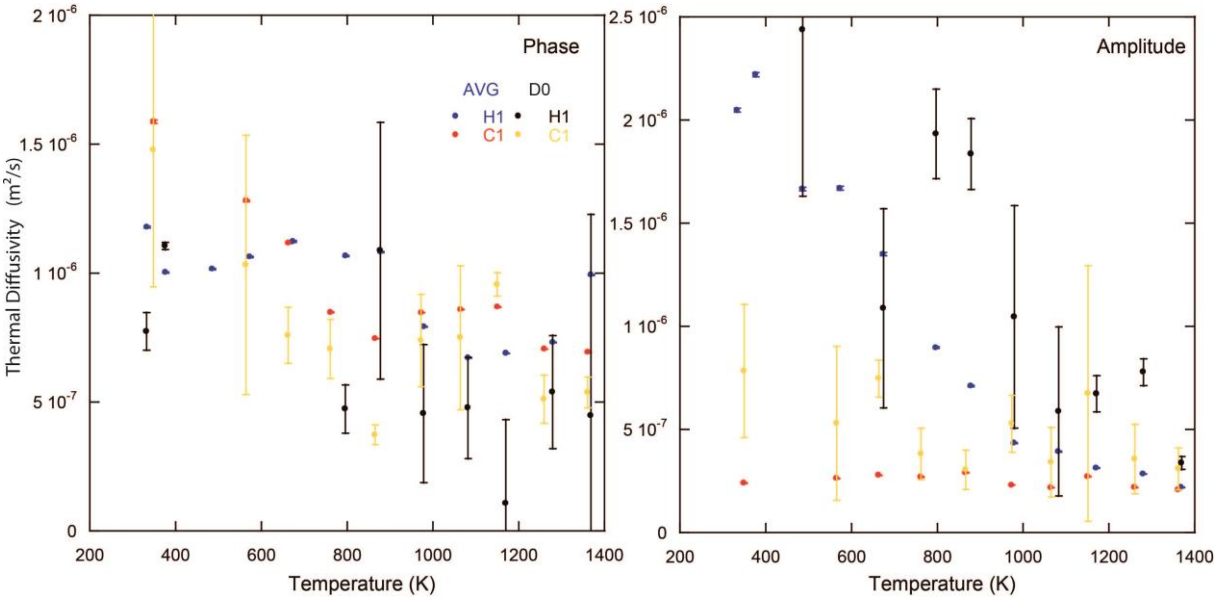

Figure D.16 M619Thermal diffusivities obtained after fitting (D_0) and average (AVG) methods on diffusivities obtained at different frequencies at a fixed temperature. Phase and amplitude estimated are given in left and right panels respectively.

M661

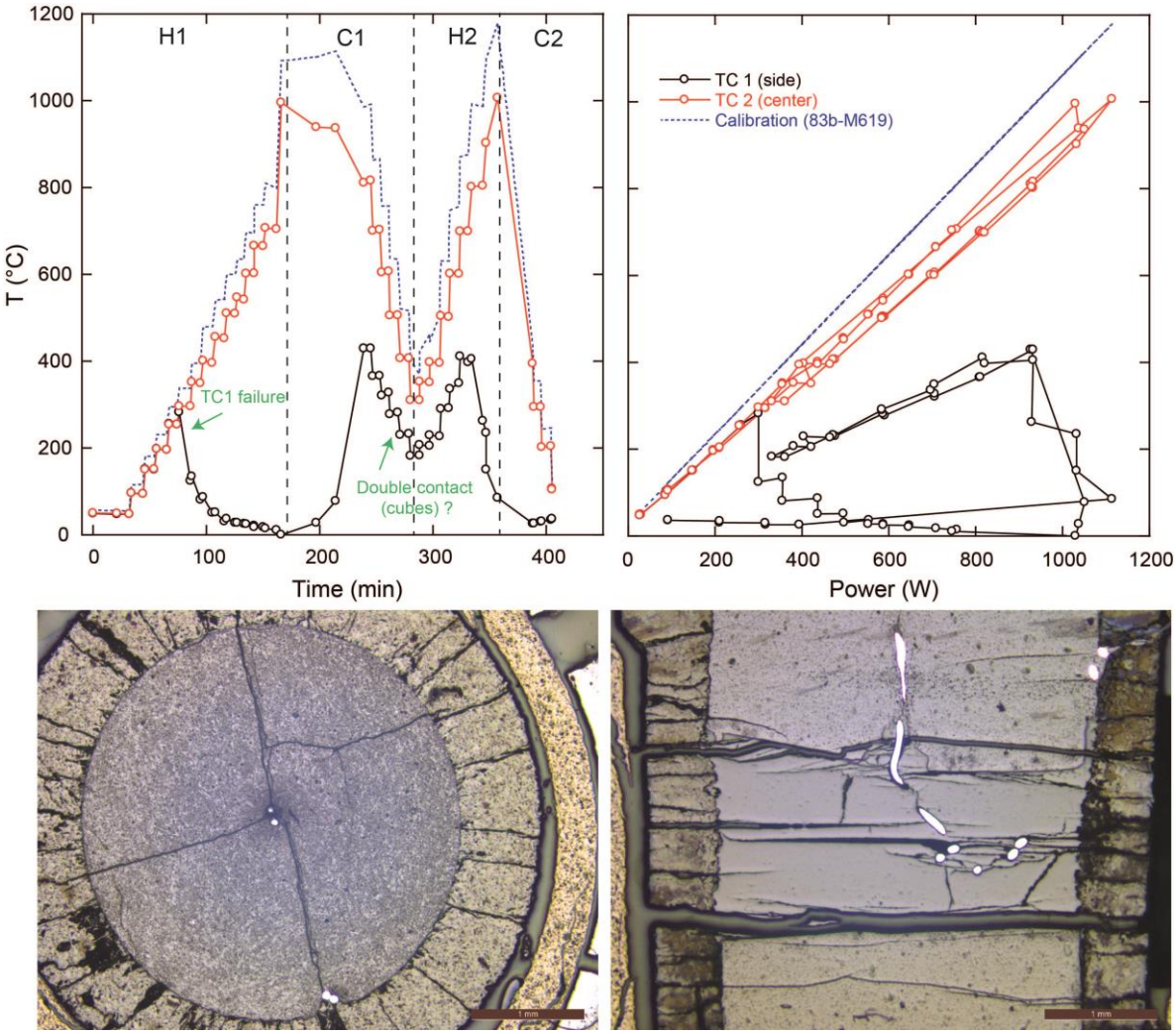

Figure D.17 M661 experimental procedure with temperature history with time and power/temperature calibration. Microphotographs of recovered sample are provided perpendicular (left) and parallel (right) to sample cylinder axis.

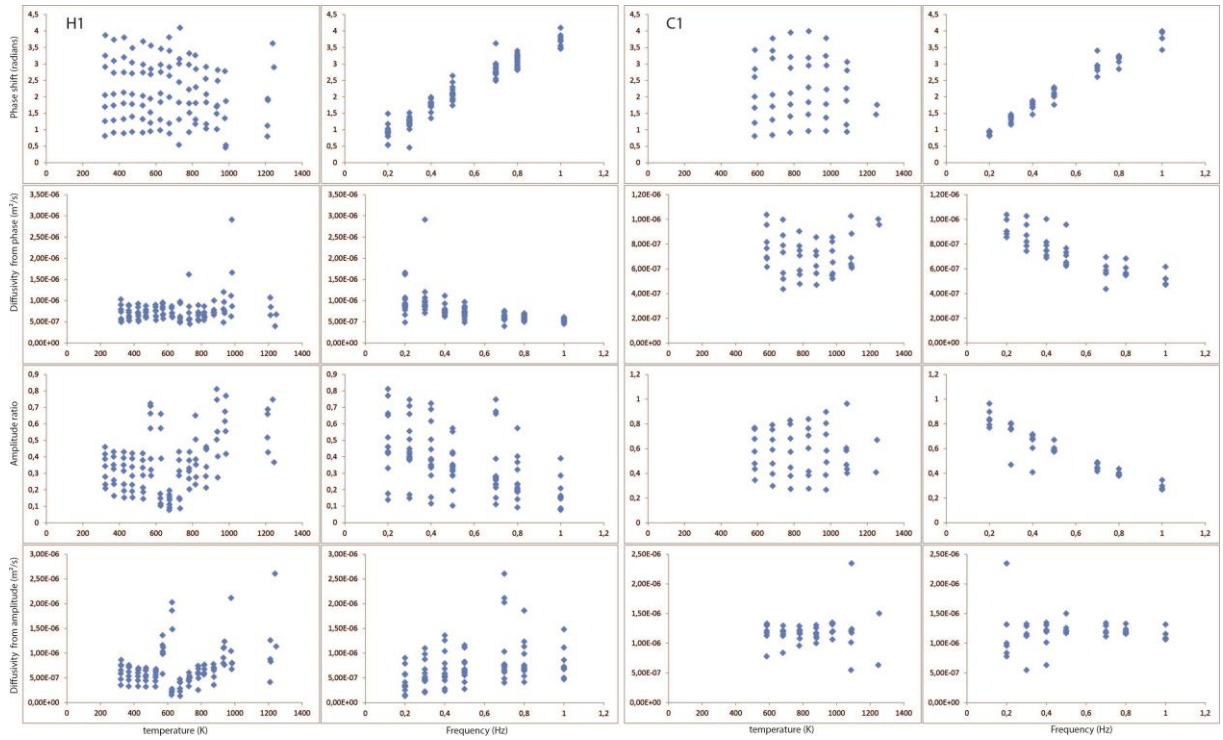

Figure D.18 M661 Experimental results for the first cycle. Phase shift (first raw), amplitude ratio (third raw) and inferred diffusivities (second and fourth raw respectively), are represented as function of temperature and frequency.

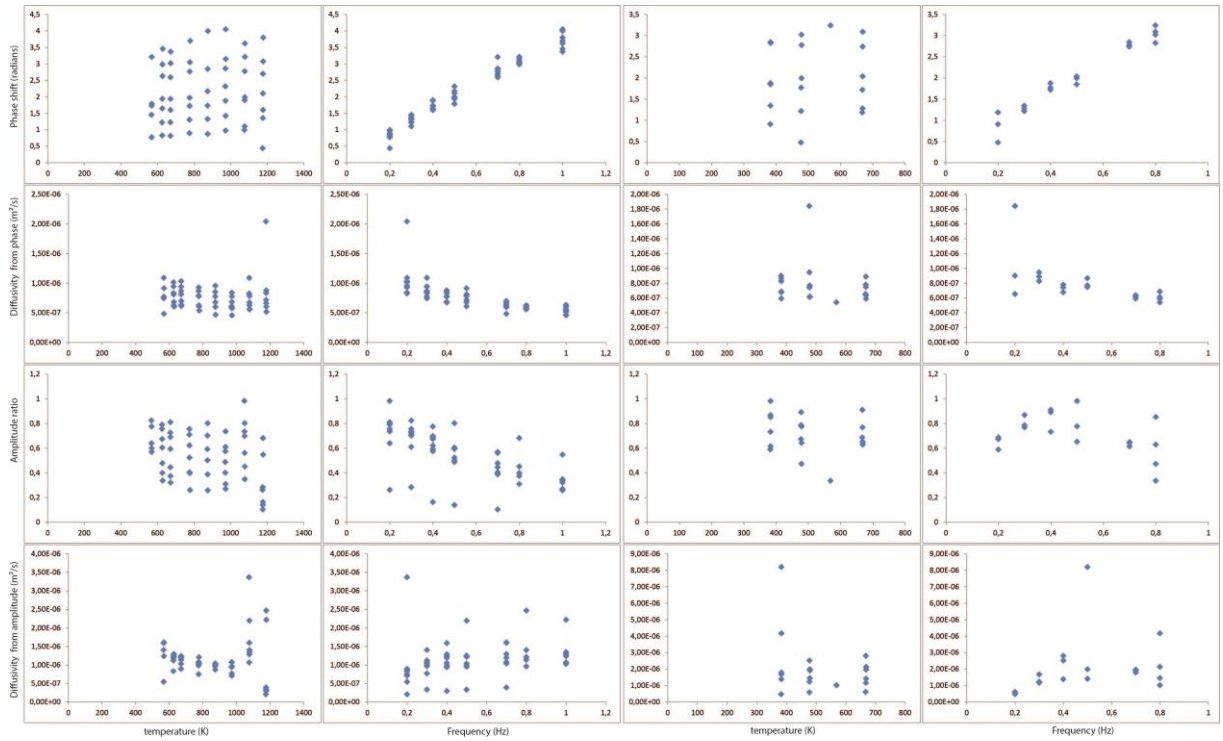

Figure D.19 M661 Experimental results for the second cycle. Phase shift (first raw), amplitude ratio (third raw) and inferred diffusivities (second and fourth raw respectively), are represented as function of temperature and frequency.

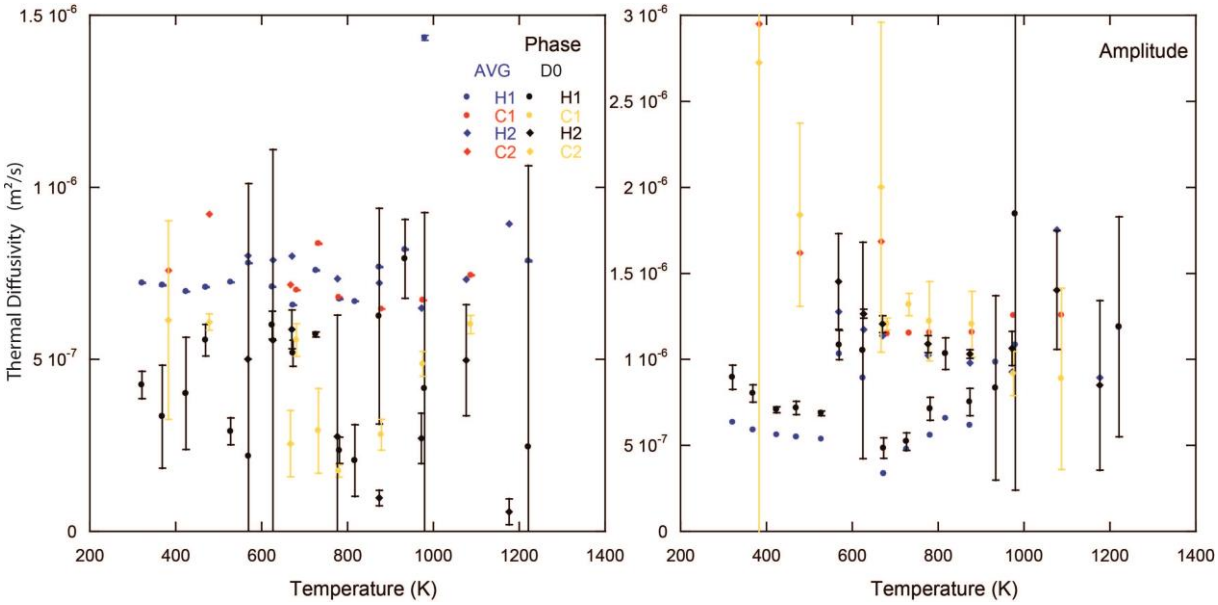

Figure D.19 M661 Thermal diffusivities obtained after fitting (D_0) and average (AVG) methods on diffusivities obtained at different frequencies at a fixed temperature. Phase and amplitude thermal diffusivity estimations are given in left and right panels respectively.

M662

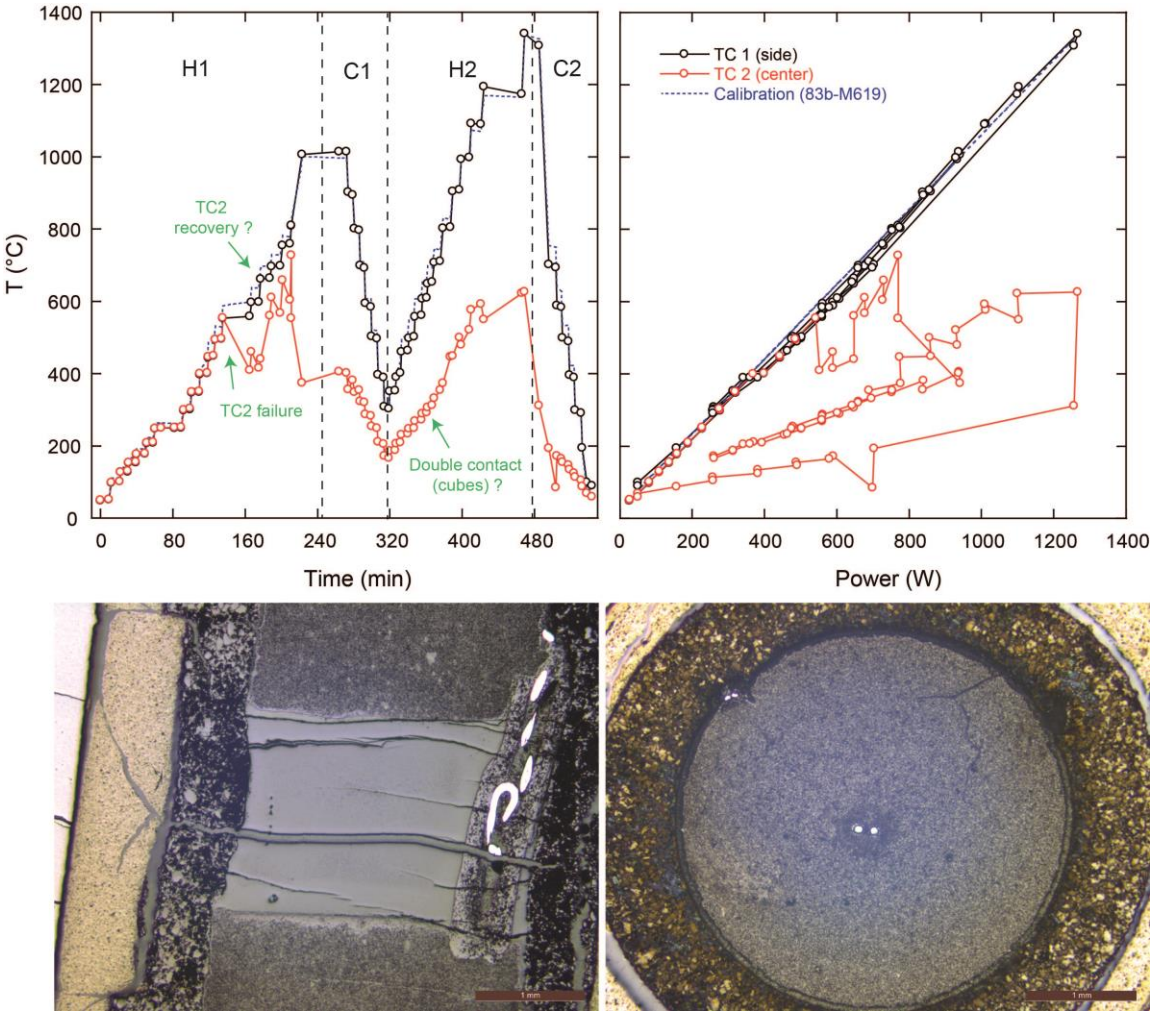

Figure D.20 M662 experimental procedure with temperature history with time and power/temperature calibration. Microphotographs of recovered sample are provided perpendicular (left) and parallel (right) to sample cylinder axis.

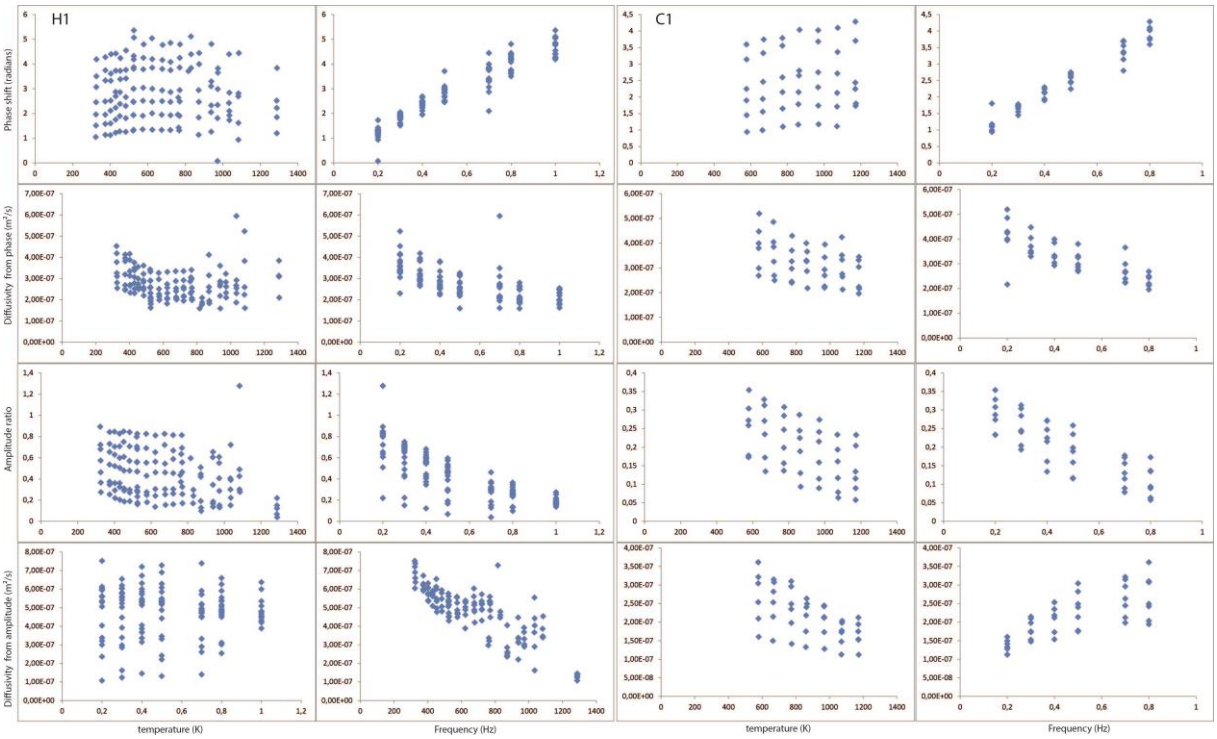

Figure D.21 M662 Experimental results for the first cycle. Phase shift (first raw), amplitude ratio (third raw) and inferred diffusivities (second and fourth raw respectively), are represented as function of temperature and frequency.

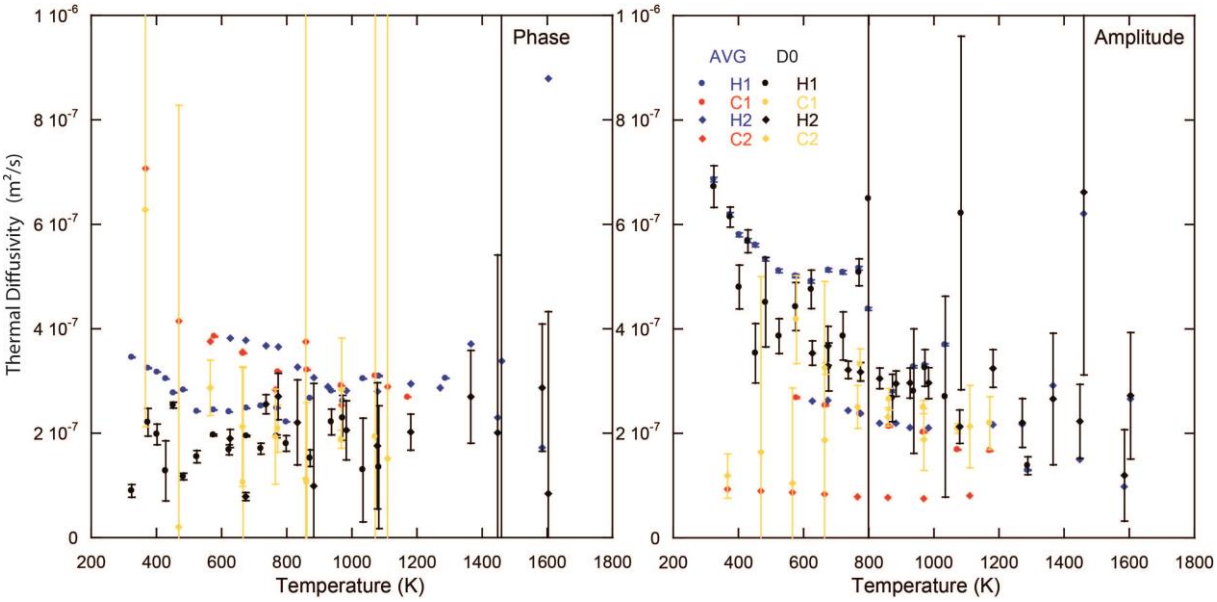

Figure D.22 M662 Thermal diffusivities obtained after fitting (D_0) and average (AVG) methods on diffusivities obtained at different frequencies at a fixed temperature. Phase and amplitude thermal diffusivity estimations are given in left and right panels respectively.

M770

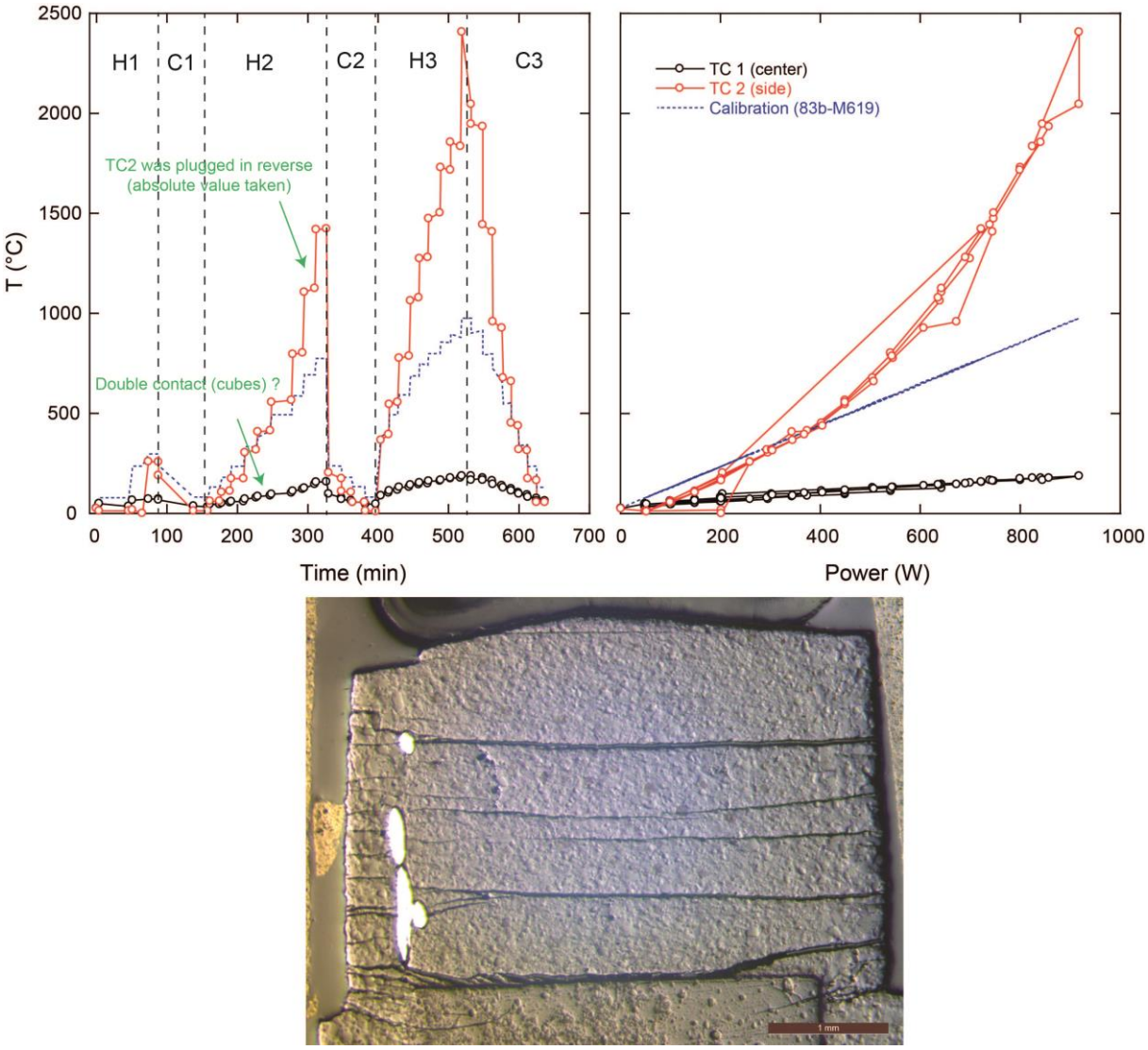

Figure D.23 M770 experimental procedure with temperature history with time and power/temperature calibration. Microphotographs of recovered sample are provided parallel to sample cylinder axis.

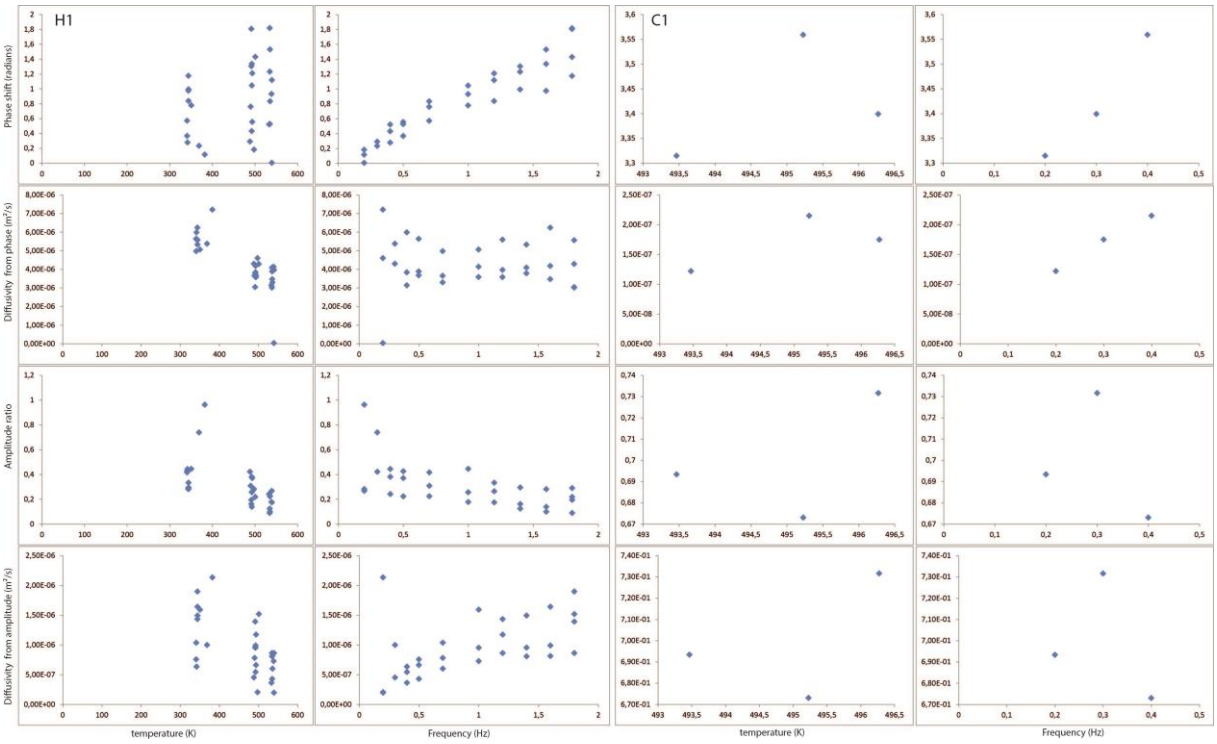

Figure D.24 M770 Experimental results for the first cycle. Phase shift (first raw), amplitude ratio (third raw) and inferred diffusivities (second and fourth raw respectively), are represented as function of temperature and frequency.

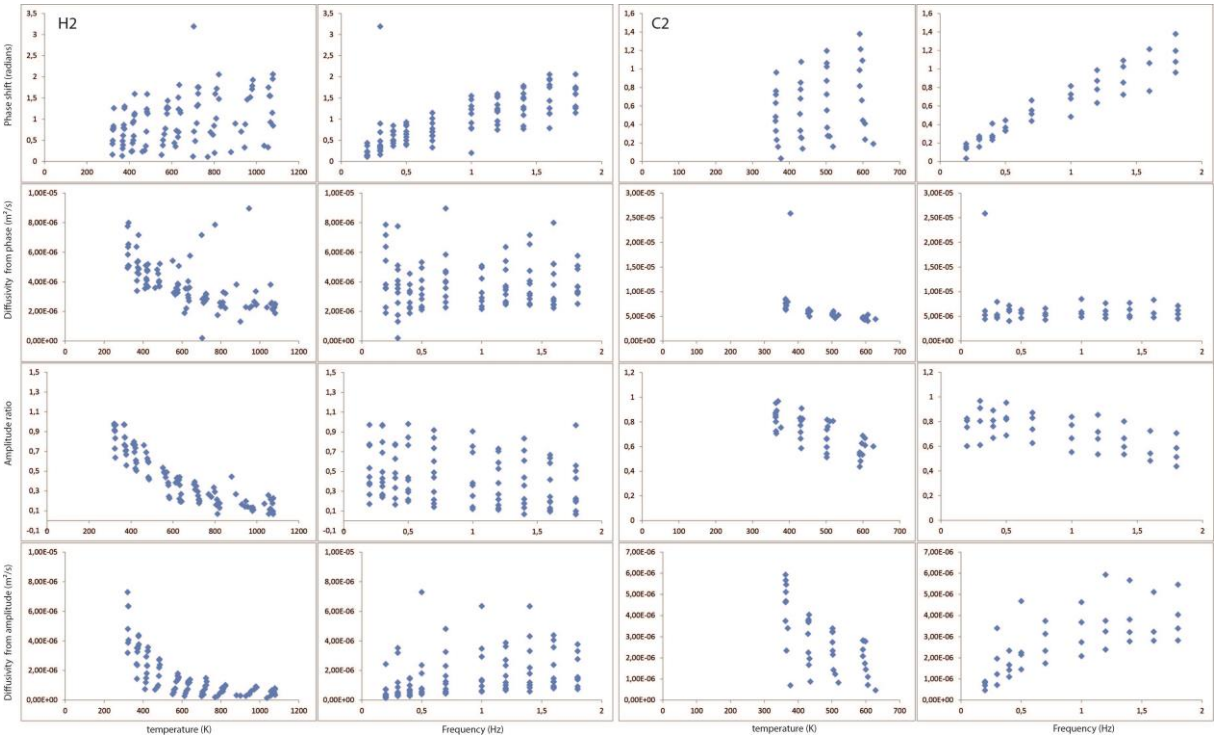

Figure D.25 M770 Experimental results for the second cycle. Phase shift (first raw), amplitude ratio (third raw) and inferred diffusivities (second and fourth raw respectively), are represented as function of temperature and frequency.

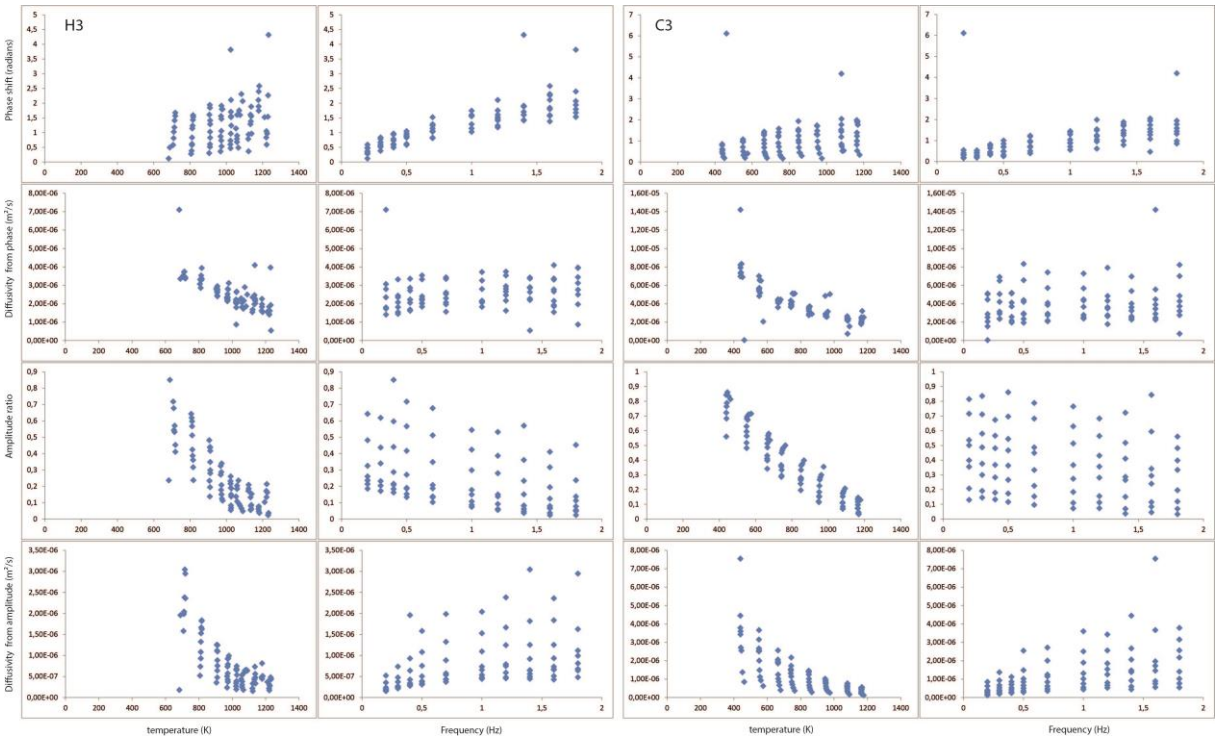

Figure D.26 M770 Experimental results for the third cycle. Phase shift (first raw), amplitude ratio (third raw) and inferred diffusivities (second and fourth raw respectively), are represented as function of temperature and frequency.

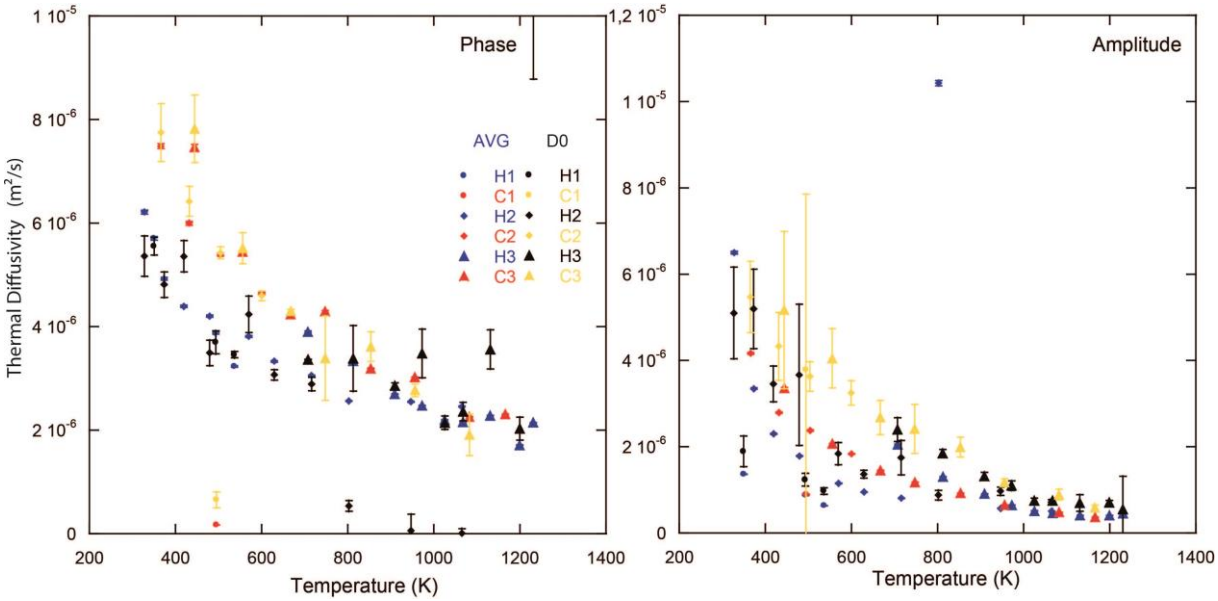

Figure D.27 M770 Thermal diffusivities obtained after fitting (D_0) and average (AVG) methods on diffusivities obtained at different frequencies at a fixed temperature. Phase and amplitude thermal diffusivity estimations are given in left and right panels respectively.

M773

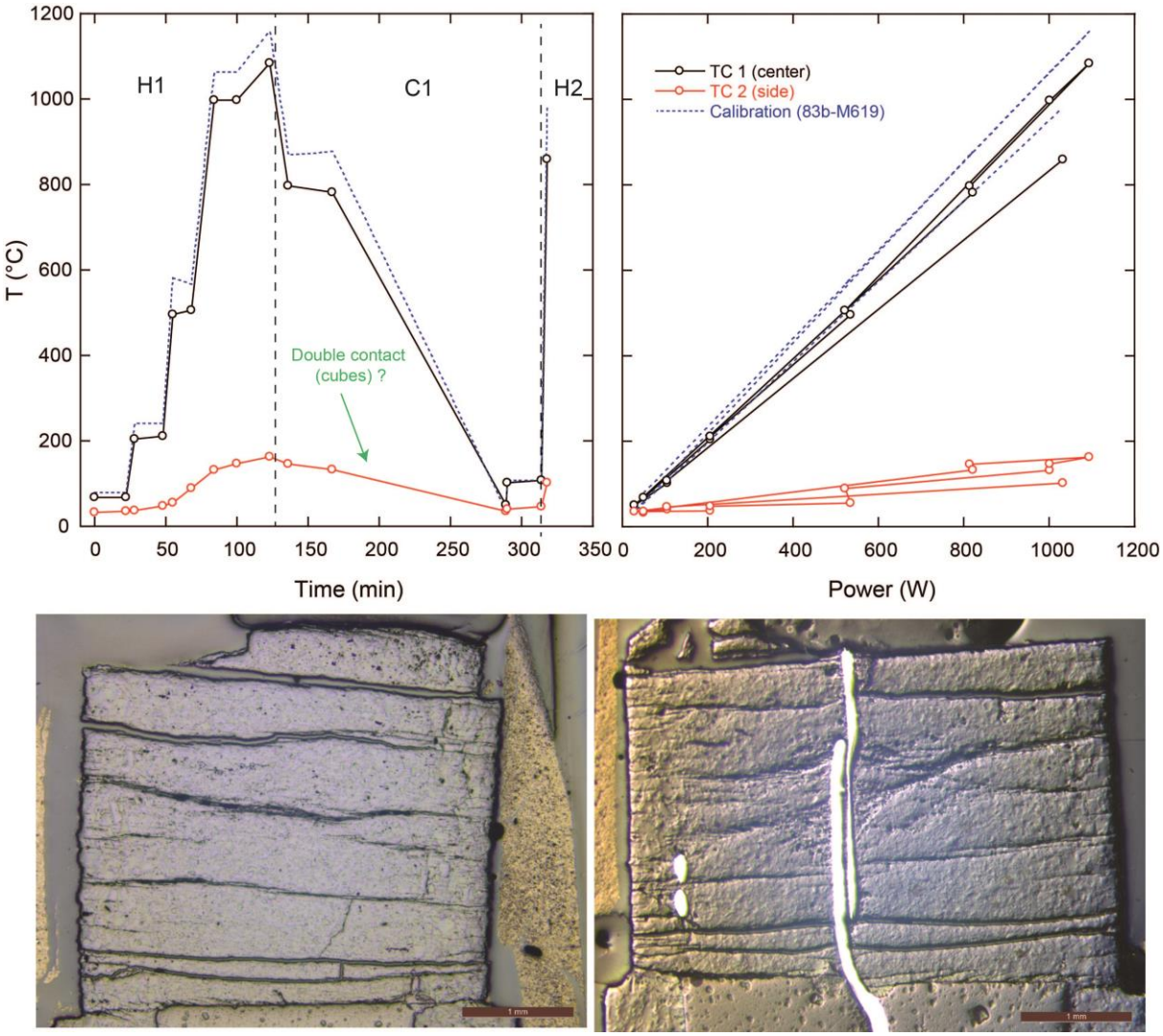

Figure D.28 M773 experimental procedure with temperature history with time and power/temperature calibration. Microphotographs of recovered sample are provided perpendicular (left) and parallel (right) to sample cylinder axis.

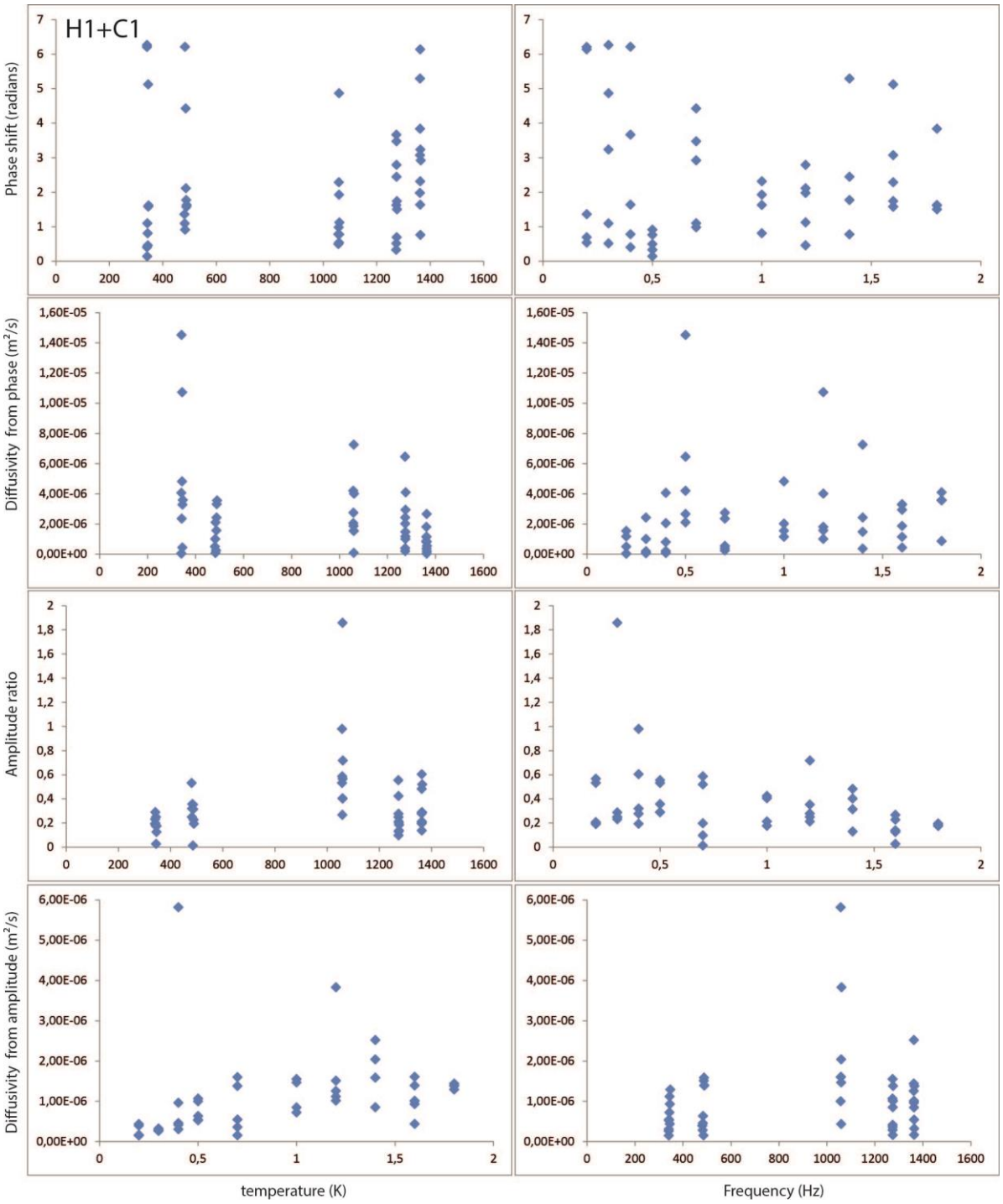

Figure D.29 M773 Experimental results for the first cycle. Phase shift (first raw), amplitude ratio (third raw) and inferred diffusivities (second and fourth raw respectively), are represented as function of temperature and frequency.

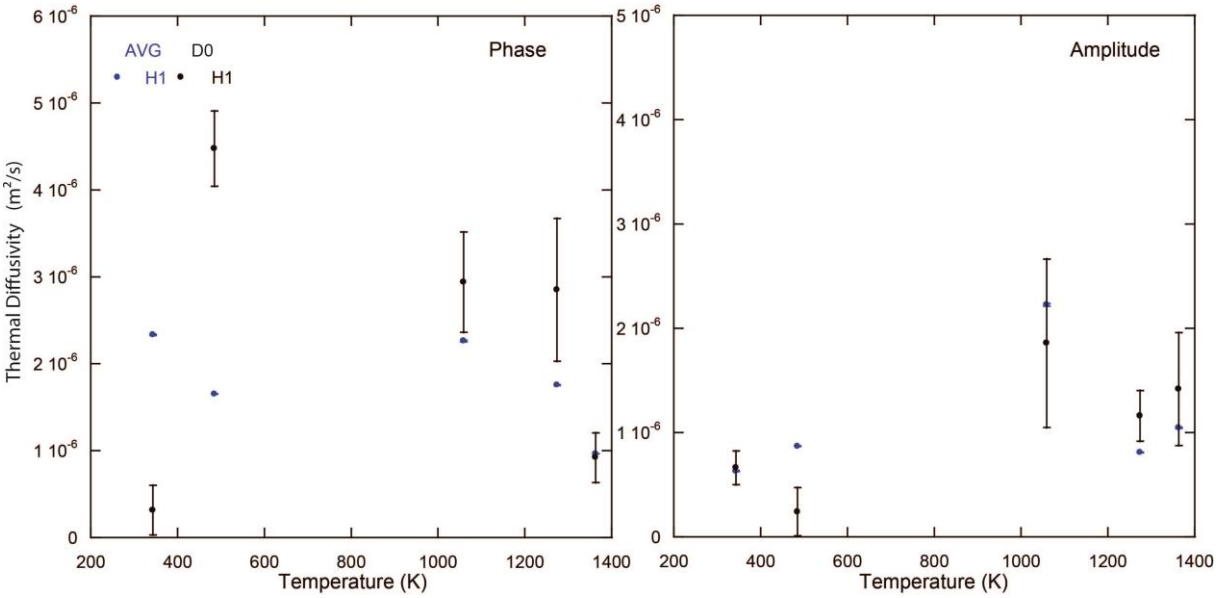

Figure D.30 M773 Thermal diffusivities obtained after fitting (D_0) and average (AVG) methods on diffusivities obtained at different frequencies at a fixed temperature. Phase and amplitude thermal diffusivity estimations are given in left and right panels respectively.

M774

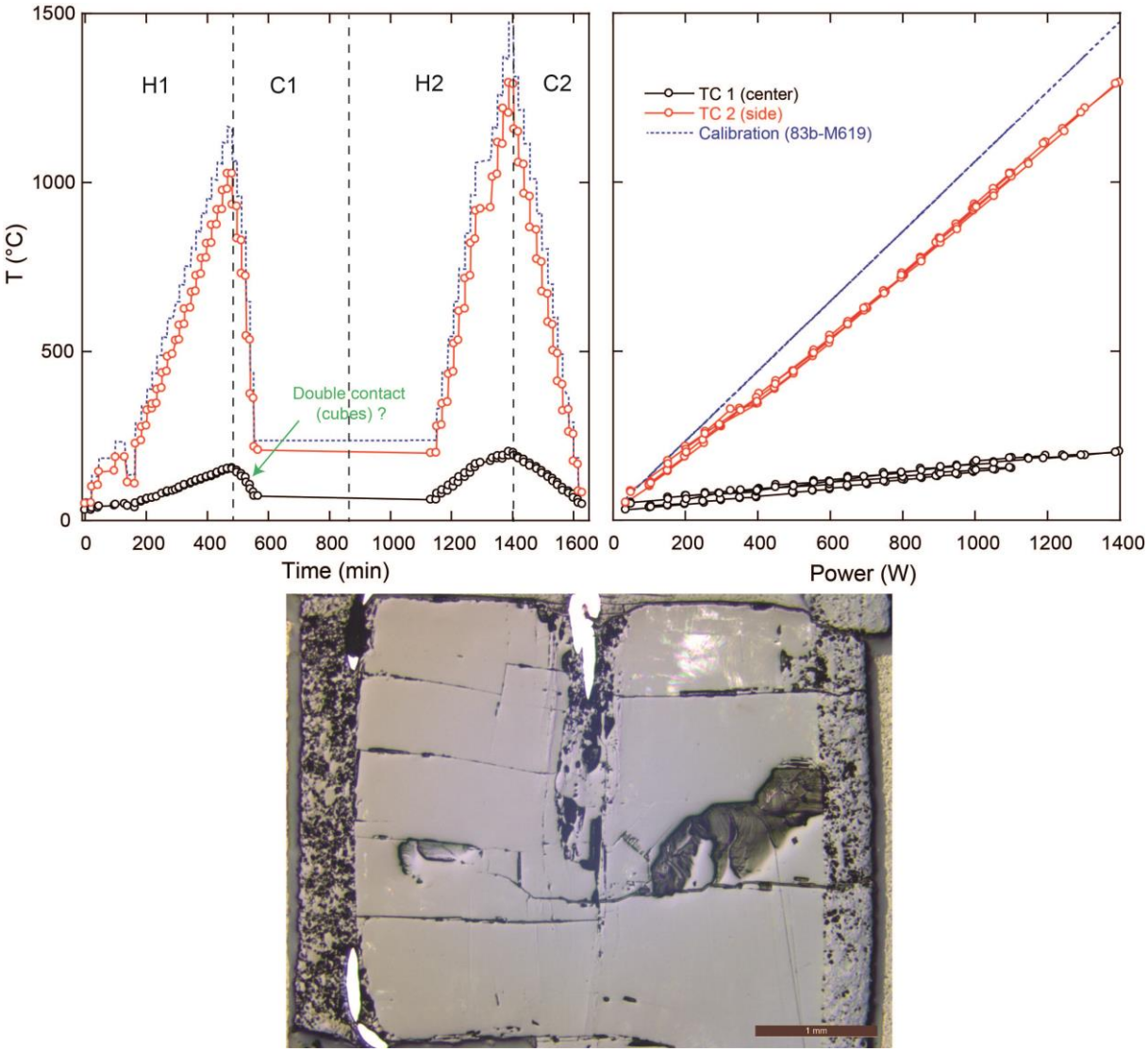

Figure D.31 M774 experimental procedure with temperature history with time and power/temperature calibration. Microphotographs of recovered sample are provided parallel to sample cylinder axis.

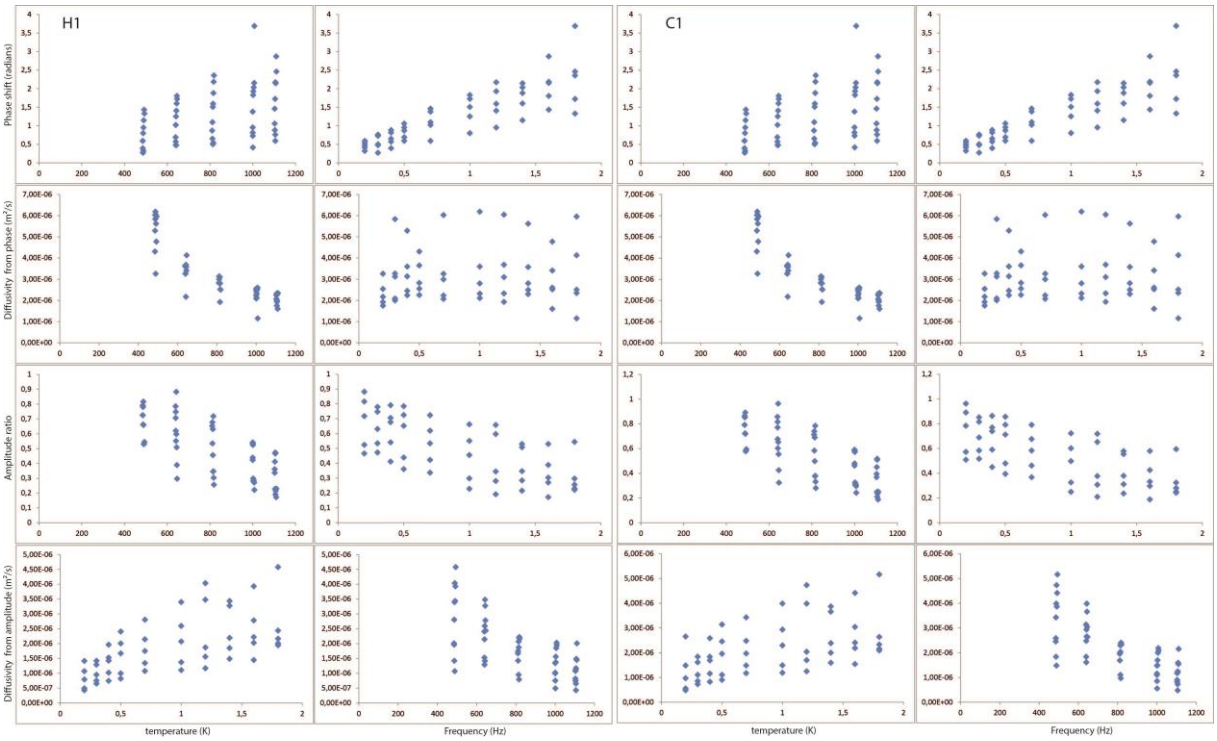

Figure D.32 M774 Experimental results for the first cycle. Phase shift (first raw), amplitude ratio (third raw) and inferred diffusivities (second and fourth raw respectively), are represented as function of temperature and frequency.

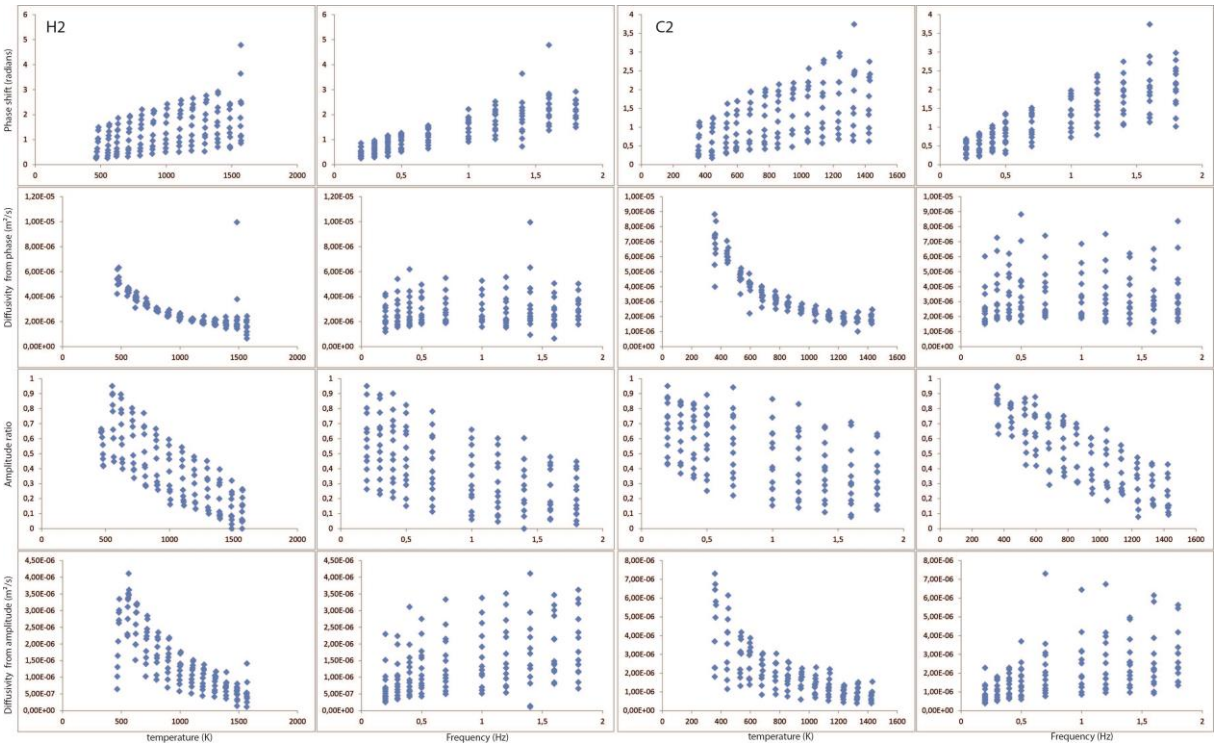

Figure D.33 M774 Experimental results for the second cycle. Phase shift (first raw), amplitude ratio (third raw) and inferred diffusivities (second and fourth raw respectively), are represented as function of temperature and frequency.

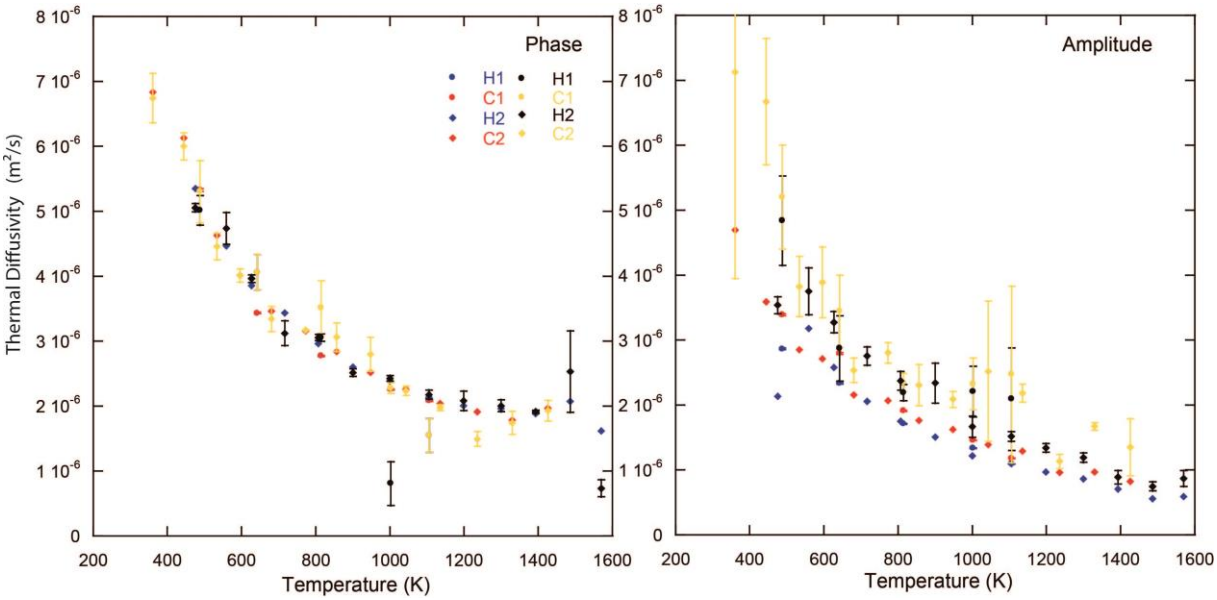

Figure D.34 M774 Thermal diffusivities obtained after fitting (D_0) and average (AVG) methods on diffusivities obtained at different frequencies at a fixed temperature. Phase and amplitude thermal diffusivity estimations are given in left and right panels respectively.

M802

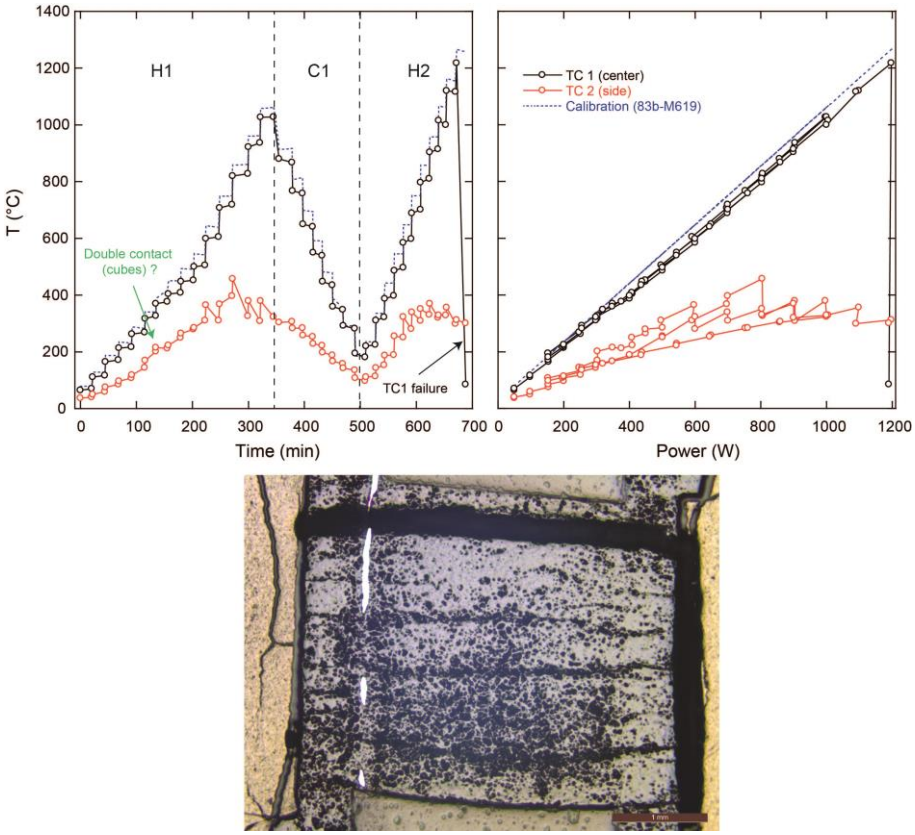

Figure D.35 M802 experimental procedure with temperature history with time and power/temperature calibration. Microphotographs of recovered sample are provided parallel to sample cylinder axis.

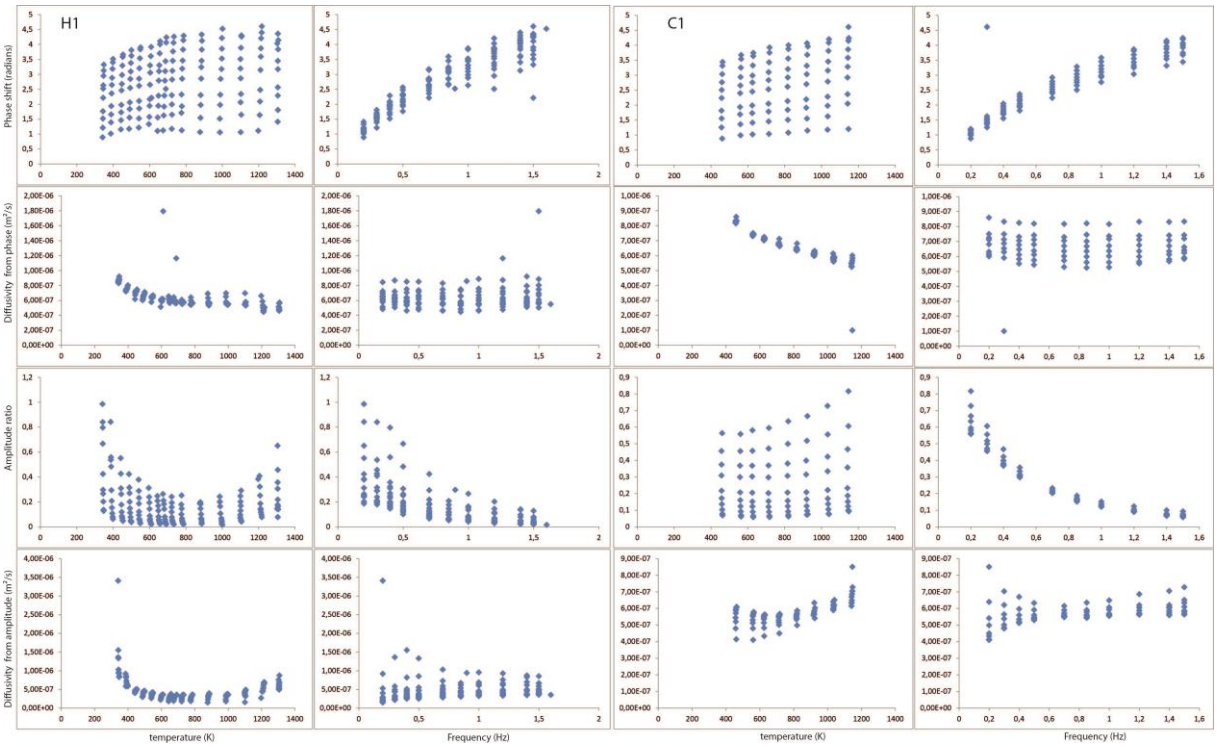

Figure D.36 M802 Experimental results for the first cycle. Phase shift (first raw), amplitude ratio (third raw) and inferred diffusivities (second and fourth raw respectively), are represented as function of temperature and frequency.

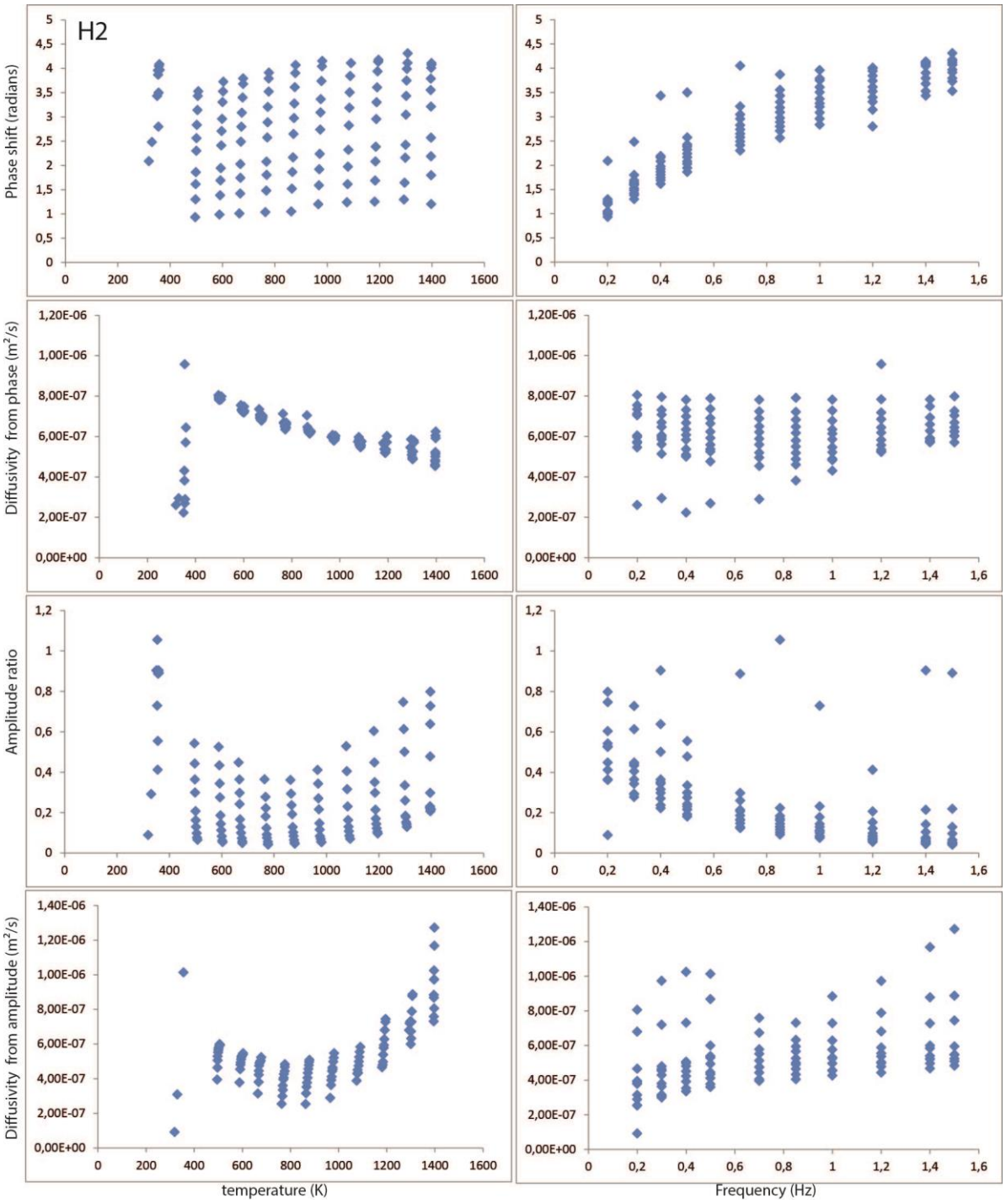

Figure D.37 M802 Experimental results for the first cycle. Phase shift (first raw), amplitude ratio (third raw) and inferred diffusivities (second and fourth raw respectively), are represented as function of temperature and frequency.

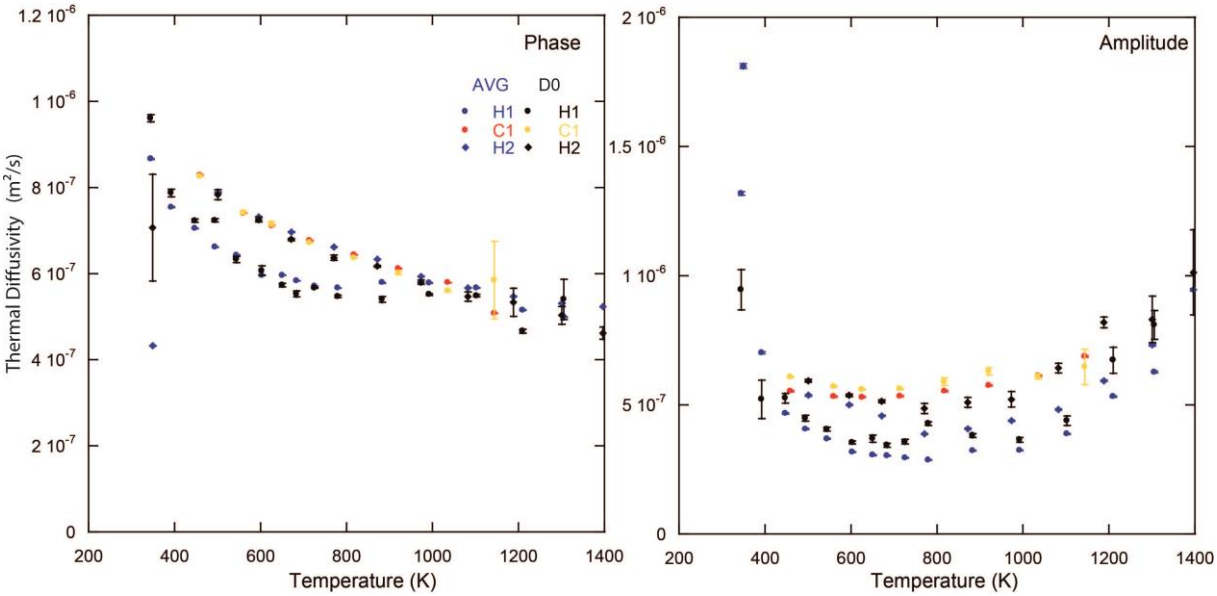

Figure D.38 M802 Thermal diffusivities obtained after fitting (D_0) and average (AVG) methods on diffusivities obtained at different frequencies at a fixed temperature. Phase and amplitude thermal diffusivity estimations are given in left and right panels respectively.

M804

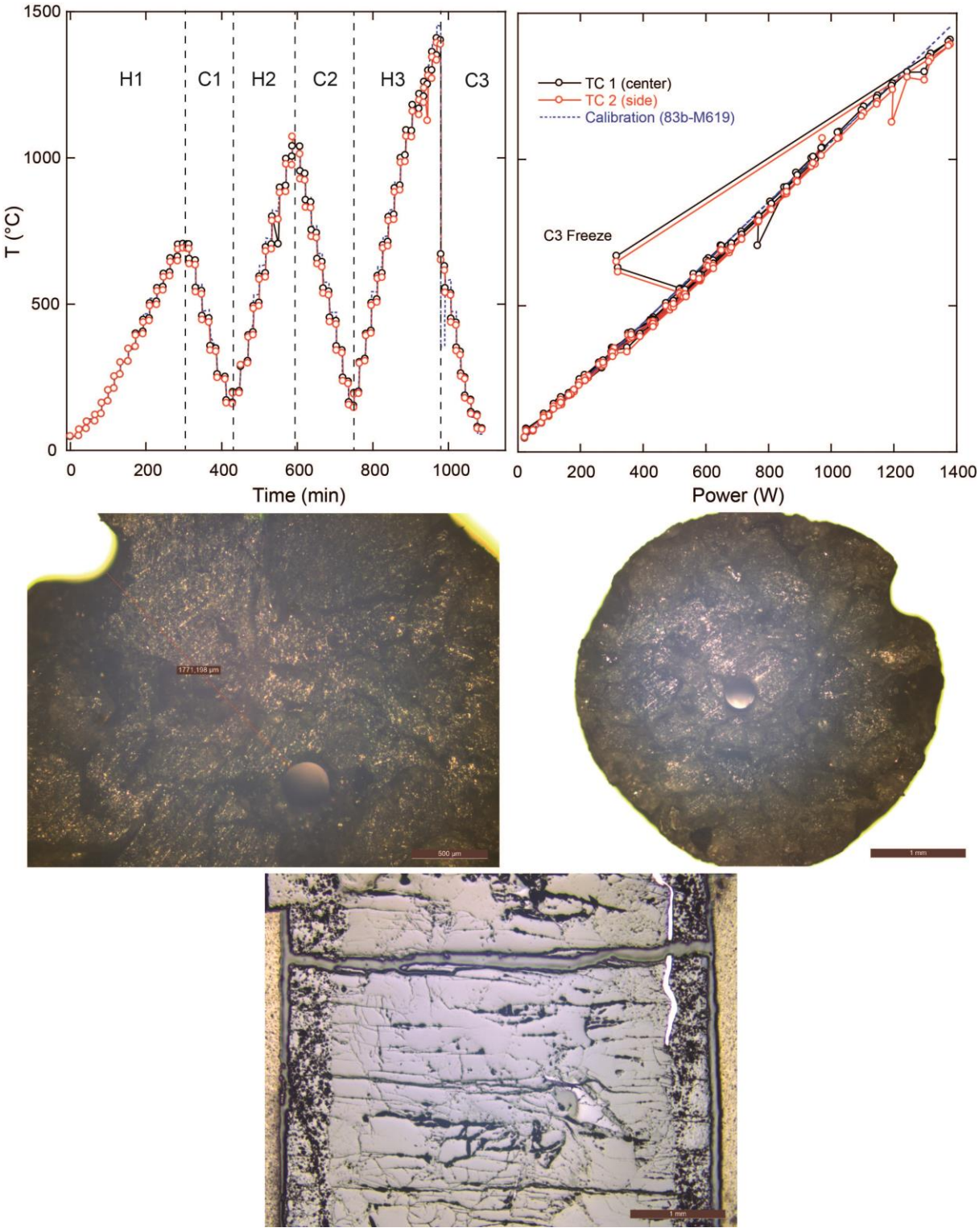

Figure D.39 M804 experimental procedure with temperature history with time and power/temperature calibration. Microphotographs on starting material and recovered sample parallel to sample cylinder axis are provided.

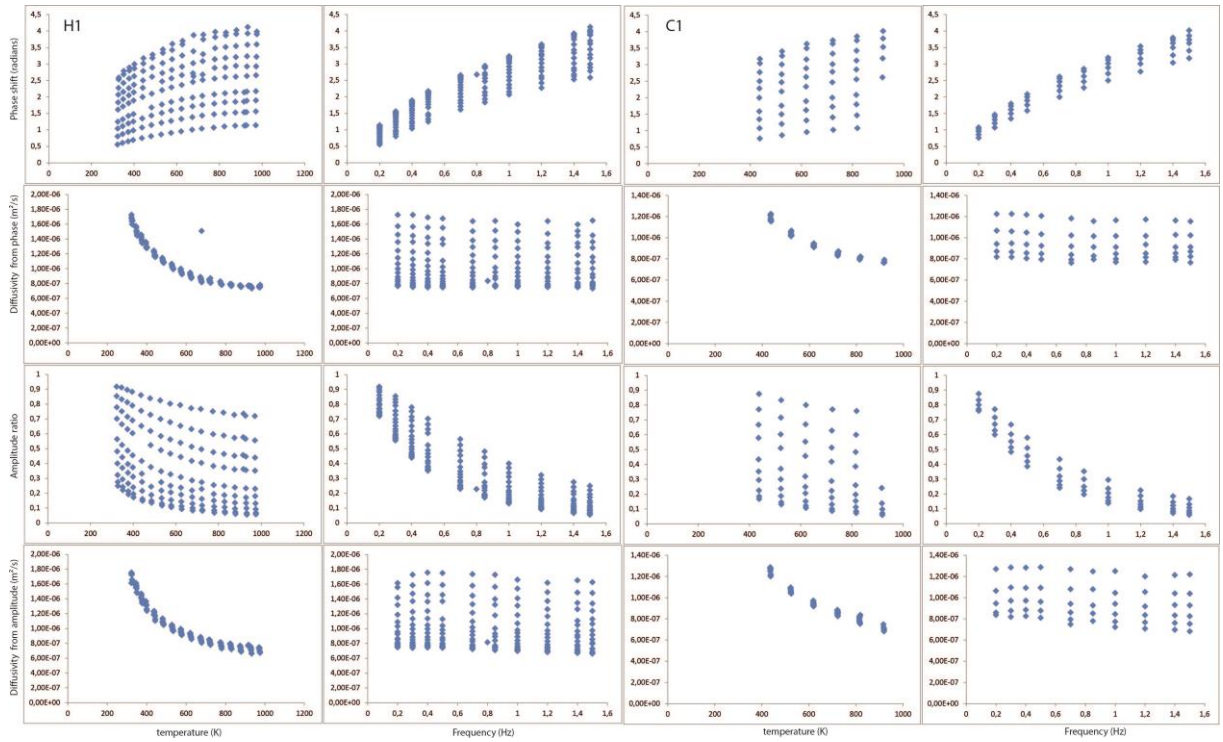

Figure D.40 M804 Experimental results for the first cycle. Phase shift (first raw), amplitude ratio (third raw) and inferred diffusivities (second and fourth raw respectively), are represented as function of temperature and frequency.

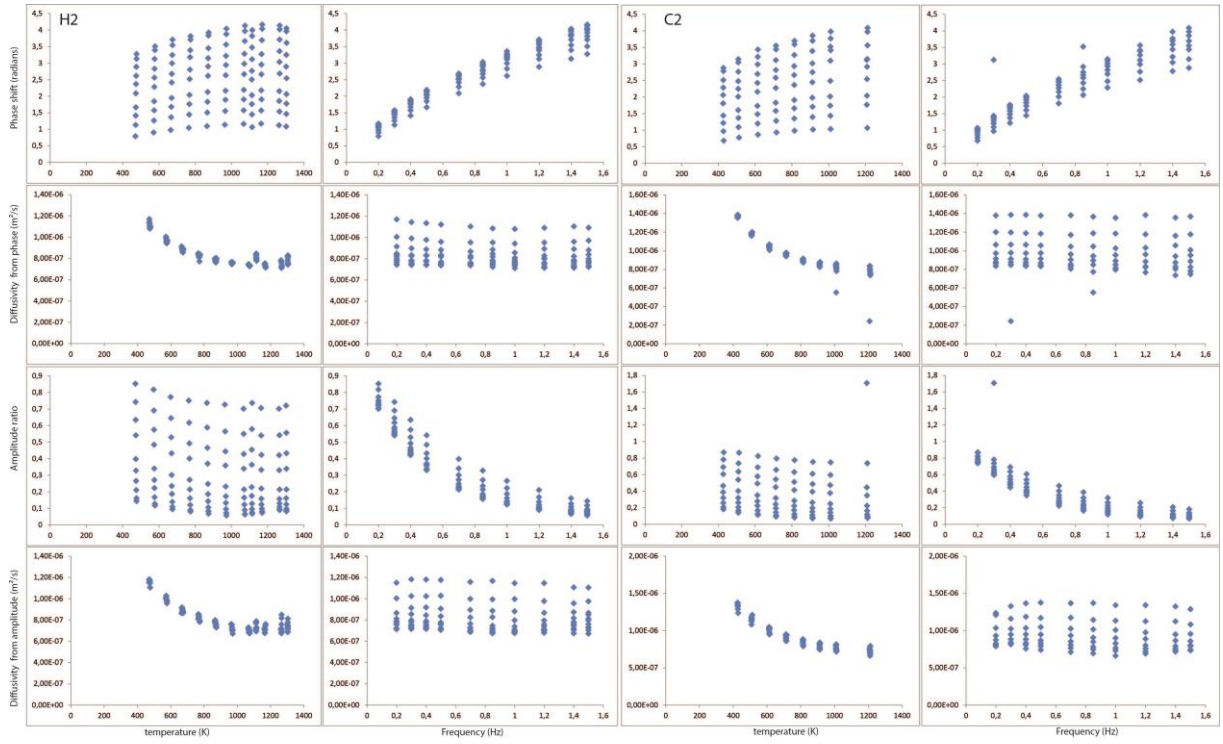

Figure D.41 M804 Experimental results for the second cycle. Phase shift (first raw), amplitude ratio (third raw) and inferred diffusivities (second and fourth raw respectively), are represented as function of temperature and frequency.

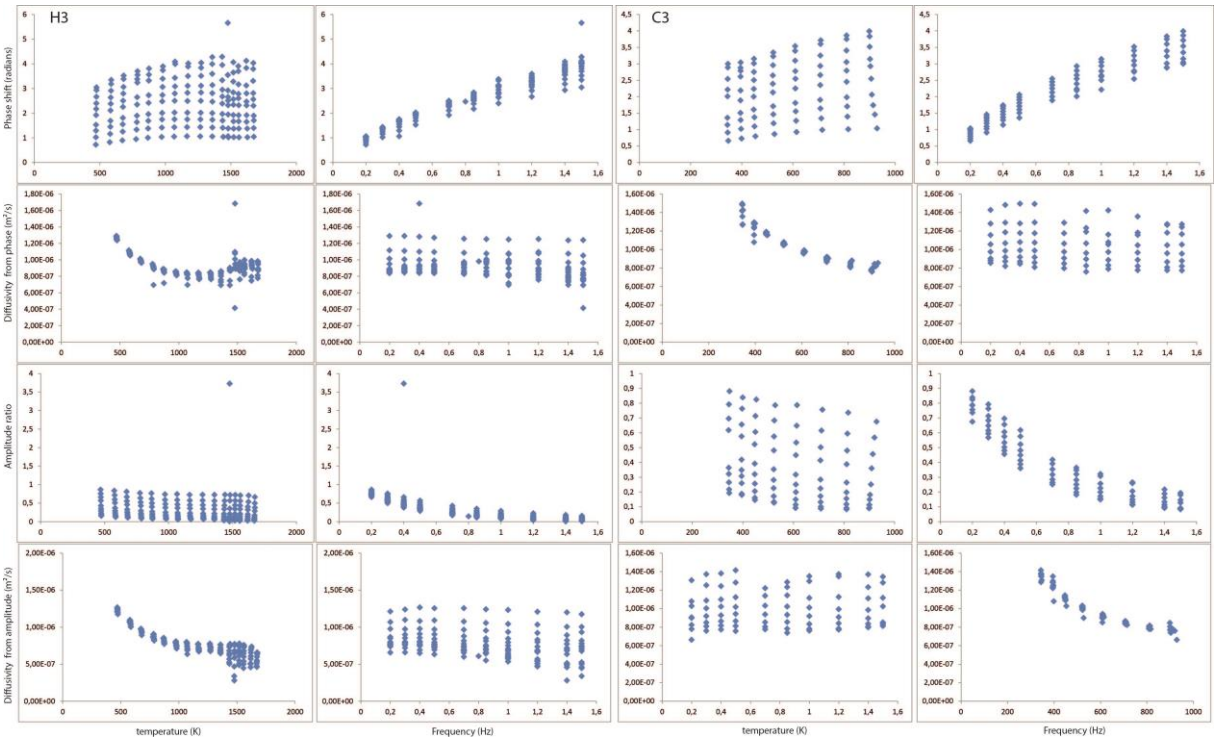

Figure D.42 M804 Experimental results for the third cycle. Phase shift (first raw), amplitude ratio (third raw) and inferred diffusivities (second and fourth raw respectively), are represented as function of temperature and frequency.

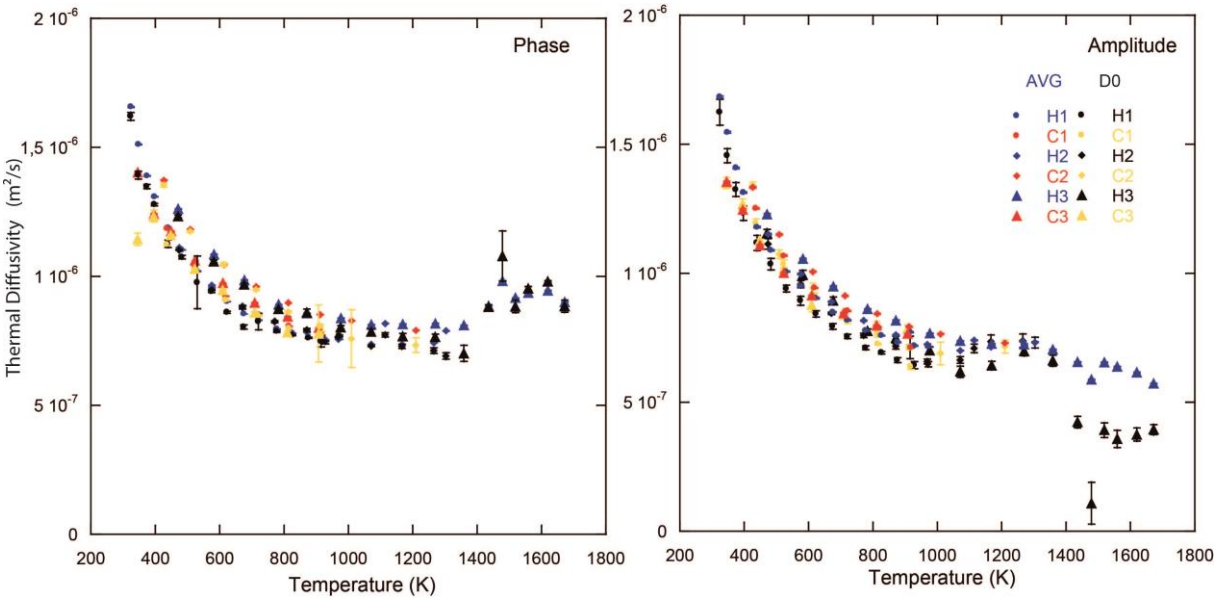

Figure D.43 M804 Thermal diffusivities obtained after fitting (D_0) and average (AVG) methods on diffusivities obtained at different frequencies at a fixed temperature. Phase and amplitude thermal diffusivity estimations are given in left and right panels respectively.

M807

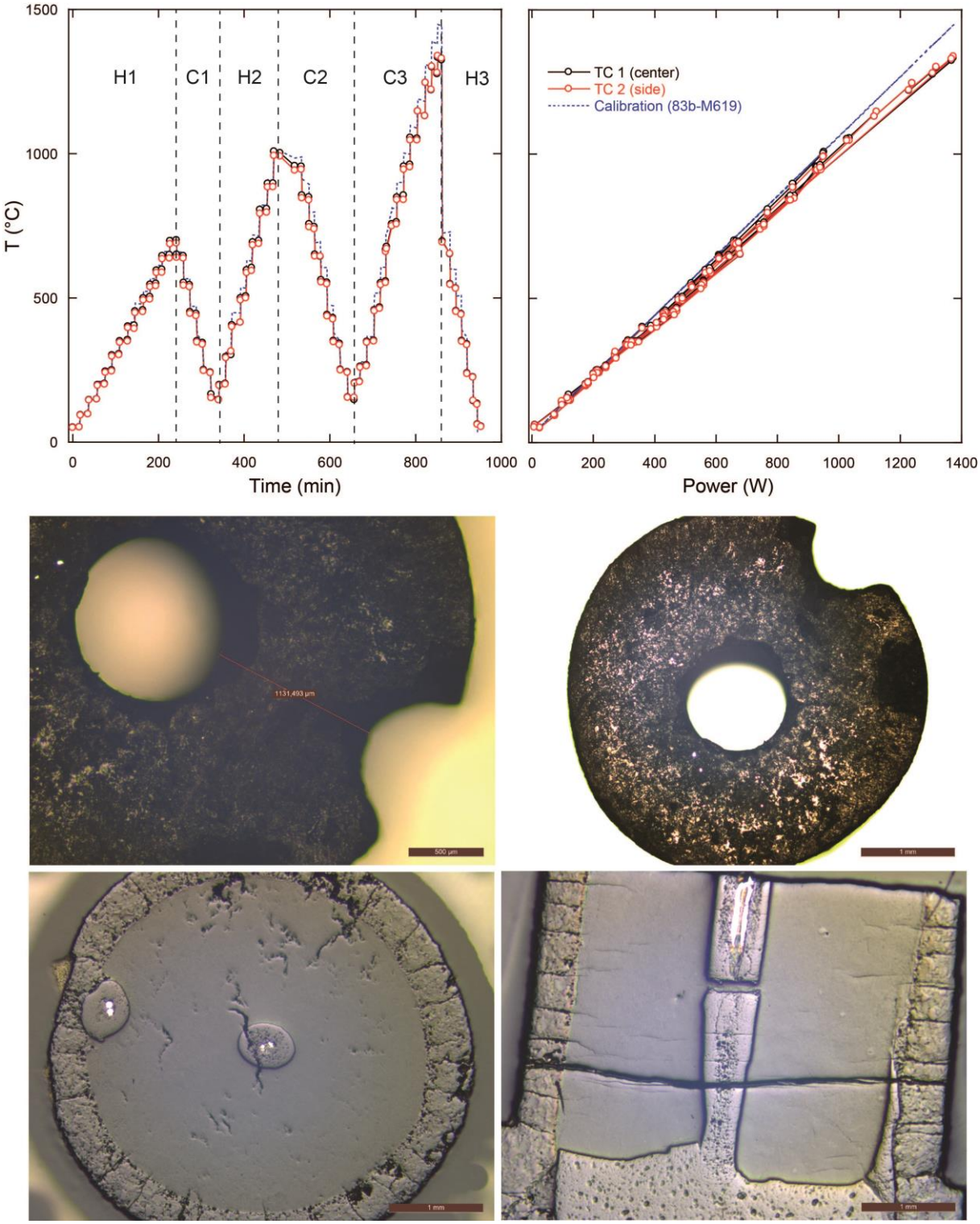

Figure D.44 M807 experimental procedure with temperature history with time and power/temperature calibration. Microphotographs o starting material and recovered sample cut perpendicular (left) and parallel (right) to sample cylinder axis are provided.

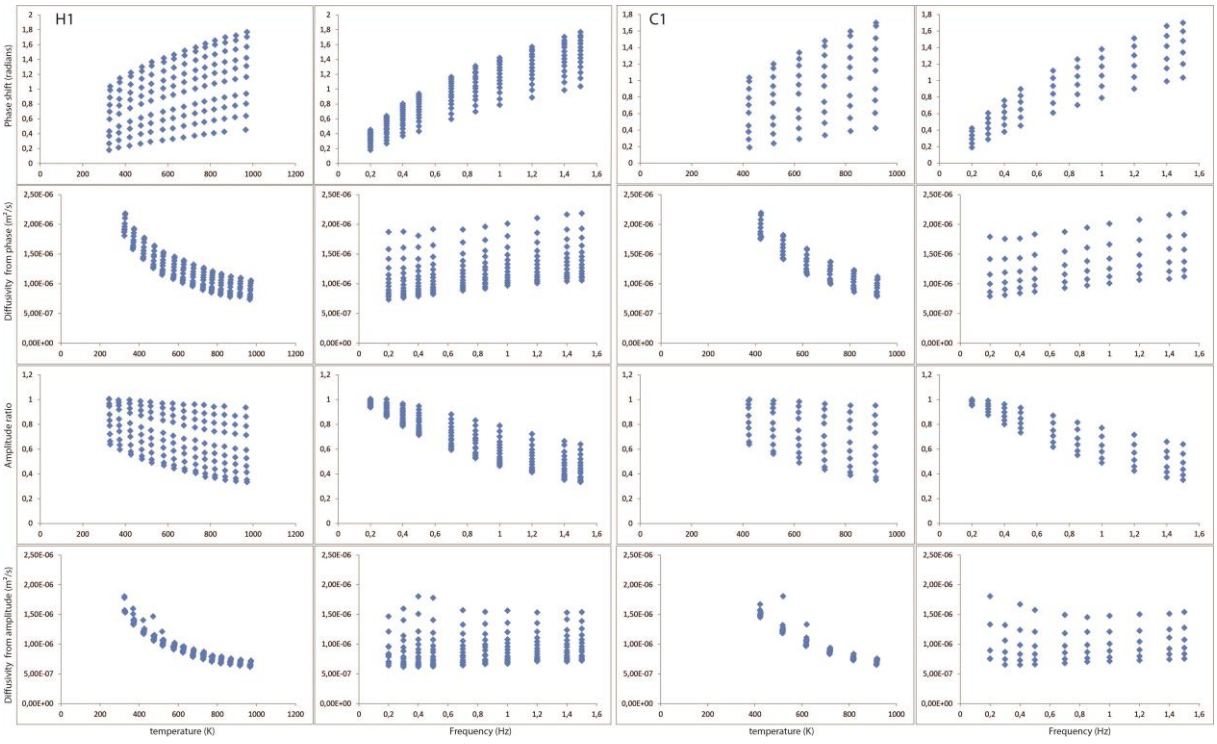

Figure D.45 M807 Experimental results for the first cycle. Phase shift (first raw), amplitude ratio (third raw) and inferred diffusivities (second and fourth raw respectively), are represented as function of temperature and frequency.

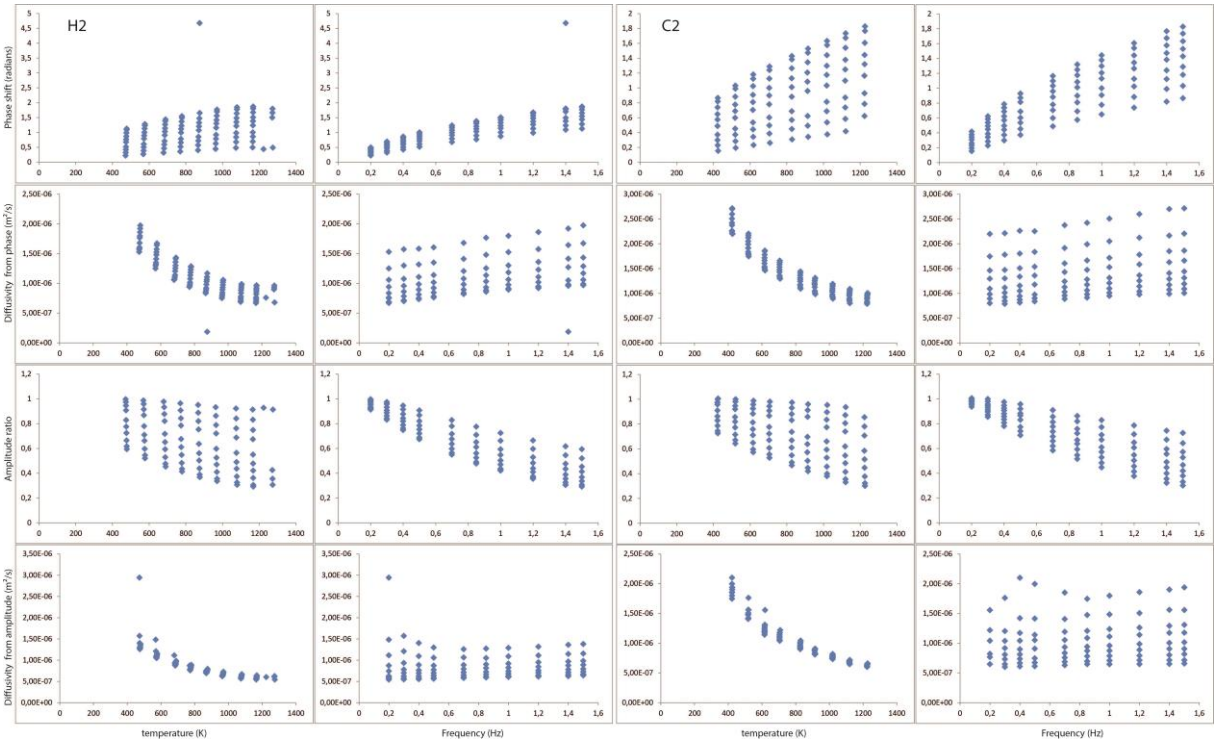

Figure D.46 M807 Experimental results for the second cycle. Phase shift (first raw), amplitude ratio (third raw) and inferred diffusivities (second and fourth raw respectively), are represented as function of temperature and frequency.

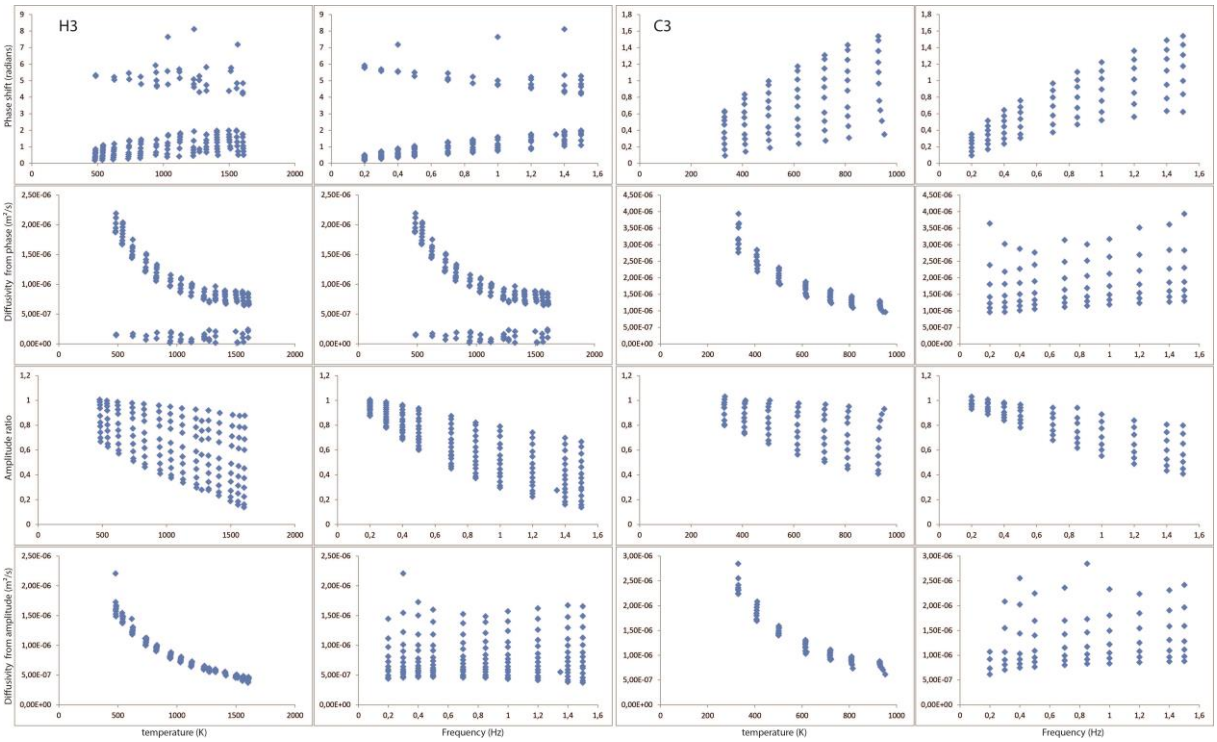

Figure D.47 M807 Experimental results for the third cycle. Phase shift (first raw), amplitude ratio (third raw) and inferred diffusivities (second and fourth raw respectively), are represented as function of temperature and frequency.

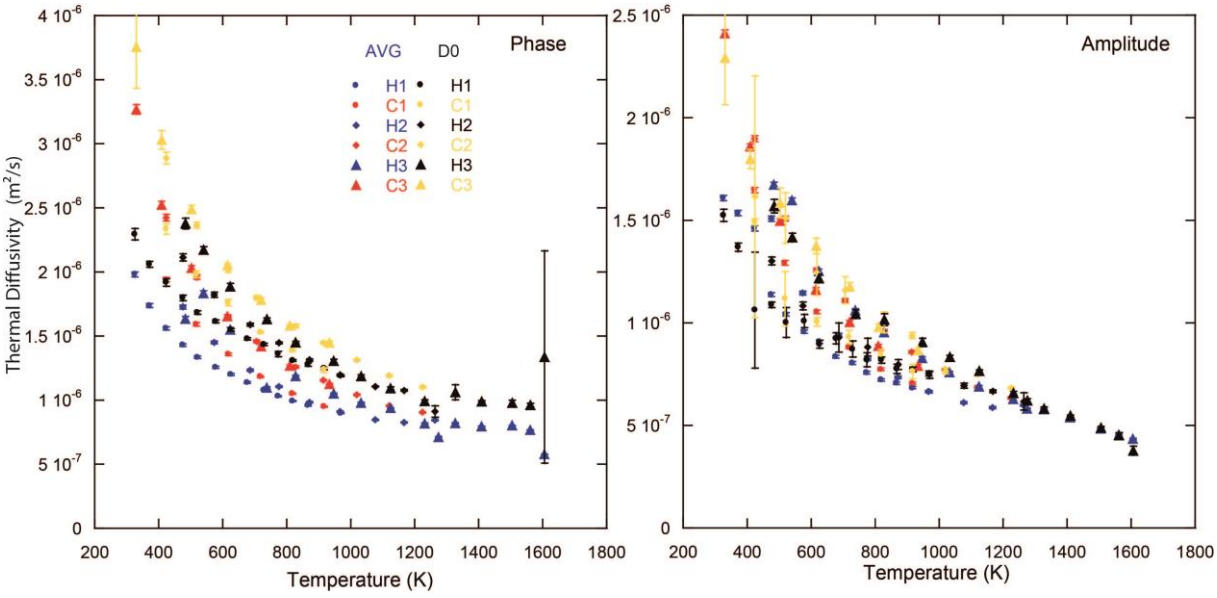

Figure D.48 M807 Thermal diffusivities obtained after fitting (D_0) and average (AVG) methods on diffusivities obtained at different frequencies at a fixed temperature. Phase and amplitude thermal diffusivity estimations are given in left and right panels respectively.

M808

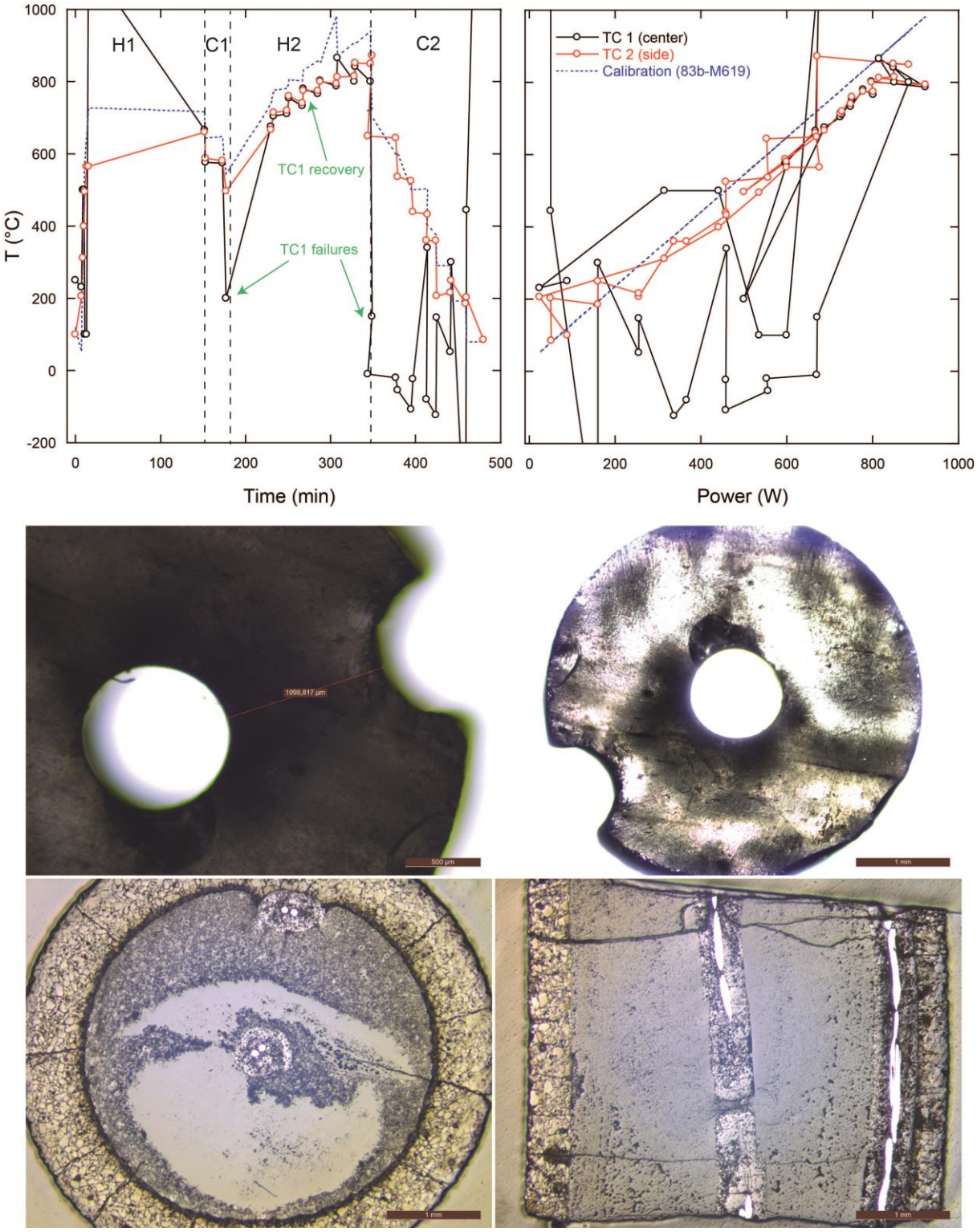

Figure D.49 M808 experimental procedure with temperature history with time and power/temperature calibration. Microphotographs o starting material and recovered sample cut perpendicular (left) and parallel (right) to sample cylinder axis are provided.

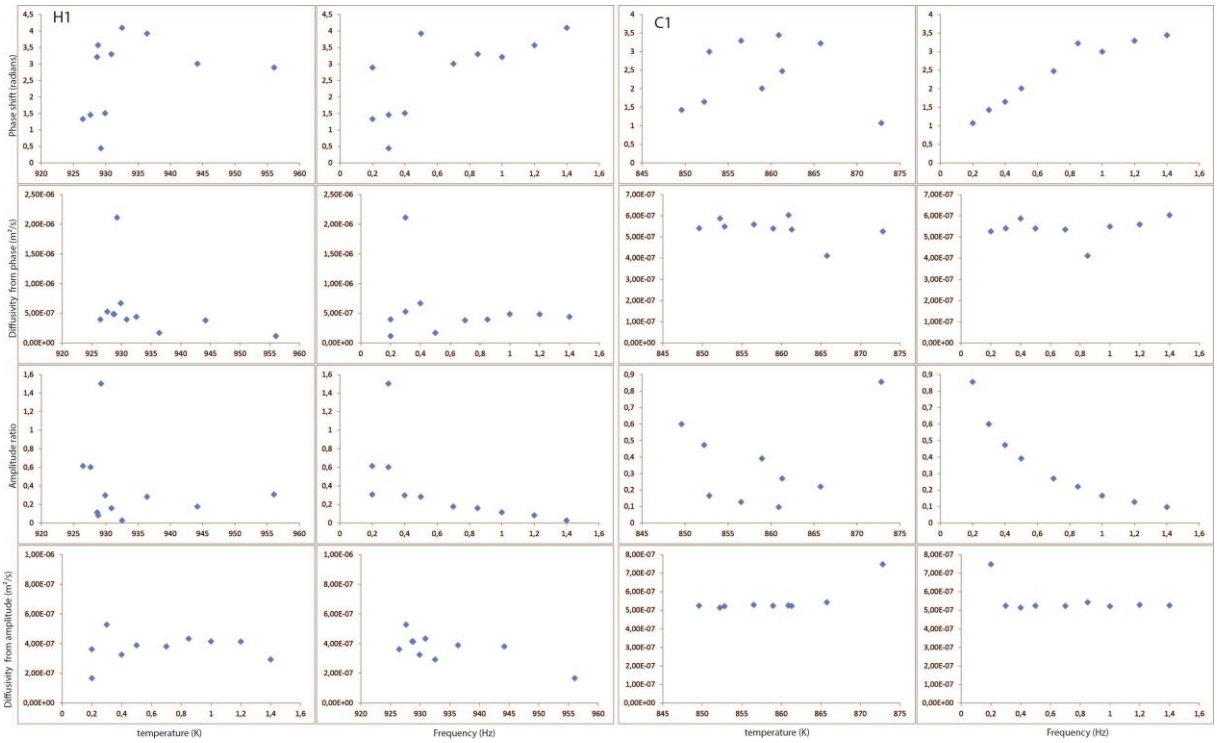

Figure D.50 M808 Experimental results for the first cycle. Phase shift (first raw), amplitude ratio (third raw) and inferred diffusivities (second and fourth raw respectively), are represented as function of temperature and frequency.

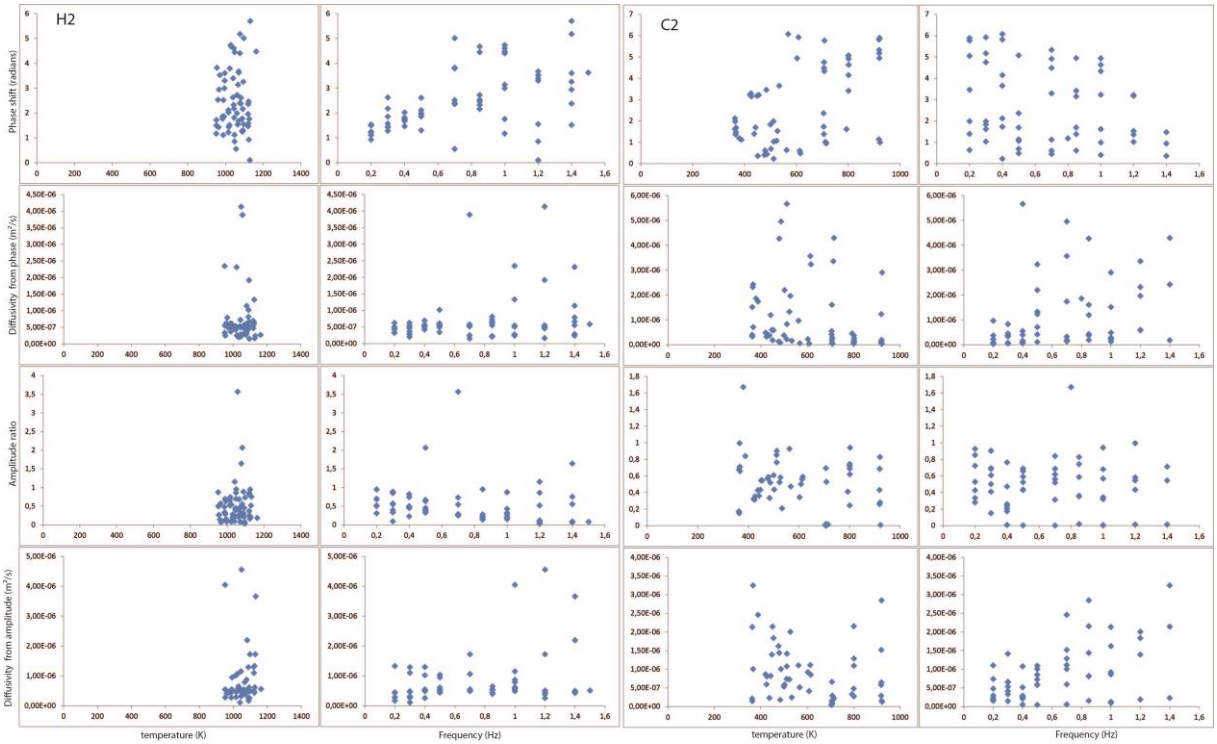

Figure D.51 M808 Experimental results for the second cycle. Phase shift (first raw), amplitude ratio (third raw) and inferred diffusivities (second and fourth raw respectively), are represented as function of temperature and frequency.

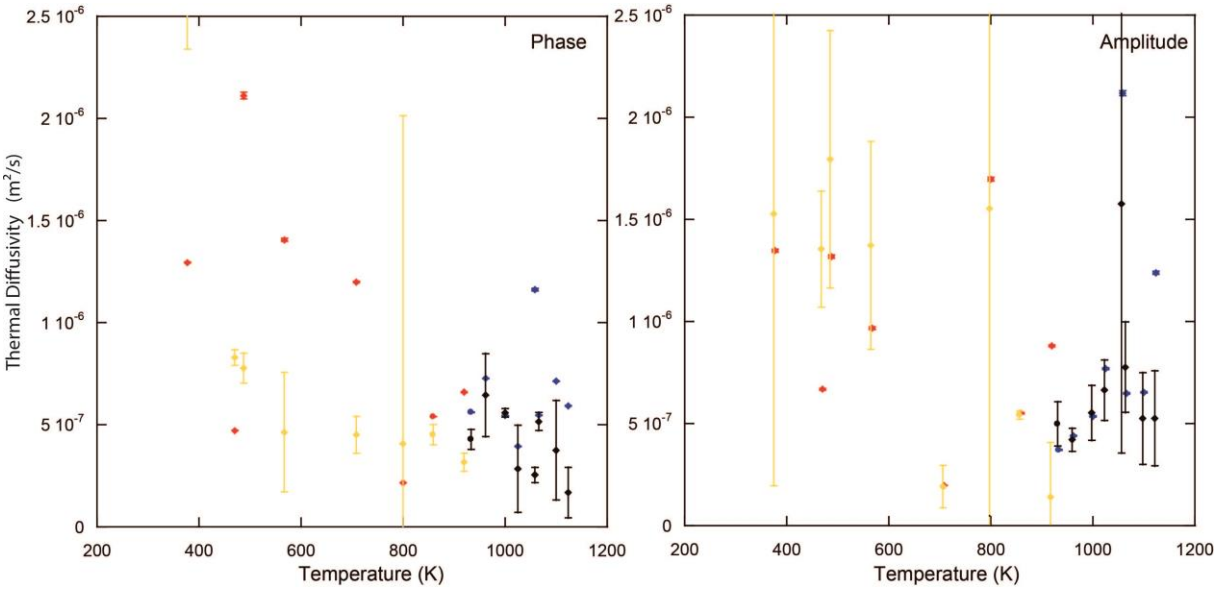

Figure D.52 M808 Thermal diffusivities obtained after fitting (D_0) and average (AVG) methods on diffusivities obtained at different frequencies at a fixed temperature. Phase and amplitude thermal diffusivity estimations are given in left and right panels respectively.

M833

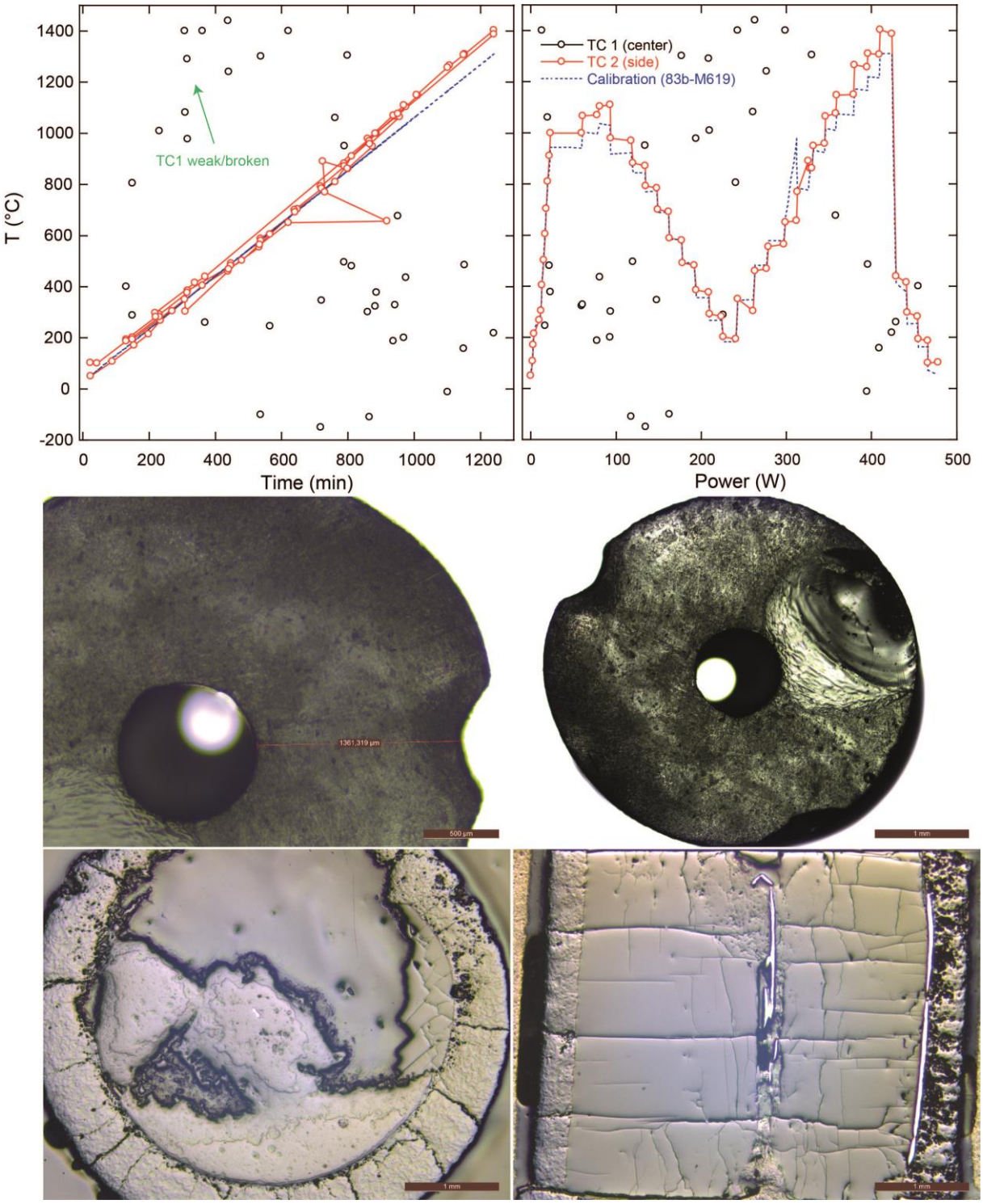

Figure D.53 M833 experimental procedure with temperature history with time and power/temperature calibration. Microphotographs o starting material and recovered sample cut perpendicular (left) and parallel (right) to sample cylinder axis are provided.

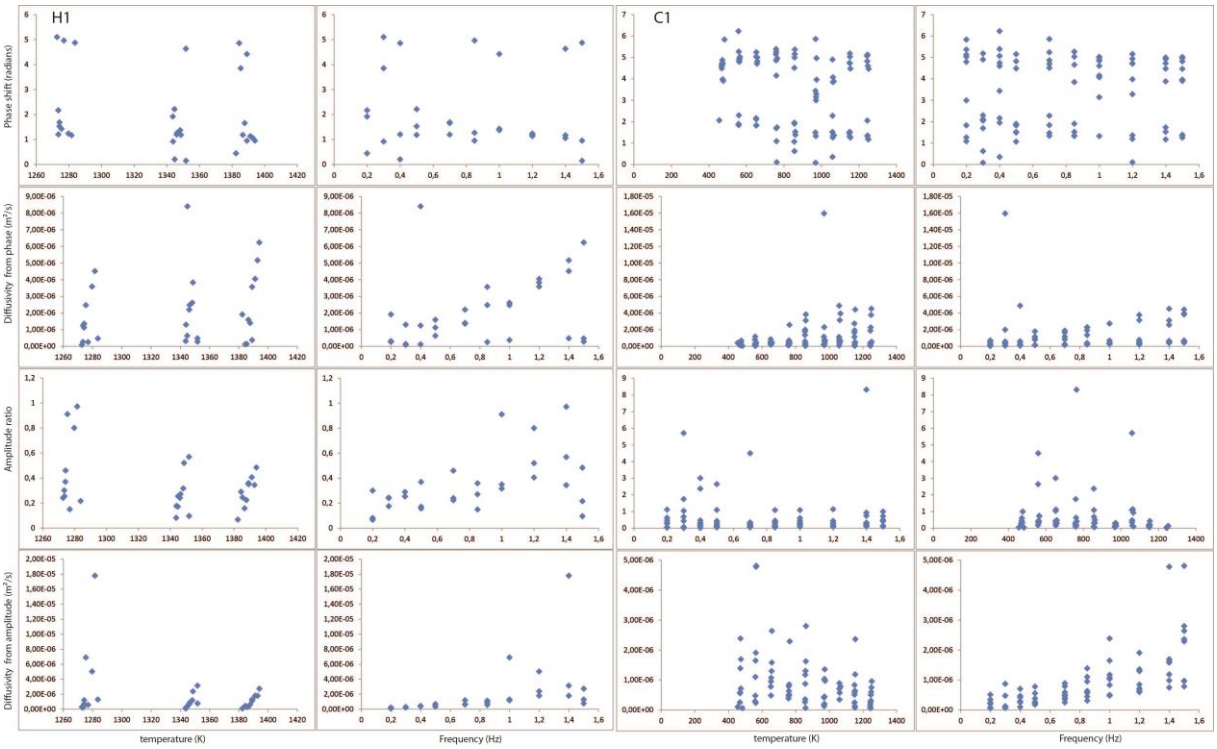

Figure D.54 M833 Experimental results for the first cycle. Phase shift (first raw), amplitude ratio (third raw) and inferred diffusivities (second and fourth raw respectively), are represented as function of temperature and frequency.

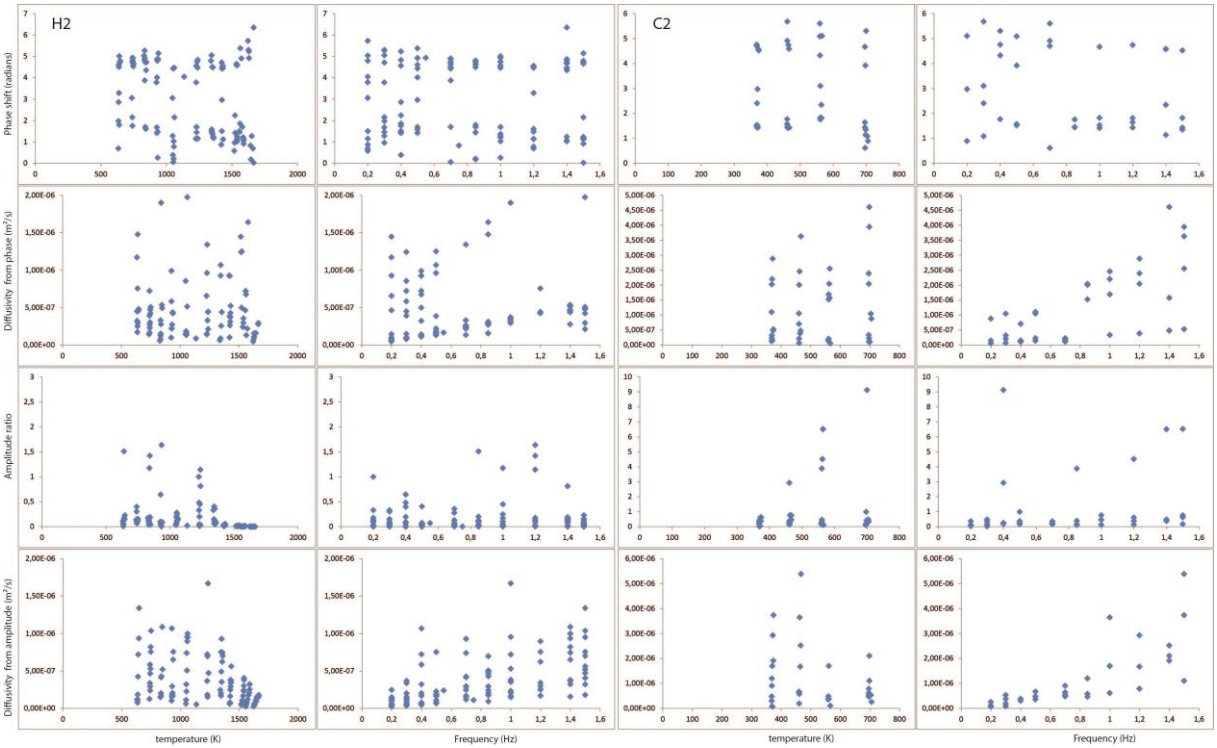

Figure D.55 M833 Experimental results for the second cycle. Phase shift (first raw), amplitude ratio (third raw) and inferred diffusivities (second and fourth raw respectively), are represented as function of temperature and frequency.

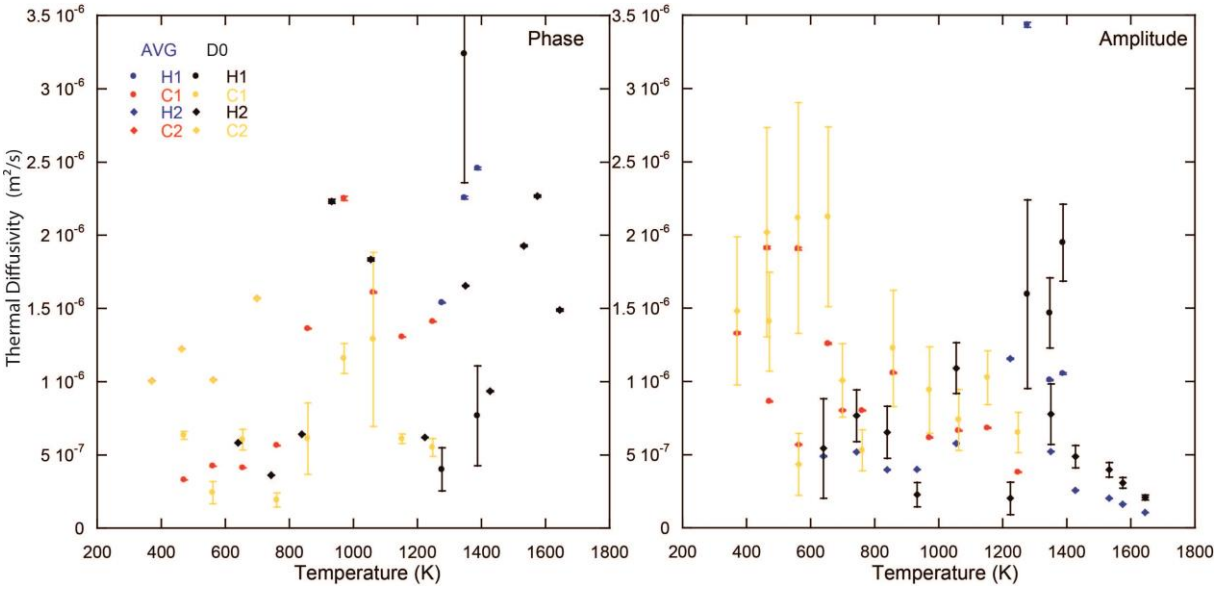

Figure D.56 M833 Thermal diffusivities obtained after fitting (D_0) and average (AVG) methods on diffusivities obtained at different frequencies at a fixed temperature. Phase and amplitude thermal diffusivity estimations are given in left and right panels respectively.

M836

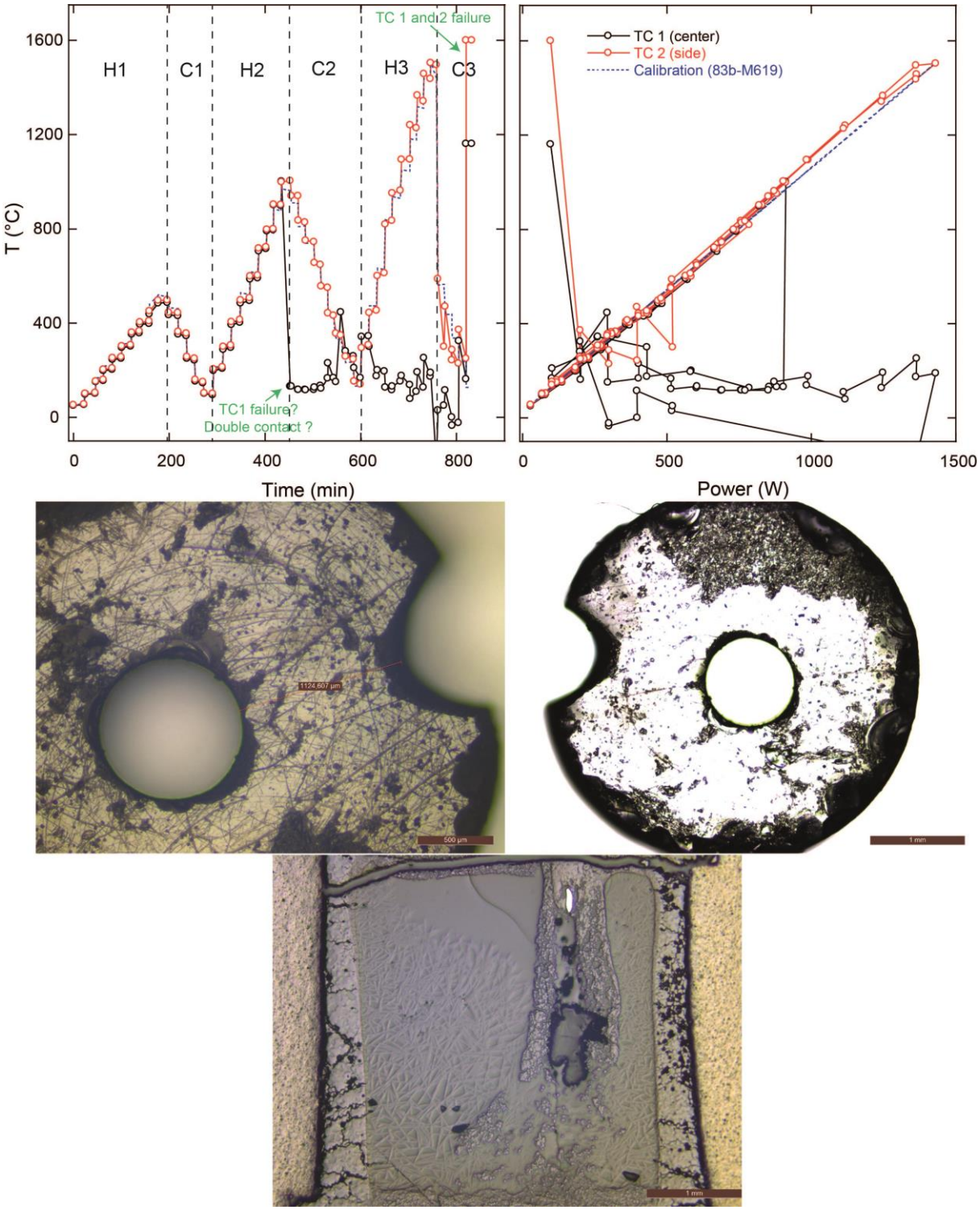

Figure D.57 M836 experimental procedure with temperature history with time and power/temperature calibration. Microphotographs o starting material and recovered sample parallel to sample cylinder axis are provided.

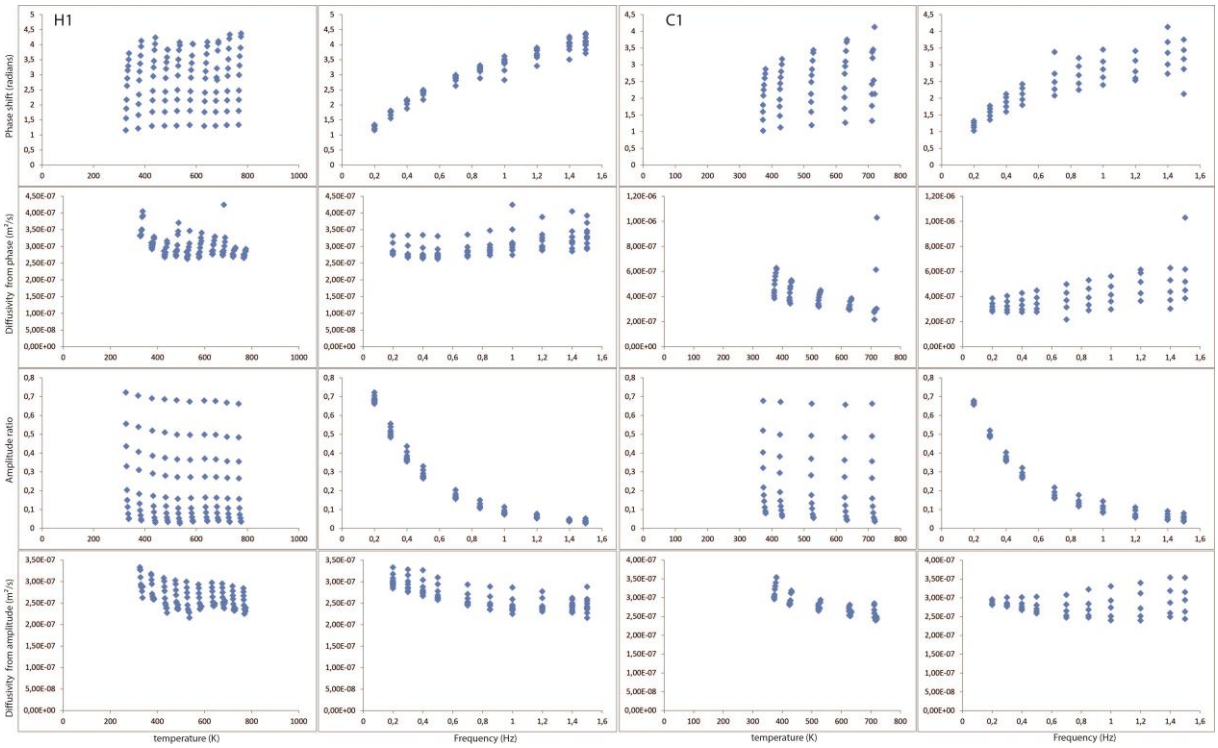

Figure D.58 M836 Experimental results for the first cycle. Phase shift (first raw), amplitude ratio (third raw) and inferred diffusivities (second and fourth raw respectively), are represented as function of temperature and frequency.

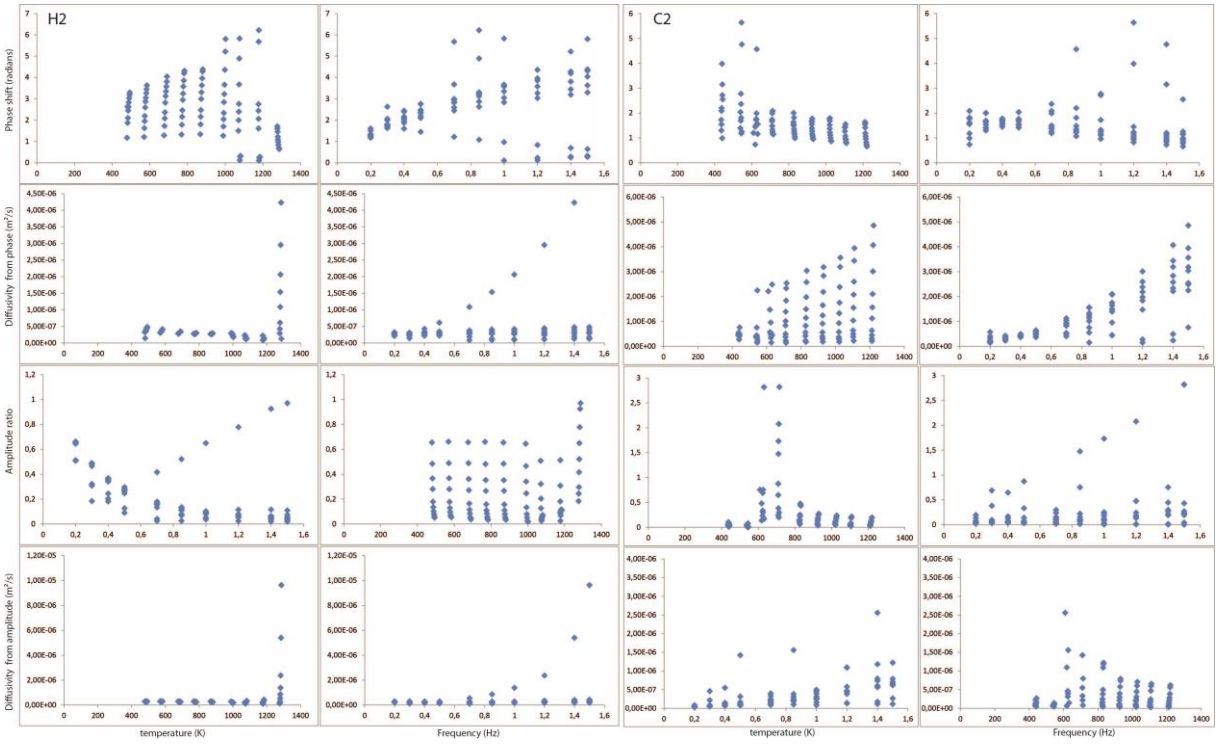

Figure D.59 M836 Experimental results for the second cycle. Phase shift (first raw), amplitude ratio (third raw) and inferred diffusivities (second and fourth raw respectively), are represented as function of temperature and frequency.

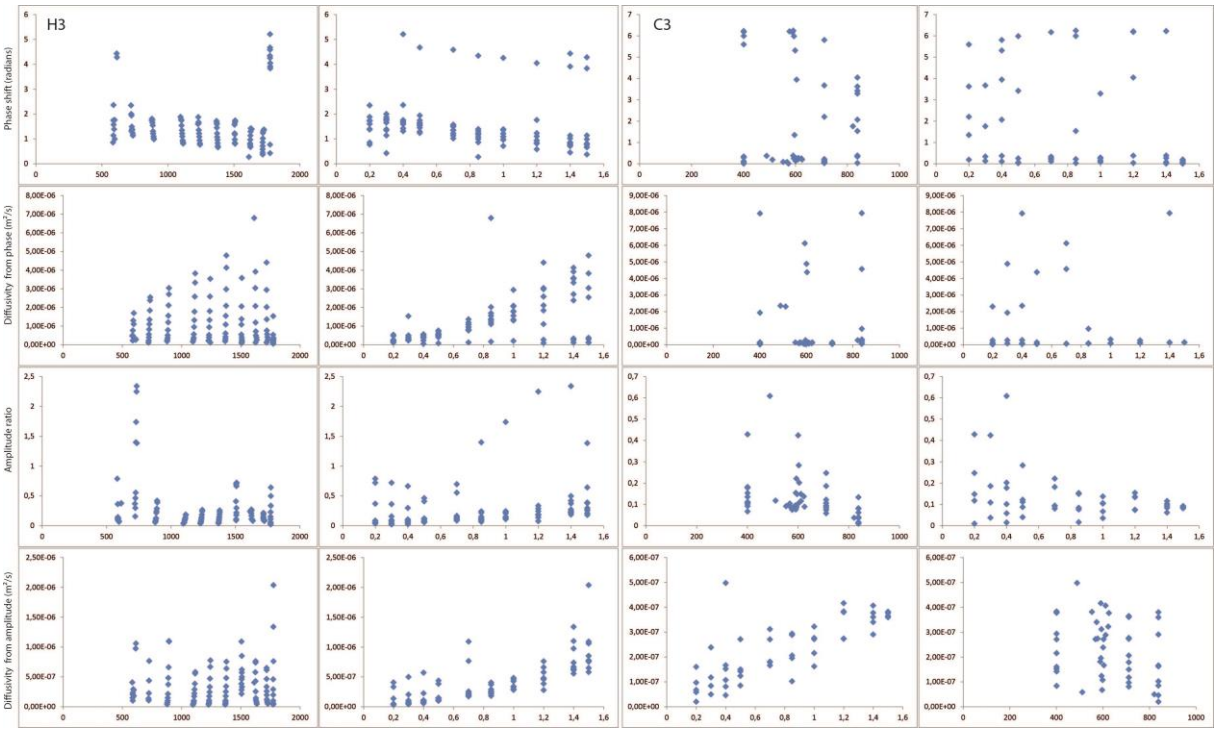

Figure D.60 M836 Experimental results for the third cycle. Phase shift (first raw), amplitude ratio (third raw) and inferred diffusivities (second and fourth raw respectively), are represented as function of temperature and frequency.

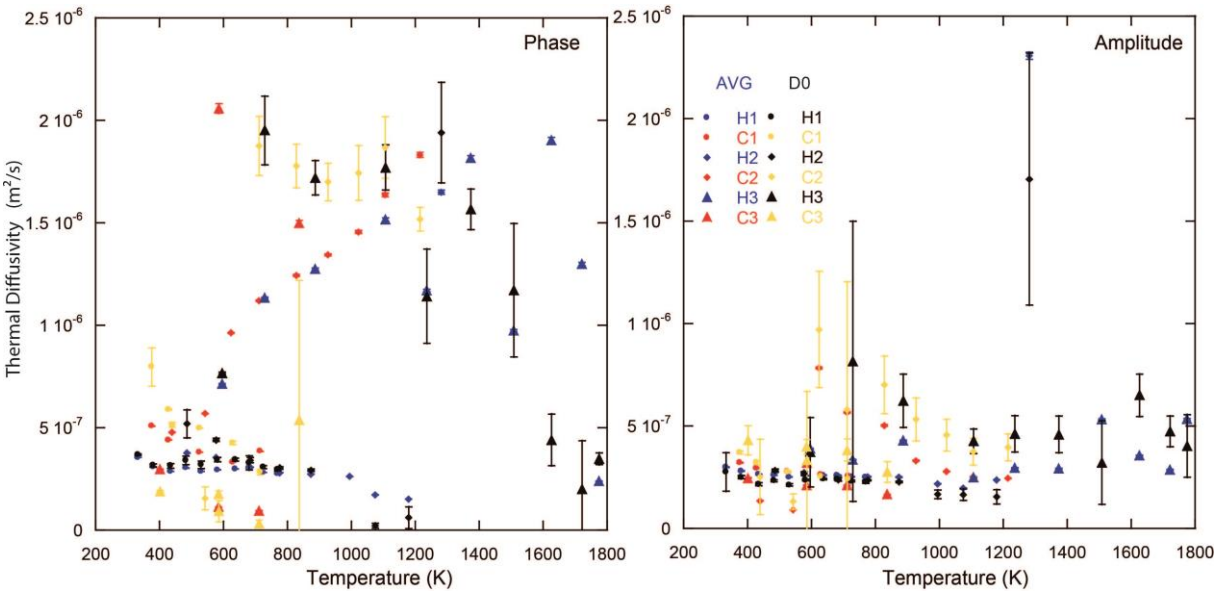

Figure D.61 M836 Thermal diffusivities obtained after fitting (D_0) and average (AVG) methods on diffusivities obtained at different frequencies at a fixed temperature. Phase and amplitude thermal diffusivity estimations are given in left and right panels respectively.

M843

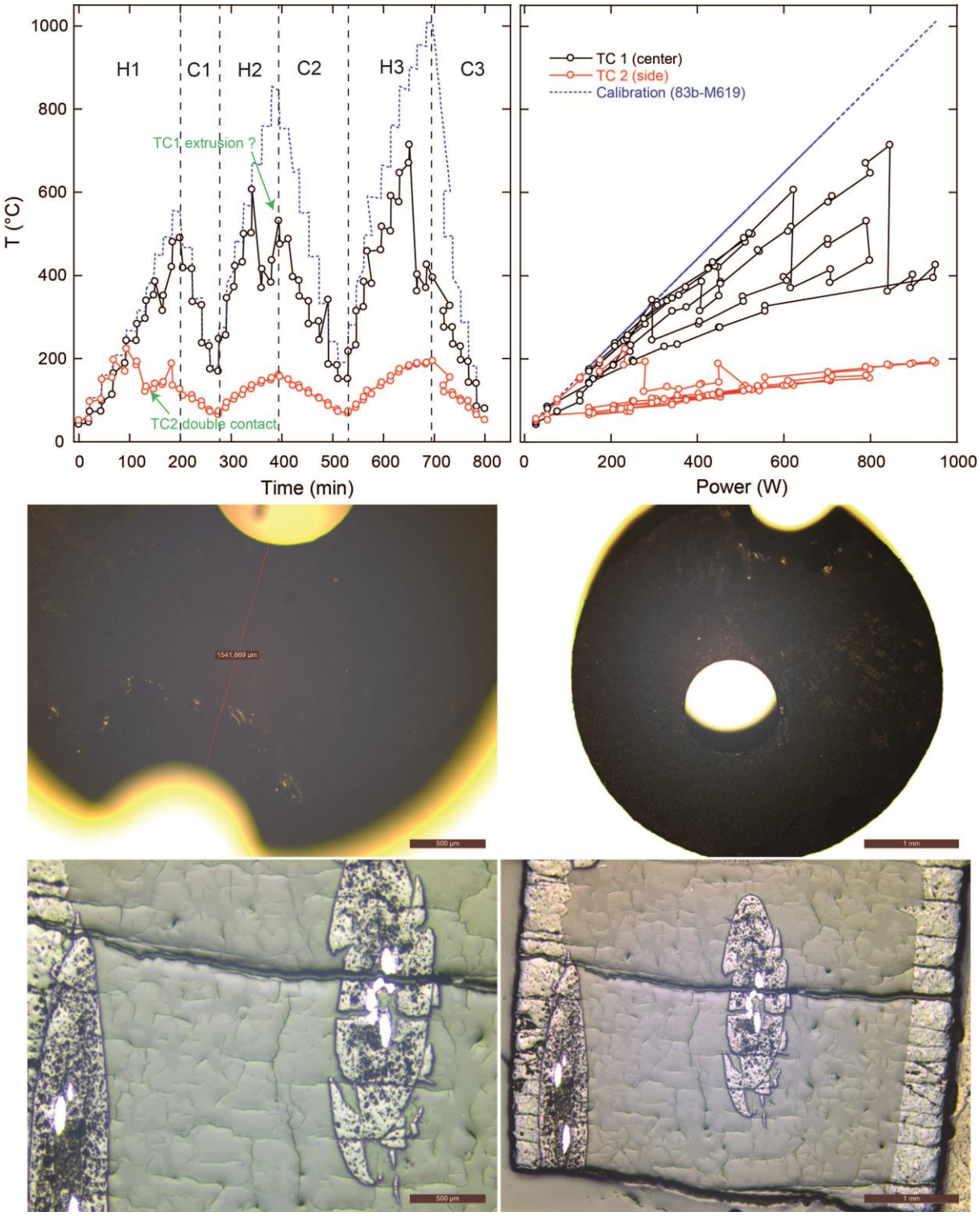

Figure D.62 M843 experimental procedure with temperature history with time and power/temperature calibration. Microphotographs o starting material and recovered sample cut perpendicular (left) and parallel (right) to sample cylinder axis are provided.

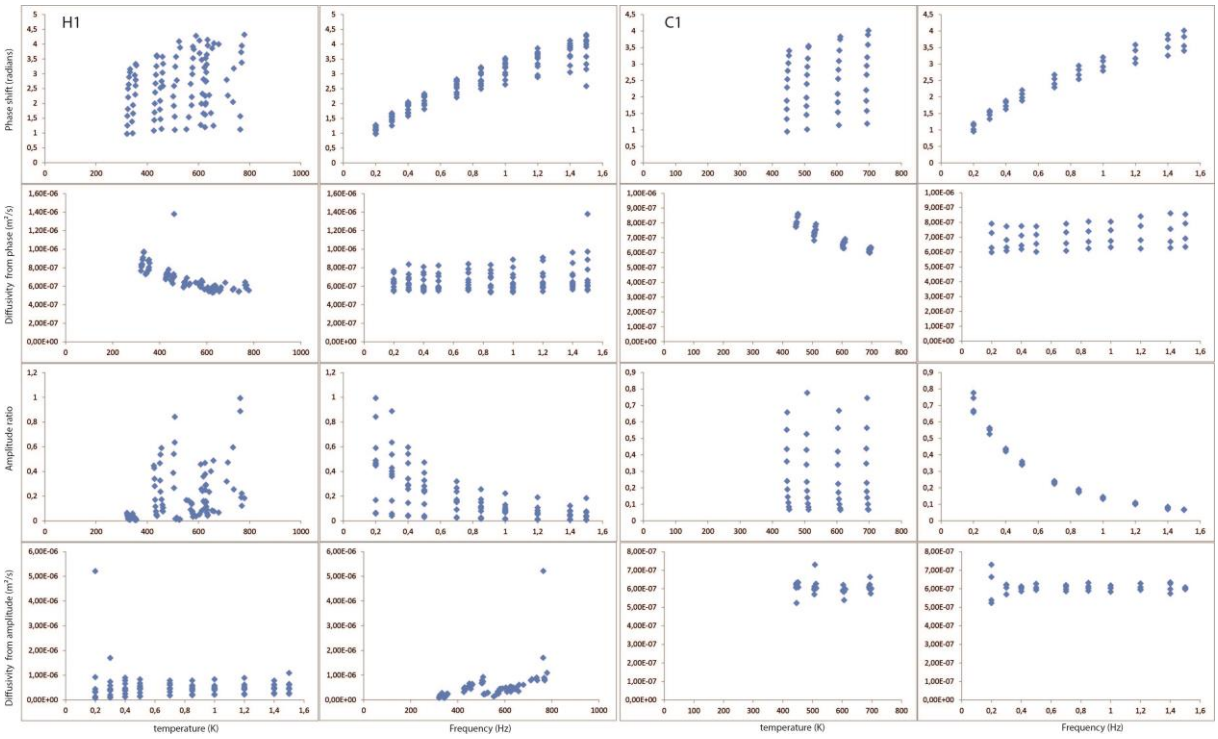

Figure D.63 M843 Experimental results for the first cycle. Phase shift (first raw), amplitude ratio (third raw) and inferred diffusivities (second and fourth raw respectively), are represented as function of temperature and frequency.

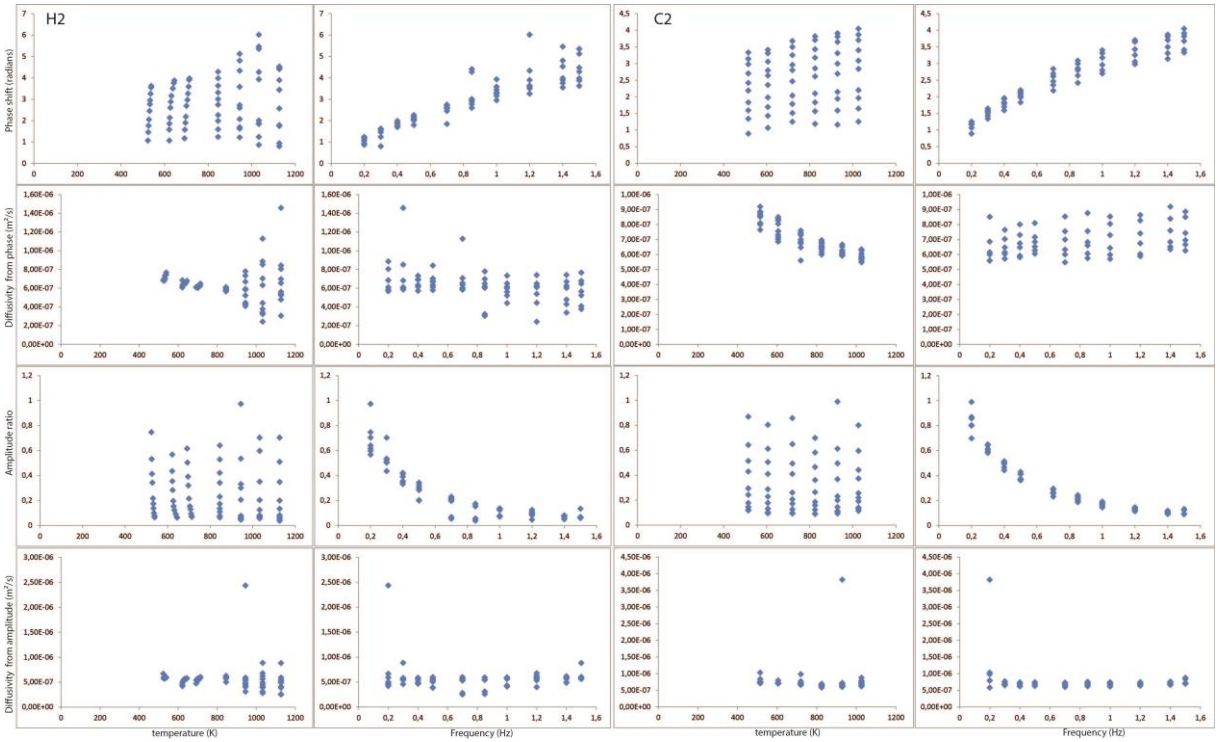

Figure D.64 M843 Experimental results for the second cycle. Phase shift (first raw), amplitude ratio (third raw) and inferred diffusivities (second and fourth raw respectively), are represented as function of temperature and frequency.

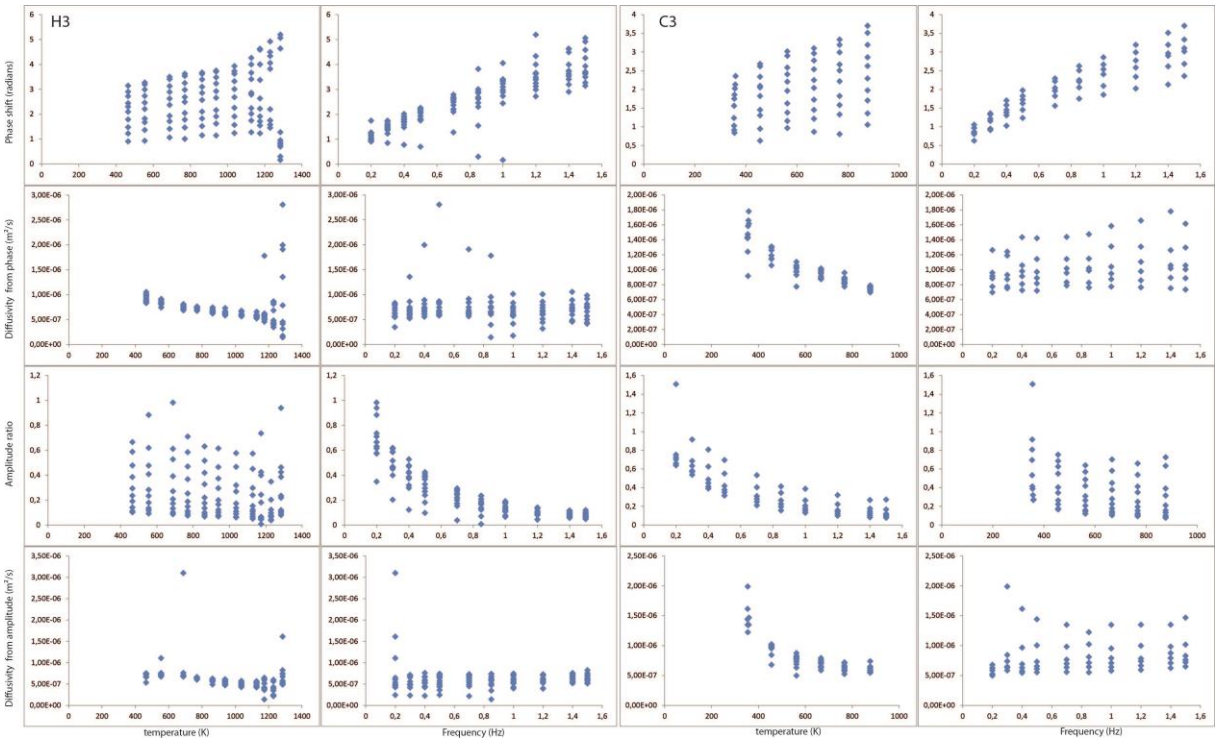

Figure D.65 M843 Experimental results for the third cycle. Phase shift (first raw), amplitude ratio (third raw) and inferred diffusivities (second and fourth raw respectively), are represented as function of temperature and frequency.

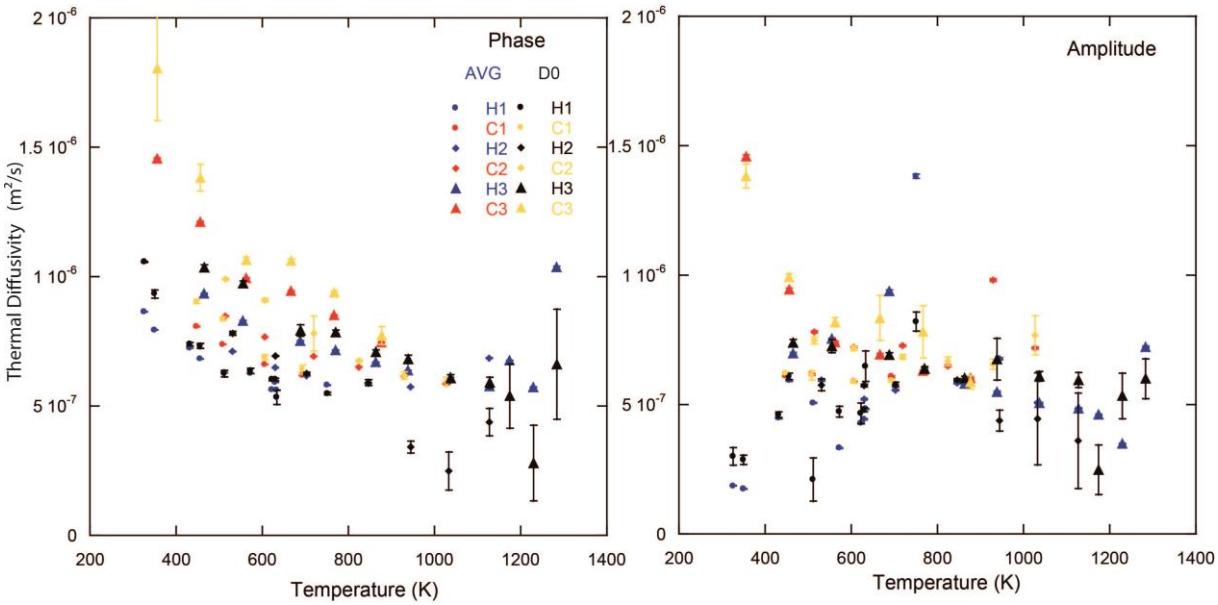

Figure D.66 M843 Thermal diffusivities obtained after fitting (D_0) and average (AVG) methods on diffusivities obtained at different frequencies at a fixed temperature. Phase and amplitude thermal diffusivity estimations are given in left and right panels respectively.

M844

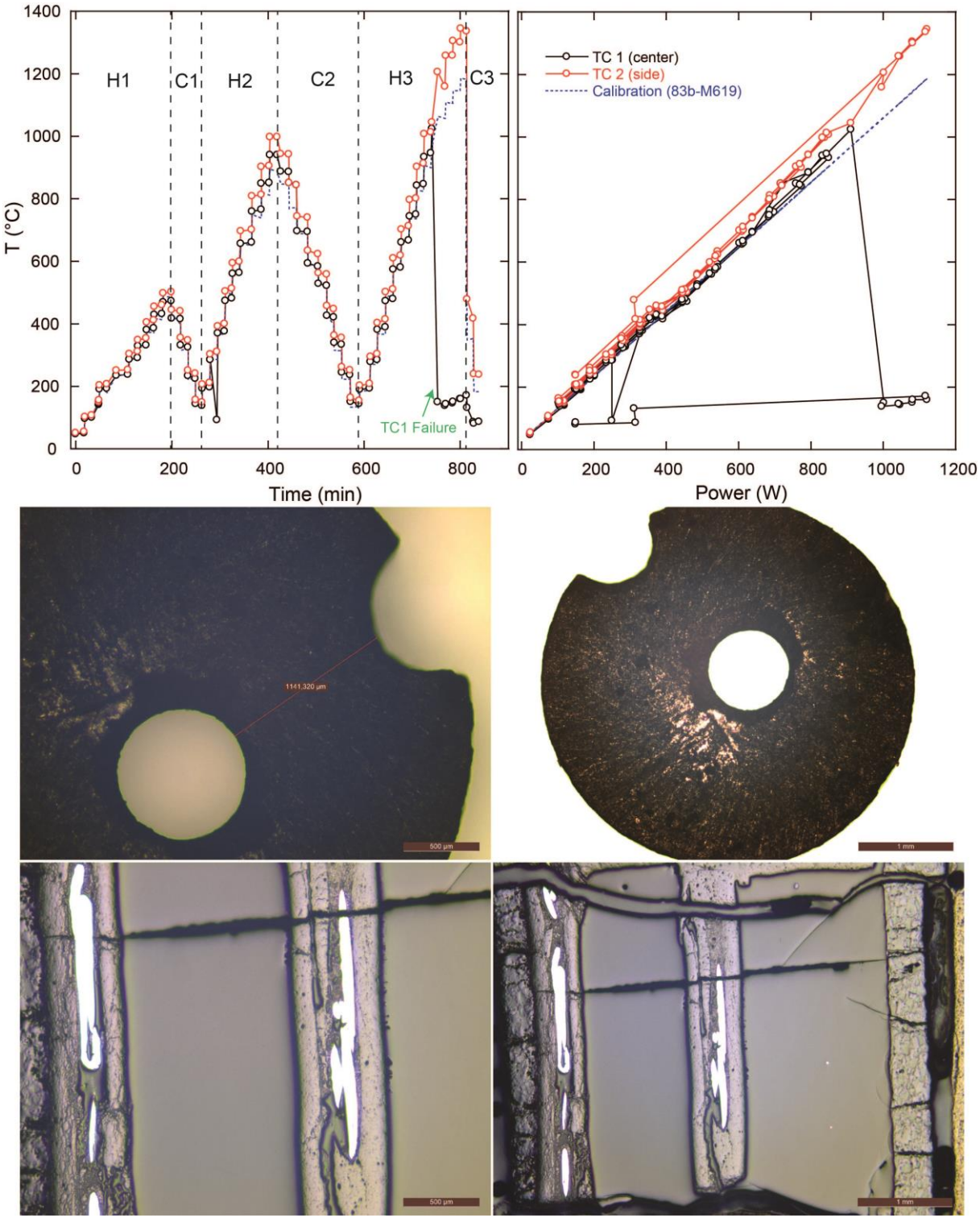

Figure D.67 M844 experimental procedure with temperature history with time and power/temperature calibration. Microphotographs o starting material and recovered sample cut perpendicular (left) and parallel (right) to sample cylinder axis are provided.

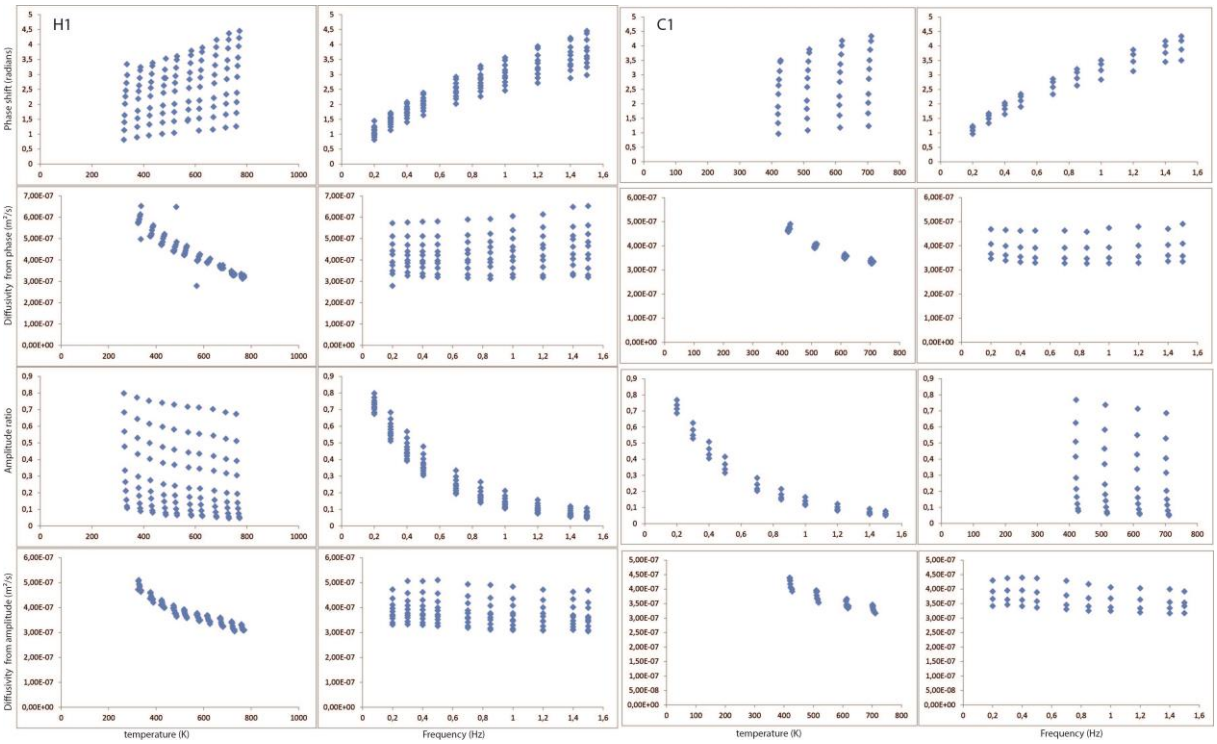

Figure D.68 M844 Experimental results for the first cycle. Phase shift (first raw), amplitude ratio (third raw) and inferred diffusivities (second and fourth raw respectively), are represented as function of temperature and frequency.

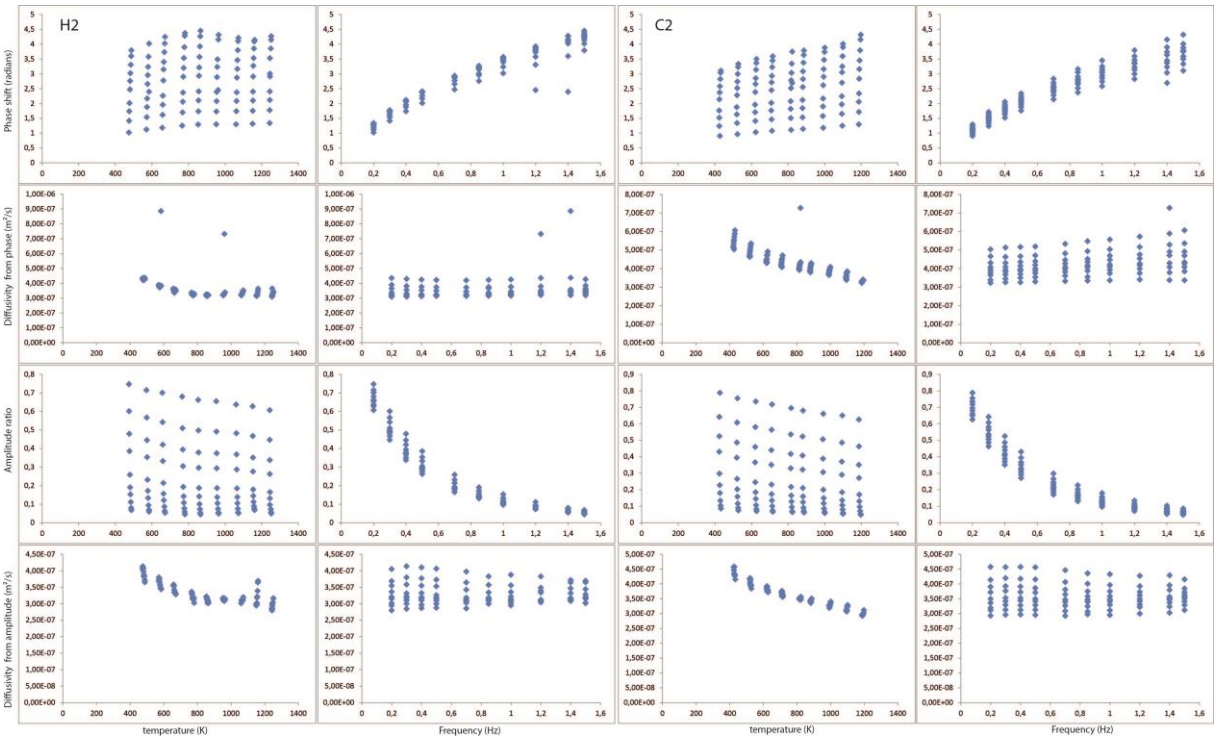

Figure D.68M844 Experimental results for the second cycle. Phase shift (first raw), amplitude ratio (third raw) and inferred diffusivities (second and fourth raw respectively), are represented as function of temperature and frequency.

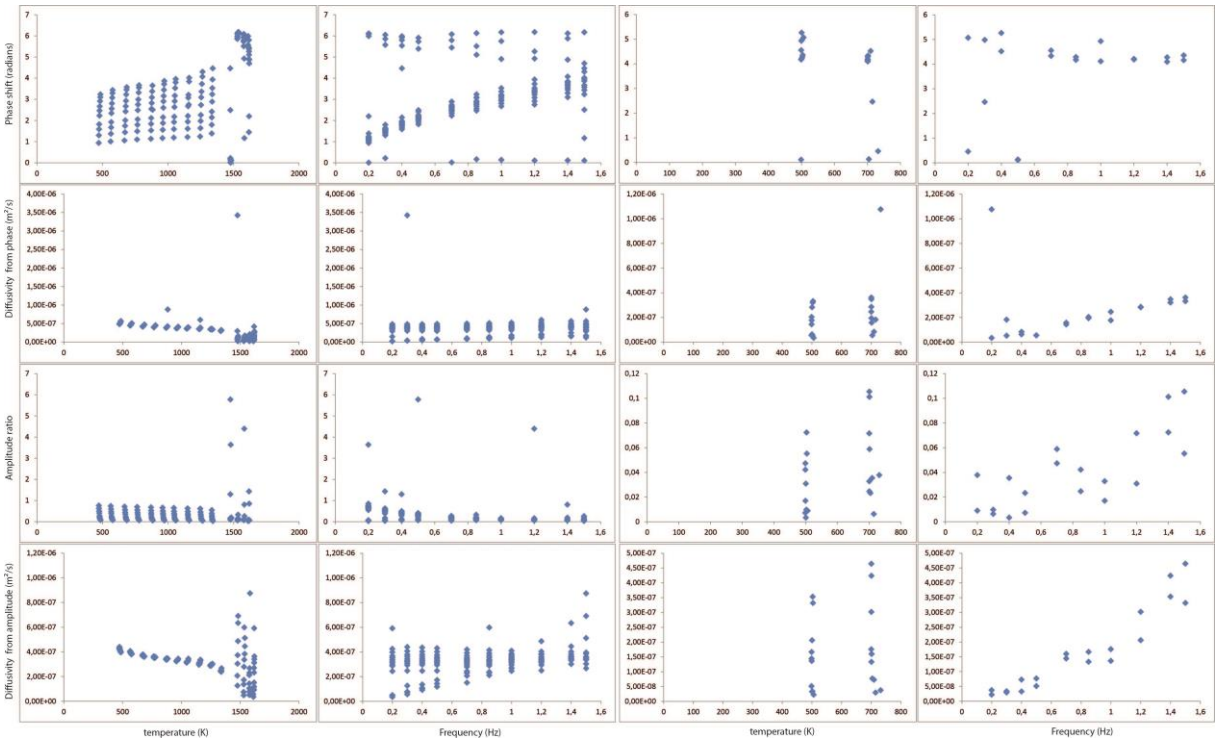

Figure D.69 M844 Experimental results for the third cycle. Phase shift (first raw), amplitude ratio (third raw) and inferred diffusivities (second and fourth raw respectively), are represented as function of temperature and frequency.

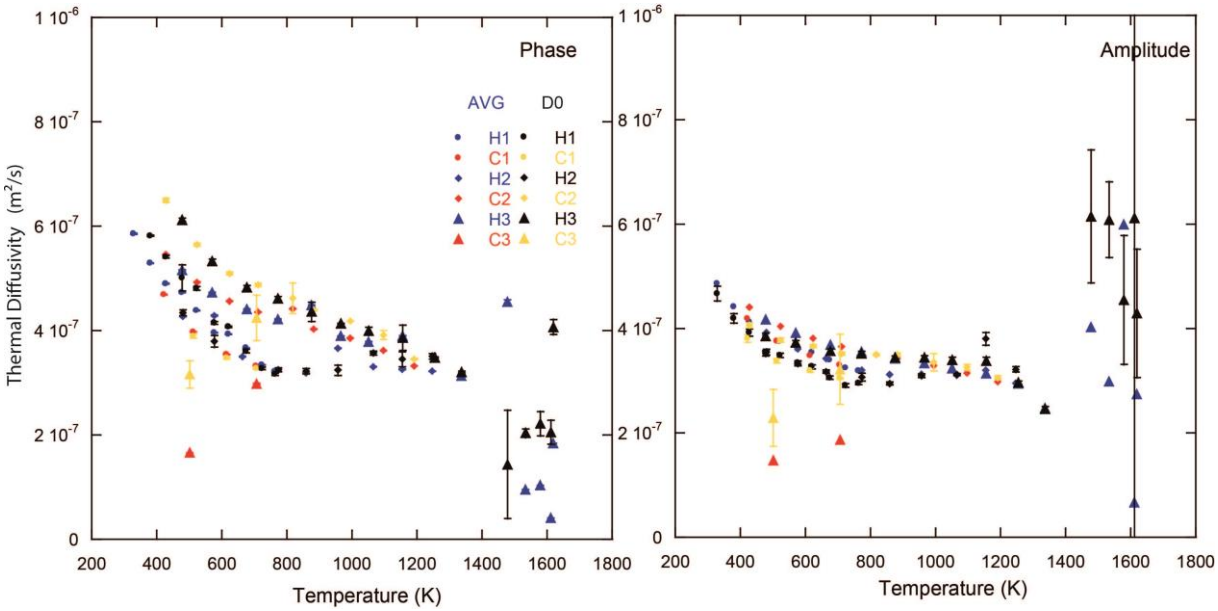

Figure D.70 M844 Thermal diffusivities obtained after fitting (D_0) and average (AVG) methods on diffusivities obtained at different frequencies at a fixed temperature. Phase and amplitude thermal diffusivity estimations are given in left and right panels respectively.

M846

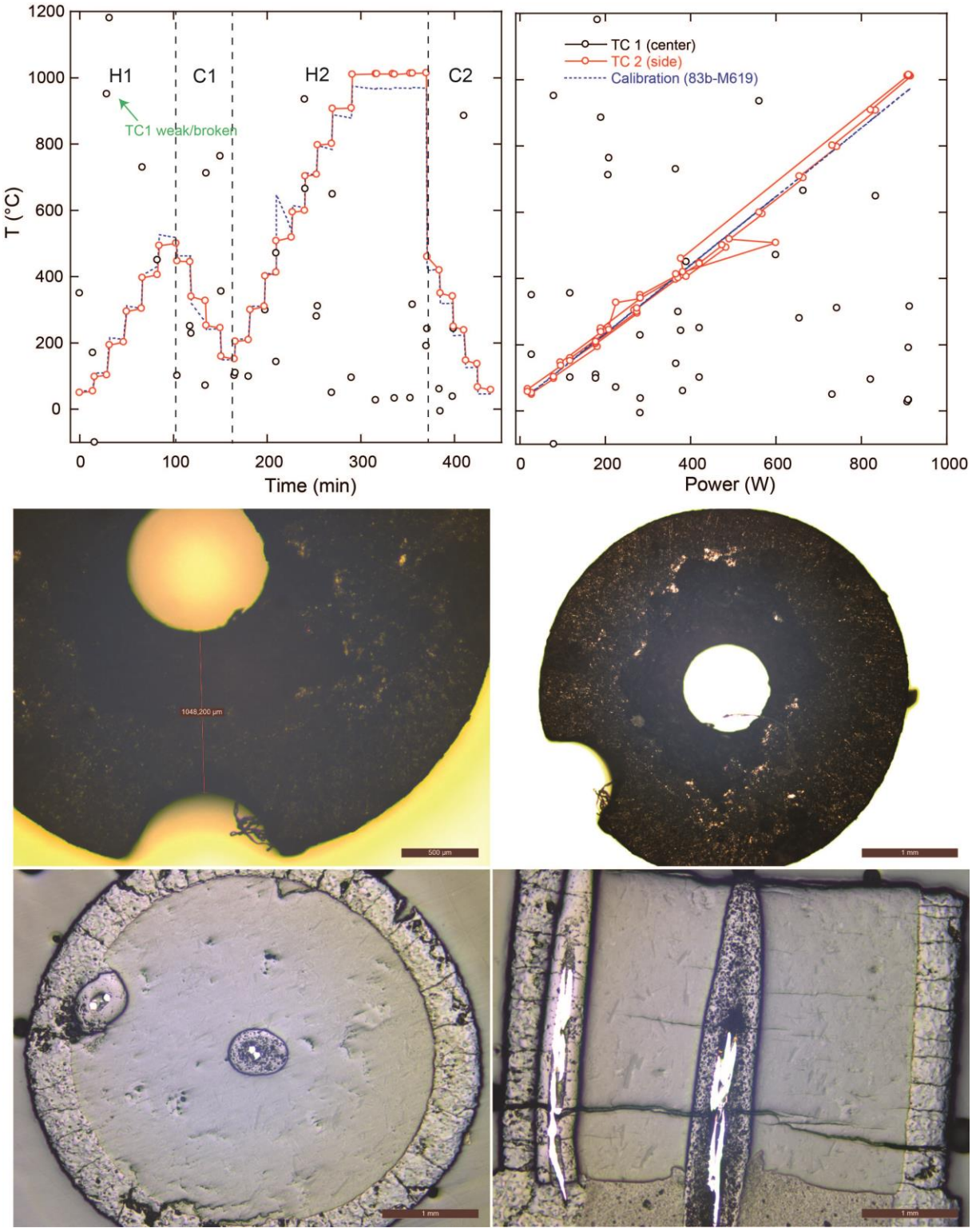

Figure D.71 M846 experimental procedure with temperature history with time and power/temperature calibration. Microphotographs o starting material and recovered sample cut perpendicular (left) and parallel (right) to sample cylinder axis are provided.

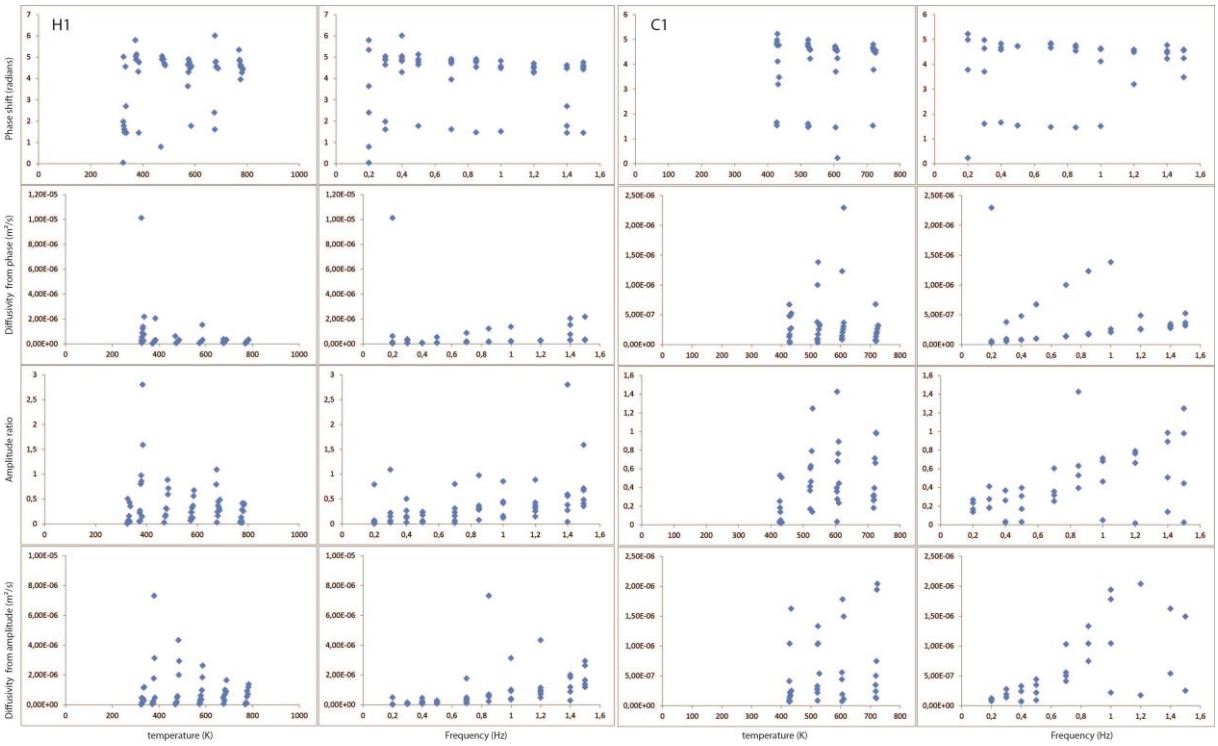

Figure D.72 M846 Experimental results for the first cycle. Phase shift (first raw), amplitude ratio (third raw) and inferred diffusivities (second and fourth raw respectively), are represented as function of temperature and frequency.

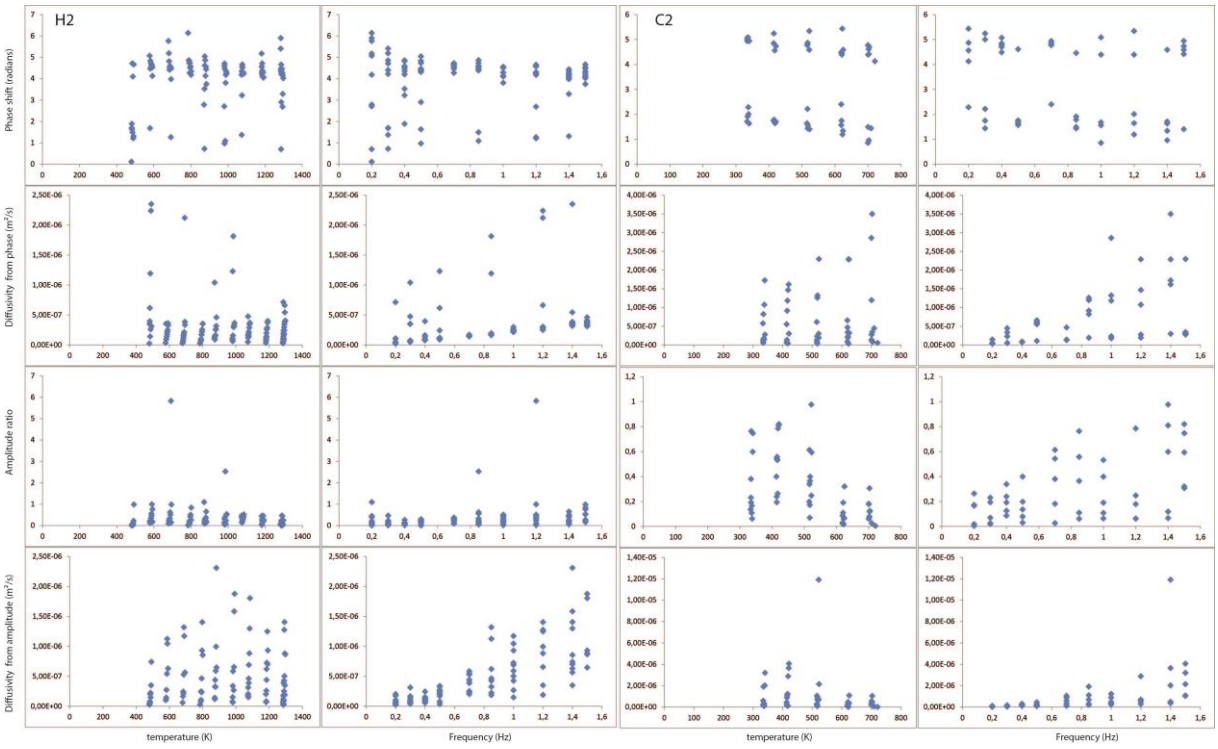

Figure D.73 M846 Experimental results for the second cycle. Phase shift (first raw), amplitude ratio (third raw) and inferred diffusivities (second and fourth raw respectively), are represented as function of temperature and frequency.

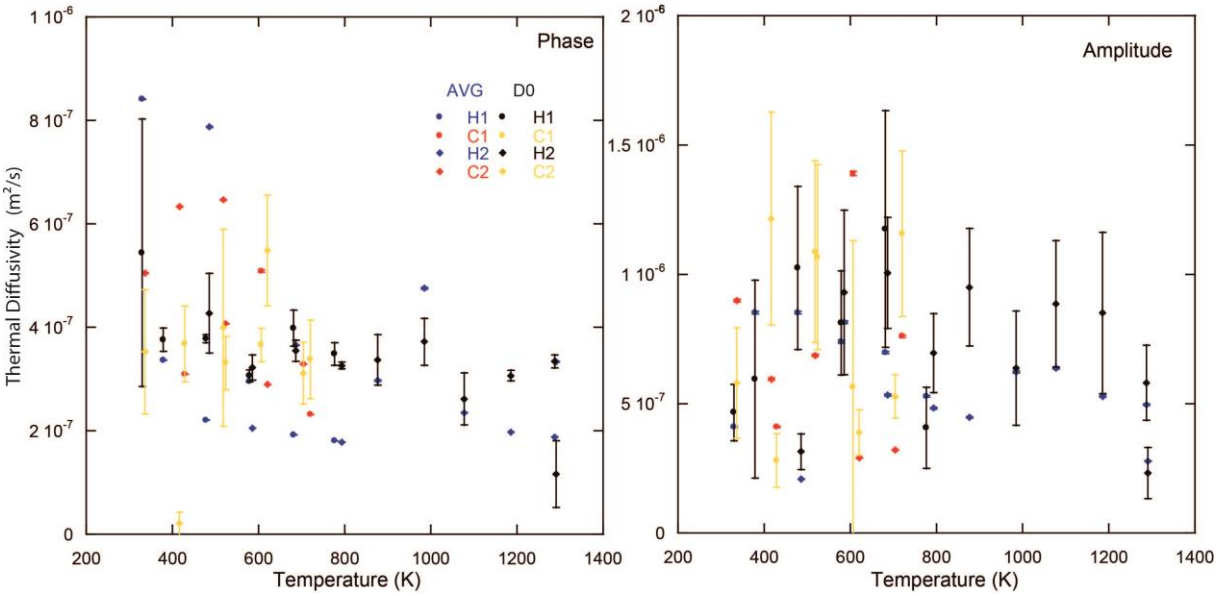

Figure D.74 M846 Thermal diffusivities obtained after fitting (D_0) and average (AVG) methods on diffusivities obtained at different frequencies at a fixed temperature. Phase and amplitude thermal diffusivity estimations are given in left and right panels respectively.

M847

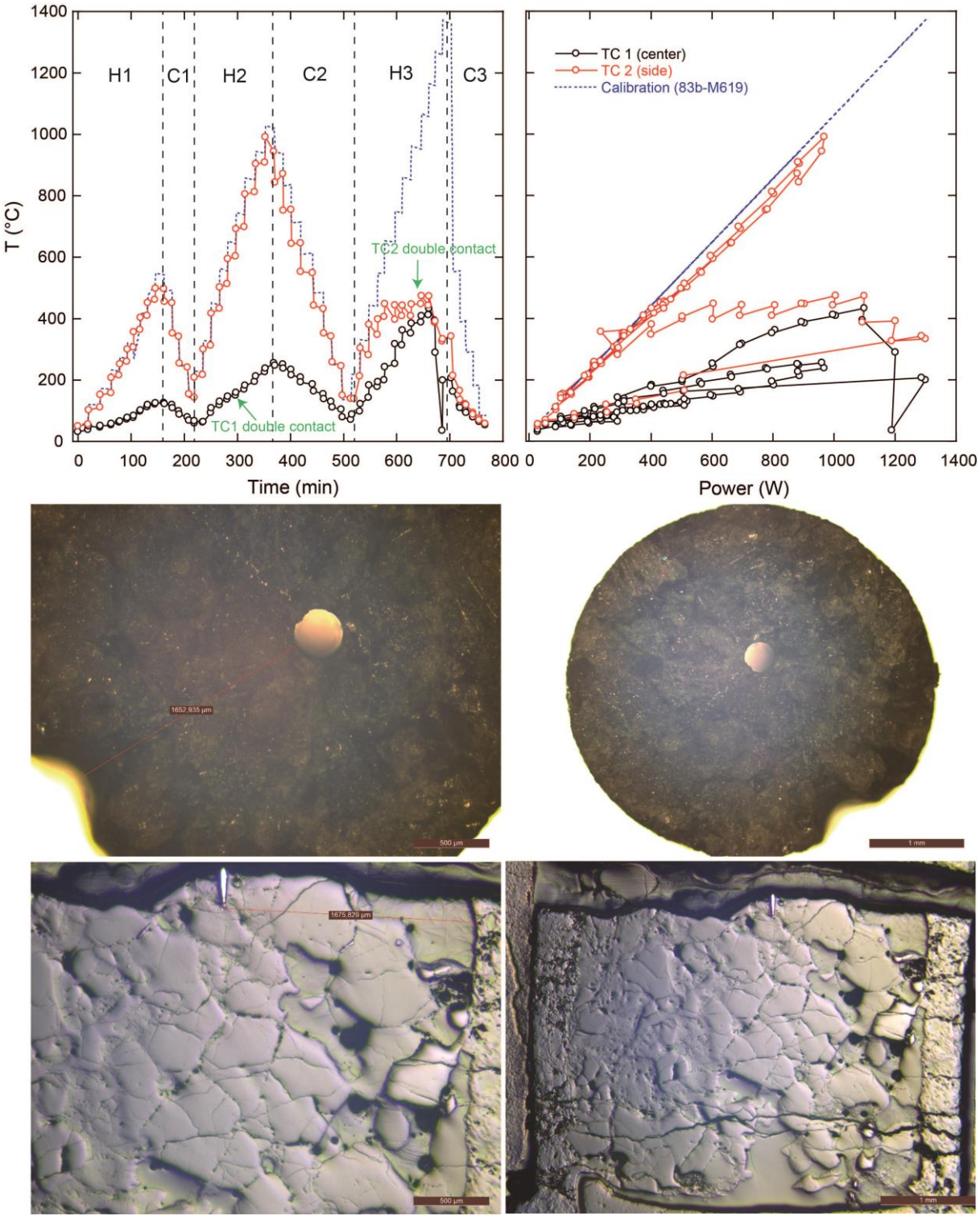

Figure D.75 M847 experimental procedure with temperature history with time and power/temperature calibration. Microphotographs o starting material and recovered sample cut perpendicular (left) and parallel (right) to sample cylinder axis are provided.

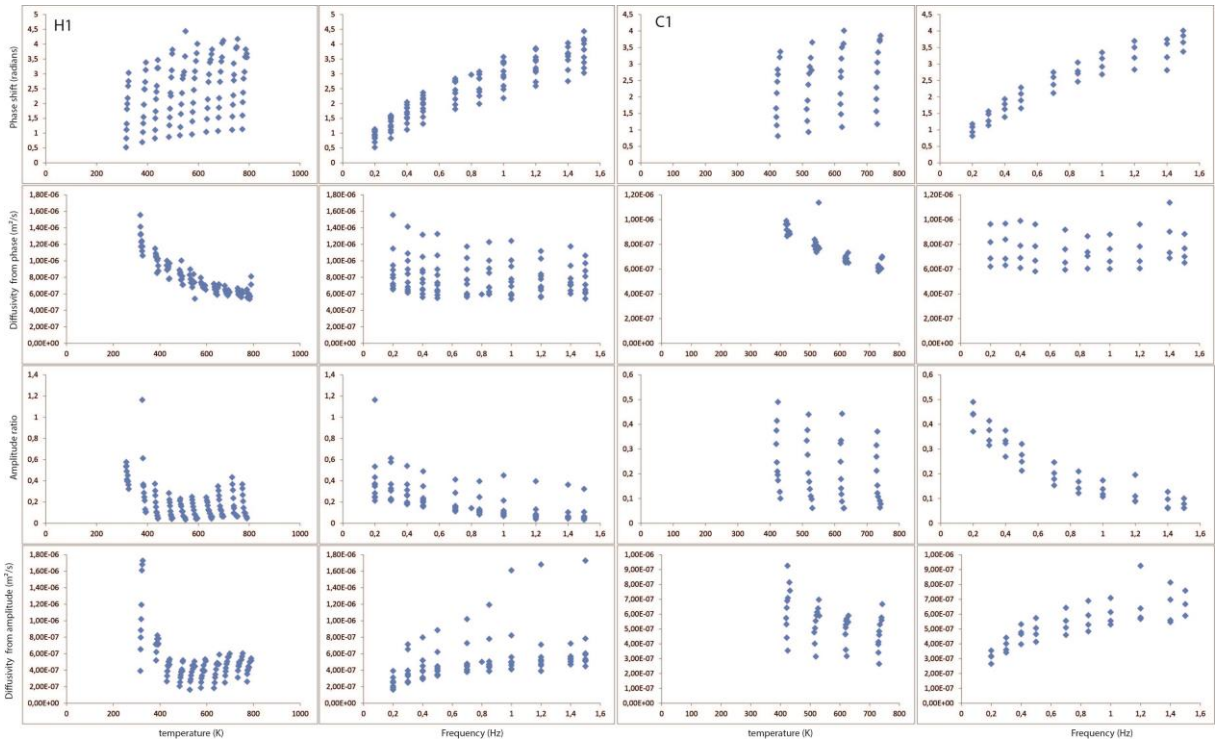

Figure D.76 M847 Experimental results for the first cycle. Phase shift (first raw), amplitude ratio (third raw) and inferred diffusivities (second and fourth raw respectively), are represented as function of temperature and frequency.

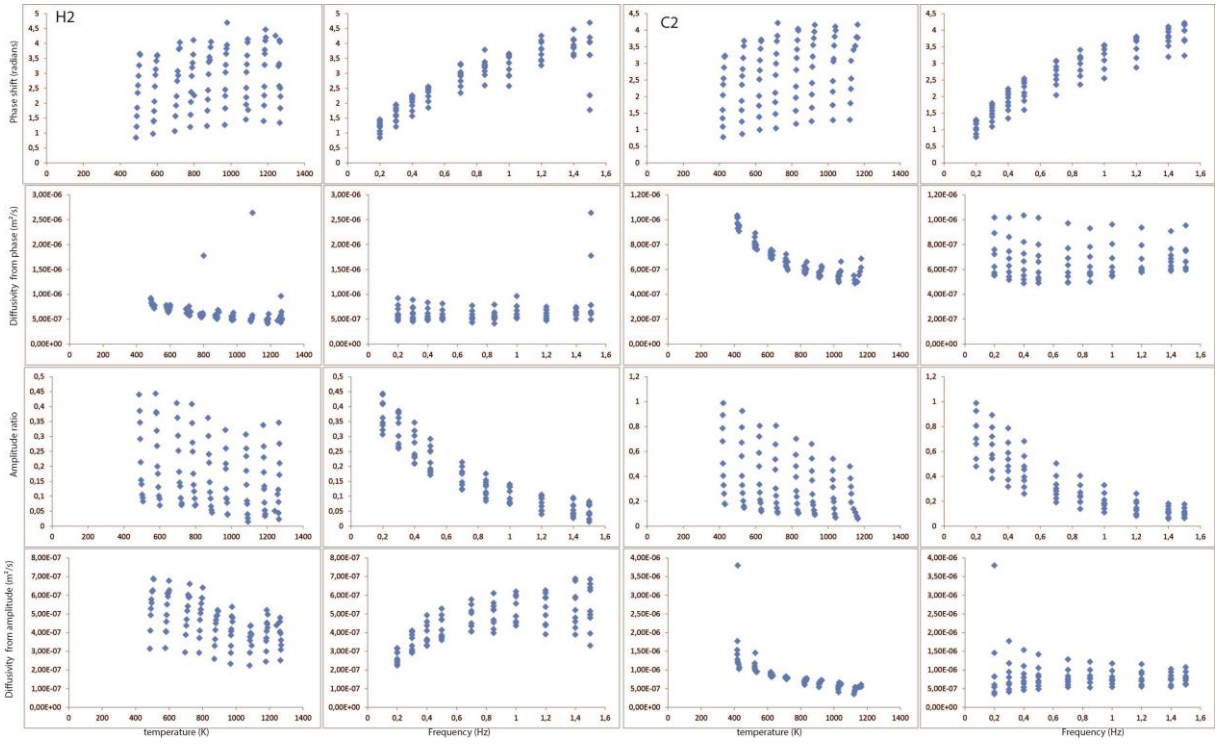

Figure D.77 M847 Experimental results for the second cycle. Phase shift (first raw), amplitude ratio (third raw) and inferred diffusivities (second and fourth raw respectively), are represented as function of temperature and frequency.

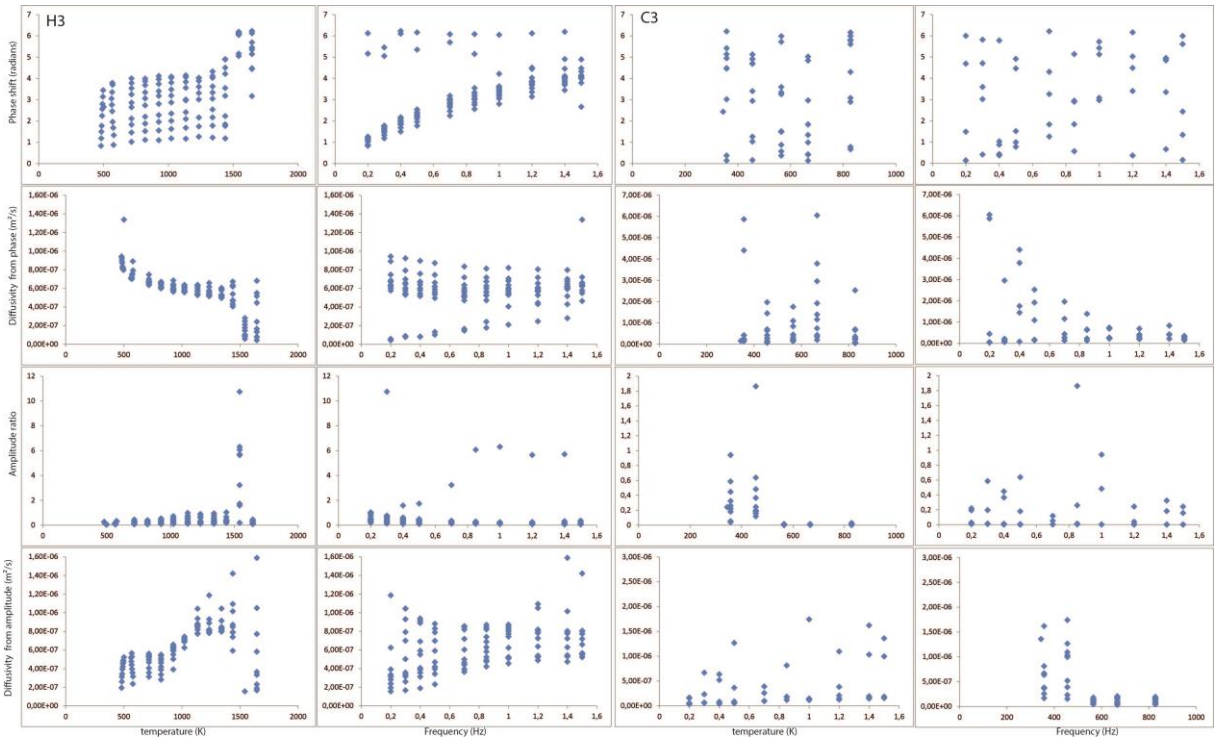

Figure D.78 M847 Experimental results for the third cycle. Phase shift (first raw), amplitude ratio (third raw) and inferred diffusivities (second and fourth raw respectively), are represented as function of temperature and frequency.

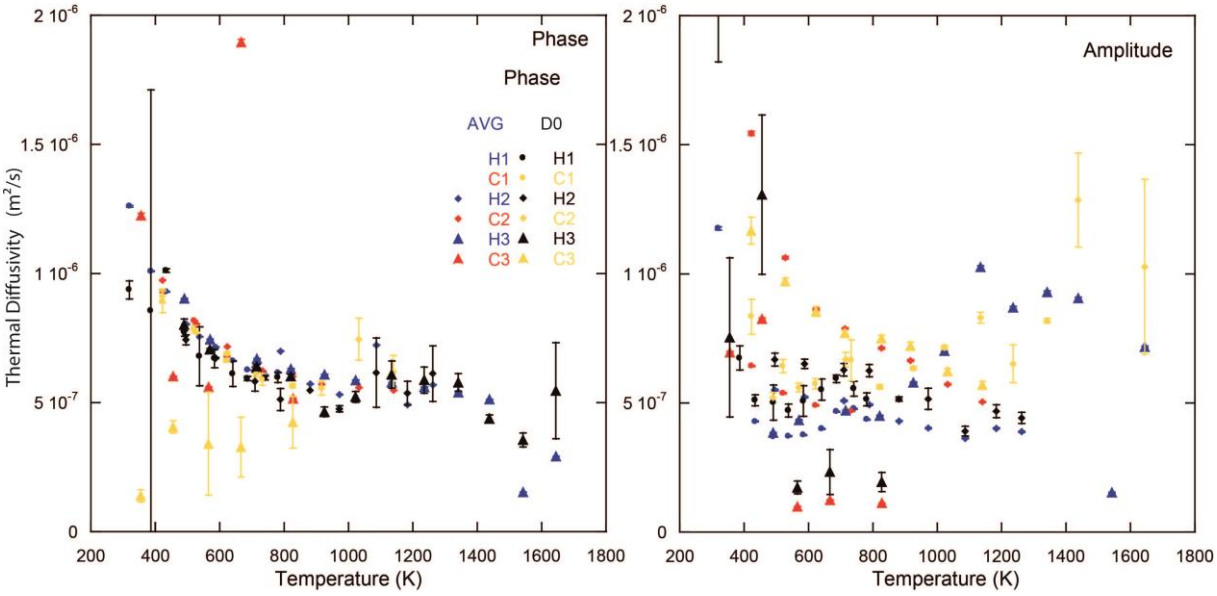

Figure D.79 M847 Thermal diffusivities obtained after fitting (D_0) and average (AVG) methods on diffusivities obtained at different frequencies at a fixed temperature. Phase and amplitude thermal diffusivity estimations are given in left and right panels respectively.

M848

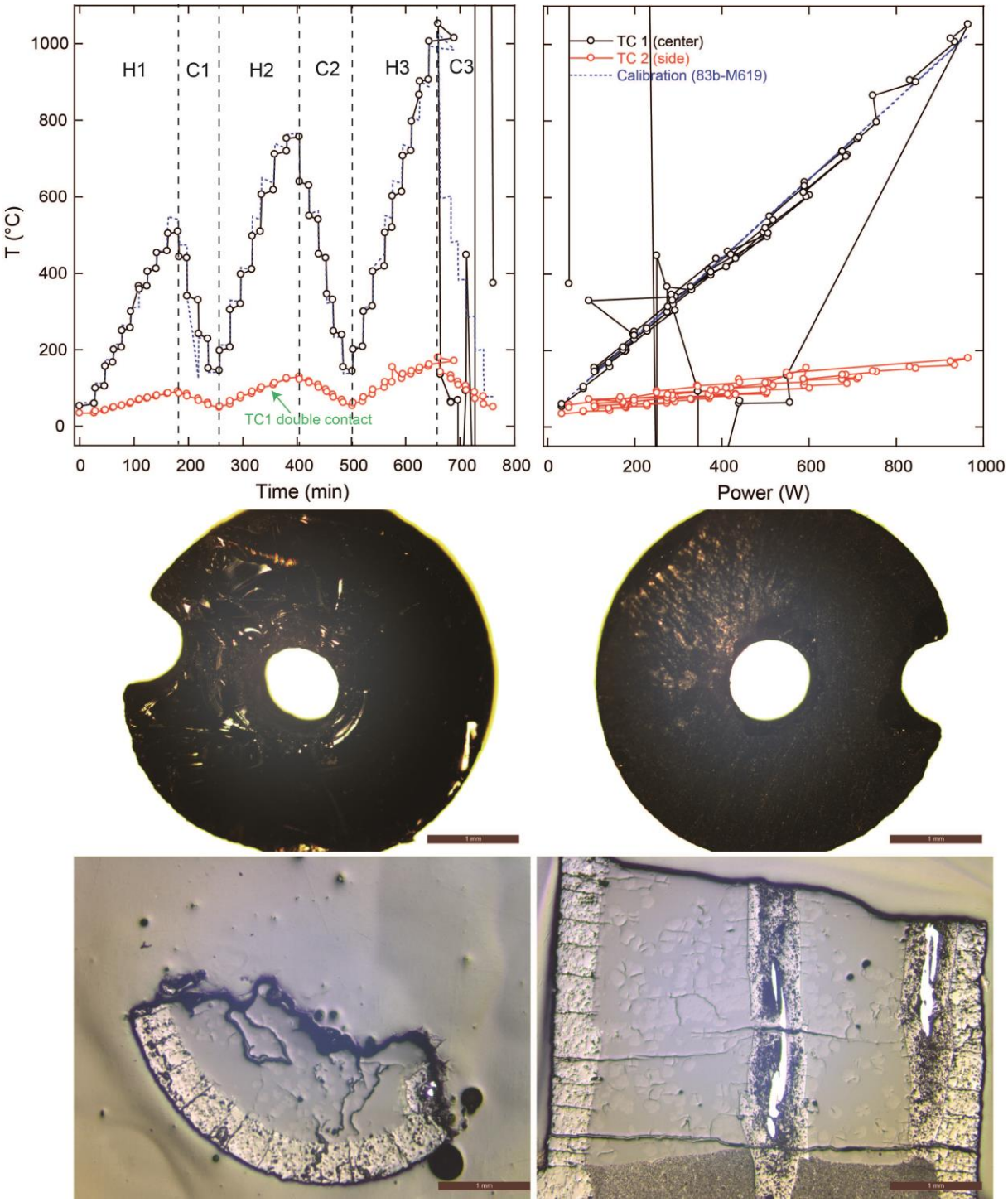

Figure D.80 M848 experimental procedure with temperature history with time and power/temperature calibration. Microphotographs o starting material and recovered sample cut perpendicular (left) and parallel (right) to sample cylinder axis are provided.

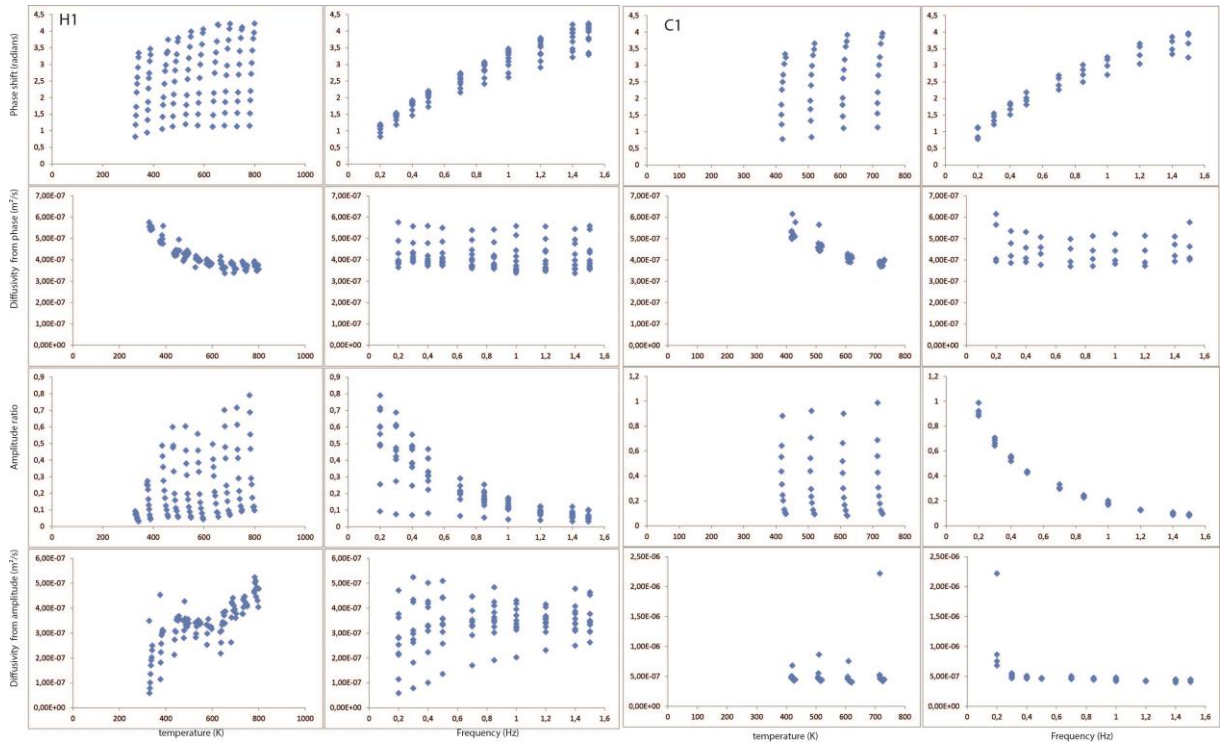

Figure D.81 M848 Experimental results for the first cycle. Phase shift (first raw), amplitude ratio (third raw) and inferred diffusivities (second and fourth raw respectively), are represented as function of temperature and frequency.

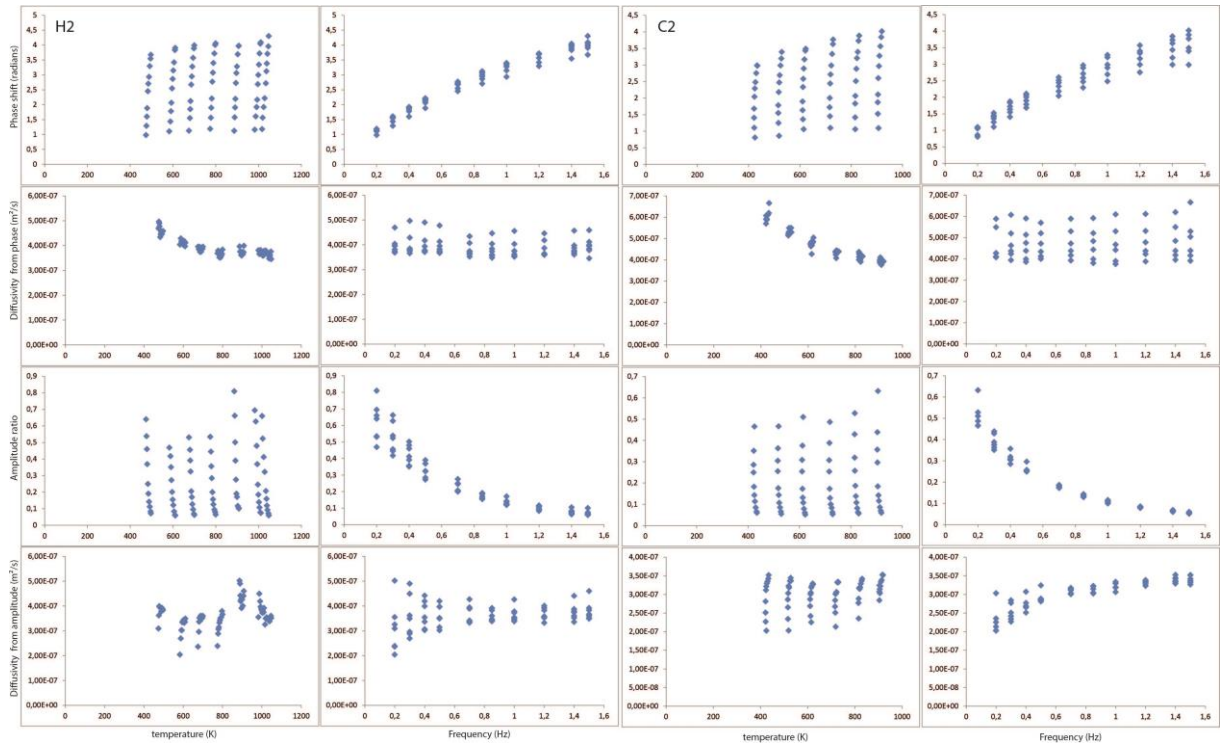

Figure D.82 M848 Experimental results for the second cycle. Phase shift (first raw), amplitude ratio (third raw) and inferred diffusivities (second and fourth raw respectively), are represented as function of temperature and frequency.

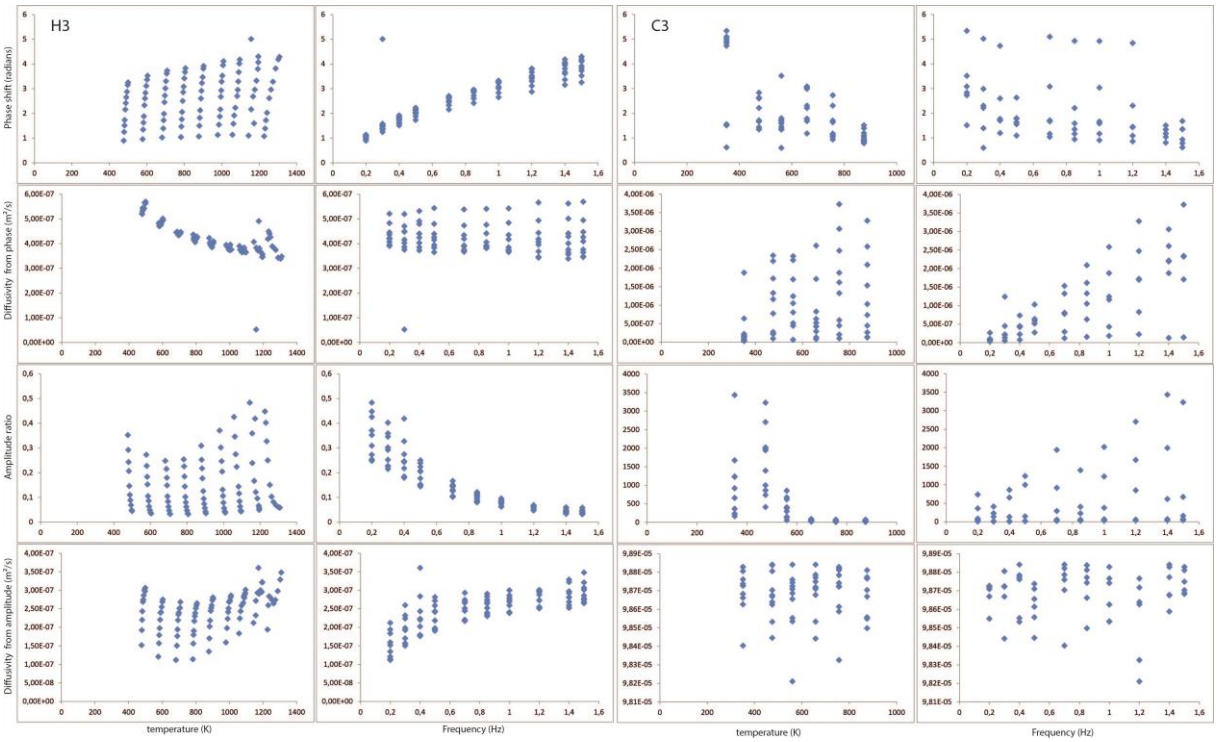

Figure D.83 M848 Experimental results for the third cycle. Phase shift (first raw), amplitude ratio (third raw) and inferred diffusivities (second and fourth raw respectively), are represented as function of temperature and frequency.

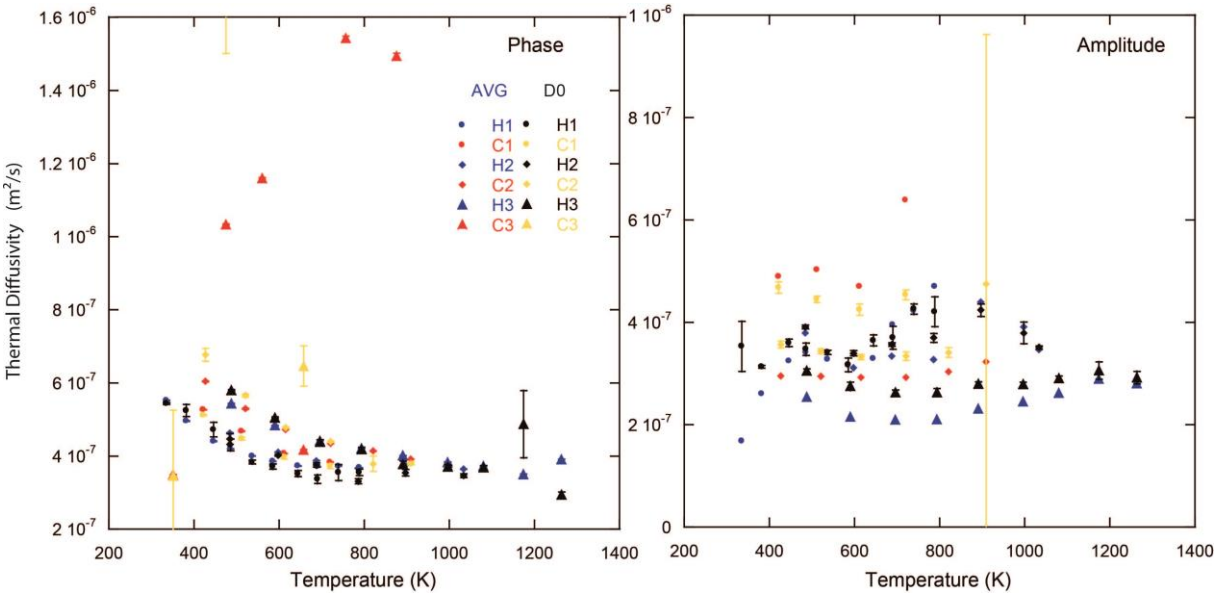

Figure D.84 M848 Thermal diffusivities obtained after fitting (D_0) and average (AVG) methods on diffusivities obtained at different frequencies at a fixed temperature. Phase and amplitude thermal diffusivity estimations are given in left and right panels respectively.

M850

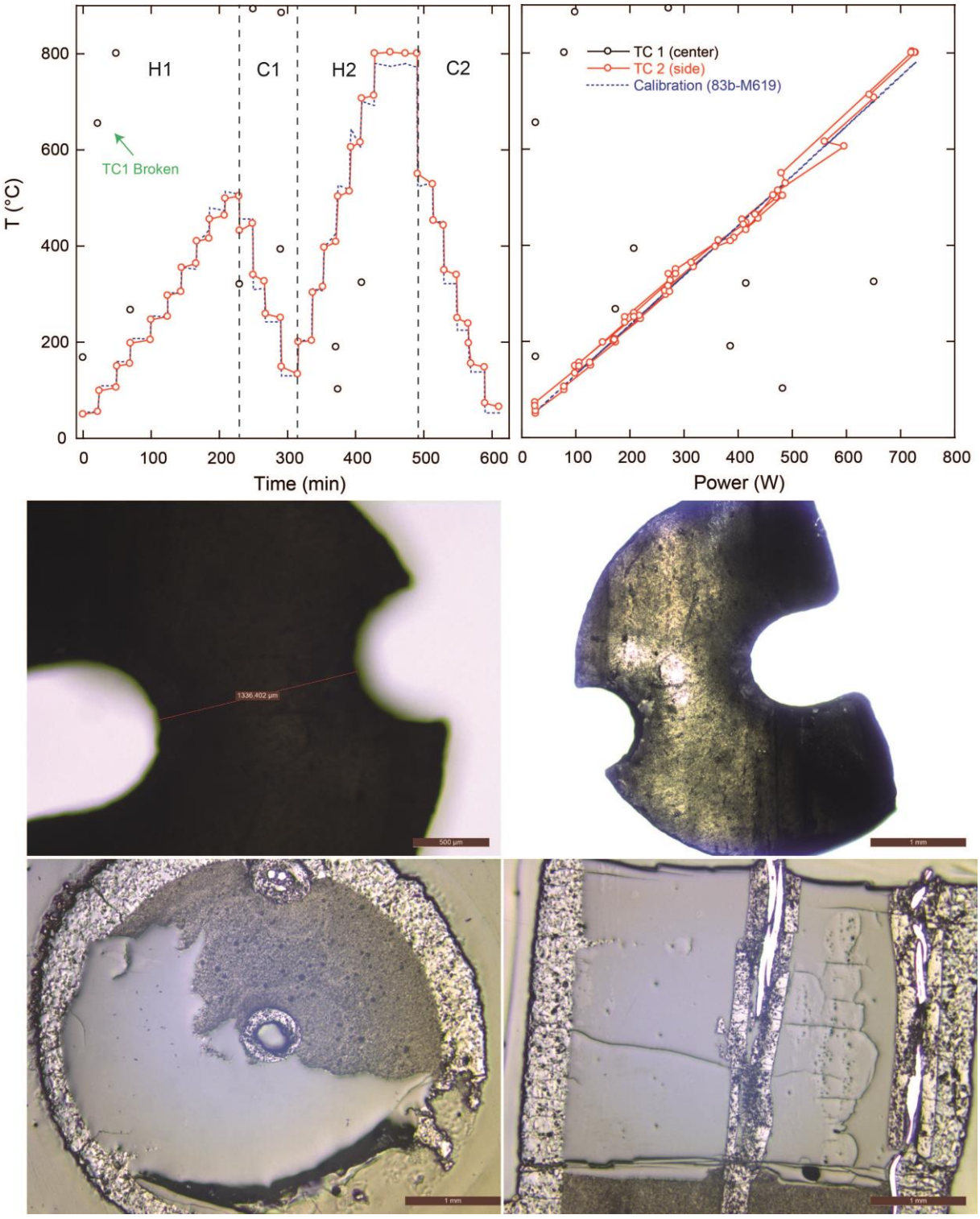

Figure D.85 M850 experimental procedure with temperature history with time and power/temperature calibration. Microphotographs o starting material and recovered sample cut perpendicular (left) and parallel (right) to sample cylinder axis are provided.

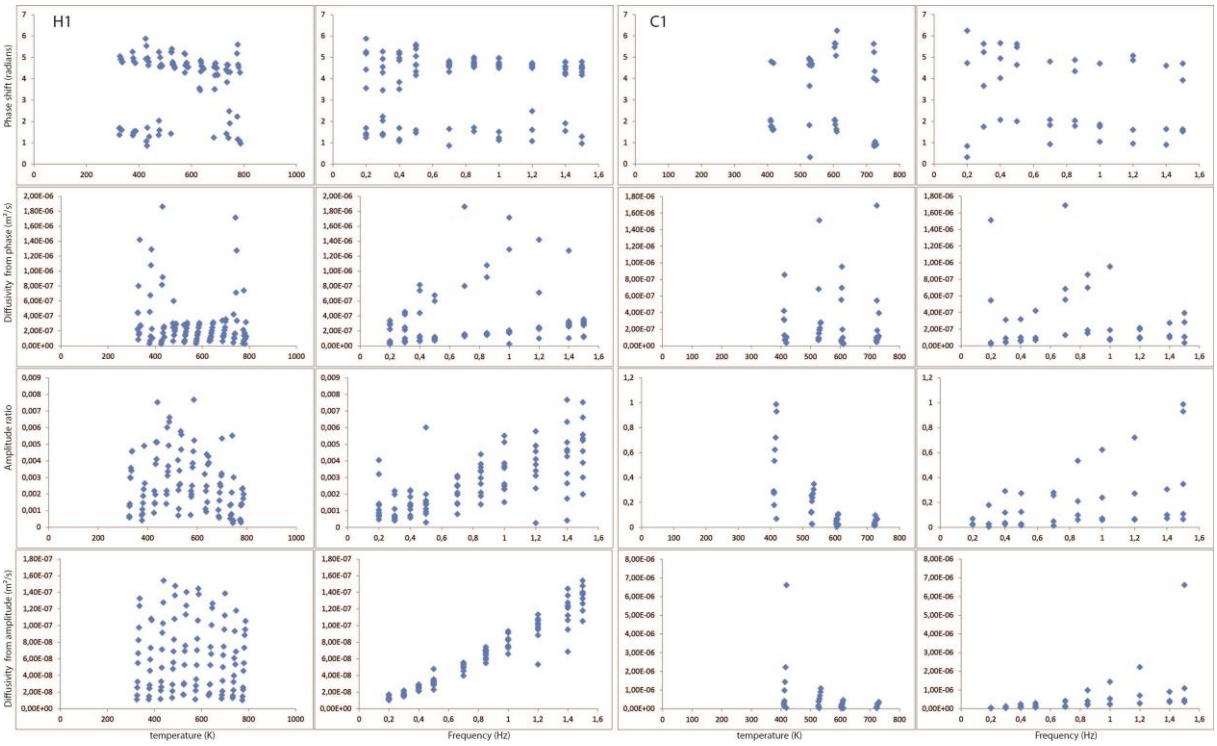

Figure D.86 M850 Experimental results for the first cycle. Phase shift (first raw), amplitude ratio (third raw) and inferred diffusivities (second and fourth raw respectively), are represented as function of temperature and frequency.

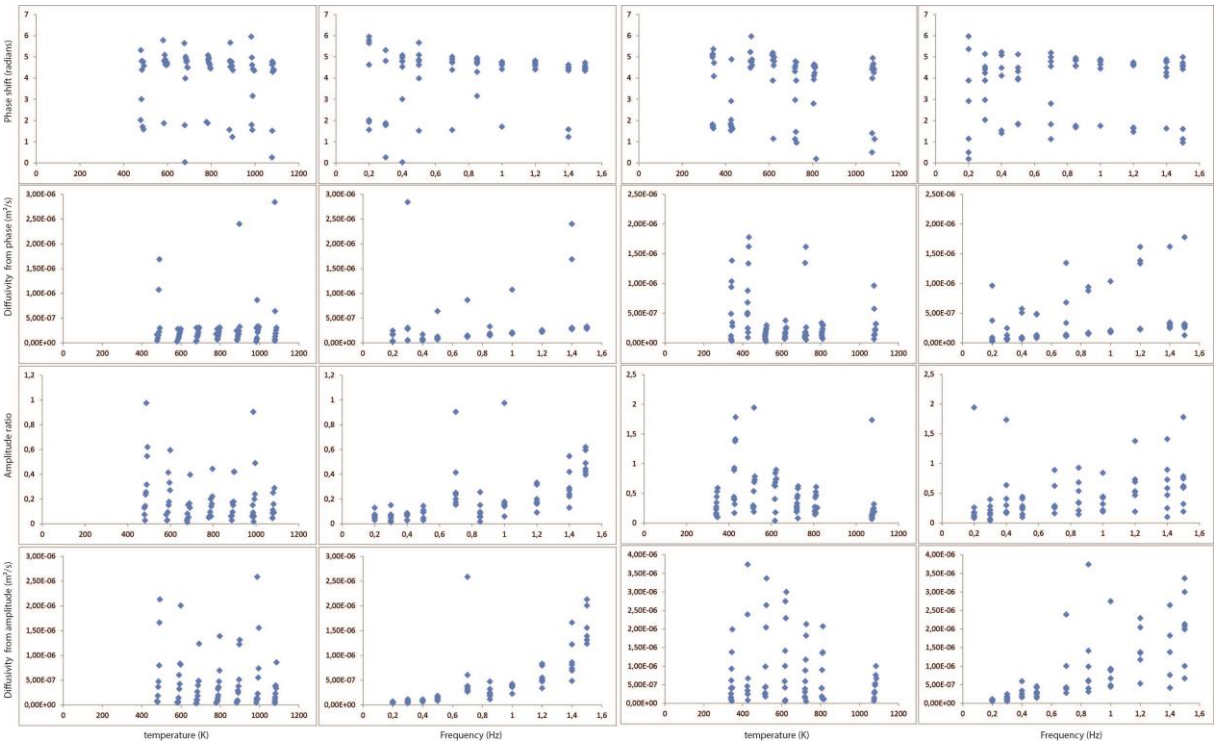

Figure D.87 M850 Experimental results for the second cycle. Phase shift (first raw), amplitude ratio (third raw) and inferred diffusivities (second and fourth raw respectively), are represented as function of temperature and frequency.

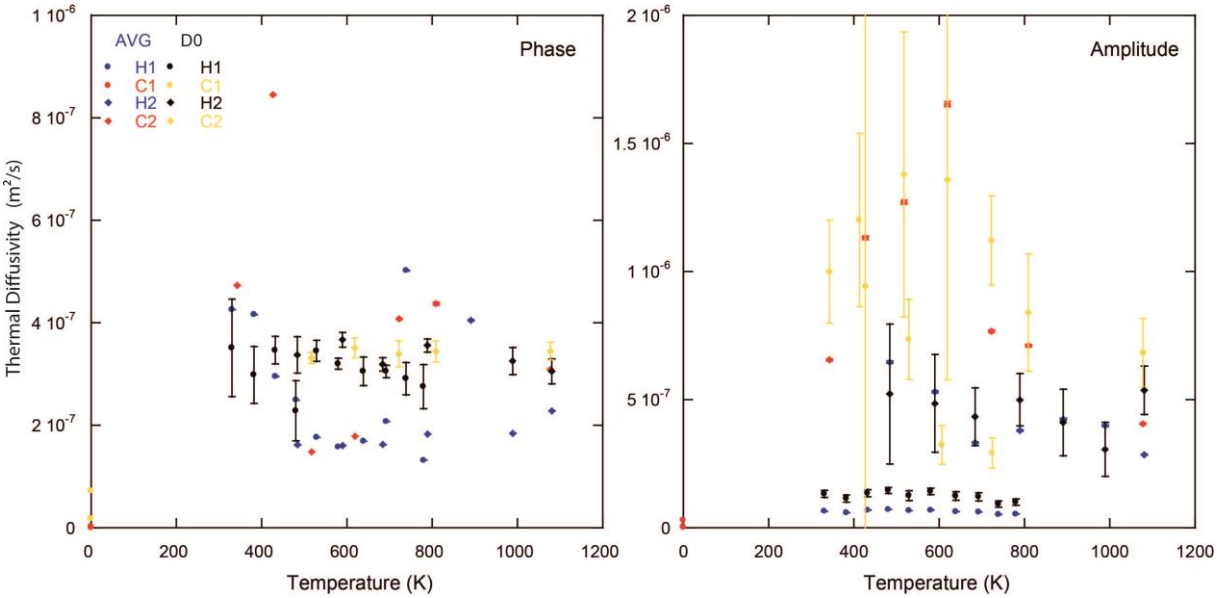

Figure D.88 M850 Thermal diffusivities obtained after fitting (D_0) and average (AVG) methods on diffusivities obtained at different frequencies at a fixed temperature. Phase and amplitude thermal diffusivity estimations are given in left and right panels respectively.

M851

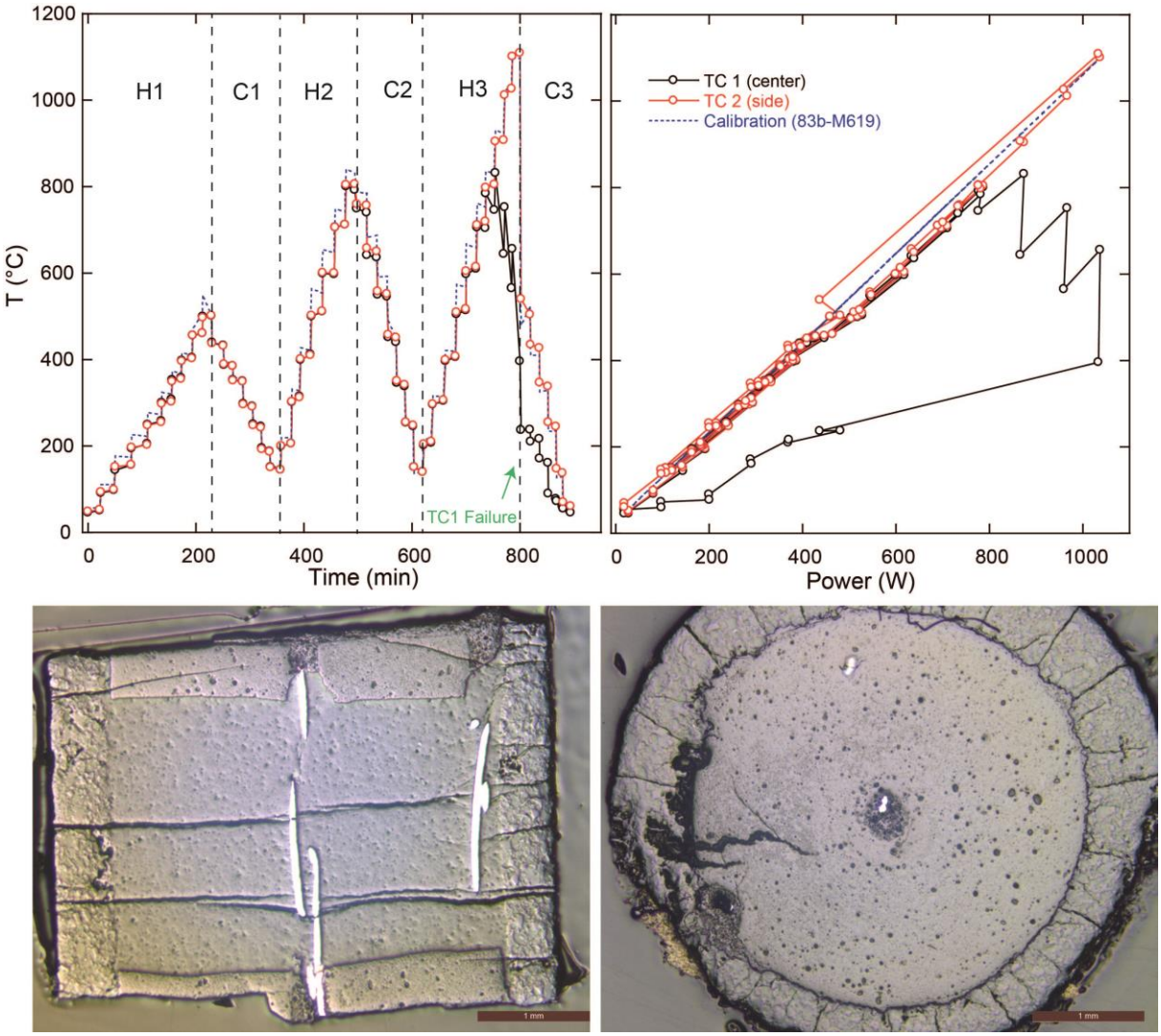

Figure D.89 M851 experimental procedure with temperature history with time and power/temperature calibration. Microphotographs o starting material and recovered sample cut perpendicular (left) and parallel (right) to sample cylinder axis are provided.

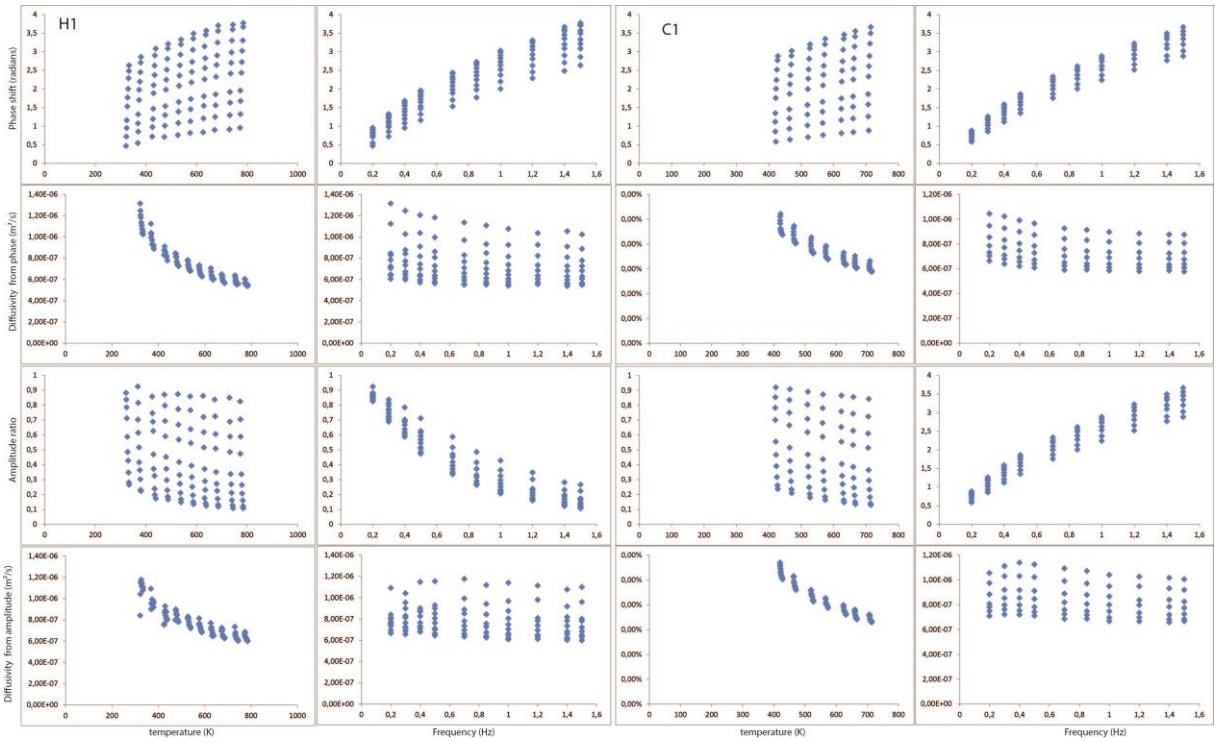

Figure D.90 M851 Experimental results for the first cycle. Phase shift (first raw), amplitude ratio (third raw) and inferred diffusivities (second and fourth raw respectively), are represented as function of temperature and frequency.

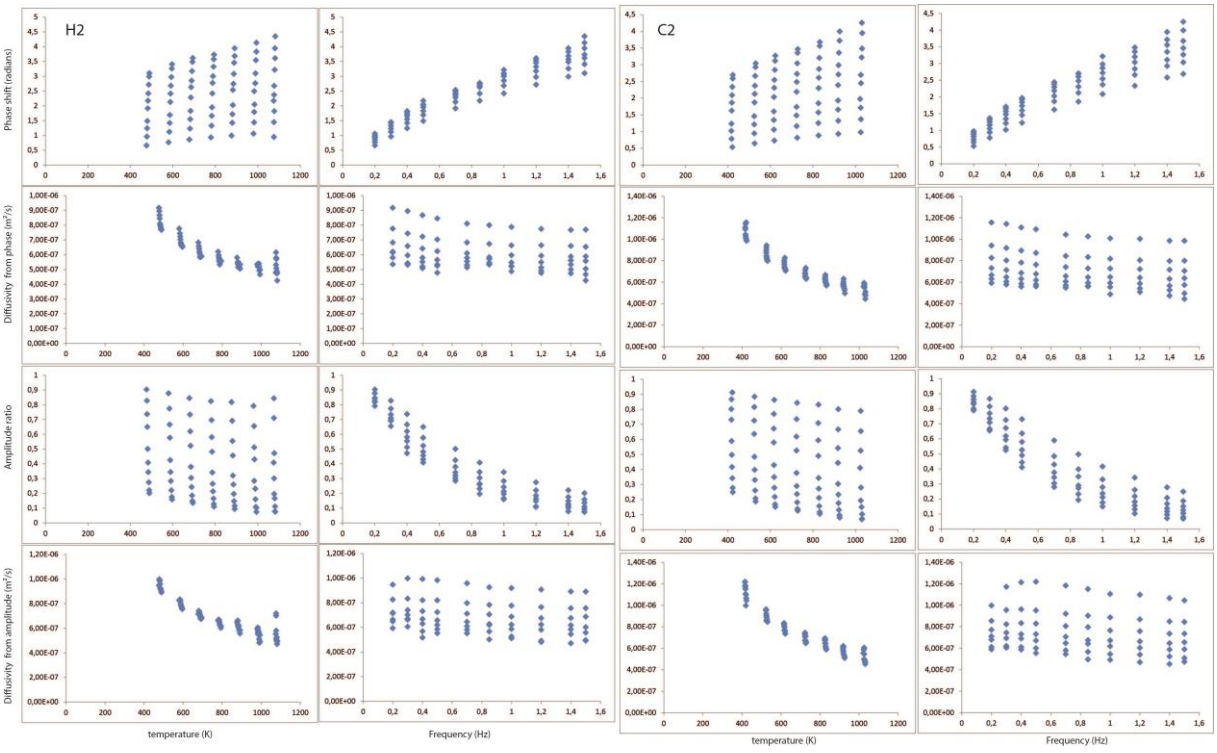

Figure D.91 M851 Experimental results for the second cycle. Phase shift (first raw), amplitude ratio (third raw) and inferred diffusivities (second and fourth raw respectively), are represented as function of temperature and frequency.

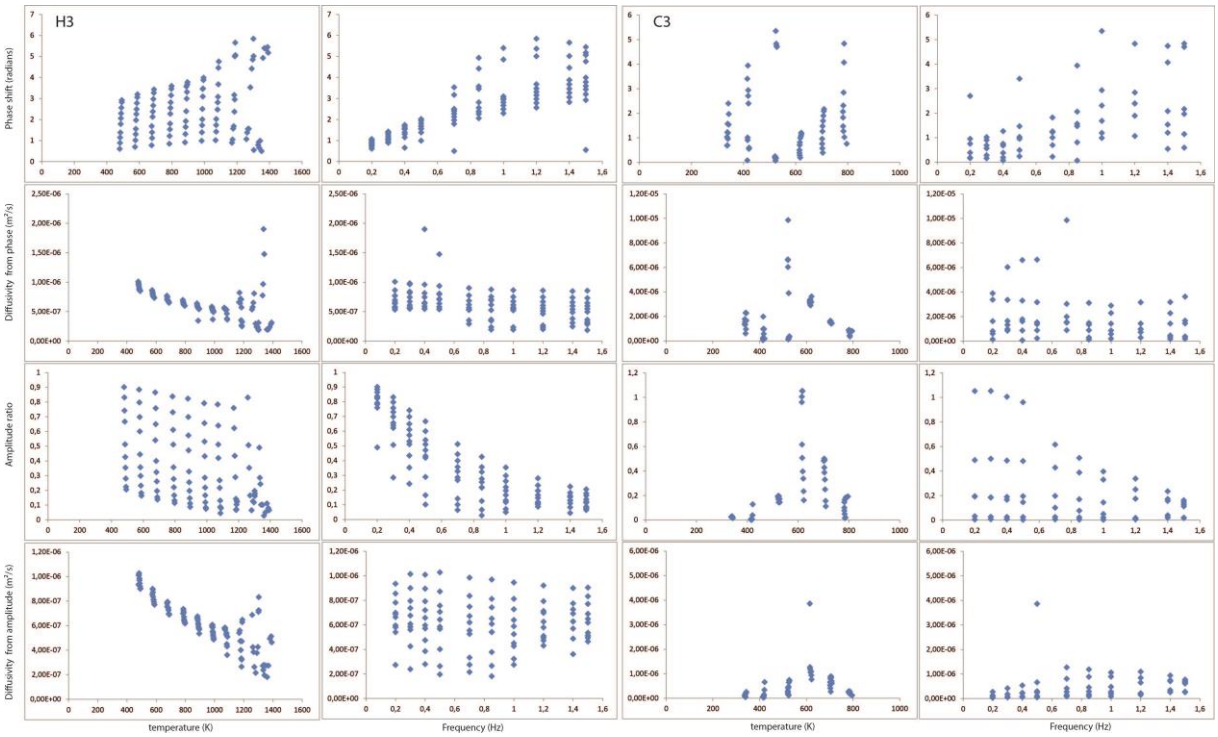

Figure D.92 M851 Experimental results for the third cycle. Phase shift (first raw), amplitude ratio (third raw) and inferred diffusivities (second and fourth raw respectively), are represented as function of temperature and frequency.

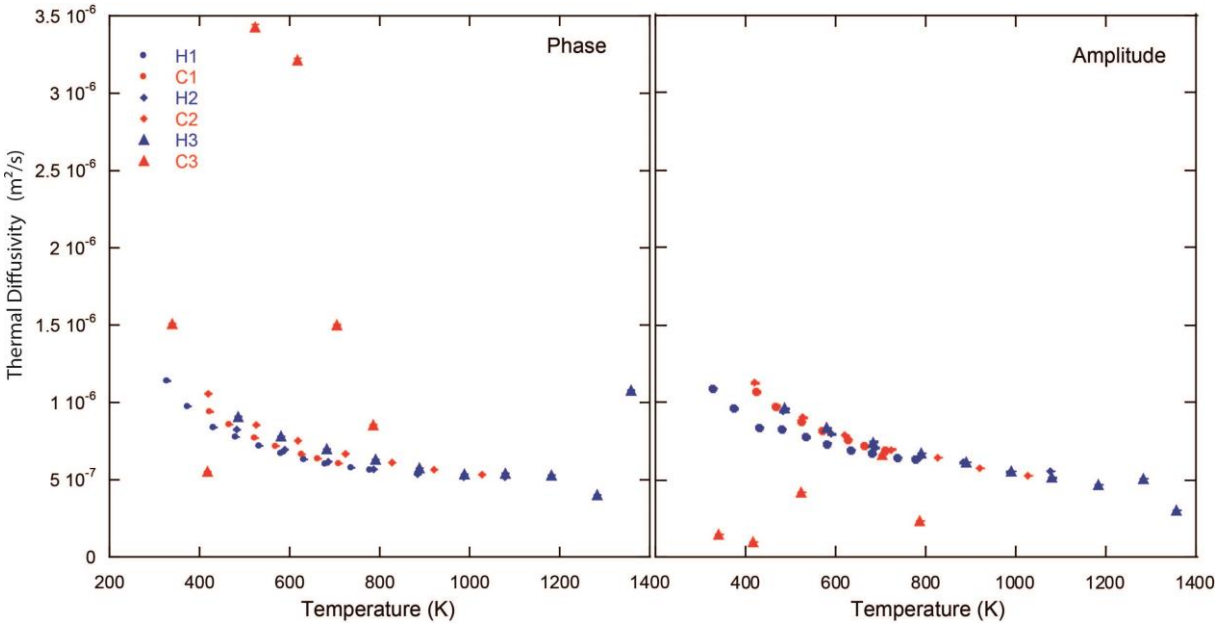

Figure D.93 M850 Thermal diffusivities obtained after average (AVG) method (D_0 values are represented in chapter VI) on diffusivities obtained at different frequencies at a fixed temperature. Phase and amplitude thermal diffusivity estimations are given in left and right panels respectively.

Appendix E

Optical thickness estimation for radiative and ballistic heat transfers

Appendix E: Optical thickness estimation for radiative and ballistic heat transfers

Optical conditions are a major point to consider before the interpretation of the experimental thermal diffusivity data. In fact, numerous arguments to reject given techniques or measurements have been based on the low optical thickness of the studied samples. In optically thin conditions, the photons are partially/not interacting with the sample and so inferred thermal conductivity is underestimated. The degree of underestimation is however unknown when optical conditions are unconstrained. Such argument has already been formulated against multi-anvil characterization because the used samples must be small. For these reasons, we consider this aspect in this appendix and try to provide an estimation of the optical thickness for our samples characterized in thermal diffusivity experiments. These calculations were performed on olivine and can be adapted to other phases if absorption spectra are provided.

We used absorption spectra from InfraRed spectroscopy measurements by Shankland et al. (1979). These spectra measured parallel to olivine *a* and *c* axis were digitalized for the different available temperatures. Digitalized spectra were inserted in Matlab® and fitted with the upgraded type of cubic fit PCHIP function (Piecewise Cubic Hermite Interpolating Polynomial). This function allows having a numerical function of the recorded spectra that cover the entire wavelength range.

The effect of temperature for each kind of spectrum (// to *a* or *c*), was assumed using linear evolution form RT spectrum to 1400°C. The calculated spectrum use affine relation ($y = ax+b$) with RT and 1400°C spectra. The assumption of linear evolution with temperature was tested against measurements of Shankland et al. (1979). Spectrum calculated at 800°C was compared to digitalized measurements at the same temperature. Results were found to be comparable (see next figure E.1). Hence, using linear evolution of absorption spectra with temperature seems to be a reasonable assumption compared to the level of precision required for this estimation.

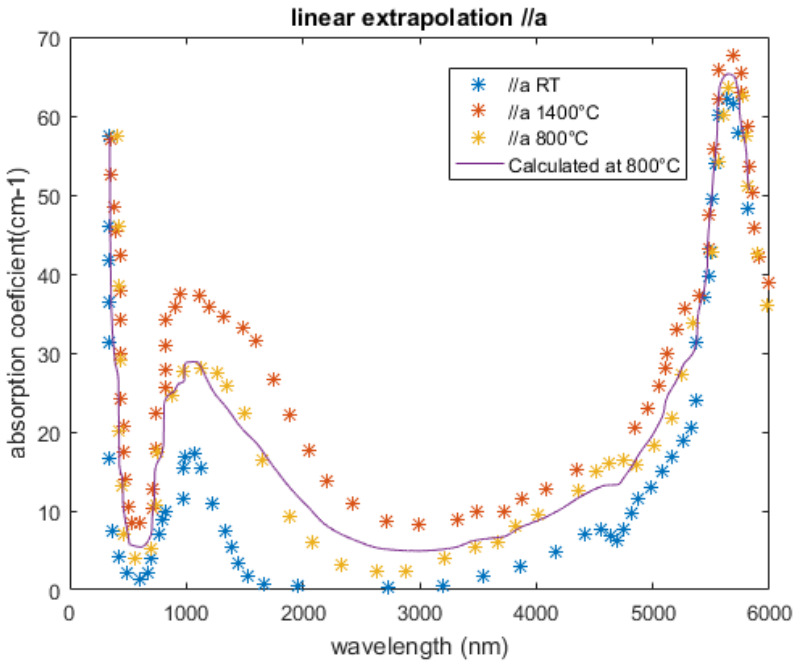

Figure E.1 Digitalized spectra //a from Shankland 1979 at RT, 800 and 1400°C: stars, and calculated spectra using linear spectra variation for 800°C (to be compare with yellow stars)

To approximate polycrystalline middle (as it should be in our experiments) absorption spectra parallel to *a* and *c* axis were averaged. This assumption can be strong in a non-hydrostatic medium but is believed to be true in multi-anvil press (see EBSD maps in appendix B and Chapter VI). Hydrostatic conditions correspond to randomly oriented grains. Thus, the average of the two perpendicular directions should provide a reasonable estimation of the real polycrystalline absorption, even if potential grain boundary effect is not evaluated.

Finally, the grain size or sample size (*d*) was inserted in calculations to provide an estimation to *A(λ)*d* product. The value of this product was argued to be crucial for optical thickness quantification. Indeed, according Hofmeister and Brandlund (2015) a sample is considered as optically thin if the product *A(λ)*d* is lower than 1. Sample is considered as optically thick if *A(λ)*d* is greater than 2 and optically opaque if the product is higher than 7.

From these values, the mode of heat transfer in the sample and equations governing it are different (Fig E.2). The values of the product are provided, in the next figures in function of temperature and sample size (Figs. E.3, 4 and 5).

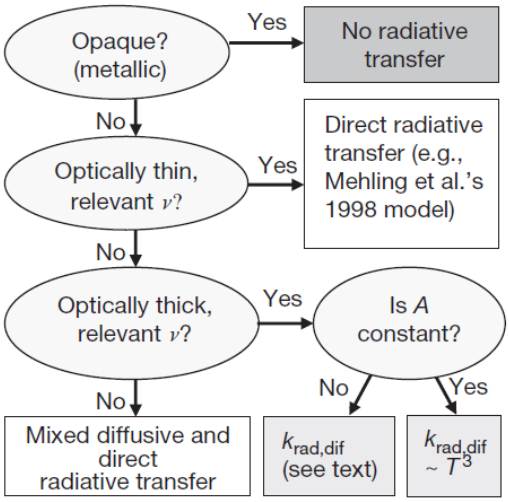

Figure 5 Flow chart for discerning whether radiative transfer is diffusive or ballistic, with links to appropriate models, discussed in the text. 'All relevant ν' refers to frequencies up to where I_{bb} is negligible at the temperature of interest.

Figure E.2 Chart of heat transfer type according optical thickness, from treatise of geophysics Hofmeister and Brandlund (2015).

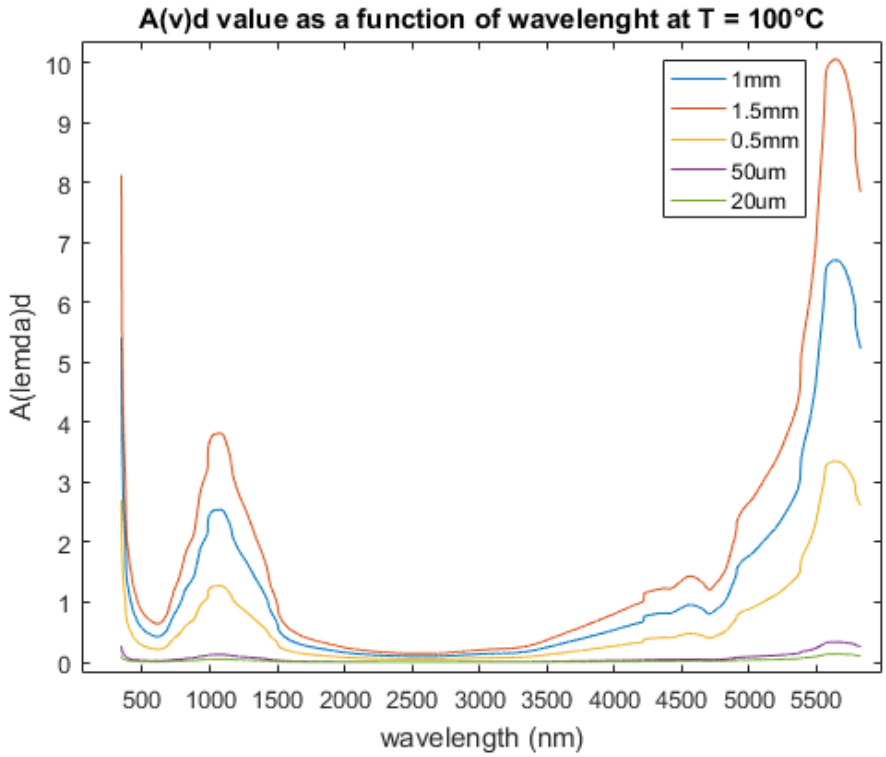

Figure E.3Calculated absorption spectra for olivine at 100°C (averaged orientation) and various olivine sizes

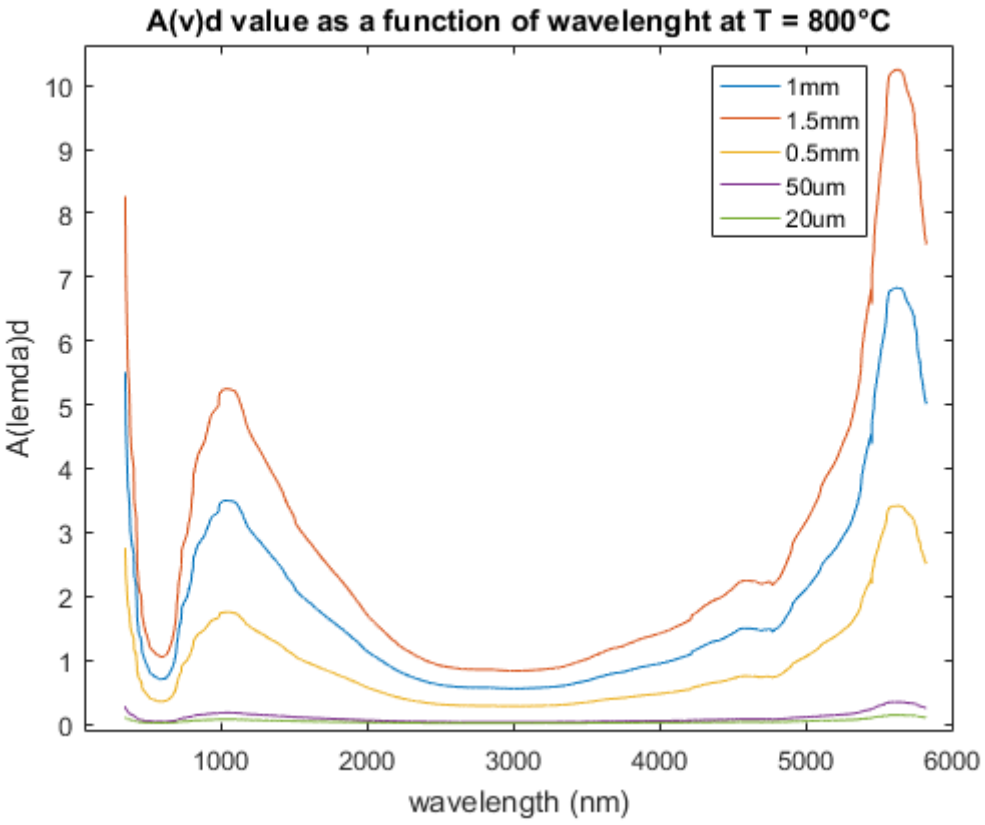

Figure E.4 Calculated absorption spectra for olivine at 800°C (averaged orientation) and various olivine sizes

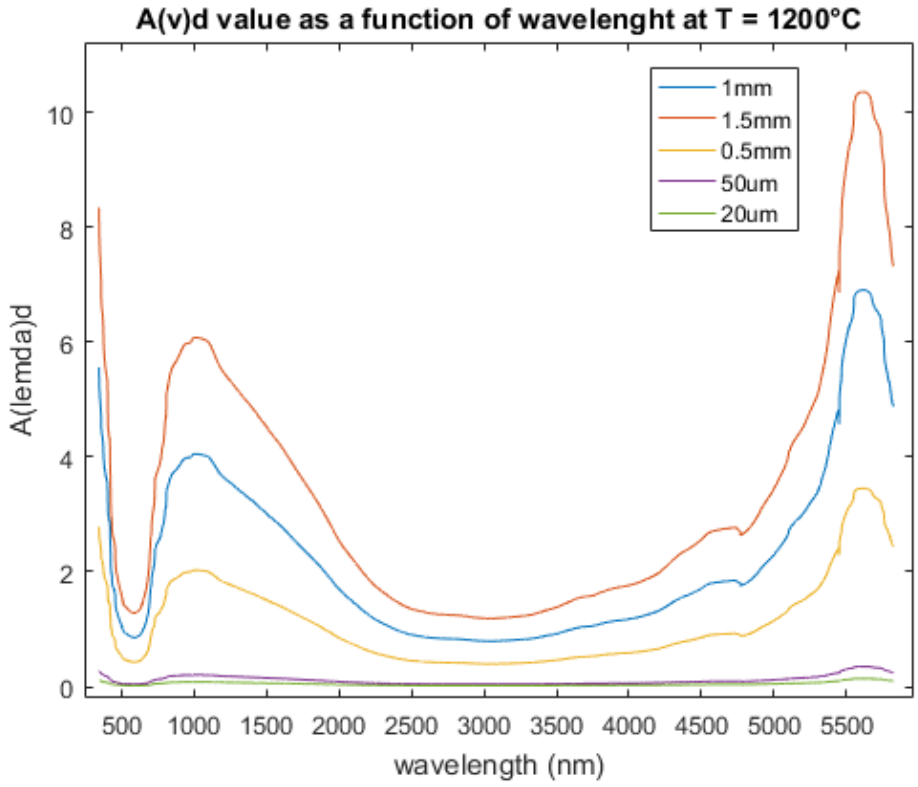

Figure E.5 Calculated absorption spectra for olivine at 1200°C (averaged orientation) and various olivine sizes

The series of figures presented above represent the *A(λ)*d* product in function of wavelength at three different temperatures and using different sample size. The thicker is the sample, the higher is the product and the optically thicker is the sample. Temperature also increases the value of absorption on whole wavelength range.

The effect of temperature on a given sample thickness is provided in the two following figures E.6 and E.7.

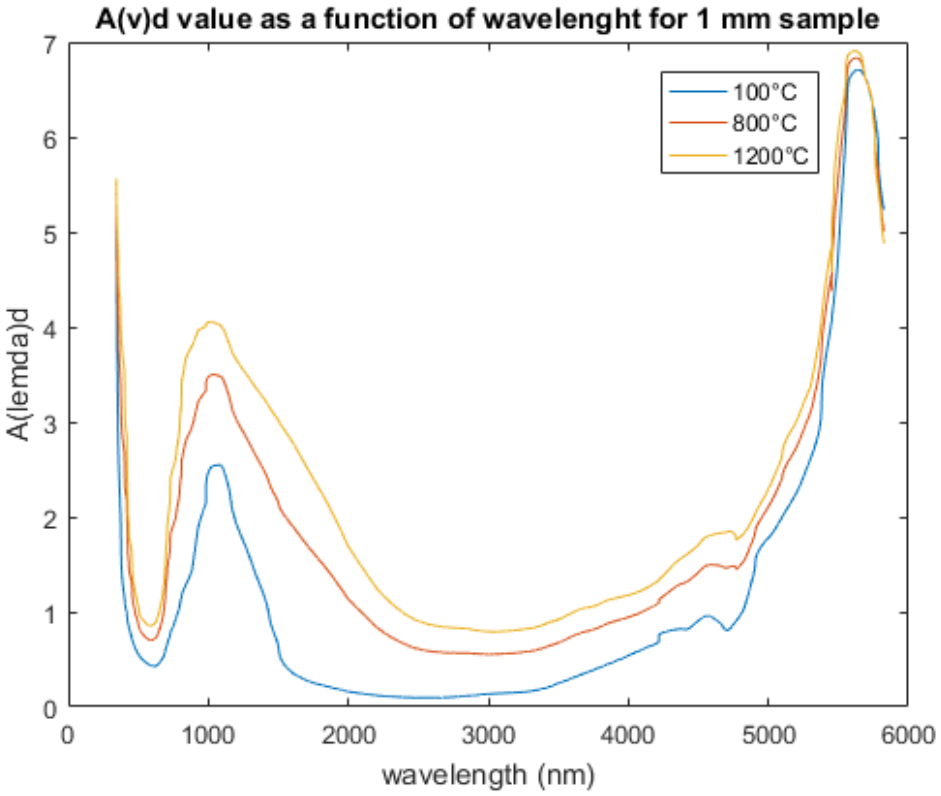

Figure E.6 Calculated absorption spectra for olivine of 1mm thickness (averaged orientation) and various temperatures

The figures presented above show that olivine is absorbing only on specific bands. In fact absorption is nearly null in visible (around 500 nm) and in IR regions (from 2000 nm to 4000 nm). This effect is even greater as temperature is low. In these zones, sample is always considered as optically thin. At the opposite, on bands around 300 nm, 1000 nm and above 4000 nm sample can be considered as thick for sample thickness in the order of 1 mm.

Silicate samples correspond then to the worst case, where they are optically thick at given wavelength and thin at some others. This state is the most difficult to describe in terms of heat transfers with combination of diffusive and direct radiative transfer. Direct radiative transfer is unwanted in experiments because photons heat the thermocouple without participation of the sample medium and so cannot account for thermal conductivity estimation.

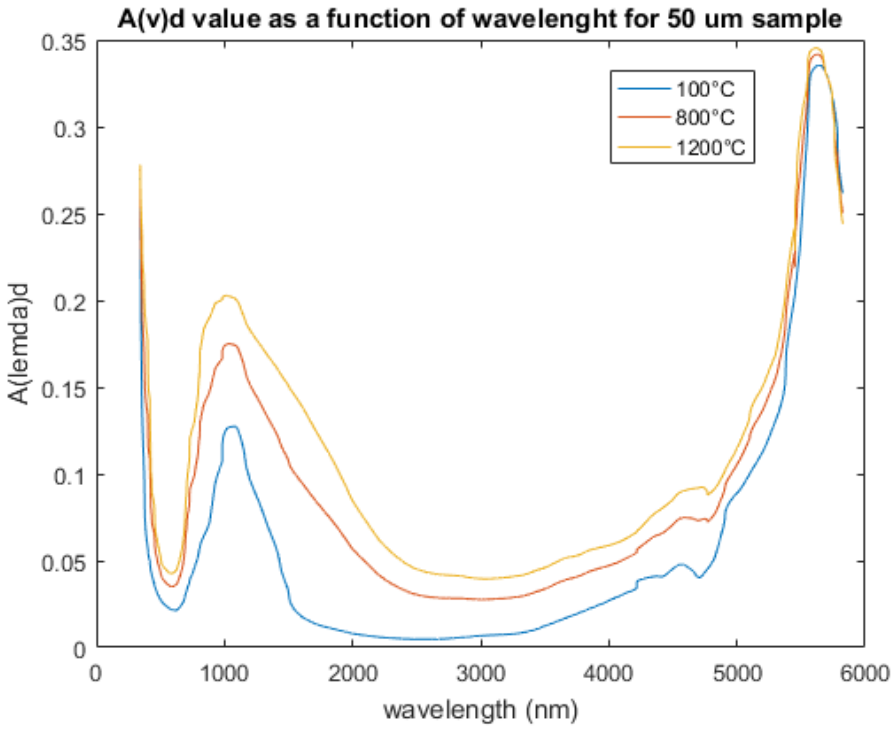

Figure E.7 Calculated absorption spectra for olivine of 50 microns thickness (averaged orientation) and various temperatures (1 grain)

To estimate if sample is thick or thin, the photon wavelength have to be taken in account in order to constrain experimental range of possible wavelengths. If we consider the main and additional furnaces the pulse heater of the assembly are blackbodies, their radiative emissions are governed by Planck's law of blackbodies radiations. The maximum radiation frequency at a given temperature is given by Wien's law. Wien's law expresses the maximum wavelength of photon emission in function of temperature:

$$\lambda_{max} = \frac{b}{T} = \frac{2.897E^{-3}}{T}$$

Values of photons wavelengths in the experimental range, from room temperature to values up to 1500 K, are covering an important part of the absorption spectrum. The maximum wavelengths are lying between 10600 nm at 273 K to 1950 nm at 1500 K.

Some key values are represented in the following figure E.9: *A*d* products for a 1mm sample at different temperatures. Values of the maximum wavelength of photon emission are represented for different temperatures. As suggested by Wien's the peak in wavelength is decreasing with the increasing temperature of the photon source. The value is for high temperature measurements (above 800K) in the middle of the transparent band.

Given the shape of blackbody radiations in function of wavelength (Fig. E.9) and relative extension of the emissions from each side of the frequency peak the samples can't be considered as optically thick even for 1.5 mm thickness. Samples must be considered as hybrid optically because of the position of the emission peak and their absorption spectra.

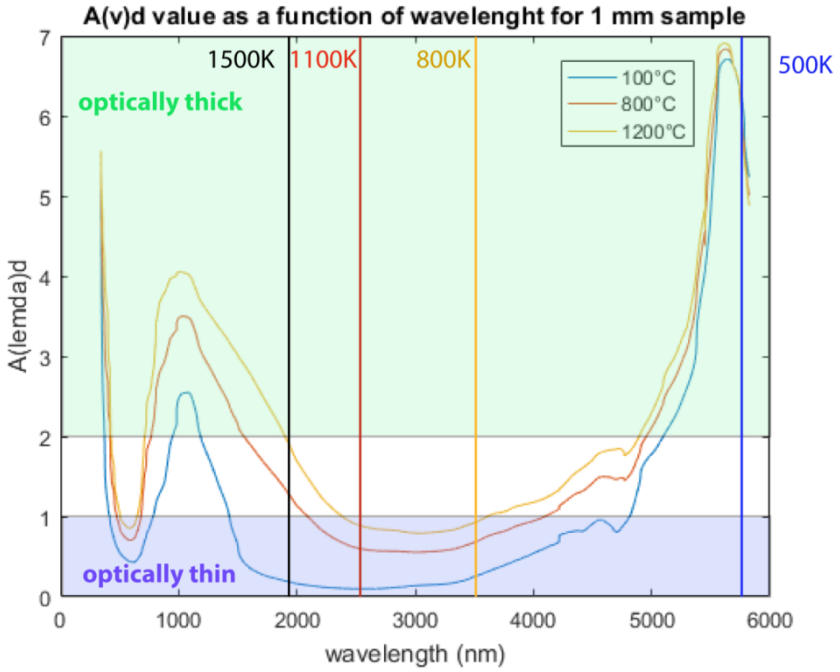

Figure E.8 Calculated absorption spectra for olivine of 1mm thickness (averaged orientation) and various temperatures, conditions of optical thickness are highlighted with the color domains, position of the wavelength for maximum intensity for photons calculated for blackbodies are given with vertical solid lines

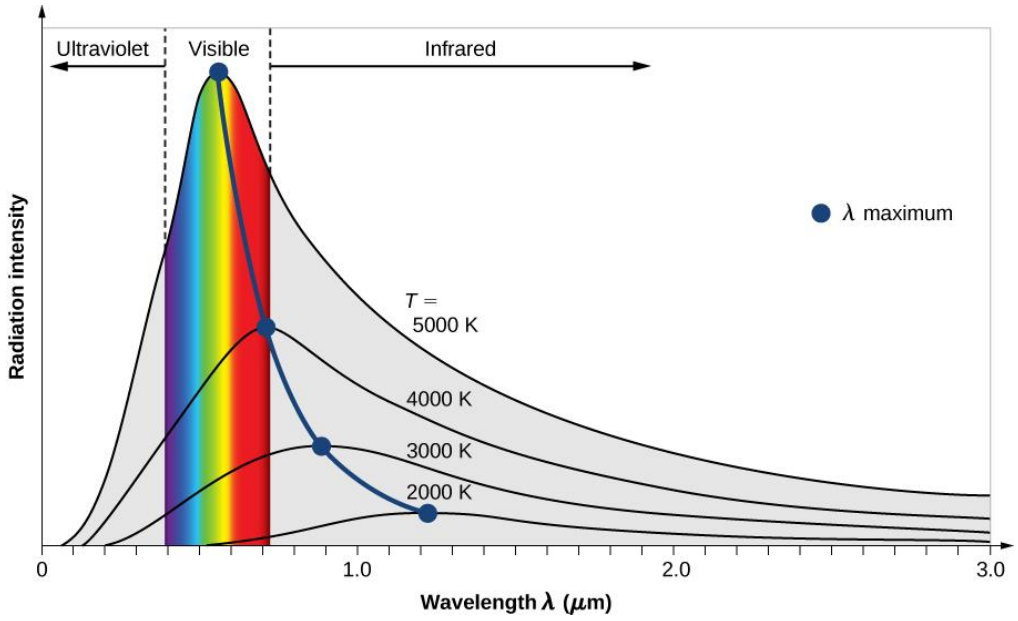

Figure E.9 Illustration of Wien's law with position of maximum wavelength with respect of temperature and emission spectrum shape

The remaining problem of the theory of optical thickness, brought by Hofmeister et al., is that value of *d* can be either grain size or whole sample size. In fact, grains boundaries should have a non-negligible effect on photon emission and reabsorption (even if tight variation of refractive index between two crystals would play a minor role). There is no reason to believe that important concentration of grain boundaries on photons path (and phonon during absorption to re-emission) would not play an important role and would increase optical thickness of the sample such as defects in crystals. The formula given by Hofmeister and Brandlund (2015) considers single crystals and approximate polycrystalline samples with the single crystal theory. In high pressure experiments, sample is in the order of 1mm for pulse heating and 2 mm thick by 4 mm long for Ansgtröm method in large assemblies. However, the grain size of our samples are often very small (appendix B), usually between 50 and 20 microns or less. Multi-anvil samples are composed of a succession of at least 20 to 50 grains and generally appear completely black/opaque to eye observation, at the opposite of single crystals that are transparent green even for thicknesses of few millimeters. This difference, in the visible spectrum (where absorption should be almost null), highlights that polycrystalline sample should be much thicker in optic term than single crystals (for a given sample thickness). This effect is not yet understood and not present in the equations but one should consider inserting both sample size and average grain size for absorption estimations.

To sum up, multi-anvil samples can either be considered as optical thin of thick (or both depending the sample nature, structure, chemical composition, thickness and the pressure and temperature conditions. Most of the polycrystalline samples used during our mantle anvil experiments such as Angström and pulse heating method are probably thick due to important absorption in the visible (black/dark color) and small grain size. For single crystals and small samples optically mixed of thin conditions must be carefully considered.